Influence of permafrost thaw on mineral organic carbon interactions

Arthur Monhonval

Thèse présentée en vue de l'obtention du grade de
Docteur en sciences agronomiques et ingénierie biologique

19th October 2022

EARTH AND LIFE INSTITUTE
UNIVERSITÉ CATHOLIQUE DE LOUVAIN

THESIS EXAMINING BOARD

President	Pr. Emmanuel Hanert (UCLouvain, Belgium)
Jury members	Pr. Reiner Giesler (Umeå University, Sweden) Pr. Frédéric Bouchard (USherbrooke, Canada) Dr. Jens Strauss (AWI Potsdam, Germany) Pr. Pierre Delmelle (UCLouvain, Belgium)
Supervisor	Pr. Sophie Opfergelt (UCLouvain, Belgium)

European Research Council

CREDITS

This Ph.D. thesis was funded by the European Union's Horizons 2020 research and innovation program (grant agreement NO. 714617, 2017-2022).

This work is part of the WeThaw (Weathering and Thawing permafrost) project at UCLouvain and results from collaboration with the Alfred Wegener Institute Helmholtz Center for Polar and Marine Research (Potsdam, Germany) and the Center for Ecosystem Society and Science at the Northern Arizona University (Flagstaff, USA).

Been spending most our lives livin’ in a tundra’s paradise,
Why spending most our lives livin’ in a tundra’s paradise.

Tell me why are we so blind to see
Minerals are key to help the IPCC.

~ Tundra Paradise ~

Gangsta team, Eight Mile Lake, August 2019

Acknowledgments

Une thèse est une aventure de vie qui se partage. Depuis 4 ans, je ne peux que remercier du plus profond de mon cœur chaque personne qui ont pu partager un bout de leur vie pour m'accompagner dans ce projet. Votre aide, vos connaissances ou encore votre soutien m'ont permis de vivre un extraordinaire projet de doctorat.

Mes remerciements vont tout d'abord à toi Sophie, qui a chapeauté cette thèse de main de maître. Le projet WeThaw obtenu pour 5 ans, tu m'embarques dans un mémoire et me permets de continuer l'aventure pour les 4 années suivantes avec la réalisation de cette thèse. Certains diront que c'était écrit d'avance. Aujourd'hui, je suis honoré de pouvoir dire que je l'ai écrite à tes côtés. Bien plus qu'une thèse, tu m'as permis de me révéler, de m'affirmer au fil dans années. Ce doctorat m'a apporté énormément de richesse, scientifiquement et humainement. J'ai apprécié ta bienveillance au quotidien, de l'aurore aux aurores, à défaut pour moi de ne l'être qu'un jour sur deux ; ta disponibilité, mais surtout ton aide plus que précieuse à chaque étape que constitue le parcours doctoral du combattant. Merci pour les missions de terrains, merci pour les missions de vulgarisations, merci tout simplement.

I would like to sincerely thank the members of the jury for their help and constructive suggestions during the revision process. Thank you to Pr. Reiner Giesler for your will to share and for all your help to switch from an Alaskan field campaign to an Abisko field campaign. Thank you to Pr. Frédéric Bouchard for your collaboration to this thesis and for your great inputs from the Artic Week back in 2019 until today. I thank Dr. Jens Strauss for all his incredible help and support along the thesis, from sharing samples to sharing knowledge and even your facilities in Potsdam. Thank you for your collaboration for the publication processes of the first chapters of this thesis. I would also like to thank Pr. Pierre Delmelle for all you have done for me, thank you for accepting being part of the support committee and to contribute to this thesis through your suggestions and your scientific rigor. I would also like to thank Pr. Emmanuel Hanert for having accepted to be president of this "énième" jury. All of you inspired me so much as a young scientist and made me wanted to give everything for these 4-years of research.

Thank you to the best lab of the world and of the universe. A family that adopts you no matter what. Merci au bubrow, Benoit, Aubry et FranFran, une team solide dans les bons et dans les très bons moments. De la hotte de l'enfer à

l’angoissomètre, il n’y a qu’un pas qu’on s’est toujours permis de franchir. Merci aux académiques Yannick, Pierre et Sophie. Grâce à vous, l’ambiance au sein de l’équipe a toujours été extraordinaire car chacun se soutient moralement et physiquement pour pouvoir donner le meilleur de soi-même. Merci à l’équipe WeThaw, Catherine, Babounette, Maxime T., Maëlle, merci pour ces moments de recherche et les autres moments, en Alaska, en Suède, en Arizona. Des souvenirs mémorables ! Je n’ai pas les mots pour décrire tout ce que vous m’avez apporté au fil des années. Merci à tous les chercheurs et toutes les chercheuses partis trop tôt de la famille SOLS (Mathilde, Charles, Yoli, Zimin, Carlos, Inga, Marlon, Michelle, Claira, Gaby, Fidèle) et merci à la nouvelle génération d’avoir apporté cette fraicheur et ce dynamisme qui l’accompagne (Noa, Bryan, Romain, Maxime D, Arnaud, Nathan, Sophie, Hugo, Clélia, Juliette). Vous êtes top, restez comme vous êtes.

Merci à l’ensemble des mémorants qui m’ont aidé tout au long de cette thèse. Un tout grand merci à Maxime (encore toi), Nathan (encore toi), Aurélien, Alexia, Justin, Elodie, Virginie pour votre bonne humeur et votre sourire au quotidien. Merci à Simon et à Eléonore pour votre aide sur le terrain et pour votre rire communicatif. Merci à l’ensemble de la plateforme MOCA : Anne, Claudine, Laurence, Elodie, Mathieu, Etienne, Karine, Hélène, merci pour le temps que vous passez pour chacun d’entre nous. Merci à la cellule technique, tout particulièrement à Sébastien, pour votre aide à la préparation du terrain, à la création du steel pipe, un matériel robuste qui n’a jamais failli. Merci à Françoise et Jasmine de nous avoir accueillis au laboratoire et aidés dans toutes les démarches parfois compliquées qui se dressent devant chaque doctorant.

Parce que l’aventure d’une vie se partage aussi en dehors du laboratoire, merci à toutes et tous, Kotéflammes, Kotécaps, Benoit, Zoui, Sebi, Marius, Pierre, les amis du GERU (je vous mets ici parce que vous n’êtes pas vraiment dans la recherche ☺), merci à ma belle-famille, Anne, Philou, Toinou, Charles et Chaewon de m’avoir accompagné dans ce parcours de vie. Merci aux amis du foot de m’avoir permis de continuer ma passion pendant ces longues années d’études en suivant un régime d’entrainements pour le moins particulier. Merci au groupe des Village People pour leur chanson YMCA sortie en 1978 sans qui la base de données des éléments minéraux dans le domaine de Yedoma serait orpheline d’un acronyme percutant. Et tous ceux que j’oublie merci pour tout.

Maman et Papa, je vous remercie de m'avoir élevé, éduqué, rendu curieux. Merci d'avoir séché mes larmes en première primaire, en première secondaire… avec le temps ça a été de mieux en mieux et l'université n'aura connu aucun chagrin. Merci pour votre amour et votre soutien à toute épreuve. Je suis fier d'avoir des parents comme vous. Merci à toute la famille, mes chères sœurs Sarah, Laure et Anna pour vos petits mots d'encouragements, merci à tous les beaux-frères d'avoir pu se libérer un mardi. Merci à Mila et Oscar d'essayer de relever notre monde. Merci à Mai et Leti, à Oscar, Jean-Paul et tous les autres, merci d'avoir demandé des nouvelles, d'avoir fait semblant de comprendre ce que je racontais, merci d'avoir essayé de lire les articles, d'être venus aux conférences de vulgarisations. Cela m'a toujours fait chaud au cœur.

Et enfin, merci à toi Loulou. Comme un docteur a toujours besoin d'une infirmière à ses côtés pour l'aider, je te dédie cette thèse. Merci de me rendre heureux, merci de toujours être présente pour moi. Merci de m'avoir poussé à écrire pendant ces jours de confinement. Avec toi, même l'enfermement devient un paradis sur Terre. Maintenant en route pour un nouveau chapitre de notre vie. Hâte de pouvoir profiter de la vie avec toi comme on a toujours eu l'habitude de le faire.

Merci et surtout, ne changez rien, restez comme vous êtes. Merci 100000 x !

Arthur

Author contributions

Journal articles as first author:

Monhonval, A., Mauclet, E., Pereira, B., Vandeuren, A., Strauss, J., Grosse, G., Schirrmeister, L., Fuchs, M., Kuhry, P., Opfergelt, S., 2021. Mineral Element Stocks in the Yedoma Domain: A Novel Method Applied to Ice-Rich Permafrost Regions. *Front. Earth Sci*. 9, 773. https://doi.org/10.3389/feart.2021.703304

Monhonval, A., Strauss, J., Mauclet, E., Hirst, C., Bemelmans, N., Grosse, G., Schirrmeister, L., Fuchs, M., Opfergelt, S., 2021. Iron Redistribution Upon Thermokarst Processes in the Yedoma Domain. *Front. Earth Sci*. 9, 629. https://doi.org/10.3389/feart.2021.703339

Monhonval, A., Strauss, J., Thomas, M., Hirst, C., Titeux, H., Louis, J., Gilliot, A., du Bois D'Aische, E., Pereira, B., Vandeuren, A., Grosse, G., Schirrmeister, L., Jongejans, L.L., Ulrich, M., Opfergelt, S., 2022. Thermokarst processes increase the supply of stabilizing surfaces and elements (Fe, Mn, Al, Ca) for mineral-organic carbon interactions. *Permafrost and Periglac Processes*, 1-18. https://doi.org/10.1002/ppp.2162

Monhonval, A., Mauclet, E., Hirst, C., Bemelmans, N., Eekman, E., Schuur., E.A.G., Opfergelt, S., 2022. Mineral organic carbon interactions in dry versus wet tundra soils, *Geoderma* (submitted).

Monhonval, A., Hirst, C., Strauss, J., Schuur., E.A.G., Opfergelt, S., 2022. Strontium isotopes trace the dissolution and precipitation of mineral organic carbon interactions in thawing permafrost, *Geoderma* (submitted).

The first two papers are part of a special collection "*Yedoma Permafrost Landscapes as Past Archives, Present and Future Change Areas*" and available as an e-book.

Journal articles as co-author:

Hirst, C., Mauclet, E., **Monhonval, A.**, Tihon, E., Ledman, J., Schuur, E. A. G., & Opfergelt, S. (2022). Seasonal changes in hydrology and permafrost degradation control mineral element-bound DOC transport from permafrost soils to streams. *Global Biogeochemical Cycles*, 36, e2021GB007105. https://doi.org/10.1029/2021GB007105.

Mauclet, E., Agnan, Y., Hirst, C., **Monhonval, A.**, Pereira, B., Vandeuren, A., Villani, M., Ledman, J., Taylor, M., Jasinski, B. L., Schuur, E. A. G., and Opfergelt, S., 2022. Changing sub-Arctic tundra vegetation upon permafrost degradation: impact on foliar mineral element cycling, *Biogeosciences*, 19, 2333–2351. https://doi.org/10.5194/bg-19-2333-2022.

Shmelev, D., Cherbunina, M., Rogov, V., Opfergelt, S., **Monhonval, A.,** and Strauss, J., 2021. Reconstructing Permafrost Sedimentological Characteristics and Post-depositional Processes of the Yedoma Stratotype Duvanny Yar, Siberia. *Front. Earth Sci.* 9:727315. https://doi.org/10.3389/feart.2021.727315.

Online dataset repository:

Monhonval, A., Opfergelt, S., Mauclet, E., Pereira, B., Vandeuren, A., Grosse, G., Schirrmeister, L., Fuchs, M., Kuhry, P., Strauss, J., 2020. Yedoma domain Mineral Concentrations Assessment (YMCA). https://doi.org/10.1594/PANGAEA.922724.

Mauclet, E., Villani, M., **Monhonval, A.,** Hirst, C., Schuur, E. A. G., Opfergelt, S., 2022, "Characterization of permafrost soil exchange properties and quantification of stocks in soil exchangeable base cations", https://doi.org/10.14428/DVN/FQVMEP, Open Data @ UCLouvain, V1, UNF:6:akHDgX5sDk1HJ0WybUVggA== [fileUNF].

Opfergelt, S., C. Hirst, E.A. Schuur, E. Mauclet, **A. Monhonval**, J. Ledman, and Bonanza Creek LTER. 2021. Eight Mile Lake Research Watershed, Thaw Gradient: Geochemical data from perched waters collected from boreholes on Gradient site during August-September 2019 ver 2. Environmental Data Initiative. ttps://doi.org/10.6073/pasta/826550e1b769269eafe11db438a79bde (Accessed 2022-07-11).

Opfergelt, S., C. Hirst, E.A. Schuur, E. Mauclet, **A. Monhonval**, J. Ledman, and Bonanza Creek LTER. 2021. Eight Mile Lake Research Watershed, Thaw Gradient: Geochemical data collected daily in Panguingue Creek during spring thaw and summer rain events, 2018-2019 ver 2. Environmental Data Initiative. https://doi.org/10.6073/pasta/e5759a95d453f28cc1b35e5ccef78f78 (Accessed 2022-07-11).

Opfergelt, S., C. Hirst, E.A. Schuur, E. Mauclet, **A. Monhonval**, J. Ledman, and Bonanza Creek LTER. 2021. Eight Mile Lake Research Watershed, Thaw Gradient: Geochemistry of soil pore waters sampled in May 2018 (0 - 20 cm depth) and August 2019 (0-120 cm depth) at Gradient site, 2018-2019 ver 2. Environmental Data Initiative. (Accessed 2022-07-11). https://doi.org/10.6073/pasta/f3b2f5aa791f8df5f7bae640f079296b

Mauclet, E., S. Opfergelt, Y. Agnan, C. Hirst**, A. Monhonval**, J. Ledman, M. Taylor, E. Schuur, and Bonanza Creek LTER. 2021. Eight Mile Lake Research Watershed, Thaw Gradient: Foliar mineral element concentrations, stocks and annual litterfall fluxes estimated for July 2017 ver 3. Environmental Data Initiative. (Accessed 2022-07-11). https://doi.org/10.6073/pasta/7fad9398ec3a596b8efc092fc8fbf55d

Mauclet, E., S. Opfergelt, Y. Agnan, C. Hirst, **A. Monhonval**, J. Ledman, M. Taylor, E. Schuur, and Bonanza Creek LTER. 2021. Carbon in Permafrost Experimental Heating Research (CIPEHR) project: Foliar mineral element concentrations, stocks, and annual litterfall fluxes in July 2009 and 2017 ver 3. Environmental Data Initiative. (Accessed 2022-07-11). https://doi.org/10.6073/pasta/597c40c5d699eec918da3e9c2eaa7bea

Active conference contributions:

Monhonval, A., Opfergelt, S., Mauclet, E., Hirst, C., Strauss, J., Grosse, G., Schirrmeister, L., Kuhry, P., Influence of Holocene thermokarst activities on mineral element content in Yedoma deposits, 2019. Presentation and poster at the Arctic week conference (Paris, France) on the 9/12/2019.

Monhonval, A., Strauss, J., Mauclet, E., Hirst, C., Pereira, B., Vandeuren, A., Bemelmans, N., Grosse, G., Schirrmeister, L., Fuchs, M., Opfergelt, S., 2020. Iron Dynamics during Thermokarst Processes in the Yedoma Domain and Implications for Interactions between Iron and Organic Carbon. E-poster

presentation at the AGU Fall meeting 2020 on the 6/12/2020 (online conference).

Monhonval, A., Mauclet, E., Hirst, C., Pereira, B., Vandeuren, A., Bemelmans, N., Opfergelt, S., 2021. Iron dynamics upon thermokarst formation in the Yedoma domain. Oral presentation at the ELI-Day seminar on the 27/05/2021 (UCLouvain, Belgium).

Outreach:

Monhonval, A., 2021, Geological archives in the Arctic. In: Open Access Government, Vol. 80, no.1, p. 454-455.

Monhonval, A., Villani, M., Thomas, M., Opfergelt, S., Arctique : quand le sol dégèle sous nos pieds, conférence au Printemps des Sciences organisée par l'UCLouvain, 21 mars 2022.

Table of content

Part I
General overview

1. INTRODUCTION

Climate change is a threat to the global permafrost regions. The increase in anthropogenic emissions of greenhouse gases such as carbon dioxide and methane have triggered a global warming, which represents the biggest challenge of our generation. In Arctic regions, the warming of air temperature is particularly marked resulting in the thawing of permafrost. Permafrost contains significant amount of ice and partially decomposed organic matter highly vulnerable to thaw and likely to be decomposed as greenhouse gases. The rise in ground temperature promotes the degradation of organic carbon in unfrozen and previously frozen portion of the soil. The decomposition of organic carbon by microorganisms releases additional carbon dioxide and methane which amplifies the amounts of greenhouse gases emitted. Permafrost contains twice the amount of carbon currently stored in the atmosphere and the release of even a small portion of this carbon reservoir will add to the remaining carbon budget target to stay within the 2°C Paris agreement threshold. While the quantification of the carbon reservoir in permafrost is well constrained, how much and how fast this organic carbon pool will be released as greenhouse gases remains uncertain.

Mineral surfaces and cations can stabilize organic carbon in soils and sediments and mitigate its degradation as greenhouse gases. We argue that mineral organic carbon interactions in permafrost influence the portion of mineral-protected organic carbon, less likely to be mineralized as greenhouse gases. Therefore mineral organic carbon interactions in permafrost could protect and preserve organic carbon from microbial degradation upon thawing permafrost. Yet, the interactions between minerals and organic carbon in permafrost and the consequences of changing soil conditions upon thawing are still poorly understood. This Ph.D. thesis tackles the influence of permafrost thaw on mineral organic carbon interactions and investigates how changing soil conditions may promote or mitigate organic carbon stabilization mechanisms.

Mineral organic carbon interactions are not irreversible and are sensitive to changing physico-chemical conditions such as water saturation (redox) or soil acidity (pH). Permafrost thaw can be gradual or abrupt. Gradual thaw is characterized by the deepening of the top layer that thaws each summer and may release organic carbon and minerals previously locked in permafrost. Abrupt thaw, which takes place in ice-rich permafrost regions, is characterized

by the formation of lakes resulting from subsidence subsequent to ice volume loss and which may drain with time. Both thawing processes lead to changes in soil physico-chemical conditions that likely influence the type and abundance of mineral organic carbon interactions and drive organic carbon stabilization in soils or sediment. Until recently, permafrost greenhouse gas release was omitted from the Earth system models used to predict climate change trajectories and inform international climate targets. New Earth system models are beginning to integrate permafrost carbon feedbacks, but estimates remain preliminary and lack a number of important processes such as organic carbon decomposition rates and stability of protection mechanisms. This study aims to better constrain organic carbon stabilization mechanisms in permafrost soils and contributes to fill the knowledge gap related to the evolution of organic carbon accessibility for microorganisms and carbon emissions upon permafrost thaw. To reach this goal, this study investigates mineral organic carbon interactions involving Fe, Mn, Al and Ca metals under changing soil conditions following gradual and abrupt permafrost thaw across multiple permafrost regions.

2. LITERATURE REVIEW

2.1 Permafrost definition

Permafrost is defined as "ground (soil or rock and included ice and organic material) that remains at or below 0°C for at least two consecutive years" (van Everdingen, 1998). Given this definition, permafrost should not be regarded as permanent, because natural or man-induced changes in the climate or terrain may cause the temperature of the ground to rise above 0°C. Permafrost is a major feature of the cryosphere. Cryosphere is a term that collectively describes the portions of the Earth's surface where water exists in solid form (ice). Therefore, permafrost do not include sea ice, lake ice, river ice, snow cover, ice caps and ice sheets (Jones et al., 2009).

The surface layer of the soil that thaws each year is not comprised in the permafrost definition. That top surface layer, that thaws seasonally (i.e. in summer) to a depth of 10 cm to more than 2 meters and refreezes each winter is referred as the active layer (Schuur et al., 2008). Active layer thickness is controlled by regional climate but also by local factors (i.e., topography, hydrology, vegetation, snow cover, and subsurface material properties). The active layer is found close to the surface above the permafrost and is thawing deeper and deeper with current climate warming in the Arctic (Åkerman and Johansson, 2008; Luo et al., 2016). The active layer is important since it influences rooting depth, hydrological processes, and quantity of soil organic matter and minerals exposed to above-freezing seasonal temperature (Schuur et al., 2008). The boundary that marks the transition between frozen (i.e. permafrost) and unfrozen (i.e., active layer) soil layer is called the permafrost table (French, 2007).

Much of the permafrost that can be found today actually formed during past ice ages when conditions were much colder. Maximum permafrost extent during the Last Glacial Maximum (LGM; 27 and 15 thousand years before present (ka BP); Schirrmeister et al., 2008; French and Millar, 2014) was about 35 millions km^2, or about 52% larger than today (Lindgren et al., 2016). Today, the permafrost region covers approximately 23 million km^2 or ~24% of terrestrial area in the Northern Hemisphere (Brown et al., 1998; Zhang et al., 1999; Obu et al., 2019) (Figure 2.1). In the Northern Hemisphere, 50% of the permafrost region is located in Russian territories, while the North

American continent (Canada and Alaska) holds further 30% of its extent (French, 2007). The Qinghai-Tibet Plateau is the largest low-latitude and high altitude permafrost region on Earth where permafrost occupies approximately 8% of the global permafrost area (Jin et al., 2007). In mountain regions, the occurrence of permafrost is strongly controlled by the elevation, slope gradient, aspect, vegetation and snow cover. Closer from Europe, permafrost can also be found at high latitude in Scandinavian countries and at high altitude in the Alps. In addition, permafrost is also present in vast areas of the continental shelves of the Arctic Ocean and referred as submarine permafrost (Rekant et al., 2015; Angelopoulos et al., 2020). This submarine permafrost was formed during the late Pleistocene period, when ocean levels were about 120 m lower than today's level and slowly immerged with rising sea level during the Holocene (starting about 11 ka BP). In the Southern Hemisphere, permafrost occurs in mountains, in sub-Antarctic islands and in the Antarctic continent (Bockheim, 1995).

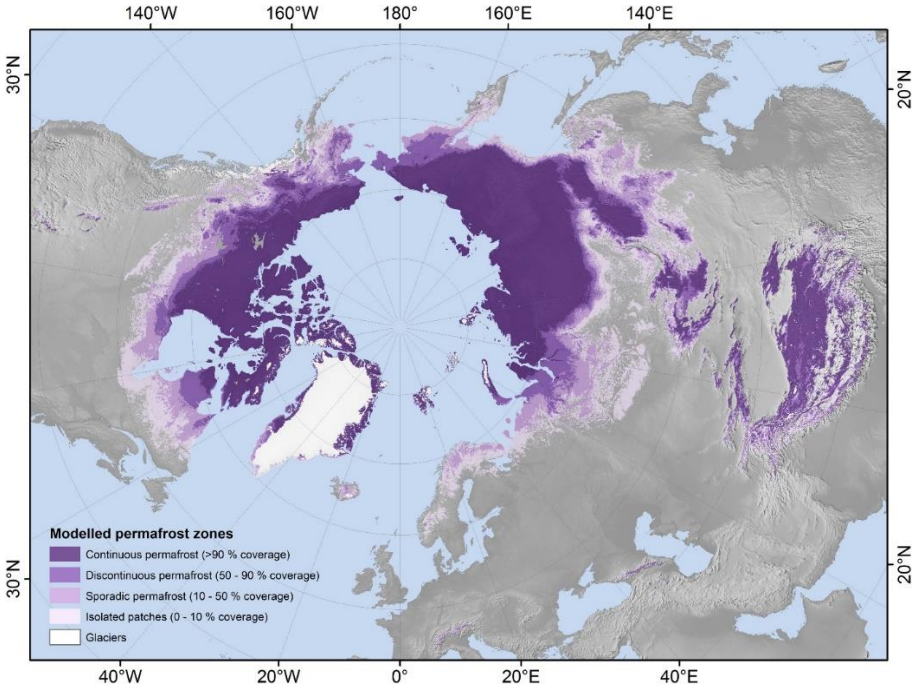

Figure 2.1: Permafrost zonation based on classified modelled permafrost probabilities which correspond with the fraction of each 1 km² pixel underlain by permafrost (Obu et al., 2019).

Topographic features (relief and aspect), snow cover, vegetation, moisture content and subsurface material influence permafrost conditions. The intensity

and extent of permafrost in the Northern Hemisphere is commonly divided in four broad zones: continuous, discontinuous, sporadic and isolated (Figure 2.1). These zones are defined based on the coverage of permafrost found in these areas: continuous (90%-100%), discontinuous (50%-90%), sporadic (10%-50%) and isolated permafrost (<10%). Continuous permafrost occupies the coldest climate zones (high latitude or high altitude) where climate conditions are favorable for active formation of frozen ground. In colder areas, permafrost is massive and active layer thickness is generally shallow. In zones of sporadic or isolated permafrost, the active layers can be several meters thick and taliks (i.e., unfrozen ground occurring in a permafrost area due to a local anomaly in thermal, hydrological conditions) are widespread (O'Neill et al., 2020). The thickness of the permafrost can range from a few tens of meter in boreal regions to hundreds of meters in the High Arctic (even as much as 1,400 m; Jones et al., 2009). Typically, permafrost thickness ranges between 350 m and 650 m in the continuous zone while it ranges from less than 1 m to 50 m in the discontinuous zone (Yershov, 2004). The heat from the interior of Earth counteracts the growth of permafrost and limits the depth it attains. Geothermal variations, ground material with higher thermal conductivity, and long-term atmospheric cool temperatures are responsible for the variable permafrost depths across permafrost regions (Rowley et al., 2015).

2.2 Permafrost formation

2.2.1 Syngenetic and epigenetic permafrost

During the late Pleistocene, up to ~50% of the land area of the Northern Hemisphere was covered by permafrost (French, 2007). Permafrost forms in materials (i.e., soil, rock, organic matter) i) through the lowering of the permafrost base in previously deposited sediment or other earth material (epigenetic permafrost formation) or ii) through the rise of the permafrost table at the time of deposition of additional sediment or other earth material on the ground surface (syngenetic permafrost formation; French, 2007). Ice-rich permafrost deposits (i.e., with 50-90% volume of ice) were typically formed by syngenetic permafrost formation.

2.2.2 Ice-rich permafrost deposits - Yedoma deposits

During the late Pleistocene until the LGM period, continuous accumulation of ice-rich permafrost deposits were promoted by very cold and dry climate conditions (Schirrmeister et al., 2008). These ice-rich permafrost deposits (in the following referred as Yedoma deposits) developed over the past 50 ka BP or more and cover vast areas of Siberia and Alaska (remnant of Beringia[1]) that remained unglaciated during the Pleistocene (Romanovskii, 1993; Schirrmeister et al., 2002a; Zimov, 2006). Extreme continental climate conditions were connected to the presence of a largely exposed continental shelf, a likely perennially Arctic sea-ice cover and the existence of large ice sheets to the west (Eurasian ice sheet) and to the east (Laurentide and Cordilleran ice sheets). Most recent estimates indicate that the Yedoma domain (i.e., ice-rich permafrost region) covers 2,587,000 km^2 with areas of Yedoma deposits of 480,000 km^2 (Strauss et al., 2021b).

Yedoma deposits were at first characterized as homogeneous silty fine, ice- and organic-rich sediments with primary or secondary aeolian processes being the main transport driver during the time of Yedoma aggradation. Hence often described as loess or loess-related deposits (Pewe and Journaux, 1983; Tomirdiaro and Chernen'kiy, 1987; Murton et al., 2015). It is now considered that the aggradation of Yedoma deposits is not the result of a single process of aeolian deposition but rather the result of a polygenetic origin with probable seasonally differentiated deposition mechanisms controlled by local environmental conditions, including local fluvial, colluvial and alluvial sediments (Schirrmeister et al., 2013, 2020). Yedoma deposits in Alaska and Siberia are dominated by silt-sized particles, abundant organic matter, ice-rich syngenetic permafrost and ice-wedges and may reach up to 40 m in thickness (Figure 2.2). These grayish deposits when wet are commonly nearly black in color from the abundant organic matter. Yet the most distinctive property is the pungent odor they give off from the incompletely decomposed organic matter that is exposed as they thaw (Schirrmeister et al., 2013).

[1] Beringia is a terrestrial bridge that extended between the Lena Delta in Siberia to the Mackenzie river in Canada at lower sea level during Pleistocene. Beringia is now divided by the Bering Strait.

Figure 2.2: Ice-rich permafrost (Yedoma) bluff of 30 meters found in Itkillik, northern Alaska. Silty deposits regularly separated by vertical ice-wedges are visible (photographer: J. Strauss).

2.2.3 Yedoma deposit characteristics and thawing features

Ice-rich permafrost areas from the Yedoma domain are characterized with typical features including, polygonal permafrost soils, ice-wedges, thermokarst lakes and drained thermokarst lake basins (also called Alas; Sect. 2.5.3). Under dry and cold conditions, frost cracks often appear on the soil surface. Rain or snowmelt water can fill the cracks and expand with freezing. Water is increasing its volume by 9% when changing from liquid to solid state. With multiple freezing and thawing, the frost cracks open wider and wider with ice expanding volume. Ice-wedges can end up to be several meters wide and tens of meters high (Schirrmeister et al., 2013). The presence of these ice-wedges creates the typical polygonal soils in high northern latitudes (Figure 2.3). The main feature that distinguishes permafrost from unfrozen ground is the presence of ground ice. The absolute ground ice content in permafrost can vary from a tenth of percent up to 90% or more of the total volume. Ice-rich permafrost deposits typically display between 50-90% ice volume which means there is an excess ice compare to the maximum retention of water within sediments porosity.

Figure 2.3: Helicopter view of the polygonal permafrost soils from Buor Khaya Peninsula, Siberia, Russia (photographer: P. Overduin). The typical polygonal form reveals the presence of underlying ice-wedges. These polygonal shapes can be several meters wide (the arrow on the picture shows a 30 meters wide polygon).

Upon thawing, ice-wedges melt and ice-rich permafrost collapse due to the volume loss caused by the void created upon ice melting and water leaching. In Yedoma deposits, thawing often lead to dramatic collapsing features. The most known include thermokarst lakes, Alas (i.e., drained thermokarst lake basin) or coastal erosion. After the LGM, permafrost started to thaw rapidly[2] and by the time of the Holocene Optimum (9-5 ka BP; warmer interglacial period), permafrost had completely disappeared from most of Europe, and the continental United States, and from significant portion of western Siberia (Yershov, 2004). During this time, the zonal distribution of permafrost was relatively stable in north-central Siberia, northeastern Siberia, and the Russian far East, although rapid development of thermokarst lakes caused increase permafrost thaw (Shur et al., 2012). Nowadays, climate warming triggers ongoing thawing of ice-rich deposits with new thermokarst lake formation that may drain/evaporate or not with time (Figure 2.4).

[2] During the Holocene period, the climate warmed at a rate of 0.05°C per century (~5°C in thousands of years), a hundred times slower than actual global warming. The main drivers of Holocene warming were the modulation of the orbital parameters, change in solar irradiance or volcanic activity (Borzenkova et al., 2015).

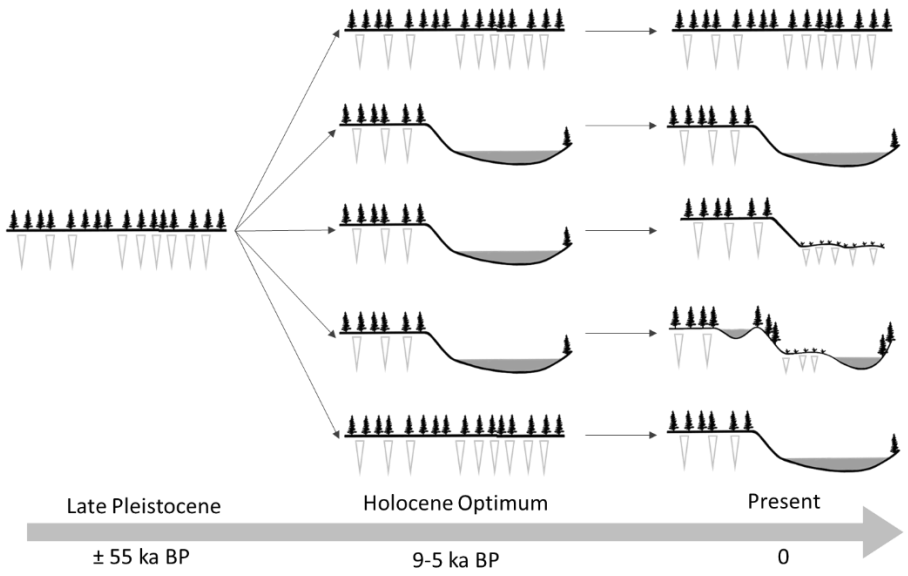

Figure 2.4: Different scenarios related to ice-rich permafrost (i.e., Yedoma) deposits thawing. Yedoma deposits formed during the late Pleistocene about 55 thousands years before present (ka BP). During the Holocene Optimum (9-5 ka BP) until now, these Yedoma deposits can follow multiple trajectories. Some colder areas never thawed until present but other areas have already thawed during the Holocene Optimum or more recently, creating thermokarst lakes that may have drained/evaporated or not with time. Others scenarios, not represented here, such as multiple thermokarst lake cycles are also possible.

2.2.4 Geological archives

Similarly to ice cores from Greenland and Antarctica used to learn about our past climates, deposits from ice-rich permafrost regions are a relic of the late Pleistocene and Holocene climate, fauna and flora, preserved in their frozen deposits (e.g., Schirrmeister et al., 2002, 2013; Murton et al., 2015; Porter and Opel, 2020). These deposits are important paleoclimate and paleoenvironmental records that allows the scientific community to trace ancient climate, life or processes: ice-rich permafrost acts as geological archives of past time. Paleoenvironmental archives, as the one found in Yedoma deposits or Alas deposits, offer an interesting source of data on past climate and environmental changes. Alas deposits are witnesses which experienced the consequences following the warmer Holocene period and may be especially relevant to investigate for anticipating the consequences of

a future warmer Arctic on permafrost soils (Miller et al., 2013; Porter et al., 2019).

2.3 Development of the permafrost carbon pool

2.3.1 Organic carbon accumulation in permafrost deposits

Total soil organic carbon (OC) in the northern circumpolar permafrost region is estimated to be 1,440-1,600 PgC (Pg is equivalent to Gt or billion tons), stored in surface and deeper (more than 3 meters deep) soil layers (Hugelius et al., 2014; Strauss et al., 2017; Canadell et al., 2021). This permafrost OC pool is large compared to all other Earth's biomes carbon pool estimated to contain 2,050 to 2,800 Pg soil OC in the top 3 m of soil, excluding the Arctic and Boreal regions (Schuur et al., 2015; Jackson et al., 2017). More surprisingly, permafrost OC is concentrated in only 15% of the world's soil area (Schuur et al., 2015). The very high OC storage from permafrost region is due to (i) the substantial carbon stored at depth in permafrost (> 1 meter deep) which is below the traditional zone accounted for soil carbon pool and (ii) the increased peat accumulation under cold climates.

The OC accumulation in permafrost soil is related to the lack of organic matter decomposition under cold climate and to the persistent frozen state offering protection to organic matter (French, 2007). This permafrost carbon comprises the remnant of plant and animals accumulated in perennially frozen soil or sediments over thousands of years. The development of soil C pool and its accumulation in northern regions occurs through the action of several processes specific to permafrost environments (syngenetic or epigenetic freezing of organic matter, peat formation and cryoturbation). More specifically, the syngenetic or epigenetic permafrost formation locks up undecomposed or partially decomposed organic material in frozen deposits. The cold climate associated to poorly drained areas due to the impermeable permafrost table both enhance peat formation. Finally, cryoturbation results in the storage of soil OC in deeper soil layers (Schuur et al., 2008). Cryoturbation can redistribute OC away from the surface to greater depth in the soil profile (Michaelson et al., 1996; Bockheim, 2007). Cryoturbation refers collectively to all soil movements due to frost action (Washburn, 1980).

2.3.2 Permafrost organic carbon stock inventory

The northern permafrost zone carbon inventory reports the surface carbon pool (0-3 m) to be 1,035 ± 150 Pg carbon (mean ± 95% confidence interval; Hugelius et al., 2013, 2014; Figure 2.5). At first, it was expected that because OC originates from plant photosynthesis and growth, there is typically higher OC density in near-surface permafrost (upper 3 m). However, carbon inventory in deep sediments (exceeding 3 m) from the ice-rich permafrost region is much larger than previously recognized and is estimated to be between 327-466 PgC (Strauss et al., 2013; Anthony et al., 2014; Fritz et al., 2015). A remaining 41-151 PgC is estimated for deep alluvial sediments accumulation below 3 m in the river deltas of major Arctic rivers (Strauss et al., 2017). In addition to this relatively well-constrained soil OC pool, there could be an additional deep permafrost pool of 350-465 PgC. This additional pool would add to the already included deep carbon pool from the Yedoma domain (Strauss et al., 2017) and estimated using an interval depth of 3-10 m and carbon content of 11-14 kg C m^{-3} (Schuur et al., 2015). In the Southern Hemisphere, the carbon content in permafrost regions is low and represents a negligible reservoir regarding the global C cycle (Bockheim, 1995). As a comparison, the carbon stock within the atmosphere or the global fossil fuels reserves are 870 and 1,106 PgC, respectively (Strauss et al., 2017; Canadell et al., 2021). Therefore, the northern permafrost region (1,460 – 1,600 PgC) stores about twice more carbon than what is currently stored in the atmosphere (Figure 2.5). Note that most recent estimates indicate that atmospheric CO_2 growth was 5.1 ± 0.02 PgC per year during the decade 2011-2020 (Friedlingstein et al., 2022), meaning that previous estimates of 829 PgC stock in the atmosphere (in 2011; Ciais et al., 2014) are now reviewed to reach 870 ± 5 PgC (Canadell et al., 2021).

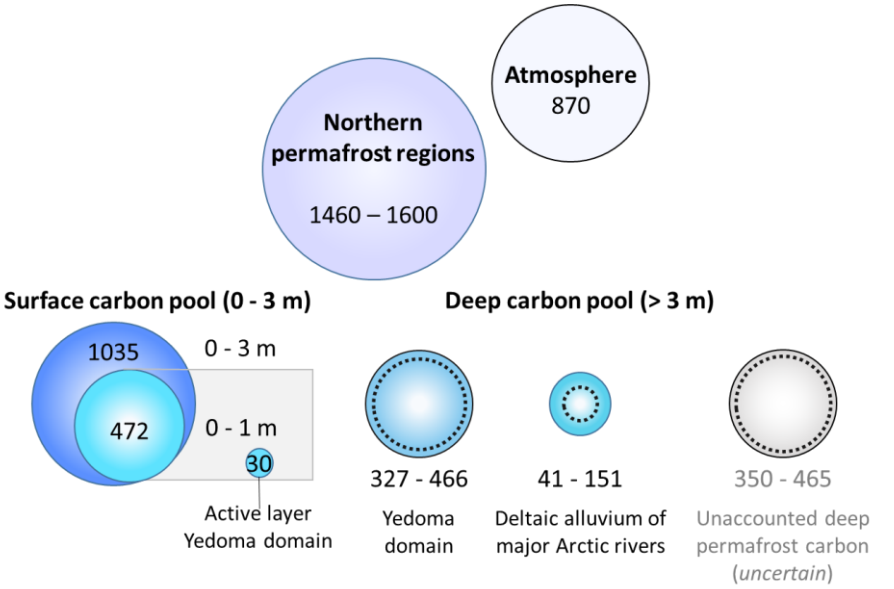

Figure 2.5: Carbon stock (in Gt or Pg carbon) of the northern permafrost region (1,460 – 1,600 PgC) across surface soils and deeper deposits compared to the carbon stock in the atmosphere (Canadell et al., 2021). Surface pool includes the stocks within 0-1 m and 0-3 m deep (Hugelius et al., 2014). The deep carbon pool, exceeding 3 m, combines the stock within the Yedoma domain (as defined by Strauss et al. (2013)) and deltaic alluvium of major Arctic rivers based on Hugelius et al. (2014) and reviewed by Strauss et al. (2017) to account for active layer. The unaccounted deep permafrost carbon is uncertain and estimated based on carbon content of 11-14 kg C m^{-3} for a 3-10 m depth interval (Schuur et al., 2015). The scheme is adapted and updated from Strauss et al. (2017).

2.4 Global and Arctic climate warming

The climate response to man-caused (anthropogenic) greenhouse gas emissions is strongly influenced by internal Earth system feedbacks (Schneider von Deimling et al., 2012). With polar amplification, the high latitude regions temperature have risen 0.6°C per decade over the last 30 years, more than twice as fast as the global average (Winton, 2006; Schuur et al., 2015). The Arctic has warmed nearly four times faster than the globe since 1979 (Rantanen et al., 2022). The ice albedo feedbacks associated with variations in snow and sea ice coverage are key factors in positive feedback mechanisms which amplify climate change at northern latitudes (e.g., Manabe and Stouffer (1980)).

The climate warming in northern regions is causing perennially frozen ground to thaw, exposing substantial quantities of poorly decomposed OC to microbial degradation in soils. As the climate warms, the carbon balance of Arctic ecosystems is regulated in two opposing ways: i) plants will grow faster and act as a carbon sink by taking carbon out of the atmosphere and ii) thawing permafrost will lead to decomposition and loss of soil carbon making it a carbon source. The prevalent mechanism will balance the Arctic ecosystem to be a carbon sink or a carbon source (Koven et al., 2015). It is now recognized that permafrost thaw is leading the system to be a carbon source (Canadell et al., 2021).

2.4.1 Permafrost carbon feedback and Earth System models

The permafrost carbon feedback and its importance for the future climate is rather unconstrained. While the OC stock in permafrost is relatively well quantified and now included in recent IPCC report (IPCC, 2021), many uncertainties still remain. The overall availability and quality of the carbon stored in frozen soils, permafrost thawing rates, organic matter decomposition rates and, more importantly, the relative proportion of aerobic decomposition (resulting in CO_2 emissions) versus anaerobic decomposition (resulting in both CO_2 and CH_4 emissions) are still poorly constrained. Because of these reasons, the carbon feedback from high latitudes is only recently included in Earth System models. Estimates of future C emissions from permafrost thaw are based on simulated volume of OC exposed upon gradual deepening of the active layer during the growing season (Dobricic and Pozzoli, 2019). However, the permafrost scientific community warns that these estimates are highly underestimated and that additional processes or C pools should be taken into account (Opfergelt, 2020). Briefly, these processes or C pools include: i) the winter season that is a significant source of C emissions and may offset the growing season carbon uptake (Natali et al., 2019); ii) soil OC loss by lateral export with greenhouse gas emissions that may occur along waterborne pathways (Vonk et al., 2019) that is likely to be amplified with increase hydrological connectivity in permafrost ecosystems; iii) deep OC pools from ice-rich permafrost sediments highly vulnerable to abrupt thaw: this would increase anaerobic decomposition pathway and hence CH_4 emissions due to thermokarst lake and wetlands formation upon ground collapse (Strauss et al., 2017; Turetsky et al., 2020); iv) rapidly eroding coastline of the Arctic ocean and additional OC loss to the ocean with

potentially similar anaerobic decomposition pathway (Tanski et al., 2019). None of these process are accounted for in current models used to simulate permafrost C emissions. One additional unaccounted process is that **models do not resolve the complexity of OC decomposition and mineral protection known to stabilize a significant portion of OC in many soil and sediment environments is strictly discarded** (Opfergelt, 2020).

2.4.2 The uncertain future of permafrost

Ground temperature is increasing rapidly in permafrost regions. There has been a global increase of 0.3 ± 0.1°C per decade at depth of no seasonal temperature fluctuation, that is, between 10 to 20 m where seasonal soil temperature vanishes (Romanovsky et al., 2010; Biskaborn et al., 2019; Meredith et al., 2019). There is *very high confidence* that record high temperature at the zero annual temperature depth were attained in recent decades (Meredith et al., 2019). In colder permafrost (temperatures less than −2°C), warming of up to about 1°C per decade is apparent, as in the high-latitude Arctic (Smith et al., 2022). This indicates a warming of permafrost even at depth. However, the pace at which permafrost will disappear and carbon cycle will change is still highly uncertain. The uncertainty in the future greenhouse gas emissions trajectory as well as the climate change resulting from these emissions explains the large uncertainty in model projections. However, the Coupled Model Intercomparison Project Phase 5 (CMIP5) models project with *high confidence* that thaw depth will increase and areal extent of near-surface permafrost will decrease substantially. Depending on the Representative Concentration Pathway (RCP) scenario, models projected near-surface permafrost loss by 2100 of: 2-66% for RCP2.6 (24 ± 16%; *likely* range) and 30-99% (69 ± 20%; *likely* range) under RCP8.5 (Meredith et al., 2019; Figure 2.6).

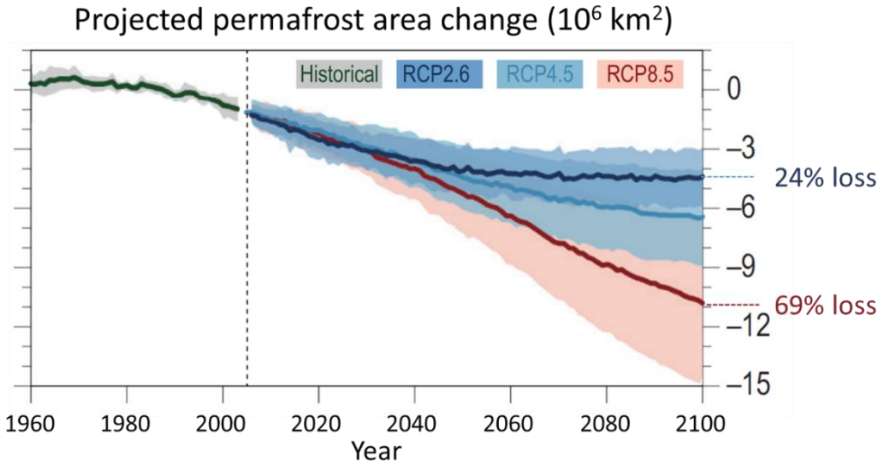

Figure 2.6: Coupled Model Intercomparison Project Phase 5 (CMIP5) multi-model average (± 1 standard deviation) projections for different Representative Concentration Pathway (RCP) scenarios for area change of near-surface permafrost (based on Meredith et al. (2019)).

2.4.3 The fate of carbon from thawed permafrost

As long as it is frozen in the ground, permafrost organic matter is not part of the active carbon cycle and can be considered as mainly inert (Schneider von Deimling et al., 2015). Note that unfrozen portion of the soil (taliks) or below 0°C microsites with liquid water may keep degrading OC at subzero temperatures (Natali et al., 2019). Once OC is thawed and exposed to microbial degradation, the key question concerns the amount and rate at which C will be transferred to the atmosphere as opposed to terrestrial or marine C long-term storage pools (i.e., sequestration)(Schädel et al., 2014). Soil organisms oxidize organic C to inorganic forms primarily as a source of energy for growth and metabolic activity. The quality (i.e., decomposability) of the organic matter in permafrost varies with OM composition and processes before permafrost burial. Note all carbon is not equally vulnerable to microbial degradation: some soil carbon is easily metabolized and transformed to gas, but more complex molecules are harder to break down. The bulk of permafrost C will be released slowly over decades after thaw but a smaller fraction could remain within the soil for centuries or longer (Schuur and Abbott, 2011). In addition, microbial decomposition rates depend strongly on environmental conditions, which exert strong control over C emissions from thawing

permafrost. Properties such as temperature, moisture availability, nutrient availability, and electron acceptor availability regulate OC decomposition rates. Microbial decomposition produces CO_2, CH_4 and nitrous oxide (N_2O), the three most influential long-lived greenhouse gases (Schuur et al., 2015; Voigt et al., 2020).

In a warming world, even if a small portion of the 1,440-1,600 Pg OC is emitted as greenhouse gases, this will have substantial effects on future climate. Evidence from independent scientific approaches (e.g., dynamic models, laboratory incubations) seems to converge on the fact that 5-15% of this C pool could be emitted as greenhouse gases by 2100 under current path of global warming (Schuur et al., 2015), but uncertainties remain. Ten percent of the permafrost OC pool, equivalent to ~144 – 160 Pg carbon, would make it similar in magnitude to other historically important biosphere C sources, such as land-use change (1.4 ± 0.7 Pg carbon per year over the last half-century), but far less than fossil CO_2 emissions (9.9 ± 0.5 Pg carbon per year in 2019; Friedlingstein et al., 2020). On an annual basis, the permafrost C emitted in the atmosphere would represent 22-31% of the current anthropogenic C emissions (Opfergelt (2020); considering anthropogenic emissions from 2019, IPCC (2019)). Most of that carbon from permafrost thaw would be emitted as CO_2 but it is estimated that 2.3% of the permafrost C emissions would be emitted as CH_4 (Schuur et al., 2013). This has great implication because of the greater warming potential of CH_4 compare to CO_2. Indeed, methane has the property to have a 25 times more important greenhouse warming potential than CO_2, on a century timescale (Bridgham et al., 1998).

2.4.4 Permafrost carbon emission estimates

Permafrost carbon emissions are likely to occur over decades and centuries as the permafrost region warms, making the carbon reservoir in the atmosphere grow even faster than what is projected based on anthropogenic emissions alone (Schuur et al., 2015). Knowing how much carbon will be released from permafrost zone in this century and beyond is crucial for determining the appropriate response in the decrease of anthropogenic carbon emissions and

prevent an overshoot of the remaining carbon budget[3] based on Paris agreement temperature target (van Huissteden, 2020). But despite the massive amount of OC in permafrost soils, C emissions from these soils are unlikely to overshadow those form burning fossil fuels, which will continue to be the main source of climate forcing (Schuur and Abbott, 2011). The effort made to mitigate climate change by reducing anthropogenic greenhouse gas emissions can strongly reduce greenhouse gas emissions from permafrost thaw in the near-future (Abbott et al., 2022).

Without taking into account permafrost emissions, the remaining carbon budget (counting emissions through 2020) for a likely chance (>66%) of remaining below 1.5°C has been estimated at ~400 Gt of CO_2 equivalent and at ~ 1,150 Gt of CO_2 equivalent for 2°C (IPCC, 2021). Recent estimates of carbon emissions from gradual permafrost thaw (i.e., deepening of the active layer) alone range from ~6 Pg to 118 Pg OC (about 22 Gt to 432 Gt of CO_2 equivalent; 1Pg C = $\frac{44}{12}$ Gt CO_2) by 2100 with reduced anthropogenic emissions and up to 550 Gt CO_2 equivalent with weaker climate policies (Koven et al., 2015; MacDougall and Knutti, 2016; Gasser et al., 2018). These are underestimates since it does not take into account abrupt thaw or wildfires which can increase the permafrost carbon emissions by 40% and 30 %, respectively (Genet et al., 2013; Turetsky et al., 2020; Natali et al., 2021). Within this context, the carbon emissions from permafrost thaw make the Paris agreement to stay within the 1.5°C scenario without overshoot likely unattainable (Natali et al., 2021). Projections from models of permafrost ecosystems suggest that future permafrost thaw will lead to some additional warming – enough to be important, but not enough to lead to a "runaway warming" situation, where permafrost thaw leads to a dramatic, self-reinforcing acceleration of global warming (Canadell et al., 2021).

2.5 Permafrost features

Ice melting and permafrost thawing in permafrost landscapes has a cascade of effects within ecosystems leading to specific permafrost features (Figure 2.7). Depending on ground ice content and topography, the consequences of

[3] The remaining carbon budget is defined as cumulative amount of anthropogenic CO_2 emission compatible with a global temperature change target (IPCC, 2022).

permafrost thaw on the landscape will differ. In this Ph.D. thesis, we focused on some major permafrost features resulting from different thaw processes such as gradual and abrupt thaw.

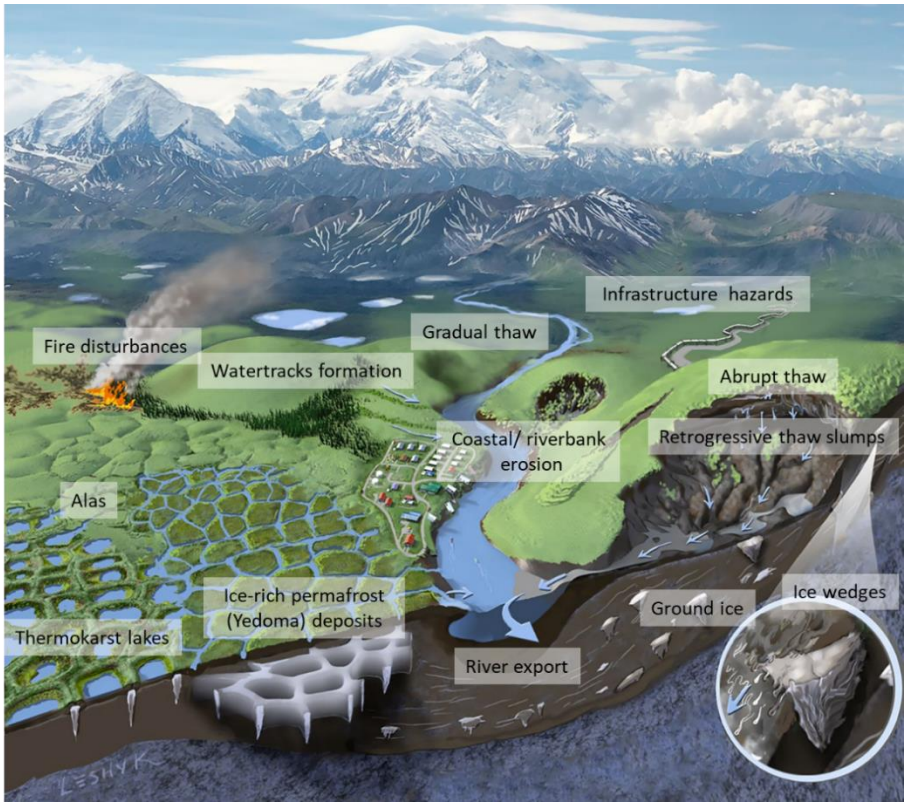

Figure 2.7: Scheme of different features found in permafrost landscapes. This Ph.D. thesis focuses on some specific permafrost features: Ice-rich permafrost (Yedoma) deposits, thermokarst lakes and Alas, gradual thaw, watertrack formation. Image drawn by Victor Leshyk, Northern Arizona University and modified from Schuur and Mack (2018).

2.5.1 Ground ice

Ground ice is fundamental in the glacial and periglacial environments (i.e., landforms associated with cold, nonglacial environment). Ice is present in multiple different shapes and sizes and is responsible of the multiple permafrost features found in northern latitudes (Figure 2.7). Ground ice varies between massive buried glacial ice to smaller-scale *in situ* ice-segregation processes. All this ice is vulnerable to thaw with global and local consequences on permafrost-affected environments (Figure 2.8). Because of types variability, the identification of typical cryostructures are used to

provide insight into ground-freezing processes (Rowley et al., 2015). Classification of the structure of ice in permafrost are useful to unravel genesis and history of permafrost and sedimentation at a particular location (van Huissteden, 2020):

- **Pore ice** includes individual ice crystals within the porosity of sedimentary rocks or unconsolidated deposits. Pore ice can act like a cement, holding soil particle together and giving structure to the ground. Pore ice does not excess natural void volume of sediments and therefore no excess water results from its thaw (French, 2007; Williams Jr and Ferrigno, 2012).
- **Segregated ice** is a broad term referring to high ice content, which often includes ice lenses visible to the naked eye. Ice lenses are defined as horizontal segregated ice layers that can be from few millimeters to several meters thick.
- **Vein ice** is formed mostly by the infiltration of water into dilatation cracks and have a vertical foliation and structure (opposingly to horizontal segregated ice).
- **Ice-wedges** are massive, generally wedge-shaped body with their apex pointing downward, composed of foliated or vertically banded ice. They are the most characteristics ice features from periglacial environments and constitute the third most important ground ice type in terms of volume (French, 2007).

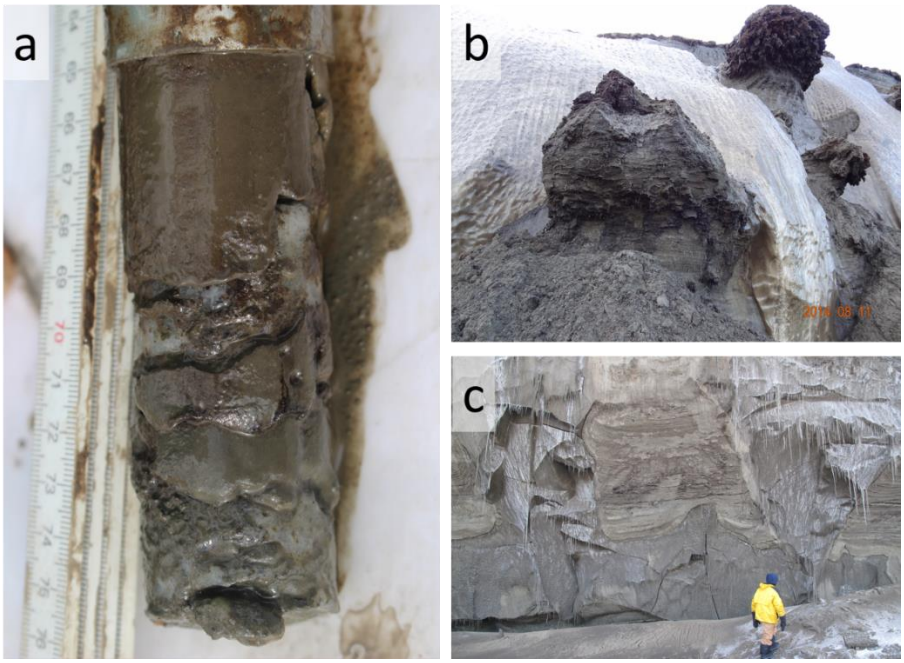

Figure 2.8: (a) Transition between active layer (upper part) and permafrost (lower part) in Eight Mile Lake tundra soil (AK, USA). Ice lenses are visible in the permafrost part of the sample (photographer: C. Hirst). (b) Coastal bluff of Sobo Sise where huge ice-wedges are visible (photographer: J. Strauss). (c) Bluff with visible ice-wedges in Itkillik, north Alaska (photographer: J. Strauss).

2.5.2 Gradual thaw and deepening of the active layer

The simplest form of permafrost thawing to consider from a conceptual and modelling standpoint is the active layer thickening, often referred to as gradual thaw. Gradual thaw include the deepening of the seasonally thawed active layer into perennially frozen permafrost layers and lengthening of the thawed season within the active layer. Gradual processes increase the amount of organic carbon and minerals that is thawed and the duration of thaw (Canadell et al., 2021). Gradual thaw occurs directly as a result of higher summer air temperature and infiltration of rain water. Water infiltration increases soil heat content and thermal conductivity. Permafrost beneath ponds or standing water is usually thawed deeper than drier surrounding areas. Winter temperatures and precipitation can also have an indirect but yet significant impact on active layer thickness and permafrost thawing (Schuur et al., 2008). Eventually, gradual thaw can be of magnitude such that winter temperatures are not

refreezing the active layer entirely, leading to the formation of a talik (i.e., a residual unfrozen soil layer with above-freezing conditions favorable for organic carbon decomposition).

With gradual thaw, the permafrost becomes part of the active layer. As a result, thawing triggers changes in the interactions between the different soil components. **Changing soil water saturation conditions modify the time for exchange between water and constituents which modifies the interactions between minerals, organic matter and microorganisms**.

2.5.3 Abrupt thaw and thermokarst landforms

Although gradual thaw and talik formation generally proceed with yearly small fluctuations, permafrost thawing can have a different outcome and occur much more rapidly or even catastrophically. This rapid scenario of permafrost thawing is usually referred to as abrupt thaw. While gradual thaw slowly affects soil by centimeters over years or decades, abrupt thaw can affect several meters of permafrost soil in periods of days to several years (Grosse et al., 2011; Turetsky et al., 2020). Greenhouse gas emissions across 2.5 million km^2 of abrupt thaw could provide a similar climate feedback as gradual thaw emissions from the entire 18 million km^2 permafrost region under RCP8.5. Abrupt thaw may also increase by 40% the current estimates of permafrost carbon emission based on gradual thaw alone (Natali et al., 2021).

Thermokarst lakes

Thermokarst is the process whereby the thawing of ice-rich permafrost ground or melting of massive ice causes land subsidence, resulting in development of distinctive landforms such as thermokarst lakes or ponds (Burn, 2013; Olefeldt et al., 2016). Ice-rich permafrost has a larger pore volume filled with ice than would normally exist in a water-saturated soil or sediment of the same material (van Huissteden, 2020). Permafrost thaw in ice-rich grounds where excess ground ice is present (Grosse et al., 2013) leads to thermokarst terrain, a patchwork of localized features that form when ground ice melts in reaction to ground warming and the surrounding ground subsides into the area previously occupied by ice (Figure 2.9). This uneven ground level greatly modifies surface water patterns within soils, wetlands, lakes and hydrology

networks. This changes the overall hydrology of permafrost landscapes, with some drier or wetter places and alter the vegetation that can thrive under waterlogged or dry conditions. A period of pronounced permafrost degradation occurred at the transition between the late Pleistocene and the early Holocene period. At that period, many regions of the Arctic suffered of warming atmospheric temperature and hence on the degradation of ground ice within permafrost regions (Grosse et al., 2013). Depending on the region of the Arctic considered, the Holocene Thermal Maximum peaked between 11-5 ka BP (Velichko et al., 2002; Kaufman et al., 2004). Note that thermokarst lake formation can be driven by other factors than warming air temperatures such as local topography, snow cover distribution and depth, and surface hydrology (Bouchard et al., 2020).

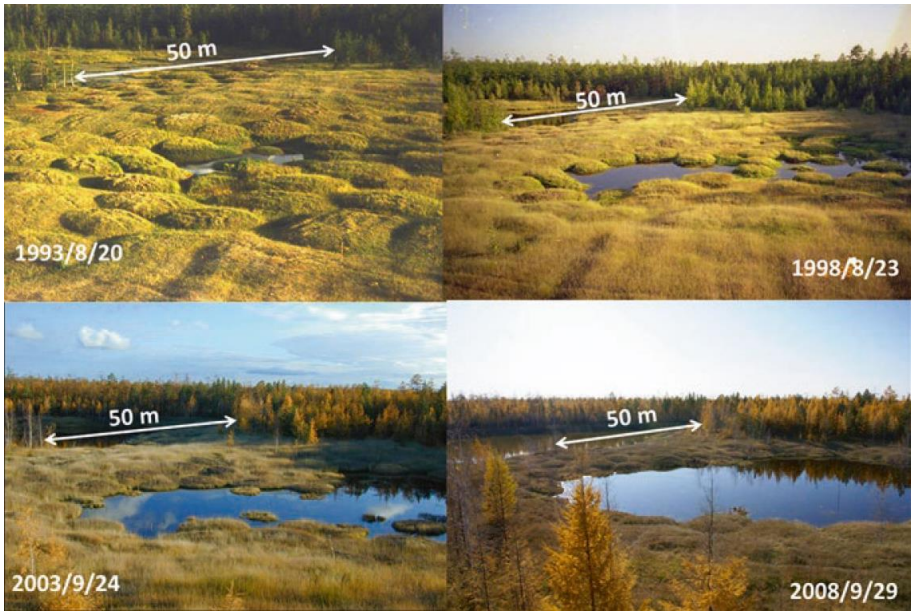

Figure 2.9: Landscape change with thermokarst lake formation at Yukechi in Central Siberia, 50 km SE from Yakutsk (Fedorov et al., 2014).

Approximately one quarter of all lakes on Earth occur in the northern regions (Lehner and Döll, 2004) and 75% of all lakes north of 45.5°N are located in permafrost landscapes (Smith et al. 2007). These numbers are underestimated because only waterbodies between 0.1 – 50 km^2 are included while many thermokarst lakes are smaller. Thermokarst lakes vary greatly in size, depth and area, from small ponds of few meters across (Breton et al., 2009) to large lakes spanning several many square kilometers (Côté and Burn, 2002). Thermokarst lakes are typically shallow (few meters deep) but some other

lakes generally found in the Yedoma region can be much deeper (i.e., several tens of meter deep; e.g., Schirrmeister et al., 2011; Morgenstern, 2012). The existence of even shallow ponds slows down freezing of the active layer in winter and induces deeper thaw in summer (Langer et al., 2015). At the Arctic scale, lake and drained lake basin systems can represent up to ~50% of the circumpolar Northern Hemisphere permafrost region lowland areas (Jones et al., 2022). Today, northern lowland permafrost regions are dotted with tens of thousands of thermokarst lakes and remnant basins (also called Alas) that resulted from partial or complete drainage or evaporation of lakes (Grosse et al., 2013).

Alas

The presence of many thermokarst basins that contain no or only small remnant lakes in many northern regions indicates that thermokarst lakes commonly lost surface area due to drainage or drying in the past (Grosse et al., 2013). The possible lifespan of a thermokarst lake from initiation to drainage or evaporation is poorly understood and rather unpredictable. Yet, it is believed to be function of regional landscape properties (i.e., relief gradient) and long-term water balance (i.e., precipitation – evaporation ratio). While climatic conditions are important drivers for thermokarst lake water balance, an even more important driver is the tendency of a lake to expand in depth and/or laterally and eventually encounter an alternative drainage mechanism (Figure 2.10). High water level, for instance, promote lakeshore erosion and may cause thermokarst lake to overflow their banks and drain. Melting of ice-wedges network may also create an abrupt thaw process leading to the creation of a drainage pathway towards downstream (i.e., lower altitude) depressions, river, ocean or other lakes (Marsh and Neumann, 2001; Hinkel et al., 2007; Grosse et al., 2013). However since most lakes are shallow, evaporation mechanism is also a key driver of thermokarst lake drying. Similar to the abrupt formation of thermokarst lake that can be rapid, deepening and widening of the drainage channels in ice-rich permafrost can take place within hours, leading to complete lake drainage within hours or days (Mackay, 1988). The degradation of ice-wedges network is likely to trigger the formation of a drainage outlet resulting in the partial or complete drainage of many thermokarst lakes (Mackay, 1988; Grosse et al., 2013). Man-induced modification of the landscape (i.e., road infrastructure, mines or construction work) was also spotted as a trigger of thermokarst lake drainage in some

studies (Mackay, 1992; Hinkel et al., 2007). The drainage of thermokarst lakes often triggered epigenetic permafrost formation and the deposits within the Alas depression freeze again with the absence of the latent heat of water to protect from subzero temperatures.

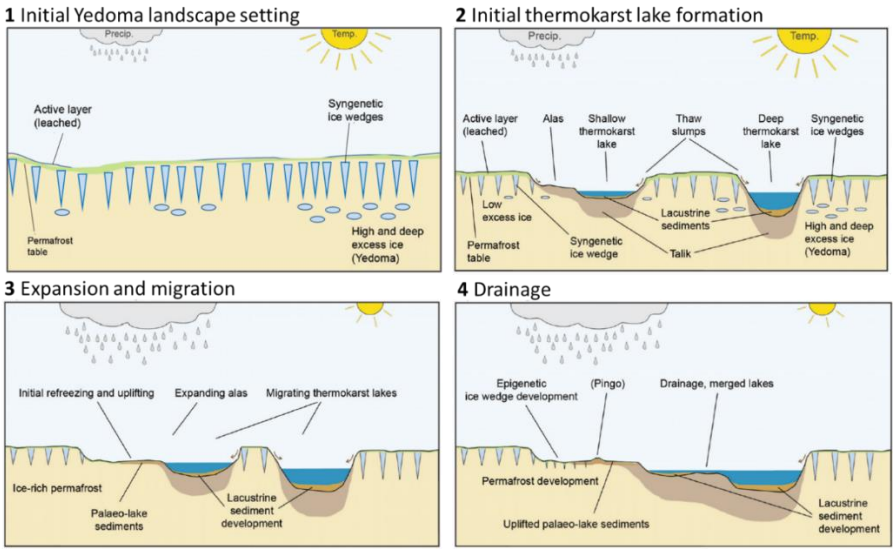

Figure 2.10: Conceptualization of typical thermokarst development in Yedoma deposits considering the finding from Soloviev (1973), French (2007) and Van Huissteden et al. (2011). Scheme adapted from Bouchard et al. (2017).

In many regions, coalesced and overlapping thermokarst lake generations are present forming complex landscape systems which can result in very large, deep and interconnected basins. Thermokarst lake cycle consisting of at least two or more cycles comprises the following steps: i) lake formation in ice-rich permafrost starting with ice-wedges degradation; ii) lake growth and eventual drainage; iii) aggradation of new ice-wedge network within the drained basin and ground elevation due to ice volume expand; iv) degradation of the newly formed ice-wedges resulting in lake formation. The massive overlap of lake basins observed in some regions likely indicate recurring thermokarst lake formation and drainage on the landscape (Lenz et al., 2016). **Changing water saturation in deposits after thermokarst lake formation or thermokarst lake drainage modify the time for exchange between the water and the mineral and organic constituents within soils or sediments.**

2.6 Mineral organic carbon interactions

Mineral organic carbon interactions have received increased attention because they were identified as one of the main control on OC long-term storage in soils (Oades, 1988; Torn et al., 1997; Baldock and Skjemstad, 2000; von Lützow et al., 2006). Mineral OC interactions include physical protection (i.e., aggregation) and physico-chemical protection of OC (organo-mineral association and organo-metallic complexes) (Sect. 2.6.3). These interactions depend on the characteristic properties of the individual organic and the mineral phases as well as their binding mechanisms. Mineral OC interactions play a critical role in structuring and compartmentalizing the biological reaction space of soils and sediments into microsites, and also determine the extent to which microsites are connected (in combination with water potential). This section presents an overview of such organic and mineral properties and how they interact in relation to each other. The formation of mineral OC interactions are facilitated by (i) the presence of liquid water, (ii) the presence of plants or buried organic matter, (iii) the presence of microbiota with the ability to degrade larger plant biopolymers to smaller, more soluble organic acids, (iv) the presence of reactive mineral phases with large surface specific area and (v) a low pH that favors weathering of minerals (Kleber et al., 2015).

In thawing permafrost, all these factors are present or were present in soil before freezing process. More specifically, the presence of water inferred by snow, rain and ice melt. The accumulation of plants and roots over thousands of years in permafrost or the accumulation of peat under cold conditions. The presence of multiple microbial communities, and minerals with high specific surface area present in the loess-like material upon deposition. These factors together with the acidic soil solution promoted by organic-rich surface soils make the thawing permafrost a rather beneficial environment to create mineral OC interactions. **We argue that mineral OC interactions in permafrost regions may increase OC stabilization and mitigate OC microbial degradation upon permafrost thaw and should be better constrained**.

2.6.1 Organic matter breakdown

All processes required to prepare organic compounds for their eventual attachment to mineral surfaces occur in the aqueous phase (Kleber et al.,

2015). Soil organic matter is defined as the sum of all naturally derived organic materials (Baldock and Nelson, 2000). Soil organic matter consists of various functional pools that are stabilized by specific mechanisms and have certain turnover rates but cannot be considered as equally involved in the formation of mineral OC interactions (von Lützow et al., 2007). The organic matter interacting with mineral surfaces display a myriad of molecular composition and sizes/weights (Kleber et al., 2007). The breakdown of organic matter from large biopolymers to monomers is therefore a necessary step to reduce the size, increase the solubility of organic compounds and increase their reactivity towards mineral surfaces and cations (Figure 2.11).

Organic matter breakdown includes depolymerization and oxidation reactions (Hedges and Keil, 1999). Depolymerization reduces molecular size and enhance aqueous solubility, while oxidation mechanisms both reduce molecular size and add oxygen-containing functional groups which also increase chemical reactivity. The increased density of polyfunctional groups (i.e., acting as ligands) enhance the aqueous solubility of the products and their reactivity towards mineral surfaces and cations, particularly when these functional groups are ionized (i.e., when they hold a charge). Polyfunctional groups combine alkyl and O-alkyl compounds (termini used to identify lipid and carbohydrate structures), carboxyls and sulfhydryl or amino groups. Carboxylic groups have the specificity to be ionized (as COO^-) in the soil pH range. Therefore, any addition of carboxyl groups to decaying organic fragments, such as in the course of depolymerized oxidation, renders these materials more likely to (1) mobilize in an aqueous soil environment and to (2) engage in electrostatic bonding with suitable mineral surfaces and/or metal cations (Kleber et al., 2015). Organic fragments diffuse toward mineral surfaces and may sorb (or not) depending on the available functional groups of the organic compound, the available mineral surfaces, and soil solution parameters (pH, and ionic strength). Adsorption between the low molecular organic acids and the mineral surfaces might be followed by desorption, exchange reaction, and biotic or abiotic degradation. Once an organic molecule come close to contact with a mineral surface, the abundance and type of organic functional groups constrain options for further reaction between the organic and the mineral matrix surfaces (Kleber et al., 2021).

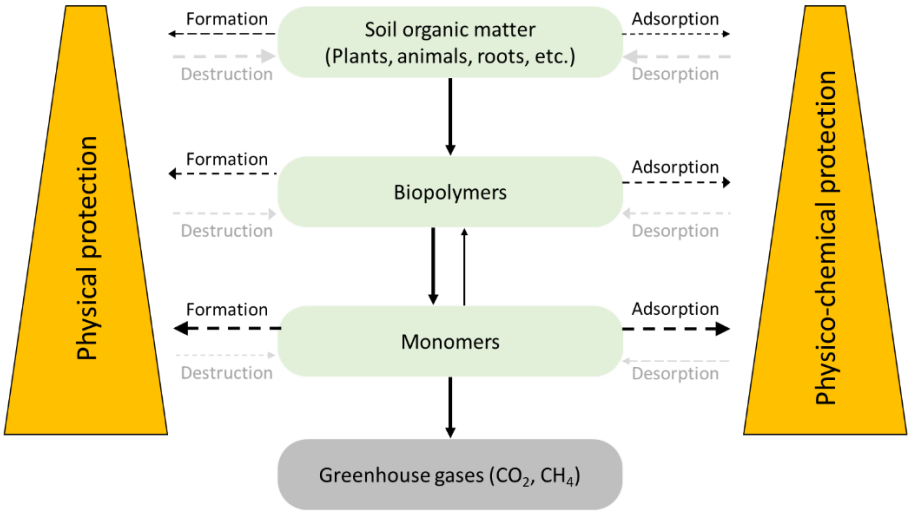

Figure 2.11: Conceptual scheme of organic matter breakdown and interactions via physical protection (aggregation) or physico-chemical protection (organo-mineral association and organo-metallic complexes). With reduction in size and increasing reactivity of the organic matter, mineral organic carbon interactions (physical and physico-chemical protection) are promoted and mitigate greenhouse gas emissions (carbon dioxide and methane) via microbial degradation. Scheme is adapted from Lehmann and Kleber (2015).

2.6.2 Microbial communities and organic matter decomposition pathways

After organic matter breakdown, the smaller and more reactive organic acids can be degraded by microorganisms or be stabilized via mineral OC interactions (Kaiser and Guggenberger, 2003; Keil and Mayer, 2014; Kleber et al., 2015). The first scenario triggers greenhouse gas emissions (as CO_2 or CH_4) while the second scenario stabilizes OC in soils and may prevent its degradation on millennial timescale (von Lützow et al., 2006). Decomposition of organic carbon is mainly microbially mediated (biotic oxidation) while a smaller part is degraded via chemical (abiotic) oxidation. The decomposition rates of protected OC can be 100 to > 1,000 years for which protection mechanisms are not entirely clear (von Lützow et al., 2006). Microorganisms (bacteria, archaea as well as most protozoa, fungi and algae) are in close interactions with minerals via i) microbially mediated formation and dissolution of minerals; ii) formation of mineral OC interactions through deposition of microbial products on mineral surfaces; and iii) acquisition and

utilization of organic material for microbial metabolic activity and growth (Kleber et al., 2015). Electron transfer reactions between organic matter and minerals can also be mediated by microbes as primary pathway contributing to the oxidation, transformation and mineralization of carbon within soil and sediments (Kleber et al., 2021). Microorganisms represent a key step in OC mineralization and greenhouse gas emissions outputs.

The decomposition pathways of OC and the relative amounts of CO_2 and CH_4 that are produced upon microbial degradation depend largely on environmental factors, particularly soil saturation (Herndon, 2018). Drier soils, where decomposer organisms use abundant oxygen to break down organic compounds, release CO_2. Under wetter conditions, CO_2 and CH_4 are more slowly released because decomposition is limited by low oxygen availability. However, in absence of oxygen, other electrons acceptors including Fe or Mn species are possible (Melton et al., 2014; Chen et al., 2020; Li et al., 2021). While this PhD thesis mainly focuses on the influence of changing soil conditions on mineral OC interactions, additional factors not considered here such as the diversity of microbial communities (e.g., modulating CO_2:CH_4 ratio or oxide dissolution rates), the spatial and functional complexity in the sediment (e.g., the structuring of space into a network of more or less connected microsites that determine local environment conditions), or the catalyst role of mineral elements for organic reactions (e.g., through the creation of centre of reactivity, proton transfer or electron acceptor) may contribute to influence mineral OC interactions to some extent (Kleber et al., 2021).

2.6.3 Mineral surfaces and metals cations

Many terminologies exist when it gets to the interaction between mineral and OC. In this thesis, we will define mineral OC interactions as a combination of both physical protection (i.e., spatial inaccessibility; aggregation) and physico-chemical protection (i.e., organo-mineral associations and organo-metallic complexes). Selective preservation of recalcitrant molecules is not included as mineral protection but rather function of the indigenous molecular characteristics of plant litter and rhizodeposits (von Lützow et al., 2006). The general term stabilization is defined as protection of organic matter from mineralization and integrates effect of recalcitrance, physical and physico-chemical protection. Generally, stabilized OC is older than unstabilized OC

and hence stabilized OC is characterized by longer turnover time and mean residence time in soils or sediments (von Lützow et al., 2006).

Physical protection (i.e., spatial inaccessibility) is the spatial localization of OC that influences access by microbes and enzymes (von Lützow et al., 2006). Physical protection is caused by occlusion of OC by aggregation, intercalation within phyllosilicates, hydrophobicity, and encapsulation in organic molecules (Figure 2.12). The content of soil OC, metal oxides, carbonates, cations and clay minerals act as a binder that improve the stability of aggregates (Colombo and Torrent, 1991; Peng et al., 2015; Wang et al., 2016; Souza et al., 2017; Xue et al., 2019). Occluded OC within aggregates is spatially protected against decomposition due to: i) reduced access for decomposers and their enzymes; ii) reduced diffusion of enzymes into the intra-aggregate space; and iii) restricted aerobic decomposition because of the reduced oxygen diffusion within the aggregate intra-space (von Lützow et al., 2006). Aggregates physically protect soil OC by forming physical barriers between microbes and enzymes and their substrates, controlling food web interactions and consequently microbial turnover (Six et al., 2002). Nearly 90% of soil OC in surface temperate soils was found to be located within aggregates (Jastrow et al., 1996).

Physico-chemical protection is defined as interactions with metal oxides or clay surfaces (organo-mineral associations) and metal polyvalent cations (e.g., Fe, Al, Mn, Ca as organo-metallic complexes) (Figure 2.12). Stabilization with mineral surfaces are inter-molecular interactions including ligand exchange, polyvalent cation bridges or weak interactions (Van der Waals forces, H-bonding, hydrophobic interactions) (von Lützow et al., 2006; Keil and Mayer, 2014). A diverse suite of mineral surfaces capable to bind with OC occur in soils and sediments, including metal oxides, hydroxides, and oxyhydroxides (herein collectively referred to as metal oxy(hydr)oxides); phyllosilicates and short range ordered aluminosilicates (Table 2.1); and metal carbonates and sulfides (Kleber et al., 2021). Surface interactions of these minerals with organic molecules depend on i) the type, abundance, and charge characteristics of their surface functional groups; ii) the size, shape, and surface topography of the primary mineral particles, and; iii) the degree of particle aggregation (Kleber et al., 2015). In organo-metallic complexes, the polyvalent metal cations (e.g., Fe^{3+}, Fe^{2+}, Al^{3+}, Ca^{2+}, Mn^{3+}) in solution can coordinate with negatively charged polyfunctional groups of organic acids (Boudot et al., 1989). Complexation between organic acids and metals lowers

the solubility of organic acids and hence their availability to microorganisms (Baldock and Skjemstad, 2000).

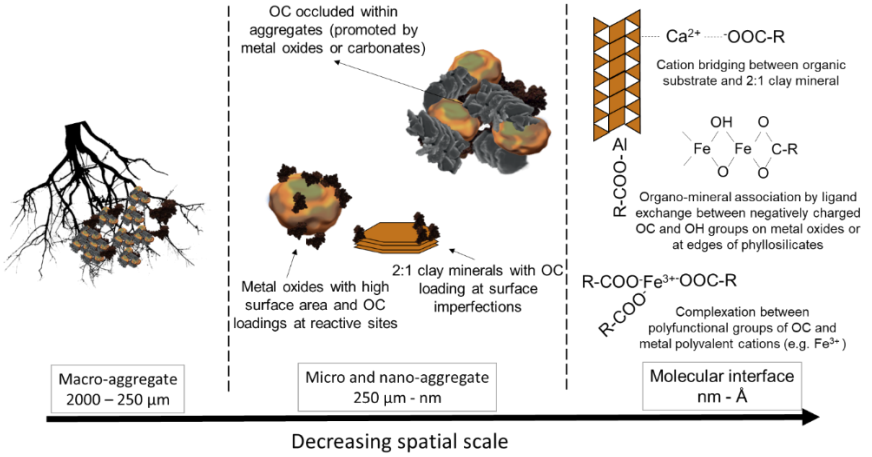

Figure 2.12: Mineral interactions with organic carbon (OC) occur at a variety of spatial scales and topography in soils and sediments, where a diversity of organic ligand may reach the solid-solution interface. At the molecular interface organic acids are represented as R-COO$^-$ molecules (adapted from Rowley et al. (2018)).

Mineral surfaces participating in organo-mineral associations may be divided in three categories: 1) variably charged (pH-dependent); 2) permanently charged (structural) and; 3) permanently non-charged.

On *variably charged surfaces*, metal oxides and phyllosilicate crystallite edges carry hydroxyl groups (OH^-) that are increasingly protonated with decreasing pH, thereby acquiring positive charge. The positive charge enables the retention of negatively charged polyfunctional groups of organic acids via ligand exchange (Kleber et al., 2021). Specific adsorption through ligand exchange is not readily reversible. Variably charged metal oxides can adsorb low molecular weight organic ligands (such as aliphatic and aromatic carboxylate, amino acids, hydroxamate ligands or phospholipid). Natural OM features similar functional groups (mainly carboxyl and alcoholic/phenolic OH groups) and hence react in a similar way. Surface hydroxyl of metal oxides undergo rapid ligand-exchange reactions with carboxyl or other usually occurring functional groups of OM, resulting in the formation of polar covalent metal-O-C bonds and the release of OH^- ions or water (Kleber et al., 2015). Metal here can refer to Fe-, Mn- or Al-oxides. Polyvalent (valence

greater than one) metals can bind with more than one functional group at the same time, thereby forming very stable ring structures (Pohlman and McColl, 1988). Polyvalent cation bridges are formed by the coordination of anionic or polyfunctional groups (e.g., carboxyl, amino, or hydroxyl groups) of OM to adsorbed polyvalent inorganic cations (Figure 2.12). The metal oxides involving Fe and Mn are interesting to investigate relative to their redox sensitivity. Reducing soil conditions are likely to dissolve Fe- and Mn-oxides with the potential release of previously stabilized OC.

The second category with *permanently charged surface* comprise surfaces of phyllosilicates with significant isomorphic substitutions (e.g., vermiculite, illite, and smectite). Common isomorphic substitutions exist when Al^{3+} is replaced by Mg^{2+} or when Si^{4+} is replaced by Al^{3+} or Fe^{3+}, resulting in a permanent (pH-independent) net negative charge on phyllosilicate surfaces. The negative charge created must be counterbalanced by adsorbed cations to maintain electro-neutrality. As a result, minerals after isomorphic substitution as in vermiculite yields in a higher surface charge density and thus a stronger electrostatic interaction with cationic solution species (Sposito et al., 1999). Phyllosilicates and their ability to retain exchangeable cations will depend on the extent of permanent charges and thus the amount of isomorphic substitution within the mineral (Kleber et al., 2015). While monovalent cations (K^+, Na^+) will only equilibrate the negative charge of the clay surface, polyvalent cations (e.g., Fe^{3+}, Al^{3+}, Ca^{2+}) act as a cation bridge between the negatively charged clay surfaces and negatively charged organic functional group (Keil and Mayer, 2014; Kleber et al., 2021). Cation bridging mechanism has been frequently observed for clay minerals, which remain negatively charged over a wide range of pH. Ligand exchange and polyvalent cation bridges are binding mechanisms that both can last for more than 100 years (von Lützow et al., 2006). Phyllosilicates are important player in OC stabilization in soils but will not be extensively investigated in this Ph.D. thesis because of their lower sensitivity to changing soil conditions compared to metal oxy(hydr)oxides.

Finally, *non-charged surfaces* (2:1 phyllosilicates with no or little substitution and those of 1:1 phyllosilicates such as kaolinite) allow nonpolar organic molecules to accumulate via entropy-driven hydrophobic exclusion phenomena in combination with Van der Waals forces and H-bond formation (Kleber et al., 2015). The Ph.D. thesis will focus mainly on variably charged oxides and organo-metallic complexes owing to their changing stability depending on soil redox and pH conditions. Permanently charged and non-

charged phyllosilicates will not be extensively detailed in the following, although we acknowledge their contribution to mineral OC interactions as well.

Table 2.1: Key properties of fine-grained minerals and related solids in organo-mineral associations (modified from Kleber et al., 2021). In the PhD thesis, the focus is on metal oxides.

Mineral type	Mineral name	Charge (σ, mmolc g^{-1})	Crystal size (nm)	Area (a_s, $m^2 g^{-1}$)
Phyllosilicates				
2:1 Layer type (Illite ≥ smectite ≥ vermiculite, chlorite)	Illite Smectite	-0.16 to -0.22 -0.7 to -1.2	~50 – 100 ~50 – 1,000	20 to 200 740 to 780
1:1 Layer type	Kaolinite	0 to -0.02	~200 to > 1 µm	7 to 80
Metal oxides (Fe, Mn, Al)				
FeOOH	Goethite	0 to 0.15	~50 – 100 wide; ~100 – 300 long	40 to 90
Fe_2O_3	Hematite	0 to 0.02	~50 – 100	10 to 35
$Fe_{10}O_{14}(OH_2)$	Ferrihydrite	0 to 1.3	~3 – 5	200 to 800
$(Na,Ca)Mn_7O_{14}$	Birnessite	-1.3 to -2.8	~6 – 35	1,200
$Al(OH)_3$	Gibbsite	0 to 0.02	50 – 200 long; < 20 wide	1 to 100

Particle size and topography features (i.e., edges, pits, steps or vacancies) are important control on the ability of minerals to interact with inorganic or organic solutes. The amount of reactive surface groups per unit of mass of mineral available for organic ligand binding generally increases with decreasing particle size due to an increase in specific surface area (Table 2.1). Nanoparticulate phyllosilicates, short-range ordered aluminosilicates and metal oxides with crystalline size of 2 -100 nm and specific surface area (SSA) values exceeding 200 m^2 g^{-1} are usually found in soils (Cornell and Schwertmann, 2003; Wilson, 2013; Kleber et al., 2015). A high specific surface area promotes a higher proportion of reactive site for binding between mineral surfaces and organic carbon.

2.6.4 Metals involved in the physico-chemical protection of organic carbon

Four metals are specifically involved in mineral surfaces or in organo-metallic complexes forming interactions with OC, and will be described here below: iron, aluminum, manganese, calcium (Figure 2.13).

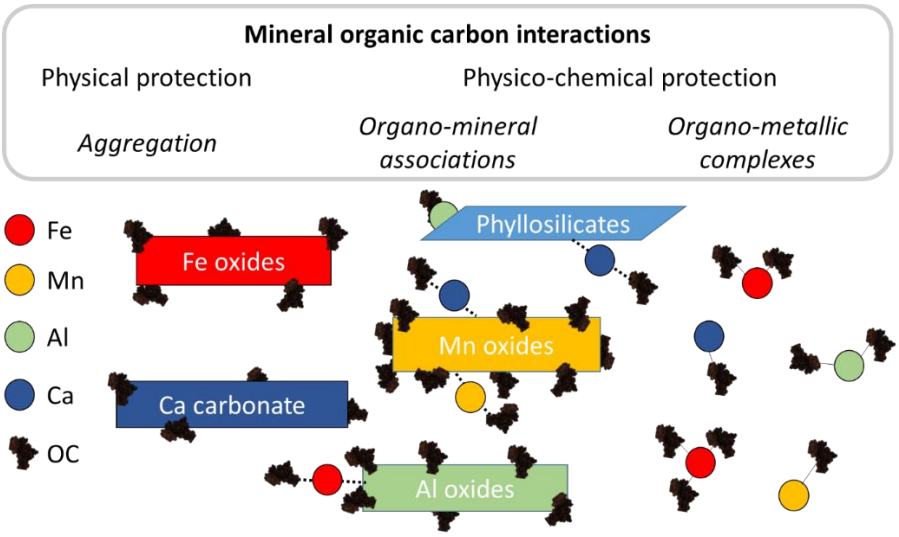

Figure 2.13: Schematic of the different metals (Fe, Mn, Al and Ca) involved in mineral organic carbon interactions. Organic carbon (OC) can be physically protected or physico-chemically protected. Metal surfaces can stabilize OC via organo-mineral associations as metal oxy(hydr)oxides (referred here as oxides) with Fe, Mn or Al, carbonates or phyllosilicates. Organo-metallic complexes are the association between the positively charged polyvalent cations (Fe, Mn, Al and Ca) and the negatively charged functional groups of organic acids. Dashed lines represent cation bridging mechanism. Mineral surfaces are schematized with polygons and polyvalent cations with circles. The number of reactive sites and the abundances of the different types of mineral OC interactions vary with soil properties, composition, and geochemical conditions.

Iron

Iron is an element relatively abundant in many soils and sediments with, on average, a total concentration of 20 to 40 g kg^{-1} (Cornell and Schwertmann, 2003). Iron minerals can be of different kind with different properties. Among pedogenetic Fe, crystalline Fe (hydr)oxides like goethite (α-FeOOH), and hematite (α-Fe_2O_3) are the most abundant mineral in well drained soils. In poorly drained conditions, lepidocrocite (γ-FeOOH), maghemite (γ-Fe_2O_3)

and magnetite, or short range ordered (in the following referred as poorly crystalline) ferrihydrite ($5Fe_2O_3 \bullet 9H_2O$) and ferroxite or even non crystalline precipitates may exist (Schwertmann et al., 1986; Cornell and Schwertmann, 2003). Each mineral may vary in crystal size and structural order and thereby in surface reactivity and solubility. The general parameters governing the behavior of Fe are redox (i.e., oxidizing or reducing conditions) and pH. Goethite and hematite are characterized by high stability (lower solubility) in the most habitual Eh-pH soil conditions. In spite of their lower stability, lepidocrocite and ferrihydrite often occur in many soils, especially in younger soils characterizing the non-equilibrium state in the pedo-environment as cold climate and acidic soils (Schwertmann, 1988). The solubilization of Fe from mineral sources is a slow process regulated by pH and by the dissolution-precipitation phenomena of both crystalline and poorly ordered Fe-hydroxide minerals.

The species of Fe in the soil environment can be summarized the following way: (1) Fe^{II} in primary minerals; (2) Fe^{III} in secondary minerals, as crystalline or poorly crystalline Fe oxy(hydr)oxides; (3) Fe bound to organic matter in soluble or insoluble forms; and (4) soluble and exchangeable Fe. Iron is considered as an essential micronutrient because it participates in many life-sustaining processes (Colombo et al., 2014). Iron is important to plant and is often deficient because of low solubility. However, here, Fe is studied regarding its sorptive and protective role relative to organic carbon. For instance, in cold-temperate climates, the carbon storage in soils is largely function of the content in crystalline and poorly crystalline Fe oxides (Wiseman and Püttmann, 2005). In permafrost regions, Herndon et al. (2017) suggested that precipitation of Fe oxides at the redox interface has the potential to contribute to mineral protection of organic matter and increase the residence time of organic carbon in Arctic soil. Overall, in well-drained soils that remain oxic (i.e., presence of O_2), Fe released from silicate minerals as Fe^{II} during weathering precipitates as Fe^{III} oxy(hydr)oxides such as goethite or hematite (Cornell and Schwertmann, 2003). Re-oxidation of this Fe^{II} is often rapid when it encounters molecular oxygen, generating Fe-OC associations when dissolved organic carbon (DOC) is present (Chen and Thompson, 2018). In poorly drained soils that suffer from periodic or persistent period of anoxia, microorganisms reduce Fe^{III} oxides to generate magnetite or release Fe^{II} into solution where it can leach or diffuse to oxic zones of the soil environment and precipitate as poorly crystalline ferrihydrite (Riedel et al., 2012; Herndon et al., 2017). At very high organic matter

content, all the Fe may be organically complexed such as in O horizons or in peaty environments and no more iron oxides will be formed (Schwertmann et al., 1986). Lalonde et al. (2012) proposed that the associations between organic matter and Fe are formed primarily through co-precipitation and/or direct chelation (i.e., complexation) and that these processes are able to promote the preservation of OC in marine sediments and act as a key factor in the long-term storage of OC. Overall, in cold climate, adsorption of organic acids on Fe oxy(hydr)oxides has become more relevant because of its impact on the carbon balance and the additional OC pool exposed to thawing in coming years (Colombo et al., 2014).

Aluminum

Similar to Fe, Al as cation can bind to organic ligands (i.e., mainly carboxylic group under acidic conditions) to form organo-metallic complexes. As solid Al oxides, bonding between hydroxyls on Al oxides surfaces and organic matter can stabilize OC against microbial degradation. Aluminum reacts with organic matter in many soils to form stable complexes and the Al may be monomeric or it may be in hydroxyl polymer (Wagai et al., 2013). In acid soils, the dynamic of organic matter and Al are strongly interdependent and Al is reported to stabilize OC upon Al precipitation (Schwesig et al., 2003; Scheel et al., 2007). Multiple evidence can support this statement: i) complexation by solid phase organic matter controls the solubility of Al, even in mineral horizons with low OC content; ii) dissolved OC solubilizes Al by complexation, and thus Al in soil solution and rivers is strongly associated with DOC (van Hees et al., 2000); and iii) the inhibitory influence of Al on the mineralization of OC is well documented (e.g., Brunner and Blaser, 1989). Sorption of organic compounds on Al constituents decreases OC mineralization (Boudot, 1992). Upon weathering under oxic conditions, Al-bearing minerals (i.e., gibbsite and alumino-silicate) are typically dissolved at greater pH than Fe-bearing minerals (i.e., ferrihydrite, goethite). Solubilized Al outcompete base cation on exchange sites and as a result buffer the soil pH between 4 and 5.5, which further limits Fe dissolution (Hall and Thompson, 2022). Because Al is abundant, this should lead to preferential dissolution of Al and formation of Al-rich organo-metallic complexes compare to Fe-complexes. Therefore, strictly as a consequence of differences in proton-mediated mineral dissolution, we might expect a greater abundance of Al-OC complexes than Fe-OC complexes unless the soil pH is very low (e.g., <4),

which is uncommon (Hall and Thompson, 2022). It is reported that Fe^{III} is more likely to hydrolyze than Al^{III} to form a solid phase which may influence the organo-metallic complexes stability (Crumbliss and Garrison, 1988). Overall, more comprehensive datasets are needed in varying soils types with varying soils conditions to better test hypothesis regarding the importance of Al^{III} vs. Fe^{III} complexes for soil OC abundance and persistence (Hall and Thompson, 2022).

Manganese

Although substantial research has demonstrated the ability of Fe- and Al-oxides and cations to stabilize OC, there is a scarcity of similar information regarding Mn oxides. Manganese oxides possess many similar properties to Fe oxides (i.e. redox-sensitive metal) that exert a poorly recognized control on C cycling in terrestrial ecosystems (Estes et al., 2017). Manganese oxides are characterized by high oxidation potential and display unusually high specific surface area, thus they exert strong control on OC adsorption and stabilization (Stone and Morgan, 1984; Roy et al., 2013; Johnson et al., 2015). Birnessite was even reported to have a higher surface area than ferrihydrite (1,200 $m^2 g^{-1}$ for birnessite compare to 200-800 $m^2 g^{-1}$ for ferrihydrite; Kleber et al., 2021)). Manganese is a redox-sensitive element that is stable under various state of oxidation. The Mn^{II}, released from primary minerals weathering, is readily oxidized to $Mn^{III/IV}$ to form Mn (hydr)oxides in soils and sediments (i.e., birnessite, manganite and hausmannite). Manganese is a critical micronutrient that is readily soluble under acidic conditions, cycling through vegetation (i.e., uptake and litterfall) and result in Mn accumulation in surface soils (Jobbágy and Jackson, 2004). The Mn^{II} species in litter are oxidized to insoluble $Mn^{III/IV}$ oxide during decomposition, facilitating their accumulation in surface soils. Most Mn oxides are net negatively charged on the surface at neutral pH and have high potential to sorb positive cations or polyfunctional groups. With decreasing pH, electrostatic interactions between Mn oxides and organic compounds increase as organic compounds protonate and associate with Mn oxide surface (Li et al., 2021). Additionally, Mn^{2+} can act as polyvalent cation bridge that can partially neutralize the negative surface charges and facilitate adsorption of organic acids. For Mn oxides, also true for Fe oxides, adsorption and reaction rates tend to be higher at low pH (<4) where increasingly positive surface charge facilitates interactions with negatively charged organic compounds (Li et al., 2021).

Manganese has also a high potential to degrade organic molecules through abiotic and microbially mediated oxidation (Remucal and Ginder-Vogel, 2014; Li et al., 2021). Manganese oxides can decompose organic matter via oxidative reactions into smaller compounds that can ultimately be transformed to greenhouse gases (Sunda and Kieber, 1994). Under permafrost soil conditions (i.e., organic-rich soils with low level of oxygen under poorly drained conditions), Mn is expected to serve as an important terminal electron acceptor thus increasing DOC mobilization in soils (Grybos et al., 2009), potentially increasing OM bioavailability to microorganisms.

Calcium

Calcium, along with Mn, is often discarded for OC stabilization, although it has widely been established that exchangeable Ca positively correlates with soil OC and its resistance to oxidation (Rowley et al., 2018). Calcium has a significant positive effect on aggregation and hence promote physical protection of OM. In addition, Ca^{2+} can be involved in complexation with organic acids or in cation bridging mechanism (Keil and Mayer, 2014; Rowley et al., 2018). Above pH 7, it is recognized that the influence of Ca^{2+} or sorption of OC to Ca carbonate dominate the influence of Fe and Al oxides and cations (Rowley et al., 2018). As pH shifts from acidic to basic conditions, polyvalent cations shift from Fe^{3+} and Al^{3+} to Ca^{2+} and influence soil OC stabilization (Tipping, 2005). Alkaline conditions are not predominant in organic-rich surface soils but yet many parts of the permafrost regions are covered by carbonates sediments with rather basic conditions (Hartmann and Moosdorf, 2012; Schirrmeister et al., 2013). Hence, Ca-mediated stabilization should not be overruled stricto senso.

2.6.5 Mineral organic carbon interactions in permafrost soils relative to other environments

The OC stabilizing mechanisms involving metal oxy(hydr)oxide have been extensively studied in i) controlled conditions (Schwertmann, 1991; Eusterhues et al., 2008; Huang and Hall, 2017; Liao et al., 2017; Zhao et al., 2017), ii) agricultural or forest soils (Wang et al., 2019; Possinger et al., 2020), iii) tropical lateritic soils (Fritsch et al., 2009; Mikutta et al., 2009; Bhattacharyya et al., 2018a; Inagaki et al., 2020), iv) peatlands and rice paddy soils (Fiedler and Sommer, 2004; Kögel-Knabner et al., 2010; Pan et al., 2014;

Bhattacharyya et al., 2018b; Xue et al., 2019), and v) lake and marine sediments (Eglinton, 2012; Lalonde et al., 2012; Barber et al., 2017), and more recently in permafrost regions (Fiedler et al., 2004; Gundelwein et al., 2007; Höfle et al., 2013; Gentsch et al., 2015b; Mu et al., 2016; Herndon et al., 2017, 2020b; Patzner et al., 2020; Sowers et al., 2020; Joss et al., 2022; Lim et al., 2022b).

A review from Kleber et al. (2015) highlighted that the carbon content within mineral–organic associations (MOAs; defined based on density) is rather low with a median of 1.3%. However, mineral-organic associations account for up to 91% of the total soil OC and substantially increase the turnover time of OC stored in such mineral-organic associations (Figure 2.14). There is a consensus that strong adsorption of organic compounds to mineral surfaces renders organic molecules at least temporarily inaccessible for enzymatic attack (Kleber et al., 2015). Yet, the relationship between the mode of adsorption of organic compounds to minerals surfaces and their residence time in soil cannot be answered conclusively. Disentangling individual adsorption mechanisms which operate simultaneously and may evolve with ligand type and concentration, ionic strength and pH is a scientifically challenging task. Here, the Ph.D. thesis focuses on the abundance and evolution of the different OC stabilization mechanisms (organo-mineral associations and organo-metallic complexes) with changing soil conditions. However, the link between mineralization rates of mineral-protected OC and particular adsorption mechanisms as a function of environmental variables will not be systematically addressed.

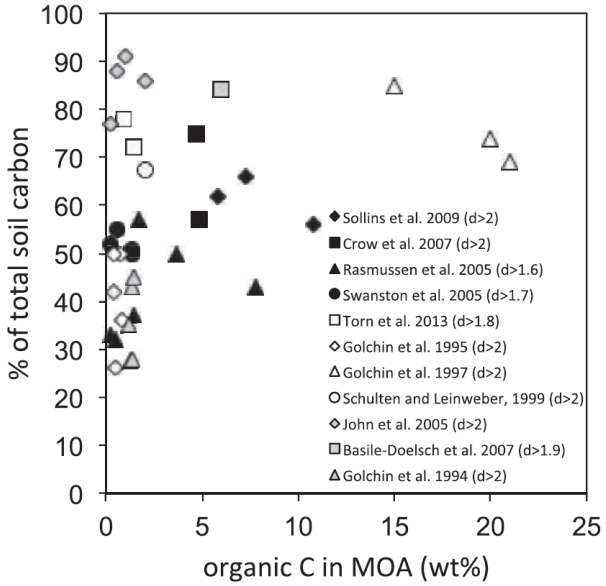

Figure 2.14: Percentage of total soil C residing in mineral-organic associations (MOAs) in a given soil ecosystem as a function of the weight percent carbon in those MOAs. MOAs were isolated using density fractionation procedures, with density cutoffs provided in parentheses (figure from Kleber et al., 2015).

Estimates of mineral-associated OC in permafrost soils range from ~30% (Mueller et al., 2015) to ~80% (Dutta et al., 2006). In permafrost regions, stabilization of OC by poorly crystalline Fe, Al oxy(hydro)xide and metal cations were shown to mitigate OC mineralization and decrease temperature sensitivity of OC towards degradation (Gentsch et al., 2018). In the permafrost region of the Qinghai-Tibetan Plateau, 20% of total OC was associated and protected by Fe (Mu et al., 2016). Mineral OC interactions in permafrost soil significantly decrease permafrost carbon emissions upon thaw since a minor portion of mineral-associated OC can be released as greenhouse gases (Gentsch et al., 2015b).

Mineral protection has been accounted as main regulator for long-term preservation of natural OC in permafrost environments (Hemingway et al., 2019). However, water-driven changes in soil properties may exert strong control over the percentage of OC stored by mineral or the loss of OC previously protected (Kramer and Chadwick, 2018). The evolution of permafrost landscapes into drier or wetter conditions influenced by permafrost degradation may lead to changes in the amount of OC available to microorganisms as DOC (Figure 2.15). Theory and models posit that OC

mineralization declines under elevated moisture and associated anaerobic conditions, leading to soil OC accumulation. Yet, the dissolution of Fe oxides via Fe reduction potentially releases previously protected OC, providing a mechanism for enhanced C destabilization under elevated moisture, especially in persistently waterlogged permafrost soils (Lawrence et al., 2015; Huang and Hall, 2017). Overall, geochemical interactions between soil organic matter and minerals influence decomposition rates in many environments but remain poorly understood in Arctic tundra systems and are not considered in organic matter decomposition models (Herndon et al., 2017). **To the best of our knowledge, the contribution of Fe, Al- and Mn- oxy(hydr)oxides participating in organo-mineral associations or polyvalent metal cations Fe, Al, Mn, and Ca involved in organo-metallic complexes is never considered as a whole.**

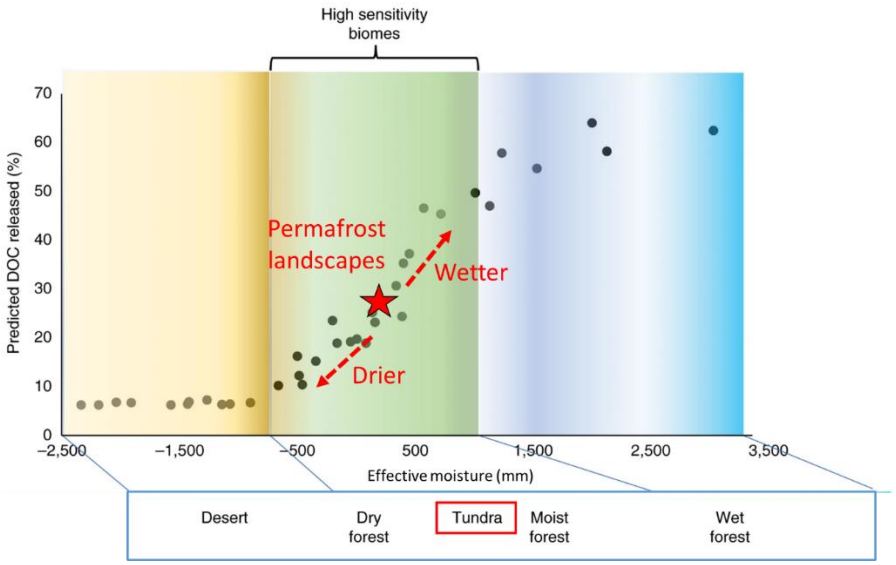

Figure 2.15: Predicted percentage of organic carbon (OC) released as dissolved organic carbon (DOC) by mineral surfaces involved in mineral OC interactions by biome as predicted by effective moisture (difference between mean annual precipitation and potential evapotranspiration, expressed in mm). The figure shows that permafrost landscapes are considered as high sensitivity biomes with potentially different evolution under drier or wetter conditions. Figure adapted from Kramer and Chadwick (2018).

2.6.6 Influence of geochemical conditions in permafrost soils for organic carbon stabilization

Permafrost gradual and abrupt thaw substantially modifies soil or sediment local geochemical conditions. Indeed, active layer deepening, subsidence, thermokarst lake formation and drainage/evaporation induces redox or pH shift. Redox and pH conditions are the main drivers controlling mineral element solubility, oxidation state and hence can trigger metal oxide dissolution or precipitation, and protonation or deprotonation of specific functional groups of organic acids (Keil and Mayer, 2014; Pan et al., 2014; Kleber et al., 2015; Kappler et al., 2021). These conditions will either increase or decrease the potential for OC stabilization.

Redox conditions are affected by thermokarst lake formation or subsidence which modifies the hydrological connectivity of the landscape and leads to wetter or drier areas with alternating oxic and anoxic conditions (Wrona et al., 2016; Vonk et al., 2019). Waterlogged conditions can mitigate oxygen diffusion and promote reduction reactions such as methanogenesis (Herndon, 2018). Anoxic conditions also enhance oxide dissolution and disintegration of aggregates releasing OC but also cations able to form organo-metallic complexes with OC polyfunctional groups. Upon oxic conditions, Fe- and Mn-oxides precipitation and aggregation increases which provides additional stabilizing surfaces to stabilize OC as previously shown in Arctic soils (Herndon et al. (2017); Figure 2.17). The magnitude of the redox processes is determined by soil properties, especially pH. However, the current knowledge of the effects of pH and buffering compounds on the redox chemistry of metal (hydr)oxides and organic matter in soil systems with alternating flooding and drainage conditions is still limited (Pan et al., 2014). The speciation of redox-sensitive elements and hence mineral solubility is governed by redox and acid-base reactions that can be summarized using Pourbaix diagrams (Figure 2.16). In Pourbaix diagrams, pure redox reactions, independent of pH, are indicated by horizontal lines (blue lines; Figure 2.16). The horizontal line between Fe^{3+} and Fe^{2+} represents the reaction:

$$Fe^{3+}_{(aq)} + e^{-} = Fe^{2+}_{(aq)} \quad (Eq.\,2.1)$$

Which has a standard potential of +0.77V. The Pourbaix diagram marks regions where a single species is stable. Similarly, pure acid-base reactions, independent of redox state, are indicated by vertical lines (red lines; Figure 2.16). Reactions that are both acid-base and redox dependent are represented

by slanted lines because of the interdependence between pH and redox potential (Eh). In soils, redox potential can range from -0.3 to +0.7 V, approximatively, with lower values found in permanently waterlogged and reduced soils depleted in O_2 and higher values (Eh > +0.4 V) found in aerated soils (Pearsall and Mortimer, 1939; Fiedler and Sommer, 2004; Mitsch et al., 2013).

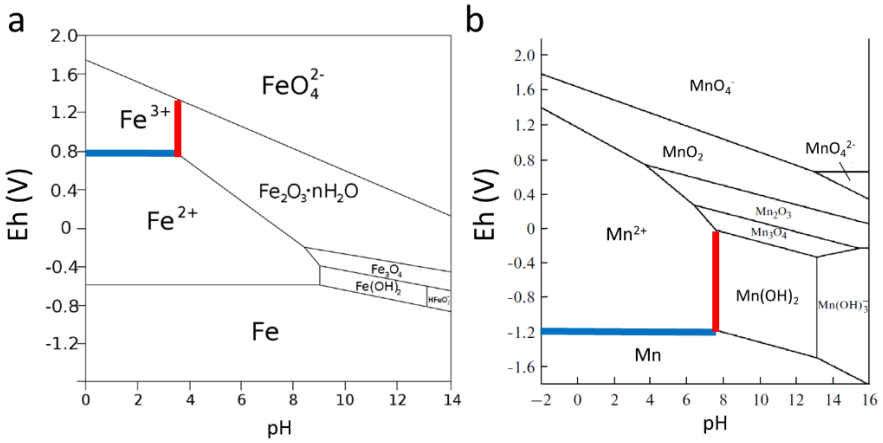

Figure 2.16: Pourbaix diagrams of (a) Fe (10^{-6} M, 25°C) and (b) Mn (1 M, 25°C). Pourbaix diagrams mark regions where a single species is stable. Horizontal lines are pure redox reactions (blue lines) and vertical lines are pure acid-base reactions depending on pH (red lines). Changing soil conditions may shift both redox potential (Eh) and pH (Verink, 2011).

The *pH* of acid soils increases after water saturated conditions because reduction processes consume protons, while the pH of alkaline soils decreases because the increased CO_2 concentration in soil solution resulting from the mineralization of organic matter causes acidification (Pan et al., 2014). The solubility of Fe-bearing minerals is controlled by dissolution–precipitation equilibria, and its extent is dependent on soil pH and ionic strength (Colombo et al., 2014). Active layer deepening or Yedoma deposits abrupt thaw releases soluble cations and poorly weathered loess material more abundant in permafrost relative to the active layer (Kokelj et al., 2002). This may influence pH conditions within the unfrozen portion of soil and the release of basic cations. In addition, this reservoir of primary and secondary minerals in permafrost may increase the abundance of mineral surfaces and cations available to stabilize OC (Figure 2.17). The more acidic conditions in organic-rich layers may increase Fe and Al solubility promoting the formation of organo-metallic complexes at the expense of metal oxides while neutral or

alkaline conditions promote Ca-mediated OC stabilization (Rowley et al., 2018).

Mineral OC interactions were extensively studied in temperate soils and processes are rather well constrained. **However, the quantification, distribution, and fate upon thawing of such mineral OC interactions in permafrost environments are still poorly studied.** Mineral OC interactions can be reversible with changing redox conditions and pH but yet there is a critical lack of data in permafrost soils and sediments vulnerable to thaw. Overall, a better understanding on the processes that influence the stabilization of OC substantial pool in thawing permafrost regions is needed to improve our projections on permafrost carbon emissions at the global scale.

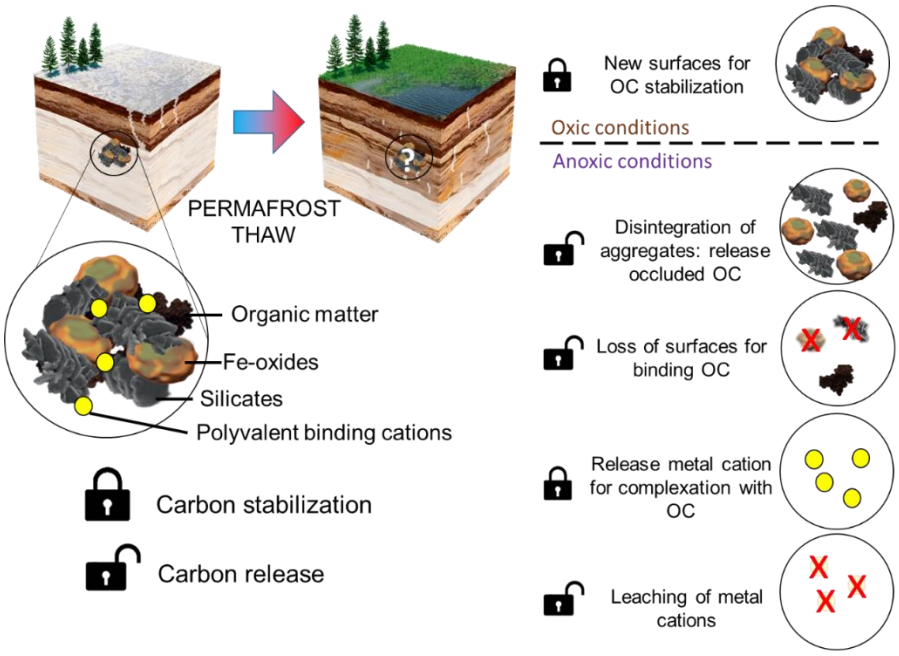

Figure 2.17: Potential evolution of the interactions between organic carbon (OC) and minerals upon permafrost thaw and subsequent changing redox conditions (modified from Opfergelt (2020)).

2.7 Radiogenic strontium isotopes as a source tracer

2.7.1 What is radiogenic strontium isotope?

Radiogenic strontium (Sr) isotopes have wide applications to chemical stratigraphy, geochronology, provenance studies, and studies of temporal changes in Earth surface processes (Capo et al., 1998). Different isotopes of an element have the same atomic number but different atomic mass by virtue of having different numbers of neutrons (Banner, 2004). For example, the oxygen atoms within a sample of rock or water will be characterized with some mixture of the oxygen-16, oxygen-17, and oxygen-18 (i.e., noted ^{16}O, ^{17}O and ^{18}O). The isotopes of oxygen have negligible radioactivity and are thus termed *stable isotopes*. Conversely, a radiogenic isotope is a daughter isotope produced from the decay of a radioactive parent isotope (Figure 2.18). In the element of interest studied here, the long term decay of rubidium-87 (^{87}Rb) produces ^{87}Sr, and so, the relative abundance of this radiogenic isotope, relative to a stable isotope such as ^{86}Sr, varies according to the following equation:

$$\frac{^{87}Sr}{^{86}Sr} = \left(\frac{^{87}Sr}{^{86}Sr}\right)_0 + \frac{^{87}Rb}{^{86}Sr}\left(e^{\lambda_{87}t} - 1\right) \qquad (Eq.\,2.2)$$

where the $(^{87}Sr/^{86}Sr)_0$ ratio is the initial isotope ratio and λ_{87} is the decay constant of ^{87}Rb. A sample with a higher $^{87}Sr/^{86}Sr$ ratio is called more radiogenic, whereas a sample with a lower $^{87}Sr/^{86}Sr$ ratio is called less radiogenic.

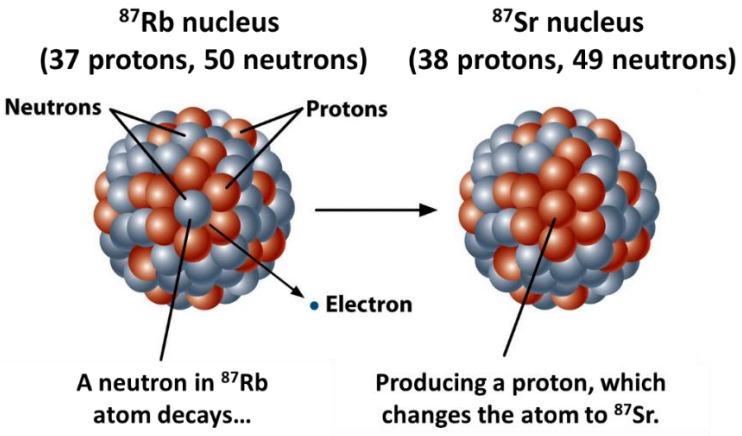

Figure 2.18: The decay of ^{87}Rb to ^{87}Sr with electron loss. The amount of ^{87}Sr is function of the radioactive decay of isotope ^{87}Rb. Image adapted from Grotzinger et al. (2010).

Since Rb and Sr belong to alkali metal and alkaline earth group, respectively, these elements behave differently in geological processes. This results in large variations in the Rb/Sr, and so large variations in the ^{87}Sr/^{86}Sr ratio. Radiogenic Sr isotopes is a powerful tool that is commonly used in studies of chemical weathering and soil genesis, cation provenance and mobility or even the chronostratigraphic correlation of marine sediments (Baskaran, 2011). Strontium (exclusively present in the oxidation state + II) has four naturally occurring stable isotopes (^{84}Sr, 0.56%; ^{86}Sr, 9.87%; ^{87}Sr, 7.04% and ^{88}Sr, 82.53%). All four isotopes are stable, although the fraction of ^{87}Sr varies with radioactive decay of ^{87}Rb. In the modern environment, ^{90}Sr radioactive isotope is produced by fission reactions. Given that isotopes ratios can be measured more precisely than absolute abundances, the stable isotope ^{86}Sr is systematically used as an index of ^{87}Sr enrichment (Capo et al., 1998). The ^{86}Sr is used preferentially to the ^{88}Sr as an index because of the similar abundance of ^{86}Sr and ^{87}Sr about 10% and 7%, respectively. Note that because of the long half time of ^{87}Rb decay (i.e., 4.89 x 10^{10} years) and small abundance, Rb and Sr inventories are considered to be only marginally affected by the radioactive decay of ^{87}Rb.

If Rb and Sr are incorporated into a mineral or rock at its formation and the system remains closed with respect to those elements, the amount of ^{87}Sr increases over time due to ^{87}Rb decay to ^{87}Sr: the amounts of ^{84}Sr, ^{86}Sr and ^{88}Sr being stable. Over geological timescale, rocks of a given age composed of minerals with a high Rb/Sr (e.g., granites in the continental crust), will

develop a higher $^{87}Sr/^{86}Sr$ ratio than minerals with a low Rb/Sr (e.g., oceanic basalt). This is explained by the significant elemental fractionation during the early separation of crust and mantle. Incompatible elements like Rb were excluded from basaltic melts and incorporated into silicic residues (continental crust). Hence, continental crust developed with a larger Rb/Sr ratio than the upper mantle and result in ^{87}Sr enrichment in old continental rocks while low $^{87}Sr/^{86}Sr$ ratios are found in the mantle and rocks derived from it (basalt). The Earth crust and mantle have distinct ranges of Rb/Sr ratios owing their distinct mineral assemblages. Therefore the Sr isotope ratio is characteristic of different rock types. In addition, marine sedimentary rocks will reflect the seawater composition which in turn depends on the relative input from different weathering and hydrothermal vents (e.g., between continental rocks and basalt).

Strontium is a high-mass element and therefore mass-dependent fractionation (i.e., the preferential removal of a specific isotope depending on mass differences resulting in the shift in their relative abundances) from geological, physico-chemical or biological processes is very small compared to the mass-dependent fractionation of low-mass element (e.g., H, C, O, S) (Capo et al., 1998). The reason is that the magnitude of the "mass-dependent" isotope fractionation is high when the relative mass difference between isotopes is high (Hajj et al., 2017): therefore, heavier elements (e.g., Sr) show less mass-dependent fractionation than the lighter elements (e.g., O). The main advantage of this negligible fractionation is that weathering, root assimilation or other processes do not change the original $^{87}Sr/^{86}Sr$ ratio and allow to use radiogenic Sr as a tool for provenance studies (Baskaran, 2011). Hence studies from multiple scientific fields have used radiogenic Sr isotopes (Capo et al., 1998; Alexander Bentley, 2006), including large scale provenance studies based on variations in bedrock and water (Bataille and Bowen, 2012), or provenance studies for weathering in rivers from across Alaska (Brennan et al., 2014).

2.7.2 Radiogenic Sr isotopic variation in terrestrial environments

The $^{87}Sr/^{86}Sr$ ratio in bulk rocks is highly variable according to the rock type, mineralogy and age (Faure, 1977; Capo et al., 1998; Faure and Mensing, 2005). Because Sr easily substitutes to Ca and Rb easily substitutes to K because of similar ionic radius, the $^{87}Sr/^{86}Sr$ ratio of K-bearing minerals is

higher (due to Rb decay in ^{87}Sr) than in Ca-bearing minerals. The higher the Rb/Sr ratio in a mineral, the more radiogenic this mineral will be. Strontium is a fairly soluble element and is re-incorporated only to minor extent to secondary phases (oxides or clays). Since the $^{87}Sr/^{86}Sr$ ratio is not affected by mass-dependent fractionation, Sr^{2+} dissolved in rivers or incorporated in neoformed materials transported as suspended material or colloids, should inherit the signature from minerals undergoing dissolution. Variations of the $^{87}Sr/^{86}Sr$ values in river water depends on the drained bedrock materials (Krishnaswami et al., 1992; Palmer and Edmond, 1992; Hajj et al., 2017; Holland, 2020). Nonetheless, it should be noted that the dissolved $^{87}Sr/^{86}Sr$ ratio is not an exact mirror of the bulk rock undergoing dissolution, as the different minerals within a given rock are subjected to varying weathering rates (Banner, 2004). Some minerals will weather more easily than others and will likely dominate the signature of the solution upon weathering.

In soils, minerals are either derived from erosion or are secondary minerals derived from pedogenic processes, as for oxides, clay minerals or pedogenic carbonates formed upon water-rock interactions. The bulk soil $^{87}Sr/^{86}Sr$ composition is influenced by the signature of the parent material, modified by weathering processes leading to the loss of Sr from the more weatherable minerals (Capo et al., 1998). As a consequence, if easily weatherable minerals have low $^{87}Sr/^{86}Sr$ values, the resulting bulk soil will show higher $^{87}Sr/^{86}Sr$ compared to the parent rock. Conversely, if the easy weatherable minerals have high $^{87}Sr/^{86}Sr$ values, the resulting bulk soil will display lower $^{87}Sr/^{86}Sr$ values than parent rock (Capo et al., 1998). For the secondary weathering products (i.e., oxides), their $^{87}Sr/^{86}Sr$ ratios will be similar to those of the dissolved Sr pool from which they precipitate.

Like many cations, Sr released into soil pore water solution can be adsorbed onto the soil exchangeable complex formed by clay minerals and organic matter. The $^{87}Sr/^{86}Sr$ ratio of the Sr on this exchangeable complex result from a mixing of two main sources: i) the weathering flux from bedrock; and ii) the atmospheric dust deposition input. As a result, the exchangeable Sr isotopic ratio may vary with depth in soil profiles (Chadwick et al., 2009; Bullen and Chadwick, 2016).

2.7.3 Radiogenic Sr isotopes in permafrost environments

In permafrost regions, the use of radiogenic Sr isotopes as a source tracer is particularly relevant to highlight processes following changing soil conditions. The hydrological and soil systems of permafrost regions are dynamic, with seasonal fluctuations and long-term modifications of these systems subsequent to permafrost thaw. Hence multiple studies have used radiogenic Sr isotopes to trace weathering, active layer dynamic, nutrient uptake processes within permafrost regions. For instance, radiogenic Sr isotopes can be used to trace the portion of soil participating in lateral water flow path and can be used as a proxy of active layer thickness dynamic at the catchment scale (Lehn et al., 2017). The modifications in hydrological connectivity which is highly influenced by permafrost degradation can also be investigated using radiogenic Sr isotopes (Bataille and Bowen, 2012; Bataille et al., 2014; Brennan et al., 2014; Streletskiy et al., 2015). Since radiogenic Sr signature varies with depth in permafrost soils, the monitoring of Arctic rivers Sr isotopic signature can be used as an indicator of increasing permafrost thaw depth (Keller et al., 2007, 2010). Similarly, the radiogenic Sr in plants are indicators of their source provenance indicating root assimilation processes (Bagard et al., 2013; Mauclet, 2022). Chemical weathering rates and the main parameters controlling weathering processes in Arctic rivers can be determined using Sr isotopes (Millot et al., 2003; Stevenson et al., 2016). Eventually, Sr isotopes were also used to trace the location of Fe aggregates formation in a permafrost-affected catchment. To do that, the isotopic signature of Sr which co-precipitate upon Fe aggregate formation and then transported by rivers was investigated (Wortberg et al., 2017).

From these studies, **it appears that Sr isotopes represent an ideal tool to test the stability of mineral OC interactions and whether these interactions will be modified upon permafrost thaw**. Indeed, because Sr can adsorb to or be occluded within Fe oxide upon precipitation (Andersson et al., 1994), the radiogenic Sr signature in such mineral OC interactions might give an indication of the Fe oxide stability with changing soil conditions. Upon changing soil conditions, the dissociation between Sr and the mineral OC interactions should release the original Sr in the soil solution and may be substituted upon subsequent association with Sr from the new soil environment of different origin with a potentially different Sr isotopic signature. If this hypothesis is true, a similar Sr isotopic signature in mineral OC interactions before and after changing soil conditions would indicate that

mineral OC interaction bonds with Sr are stable (no dissolution) or that the ultimate Sr from the new soil environment is characterized with similar Sr isotopic signature as the original Sr (Figure 2.19a). However, a change in the isotopic signature of Sr within mineral OC interactions would suggest a dissolution step followed by the adsorption of ultimate Sr from an external source with a contrasting Sr isotopic signature (Figure 2.19b). **With the right methodological approach, one could use radiogenic Sr isotopes to trace the stability of mineral OC interactions with changing soil conditions upon permafrost thaw**.

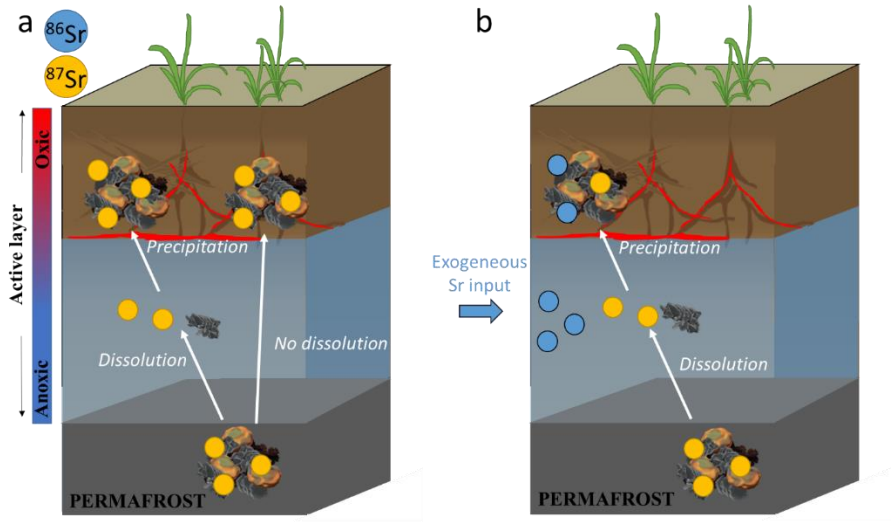

Figure 2.19: Hypothesis of use of Sr isotopes to test the stability of mineral organic carbon interactions upon permafrost thaw. (a) There is no change in the radiogenic Sr signature indicating either no dissolution of the mineral OC interactions or no exogenous inputs of different isotopic signature. (b) The change in isotopic signature within mineral OC interactions indicate a dissolution step and a precipitation step integrating Sr of different isotopic signature.

3. RESEARCH OBJECTIVES AND THESIS OUTLINE

The aim of this PhD thesis is to improve our knowledge on mineral surfaces and cations involved in interactions with organic carbon (OC) in permafrost soils and sediments, and investigate the evolution of mineral OC interactions upon permafrost thaw. The emissions of greenhouse gases from thawing permafrost are considered as a tipping point in Earth climate system but remain poorly quantified. Mineral OC interactions contribute to substantially decrease the proportion of OC likely to contribute to permafrost C emissions. However, there is a gap in knowledge on the fate of these mineral OC interactions upon changing soil conditions arising upon permafrost thaw.

This Ph.D. thesis investigates the following overarching research question: "*What is the influence of permafrost thaw on mineral organic carbon interactions?".* This work offers a comprehensive assessment of mineral OC interactions involving metal oxy(hydr)oxides and organo-metallic complexes in permafrost subjected to abrupt thaw (i.e., thermokarst lake formation and drainage) and gradual thaw (i.e., deepening of the seasonally thawed active layer).

Three specific research questions (**Q1**, **Q2**, **Q3**) have been identified (Figure 3.1):

1. How do mineral organic carbon interactions change with thermokarst lake formation and drainage upon ice-rich permafrost *abrupt thaw*?
2. How do mineral organic carbon interactions change with the deepening of the active layer upon permafrost *gradual thaw*?
3. To what extent can we trace the dissolution-precipitation processes of mineral organic carbon interactions upon both gradual and abrupt thaw?

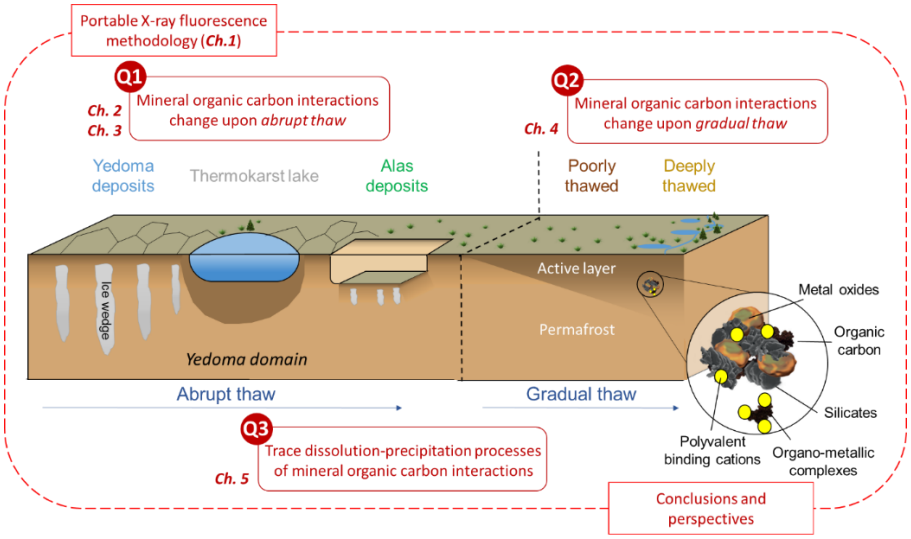

Figure 3.1: Schematic of the thesis outline. The objectives of the study are represented as three research questions (Q1, Q2 and Q3). The Data Chapters are represented (*Ch.1*, *Ch.2*, *Ch.3*, *Ch.4* and *Ch.5*).

To answer these questions, an analytical development was performed to determine mineral element concentration in a large set of permafrost and active layer soil and sediment samples using the X-ray fluorescence (pXRF) method, and this is presented as a methodological data chapter (*Ch.1*).

The Ph.D. thesis is organized in four different parts:

Part I: *General Overview*. This part provides a background on permafrost features development and recent vulnerability towards climate warming. The importance of mineral organic carbon interactions and their mechanisms to protect and stabilize OC from microbial degradation is presented. Eventually, this section also lays the foundations on radiogenic Sr isotopes as a source tracer in Earth surface processes and how useful Sr isotopes are for provenance or cations mobility studies.

Part II: *Material and methods.* This part provides an overview of the sampled material and sampling techniques used in the Yedoma domain and Eight Mile Lake study sites. Then, all methods used along this PhD thesis are presented. Methods further detailed in Data Chapters (Part III) are only briefly described.

Part III*: Data Chapters (Ch.1, Ch.2, Ch.3, Ch.4 and Ch.5).* This part includes the different chapters discussed in order to answer every research question

afore-mentioned. The *Ch.1* is a methodological data chapter dedicated to the validation of pXRF method to accurately assess mineral element concentration in permafrost soils and sediments and includes a first estimation of mineral element stocks within the Yedoma domain (Yedoma domain Mineral Concentration Assessment; YMCA). The *Ch.2* and *Ch.3* are dedicated to assess the influence of abrupt thaw on mineral OC interactions in ice-rich permafrost regions (**Q1**), in the Yedoma domain (*Ch.2*) and at the Siberian site of Yukechi in particular (*Ch.3*). The *Ch.4* investigates the influence on mineral OC interactions of active layer deepening and water table rise due to subsidence upon gradual permafrost thaw at the Alaskan tundra site of Eight Mile Lake (**Q2**). Eventually, the *Ch.5* aims to open a new way to approach the *in situ* tracing of mineral OC interactions precipitation-dissolution processes and the stability of these interactions upon gradual or abrupt permafrost thaw using radiogenic Sr isotopes (**Q3**).

Part IV: *Conclusions and perspectives.* This section summarizes the findings of the Ph.D. thesis and its contribution to the scientific community. This section includes the answer to the three specific research questions raised in the thesis, connects the implications of the different chapters and shares potential perspectives outlined in this work for further investigations.

The Ph.D. thesis is structured as a collection of articles already published (*Ch.1, Ch.2 and Ch.3)* and submitted work *(Ch.4 and Ch.5)*. The different chapters can be read independently, involving some redundancies between the method sections.

Part II
Material and methods

4. MATERIAL

A large number of sites have been investigated in the Ph.D. thesis (23 sites for a total of 1,455 samples; Figure 4.1; Table 4.1). The different chapters either cover multiple sites (22 sites in *Ch.1* and *Ch.2*) or focus on one or couple of specific sites (*Ch.3* - Yukechi; *Ch.4* - Eight Mile Lake; and *Ch.5* - Eight Mile Lake and Duvanny Yar) (Figure 4.2). The materials have been collected i) by the Permafrost Research Section, Alfred Wegener Institute Helmholtz Centre for Polar and Marine Research, Potsdam, Germany (i.e., exclusively in the Yedoma domain) or ii) by the WeThaw group from UCLouvain with which I took part in the sampling campaign of moist acidic tundra soils at Eight Mile Lake watershed, Healy, AK, USA in 2019. Sediment or soil materials from the Yedoma domain were shared by the Alfred Wegener Institute from several decades of sampling campaigns across the Yedoma region in Siberia and Alaska. Since their field campaigns are numerous, we kindly refer the readers to the site-specific publications for detailed description of each study site (Table 4.1). Nonetheless, this section provides a summary of sampling techniques typically used. In addition, study sites are described in details in *Ch.1* and *Ch.2* (Yedoma domain study sites), *Ch.3* (Yukechi), *Ch.4* (Eight Mile Lake) and *Ch.5* (Duvanny Yar and Eight Mile Lake).

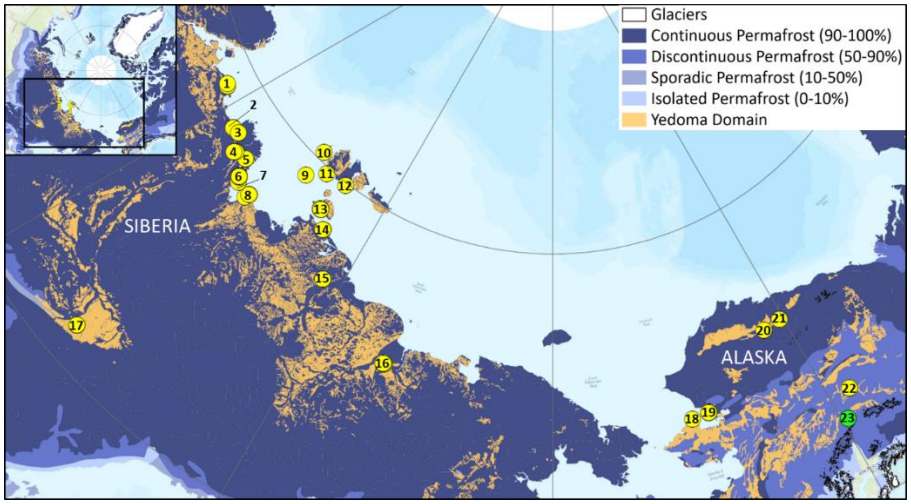

Figure 4.1: Studied permafrost sites from the Yedoma domain (yellow points) and from Eight Mile Lake watershed (green point). 1. Cape Mamontov Klyk; 2. Nagym (Ebe Sise Island); 3. Khardang Island; 4. Kurungnakh Island; 5. Sobo Sise Island; 6. Bykovsky Peninsula; 7. Muostakh Island; 8. Buor Khaya Peninsula; 9. Stolbovoy Island; 10. Belkovsky Island; 11. Kotel'ny Island; 12. Bunge Land; 13. Bol'shoy Lyakhovsky Island; 14. Oyogos Yar coast; 15. Kytalyk; 16. Duvanny Yar; 17. Yukechi; 18. Kitluk; 19. Baldwin Peninsula; 20. Colville; 21. Itkillik; 22. Vault Creek tunnel; 23. Eight Mile Lake (Healy, AK, USA). Permafrost coverage layer is derived from the Circum-Arctic map of permafrost and ground-ice conditions shapefile (Brown et al., 1998). Yedoma domain coverage from Strauss et al. (2016) (Database of Ice-Rich Yedoma Permafrost - IRYP).

Table 4.1: Study sites, coordinates, site label, number of samples characterized by each method, PhD data chapters involving the sites, and site-specific reference publications.

Site Nb	Site Name	Elevation (m a.s.l.)	°N	°E	Label	pXRF method	Alkaline fusion and ICP-OES	Selective extractions	X-ray diffraction	Radiogenic Sr isotopes	Chapters involving	Reference papers
Western Laptev Sea												
1	Cape Mamontov Klyk	30	73.61	117.18	Mak	80	-	-	-	-	1-2	Schirrmeister et al., 2008, 2011
Lena Delta												
2	Nagym (Ebe Sise Island)	25	72.88	123.32	Nag	29	-	-	-	-	1-2	Schirrmeister et al., 2003b
3	Khardang Island	20	72.95	124.21	Kha	31	1	-	-	-	1-2	Schirrmeister et al., 2007, 2011
4	Kurungnakh Island	35	72.33	126.30	Bkh, KUR	143	2	-	-	-	1-2	Schirrmeister et al., 2003b, 2008; Wetterich et al., 2008
Central and Eastern Laptev Sea												
5	Sobo Sise Island	30	72.48	128.27	Sob	58	58	6	13	-	1-2	Fuchs et al., 2018
6	Bykovsky Peninsula	40	71.78	129.43	Mkh, BYK	150	2	-	-	-	1-2	Andreev et al., 2002; Grosse et al., 2007; Schirrmeister et al., 2002, 2011
7	Muostakh Island	20	71.60	129.99	Muo	11	-	-	-	-	1-2	Grigoriev et al., 2003; Schirrmeister et al., 2011
8	Buor Khaya Penisula	35	71.42	132.11	Buo	80	44	9	9	-	1-2	Schirrmeister et al., 2017
New Siberian Archipelago and the Dmitry Laptev Strait												
9	Stolbovoy Island	30	74.06	136.08	Sto	16	1	-	-	-	1-2	Grigoriev et al., 2003; Schirrmeister et al., 2003a
10	Belkovsky Island	15	75.37	135.59	Bel	12	-	-	-	-	1-2	Grigoriev et al., 2003; Schirrmeister et al., 2003a, 2011
11	Kotel'ny Island	20	76.17	139.01	KyS	10	-	-	-	-	1-2	Grigoriev et al., 2003; Schirrmeister et al., 2003a, 2011

Table 4.1: (continued)

Site Nb	Site Name	Elevation (m a.s.l.)	°N	°E	Label	pXRF method	Alkaline fusion and ICP-OES	Selective extractions	X-ray diffraction	Radiogenic Sr isotopes	Chapters involving samples	Reference papers
12	Bunge Land	~10	74.87	142.16	Bun	8	-	-	-	-	1-2	Schirrmeister et al., 2010
13	Bol'shoy Lyakhovsky Island	35	73.30	141.5	TZ, R, L	150	3	-	-	-	1-2	Andreev et al., 2009; Wetterich et al., 2011a, 2014
14	Oyogos Yar coast	30	72.68	143.53	Oy	50	1	-	-	-	1-2	Wetterich et al., 2009; Schirrmeister et al., 2011; Opel et al., 2017
Yakutian inland												
15	Kytalyk	30	70.84	147.45	KY, KH	50	4	6	4	-	1-2	Weiss et al., 2016
16	Duvanny Yar	50	68.63	159.14	DY	143	5	46	-	46	1-2-5	Strauss et al., 2010
17	Yukechi	200	61.76	130.47	Yuk-Yul YY, YA	126	41	39	39	-	1-2-3	Windirsch et al., 2020
Alaska												
18	Kitluk River	~30	66.55	-164.45	Kit	45	2	-	-	-	1-2	Unpublished data ; Wetterich et al., 2012
19	Baldwin Peninsula	~30	66.73	-162.45	Bal	70	1	-	-	-	1-2	Jongejans et al., 2018
20	Colville River	250	69.03	-155.44	Col	23	8	-	3	-	1-2	Grosse et al., 2015 ; unpublished data
21	Itkillik River	85	69.57	-150.32	Itk, It	22	10	-	10	-	1-2	Kanevskiy et al., 2011
22	Vault Creek Tunnel	200	65.03	-147.71	FAI	24	-	-	-	-	1-2	Schirrmeister et al., 2016
23	Eight Mile Lake	700	63.88	-149.25	EML19	124	39	124	19	72	4-5	Osterkamp et al., 2009; Schuur et al., 2009
Total						1,455	222	230	97	118		

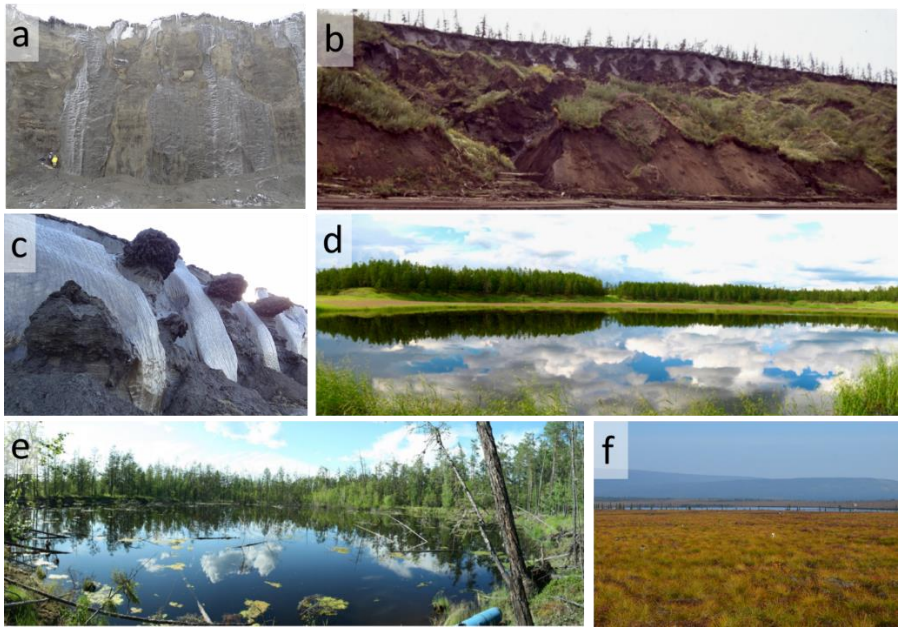

Figure 4.2: Overview of permafrost sites investigated in the Ph.D. thesis: (a) Yedoma deposits exposure at Itkillik, Alaska, USA (photographer: V. Tumskoy); (b) Yedoma deposits and thermokarst mound from Duvanny Yar site, Siberia, Russia (photographer: L. Schirrmeister and S. Wetterich); (c) Yedoma deposits cliff from Sobo Sise Island in the Lena Delta, Siberia, Russia (photographer: J. Strauss); (d) Alas lake and (e) Yedoma lake drilled at the Yukechi site (photographer: M. Ulrich); (f) Tundra from Eight Mile Lake study site, Alaska, USA (photographer: E. Mauclet).

4.1 Yedoma domain sites and sampling protocols

Study sites in eastern Beringia are located on the Alaska North Slope with exposures along the Itkillik and Colville rivers, on the northern part of the Seward Peninsula and western coast of the Baldwin Peninsula, and in the Vault Creek tunnel near Fairbanks in Interior Alaska. In western Beringia, Yedoma exposures and drill cores from numerous coastal and delta sites in the Laptev and East Siberian seas region were studied between 1998 until today, mainly along the Laptev Sea and New Siberian Islands coasts. In addition, Yedoma sites were studied in the Yakutian inland, at the key site of Duvanny Yar in the Kolyma lowlands, at the Kytalyk site in the Yana-Indigirka Lowland, and in Central Yakutia (Figure 4.1; Table 4.1).

4.1.1 Sampling from exposures

In ice-rich permafrost sites from coastal or riverbank regions, sampling usually takes place on cliffs or natural exposure. Cliffs and exposure provide sediment records of substantial depth and hence of substantial paleoenvironmental information back from Pleistocene to the more recent Holocene period. Before the sampling, the outcrop is cleaned up by scratching out the first centimeters of sediments to avoid any contamination from aerosol or mudflow from upper sections in the profile. Samples are collected using hammers, small axes or hand-held drills (Figure 4.3). Typically, vertical position between two samples ranges between 0.5 and 1.0 m intervals. Frozen sediments are placed in plastic bags. The position of the samples along the outcrop is often referred to height above river or sea level using laser theodolite and measuring tapes.

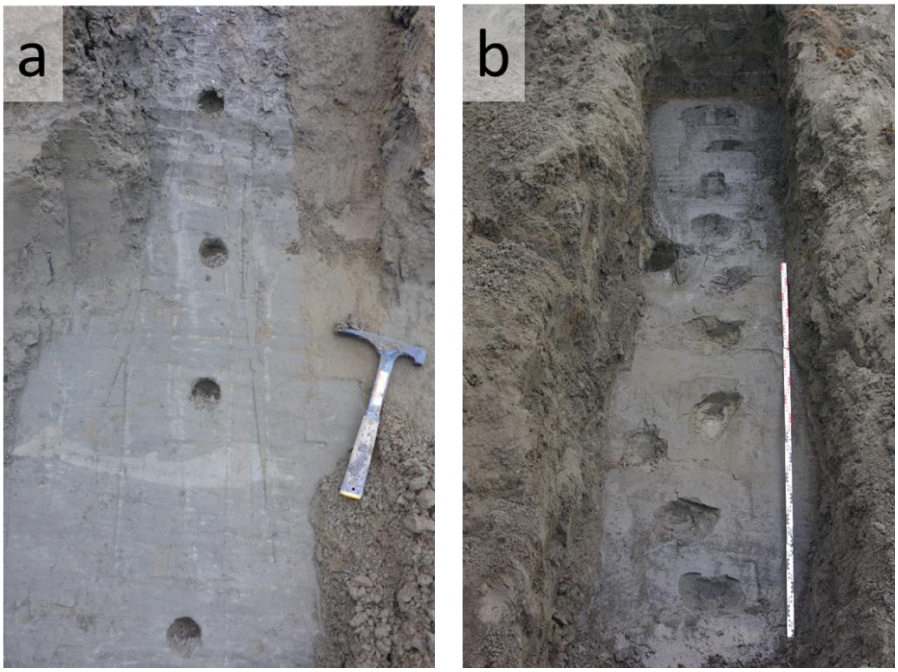

Figure 4.3: Sampling from Yedoma exposure after cleaning the profile and sampling using (a) portable hand-held drill in Baldwin Peninsula (AK, USA) and (b) hammer and axes in Buor Khaya peninsula (Siberia, Russia) (photographer: J. Strauss).

Although the steep permafrost outcrops are generally well exposed, it is often necessary to combine accessible subsections into complete vertical profiles. For instance, in the Duvanny Yar outcrop, no less than eight sub-profiles were combined together to create a complete vertical profile (i.e., DY-01; Figure 4.4). Subsections consist of sediment sequence located between ice-wedges or in still-frozen, undisturbed thermokarst mound (also called baydzherakhs). Limiting factors for accessibility combine steepness of bluffs, overhanging frozen sediment and peat, and extensive mudflows from melting ground ice.

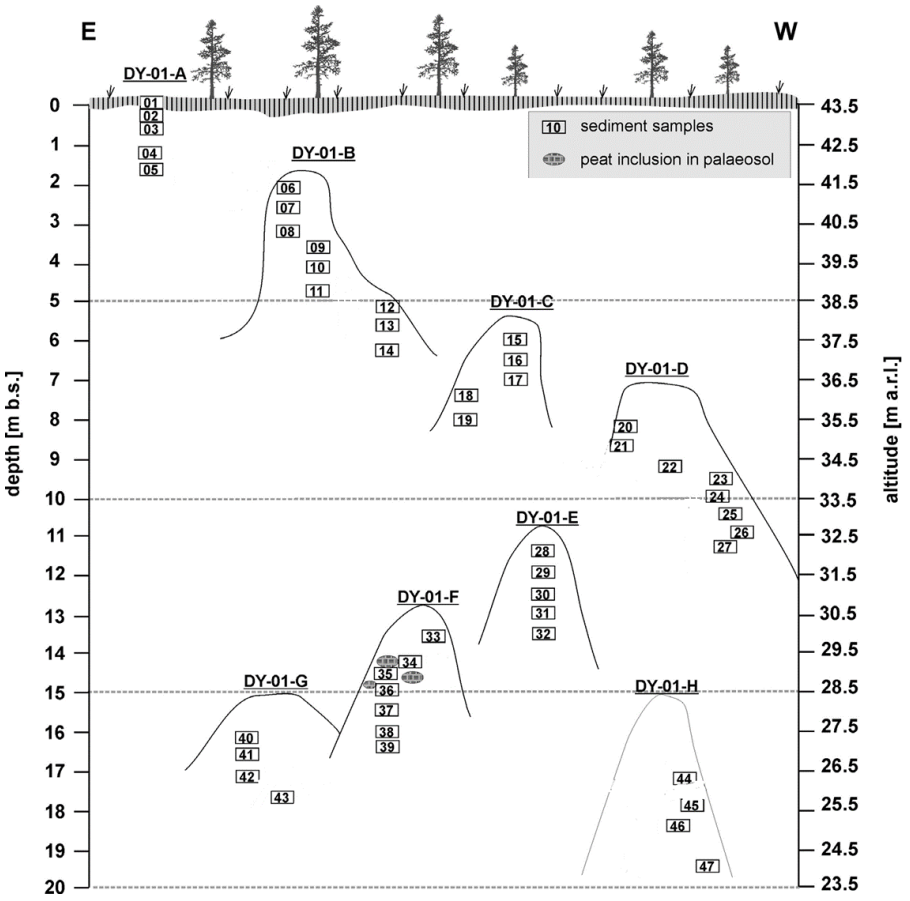

Figure 4.4: Scheme of the composite profile DY-01 from the Duvanny Yar outcrop (Siberia, Russia) with position of the sub-profiles and sample locations (modified from Wetterich et al. (2011b)).

4.1.2 Sampling using drilling ice corer

Where no natural exposure is present, samples are collected using coring techniques. After excavation of the surface layer down to the bottom of the active layer. Fixed-volume samples are collected using a metal cylinder of known volume. After sampling of the active layer, permafrost cores are collected using a drilling SIPRE (Snow, Ice and Permafrost Research Establishment) auger barrel drill. The cores (of varying length for each field campaign) are subdivided in the field in 5 to 10 cm intervals depending on facies horizons (Figure 4.5).

Figure 4.5: Coring technique after SIPRE (Snow, Ice and Permafrost Research Establishment) auger barrel drill and sampling subdivision for a permafrost core in Sobo Sise Island, Siberia (Russia) during 2014 field campaign (photographer: J. Strauss).

4.2 Eight Mile Lake site and sampling protocols

Unlike other sites, Eight Mile Lake is not part of the Yedoma (i.e., ice-rich permafrost) region *stricto senso*, although the EML watershed was reported in the *uncertain* Yedoma confidence class in the updated circum-Arctic Map

of the Yedoma permafrost domain (Strauss et al., 2021b). The site lies at the continuous-discontinuous border. Eight Mile Lake site remained unglaciated during the LGM. The area is characterized with thick peat accumulation over fine-grained soils of loess origin associated with colluvial deposits (Osterkamp et al., 2009). The Eight Mile Lake study site is detailed in *Ch.4* and *Ch.5*.

For active layer and permafrost layers of the Eight Mile Lake watershed, different sampling techniques were used (Figure 4.6). For the unfrozen active layer, samples were collected using chisel and knife in 5 cm increments and stored in plastic bags. Below water table (when chisel and knife was not applicable), soil and sediments were retrieved using a stainless-steel pipe (diameter 44 mm) protected by a metal cap on top, manually hammered down into active layer and permafrost. A thinner steel pipe of 40 mm with full-section was used to push the core out. The core within the steel pipe was subdivided in 10 cm increments and stored in plastic bags. More detailed information on site characteristics and sampling techniques are provided in *Ch.4*.

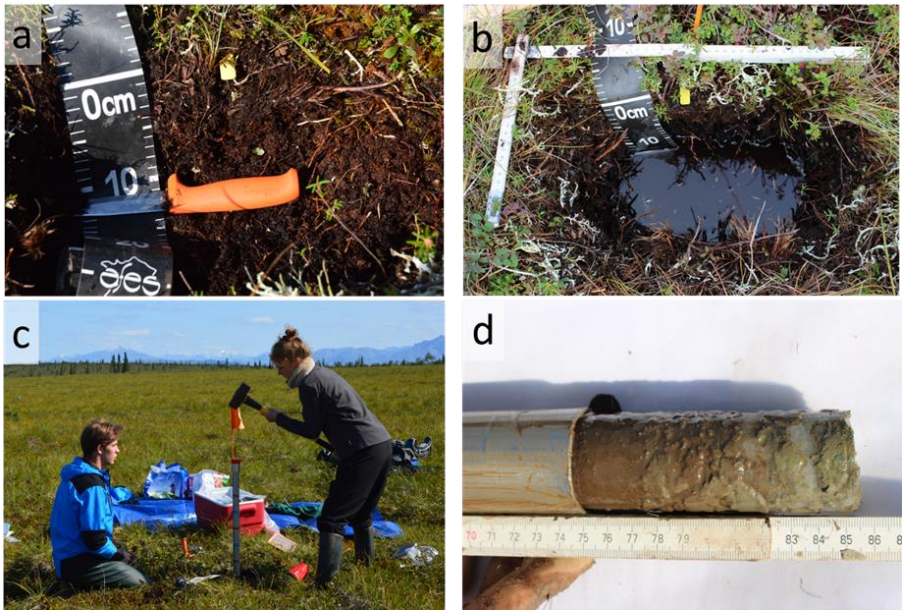

Figure 4.6: Sampling techniques for Eight Mile Lake active layer (a and b) using chisel and knife technique and permafrost retrieval (c and d) using steel pipe technique (photographer: C. Hirst).

5. METHODS

This section briefly overviews the different methods used along the Ph.D. chapters. Many of those methods are extensively detailed in the Data Chapters. The Data chapters in which the methods have been used are summarized (Table 5.1). The analyses were carried out with the "Mineral and Organic Chemical Analysis" (MOCA) analytical platform from the Earth and Life Institute at UCLouvain.

Table 5.1: Overview of the methods used in the different data chapters of the Ph.D. thesis and described in this section. The acronyms are explained in the related sections here below.

	ICP-OES	pXRF	XRD	DCB	Oxalate	Pyro	ODOE and Cp	pH	TOC	Radiogenic Sr isotope
Section	5.1	5.2	5.3	5.4	5.4	5.4	5.5	5.5	5.5	5.6
Ch.1	X	X	X							
Ch.2	X	X		X	X	X	X		X[b]	
Ch.3	X	X	X	X	X	X	X	X	X[c]	
Ch.4	X	X	X[a]	X	X	X	X	X[a]	X	
Ch.5	X	X	X[a]	X				X[a]	X[d]	X

[a] Data available from Mauclet (2022).
[b] Data available from multiple studies (see reference papers from Table 4.1).
[c] Data available from Windirsch et al. (2020); Ulrich et al. (2021).
[d] Data available from Strauss (2010).

5.1 Alkaline fusion and inductively coupled plasma optical emission spectrometry (ICP-OES) for total element concentration

The alkaline fusion and inductively-coupled plasma optical emission spectrometry (ICP-OES) method is extensively detailed in *Ch.1* and briefly detailed here. This method is used to assess mineral element concentration of all element of interest from bulk soil (i.e., total concentration). First, the alkaline fusion is used to dissolve the sample. A portion of milled sample (80 mg) is mixed with lithium metaborate and Li tetraborate and heated for 10 minutes in a pre-heated 1,000°C oven (Chao and Sanzolone, 1992). Upon cooling, a fusion bead is formed and introduced in a HNO_3 2.2N solution heated at 80°C for dissolution. After complete dissolution, the mineral

element concentration in solution is measured by ICP-OES (iCAP 6500 Thermo Fisher Scientific).

The combined alkaline fusion and ICP-OES method was used on 222 samples from both the Yedoma domain and Eight Mile Lake study sites. The samples were selected to span a large range of different lithologies and matrices (organic-rich, carbonate-rich, etc.) in order to calibrate portable X-ray fluorescence measurement on a wide variety of soil and sediment samples from the permafrost region (Sect. 5.2).

5.2 Portable X-ray fluorescence for total element concentration

The portable X-ray fluorescence (pXRF) method is extensively detailed in *Ch.1* and briefly detailed here. This method allows to measure mineral element concentration of all element of interest from bulk soil. This technique stands out from the alkaline fusion and ICP-OES measurement by its minimal pre-treatment and rapid analytical procedure. For the pXRF measurement, a few grams of sample are placed in a circular plastic cap (2.5 cm diameter) provided with a thin 4 µm prolene film at its base (Shand and Wendler, 2014; Ravansari and Lemke, 2018). The sample is placed on a measuring lead stand with the plastic film in close contact with the pXRF instrument *Niton XL3t GOLDD+* (Thermo Fisher Scientific, Waltham, USA). The pXRF is fixed to the lead stand with the X-ray beam directed in the upward direction (Figure 5.1). The high energy beam excites atoms present in the sample from which some electrons are ejected. This electron loss destabilizes the overall atom from which an electron from outer orbitals moves to lower energy orbitals releasing energy in the form of fluorescence. This fluorescence is specific to each atom and detected by the pXRF device. The fluorescence (measured as count per second) is converted to concentration in mg kg^{-1} for elements from Mg to U. Portable X-ray fluorescence concentrations must be corrected with another method where trueness is validated using certified reference material.

The pXRF method was used to accurately assess mineral concentrations of ten elements (Si, Al, Fe, Ca, K, Ti, Mn, Zn, Sr, and Zr) on 1,331 samples from the Yedoma domain and 124 samples Eight Mile Lake study sites. The mineral concentrations measured by pXRF were corrected using alkaline fusion and

ICP-OES method (Sect. 5.1). The corrected pXRF concentrations are used in every chapter of the Ph.D. thesis (*Ch.1* to *Ch.5*).

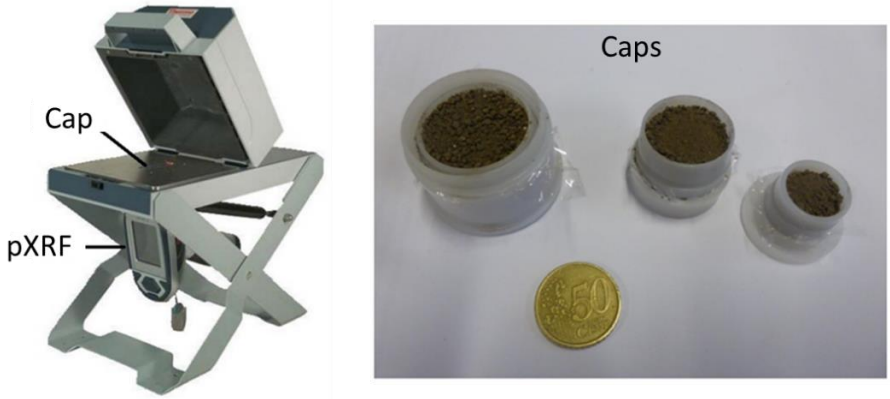

Figure 5.1: Illustration of the lead stand and portable X-ray fluorescence (pXRF) device pointing in the upward direction. The circular plasic cap is filled with soil or sediment sample and placed on the lead stand. Once the lid of the lead stand is closed, the measurement can start.

5.3 X-ray diffraction (XRD) to characterize soil mineralogy

The X-ray diffraction (XRD) method allows the characterization of the presence of crystalline mineral phases. The mineralogy of bulk samples was determined on finely ground soil or sediment fixed using toluene on a flat smooth reflecting surface and introduced in the XRD instrument (Bruker Advance D8, Cu Kα, I = 0.15418 nm, 40 kV, 30 mA, 2θ min^{-1}, detection limit 5%). Diffraction spectra were analyzed with DiffracPlus EVA© software version 10.0.0.3 and the PDF-2 (International Centre for Diffraction Data, 2013) and EVA©-embedded DiffracPlus Reference databases (Mineral and Master datasets) using peak fitting method. The X-ray diffraction method was used on 39 samples from the Yedoma domain (*Ch.*1) with additional 39 samples from Yukechi site (*Ch.3*) and 19 samples from Eight Mile Lake site (Mauclet, 2022).

5.4 Selective extractions to identify crystalline and amorphous oxides or complexed metals

The selective extractions used i) dithionite-citrate-bicarbonate (DCB; Mehra and Jackson, 1960), ii) ammonium oxalate (Blakemore et al., 1981), and iii) sodium pyrophosphate (Bascomb, 1968; Parfitt and Childs, 1988) are extensively detailed in *Ch.2* and summarized here. The DCB extraction mixes 0.75 g of milled sediment/soil sample with sodium citrate $Na_3C_6H_5O_7$ $2H_2O$ solution buffered with 0.3 M sodium bicarbonate $NaHCO_3$. Sample is placed on hot bath (80°C) and dithionite ($Na_2S_2O_4$; three times 0.75 g) is added while stirring. Rinsing with NaCl three times is done for complete extraction. The oxalate extraction mixes 0.4 g of milled sediment/soil sample with ammonium oxalate ($(NH_4)_2C_2O_4$ H_2O) and oxalic acid ($H_2C_2O_4$ $2H_2O$). The tubes are agitated in the dark for four hours at room temperature and centrifuged at 2,000 rpm for 10 minutes. The pyrophosphate extraction mixes 0.4 g of milled sediment/soil sample with sodium pyrophosphate ($Na_4P_2O_7$ $10H_2O$) 0.1M. Tubes are agitated for 16 hours at room temperature and centrifuged at 4,000 rpm for 30 minutes. All sample solutions were filtered (Whatmann 41; 20µm retention size) prior to ICP-OES measurement for metals element concentrations investigated in the Ph.D. thesis (Fe, Mn, Al, Ca and Sr).

Selective extractions were used on 106 samples from Yedoma domain and 124 samples from Eight Mile Lake study sites. Selective extractions are used in *Ch.2* (Yedoma domain), *Ch.3* (Yukechi site), *Ch.4* (Eight Mile Lake site) and *Ch.5* (Duvanny Yar site).

5.5 Other soil characterization methods

5.5.1 Organic acids within selective extractions

In the solution extracted with ammonium *oxalate*, we measured the presence of organic acids via an indirect method. The optical density of the oxalate extract (ODOE) is measured by absorbance at 430 nm on a Genesys 10 S VIS spectrophotometer using the oxalate solution as a blank (Daly, 1982). The higher the absorbance, the higher the proportion of organic acids within the solution. In the solution extracted with sodium *pyrophosphate*, we measured the concentration of dissolved organic carbon released after dispersion of

organo-metallic complexes using a Shimadzu (TOC-L) analyzer. The limit of detection is 0.1 mg L^{-1} and precision is 2%. Repetitions on permafrost samples and standard deviations are presented in *Ch.3*. These two methods were used on identical samples as the one for selective metal extractions (106 samples from the Yedoma domain and 124 samples from the Eight Mile lake study site; *Ch.2*, *Ch.3*, *Ch.4*).

5.5.2 Soil pH

The soil pH_{H2O} and pH_{KCl} were measured with the pH probe (Inlab micro) connected to the pH-meter (Mettier Toledo SevenCompact DuoS213). Samples were mixed with a 1:5 solid:solution ratio with H_2O or 1M KCl solution (Page et al., 1982). The pH probe was calibrated to pH 4 and pH 7 before measurement. The pH data are used in the *Ch.3* (n = 39) and in the *Ch.4* (n = 87) on samples from Eight Mile Lake.

5.5.3 Total organic carbon (TOC) content

The total organic carbon (TOC) content was measured with the C, N, S elemental analyzer vario El Cube (Elementar, Germany). Dried samples are finely milled (~5 µm powder) and 5-7 mg is loaded in the analyzer. Each sample is flushed with carrier gas (oxygen and helium) to remove atmospheric nitrogen. During the catalytic combustion (1,200°C), carbon is oxidized to carbon dioxide, separated from other gases by gas chromatography and analyzed through a thermal conductivity detector. Each sample is measured twice and the average standard deviation for C content is ~5% and the detection limit is <0.1%. Total C measurements are expressed as weight percentage (i.e., wt%) in reference to the soil dry weight at 105°C. As the presence of carbonate was not detected by XRD for the sample characterized for TOC, the total soil carbon content is considered equivalent to soil organic carbon content. Total soil organic carbon content was measured on 124 samples from Eight Mile Lake study site (*Ch.4*) and available from reference papers for samples from the Yedoma domain (Table 4.1).

5.6 Radiogenic Sr isotope measurement

5.6.1 Multicollector- ICP-MS principle

The multicollector - inductively coupled plasma - mass spectrometer (MC-ICP-MS) is a double focusing, high-resolution mass spectrometer for high precision isotope ratio measurements used in *Ch.5*. The Neptune Plus™ High resolution Multicollector-ICP-MS (Thermo Fisher Scientific, Waltham, USA) used for this thesis is located at the Earth and Life Institute from UCLouvain. Mass spectrometry is the detection of ionized particles (ions, molecules) of different mass. The mass difference of two isotopes of a same element conferred by different numbers of neutrons (for instance ^{86}Sr and ^{87}Sr) makes mass spectrometry capable to determine isotopic ratios (i.e., the relative abundance of the two different isotopes). To do that, the MC-ICP-MS instrument is composed of four different modules i) the inductively coupled plasma (ICP) module, ii) the electrostatic analyzer (ESA) module, iii) the magnet module and iv) the multicollector module, each dedicated to a specific task: ionize, focus, separate by mass and detect particles of varying mass relative to each other (Figure 5.2).

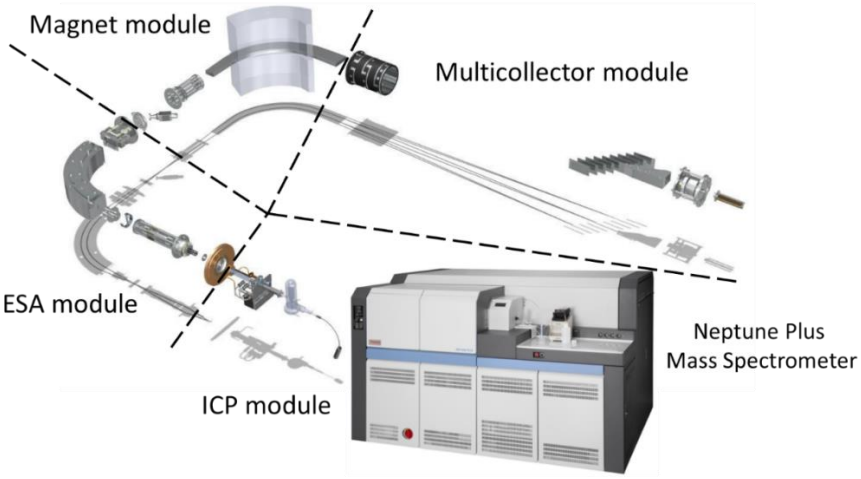

Figure 5.2: Illustration of the Neptune Plus™ High resolution multicollector ICP-MS (Thermo Fisher Scientific) and internal composition of the instrument with the inductively coupled plasma (ICP) module, the electrostatic analyzer (ESA) module, the magnet module and the multicollector module (image adapted from Thermo Fisher Scientific, 2018).

The *ICP module* covers the hardware related to plasma and ion generation. Its role is to provide a sustained amount of energy (> 8,000°C) and to ionize isotopes to be measured. The sample (always liquid for this Ph.D. thesis) is continuously fed into a nebulizer, where an argon/sample mixture aerosol is generated with usually low efficiency (< 5% of the sample is converted in fine droplets introduced in the plasma). The spray chamber eliminates the larger droplets so that only very fine aerosol mixture is injected in the center of the plasma torch. The aerosol is instantly desolvated and ionized.

The *ESA module* role is to focus and accelerate the ions through a combination of lenses, slits and voltage difference. A high voltage between the ion source and analyzer is needed. In the Neptune Plus MS, the plasma source is at ground potential and the analyzer at high voltage (10 kV). The higher the accelerating voltage, the better the mass separation in the magnet.

The *magnet module* is used to separate the different isotopes relative to their mass using a magnetic field.

$$\mathrm{r} = \frac{1}{\mathrm{B}}\sqrt{\frac{2\mathrm{Um}}{\mathrm{q}}} \rightarrow r = \frac{m \times v}{q \times B} \quad (Eq.\,5.1)$$

The equation (Eq. 5.1) means that with constant field strength (B) and accelerating voltage (U), the radius (trajectory of the particle) depends on the ion's mass (m) and charge (q). The modulation of field strength is used so that the dispersion of ions beam is directed to the detector. All spectrometers operate at very low pressure to allow for free movement of ions. Here, focusing ions, mass separation and mass detection takes place in the high vacuum ($<10^{-9}$ mbar).

The *multicollector module* is composed of nine independent detectors (i.e., Faraday cups) that allow the simultaneous measurement of up to nine isotopes. Cups are mobile (with the exception of the central cup) to adjust to the expected position of a given isotope. When the charged ion enters a Faraday cup, the charge is neutralized by inducing a current through the resistor and recorded as a change of voltage. The more charged particle of a specific isotope is hitting the detector, the higher the voltage. With multiple Faraday cups, the signals of isotope presence are collected simultaneously and the signal measured reflects time-specific background noise from the instrument. For instance, intensity variations caused by plasma flicker are cancelled out

and allow to be much more precise than signals from each isotope being collected at two different moments.

5.6.2 Radiogenic Sr isotope measurements with Neptune Plus TM High Resolution Mass Spectrometry

Strontium isotopes (^{84}Sr, ^{86}Sr, ^{87}Sr and ^{88}Sr) measurements can interfere with the presence of isotopes from similar mass elements such as krypton (^{84}Kr and ^{86}Kr) or rubidium (^{86}Rb and ^{87}Rb). To correct for such interferences, the ^{83}Kr isotopes are measured and allow to infer for ^{84}Kr and ^{86}Kr since $^{83}Kr/^{84}Kr$ ratio (0.201750) and $^{84}Kr/^{86}Kr$ (0.664740) are known. Similarly, ^{85}Rb is measured to subtract the ^{87}Rb interference ($^{85}Rb/^{87}Rb$ = 2.592310). Thanks to the multiple detectors, each isotope is measured simultaneously with the following cup configuration (Table 5.2).

Table 5.2: Configuration of the Faraday cups for the Sr isotopes measurements with the Neptune MC-ICP-MS. Isotopes that interfere with Sr isotopes are in bold character. The Faraday cups are named according to their position: central cup (C), heavy cups (H) or light cups (L).

Sr isotopes			^{84}Sr		^{86}Sr	^{87}Sr	^{88}Sr		
Interferences	^{82}Kr	^{83}Kr	**^{84}Kr**	^{85}Rb	**^{86}Kr** **^{86}Rb**	**^{87}Rb**			
Faraday cup	L4	L3	L2	L1	C	H1	H2		

Part III
Data chapters

6. Chapter 1: Mineral element stocks in the Yedoma domain: a novel method applied to ice-rich permafrost regions

This chapter is a modified version of a research paper published in Frontiers in Earth Science special collection "Yedoma Permafrost Landscapes as Past Archives, Present and Future Change Areas":

Monhonval A, Mauclet E, Pereira B, Vandeuren A, Strauss J, Grosse G, Schirrmeister L, Fuchs M, Kuhry P and Opfergelt S (2021) Mineral Element Stocks in the Yedoma Domain: A Novel Method Applied to Ice-Rich Permafrost Regions. Front. Earth Sci. 9:703304. doi: 10.3389/feart.2021.703304.

Data produced in this chapter are available in the Pangaea repository:

Monhonval, Arthur; Opfergelt, Sophie; Mauclet, Elisabeth; Pereira, Benoît; Vandeuren, Aubry; Grosse, Guido; Schirrmeister, Lutz; Fuchs, Matthias; Kuhry, Peter; Strauss, Jens (2020): Yedoma domain Mineral Concentrations Assessment (YMCA). PANGAEA, https://doi.org/10.1594/PANGAEA.922724.

Abstract

With permafrost thaw, significant amounts of organic carbon (OC) previously stored in frozen deposits are unlocked and become potentially available for microbial mineralization. This is particularly the case in ice-rich regions such as the Yedoma domain. Excess ground ice degradation exposes deep sediments and their OC stocks, but also mineral elements, to biogeochemical processes. Interactions of mineral elements and OC play a crucial role for OC stabilization and the fate of OC upon thaw, and thus regulate carbon dioxide and methane emissions. In addition, some mineral elements are limiting nutrients for plant growth or microbial metabolic activity. A large ongoing effort is to quantify OC stocks and their lability in permafrost regions, but the influence of mineral elements on the fate of OC or on biogeochemical nutrient cycles has received less attention and there is an overall lack of mineral element content analyses for permafrost sediments. Here, we combine portable X-ray fluorescence (pXRF) with a bootstrapping technique to provide (i) the first large-scale Yedoma domain Mineral Concentrations Assessment (YMCA) dataset, and (ii) estimates of mineral element stocks in never thawed (since deposition) ice-rich Yedoma permafrost and previously thawed and partly refrozen Alas deposits. The pXRF method for mineral element quantification is non-destructive and offers a complement to the classical dissolution and measurement by optical emission spectrometry (ICP-OES) in solution. Using this method, mineral element concentrations (Si, Al, Fe, Ca, K, Ti, Mn, Zn, Sr and Zr) were assessed on 1,292 sediment samples from the Yedoma domain with lower analytical effort and lower costs relative to the ICP-OES method. The pXRF measured concentrations were calibrated using alkaline fusion and ICP-OES measurements on a subset of 144 samples (R^2 from 0.725 to 0.996). The results highlight that (i) the mineral element stock in sediments of the Yedoma domain (1,387,000 km^2) is higher for Si, followed by Al, Fe, K, Ca, Ti, Mn, Zr, Sr, and Zn, and that (ii) the stock in Al and Fe (598 ± 213 and 288 ± 104 Gt) is in the same order of magnitude as the OC stock (327-466 Gt).

6.1 Introduction

The ice-rich deposits of the Yedoma domain hold more than 25% (213 Gt) of the frozen organic carbon (OC) of the northern circumpolar permafrost region, while covering only about 8% of its total soil area (c. 1.4 of 17.8 million km²; Schirrmeister et al., 2013; Hugelius et al., 2014; Strauss et al., 2017). This carbon- and ice-rich region is particularly vulnerable to abrupt thawing processes (Nitzbon et al., 2020; Turetsky et al., 2020). This is the reason why Yedoma deposits are considered as a potential "tipping element" for future climate warming (Lenton, 2012). The key features of Yedoma deposits relative to other permafrost deposits are (i) their ground ice properties, with 50-90% volume percent ice (Schirrmeister et al., 2013) and (ii) their large spatial extent and thickness, resulting in a large total volume (Strauss et al., 2017). Thawing of ice-rich sediments has severe geomorphological consequences for the landscape (Kokelj and Jorgenson, 2013). Striking examples are collapsing river and coastal bluffs (Günther et al., 2015; Kanevskiy et al., 2016; Fuchs et al., 2020). But a spatially more important process is thermokarst lake formation, caused by surface subsidence due to excess ground ice melting in Yedoma deposits and leading to the formation of vast thermokarst depressions. The process not only affects the superficial soil horizons but also deep mineral horizons (Strauss et al., 2013; Walter Anthony et al., 2018). Thermokarst processes were highly active during the Deglacial and early Holocene period (Walter et al., 2007; Brosius et al., 2021) and shaped the Yedoma domain region with numerous lakes. Following drainage of lakes, a widespread process across lake-rich lowlands (Grosse et al., 2013), renewed permafrost aggradation and new soil development could occur in the drained thermokarst lake basins also called Alas. The Yedoma domain therefore includes Yedoma deposits never affected by thaw and frozen deposits that accumulated after Yedoma degradation in Alas landforms (Olefeldt et al., 2016; Strauss et al., 2017).

In permafrost soils, between ~30% (Mueller et al., 2015) and ~80% (Dutta et al., 2006) of the total soil OC is associated to minerals through various mechanisms, as detailed below. It is well known that interactions between minerals and OC can have a stabilizing effect on OC (Kaiser and Guggenberger, 2003; von Lützow et al., 2006; Kögel-Knabner et al., 2008; Kleber et al., 2015; Gentsch et al., 2018; Wang et al., 2019). Mineral-protected OC is less bioavailable than mineral free OC (Schmidt et al., 2011; Kleber et al., 2015), thereby contributing to the long term carbon storage (Hemingway

et al., 2019). Mineral protection of OC includes aggregation, adsorption and/or complexation or co-precipitation processes (Kaiser and Guggenberger, 2003). These protection mechanisms involve i) clay minerals, Fe-, Al-, Mn-oxy(hydr)oxides, or carbonates (aggregation); ii) clay minerals and Fe-, Al-, Mn-oxy(hydr)oxides using polyvalent cation bridges such as Fe^{3+}, Al^{3+}, Ca^{2+} or Sr^{2+} (adsorption); or iii) Fe^{3+}, Fe^{2+} and Al^{3+} ions (complexation). In addition, mineral elements (e.g., Si, Al, Fe, Ca, K, Mn, Zn, Sr) drive nutrient supply to plants or microorganisms, including algae such as diatoms. Nutrient supply is essential for plants growth and/or microbes metabolic activity and therefore indirectly influences C storage or degradation. It remains however unclear how mineral OC interactions and nutrient supply will evolve upon permafrost thaw (Opfergelt, 2020), especially in ice-rich permafrost regions. This is mainly due to a lack of knowledge about the mineral element content in permafrost regions, relative to the well-known OC stocks in permafrost soils (Harden et al., 2012; Hugelius et al., 2014, 2020; Strauss et al., 2017; Kuhry et al., 2020) and the increasing knowledge on N stocks (Fuchs et al., 2018, 2019; Fouché et al., 2020; Hugelius et al., 2020).

To improve our understanding on the potential effects mineral elements can have on OC from permafrost regions, it is essential to have better knowledge on mineral element stocks in these regions, and on the changes in mineral element stocks upon thawing with changing conditions for mineral weathering (Zolkos and Tank, 2020). Ice-rich permafrost regions are particularly well suited areas to study the impact of thawing processes on the mineral elemental stocks in deposits. Indeed, "never" (since deposition) thawed deposits can be compared with previously thawed deposits resulting from thermokarst processes during warmer and wetter periods in the Deglacial and early Holocene periods (13 to 9 ka BP; Morgenstern et al., 2013; Walter et al., 2007). Assessing the evolution of the mineral element stocks between never thawed (since deposition) and previously thawed, refrozen as well as newly formed deposits will contribute to a better understanding of the impact of past thawing processes on the evolution of the pool of mineral elements available for mineral OC interactions. It also provides insights into how ongoing permafrost thaw and thermokarst processes may impact mineral elements and what the potential implications are for the fate of OC in ice-rich deposits (Strauss et al., 2017). This is particularly relevant given that thermokarst processes are projected to spread across the Arctic and will potentially unlock additional OC stocks (Lacelle et al., 2010; Abbott and Jones, 2015; Schneider von Deimling et al., 2015; Nitzbon et al., 2020; Turetsky et al., 2020).

The objective of this study is to provide a method to assess the mineral element content on a large sample set in order to cover the different types of deposits from the Yedoma domain. Using this method, we provide a Yedoma domain Mineral Concentrations Assessment (YMCA) dataset for ten mineral elements (Si, Al, Fe, Ca, K, Ti, Mn, Zn, Sr, and Zr) and the stocks for these mineral elements in deposits from ice-rich permafrost regions. This assessment comprises "never" thawed since syngenetic freezing Yedoma Ice Complex deposits (in the following referred as Yedoma) and at least once previously thawed and then refrozen drained thermokarst lake basin deposits (in the following referred as Alas).

6.2 Materials

6.2.1 Environmental settings

The Yedoma domain is part of the permafrost region characterized by organic- and ice-rich deposits as well as thermokarst features. Today, the Yedoma domain predominantly covers areas in Siberia and Alaska (Figure 6.1) which were not covered with ice sheets during last glacial period (110 ka – 10 ka BP; Schirrmeister et al., 2013).

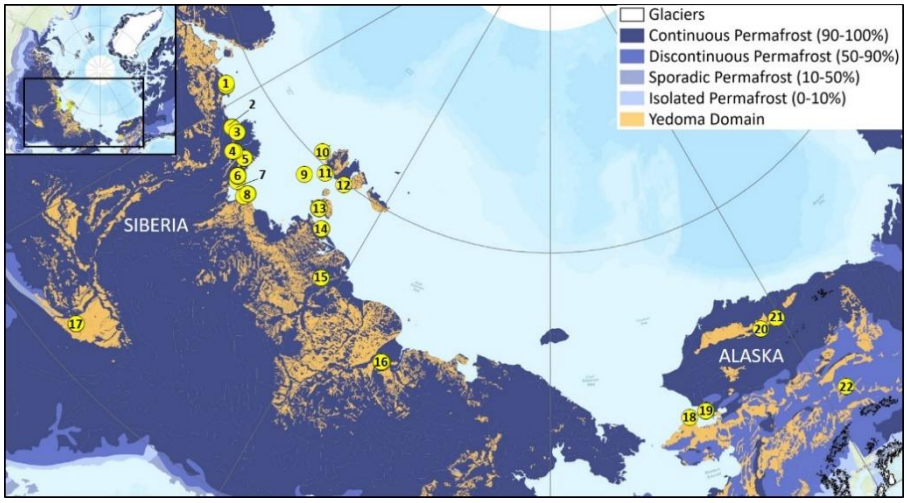

Figure 6.1: Studied permafrost sites from the Yedoma domain. 1. Cape Mamontov Klyk; 2. Nagym (Ebe Sise Island); 3. Khardang Island; 4. Kurungnakh Island; 5. Sobo Sise Island; 6. Bykovsky Peninsula; 7. Muostakh Island; 8. Buor Khaya Peninsula; 9. Stolbovoy Island; 10. Belkovsky Island; 11. Kotel'ny Island; 12. Bunge Land; 13. Bol'shoy Lyakhovsky Island; 14. Oyogos Yar coast; 15. Kytalyk; 16. Duvanny Yar; 17. Yukechi; 18. Kitluk; 19. Baldwin Peninsula; 20. Colville; 21. Itkillik; 22. Vault Creek tunnel. Permafrost coverage layer is derived from the Circum-Arctic map of permafrost and ground-ice conditions shapefile (Brown et al., 1998). Yedoma domain coverage from Strauss et al. (2016) (Database of Ice-Rich Yedoma Permafrost - IRYP).

Recent estimates indicate that the current Yedoma domain has an extent of ~1.4 million km² and contains between 327 – 466 Gt OC (Strauss et al., 2017). Frozen deposits from the Yedoma domain alone store probably at least as much carbon as the tropical forest biomass (Lai, 2004). These deposits were formed by long-term continuous sedimentation and syngenetic freezing. Yedoma deposits were first described as homogeneous silty fine, ice-, and organic-rich sediments derived from aeolian processes (i.e., loess or loess-related deposits) (Murton et al., 2015; Pewe and Journaux, 1983; Tomirdiaro and Chernen'kiy, 1987). Current evidence indicates that depositional processes are polygenetic including alluvial and aeolian deposition and re-deposition, as well as *in situ* weathering during the late Pleistocene cold stages (Konishchev and Rogov, 1993; Schirrmeister et al., 2013). Despite evidence of homogeneity of Yedoma deposit aggradation, grain-size analyses show the large diversity of Yedoma deposits, pointing at multiple origins and transport pathways of sediments as well as a diverse interplay of (post)depositional sedimentary processes (Strauss et al., 2012; Schirrmeister et al., 2020; Sizov et al., 2020). For tens of millennia, continuous sedimentation led to the

accumulation of several tens of meters thick permafrost deposits with characteristic syngenetic ice-wedge formation. Harsh, cold late Pleistocene winter climate triggered the formation of vertical frost cracks within surface deposits in which snow melt water percolated during spring and refroze into vertical ice veins in the permafrost. Over time and with annual repetition of this process, many meters wide and up to 40 m high ice-wedges were formed. Those large volumes of icy sediments together with the rise in temperature during the Holocene Thermal Maximum (HTM between 11-5 ka BP depending on the region; HTM reached at 7.6 - 6.6 ka BP in North Alaska and variable with time in Siberian regions) (Velichko et al., 2002; Kaufman et al., 2004; Porter and Opel, 2020) lead to a vast reshaping of the landscape with formation of thermokarst lakes and drained Alas basins (Grosse et al., 2013). Alas deposits in drained thermokarst lake basins are composed of reworked Yedoma deposits as well as Holocene accumulation during sub-aquatic and sub-aerial phases (Strauss et al., 2017; Windirsch et al., 2020). The Yedoma domain area includes 30% of unthawed Yedoma deposits composed of homogeneous silty deposits with polygenetic origins (eolian, alluvial or colluvial deposition) between large ice-wedges. Alas deposits have experienced thawing processes and drainage during early Holocene until more recently and account for 56% of the Yedoma domain area. Deltaic deposits (4%) as well as lakes and rivers (10%) complete the Yedoma domain deposits area distribution (Figure 6.2).

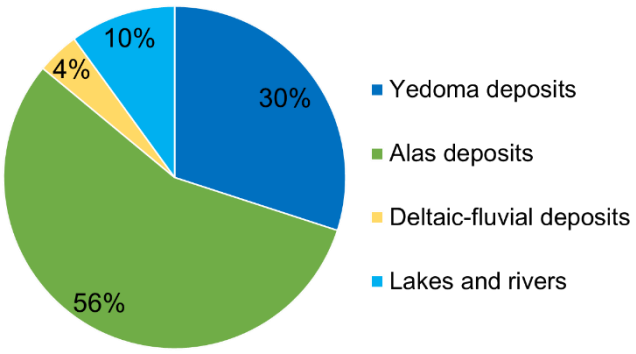

Figure 6.2: Distribution of the area coverage (percentage) in the Yedoma domain region. The total Yedoma domain area is estimated at 1,387,000 km² (based on Strauss et al., 2017).

In this study, mineral element stocks are evaluated in Yedoma and Alas deposits (for a mean deposit thickness of 19.6 m and 5.5 m, respectively; Figure 6.3a), but the evaluation does not include sediments underlying extant thermokarst lakes, active layer sediments or fluvial sediments (Figure 6.3b).

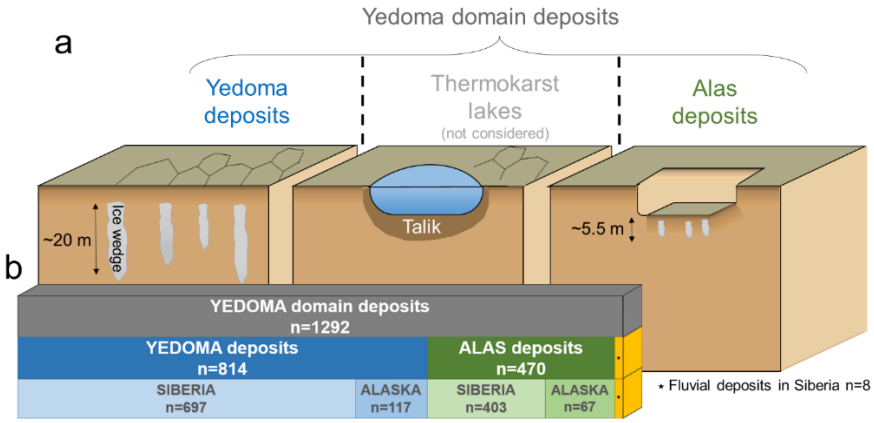

Figure 6.3: (a) Schematic view of Yedoma and Alas (drained thermokarst lake basins) deposits considered for mineral element stock calculations (modified from Nitzbon et al., 2020); sediments underlying thermokarst lakes or river floodplains are excluded. (b) Number of samples from Yedoma domain deposits included in the Yedoma domain Mineral Concentrations Assessment (YMCA) dataset (see Sect. 6.4.2).

6.2.2 Sample collection

This large-scale mineral element concentration assessment from Yedoma and Alas deposits is based on samples collected in two major Arctic regions, Alaska and Siberia. More specifically, the dataset includes 22 locations and compiles 75 different profiles from West, North and Interior Alaska, the Kolyma region, the Indigirka region, the New Siberian Archipelago, the Laptev Sea coastal regions, and Central Yakutia (Figure 6.1). About 64% of the profiles are from Yedoma deposits, 33% from Alas deposits and 3% from deltaic deposits, and the sites cover a range of geomorphological settings (Table S.6.1). For each location, Yedoma and Alas deposits profiles were sampled if both types of deposit were present. In total, 1,292 different samples were analyzed for their mineral element concentration. Sampling strategies were as follows: during the cold season, frozen samples were collected by drilling from the surface down with drilling rigs, whereas during the mid-

summer season, drilling was performed in frozen ground below the existing thawed active layer. Cliffs or headwall exposures along coasts, rivers, or lakes were cleaned and frozen *in situ* sediments sampled with hammer and ax. For headwall or cliff sampling, sub-profiles from different vertical exposures were included when needed to reconstruct a complete stratigraphical composite profile. Additional information on specific site sampling techniques can be found in the reference papers cited in Table 6.1. Recovered samples were air- or freeze-dried before being stored and archived. The number of samples collected in each location and the number of samples analyzed with the different methods presented in section 6.3 are provided in Table S.6.1.

Table 6.1: Studied locations from the Yedoma domain with associated labels, the number of profiles assessed for each type of deposits and the associated reference papers for site description. The site numbers (Site Nb) 1-17 are from Siberia, and 18-22 are from Alaska (located on the map in Figure 6.1). The labels are used in the Yedoma domain Mineral Concentrations Assessment (YMCA) dataset (doi:10.1594/PANGAEA.922724) (see Sect. 6.4.2 for details). * Sobo Sise Yedoma profiles were collected from the top of Yedoma hills but radiocarbon dating indicates that those are actually cover deposits of Holocene age. Information on site geomorphology, number of samples collected in each location, and samples selected for specific analyses (Sect. 6.3) are given in Table S.6.1.

Site Nb	Site Name	Label	Yedoma deposits	Alas deposits	Deltaic deposits	Reference papers
1	Cape Mamontov Klyk	Mak	2	1	0	Schirrmeister et al., 2008, 2011
2	Nagym (Ebe Sise Island)	Nag	2	1	0	Schirrmeister et al., 2003b
3	Khardang Island	Kha	1	0	0	Schirrmeister et al., 2007, 2011
4	Kurungnakh Island	Bkh, KUR	2	2	0	Schirrmeister et al., 2003b; Schirrmeister et al., 2008; Wetterich et al., 2008
5	Sobo Sise Island	Sob	2*	1	1	Fuchs et al., 2018
6	Bykovsky Peninsula	Mkh, BYK	5	2	0	Andreev et al., 2002; Grosse et al., 2007; Schirrmeister et al., 2002, 2011
7	Muostakh Island	Muo	1	0	0	Grigoriev et al., 2003; Schirrmeister et al., 2011
8	Buor Khaya Peninsula	Buo	2	3	0	Schirrmeister et al., 2017
9	Stolbovoy Island	Sto	3	1	0	Grigoriev et al., 2003; Schirrmeister et al., 2003a
10	Belkovsky Island	Bel	0	2	0	Grigoriev et al., 2003; Schirrmeister et al., 2003a, 2011
11	Kotel'ny Island	KyS	1	0	0	Grigoriev et al., 2003; Schirrmeister et al., 2003a, 2011
12	Bunge Land	Bun	0	0	1	Schirrmeister et al., 2010
13	Bol'shoy Lyakhovsky Island	TZ, R, L	11	4	0	Andreev et al., 2009; Wetterich et al., 2011, 2014
14	Oyogos Yar coast	Oy	1	1	0	Wetterich et al., 2009; Schirrmeister et al., 2011; Opel et al., 2017
15	Kytalyk	KY, KH	2	1	0	Weiss et al., 2016
16	Duvanny Yar	DY	5	1	0	Strauss, 2010
17	Yukechi	Yuk-Yul	2	2	0	Windirsch et al., 2020
18	Kitluk	Kit	1	1	0	Unpublished data ; Wetterich et al., 2012
19	Baldwin Peninsula	Bal	1	3	0	Jongejans et al., 2018
20	Colville	Col	1	0	0	Grosse et al., 2015; unpublished data
21	Itkillik	Itk, It	1	0	0	Kanevskiy et al., 2011
22	Vault Creek Tunnel	FAI	1	0	0	Schirrmeister et al., 2016

6.3 Methods

6.3.1 Total elemental analysis by ICP-OES measurement after alkaline fusion

Inductively coupled plasma optical-emission spectrometry (ICP-OES) is a classical method to assess mineral element concentrations in solutions from the environment accurately. Solid phases such as soil samples should be first digested prior to ICP-OES analysis. Here, soils were digested by alkaline fusion. Briefly, air- or freeze-dried soil samples were carefully milled for homogenization (agate mill). We mixed a portion of the milled sample (80 mg) with Lithium metaborate and Lithium tetraborate and heated it up to 1,000°C for 10 minutes. Then we dissolved the fusion bead in HNO_3 2.2N at 80°C and stirred until complete dissolution (Chao and Sanzolone, 1992). We measured the mineral element concentrations in that solution by ICP-OES (iCAP 6500 Thermo Fisher Scientific). We assessed the loss on ignition at 1,000°C, the sum of oxides was between 98-102%, and the total element content in soils is expressed in reference to the soil dry weight at 105°C. To assess the accuracy (i.e., trueness and precision) of the method, the analytical measurement was validated by repeated measurements on three certified materials; i) USGS basalt reference material BHVO-2 (Wilson, 1997), ii) GBW07401 podzolitic soil, and iii) GBW07404 limy-yellow soil (National Research Center for CRM, 1986; Table S.6.2). To assess the precision of the method on a matrix similar to samples from the Yedoma domain, we conducted three repetitions on three individual samples from Yedoma and Alas deposits. For each mineral element, standard deviations on the repetitions, expressed in mg kg^{-1}, are available in Table 6.2.

Out of the 1,292 deposit samples retrieved from the Yedoma domain (Sect. 6.2.2), a subset of 144 samples was analyzed by ICP-OES after alkaline fusion to determine their mineral element concentrations (sample list is provided in Table S.6.3). We used this subset of analysis to calibrate element concentrations measured by portable X-ray fluorescence (Sect. 6.3.2) for accurate determination of concentration values. For this first assessment, we measured the following elements on the subset of samples (except for Zn, which was measured on 119 out of the 144 samples): Si, Al, Fe, Ca, Mg, Cr, Ba, K, Ti, P, Cu, Mn, Ni, Zn, Sr, and Zr.

Table 6.2: Precision of the element concentrations expressed as pooled standard deviations (i.e., two pooled standard deviations, expressed in mg kg^{-1}) for the 10 elements considered. The values are based on three repetitions of three identical samples for both ICP-OES and raw concentrations from pXRF method. The coefficient of variation (CV; expressed in %), defined as the ratio of the standard deviation to the mean is also provided.

		Si	Al	Fe	Ca	K	Ti	Mn	Zn	Sr	Zr
ICP-OES	$\pm 2SD_{pooled}$ (mg kg^{-1})	± 1858	± 417	± 275	± 758	± 510	± 55	± 8.5	± 6.8	± 3.0	± 25
	CV (%)	0.29	0.43	0.50	0.99	2.01	0.71	0.85	4.31	1.05	4.21
pXRF	$\pm 2SD_{pooled}$ (mg kg^{-1})	± 5887	± 3830	± 401	± 627	± 386	± 210	± 27	± 8.2	± 5.17	± 11.3
	CV (%)	1.15	3.75	0.74	0.84	1.51	2.88	2.91	5.72	1.97	2.04

6.3.2 Total elemental analysis by *ex situ* direct measurement by portable X-ray fluorescence

X-ray fluorescence (XRF) spectrometry is an elemental analysis technique with broad environmental and geologic applications, from pollution assessments to mining industries (Weindorf et al., 2014a; Rouillon and Taylor, 2016; Young et al., 2016; Ravansari et al., 2020). In addition, there is a growing use of portable XRF for soil science (McLaren et al., 2012; Ravansari and Lemke, 2018). Portable XRF is used primarily for solid elemental analysis (soils, sediments, rocks or even plastics) but can also deal with oil chemical characterization (Weindorf et al., 2014a). XRF is based on the principle that individual atoms emit photons of a characteristic energy or wavelength upon excitation by an external X-ray energy source. By counting the number of photons of each energy emitted from a sample, the elements present may be identified and quantified (Anzelmo and Lindsay, 1987; Figure S.6.1). XRF-scanning results represent elements intensities in "counts per second" (cps) which are proportional to chemical concentrations in the sample but depend also on sample properties (Röhl and Abrams, 2000), ice and water content (Tjallingii et al., 2007; Weindorf et al., 2014b) and interactions between elements called "matrix effect" (Weltje and Tjallingii, 2008; Fritz et al., 2018).

In situ pXRF measurement often involves variability from uncontrolled environmental factors, such as water content, organic matter content or sample heterogeneity (Shand and Wendler, 2014; Weindorf et al., 2014b; Ravansari et al., 2020). To avoid such variability in water content, measurements were performed on dried samples in laboratory (*ex situ*) conditions with the

handheld device in the laboratory. The particle size distribution of these Yedoma domain deposits (described in reference papers from Table 6.1) is below 2 mm: therefore no sieving was necessary. For the pXRF measurement, the dried sample is placed on a circular plastic cap (2.5 cm diameter) provided at its base with a transparent thin film (prolene 4 µm). To avoid the underestimation of the detected intensities, sample thickness in the cap needs to be higher than 5 mm to 2 cm, depending on the element of interest (Ravansari et al., 2020). For a precise measurement, the sample thickness in the cap is set to >2 cm. Above 2 cm, the width is considered as "infinitely thick" for all elements. Measurements on the 1,292 samples from the Yedoma domain were performed using the pXRF device *Niton XL3t GOLDD+* (Thermo Fisher Scientific), which has two specific internal calibration modes called *mining* and *soil*. Each internal calibration is dealing with different energy range and filters to scan the complete energetic spectrum from low to high-energetic fluorescence values. Both modes were used on each sample and depending on the element, the calibration with the best correlation with the ICP-OES method (Sect. 6.3.1) was kept for further calculations (Sect. 6.3.4). To standardize the analysis, total time of measurement was set to 90 seconds. We conducted the analysis in laboratory conditions, using a lead stand to protect the operator from X-rays.

In theory, the pXRF device used to generate this dataset can measure simultaneously elements of atomic mass from Mg to U. Because ambient air annihilates fluorescence photons that do not have enough energy, low atomic mass elements from Na and lighter cannot be quantified by pXRF. Note that Na quantification would be possible in controlled void conditions during analysis (Weindorf et al., 2014a). In this study, we focused on the concentrations in 16 elements (Si, Al, Fe, Ca, Mg, Cr, Ba, K, Ti, P, Cu, Mn, Ni, Zn, Sr, Zr) by pXRF and by the ICP-OES method (Sect. 6.3.1) to allow for quality check, calibration and correction. Some elements are at the limit of detection (LOD) for pXRF device (e.g., Cu, Ni). The LOD was reached when the sample was lacking a specific mineral element. LOD concentrations were set to 0.7 times the minimal concentration measured for this element, which is an arbitrary number but conventionally used for data statistical treatment (Reimann et al., 2008). Depending on the considered element, pXRF measured concentrations were highly precise but not always accurate (far from the true value) (Figure 6.4). Trueness was achieved after correction using a regression with concentration values measured by the ICP-OES method to avoid systematic bias (Figure 6.4; Sect. 6.4.1). Using a well-defined

regression to correct pXRF measurements for trueness allowed using the pXRF method to measure mineral element concentrations on a large number of Yedoma and Alas sample (n=1,292), i.e., providing a valuable method to assess the mineral element content on a large sample set (Figure 6.4). Raw pXRF concentrations cannot be used for absolute quantification if not corrected with a reliable and accurate method. Here, only pXRF concentration values corrected using a well-defined regression were used (Sect. 6.4.1). Because of poor correlation ($R^2 < 0.5$) between pXRF and accurate ICP-OES method for Mg, Cr, Ba, P, Cu and Ni, as discussed in Sect. 6.4.1, these elements were not considered further in this study.

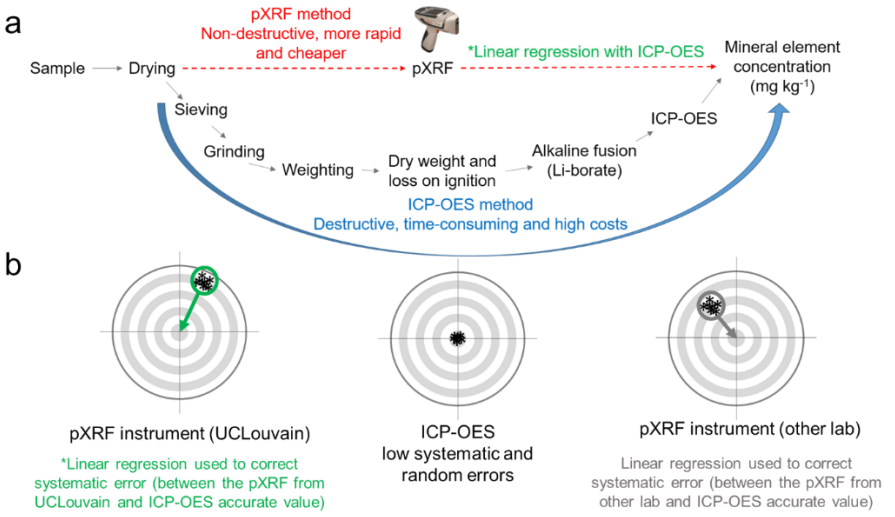

Figure 6.4: (a) Comparison between two methods to assess mineral element concentrations in deposit samples: the inductively coupled plasma optical-emission spectrometry (ICP-OES) method (large blue arrow) is destructive and time-consuming (involving several steps), whereas the portable X-ray fluorescence (pXRF) method (dotted red arrows) is non-destructive and allows a fast and reliable determination of element concentrations on a large set of samples in a cost-effective way when a correction with a linear regression is applied. (b) The pXRF bias (i.e., systematic error) is corrected with a linear regression specific to each pXRF device. Portable XRF devices from each lab require their own linear regression to correct for accurate value. The linear regression is obtained from a selection of samples (here 11 % of the samples) analysed by both methods, pXRF and ICP-OES.

To assess the precision (i.e., random errors) of the pXRF method, three repetitions were conducted on three individual samples from different

locations. Between each repetition, instrument/sample repositioning is used to mitigate the "nugget effect" due to heterogeneity in the sample (Ravansari and Lemke, 2018). Pooled standard deviations (SD_{pooled}, weighted average of standard deviations), expressed in mg kg^{-1}, of the repetitions for the ten elements used for stock calculation (Sect. 6.4.1) are available in Table 6.2. Given the influence of sample matrix on pXRF measurements, the precision of the pXRF method was also evaluated based on three to five repetitions on 20 individual samples and on average 2.6 times larger than based on three repetitions on three samples (Table S.6.4). The coefficient of variation was 20% smaller for Al but 6.5 times larger for Ca based on 20 samples. To ensure a cautious evaluation of the dataset, we decided to report the precision on the data in Figure S.6.2 based on the precisions from Table 6.2 for ICP-OES measurements, and from Table S.6.4 for pXRF measurements to use the largest set of sample with precision data available.

6.3.3 Mineralogy by X-ray diffraction

The X-ray diffraction (XRD) method allows the characterization of the presence of crystalline mineral phases. We assessed the mineralogy of 39 finely ground bulk samples and six clay fraction samples (samples selected in Siberia and Alaska detailed in Table S.6.1). The mineralogy of bulk samples was determined on powder (Cu Kα, Bruker Advance D8). Clay fraction mineralogy was assessed after K^+ and Mg^{2+} saturation, ethylene glycol (eg) solvation and thermal treatments at 300 and 550°C (Robert and Tessier, 1974). The clay size fraction (<2 µm) was recovered after sonication, sieving at 50 µm to remove the sand fraction, and dispersion with Na^+-resins to separate silt (2-50 µm) and clay fractions (Rouiller et al., 1972).

6.3.4 Mean-Bootstrapping technique for mineral element stocks calculations

Calculations of mineral element stocks are based on a mean-bootstrapping technique. From the corrected mineral element concentrations obtained via linear regression of pXRF measurements (YMCA dataset; Sect. 6.4.2), the aim is to calculate the mineral element stock in Yedoma and Alas deposits individually, in order to estimate total mineral element budget at the Yedoma

domain scale. This technique has been used to estimate OC budget from Yedoma and Alas deposits (Strauss et al., 2013) and was further improved by Jongejans and Strauss (2020). Because Yedoma domain deposits contain large ice volumes, stock calculations need to take into account not only the bulk density (BD) of the samples but also total thickness and total wedge-ice volume (WIV) of the deposits. In order to avoid overestimation of the mineral stocks, WIV was subtracted from the total Yedoma domain deposit volume, since the proportion of mineral elements locked inside ice-wedges is negligible. Indeed, Opel et al. (2018) indicate the minor contribution of mineral particles during ice-wedge formation. Fritz et al. (2011) further indicate that ion concentrations in ice is generally low, dominated by HCO_3^- (55%) and Cl^- (37%) for anions and Na^+ (58%) and Ca^{2+} (30%) for cations. Note that a flush of highly labile mineral elements (e.g., Na^+, Ca^{2+}, Cl^-) locked inside ice-wedges may increase nutrient supply for a short time scale upon Yedoma deposits degradation compared to long-term solid-liquid interactions upon thaw. Assumptions and calculations for BD determination, WIV estimations, deposits thickness, and coverage are fully explained in Strauss et al. (2013) and are summarized here. The bootstrapping statistical method use resampled (10,000 times) observed values (mineral element concentrations, BD, WIV and deposits thickness; Figure S.6.3) and derive the mean afterward. The BD determination for each sample was obtained by using an inverse relationship with porosity (ϕ) Eq. (6.1) (Strauss et al., 2013):

$$BD = (\phi - 1) \times \rho_s \quad \text{(Eq. 6.1)}$$

whereas ρ_s is the solid fraction density. We assume that pore volume in ice-saturated samples is directly measured with segregated ice volume. For samples where no BD determination is available, BD is inferred from the total organic carbon (TOC) content using equation Eq. (6.2) (Strauss et al., 2013):

$$BD = 1.126^{-0.061 \times TOC} \quad \text{(Eq. 6.2)}$$

If neither BD or TOC is available, BD is fixed to 0.88 10^3 kg m^{-3} and 0.93 10^3 kg m^{-3} for Yedoma and Alas deposits, respectively, i.e., the mean BD measured in such deposits (Strauss et al., 2013). These values are comparable with other studies on BD of Yedoma deposits (0.98 10^3 kg m^{-3}; Dutta et al., 2006). The WIV estimations were performed using ice-wedge width from field measurements (Strauss et al., 2013), ice-wedge polygon size determinations from high-resolution satellite, and additional geometrical tools (assuming ice-wedges have an isosceles triangular or rectangular shape

depending on the type of ice-wedge; see Strauss et al., 2013; Hugelius et al., 2014). Thickness used for mineral element stock estimations in Yedoma domain deposits are based on mean profile depths of the sampled Yedoma (n = 19) and Alas (n = 10) deposits (Table 6.3; Strauss et al. (2013)). Since the 10,000 step bootstrapping technique randomly picks one thickness at a time with replacement, we evaluated the stock estimation for a mean thickness of 19.6 meters deep in Yedoma deposits and 5.5 meters deep in Alas deposits.

Table 6.3: Summary of key parameters for Yedoma deposits and Alas deposits. Parameters include thicknesses (in meters) and wedge ice volume (WIV, in %) from Strauss et al. (2013). Mineral element stock estimations are based on a mean thickness of 19.6 m for Yedoma and 5.5 m for Alas deposits.

	Yedoma deposits		Alas deposits	
	Thickness (m)	WIV (vol%)	Thickness (m)	WIV (vol%)
Mean	19.6	49.1	5.5	7.8
Median	15.1	51.9	4.6	7.6
Min	4.6	34.7	1.2	0.8
Max	46	59	13.4	12.8
n	19	10	10	7

The core Yedoma domain extent was estimated to ~1,387,000 km², based on digital Siberian Yedoma region map (Romanovskii, 1993) and the distribution of Alaskan ice-rich silt deposits equivalent to Yedoma (Jorgenson et al., 2008). The Yedoma deposit extent is estimated to 410,000 km², i.e., 30% of the Yedoma domain, based on the fact that 70% of the Yedoma domain area is affected by degradation (Strauss et al., 2013). Considering 10% of the area of the Yedoma domain covered with lakes and rivers, 4% covered with other deposits including deltaic and fluvial unfrozen sediments, this leaves 56% (780,000 km²) of the Yedoma domain covered by frozen thermokarst deposits in drained thermokarst lakes (Figure 6.2). Using these parameters, the overall mineral element stock is determined with Eq. (6.3) included into the bootstrapping calculation:

$$Mineral\ element\ stock\ [Gt] = \frac{thickness\ [m] \times coverage\ [m^2] \times BD\ \left[10^3 \frac{kg}{m^3}\right] \times \frac{100-WIV}{100}[-] \times mineral\ concentration\ \left[\frac{mg_{Min\ element}}{kg_{dry\ soil}}\right]}{1{,}000{,}000{,}000} \quad \textit{(Eq. 6.3)}$$

Because Yedoma and Alas deposits have different properties for BD, ice content, and deposit thickness, mineral element stocks were estimated for each deposit type individually. For each bootstrapping step, the sample mineral element concentration and specific BD were paired (as they are not independent) and a specific stock was estimated based on one value for WIV and thickness. The stock was then multiplied by total coverage for total mineral stock estimation to the Yedoma domain scale. From these input parameters, multiple mineral element stocks were computed, one for each bootstrapping step. Eventually, from those multiple steps (n=10,000), a mineral element stock distribution was estimated from which the mean represents the best stock estimation of the considered mineral element. The error estimates in this study represent 2 standard deviations (mean ±2σ), with the assumption of a normal distribution. Computations were performed using R software (boot package; R Core Team, 2018). Supplementary information on input parameters (deposit thickness, WIV) are available in Figure S.6.3.

6.4 Data processing and results

6.4.1 Linear regression for accurate mineral element concentration measurements

Mineral element concentrations were measured with both the ICP-OES method (Sect. 6.3.1) and the pXRF method (Sect. 6.3.2) on a subset of samples (n=144) from Yedoma domain deposits (Table S.6.1 and Table S.6.3). Linear regressions can be computed from this subset of data and parameters of the regression are estimated and based on a robust linear regression (alpha=0.95; Table 6.4). Among the 16 mineral elements measured, 10 elements (Si, Al, Fe, Ca, K, Ti, Mn, Zn, Sr and Zr) display high correlations between pXRF and ICP-OES method with R^2 ranging from 0.725 (Al) to 0.996 (Ca; Table 6.4). Linear regression plots for these elements are presented in Figure S.6.2. The other six elements (Mg, Ba, Cr, Cu, Ni and P) present weak ($R^2 < 0.5$) or no correlations between the two methods. According to these correlations, the mineral element stock quantification was performed on the 10 elements reliably measured by pXRF (Si, Al, Fe, Ca, K, Ti, Mn, Zn, Sr and Zr), and the other six elements are not discussed further in this study.

Table 6.4: Robust linear regression adjusted R^2 (alpha = 0.95) between concentrations measured from pXRF and ICP-OES method in Yedoma domain deposits (n=144 for all elements, except for Zn where n=119).

Element	Si	Al	Fe	Ca	K	Ti	Mn	Zn	Sr	Zr
R^2	0.835	0.725	0.949	0.996	0.941	0.728	0.875	0.844	0.965	0.907

The uncertainty based on three identical samples on the ICP-OES measurement after alkaline fusion was lower than pXRF measurements, except for Ca, K,and Zr (Table 6.2). Nonetheless, the advantages of a non-destructive, rapid and cheaper method predominate for a large-scale mineral concentration assessment given that the coefficient of variation (2.1% to 8.7%) on the pXRF measurement was satisfying to differentiate between high and low concentrations values measured in these deposits (i.e., comparing the horizontal error bar with the total range of values represented on the X-axis in Figure S.6.2).

In this dataset, the risk of overestimating the element concentration by pXRF in organic-rich samples (Shand and Wendler, 2014) is limited. Among the 1,292 Yedoma and Alas samples used in this study to build the YMCA dataset (Sect. 6.4.2), less than 0.5% of the samples were characterized by TOC content similar to or higher than 40 wt% (Table 6.5). Overestimation of the concentration was only observed for a single sample for Fe (Figure S.6.2c) and for three samples for Ca (Figure S.6.2d) out of the 144 samples from the subset (for samples with TOC content > 40 wt%), and not observed for Si, Al, K, Ti, Mn, Zn, Sr and Zr.

Since the points corresponding to these organic-rich samples were excluded from the robust linear regressions (Figure S.6.2), we assume that the matrix effect is not a source of significant bias to correct pXRF measurements of element concentrations using these regressions. Thus, the pXRF method can be applied for this first large-scale mineral element assessment of Yedoma domain deposits.

6.4.2 Yedoma domain Mineral Concentrations Assessment (YMCA) dataset

Robust linear regression equations with reliable R^2 (Table 6.4) were applied for each pXRF-measured concentration to correct concentrations values for trueness (Figure 6.4 and Figure S.6.2). The resulting YMCA dataset, freely available under doi:10.1594/PANGAEA.922724, compiles 1,292 samples for the following elements: Si, Al, Fe, Ca, K, Ti, Mn, Zn, Sr and Zr.

In addition to the corrected mineral element concentrations, the YMCA dataset combines a wide range of relevant existing information on these 1,292 samples. Site and samples properties are integrated from AWI (Alfred Wegener Institute) Potsdam and Stockholm University data. We associated the lithology of the underlying bedrock, and the type of unconsolidated sediments at the surface characterizing each site from a spatial join using Arc Map 10.4. Specifically, coordinates from each site are joined based on their spatial location to Global Lithology Map (GLiM; Hartmann and Moosdorf, 2012) and Global Unconsolidated Sediments Map (GUM; Börker et al., 2018). Typically, we included the lithology of the underlying bedrock to evaluate its potential control on the mineral element concentrations in the deposits.

The attribute columns of this dataset are organized as follows: (i) all site and sample properties (sample ID, description (identifying active layer (AL)), type of deposit, site location, number of profile, GPS coordinates, country, GLiM-lithology, GUM-unconsolidated sediment type, GUM-age, sample depth below surface level (b.s.l) or height above sea/river level (a.s.l), sediment characteristics, BD, gravimetric and absolute ice content, TOC values); and (ii) corrected pXRF concentrations based on linear regressions from Sect. 6.4.1. Table 6.5 summarizes corrected mineral element concentration values as well as BD, TOC and ice content from the whole Yedoma domain region, with no differentiation between Yedoma and Alas deposits samples (n=1,292).

Table 6.5: Statistical summary of YMCA dataset (n=1,292) for bulk density (BD), total organic carbon content (TOC), absolute ice content, and corrected mineral element concentrations (Si, Al, Fe, Ca, K, Ti, Mn, Zn, Sr and Zr) in Yedoma domain deposit samples (grouping Yedoma and Alas deposits together). Columns stand for N (number of data); Missing (missing data); MIN (minimum value reported); Q (quantiles); Q1 (first quantile); Q3 (third quantile); MEDIAN; MEAN; MAX (maximum value reported); SD (standard deviation); MAD (median absolute deviation standardised to conform with the normal distribution); IQR (interquartile range standardised to conform with the normal distribution); CV (coefficient of variation (%)); CVR (robust coefficient of variation (%)). *For Si, excessive organic rich samples may result in lower concentration values and consequently in negative concentration value after correction. Only positive values have been considered for stock calculations.

	Units	N	Missing	MIN	Q_0.05	Q1	MEDIAN	MEAN-log	MEAN	Q3	Q_0.95	MAX	SD	MAD	IQR	CV	CVR
BD	g cm^{-3}	1292	0	0.0379	0.721	0.943	0.988	1.076	1.143	1.322	2.055	2.429	0.397	0.1083	0.2814	34.74	10.96
TOC	wt%	1182	110	0.07	0.1	1.11	1.942	1.87	3.747	3.748	13.09	44.36	5.950	1.606	1.955	159	82.74
Abs. ice content	%	703	589	0	17.76	28.83	37.5	36.66	38.94	47.8	64.69	103.9	14.99	14.08	14.06	38.48	37.56
Si	mg kg^{-1}	1292	0	-19310*	241400	284000	301000	290400	295200	316900	335700	444700	40750	24170	24330	13.8	8.031
Al	mg kg^{-1}	1292	0	6480	48630	61210	66460	63700	64820	70600	77100	101000	9978	6914	6957	15.39	10.4
Fe	mg kg^{-1}	1292	0	9591	18770	28270	31680	30970	32140	34470	45810	111000	9234	4586	4600	28.73	14.48
Ca	mg kg^{-1}	1292	0	2086	5316	7972	10380	11490	13910	15520	32910	102000	11540	4667	5594	82.94	44.97
K	mg kg^{-1}	1292	0	2097	11820	17680	19290	18300	18720	20640	22580	30380	3270	2192	2194	17.47	11.36
Ti	mg kg^{-1}	1292	0	100.2	2112	3715	4171	3867	4015	4480	5081	10970	940.1	536.9	567.5	23.41	12.87
Mn	mg kg^{-1}	1292	0	118.6	275.8	409	498	490	569.9	568.2	775.1	48690	1395	118.8	118	244.8	23.86
Zn	mg kg^{-1}	1292	0	22.1	29.88	58.45	70.86	67.01	71.28	83.37	103.8	686.8	28.81	18.47	18.48	40.41	26.07
Sr	mg kg^{-1}	1292	0	32.82	96.03	158.1	186	185	196.2	242.5	308.1	392.5	63.53	59.81	62.57	32.38	32.16
Zr	mg kg^{-1}	1292	0	43.74	158.6	242.8	278.5	269.4	280.1	314	399.8	711	73.48	53.03	52.8	26.23	19.04

6.4.3 Yedoma domain deposits mineralogy

The main mineral phases (i.e., primary and secondary minerals) identified in selected Yedoma, Alas and fluvial deposits are presented in Table 6.6. The following minerals were identified in all bulk samples: quartz, feldspar plagioclase, micas and kaolinite. Chlorite was identified in Siberian deposits from Sobo Sise, Buor Khaya and Kytalyk. Calcite and dolomite were only detected in Alaskan Yedoma deposits from Colville and Itkillik. The mineralogy is generally similar along the profile depth for each location (Figure S.6.4). In these silty-fine sediments, the clay content ranges between 6 and 18% (silt content 67-79%; sand content 3-55%), i.e., well in line with Strauss et al. (2012). The diffractograms on clay fractions from Buor Khaya highlighted the presence of kaolinite, illite, and smectite (Figure S.6.4d-i). These data highlight the co-existence in these deposits of highly stable minerals such as quartz with more weatherable minerals such as dolomite, calcite, or feldspar plagioclase (Goldich, 1938; Wilson, 2004; Cornelis et al., 2011), and the presence of clay minerals characterized by higher specific surface area relative to the other mineral constituents (i.e., smectite, kaolinite, illite) (Kahle et al., 2004; Saidy et al., 2012).

Table 6.6: Mineralogical composition in Yedoma (Y) and Alas and fluvial (A) deposits of Siberia and Alaska (Q, Quartz; Pl, Plagioclase; Ch, Chlorite; M, Mica; I, Illite; K, Kaolinite; D, Dolomite; Ca, Calcite; Sm, Smectites). The diffractograms for each profile (n = number of diffractogram per profile) are presented in Figure S.6.4.

Site	n	Fraction	Profile label	Mineralogy	Figure S.6.4
Sobo Sise	13	Bulk	Sobo T2-2 (Y), T2-3 (Y), T2-5 (A), T2-6 (A)	Q, Pl, Ch, M, K	a
Buor Khaya	3	Bulk	Buo-02 (Y)	Q, Pl, Ch, M, K	b
Buor Khaya	6	Bulk	Buo-04 (Y)	Q, Pl, Ch, M, K	c
Buor Khaya	6	Clay	Buo-04 (Y)	Q, Pl, Ch, I, K, Sm	d to i
Kytalyk	4	Bulk	KY T1-1 (Y), KY T2-2 (A)	Q, Pl, Ch, M, K	j
Colville	3	Bulk	Col (Y)	Q, Pl, M, K, D, Ca	k
Itkillik	10	Bulk	Itk (Y)	Q, Pl, M, K, D, Ca	l

6.4.4 Mineral element stocks in the Yedoma domain

The quantification of mineral element stocks is a major step to assess the distribution of mineral elements in the Yedoma domain. We performed mineral elements stock estimations with the bootstrapping technique (Sect. 6.3.4). For example, the mean Fe stock from Yedoma deposits (n=814) is 147 ± 43 Gt (±2σ) using the theoretical normal distribution (mean-bootstrapping technique; Figure 6.5).

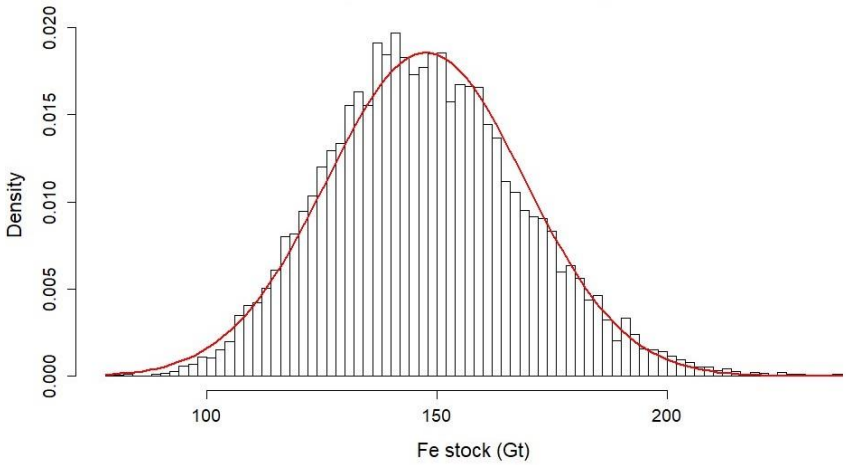

Figure 6.5: Distribution of the iron stock (Gt) in Yedoma deposits (n=814). The histogram results from the bootstrapping technique (n=10,000; Figure S.6.3). The theoretical normal distribution is shown in red.

Based on the YMCA dataset, the bootstrapping technique was applied to calculate the stocks in Yedoma deposits for the 10 elements (Si, Al, Fe, Ca, K, Ti, Mn, Zn, Sr, and Zr), basing on the same input parameters for BD, thickness, WIV and coverage. The estimate mean and standard deviation derived the best estimation of the Yedoma deposit stocks for each specific mineral element. With a similar approach, mineral element stocks (Si, Al, Fe, Ca, K, Ti, Mn, Zn, Sr, and Zr) were estimated in Alas deposits. The element stocks in the Yedoma domain were obtained by adding element stocks in Yedoma and Alas deposits (Table 6.7). The results highlight that the mineral element with the largest stock in the Yedoma domain is Si (2,739 ± 986 Gt) followed by Al, Fe, K, Ca, Ti, Mn, Zr, Sr, and Zn (Figure 6.6). In comparison, the estimated OC stock in the Yedoma domain reaches around 324-466 Gt (Strauss et al., 2017; Figure 6.6).

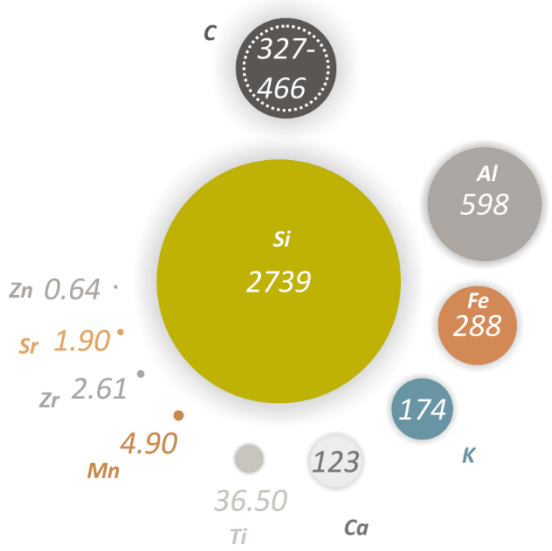

Figure 6.6: Mineral element stocks (in Gt) in the Yedoma domain deposits (including Yedoma and Alas deposits) for Si, Al, Fe, K, Ca, Ti, Mn, Zr, Sr, and Zn. The surface area of the circles is proportional to the stock of the element considered. The organic carbon stock in the Yedoma domain (Strauss et al., 2017) is provided for comparison (the dotted line represents the lower range of the estimate, i.e., 327 Gt).

Overall, Yedoma and Alas deposits (Table 6.7) represent 86% of the total Yedoma domain area (Figure 6.2): this means that mineral element stocks are based on 86% of the deposits. The remaining surfaces of the Yedoma domain correspond to deltaic deposits (4%) or lakes and rivers (10%). Element stocks in deltaic deposits have not been estimated in this study due to the scarce number of available mineral concentration data in deltaic deposits (0.6% of the YMCA dataset) and the lack of empirical estimations of their thickness, or their ice volume (even if ice volume is probably negligible in these deposits). Waterbodies, lakes and rivers are not considered in this assessment focusing on the mineral element content in surface solid materials vulnerable to thaw or already thawed in the past. Sediments underlying lakes and rivers are therefore outside the scope of this evaluation and would only become relevant if drainage occurs. Absolute stock estimates (in Gt) allow direct comparison between Yedoma and Alas deposits, despite their different thickness (19.6 m and 5.5 m, respectively), WIV and coverage. Mineral element density estimations (kg m^{-3}) are available (Table S.6.5) in which thickness and WIV have been neglected: this estimation is the product of mineral element concentrations and BD using bootstrapping technique.

Table 6.7: Mineral elements stock (Gt) summary in Yedoma, Alas and Yedoma domain deposits (n=814, 470 and 1,284, respectively). Mean and associated 2 standard deviations (σ; absolute value) are provided. Total stocks are the addition from the stocks in Yedoma and Alas deposits. Note, fluvial /deltaic deposits stocks were not estimated because of lack of data and spatial coverage (n=8).

	Stock (Gt)					
	Yedoma deposits		Alas deposits		Total Yedoma domain	
Element	Mean	± 2σ	Mean	± 2σ	Mean	± 2σ
Si	1413	408	1327	578	2739	986
Al	309	88.9	289	124	598	213
Fe	147	42.6	140	60.9	288	104
Ca	70.8	20.9	51.7	23.2	123	44.1
K	90.0	25.7	84.0	36.8	174	62.4
Ti	19.0	5.45	17.5	7.68	36.5	13.1
Mn	2.57	0.852	2.34	1.02	4.90	1.87
Zn	0.327	0.0941	0.311	0.137	0.638	0.231
Sr	0.963	0.278	0.935	0.409	1.90	0.687
Zr	1.36	0.393	1.25	0.543	2.61	0.936

6.5 Advantages and limitations of the methodological approach

6.5.1 Portable X-ray fluorescence

The main advantage of the pXRF method is to ensure a non-destructive, more rapid (less steps involved; Figure 6.4) and cheaper method for mineral element concentration measurement compared to the ICP-OES measurements after alkaline fusion. This is beneficial when dealing with large-scale assessments involving thousands of archive samples from the Yedoma domain. The concentrations of 10 elements could be reliably measured in these deposits (i.e., Si, Al, Fe, K, Ca, Ti, Mn, Zr, Sr, and Zn). The main limitation of the pXRF method is that raw concentration data cannot be used before applying a linear regression to correct for systematic error. This drawback related to inaccurate raw pXRF measurements can be rectified by correcting the raw pXRF values with accurate values obtained with the ICP-OES method after alkaline fusion (calibration based on 144 samples in this study). This

correction can only be applied when the correlation between pXRF and ICP-OES concentrations is satisfactory (here, $R^2 > 0.7$). In these deposits, the concentrations of some elements (Mg, P, Cu, Ni, Ba) could not be assessed due to poor pXRF-ICP-OES correlation ($R^2 < 0.5$). Linear regressions used to correct raw pXRF concentrations depend on internal geometry of the pXRF device used. This means that each pXRF device needs its own linear regression and that a single linear regression equation cannot be used with different pXRF devices. Moreover, pXRF measurements are also matrix-dependent. The matrix (i.e., organic content, bulk density) of a sample can affect pXRF-measured concentrations and therefore linear regressions must be calibrated with samples from the same matrix (here, we used a subset of 11% of samples from the Yedoma domain). For some other elements, pXRF measurements are not possible due to the low atomic mass of these elements (N, Na).

6.5.2 Mean-bootstrapping technique

The main advantage of the mean-bootstrapping technique is to ensure a reliable calculation of non-parametric uncertainty estimates. The bootstrapping technique allows to include variability in mineral element concentrations and BD, WIV and thickness of the deposits. However, standard deviations from stock estimations (Table 6.7) are markedly large because of the conservative (observation-based) approach using all measurement for bootstrapping and deriving the mean afterwards. The only fixed parameter included in mineral element stock calculation (Eq. 6.3) is coverage. The coverage is set to 410,000 km² and 780,000 km² for Yedoma and Alas deposits, respectively. These estimations are subject to uncertainty but are the best current estimates, identical to the ones used in Strauss et al., (2013) to allow direct comparison with OC stocks. However, with the ongoing Arctic warming, these coverage estimations are dedicated to change with time. Because mineral element stocks are based on different WIV, thickness and coverage, the mineral element density expressed in kg m^{-3} allows to compare Yedoma and Alas deposits for an identical one cubic meter of sediments (without ice-wedges volume) (Table S.6.5).

6.6 Implications upon permafrost thaw

6.6.1 Implications for the evolution of mineral organic carbon interactions

The YMCA dataset allows investigating the evolution of selected element to OC ratio upon thermokarst processes resulting from permafrost thaw, i.e., between Yedoma and Alas deposits. Organo-mineral associations with Fe-, Al-, Mn-oxides or clay minerals using polyvalent cations bridging between OC and mineral surfaces (e.g., Ca^{2+}, Sr^{2+} in neutral and alkaline soils or Fe^{3+} and Al^{3+} in acid soils), or organo-metallic complexes involving Fe^{3+}, Fe^{2+} and Al^{3+} ions are well known to contribute to OC stabilization (von Lützow et al., 2006). Some mineral elements such as Fe or Mn are known for an inhibition effect on methane production (Lovley and Phillips, 1987; Beal et al., 2009; Herndon et al., 2015; Sowers et al., 2018), despite microbial function being considered as a larger part of the limitation for methane production (Monteux et al 2020). The present dataset highlights a decrease of the Fe/TOC ratio and the Al/TOC ratio from Yedoma to Alas in Alaska, and virtually no change in these ratios in the Siberian Yedoma domain (Figure 6.7a-b). Providing evidence for changes in Fe/TOC or Al/TOC ratios upon thermokarst processes in a portion of the Yedoma domain highlights the need for further investigations regarding the evolution of interactions between OC and Fe or Al upon thawing.

In addition, the clay minerals present in these Yedoma domain deposits (confirmed by XRD; Table 6.6) can be associated to the formation of aggregates, thereby contributing to spatial inaccessibility of OC for decomposer organisms due to occlusion in aggregates (von Lützow et al., 2006). Iron oxides are also known to contribute to the formation of aggregates (Eusterhues et al., 2005; Kleber et al., 2015). Changing Fe/TOC ratio between Yedoma and Alas in Alaska (Figure 6.7a-b) reinforces the need to further investigate the potential role of the evolution of aggregates for OC availability upon thawing (*Ch.2*). Changing conditions for mineral protection of OC upon thawing is likely to influence OC microbial degradation (Kögel-Knabner et al., 2010; Gentsch et al., 2015b; Herndon et al., 2017; Opfergelt, 2020), thereby contributing to modulate the permafrost carbon feedback (Schuur et al., 2015).

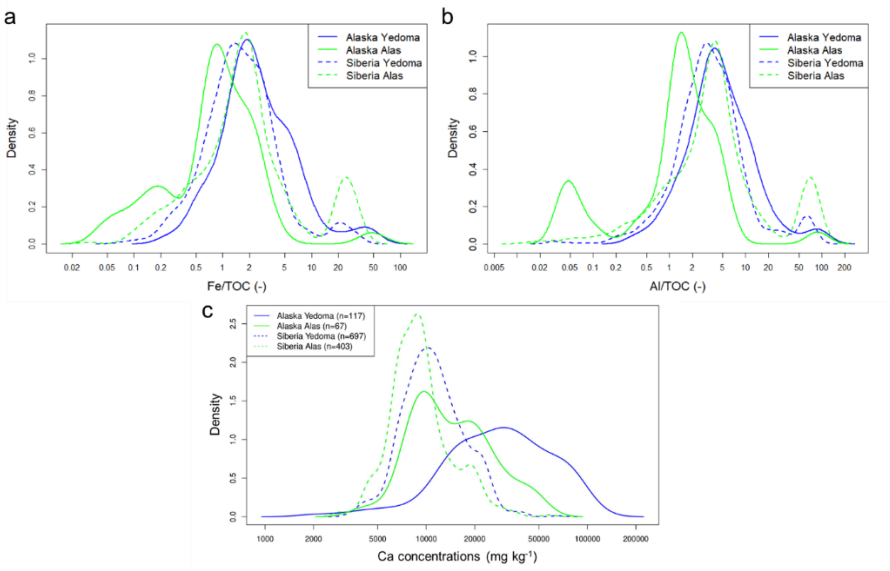

Figure 6.7: Empirical density histogram of (a) Fe/total organic carbon (TOC) ratio, (b) Al/TOC ratio and (c) Ca concentrations (mg kg^{-1}) in Yedoma domain deposits in Alaska (full line) and Siberia (dashed line) for Yedoma (blue line) and Alas (green line) deposits. The X-axis is a log scale.

6.6.2 Implications for mineral weathering and nutrient supply to ecosystems

The YMCA dataset allows investigating the change in concentration of soluble elements such as Ca upon thermokarst processes resulting from permafrost thaw, i.e., between Yedoma and Alas deposits. As shown on a density plot (Figure 6.7c), sediments from Alas deposits are characterized by lower Ca concentrations compared to Yedoma deposits. This was observed between Yedoma and Alas deposits in Alaska, and in Siberia (Figure 6.7c).

Higher Ca concentrations in Yedoma and Alas deposits from Alaska relative to the deposits from Siberia can be explained by the local lithology, i.e., carbonate rocks from the northern Brooks Range contributing to the deposits in Alaska (Till et al., 2008). The lithology of the bedrock, beneath Quaternary deposits, inferred from the GLiM map, is similar between Yedoma and Alas deposits (Figure S.6.5). This can likely be explained by the fact that the Yedoma and Alas deposits from the Yedoma domain mainly originate from the same source material on local to regional scales (Grosse et al., 2007;

Strauss et al., 2017). Since most of the studied regions are covered by thick Quaternary deposits, mineral element concentrations are likely more influenced by the mixing of the unconsolidated sediments contributing to the Quaternary deposits rather than by the lithology of the underlying bedrock. The lithological similarity between Yedoma and Alas deposits can also be explained by the fact that Alas deposits are dominated by reworked sediments from former Yedoma deposits (Schirrmeister et al., 2020). Therefore, Ca depletion in Alas deposits relative to Yedoma deposits from one region is not lithology dependent but potentially results from mineral weathering and leaching processes of soluble elements such as Ca during former thawing periods. Indeed, Alas formation history includes lake formation and drainage, and the dynamism of such formation over the past thousands of years may lead to leaching processes of soluble elements, a commonly observed process in non-cryogenic soils (Stumm and Morgan, 1995) and cryogenic soils (Ping et al., 2005).

The co-existence of more weatherable (dolomite, calcite, or feldspar plagioclase) and less weatherable (quartz) mineral constituents in Yedoma deposits (Table 6.6) is likely to lead to an increasing contribution from mineral weathering to the inorganic carbon budget (Zolkos and Tank, 2020) upon thermokarst processes. The balance between carbonate or silicate mineral weathering is known to influence the short-term and long-term atmospheric CO_2 consumption (Berner et al., 1983). Locally, the oxidation of sulfides such as pyrite present in low amount, not detected here but reported in beach deposits (Schirrmeister et al., 2010), can lead to the formation of sulfuric acid and the subsequent weathering of carbonate mineral without involving atmospheric CO_2 consumption (Zolkos and Tank, 2020).

The YMCA dataset provides total mineral element concentrations, including (i) a mineral element reservoir known to be rapidly available to vegetation and microorganisms in permafrost soils (Ping et al., 1998, 2005), and (ii) a mineral element reservoir providing a longer term supply of nutrients through mineral weathering (Zolkos and Tank, 2020). Indeed, the weathering of minerals such as dolomite, calcite, or feldspar plagioclase is expected to release soluble cations such as Ca available to supply nutrients to terrestrial and aquatic Arctic ecosystems, or to interact with OC (Sect. 6.6.1). Among the 10 elements included in the YMCA dataset, macro- (e.g., K, Ca) and micro-nutrients (e.g., Fe, Mn, Zn) are required for plant nutrition and also regulate other vital processes for plants and microorganisms growth and metabolic activity (DalCorso et al., 2014). Briefly, K regulates vital processes, such as

photosynthesis, water and nutrient transportation, or protein synthesis (Marschner, 2012). Ca is a major second messenger in plant signal transduction, mediating stress- and developmental processes (Liese and Romeis, 2013). Micro-elements are required as cofactor for some essential proteins (Fe; Morgan and Connolly, 2013), play an essential role as a photosynthetic function or in metallo-protein conformation (Mn; Yang et al., 2008) or can have enzymatic functions (Zn; Lindsay, 1972). Some non-essential elements, such as Si and Al, can stimulate plant growth by playing with abiotic-biotic stress resistance and symbiosis (Richmond and Sussman, 2003; DalCorso et al., 2014). In aquatic ecosystems, silicon is a limiting nutrient for diatoms and other siliceous organisms, thereby controlling diatom abundance and community structure in the ocean, and as a result, food web and CO_2 uptake by photosynthesis (Smetacek, 1999; Yool and Tyrrell, 2003). The leaching of the more mobile cations such as Ca or K can be estimated by comparing ratios between mobile and immobile elements: this is why assessing the concentration of elements considered as immobile such as Ti or Zr can be useful to evaluate the advance of weathering in a soil relative to its parent material, and thereby the soil mineral reserve (Kurtz et al., 2000; Hodson, 2002; Jiang et al., 2018). However, the reserve in important nutrients such as P, N, S, and Mg in the Yedoma domain could not be estimated with the method used in this study (Sect. 6.5). The YMCA dataset is a first step needed in order to evaluate the impact of widespread rapid permafrost thaw through thermokarst processes (Turetsky et al., 2020) on the mineral element concentrations in the deposits and the potential implications for OC and mineral nutrient supply.

6.7 Conclusions

This study presents a method combining portable X-ray fluorescence with a bootstrapping technique to generate the first mineral element inventory of permafrost deposits from the ice-rich Yedoma region, i.e., never thawed Yedoma deposits and previously thawed Alas deposits for a mean thickness of 19.6 m and 5.5 m, respectively. In the resulting Yedoma domain Mineral Concentrations Assessment (YMCA) dataset, the total concentrations of 10 mineral elements (Si, Al, Fe, Ca, K, Ti, Mn, Zn, Sr, Zr) in Yedoma domain deposits have been quantified in 75 different profiles. The associated mineral elements stocks are shown to be in the same order of magnitude for Al and Fe than for OC, and to decrease from Si, Al, Fe, K, Ca, Ti, Mn, Zr, Sr, to Zn. This dataset allows tracking dynamic processes controlling mineral element concentrations in thawing environments, as illustrated by lower Ca concentration in Alas deposits relative to Yedoma deposits highlighting potential Ca leaching upon thawing. Providing the YMCA dataset is contributing to improve the knowledge on the mineral constituents in ice-rich permafrost, i.e., a necessary step to better understand the evolution of mineral OC interactions, mineral weathering and mineral nutrient supply to ecosystems upon permafrost thaw. The YMCA dataset is particularly relevant given the increasing occurrence of abrupt thaw in ice-rich permafrost regions.

7. Chapter 2: Iron redistribution upon thermokarst processes in the Yedoma domain

This chapter is a modified version of a research paper published in Frontiers in Earth Science special collection "Yedoma Permafrost Landscapes as Past Archives, Present and Future Change Areas":

Monhonval A, Strauss J, Mauclet E, Hirst C, Bemelmans N, Grosse G, Schirrmeister L, Fuchs M and Opfergelt S (2021) Iron Redistribution Upon Thermokarst Processes in the Yedoma Domain. Front. Earth Sci. 9:703339. doi: 10.3389/feart.2021.703339.

Abstract

Ice-rich permafrost has been subject to abrupt thaw and thermokarst formation in the past and is vulnerable to current global warming. The ice-rich permafrost domain includes Yedoma sediments that have never thawed since deposition during the late Pleistocene and Alas sediments that were formed by previous thermokarst processes during the Lateglacial and Holocene warming. Permafrost thaw unlocks organic carbon (OC) and minerals from these deposits and exposes OC to mineralization. A portion of the OC can be associated with iron (Fe), a redox-sensitive element acting as a trap for OC. Post-depositional thaw processes may have induced changes in redox conditions in these deposits and thereby affected Fe distribution and interactions between OC and Fe, with knock-on effects on the role that Fe plays in mediating present day OC mineralization. To test this hypothesis, we measured Fe concentrations and proportion of Fe oxides and Fe complexed with OC in unthawed Yedoma and previously thawed Alas deposits. Total Fe concentrations were determined on 1,292 sediment samples from the Yedoma domain using portable X-ray fluorescence; these concentrations were corrected for trueness using a calibration based on a subset of 144 samples measured by inductively coupled plasma optical emission spectrometry after alkaline fusion ($R^2 = 0.95$). The total Fe concentration is stable with depth in Yedoma deposits, but we observe a depletion or accumulation of total Fe in Alas deposits, which experienced previous thaw and/or flooding events. Selective Fe extractions targeting reactive forms of Fe on unthawed and previously thawed deposits highlight that about 25% of the total Fe is present as reactive species, either as crystalline or amorphous oxides, or complexed

with OC, with no significant difference in proportions of reactive Fe between Yedoma and Alas deposits. These results suggest that redox driven processes during past thermokarst formation impact the present-day distribution of total Fe, and thereby the total amount of reactive Fe in Alas versus Yedoma deposits. This study highlights that ongoing thermokarst lake formation and drainage dynamics in the Arctic influences reactive Fe distribution and thereby interactions between Fe and OC, OC mineralization rates, and greenhouse gas emissions.

7.1 Introduction

Upon ice-rich permafrost thaw, substantial amounts of organic carbon (OC) stored in frozen deposits become potentially available for microbial mineralization (Strauss et al., 2017; Nitzbon et al., 2020; Turetsky et al., 2020). The Yedoma domain includes Yedoma Ice Complex deposits (50-90% volume percent ice, in the following referred as Yedoma deposits) that have never thawed since late Pleistocene deposition and Alas deposits that formed upon thermokarst processes during the Lateglacial and Holocene warmer and wetter periods (Schirrmeister et al., 2013; Strauss et al., 2013). The latest estimates show that the Yedoma domain stores around 327 – 466 Gt of OC despite covering only 8% of the circumarctic permafrost region (Hugelius et al., 2014; Strauss et al., 2017). Ongoing global warming in high northern latitudes will unlock OC frozen in ice-rich Yedoma deposits (with potential lake formation and drainage) and refrozen Alas deposits, exposing more OC to decomposition (Schneider von Deimling et al., 2015; Olefeldt et al., 2016). Thawing of present day Yedoma and Alas deposits triggers a cascade of processes, including the mineralization of previously locked carbon by microorganisms generating additional greenhouse gas emissions (Schuur et al., 2008).

For millennial-scale OC preservation, the interactions between OC and mineral surfaces, especially with iron (Fe) oxides surfaces, are of great importance in soils (Adhikari and Yang, 2015; Kögel-Knabner et al., 2008; Kögel-Knabner et al., 2010; Kaiser and Guggenberger, 2007) and sediments (Eglinton, 2012; Lalonde et al., 2012). In the Qinghai-Tibetan Plateau permafrost region, approximately 20% of the soil OC is stabilized by Fe (Mu et al., 2016) illustrating the important relationship between Fe and OC in permafrost terrain. Mineral OC interactions contribute to stabilize OC through complexation, co-precipitation or aggregation processes and thus hinder microbial degradation of OC (von Lützow et al., 2006). The OC can be i) physically protected within soil aggregates (involving Fe-Al oxy(hydr)oxides, clay minerals, or carbonates), which means that OC is spatially inaccessible for microorganisms; or ii) physico-chemically protected in organo-mineral associations and/or as organo-metallic complexes. These organo-mineral associations result from the interaction of OC with mineral surfaces such as OC adsorbed onto Fe-oxides or clay minerals, using cation bridges such as Ca^{2+} or Mg^{2+}. Organo-metallic complexes result from the complexation of OC with metal ions (i.e., OC complexed with e.g., Fe^{3+}, Al^{3+}). Overall, several

stabilizing mechanisms exist between reactive Fe (Fe-oxides or complexed Fe) and OC.

These mineral-protected pools of OC are of major concern to better understand OC mineralization rates in permafrost soils upon thawing (Opfergelt, 2020). The soil OC that interacts with reactive minerals (via aggregation, sorption, complexation, and/or co-precipitation) is less available for microbial decomposition, thus contributing to the "protected" or "stabilized" organic matter pool (Schmidt et al., 2011; Lalonde et al., 2012; Kleber et al., 2015, 2021; Salvadó et al., 2015). Yet, the "protected" OC pools are not permanent and may lose their mineral-protected status in redox changing environments (Kögel-Knabner et al., 2010; Colombo et al., 2014; Herndon et al., 2017; Huang and Hall, 2017; Opfergelt, 2020; Patzner et al., 2020). Iron-mediated OC decomposition in anoxic condition can counteract protection mechanisms of OC (Chen et al., 2020; Kappler et al., 2021). Thermokarst processes trigger redox changes in the environment (Kokelj and Jorgenson, 2013; Abbott and Jones, 2015), and Fe is a redox-sensitive element, consequently thawing of ice-rich permafrost deposits may redistribute and modify total Fe distribution, and the proportion of Fe distributed between Fe oxides and OC complexes. Overall, we expect biogeochemical Fe transformations to occur upon redox fluctuations in thermokarst-affected ice-rich permafrost soils, with potential direct implications for OC stabilization in Yedoma domain deposits (Figure 7.1), mirroring the impact of redox processes on Fe redistribution described for gradual thaw (i.e., gradual deepening of the active layer; Lipson et al., 2012; Herndon et al., 2020b; Patzner et al., 2020).

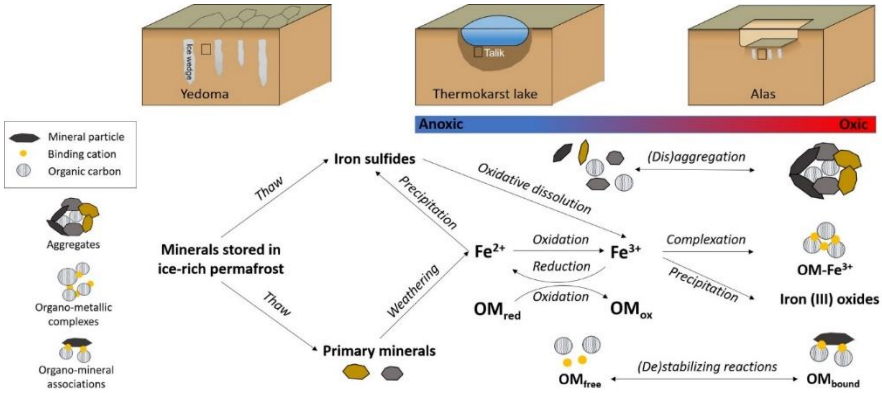

Figure 7.1: Conceptual scheme of the biogeochemical iron (Fe) transformations expected upon thermokarst lake formation and drainage in ice-rich-permafrost (Yedoma) sediments and implications for organic matter (OM) stabilization. Black rectangles in the upper schematic representation of Yedoma, thermokarst lake and Alas profile indicate the sample location. Geochemical reactions shown are both abiotic and microbially mediated. OM_{red} represents reduced organic species, which can include CH_4, and OM_{ox} represents oxidized organic species, which can include CO_2.

The dependence of Fe-bearing mineral solubilization, Fe translocation and Fe precipitation on redox conditions has been studied in polygonal permafrost soil of the Lena Delta (Fiedler et al., 2004), the Alaska North Slope (Lipson et al., 2012; Herndon et al., 2020b) and also in a thaw gradient site (i.e., palsa, bog and fen) close to Abisko in northern Sweden (Patzner et al., 2020). These studies found that redox processes drive Fe solubilization under fluctuating water-table height. Similarly, the mobilization of Fe upon thermokarst lake formation and subsequent transport in the hydrological network has been observed in several studies (e.g., Audry et al., 2011; Pokrovsky et al., 2014; Manasypov et al., 2015). However, the influence of redox fluctuations on Fe distribution in deeper deposits from ice-rich permafrost regions during the late Pleistocene and Holocene periods remains unknown. Using modern day studies of Fe dynamics in permafrost as an analogue, we hypothesize that upon thermokarst processes, the fluctuating redox conditions due to subsidence, lake formation, drainage, subaerial exposure and/or deposition, and refreezing, will drive Fe solubilization, translocation and precipitation within former Yedoma deposits, potentially affecting Fe-OC interactions in the resulting Alas deposits. To test this hypothesis, a screening of total Fe concentrations in ice-rich permafrost landscape is needed to better evaluate the potential for Fe redistribution upon thaw. Being able to identify that thaw processes have occurred in the past with potential influence on Fe-OC

interactions is valuable information in the context of a warming Arctic. Indeed, identifying potential redistribution of Fe-oxides and complexed Fe that took place in thawed, newly formed and subsequently refrozen deposits during the Lateglacial and Holocene warming periods may help to predict the fate of Fe-OC interactions upon current global warming and to better assess implications for OC stabilization. This information is relevant given that a large portion of the Arctic permafrost region is threatened by abrupt thaw and thermokarst processes (Olefeldt et al., 2016; Turetsky et al., 2020). Turetsky et al. (2020) emphasize that despite the fact that abrupt thaw will probably occur in < 20% of the permafrost zone, this thaw could affect half of the permafrost OC through collapsing ground, lake formation, rapid erosion, and thaw slumping.

The aim of this study is to investigate the Fe redistribution upon thermokarst processes during the Lateglacial and Holocene and to highlight potential implications for interactions between Fe and OC in present day ice-rich permafrost sediments. To this goal, (i) we measured the total Fe concentration on 1,292 deposits samples across the ice-rich permafrost region, including Yedoma (never thawed) and Alas (previously thawed) deposits, and (ii) we assessed the proportion of reactive Fe and the distribution between Fe oxides and Fe complexed with OC based on selective Fe extractions on a subset of Yedoma and Alas samples.

7.2 Environmental settings

The Yedoma domain is 1.4 million km² in extent and its Yedoma and thermokarst deposits contain between 327 - 466 Gt OC (Strauss et al., 2017). This region mainly includes areas of Alaska and Northeast Siberia which were not covered by ice sheets during the last glacial period (110 ka – 10 ka BP). For tens of millennia during the late Pleistocene, continuous periglacial weathering, transport, and sedimentation lead to the accumulation of several decameters thick permafrost deposits and syngenetic ice-wedge formation. The large syngenetic ice-wedges, often exceeding 50% of the soil volume, are a consequence of the late Pleistocene dry and cold climate which triggered regular frost cracking within the deposits. Subsequent filling of cracks with liquid water from rain or snowmelt resulted in the formation of vertical ice veins that over multiple millennia grew into up to 40 m deep and several meters wide ice-wedges (Schirrmeister et al., 2013). The deposits also consist

of ice-bearing sediments, which increase the total ice volume within Yedoma deposits (Strauss et al., 2017). These ice-rich deposits were then particularly sensitive to the rise in air temperature during the Pleistocene/Holocene transition period (starting around 14 ka BP; Walter et al., 2007). Ice-wedge degradation led to widespread thermokarst lake formation and subsequent lake drainage. Reworked sediments from former Yedoma deposits and newly formed peat deposits accumulated in thermokarst basins and refroze to form Alas deposits (Grosse et al., 2013). These Alas deposits are depleted in ice, compared to the original Yedoma ice-rich deposits, but still contain an important stock of OC (130-213 Gt C; Strauss et al., 2017). To perform this large-scale assessment of total Fe concentrations in Yedoma domain deposits, our set of samples (n=1,292) covers many regions of the Yedoma domain (North, West and Interior Alaska, the Kolyma region, the Indigirka region, the New Siberian Archipelago, the Laptev Sea coastal region, and Central Yakutia – Figure 7.2).

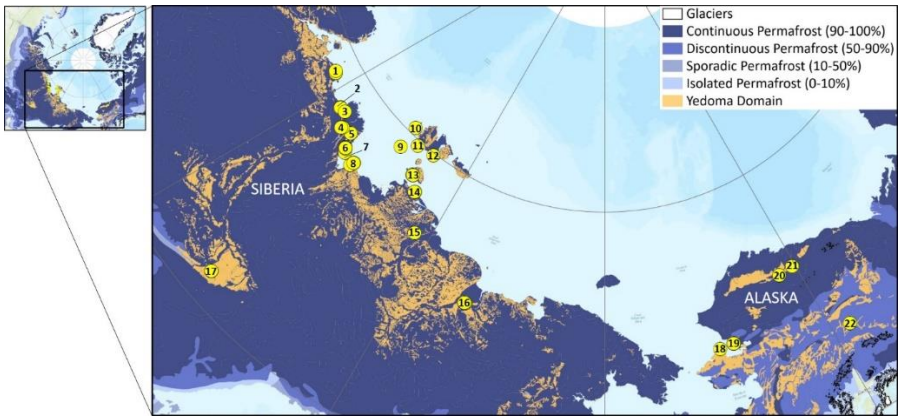

Figure 7.2: Location of the studied permafrost sites from the Yedoma Domain. 1. Cape Mamontov Klyk; 2. Nagym (Ebe Sise Island); 3. Khardang Island; 4. Kurungnakh Island; 5. Sobo Sise Island; 6. Bykovsky Peninsula; 7. Muostakh Island; 8. Buor Khaya Peninsula; 9. Stolbovoy Island; 10. Belkovsky Island; 11. Kotel'ny Island; 12. Bunge Land; 13. Bol'shoy Lyakhovsky Island; 14. Oyogos Yar coast; 15. Kytalyk; 16. Duvanny Yar; 17. Yukechi; 18. Kitluk; 19. Baldwin Peninsula; 20. Colville; 21. Itkillik; 22. Vault Creek tunnel. Yedoma domain coverage from Strauss et al. (2016, 2017).

7.3 Methods

7.3.1 Sampling

Depending on the sites, individual or multiple Yedoma/Alas deposit profiles were sampled (Figure 7.1). Samples were obtained either from cores or from natural exposures. Coring was conducted with various types of drilling rigs, from the surface during the winter season, and below the active layer during the summer season. Cliffs exposing deep permafrost deposits at coasts and river shores or headwall exposures in thaw slumps were sampled frozen with hammer and axes. Sub-profiles were sometimes needed to reconstruct a complete composite profile because of vertical discontinuities (i.e., ice-wedges presence) or sections covered by thawed mud overburden. For any additional information related to sampling techniques of a specific site, please refer to the respective reference papers for each field site (Table 7.1). Recovered samples remained frozen or were air-dried in the field before transport to the lab. The particle size distribution of these Yedoma domain deposits (described in reference papers from Table 7.1) is below 2 mm; therefore no sieving was necessary.

Table 7.1: List of the studied sites from the Yedoma domain, associated label, number of samples analyzed with portable X-ray fluorescence and inductively coupled plasma optical emission spectrometry method, number of profiles sampled for each type of deposits and associated reference papers. Sites are located in Siberia (1 to 17) and Alaska (18 to 22). The site numbers 1 to 22 are located on the map in Figure 7.2. * Sobo Sise profiles are of Holocene age on top of Yedoma Ice Complex deposits. Labels identification for each profile are detailed in Table S.7.1.

Site Nb	Site Name	Label	Samples analyzed with pXRF	Samples analyzed with ICP-	Yedoma profile	Alas profile	Fluvial profile	Reference papers
1	Cape Mamontov Klyk	Mak	80	-	2	1	0	Schirrmeister et al., 2008, 2011
2	Nagym (Ebe Sise Island)	Nag	29	-	2	1	0	Schirrmeister et al., 2003b
3	Khardang Island	Kha	31	1	1	0	0	Schirrmeister et al., 2007, 2011
4	Kurungnakh Island	Bkh, KUR	143	2	2	2	0	Schirrmeister et al., 2003b, 2008; Wetterich et al., 2008
5	Sobo Sise Island	Sob	58	58	2*	1	1	Fuchs et al., 2018
6	Bykovsky Peninsula	Mkh, BYK	150	2	5	2	0	Andreev et al., 2002; Grosse et al., 2007; Schirrmeister et al., 2002, 2011
7	Muostakh Island	Muo	11	-	1	0	0	Grigoriev et al., 2003; Schirrmeister et al., 2011
8	Buor Khaya Penisula	Buo	80	44	2	3	0	Schirrmeister et al., 2017
9	Stolbovoy Island	Sto	16	1	3	1	0	Grigoriev et al., 2003; Schirrmeister et al., 2003a
10	Belkovsky Island	Bel	12	-	0	2	0	Grigoriev et al., 2003; Schirrmeister et al., 2003a, 2011
11	Kotel'ny Island	KyS	10	-	1	0	0	Grigoriev et al., 2003; Schirrmeister et al., 2003a, 2011
12	Bunge Land	Bun	8	-	0	0	1	Schirrmeister et al., 2010
13	Bol'shoy Lyakhovsky Island	TZ, R, L	150	3	11	4	0	Andreev et al., 2009; Wetterich et al., 2011a, 2014
14	Oyogos Yar coast	Oy	50	1	1	1	0	Wetterich et al., 2009; Schirrmeister et al., 2011; Opel et al., 2017
15	Kytalyk	KY, KH	50	4	2	1	0	Weiss et al., 2016
16	Duvanny Yar	DY	143	5	5	1	0	Strauss et al., 2010
17	Yukechi	Yuk-Yul	87	2	2	2	0	Windirsch et al., 2020
18	Kitluk	Kit	45	2	1	1	0	Unpublished data ; Wetterich et al., 2012
19	Baldwin Peninsula	Bal	70	1	1	3	0	Jongejans et al., 2018
20	Colville	Col	23	8	1	0	0	Grosse et al., 2015 ; unpublished data
21	Itkillik	Itk, It	22	10	1	0	0	Kanevskiy et al., 2011
22	Vault Creek Tunnel	FAI	24	-	1	0	0	Schirrmeister et al., 2016
Total			1,292	144	47	26	2	

7.3.2 Assessment of bulk iron concentrations

We assessed the total Fe concentration on 1,292 samples from Yedoma domain deposits using a portable X-ray fluorescence (XRF) device (*Niton XL3t GOLDD+* pXRF; Thermo Fisher Scientific, Waltham, USA). The measurements were performed in laboratory (*ex situ*) conditions on air- or freeze-dried samples to avoid the introduction of additional variability (e.g., water content, sample heterogeneity). Briefly, samples are placed on a circular plastic cap (2.5 cm diameter) provided at its base with a thin transparent film (prolene 4 µm). Minimum sample thickness in the cap is set to 2 cm to prevent underestimation of the detected intensities (Ravansari et al., 2020) and total time of analysis is set to 90 seconds to standardize each measurement. The analysis is performed using a lead stand to protect operators from X-rays. To assess the precision of the pXRF method, we conducted three to five repetitions on twenty individual samples from different locations from Yedoma and Alas deposits (x-axis error bar from Figure 7.3).

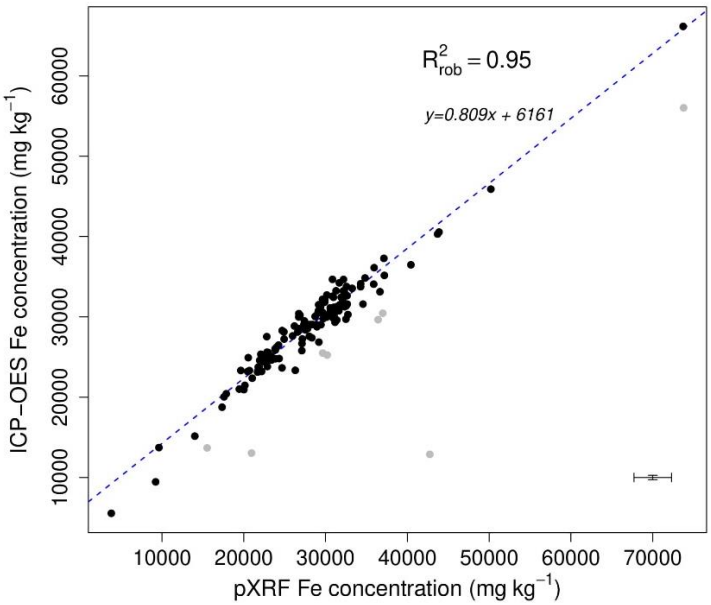

Figure 7.3: Total Fe concentrations (mg kg^{-1}) measured by the inductively coupled plasma optical-emission spectrometry (ICP-OES) method as a function of those measured by the portable X-ray fluorescence (pXRF) method on the Yedoma domain deposits. Errors bars (±2σ) are based on three repetitions of three samples for the ICP-OES method and five or three repetitions of twenty samples for the pXRF method. The robust linear regression is presented (blue line; alpha= 0.95; n=144), excluding the gray points, and the equation is provided.

To ensure trueness, the pXRF-measured concentrations were calibrated with another method. For a subset of 144 samples, we compared the total Fe concentrations measured by pXRF with Fe concentrations obtained using a method measuring Fe concentration in solution by inductively coupled plasma optical-emission spectrometry ICP-OES (iCAP 6500 Thermo Fisher Scientific) after sample dissolution by alkaline fusion. Briefly, air- or freeze-dried sediment samples are carefully milled for homogenization. A portion of the milled sample (80 mg) is mixed with lithium metaborate and lithium tetraborate and heated up to 1,000°C for 10 minutes. The fusion bead is dissolved in HNO_3 2.2 N at 80°C and stirred until complete dissolution (Chao and Sanzolone, 1992). The loss on ignition is assessed at 1,000°C and total element content is expressed in reference to the sediment dry weight at 105°C. Trueness of the analytical measurement by ICP-OES is validated by repeated measurements on the USGS basalt reference material BHVO-2 (Wilson, 1997) as well as on certified soils GSS-1 and GSS-4 (National Research Centre for CRM, 1986). The offset, defined as the difference between certified and ICP-OES value over the certified value, is -0.8%, -4.2% and -6.1% for the three certified materials, respectively. To assess the precision of the ICP-OES method, we conducted three repetitions on three individual samples from different locations from Yedoma and Alas deposits (y-axis error bar from Figure 7.3). The linear regression obtained based on Fe concentrations measured by pXRF and ICP-OES after alkaline fusion on this subset of 144 samples (robust R^2 = 0.95; Figure 7.3) was used to correct pXRF concentrations for trueness on the total set of samples (n=1,292). This linear regression is dependent on the internal geometry of the pXRF device used and should not be used for other pXRF-measured data without a calibration check. All concentrations data can be found in the Yedoma domain Mineral Concentration Assessment (YMCA) dataset (*Ch.1*). Here, only pXRF concentration values corrected using the well-defined regression are used.

7.3.3 Selective iron extractions

To test the influence of permafrost thaw on the distribution of Fe-oxides and on Fe involved in complexes, we performed selective Fe extractions on a subset of samples from Yedoma and Alas deposits (n=21) from three locations in Siberia: Sobo Sise Island, Buor Khaya Peninsula and Kytalyk (site number

5, 8 and 15 in Figure 7.2, respectively). Total Fe concentrations from Yedoma and Alas deposits in the subset are within similar range. Three standard procedures of selective Fe extraction from soil were used: dithionite-citrate-bicarbonate extraction (DCB), dark ammonium oxalate extraction (referred here as oxalate extraction), and sodium pyrophosphate extraction (referred here as pyrophosphate extraction). These extractions (DCB, oxalate and pyrophosphate) are not fully quantitative (Rennert, 2019) but can be used as indicators of the Fe-oxides phases or complexed Fe within a particular soil or sediment. More specifically, (i) DCB extractions provide an estimate of the content of free Fe oxides in soils, i.e., poorly crystalline and crystalline Fe-oxides, and should not include structural Fe from clay minerals (Mehra and Jackson, 1960; McKeague and Day, 1966); (ii) oxalate extractions target poorly crystalline Fe oxides (Blakemore et al., 1981), i.e., amorphous Fe oxides species and organo-metallic complexes; (iii) pyrophosphate extractions are used as an indicator of Fe-organic complexes (Bascomb, 1968; Parfitt and Childs, 1988). A contribution of Fe oxide nanoparticulates in addition to the Fe involved in organic complexes cannot be excluded (Jeanroy and Guillet, 1981), even if limited by the centrifugation and the filtration of the extract.

Practically, Fe concentration was measured in solution by ICP-OES after the following extraction procedures: (i) for a DCB extraction, 0.75 g of milled sediment was mixed with 30 ml of citrate solution (sodium citrate $Na_3C_6H_5O_7$ $2H_2O$) 0.3 M buffered by sodium bicarbonate $NaHCO_3$. The sample tube was placed in a hot bath (85°C) and three successive additions of 0.75 g of sodium dithionite ($Na_2S_2O_4$) were used to reduce crystallized and amorphous Fe oxides. The tube was centrifuged and the solution was filtered (Whatman 41 filter, 20 µm retention size). The residue was rinsed three times with 20 mL of NaCl 1 M and centrifuged. The rinsing solutions were filtered and pooled with the first solution to obtain a final solution; (ii) for an oxalate extraction, 0.4 g of milled sediment was mixed with 40 mL of oxalate extractant (ammonium oxalate $(NH_4)_2C_2O_4$ H_2O and oxalic acid $H_2C_2O_4$ $2H_2O$). The tube was agitated for 4 hours in the dark, given that this reagent is UV-sensitive. The tube was centrifuged and the solution was filtered (Whatman 41 filter); (iii) for a pyrophosphate extraction, 0.4 g of milled sediment was mixed with 40 mL of pyrophosphate solution (tetrasodium pyrophosphate decahydrate $Na_4P_2O_7$ $10H_2O$ 0.1 M). The tube was agitated for 16 hours. Sodium sulfate (1.4 g) was added and the solution was centrifuged (30 minutes at 4,000 rpm) and filtered (Whatman 41 filter). To assess the precision of selective Fe extractions (i.e., DCB, oxalate and pyrophosphate), three

repetitions of three different samples were performed. Samples were selected from Yedoma and Alas deposits from the Yukechi site (with similar matrix, not presented here). The mean and associated coefficient of variation (i.e., the ratio between standard deviation and the mean) were calculated for each sample and are summarized in Table S.7.2.

In the following, the Fe extracted using DCB, oxalate or pyrophosphate extraction methods will be referred to as Fe_d, Fe_o and Fe_p, respectively, whereas total Fe measured by XRF and corrected for trueness (Sect. 7.3.2) will be referred to as Fe_t. The Fe_o/Fe_d ratio will be used to reflect the relative proportion of amorphous (short-range ordered) Fe oxyhydroxides and complexed Fe within the global pool of Fe oxides. The Fe_d/Fe_t ratio will be used for the proportion of free Fe oxides and complexed Fe relative to the total Fe, the Fe_o/Fe_t ratio indicates the proportion of amorphous Fe oxides and complexed Fe relative to the global Fe pool, and Fe_p/Fe_t ratio the proportion of Fe present in organo-metallic complexes relative to the global Fe pool.

7.3.4 Selective carbon extractions

The carbon selectively extracted by oxalate and pyrophosphate has been evaluated on the same solutions used for selective Fe extractions (Sect. 7.3.3). More specifically: (i) in the solution from the oxalate extraction, we evaluate the proportion of organic acids by measuring the absorbance at 430 nm on a Genesys 10S VIS spectrophotometer, with the oxalate extractant solution as a blank. The optical density of the oxalate extract (ODOE) is mainly influenced by the extracted fulvic acids thereby indicating the concentration in organic acids present in solution (Daly, 1982); (ii) in the solution from the pyrophosphate extraction, we measure the concentration of dissolved OC released after dispersion by pyrophosphate (referred as C_p) using a Shimadzu total organic carbon (TOC) analyzer (measuring non purgeable OC). This indicates the amounts of C participating in organo-metallic complexes in soils. To assess the precision of selective C extractions (i.e., ODOE and Cp), three repetitions of three different samples were performed. Samples were selected from Yedoma and Alas deposits from the Yukechi site. The mean and associated coefficient of variation (i.e., the ratio between the standard deviation and the mean) were calculated for each sample and are shown in Table S.7.3.

7.3.5 Statistical analysis

We performed computations for statistical analysis using R software version R.3.5.1 (R Core Team, 2018). Robust linear regression (R^2_{rob}) presented in this study are implemented with an alpha of 0.95. In the following, the non-parametric statistical Wilcoxon test (median) is used in preference to the student test (mean) to statistically compare two distributions when data distribution do not follow the normality hypothesis (Shapiro-Wilk normality test p-value <0.05). Median and median absolute deviation (MAD) will be used to compare concentrations of Yedoma and Alas datasets. Mean and standard deviation (σ) will be used to compare concentrations among different sites.

7.4 Results

7.4.1 Global distribution of iron concentrations in Yedoma and Alas deposits

The median total Fe concentration (± MAD, i.e., median absolute deviation) in never thawed Yedoma deposits (31.9 ± 3.0 g kg^{-1}; n=814) and previously thawed, refrozen or newly formed Alas deposits (31.2 ± 8.2 g kg^{-1}; n=470) shows no significant differences (p-value = 0.64, Wilcoxon test). However, the dispersion (i.e., MAD) of total Fe concentrations is more than two times larger for Alas deposits compared to Yedoma deposits (Figure 7.4).

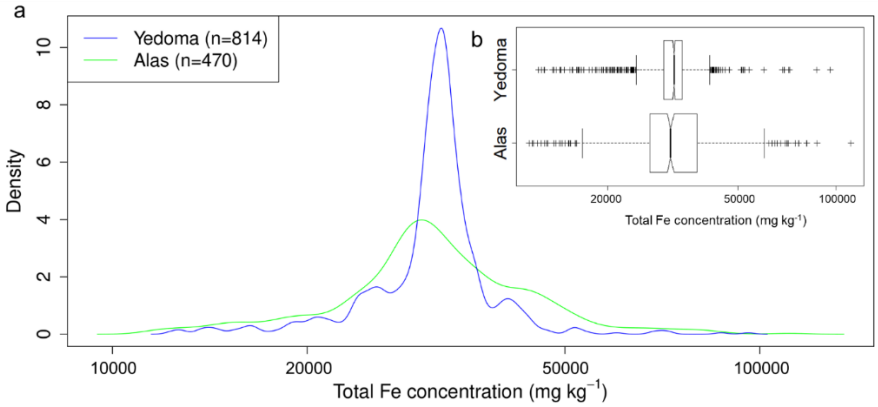

Figure 7.4: (a) Density plot and (b) fligner test (boxplot) of the total iron (Fe) concentration within Yedoma (n=814; blue line) and Alas (n=470; green line) deposits.

This implies that Alas deposits have higher probability to display either lower or higher total Fe concentrations at a certain depth, relative to Yedoma deposits. Along with this, Figure 7.5 displays profile selections (i.e., based on Yedoma deposit profiles excluding active layer) of individual Yedoma, Alas or deltaic/fluvial deposits profiles and confirm the homogenous total Fe concentrations in Yedoma deposits and heterogeneous total Fe concentrations in Alas deposits as mentioned above. Figure 7.5 highlights some additional observations. First, profiles with sediments of deltaic/fluvial origins display significantly lower total Fe concentrations compared to Yedoma or Alas deposits (p-value < 0.005, Wilcoxon test). Deltaic deposits (Bun) and fluvial deposits (Sob14 T2-6) have a median total Fe concentration equal to 12.3 ± 0.8 g kg^{-1} and 21.7 ± 6.8 g kg^{-1}, significantly lower to the median values mentioned above for Yedoma and Alas deposits. Second, Yedoma deposits from Siberia (e.g., labeled Mak, Muo, DY, TZ, L and Oy) show similar total Fe concentrations throughout the whole Siberia region, even for sites located thousands of km apart from each other. This is illustrated by equivalent mean total Fe concentrations (±2σ, i.e., two standard deviations) along the Yedoma deposit profiles from Cape Mamontov Klyk (Mak-12 to 19) 31.9 ± 1.3 g kg^{-1}, to Oyogos Yar coast (Oy-07-08) 32.6 ± 3.0 g kg^{-1}, Duvanny Yar (DY-05) 33.5 ± 2.8 g kg^{-1}, Sobo Sise Island (Sob14-T2-3) 31.6 ± 2.0 g kg^{-1}, Muostakh Island (Muo) 31.7 ± 3.7 g kg^{-1}, and even to the New Siberian Archipelago: Bol'shoy Lyakhovsky Island (L7-18) 32.7 ± 3.4 g kg^{-1} or Stolbovoy Island (Sto) 27.2 ± 1.2 g kg^{-1}. Note that the distance between profiles from Cape Mamontov Klyk (Mak-12 to 19) to Duvanny Yar (DY-05) is more than 1500 km (see Figure 7.2). Lastly, Figure 7.5 highlights that Yedoma deposit profiles from Alaska (i.e., labeled Itk, Col, Bal2 and Kit) display homogeneous total Fe concentrations along each profile (similarly to Yedoma deposits from Siberia) but with different mean total Fe concentrations between them. The Itkillik Yedoma exposure displays a mean of 24.6 ± 1.7 g kg^{-1} Fe, Colville Yedoma profile of 30.5 ± 1.9 g kg^{-1}, Baldwin Peninsula Yedoma deposits of 43.2 ± 7.4 g kg^{-1} Fe (the Fe concentration becomes 42.1 ± 3 g kg^{-1} Fe when excluding the 3 samples at the bottom of the profile considered as a separate unit), and 41.1 ± 4.7 g kg^{-1} Fe from a Yedoma exposure at the Kitluk River on the northern Seward Peninsula.

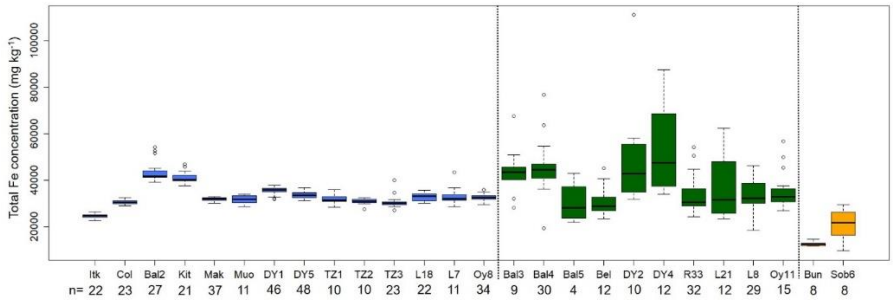

Figure 7.5: Boxplot of the Fe concentration within selected profiles from different types of deposit: Yedoma Ice Complex (blue), Alas (green), and deltaic/fluvial deposits (orange). Yedoma Ice Complex deposit profiles were selected based on the absence of active layer deposits or fluvial deposits along the profile. Alas profiles located near Yedoma profiles selected (when possible) are shown. The number of samples for each boxplot is given below labels of the x-axis. The sample labels refer to Table 7.1.

7.4.2 Variability of iron concentrations with depth in Yedoma and Alas deposits

The full dataset of total Fe concentration from Yedoma domain deposits is provided in the PANGAEA data repository (doi:10.1594/PANGAEA.922724). Here, the depth-variations of total Fe concentrations in Yedoma domain deposits are investigated in detail and linked to the specific history of the deposits from deposition during late Pleistocene to post-depositional processes during Lateglacial and Holocene warmer periods. In each location, where both Yedoma and Alas deposits were available, the vertical total Fe concentration is compared between the Yedoma profile and the Alas profile (Figure 7.6). We present each profile with a simplified stratigraphic column, which highlights the successive layers along the sampled profile (i.e., Yedoma deposits, thermokarst deposits, fluvial deposits, active layer, or peat layer). The complexity in individual profiles arises from the multiple origins of Yedoma deposition during the late Pleistocene, as well as thermokarst, soil development, cryoturbation, peat formation, or flooding processes (as indicated by fluvial sandy layers) that affected the depositional and soil environment.

Ice-rich Yedoma deposits had homogeneous Fe concentrations throughout the whole deposit thickness (Figure 7.6a, c, e, g, i, k, m, o), whereas Alas deposits were characterized by variable Fe concentrations with depth (Figure 7.6b, d,

f, h, j, l, n, p). This reflects the higher dispersion of Fe concentrations in Alas deposits compared to Yedoma deposits (Figure 7.4; Sect. 7.4.1). For example, both Duvanny Yar Yedoma deposit profiles (DY-01 and DY-05) showed constant Fe concentrations despite their large thicknesses (Figure 7.6a) and despite the fact that they are located 2 km away from each other. DY-01 had a mean of 35.5 ± 2.77 g kg^{-1} Fe (±2σ) for a total thickness of about 20 m and DY-05 of 33.5 ± 2.79 g kg^{-1} Fe for an equivalent thickness. Conversely, DY-04 Alas profile displayed a mean of 53.3 ± 37.6 g kg^{-1} (±2σ) for a deposit thickness of 3.5 m which points at the heterogeneity of the material inherent to Alas thawing history (Figure 7.6b). Deposits with fluvial origins (i.e., characterized as sandy layers) showed depleted total Fe concentrations, as highlighted in Figure 7.6d, n and p). Conversely, in sediments containing peat layers, total Fe concentrations either: i) increased in active layer deposits (Figure 7.6f, g, l) or even in peat layers from underlying permafrost (Figure 7.6d, m); ii) decreased, usually in the top horizons of the profile Figure 7.6l); or iii) remained with similar Fe concentration as deposits located above or below in the profile (Figure 7.6a, c, d, i). The data further indicate a positive correlation between total Fe concentrations and TOC content (wt%; Figure S.7.1). An exception to this trend is observed for organic-rich samples (i.e., TOC > 30 wt%) in the top surface layer (within the first centimeters) of the profile that show a depletion of total Fe concentrations.

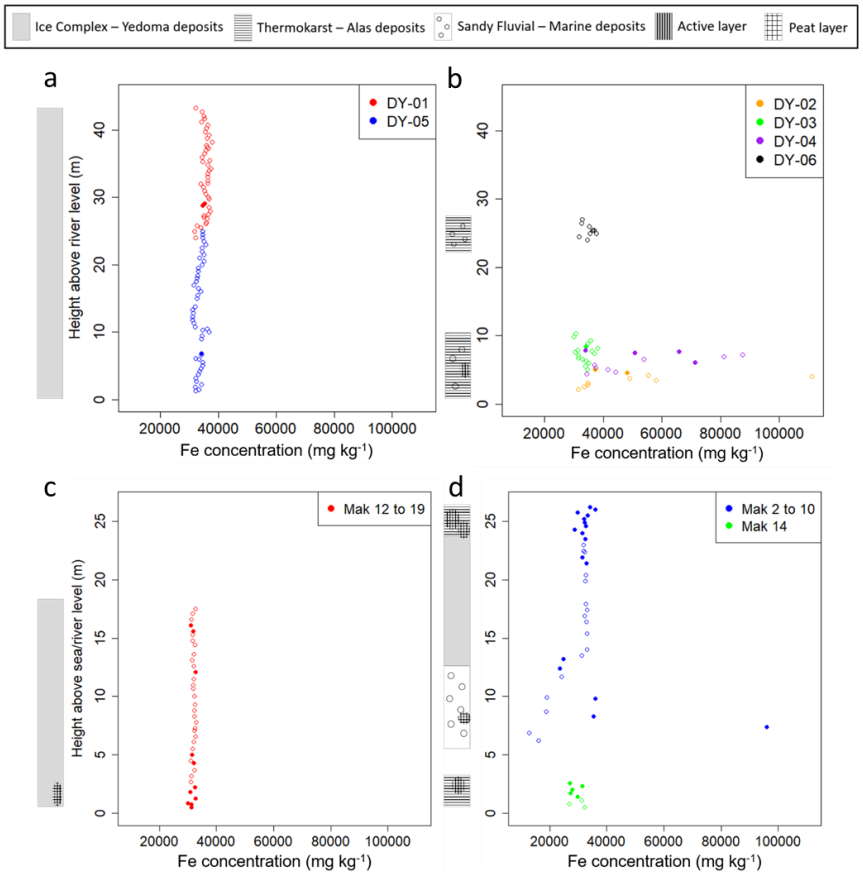

Figure 7.6: Depth-variation plot of total Fe concentrations (mg kg^{-1}) presented with the corresponding stratigraphic columns in never thawed Yedoma Ice Complex deposits (left side: a, c, e, g, I, k, m, o) and in previously thawed and newly formed Alas deposits (right side: b, d, f, h, j, l, n, p) from the following sites: Duvanny Yar (a-b), Cape Mamontov Klyk (c-d), Bol'shoy Lyakhovsky Island (e-f), Bykovsky Peninsula (g-h), Oyogos Yar coast (i-j), Baldwin Peninsula (k-l), Sobo Sise Island (m-n), New Siberian Archipelago and Muostakh Island (o-p). Samples with total organic carbon (TOC) content > 5wt% (plain circle) and < 5wt% (open circle) are identified (samples with missing information about TOC content are presented with a cross). The stratigraphic columns are based on descriptions provided in the reference papers listed in Table 7.1 for each location. Labels for each profile are explained in Table S.7.1.

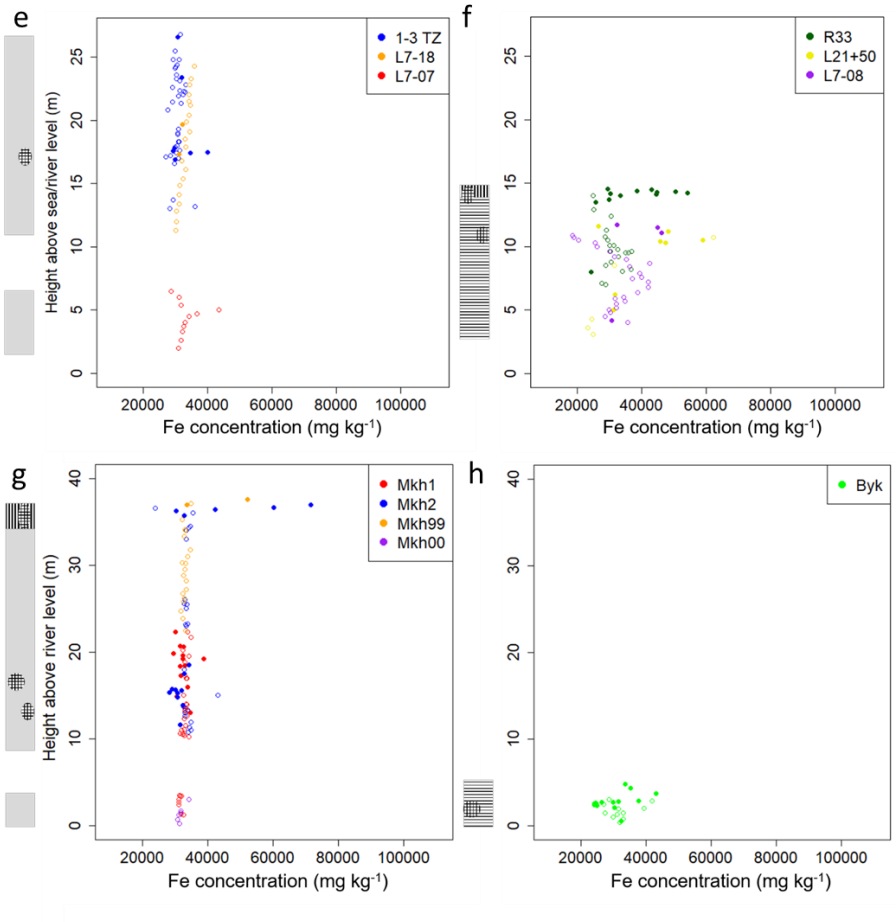

Figure 7.6: (continued)

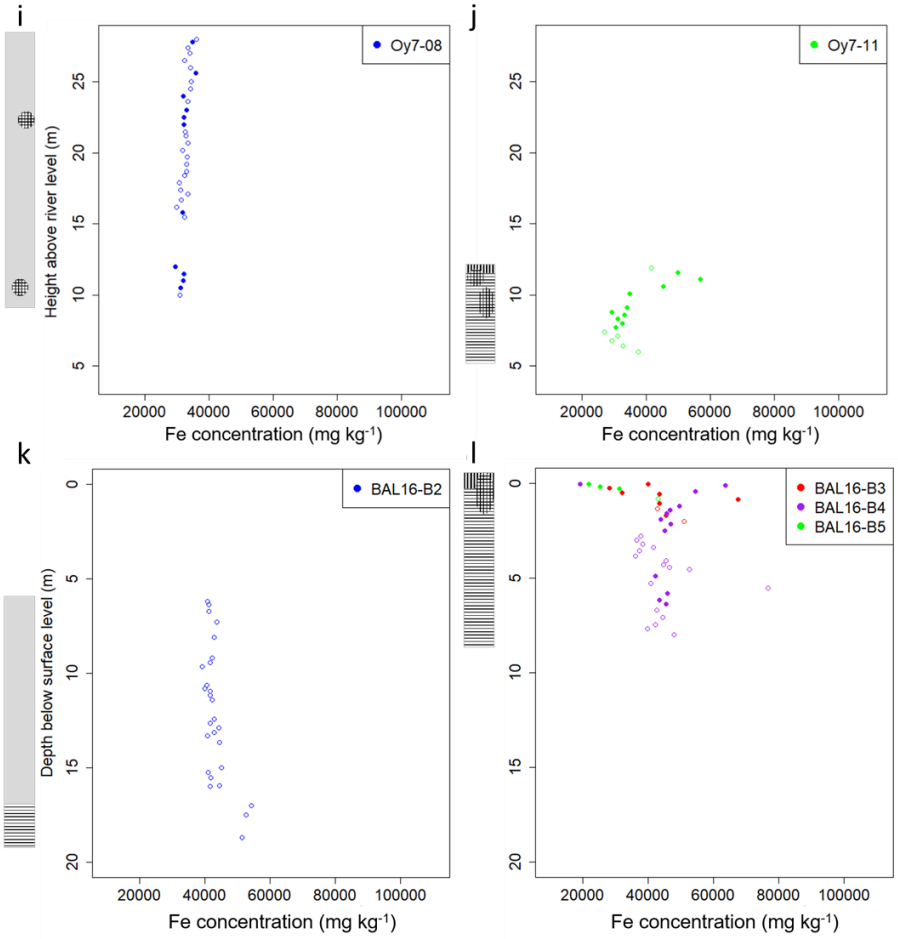

Figure 7.6: (continued)

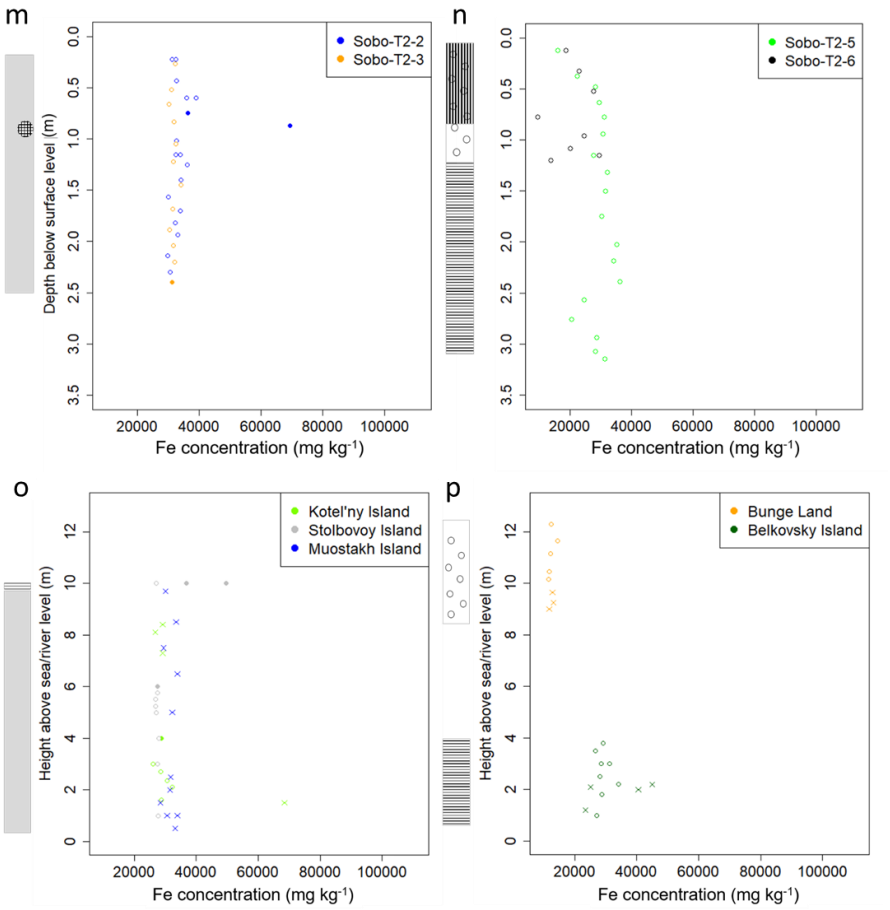

Figure 7.6: (continued)

7.4.3 Distribution of selectively extracted iron and carbon in Yedoma and Alas deposits

The Fe concentrations in selective extractions by DCB, oxalate and pyrophosphate within a subset of selected Yedoma and Alas deposits are presented in Table 7.2. Robust and Pearson correlation matrix for all studied parameters (Fe_t, Fe_d, Fe_o, Fe_p) is presented in Figure S.7.2. Based on this subset of 21 samples from the Yedoma domain, the Fe_d/Fe_t ratios in Yedoma (n=12) and Alas (n=9) deposits have a median of 26.6 % and 27.8 %, respectively, and are not statistically different (p-value 0.46, Wilcoxon test). Taking the never thawed, previously thawed and newly formed deposits together, the mean of Fe_d/Fe_t, which represents the proportion of free Fe

oxides out the global Fe pool (Sect. 7.3.3), equals 24.7 %. Within those free oxides, poorly crystalline (i.e., amorphous) Fe oxides or complexed Fe reach 80.9 % and therefore represent about 20 % of the total Fe pool (Fe_o/Fe_t; Table 7.2). The distribution of reactive Fe-oxides varies within each profile; the Fe_o/Fe_t ratio ranges from 22.8 % to 36.5 % (Sob14 T2-2), 13.8 % to 22.0 % (Sob14 T2-5), 10 % to 28.6 % (KY T1-1) and 17.2 % to 30.4 % (KY T2-2), for two pairs of Yedoma-Alas profiles (Table 7.2); the Fe_p/Fe_o ratio in the same profiles indicates that more than a third of Fe amorphous phases are involved in complexes with OC.

The C selectively extracted by the oxalate and pyrophosphate is presented in Table 7.2 and correlation matrix for all studied parameters (ODOE, C_p, TOC) is presented in Figure S.7.2. Positive correlations stand out between TOC content (in wt%) and C_p (mg kg^{-1}; R^2_{rob} = 0.80; Figure 7.7a), and between C_p and Fe_p (R^2_{rob} = 0.80; Figure 7.7b), resulting in a positive correlation between TOC content and Fe_p (R^2_{rob} = 0.77; Figure 7.7c). A positive correlation is also observed between ODOE and Fe_o (R^2_{rob} = 0.4; not shown), as well as between ODOE and Fe_p (R^2_{rob} = 0.77; Figure 7.7d). The total Fe concentration in these deposits (Fe_t) is not correlated with pyrophosphate-extractable Fe and C (Fe_p, C_p) or TOC (R^2_{rob} < 0.05), but is correlated with DCB- (Fe_d; R^2_{rob} = 0.76; Figure 7.7e) and oxalate-(Fe_o; R^2_{rob} = 0.34; not shown) extractable Fe.

Table 7.2: Concentrations in total Fe (Fe_t) and Fe selectively extracted by dithionite-citrate-bicarbonate (Fe_d), ammonium oxalate (Fe_o), pyrophosphate (Fe_p) in Yedoma and Alas deposits. Total organic carbon (TOC), optical density of oxalate extract (ODOE) and C extracted with pyrophosphate (C_p) are also presented. *Sobo Sise samples are Holocene age deposits on top of Yedoma Ice Complex deposits profile. ** The TOC data are from Fuchs et al. (2018) for Sobo Sise Island (Sob), from Schirrmeister et al. (2017) for Buor Khaya Peninsula (Buo) and from Weiss et al. (2016) for Kytalyk (KY).

Sample	Deposits	Depth	Fe_t	Fe_d	Fe_o	Fe_p	Fe_d/Fe_t	Fe_o/Fe_t	Fe_o/Fe_d	Fe_p/Fe_o	TOC**	ODOE	C_p
		cm			g kg^{-1}			%			wt%	-	g kg^{-1}
Sob14 T2-2-5	Yedoma*	43	30.3	9.75	10.2	4.65	32.2	33.7	104.8	45.6	3.26	0.335	13.1
Sob14 T2-2-19	Yedoma*	140	31.6	9.46	11.5	4.15	29.9	36.5	121.9	35.9	4.22	0.410	14.0
Sob14 T2-2-31	Yedoma*	230	30.0	6.45	6.83	1.84	21.5	22.8	105.8	27	2.68	0.369	9.74
KY (1-1) 9-14	Yedoma	11.5	27.2	7.41	5.65	2.77	27.2	20.7	76.2	49.1	2.40	0.093	7.16
KY (1-1) 40-45	Yedoma	42.5	32.8	10.0	3.29	0.217	30.5	10	32.9	6.6	0.61	0.029	1.26
KY (1-1) 90-95	Yedoma	92.5	30.8	8.25	8.81	5.45	26.8	28.6	106.9	61.8	4.94	0.409	45.8
Buo-02-A02	Yedoma	60	29.5	7.63	6.93	1.03	25.9	23.5	90.8	14.8	0.82	0.079	0.823
Buo-02-D18	Yedoma	450	20.0	0.941	0.634	0.421	4.7	3.2	67.4	66.4	4.08	0.129	5.64
Buo-02-D19	Yedoma	500	21.0	1.44	1.11	0.952	6.9	5.3	77.1	85.4	7.01	0.153	8.50
Buo-04-A01	Yedoma	100	32.2	8.72	4.06	0.644	27.1	12.6	46.5	15.9	0.86	0.062	2.33
Buo-04-B10	Yedoma	850	29.0	7.63	5.85	1.95	26.3	20.2	76.6	33.3	1.62	0.132	5.51
Buo-04-C23	Yedoma	1350	23.2	4.78	2.42	0.622	20.6	10.4	50.6	25.7	0.21	0.033	1.53
Mean (Yedoma)							23.3	19.0	79.8	39.0			
1σ							8.8	10.8	27.4	23.6			
Sob14 T2-5-5	Alas	37.5	20.9	4.69	2.88	1.14	22.4	13.8	61.4	39.7	2.15	0.097	4.31
Sob14 T2-5-17	Alas	132	33.1	7.93	4.81	1.17	23.9	14.5	60.7	24.4	1.92	0.127	4.73
Sob14 T2-5-27	Alas	239	35.2	10.5	7.72	1.68	29.9	22	73.5	21.8	2.17	0.170	5.61
KY (2-2) 27-32	Alas	29.5	26.9	5.06	4.62	2.48	18.8	17.2	91.4	53.7	3.87	0.138	7.53
KY (2-2) 42-48	Alas	45	24.9	4.76	4.55	2.56	19.1	18.2	95.6	56.4	3.66	0.153	8.41
KY (2-2) 89-94	Alas	91.5	26.8	8.27	8.17	5.62	30.8	30.4	98.7	68.8	7.20	0.310	24.0
Buo-05-A04	Alas	80	26.0	7.23	7.35	0.650	27.8	28.2	101.7	8.8	2.31	0.128	3.00
Buo-05-B12	Alas	400	29.2	9.89	6.54	1.49	33.9	22.4	66.1	22.8	1.49	0.108	4.06
Buo-05-C26	Alas	830	30.3	9.90	9.17	1.46	32.6	30.2	92.6	15.9	1.64	0.116	3.71
Mean (Alas)							26.6	21.9	82.4	34.7			
1σ							5.7	6.5	16.8	20.8			
Mean (total)							24.0	19.8	78.5	36.6			
1σ							8.0	8.9	24.6	21.1			

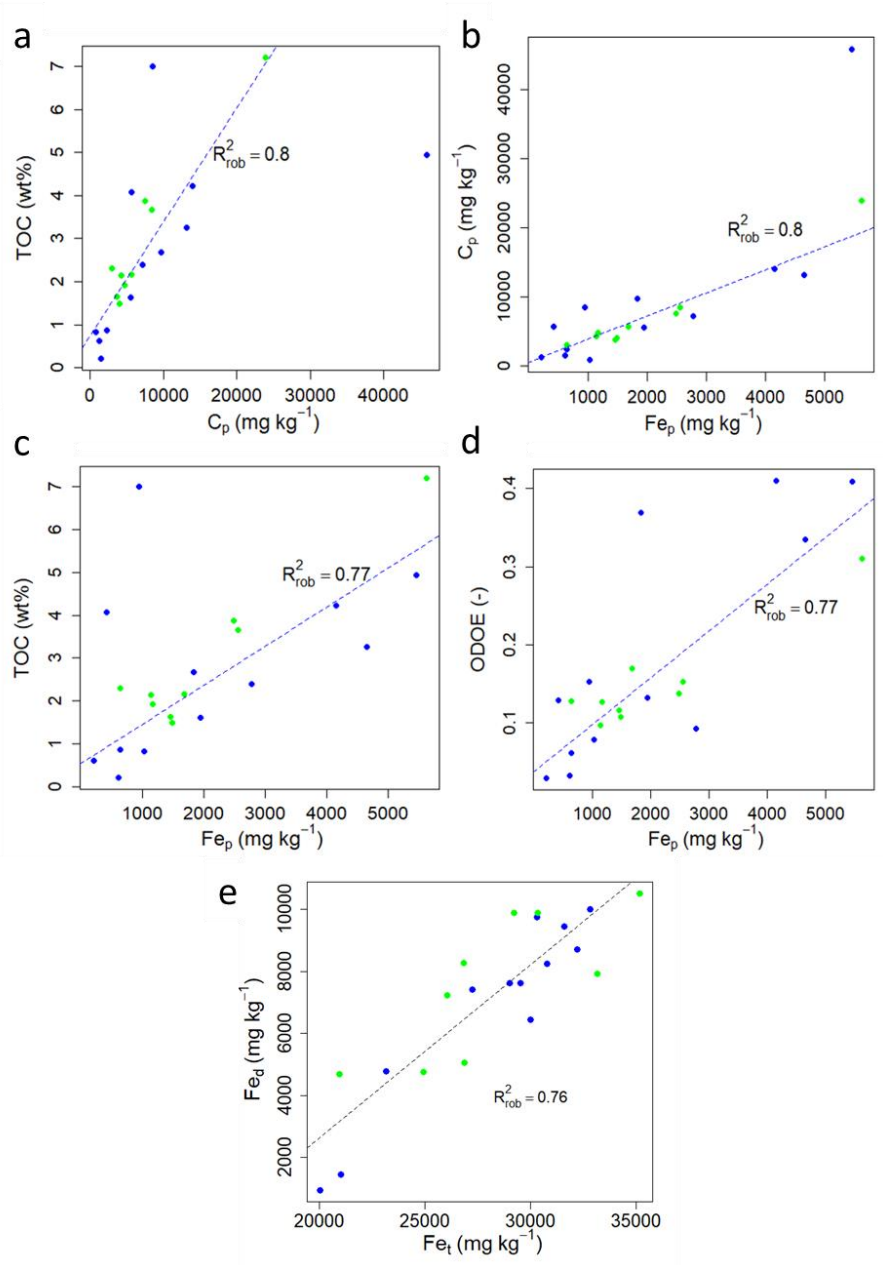

Figure 7.7 Robust linear regression plots for Yedoma Ice Complex deposits (blue dots) and Alas deposits (green dots) between (a) Total organic carbon (TOC) content (wt%) vs. C extracted with pyrophosphate (C_p); (b) C_p vs. Fe selectively extracted by pyrophosphate (Fe_p); (c) TOC vs. Fe_p; (d) Optical density of oxalate extract (ODOE) vs. Fe_p; and (e) Fe selectively extracted by dithionite-citrate-bicarbonate (Fe_d) vs total Fe concentrations (Fe_t). Dashed lines represent the robust linear regression (alpha = 0.95; n = 21).

7.5 Discussion

7.5.1 Iron distribution in Yedoma deposits

In Yedoma deposits, total Fe concentrations are stable with depth in all profiles (from both Siberia and Alaska). The standard deviation, 2σ, ranges from 1.3 to 3.7 g kg^{-1} Fe with depth for Cape Mamontov Klyk (Mak-12 to 19) and Muostakh Island (Muo), respectively (Figure 7.5 and Figure 7.6). We suggest that the conditions of formation for these ice-rich deposits can explain the stable total Fe concentrations with depth within their profiles. First, Yedoma deposits have never thawed since their late Pleistocene deposition, thereby limiting the periods of redox fluctuations which may affect Fe solubility (Schwertmann, 1991; Colombo et al., 2014). We see this supported by evidence for a rapid syngenetic freezing (on geological timescale) of the transported particles after settlement during periods of Yedoma deposit aggradation (Schirrmeister et al., 2002b) as well as overall dry conditions under late Pleistocene tundra steppe active layer conditions (Schirrmeister et al., 2013). Second, sediments along a single Yedoma profile likely result from materials with similar total Fe concentrations. Sediments contributing to Yedoma deposits are derived from a mix of lithologies being affected by intense periglacial weathering processes and getting deposited as unconsolidated sediments. The similar periglacial weathering, erosion, and sediment transport processes which were similar across large unglaciated permafrost domains in the Late Pleistocene may have contributed to the homogenization of mixed sediment lithologies before Yedoma aggradation. The origins of Yedoma sediments across the Yedoma domain have, for a long time, divided the scientific community and are still under debate (Schirrmeister et al., 2002, 2020; Murton et al., 2015). Yedoma deposits were, at first, characterized as homogeneous silty fine, ice- and organic-rich sediments with primary or secondary aeolian processes being the main contributor during the time of formation. Hence, Yedoma deposits were and still are often defined as loess or loess-related deposits (Pewe and Journaux, 1983; Tomirdiaro and Chernen'kiy, 1987; Murton et al., 2015). However, in addition to the established aeolian contribution to these ice-rich sediments, additional contributions from fluvial, colluvial, alluvial local sedimentation processes are identified in many regions of the Yedoma domain (e.g., Schirrmeister et al., 2020). It is now considered that the aggradation of Yedoma deposits is not the result of a single process of aeolian deposition, but

rather the result of a polygenetic origin with probable seasonally differentiated deposition mechanisms controlled by local environmental conditions, including the contribution from local fluvial, colluvial, and alluvial sediments (Strauss et al., 2012; Schirrmeister et al., 2013, 2020). Similar heavy mineral composition between Yedoma deposits and the nearby mountain range support a contribution from local sediments during Yedoma deposits aggradation (e.g., Schwamborn et al., 2002; Siegert et al., 2002). The largely linear relationship between sample depth (or vertical position in an exposure) and calibrated ^{14}C age reported for Yedoma deposits (Schirrmeister et al., 2002b; Wetterich et al., 2014) indicates that the material is supplied with a stable sedimentation rate. Our data are well in line with the supply of local sediments with similar Fe concentrations, which is consistent with the reported homogeneous mineralogy of Yedoma deposits with depth (Strauss et al., 2017).

Despite generally dry conditions, Yedoma deposits may have experienced short wetter periods during their formation (indicated by the presence of peat or peaty soil layers). It can be identified from some of the studied profiles, as in Cape Mamontov Klyk (Mak-2 to 10), Bol'shoy Lyakhovsky Island (1-3 TZ) or Sobo Sise Island (SobT2-2), that the formation of peat layers are associated with the highest total Fe concentrations. In Cape Mamontov Klyk (Figure 7.6d), the highest Fe concentrations occurred in a sandy peat layer underlying the typical silty Yedoma deposits. In Bol'shoy Lyakhovsky Island (Figure 7.6e), the highest total Fe concentrations occurred in a peat inclusion from a typical Yedoma Ice Complex unit. In Sobo Sise (Figure 7.6m), the total Fe concentrations are the highest in a single peaty horizon of Holocene age overlying Yedoma deposits. The higher total Fe concentration highlighted in these deposits often correspond with peat layers or inclusions. The local redistribution of total Fe in Yedoma profiles can be explained with two hypotheses: i) solubilization of Fe (from Fe oxide or complexed Fe dissolution) induced by the wetter conditions during short warmer periods and translocation of Fe to a peat layer where the microscale redox environment favors Fe oxide precipitation or ii) cryoturbation of a surface peat horizon where Fe was precipitated following a similar solubilization and precipitation process. The high TOC content in these Fe-rich samples (e.g., TOC: Mak-2-3 = 15.3 wt% and Sob14T2-2-11 = 7.6 wt%) supports the hypothesis that the presence of peat favors the precipitation of solubilized Fe. Field observations from Schirrmeister et al. (2008) indicate that the sandy-peat layer from Cape Mamontov Klyk (5 - 10 m above sea level; Figure 7.6d) have brownish to

reddish mottled layers, in a buried oxic gley–soil horizon, thereby supporting our hypothesis of Fe translocation upon water saturated conditions and Fe oxide precipitation in favorable oxic conditions. Water saturated conditions are suggested to favor the translocation of reduced Fe as already observed in previous studies (Fiedler et al., 2004; Riedel et al., 2013; Herndon et al., 2017). The accumulation of Fe is also found in active layer or Holocene deposits (located in the top of the profiles – Figure 7.6g), and comparable with Fe accumulation in organic-rich surface soils of ice-wedge polygon from arctic tundra (Herndon et al., 2020a). Thus, evidence for Fe accumulation also supports that higher TOC content, often observed in active layer, promotes Fe precipitation in favorable redox conditions. Despite the fact that Yedoma deposit formation predominantly took place during the interstadial Marine Isotope Stage (MIS) 3 and the stadial MIS 2, promoted by long-lasting continental cold and arid climate conditions, short thaw phases occurred during the late Pleistocene with potential impact on the formation of Yedoma deposits (Schirrmeister et al., 2002b, 2013; Wetterich et al., 2014). Wetter conditions trigger anoxia, which improves vegetation growth, lowers organic matter mineralization rates and thus promotes peat accumulation (Keller and Medvedeff, 2016). In northern latitudes, phases of peat expansion triggered by increasing air temperatures and moisture supply were inferred from paleo proxies (from 57 ka to 45 ka BP and from 35 ka to 29 ka BP; Treat et al., 2019). Buried peat layers found in deep Yedoma deposits could be indirect evidence of these "short" warming and wetting periods (Treat et al., 2019), and our data highlight that this likely promoted Fe precipitation. However, our data show that the presence of peat layers in Yedoma deposits does not necessarily imply accumulation of Fe (Figure 7.6). Detecting the presence or absence of Fe accumulation in these peat layers is important to identify potential accumulation of reactive Fe, which in turn can promote OC stabilization. Based on the positive correlation between total Fe concentrations and reactive Fe concentrations in the deposits (R^2 = 0.76; Figure 7.7e), we argue that Fe accumulation in peat layers likely contributes to organic matter stabilization and hence to lower organic matter mineralization rates.

Our data highlight that Yedoma deposits from Siberia show similar total Fe concentrations (Sect. 7.4.1; Figure 7.5) across deposits that span 1500 km across Siberia (Figure 7.2). In Yedoma deposits from Alaska, the mean total Fe concentration differs from one Alaskan location to another, being higher in Western Alaska (Kitluk and Baldwin Peninsula: 41.1 ± 4.7 and 43.2 ± 7.4 g

kg^{-1} Fe, respectively) than in Northern Alaska (Colville and Itkillik: 30.5 ± 1.9 and 24.6 ± 1.7 g kg^{-1} Fe, respectively; Figure 7.5; see Figure 7.2 for locations). The mineralogical variation between loess in different parts of the world reflects the nature of the surficial geology and the effectiveness of sediment mixing processes in the individual source regions (Pye, 1995). Our data suggest that across the Siberian sites, the sediments contributing to the deposits are of similar chemical composition, or of mixed lithologies with a total Fe concentration similar to the Fe concentration in the continental crust (Börker et al., 2018). The total Fe concentration reported in the upper continental crust (39 g kg^{-1}; Rudnick and Gao, 2003), in continental sediments (40 g kg^{-1}; Rauch and Pacyna, 2009) and in a typical loess (24 g kg^{-1}; Rauch and Pacyna, 2009) are likely to yield a homogeneous total Fe concentration in Yedoma deposits (32 g kg^{-1}; this study) after sediment mixing by periglacial surface abrasion and polygenetic (aeolian, fluvial, colluvial, alluvial) transport and deposition. In contrast, in Alaska, the different mean total Fe concentration in different locations suggests a range of Fe contributions from different local lithologies, such as carbonates present in North Alaska close to the Brooks Range (Walker and Everett, 1991; Till et al., 2008) or to less effective sediment mixing processes before deposition than in Siberia. Overall, despite their different mean total Fe concentrations, both Siberia and Alaska Yedoma deposits present similar Fe concentrations with depth, and can be used to investigate the influence of thermokarst process with potential redistribution of Fe during Alas deposits formation.

7.5.2 Thawing triggers iron mobility in ice-rich deposits and iron redistribution in Alas deposits

Our results show a larger variability in total Fe concentrations in Alas deposits relative to Yedoma deposits (Figure 7.4, 7.5 and 7.6) for both Siberia and Alaska. In contrast to never thawed Yedoma deposits (discussed in Sect. 7.5.1), Alas deposits, have experienced intense thawing processes with potential effects on redox-sensitive elements (e.g., Fe). Alas deposits result from the impact of thaw and post-depositional processes on ice-rich Yedoma deposits, as well as newly formed Holocene deposits. Ground collapse during thawing of ice-rich deposits, caused by the volume loss after ground ice melt, often creates favorable conditions for thermokarst lake formation. Depending on local conditions, these lakes can persist for several decades, centuries, or

even millennia, before they drain due to further permafrost degradation or dry out under unfavorable water balance conditions (e.g., shallow water bodies; Grosse et al., 2013). Moreover, several studies consider that thermokarst lakes form, drain and reform in a cycle ("thaw-lake cycle"); a process that would result in substantial changes to Alas deposits on millennial timescale because of repeatedly reworked sediments undergoing several alternating stages of lacustrine and subaerial wetland development (Jones et al., 2012). Field evidence of multiple thermokarst lake generations overlapping at sites can also be found in cores (e.g., Lenz et al., 2016). In summary, Alas deposits are the result of thermokarst dynamics during the Lateglacial and Holocene and associated reworking of deposits once or multiple times depending on overall thaw dynamics in the landscape. Additional complexity arises from the fact that thermokarst landforms undergo successional changes over time from initial towards advanced stages of degradation and possibly stabilization, during which the dominant physical and biogeochemical processes may change as these features evolve (Biskaborn et al., 2013; Kokelj and Jorgenson, 2013; Turetsky et al., 2020).

Relative to Yedoma deposits that have never thawed displaying homogeneous Fe concentrations with depth (Figure 7.6a, c, e, g, I, k, m and o; Sect. 7.5.1), Alas deposits from corresponding locations are characterized by changes in total Fe concentrations with depth (Figure 7.6b, d, f, h, j, l, n and p). This likely results from Fe becoming mobile during post-depositional processes such as thermokarst events and subsequent drainage, affecting Fe distribution in reworked and newly formed deposits. It is well established that Fe can be mobilized in water-saturated soil (Riedel et al., 2013; Colombo et al., 2014; Pokrovsky et al., 2014; Manasypov et al., 2015; Herndon et al., 2020b). The loss of Fe from alluvial plain soil horizons is correlated to low redox potential (Eh) supporting the idea that leaching of redox-sensitive elements, such as Fe, occurred during fluctuating redox conditions in thermokarst lakes (Fiedler and Sommer, 2004). Moreover, redox gradients can occur over small scale, e.g., with relief changes between high-centered and low-centered polygons in polygonal permafrost soils (Fiedler et al., 2004), or over centimeter scale (Herndon et al., 2020). It follows that solubilization, translocation and precipitation are also the major processes involved in Fe mobility in Alas deposits. Here, the data support that (i) thermokarst lake formation after ice-rich Yedoma degradation has generated reducing conditions favoring the solubilization and translocation of dissolved Fe from oxides or complexed forms in the initial Yedoma deposit, (ii) the subsequent thermokarst lake

drainage and refreezing as well as peat accumulation generated suitable oxic conditions that promote Fe precipitation in Alas deposits. The Alas deposits therefore represent reworked and newly formed deposits, which have experienced local oxidation and precipitation of dissolved Fe in favorable environments depending on microscale redox potential. This is also supported by field observations of Alas deposits profiles (e.g., DY-02) with the typical brownish color given by Fe oxides (Wetterich et al., 2011b) in the layers enriched in total Fe concentration (Figure 7.6b).

Grain-size distribution is commonly used as an indicator of major disturbances between the original Yedoma deposits and the reworked and newly formed Alas deposits induced by post-depositional processes (Strauss et al., 2012). This allows identifying contrasts between homogeneous grain-size distribution in Yedoma deposits (e.g., in Duvanny Yar DY-01 and DY-05) and the more heterogeneous distribution with coarser and finer particles in Alas deposits (e.g., DY-04 and DY-02 from the same location; Strauss, 2010; Strauss et al., 2012). The contrast between homogeneous distribution of total Fe concentration with depth in Yedoma deposits and the heterogeneous distribution of total Fe concentration with depth in Alas deposits (Figure 7.6) is in good agreement with the observations based on the grain-size distribution (Figure S.7.3), and supports that the reworking and new formation of the deposits is leading to changing conditions for the mobility of Fe. The degree of Fe redistribution within Alas deposits could be an indicator of the intensity of post-depositional processes. The study of such redistribution may give new clues on thermokarst dynamics, in particular i) drainage rate after lake formation, ii) rapid refreezing after drainage, or iii) single or multiple thaw-lake cycles. In this way, these observations of Fe mobilization in the paleo-record act as an analogue for present day and future Fe distribution in thermokarst lake deposits.

7.5.3 Changing iron and organic carbon interactions during post-depositional processes

The changing conditions for Fe mobility upon thermokarst processes potentially affect Fe-OC interactions and thereby OC stability in the reworked deposits (Colombo et al., 2014; Herndon et al., 2020b; Kleber et al., 2021). This study shows that, on average, 25% of total Fe is in Fe-oxide form (as crystalline or amorphous phases) and that out of these oxides, 80% is

amorphous or complexed Fe (Table 7.2). Based on the subset of samples analyzed for the selective extractions of Fe (n=21), it appears that the proportion of reactive Fe oxides to the global Fe pool is not significantly different between thawed and never thawed deposits, whether considering the total Fe-oxides (Fe_d/Fe_t; p-value = 0.46) or the amorphous Fe-oxides (Fe_o/Fe_t, p-value= 0.55; Table 7.2). The crystallinity of Fe-oxides phases in soils is not solely controlled by redox conditions, but other factors such as water budget, organic matter input, initial Fe phase composition, and time (potentially inducing Fe-oxide aging) are also important players (Cudennec and Lecerf, 2006; Winkler et al., 2018). In addition, microbial activity, especially from Fe-reducing microorganisms, may influence the crystallinity of Fe oxides and abundance of complexed Fe (Rivkina et al., 2020). As a result, both increases or decreases in Fe oxides crystallinity have been reported under redox fluctuations in wetlands soils (Winkler et al., 2018). This likely explains why our data indicate that the thawing history of the deposits is not leading to systematic changes in the crystallinity of Fe oxides. We observed that the concentration in reactive Fe oxides (Fe_d) in Yedoma and Alas deposits is positively correlated with their total Fe concentrations (Figure 7.7e). This result supports that total Fe accumulation (i.e., reported locally in Yedoma deposits and intensively in Alas deposits) is directly associated to the accumulation of reactive Fe oxides, thereby providing potential OC stabilizing phases in these deposits. The redistribution in total Fe concentration in the Alas deposits suggest that Fe accumulation likely occurred in oxic conditions favorable for oxy(hydr)oxides formation, whereas Fe depletion was likely associated with flooding conditions leading to dissolution in reducing conditions combined with subsequent loss of Fe via lateral or vertical leaching mechanisms.

The characterization of reactive Fe-oxides (crystalline, poorly crystalline and complexed Fe (Fe_d, Fe_o, Fe_p)) is a primary step required to track the potential driving factors linking mineral and organic components in soils and sediments. Interactions between Fe and OC, as Fe-OC complexes and as OC-Fe oxide associations, are supported by the positive correlation between (i) the complexed Fe (Fe_p) and the complexed carbon (Figure 7.7b), and (ii) the complexed Fe and the ODOE which represents organic acids associated with amorphous Fe oxides and complexed Fe (Figure 7.7d). The more TOC is present in the deposit, the more carbon is present in complexed form (Figure 7.7a). Deciphering between the many OC stabilizing processes reported in the literature, such as physical and physico-chemical protection involving Fe

oxides (aggregation, organo-mineral associations) and organo-metallic complexes (complexation) is of primary importance to better predict the fate of OC in a warming Arctic (e.g., von Lützow et al., 2006; Kögel-Knabner et al., 2008). Our work highlights that total Fe is redistributed upon thermokarst processes, but more importantly, we highlight the local (Yedoma) or intensive (Alas) redistribution of protective mechanisms associated to OC in ice-rich permafrost regions.

7.5.4 Implications of thermokarst processes for iron mobility and interactions with organic carbon

The different steps of Fe mobility between Yedoma and Alas deposits can be summarized as follows (Figure 7.8): in Yedoma deposits that never thawed since deposition, the syngenetic freezing of sediments soon after deposition limits solubilization and translocation of Fe throughout the profile (Figure 7.6a, c, e, g, I, k, m, o). Nonetheless, Yedoma deposits, which may have experienced short wetter periods (indicated by peat layers), show a local accumulation/depletion of Fe and therefore suggest Fe mobility and translocation mechanisms. In contrast, in Alas deposits, which have experienced intensive thermokarst processes, we observe a large variability of total Fe concentrations (Figure 7.8), suggesting sustained dissolution of Fe oxides and/or complexed Fe, Fe translocation and precipitation in redox favorable microscale environments with potential peat influence. Finally, fluvial deposits underlying Yedoma deposits or deposits showing marine to deltaic influence in coastal regions (e.g., Bunge Land; Figure 7.7p) display low total Fe concentrations that either suggest depletion caused by lateral loss during flood events or a different sediment origin already depleted in Fe prior to deposition. These fluvial deposits are also characterized with very low TOC values which may not facilitate Fe precipitation. Overall, the redistribution of Fe between Yedoma and Alas deposits reflects the influence of the complex history of Yedoma deposits (polygenetic origin, potential short thawing periods during late Pleistocene) and the intense post-depositional processes of Alas deposits during Lateglacial to Holocene warmer periods (Figure 7.9).

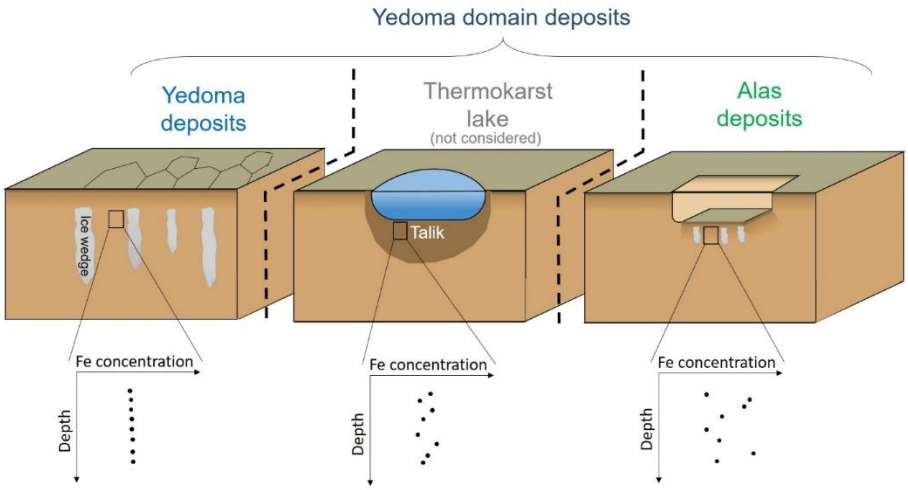

Figure 7.8: Conceptual scheme of the depth-distribution of total Fe concentration in never thawed Yedoma Ice Complex deposits, in deposits subsequently to thaw processes, i.e., below thermokarst lake (not considered in this study) and in Alas deposits. Black rectangles in the upper schematic representation of Yedoma, thermokarst lake and Alas profile indicate the sample location. The spatial coverage of the geomorphologic features is not to scale.

The Fe-OC associations are not permanent: they may disappear in a wetter, reducing environment, or form in oxic conditions resulting in a redistribution of Fe throughout the sediment profile (Opfergelt, 2020; Patzner et al., 2020). Our results highlight that specific horizons from Alas deposits have a 2 to 3-fold increase in total Fe concentration (Figure 7.7a-b) and therefore we could expect a 2 to 3-fold increase in reactive Fe, based on the positive correlation between total Fe concentrations and reactive Fe concentrations in the deposits ($R^2 = 0.76$; Figure 7.7e). In contrast, sandy layers, often depleted in TOC, have a 2.5-fold decrease in total Fe concentrations compared to the overlying typical Ice Complex deposits (Figure 7.6c-d). The redistribution of stabilizing OC phases (i.e., Fe-oxides or complexed Fe) is key for the fate of OC in a warming Arctic. The changing Fe concentration between Yedoma and Alas deposits support the idea that future thermokarst processes in the Arctic will affect Fe-OC interactions. In this study, we contend that Alas deposits which have experienced past thawing processes are key witnesses to predict what may happen next with Fe-OC interactions during the current and future Arctic warming. More specifically, it can be expected that oxic conditions would favor Fe-oxides formation, generating Fe-OC interactions thereby

contributing to mitigate OC decomposition, whereas flooding would generate reducing conditions and the lateral and vertical transport of dissolved Fe phases resulting in the depletion of total Fe concentrations, thereby contributing to decrease Fe-OC interactions, and limiting long-term OC stabilization. We also highlight that future permafrost thaw will be superimposed on deposits with a relict Fe distribution from the Holocene and Pleistocene. The paleo Fe distribution in the Yedoma domain may have a knock-on effect how Fe can be distributed during future thaw, and therefore is primed for variations in OC stabilization and OC mineralization rates. It is therefore essential to consider the permafrost history to predict the evolution of OC upon warming and permafrost thaw.

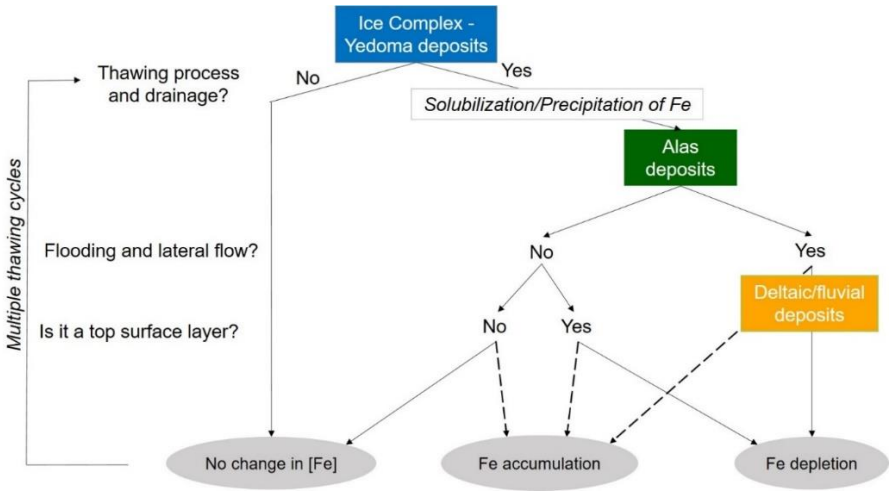

Figure 7.9: Schematic representation of the iron dynamic within Yedoma domain deposits and the resulting impact for Fe concentration ([Fe]) in Yedoma Ice Complex (blue), Alas (green), and deltaic/fluvial deposits (orange). The "Yes" and "No" correspond to the answer of the question on the left side of the scheme. Dashed lines suggest the potential influence of peat to create favorable oxic conditions.

7.6 Conclusions

We determined the total Fe concentration (n = 1,292) and distribution of Fe-oxides and Fe involved in complexes (n = 21) in unthawed Yedoma deposits and previously thawed Alas deposits from the Yedoma domain. We found:

(i) that the total Fe concentrations in never thawed Yedoma deposits are homogeneous with depth in Alaska and in Siberia, allowing for Fe concentrations in previously thawed Alas deposits to be compared with Yedoma deposits to test the impact of thermokarst processes on Fe mobility.

(ii) a local redistribution of total Fe concentration throughout Yedoma profiles (i.e., driven by short thaw phases upon Yedoma aggradation with potential peat influence) and an intensive total Fe redistribution in Alas deposits consequent to thermokarst lake formation and drainage, supporting that iron is mobile upon thaw. We suggest Fe mobility after Fe-oxides dissolution, i.e., Fe translocation within sediments followed by Fe-oxides re-precipitation in favorable microscale conditions or Fe leaching.

(iii) a positive correlation between the total Fe concentration and the reactive Fe concentration in both Yedoma and Alas deposits. On average, proportion of reactive Fe (i.e., Fe-oxides or complexed Fe) equals 25% of global Fe pool for both Yedoma and Alas deposits. The intensive redistribution of total Fe in Alas profiles imply that reactive Fe is redistributed upon thermokarst processes with direct implication on OC stabilization.

The Yedoma domain has been a highly dynamic environment since the late Pleistocene period until today, and will continue to be so with the projected rising temperatures. Our research suggests that similar processes (i.e., Fe solubilization, translocation and precipitation) occur in ice-rich permafrost degradation upon thermokarst processes as previously described for polygonal or thaw gradient permafrost landscapes. The total Fe accumulation/depletion, observed in Alas deposits is accompanied with an accumulation/depletion of reactive Fe and micro-scale implications for OC stabilization. We argue that the change from frozen to unfrozen state leads to the modifications of multiple environmental conditions (fluctuating redox conditions, subsidence, leaching, and drainage) with indirect impact on Fe-oxides distribution and hence on a portion of mineral-protected OC pools.

8. Chapter 3: Thermokarst processes increase the supply of stabilizing surfaces and elements (Fe, Mn, Al, Ca) for mineral organic carbon interactions

This chapter is a modified version of a research paper published in Permafrost and Periglacial Processes:

Monhonval, A., Strauss, J., Thomas, M., Hirst, C., Titeux, H., Louis, J., Gilliot, A., du Bois D'Aische, E., Pereira, B., Vandeuren, A., Grosse, G., Schirrmeister, L., Jongejans, L.L., Ulrich, M., Opfergelt, S., 2022. Thermokarst processes increase the supply of stabilizing surfaces and elements (Fe, Mn, Al, Ca) for mineral-organic carbon interactions. Permafrost and Periglac Processes, 1-18. doi:10.1002/ppp.2162.

Abstract

The stabilizing properties of mineral organic carbon interactions have been studied in many soil environments (temperate soils, podzol lateritic soils, paddy soils). Recently, interest in their role in permafrost regions is increasing as permafrost was identified as a hotspot of change. In thawing ice-rich permafrost regions, such as the Yedoma domain, 327-466 Gt of frozen organic carbon (OC) is buried in deep sediments. Interactions between minerals and OC are important since the OC is located in close contact with the mineral matrix. Mineral surfaces and elements could mitigate recent and future greenhouse gas emissions through physical and/or physico-chemical protection of OC. The dynamic changes of redox and pH conditions associated with thermokarst lake formation and drainage, trigger metal-oxide dissolution and precipitation, likely influencing OC stabilization and microbial mineralization. However, the influence of thermokarst processes on mineral OC interactions remains poorly constrained. In this study, we aim to characterize Fe, Mn, Al and Ca minerals and their potential protective role for OC. Total and selective extractions were used to assess the crystalline and amorphous oxides or complexed metal pools as well as the organic acids found within these pools. We analyzed four sediment cores from an ice-rich permafrost area in Central Yakutia, which were drilled i) in undisturbed Yedoma uplands, ii) beneath a recent lake formed within Yedoma deposits,

iii) in a drained thermokarst lake basin, and iv) beneath a mature thermokarst lake from the early Holocene period. We find a decrease in the amount of reactive Fe, Mn, Al and Ca in the deposits upon lake formation (promoting reduction reactions), and this was largely balanced by an increase in the amount of reactive metals in the deposits upon lake drainage (promoting oxidation reactions). We demonstrate an increase in the metal:C molar ratio upon thermokarst process, which may indicate an increase in metal-C bindings and could provide a higher protective role against microbial mineralization of organic matter. Finally, we find that an increase in mineral OC interactions corresponded to a decrease in CO_2 and CH_4 gas emissions upon thermokarst process. Mineral OC interactions could mitigate greenhouse gas production from permafrost thaw as soon as lake drainage occurs.

8.1 Introduction

Permafrost deposits are thawing at an unprecedented rate since the last century (Koven et al., 2011; Schuur et al., 2015; Biskaborn et al., 2019). Climatic warming, which is two to three times more intense in northern regions, will accentuate permafrost thaw in coming decades affecting the whole Arctic (IPCC, 2021). Thereby, the organic carbon (OC) stored in the permafrost deposits is mobilized. Even if a portion of the 1,300 Pg OC stock lying within permafrost regions (Hugelius et al., 2014; Strauss et al., 2017) is decomposed upon thawing, this would result in significant greenhouse gas emissions at the global scale (IPCC, 2021). Thawing of Yedoma (i.e., ice-rich permafrost) deposits leads to massive landscape modifications (Grosse et al., 2013; Schirrmeister et al., 2013; Strauss et al., 2021b). The melting of ice-wedge networks and other excess ice usually leads to surface subsidence followed by thermokarst lake formation. With time, the lake can extend horizontally and vertically, and eventually create a drainage pathway (Grosse et al., 2013). Upon lake drainage, sediment deposits remain within the dried basins, which are called "Alas". At the Arctic scale, lake and drained lake basin systems can represent up to ~50% of the circumpolar Northern Hemisphere permafrost region lowland areas (Jones et al., 2022). About a quarter of 21st century thermokarst lake CH_4 release stems from newly thawed OC stored in deep deposits from the Yedoma region (Schneider von Deimling et al., 2015). The thawing and draining of ice-rich deposits triggers shifts in soil or sediment properties, such as the reductive-oxidative potential (i.e., redox) or pH values. These shifts drive changes in biogeochemical processes with potential consequences for mineral OC interactions (i.e., aggregation, organo-mineral associations, organo-metallic complexes; Kleber et al., 2015) and thus OC mineralization rates (von Lützow et al., 2006; Jones et al., 2022). These processes, leading to destabilization of these mineral OC interactions, may accelerate permafrost carbon emissions, and need to be incorporated in Earth system models for more comprehensive projections of the permafrost carbon feedback (Schuur et al., 2015; Opfergelt, 2020).

Mineral elements and mineral surfaces provide stabilizing mechanisms for OC resulting in the mitigation of OC mineralization in many soils (Torn et al., 1997; Dutta et al., 2006; von Lützow et al., 2006; Mikutta et al., 2007; Kögel-Knabner et al., 2008; Wagai et al., 2013; Gentsch et al., 2015b; Kleber et al., 2015; Kramer and Chadwick, 2018; Hemingway et al., 2019). Organic carbon stabilizing mechanisms involving Fe and Al oxy(hydr)oxide have been

extensively studied in i) controlled conditions (Schwertmann, 1991; Eusterhues et al., 2008; Huang and Hall, 2017; Zhao et al., 2017), ii) agricultural soils (Wang et al., 2019), iii) tropical lateritic soils (Fritsch et al., 2009; Mikutta et al., 2009; Inagaki et al., 2020), iv) peatlands and rice paddy soils (Fiedler and Sommer, 2004; Kögel-Knabner et al., 2010; Pan et al., 2014; Xue et al., 2019), and v) lake and marine sediments (Eglinton, 2012; Lalonde et al., 2012; Barber et al., 2017). However, more recently there has been an increasing interest in permafrost regions (Fiedler et al., 2004; Mu et al., 2016; Herndon et al., 2017, 2020b; Patzner et al., 2020; Sowers et al., 2020; Joss et al., 2022; Lim et al., 2022b). In addition, Mn and Ca play a key role in OC stabilization and degradation mechanisms (Bartlett and Ross, 2005; Johnson et al., 2015; Oldham et al., 2017; Rowley et al., 2018; Sowers et al., 2020; Li et al., 2021). Together Fe, Al, Mn and Ca –bearing minerals and cations can provide physical and physico-chemical protection of OC. For microbial mineralization, OC has to be in intimate contact with microorganisms. Physical protection of OC within mineral aggregates prevents microorganisms from approaching this substrate and thus limits this contact. Physico-chemical protection, in the form of organo-mineral associations within clays or Fe-, Mn-, Al-(oxyhydr)oxides using polyvalent cation bridges such as Fe^{3+}, Al^{3+}, Ca^{2+}, Mn^{3+} (adsorption) or in the form of organo-metallic complexes (Fe-, Mn-, Al- and Ca-OC; complexation), hinders microbial degradation through diverse type of chemical bindings (e.g., von Lützow et al., 2006). Overall, physical and physico-chemical protection of OC through mineral OC interactions lower the solubility of organic acids and their availability for microorganisms.

A major concern is that mineral OC interactions that promote OC stabilization could be highly reversible under changing physico-chemical conditions, including both redox and pH (von Lützow et al., 2006; Schmidt et al., 2011; Grant et al., 2022) that occur during thermokarst processes. Fluctuating wet-dry cycles drive redox shifts in otherwise well-drained soils resulting in mineral dissolution, OC mobilization, and subsequent OC mineralization (Bartlett and Ross, 2005; Lipson et al., 2012; Ernakovich et al., 2017; Possinger et al., 2020; Kappler et al., 2021; Kleber et al., 2021). These shifts in redox potential influence redox-sensitive elements (i.e., Fe and Mn) by modifying the crystallinity of Fe- and Mn-oxy(hydr)oxides or the redistribution of stabilizing surfaces, with subsequent OC release (Winkler et al., 2018; Inagaki et al., 2020; Patzner et al., 2020). The processes of wetting and drying are also evident in thawed lake basins. The reductive conditions induced upon lake formation may have an opposite influence on mineral OC

interactions compared to the oxidative potential induced upon lake drainage. Along the redox ladder (Figure 8.1), electron acceptors follow the sequence O_2, NO_3^-, NO_2^-, Mn^{4+}, Fe^{3+}, SO_4^-, CO_2, from more to less thermodynamically efficient. However, studies show that these redox reactions often overlap under environmental conditions (e.g., Kappler et al., 2021). Besides the redox conditions, the pH is also a key driver of Al-, Fe-, Mn-oxy(hydr)oxide solubility and dissolution rates (Kleber et al., 2015). Furthermore, in soils/sediments with a high pH (neutral/alkaline), Ca promotes OC stabilization via aggregation, cation bridging and/or complexation (von Lützow et al., 2006; Rowley et al., 2018; Wang et al., 2021) and may also raise the surface potential of Fe-, Mn-, Al-oxy(hydr)oxides which lead to more effective coagulation of OC (Davis and Edwards, 2017). The contribution of Ca towards OC stabilization was even described in permafrost systems (Sowers et al., 2020). In soils with an acidic/neutral pH, the loss of Ca-based stabilizing mechanisms enables OC microbial degradation (Rowley et al., 2018).

Most mineral OC interactions studies focus on one or a few elements involved in OC stabilization but, to our knowledge, very few investigated Fe, Mn, Al and Ca interactions with OC simultaneously. In ice-rich permafrost regions, interactions between minerals and OC are crucial given that most of the OC is found in deep mineral sediments, potentially enhancing interactions between the mineral and the organic compounds upon thaw (Hemingway et al., 2019; Lim et al., 2022b, 2022a). Although the increase in Fe stabilizing surfaces from undisturbed (not thawed since deposition) Yedoma deposits to previously thawed Alas deposits was recently shown (*Ch.2*), neither the influence of thermokarst lake formation and drainage on mineral OC interactions in sediments, nor the role of all potential reactive metals (Fe, Mn, Al and Ca) were investigated. We hypothesize that lake formation and lake drainage are important intermediate steps controlling changes in mineral OC interactions upon thermokarst process, with likely opposing effects.

To test our hypothesis, we studied a landscape transect in Central Yakutia from undisturbed sediments in Yedoma uplands to drained lake sediments and sediments below thermokarst lakes from different generations (Ulrich et al., 2017). The different thawing history of these deposits allows us to dissociate thermokarst lake formation on the one hand and thermokarst lake drainage and refreezing on the other hand. This comparison provides a glance into the evolution of ice-rich permafrost deposits in the near future, and allows us to

assess how mineral OC interactions (with Fe, Mn, Al and Ca) will evolve within the thawed, drained and refrozen deposits.

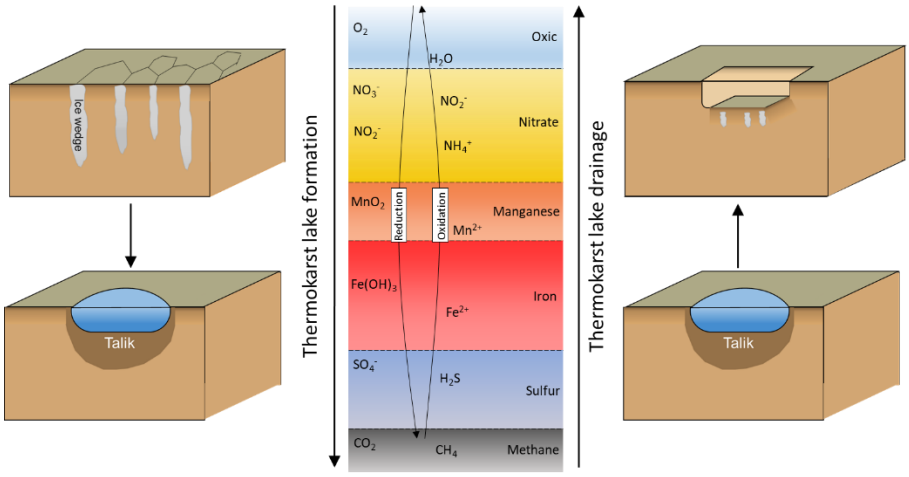

Figure 8.1: Simplified view of the oxidation/reduction couples involved in redox reactions and listed in thermodynamic order. The redox potential is decreasing towards the bottom of the column. Upon thermokarst lake formation (left), electron acceptors for reactions follow the sequence O_2, NO_3^-, MnO_2, Fe^{3+}, SO_4^- and CO_2. Upon lake drainage (right), the redox potential increases and favors oxidation reactions. The coloured panels indicate the sequence in which the different reactions are expected to occur on the basis of thermodynamics; however, these redox reactions may overlap under environmental conditions (modified from Melton et al., (2014)).

8.2 Regional settings

The studied Yukechi site is located 80 km southeast from the city of Yakutsk in the central part of the Sakha (Yakut) Republic, East Siberia, Russia (Figure 8.2a). The region is characterized by a cold and continental climate with a mean annual temperature of -10.7°C (mean January: -41°C, mean July: 18.5°C) and a mean annual precipitation of 246 mm (period: 1982–2012; Yakutsk Weather Station: RSM00024959; Climate-data.org, 2022). Between 1966 and 2016, the Central Yakutian mean annual air temperature has increased by 0.3-0.6°C per decade (Gorokhov and Fedorov, 2018). Central Yakutia lies within the continuous permafrost zone and is in a low-relief landscape, characterized by numerous Alas basins and thermokarst lakes at different evolutionary stages (Soloviev, 1959; Tarasenko, 2013), indicating past and modern active thermokarst processes (Ulrich et al., 2017).

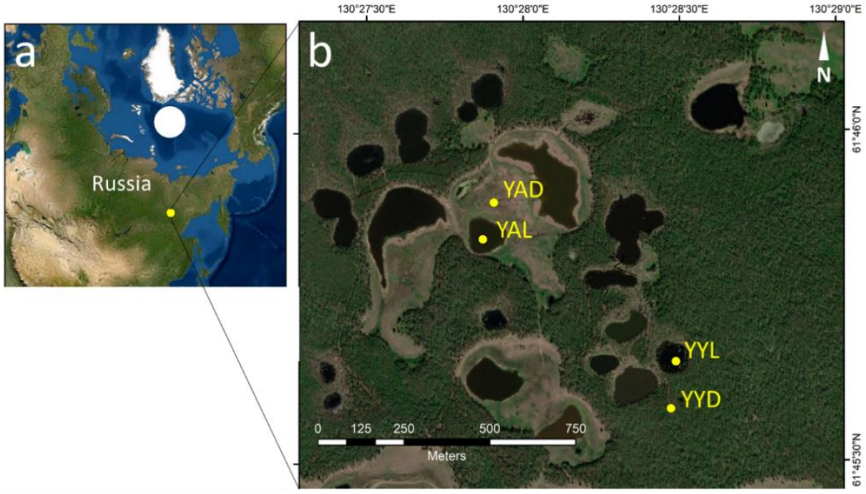

Figure 8.2: (a) Location of the Yukechi site in Russia. (b) Location of the four cores within Yukechi site: the Yedoma dry (YYD), the Yedoma lake (YYL), the Alas dry (YAD) and the Alas lake core (YAL). Source: Esri, DigitalGlobe, GeoEye, Earthstar Geographics, CNES/Airbus DS, USDA, USGS, AeroGRID, IGN, and the GIS User Community.

The Yukechi site is located within the Yedoma domain (Strauss et al., 2021b). The Yedoma deposits of this region can be more than 30 m thick (Soloviev, 1959). For tens of millennia, cold and dry conditions during late Pleistocene and continuous sedimentation led to the accumulation of several tens of meters thick Yedoma deposits with characteristic ice-wedge formation (I) (Figure 8.3a). These ice-wedges formed by the infilling of vertical frost cracks with snow melt water repeatedly (Schirrmeister et al., 2013). Warm and wet climate conditions during the Holocene period led to ice-wedge melting and a thermokarst lake formed within the subsidence area (II). With time, evaporation and thermokarst lake expansion in depth (i.e., talik deepening) or laterally (i.e., thermoerosion) led to the drying/drainage of the thermokarst basin where residual lake may have persisted, and consequent refreezing of the deposits (III) (Grosse et al., 2013). Since the onset of the Holocene until now, lake formation and potential drainage have occurred within the refrozen Alas basin or within frozen Yedoma deposits (IV).

The studied transect included four evolutionary stages: undisturbed Yedoma sediments (Yedoma dry), sediments underneath a recently formed lake (Yedoma lake), Alas sediments in a drained thermokarst lake basin (Alas dry), and sediments underneath a lake in the drained basin which have been subject to multiple lake generations (Alas lake) (Figure 8.2b and Figure 8.3b). The

Yedoma lake is a recent lake that formed in Yedoma uplands about 70 years ago (Yedoma lake), defined here as initial lake formation (lake formation timeline observed by aerial photography from 1944 until today; Ulrich et al., 2017). This recent thermokarst lake formation in the Yedoma uplands indicates still ongoing thermokarst processes (Ulrich et al., 2017, 2021). The Alas sediments experienced drainage/evaporation and refreezing in previous thermokarst lake generations (Jongejans et al., 2021b). In the following, we will split the thermokarst process using specific stages: i) thawing and initial lake formation (*), ii) lake drainage and refreezing (**), and iii) secondary thawing and mature lake formation (***) (Figure 8.3c). Yedoma and Alas deposits can be clearly subdivided in different stratigraphic units which reflect varying sedimentation processes confirmed by grain-size analysis, as described for the Yedoma dry and Alas dry cores (Windirsch et al., 2020) and for the Yedoma and Alas core beneath the lakes (Jongejans et al., 2021b; Ulrich et al., 2021).

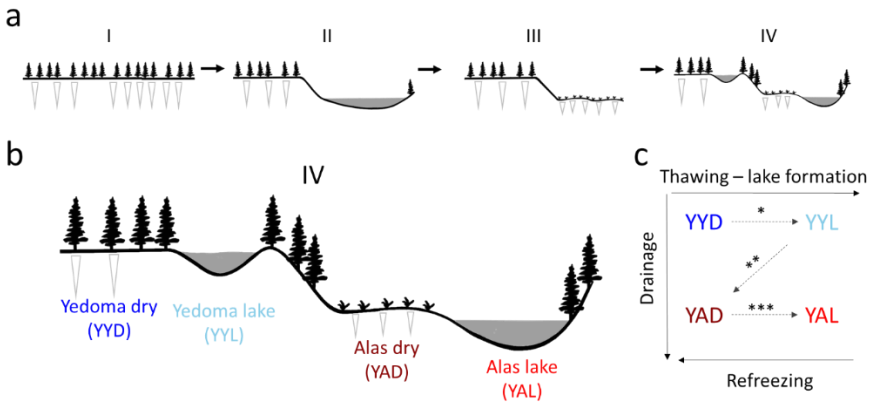

Figure 8.3: (a) Scheme of the permafrost degradation history (I-IV) of the site sampled in this study. Previous Yedoma uplands, with characteristic ice-wedges (white triangles), have experienced thermokarst process with thermokarst basin formation and drainage since the onset of the Holocene until now (I-III). More recently, about 70 years ago, a thermokarst lake formed in the Yedoma uplands (IV). (b) Sediment cores retrieved from the Yukechi site include a core from the Yedoma uplands (Yukechi Yedoma dry (YYD)), a core beneath a recent Yedoma lake (Yukechi Yedoma lake (YYL)), a core from a drained thermokarst lake basin (Yukechi Alas dry (YAD)), and a core beneath a mature Alas lake (Yukechi Alas lake (YAL)). (c) Permafrost degradation processes involved within each core: *thawing and initial lake formation, **drainage and refreezing, and * secondary thawing and mature lake formation. The combination of initial lake formation (*) and drainage and refreezing (**) will be referred as the shift from Yedoma dry to Alas dry cores.**

8.3 Materials and Methods

8.3.1 Coring and sample preparation

The field campaign to Yukechi was carried out in March 2015 to retrieve four sediment cores from different landforms features (Sect. 8.2): a Yedoma dry core (YYD), a Yedoma lake core (YYL), an Alas dry core (YAD), and an Alas lake core (YYL) (coordinates in Table S.8.1). Drilling was carried out using a URB2-4T drilling rig mounted on a truck. The cores were drilled with 15.7 cm diameter for the uppermost parts and 8 cm in diameter in the lower parts. The sediment cores were removed from the core barrel using compressed air, described, stored in plastic bags and kept frozen until laboratory analysis. The drilling depths below surface (i.e. lake-ice surface for lake cores) were 22.4 m (YYD), 17.2 m (YYL), 19.8 m (YAD) and 17.7 m (YAL), respectively (Figure S.8.1). Upon coring, the presence of taliks, i.e., portion of the sediments that remain unfrozen during winter, sometimes led to partial core loss (Jongejans et al., 2021b; Ulrich et al., 2021). The Yedoma dry core included an ice-wedge between 700 to 950 cm b.s. (below surface) and a talik section was identified between 100 and 200 cm b.s. The Yedoma lake core was frozen below 12 m with significant core loss upon core retrieval for the upper unfrozen section. In the Alas dry core, a talik was found between 160 down to 750 cm b.s. The Alas lake core was unfrozen for the entire core. The frozen cores were split lengthwise using a band saw and were subsequently subsampled in a freezer room at −5°C (sample positions along the core are shown in Figure S.8.1). Samples were then air-dried before analyses. In total, 39 samples were analyzed in this study. The locations and numbers of samples analyzed are indicated in Table S.8.1.

8.3.2 Sample characterization

pH and mineralogy

Sample pH-H_2O and pH-KCl (1M KCl solution) were measured on bulk sediment samples (n = 39) with a 1:5 sediment:solution ratio (Page et al., 1982). The pH was measured using WTW Inlolab 720 pH-meter probe after 1 hour with manual shaking every 20 minutes. Bulk sediment mineralogy was determined by X-ray diffraction (XRD; n = 39). The mineralogy of bulk

samples was determined on finely ground powder (Cu Kα, Bruker D8 Advance diffractometer, detection limit = 5%). Diffraction spectra were analyzed with DiffracPlus EVA© software version 10.0.0.3 and the PDF-2 (International Centre for Diffraction Data, 2013) and EVA©-embedded DiffracPlus Reference databases (Mineral and Master datasets) using peak fitting method.

Total Fe, Mn, Al and Ca concentrations measurement

Total mineral element concentrations (Fe, Mn, Al and Ca) were measured (n = 39) using a portable X-ray fluorescence (pXRF) device and corrected with inductively-coupled plasma optical emission spectrometry (ICP-OES) measurement after alkaline fusion. This procedure is fully described in *Ch.1*. This procedure consists in converting raw pXRF element concentrations values by a linear regression model in order to be equivalent to an ICP-OES concentration value obtained after alkaline fusion. Here, only pXRF concentration values corrected using element specific regressions with high coefficient of determination ($R^2 > 0.72$) were used.

We performed the pXRF measurements in the laboratory on dried samples to avoid variability of water content upon measurements (n = 39) (Ravansari et al., 2020). For this, air or freeze-dried samples are placed in a circular plastic cap (2.5 cm diameter) provided at its base with a transparent thin film (prolene 4 µm). Measurements were carried out using pXRF device Niton XL3t GOLDD+ (Thermo Fisher Scientific) and a lead stand to protect the operator from X-rays. Total time of measurements were set to 90 s (*Ch.1*).

For the alkaline fusion used to calibrate the linear regression, air- or freeze-dried samples were ground in an agate mill. A portion (80 mg) of the milled sample was mixed with Li-metaborate and Li-tetraborate and heated during 10 minutes in a 1,000°C oven. The fusion bead was dissolved in HNO_3 2.2N at 80°C and stirred until complete dissolution. We measured mineral element concentrations in that solution by ICP-OES (iCAP 6500 Thermo Fisher Scientific). Loss on ignition was measured to evaluate the sum of oxides (between 98 and 102%) and the concentration values were reported in reference to the sediment dry weight (105°C). The ICP-OES method was performed on a subset of Yukechi samples (n = 6) to confirm that the linear regression from the Yedoma domain (n = 144; *Ch.1*) was appropriate for Yukechi samples (Figure S.8.2).

Selective Fe, Mn, Al, Ca and organic carbon extraction methods

Commonly-used selective extraction methods have been chosen to identify the Fe, Mn, Al, Ca and OC phases. The Fe, Mn, and Al were measured in filtered solution (Whatman 41 filter, 20 µm size) by ICP-OES after the following extraction procedures: i) dithionite-citrate bicarbonate (DCB) (Mehra and Jackson, 1960), ii) ammonium oxalate in the dark 4h (oxalate) (Blakemore et al., 1981), and iii) sodium pyrophosphate (pyrophosphate) (Bascomb, 1968). In soils/sediments with a high pH, Ca could be an important contributor to the stabilizing mechanisms affecting OC (Rowley et al., 2018; Boiteau et al., 2020). Therefore, we measured Ca concentrations within the pyrophosphate extract. Extraction methods using DCB, oxalate and pyrophosphate are standard procedures to determine Fe- and Al-(oxyhydr)oxides phases or complexed ions (Table S.8.2). Here, we tested these extractions to decipher the different Mn phases. We found that the different extraction methods extracted different pools of Mn (Figure S.8.3). In addition, the Mn concentrations measured by ICP-OES on the solid residue after the different extractions support that DCB, oxalate and pyrophosphate extractions target different Mn pools. Repetitions (n = 3) for three different samples were conducted to assess precision of the different methods (Table S.8.3). This analysis supports that these extractions can also be used to assess Mn pools.

Extraction with DCB is presumed to remove well crystalline, poorly crystalline Fe oxides and Fe complexed with organic matter from soil or sediment (Rennert, 2019), also called ‘free iron’. Extraction with dithionite reduces Fe(III) from oxides. Similarly, Mn(IV) should be reduced to Mn(II) since Mn is redox-sensitive. The reduction of Mn(IV) is effective with hydroxylamine (NH_2OH), a weaker reductant than dithionite (Chao, 1972). Therefore, we assume that dithionite reduces Mn(IV) within Mn-oxides as well. Substantial amounts of Al and Ca are released via dithionite without targeting specific Al or Ca pools. The released Fe(II), Mn(II) and Al^{3+} and Ca^{2+} ions remain in solution and complexes with citrate (complexing agent).

Extraction with oxalate at pH 3 targets poorly crystalline oxides and complexed forms. At pH < 3.5, oxides are protonated weakening the metal-O bond, which is the first stage of dissolution, followed by the adsorption of oxalate and release of complexed Fe^{3+} and Al^{3+}. The oxalate extraction (4h in

the dark procedure) is a rate-limited process, which targets poorly crystalline phases and complexed metals while longer procedures target more crystalline phases (Rennert, 2019). Unlike in the DCB extraction, several Al-containing minerals are dissolved by oxalate. These include hydroxyl-interlayer Al, poorly crystalline Al oxides, allophane, imogolite and other poorly crystalline aluminosilicates (Rennert et al., 2019). We emphasize that oxalate-extracted Ca cannot be discussed because of the precipitation of Ca with oxalate upon extraction.

Pyrophosphate extraction at pH 10 chelates polyvalent cations and therefore targets metals (Fe, Mn, Al and Ca) complexed with organic species. It has been reported that Na-pyrophosphate does not only target organically bond Fe but may also include nanoparticulate poorly crystalline Fe oxides (Regelink et al., 2014). Therefore, the release of Fe and Al from small particles that have not complexed with soil organic acids is not excluded during pyrophosphate extraction (Rennert, 2019).

The well crystallized (DCB-extracted) oxides are less reactive towards organic compounds because they offer less specific surface area than poorly crystalline oxides (Cornell and Schwertmann, 2003; Gentsch et al., 2015a). Moreover, DCB-extracted Al cannot be attributed to distinct Al minerals and does not target well-crystalized Al-oxides (Rennert, 2019). Dithionite-extraction was also reported to be unexpectedly less efficient within some permafrost soils (Jakobsen et al., 1996). Because it is difficult to decipher which phases are extracted by using DCB extraction method, we define our "reactive" pool (i.e., the pool highly reactive towards organic species) by the pool extracted by ammonium-oxalate. This pool should combine all poorly crystalline, amorphous and complexed pools of Fe, Mn and Al. Similarly, we define our reactive Ca as the pyrophosphate extracted Ca because of the drawback related to Ca oxalate precipitation and should include Ca under complexed forms or interacting via cation bridging.

Organic carbon was quantified in oxalate extract and in pyrophosphate extract. The optical density of oxalate extract (ODOE), considered as an indicator of reactive polyaromatic acid concentration, was measured by determining the absorbance at 430 nm on a Genesys 10 S VIS spectrophotometer, with the ammonium oxalate reagent as a blank (Daly, 1982). Note that the direct measurement of OC within oxalate extract is not possible because of the organic composition of oxalate. From the pyrophosphate extract, the concentration in dissolved OC released after dispersion by pyrophosphate

(referred as Cp) was measured using a Shimadzu total organic carbon (TOC) analyzer (measuring non-purgeable OC). This indicates the amounts of C participating in organo-metallic complexes in soils or sediments (Bascomb, 1968). Repetitions (n = 3) for three different samples were conducted to assess the precision of the method (Table S.8.3).

8.3.3 Statistical analysis

The Wilcoxon-test (two-sided) was used to assess statistical differences within reactive metals and organic compounds (C_p) between the different cores. In addition, correlation matrices using Pearson method were constructed using *corrplot* package, performed with R software version 4.1.1 (R Core Team, 2018).

8.4 Results

8.4.1 Sediment core pH and mineralogy

The pH-H_2O ranged between 8.22 and 10.05 with a mean of 8.97 and pH-KCl ranged between 7.61 and 8.73 (mean = 8.18) (Figure S.8.4). Diffractograms indicate the presence of quartz, plagioclase, mica, pyroxene, amphibole, dolomite, serpentine and vermiculite (Table S.8.4). Mineral phases below 5% may be present but undetected.

8.4.2 Total and selectively extracted Fe, Mn, Al and Ca concentrations in sediment cores

The mean (± standard deviation) total concentrations in Fe, Al and Mn among all studied sediment cores are 26.1 ± 4.9 g kg^{-1}, 64.5 ± 5.2 g kg^{-1} and 0.50 ± 0.10 g kg^{-1}, respectively. Total Ca concentration reaches 23.6 ± 6.8 g kg^{-1}. Total Al concentration is 2-3 times higher than Fe concentrations and more than two orders of magnitude higher than Mn concentrations on mass concentration basis. The DCB-extracted Fe (mean: 5.41 g kg^{-1}) is almost one order of magnitude greater than DCB-extracted Al (mean: 0.63 g kg^{-1}) which is about two times greater than Mn (mean: 0.28 g kg^{-1}). Reactive Fe, Mn and Al (defined here as the oxalate-extracted pool) represent about ~12% (3.3 g

kg^{-1}), 28% (0.15 g kg^{-1}) and 1.3% (0.85 g kg^{-1}) of the bulk total concentration, respectively (Figure 8.4a). Finally, pyrophosphate-extracted Fe represents ~3% (0.82 g kg^{-1}) of total Fe. Pyrophosphate-extracted Mn (0.13 g kg^{-1}) and Al (0.10 g kg^{-1}) concentrations are smaller compared to Fe but falls within the same order of magnitude and represents ~25% and 0.2%, respectively of total Mn and total Al (Figure 8.4b). Pyrophosphate-extracted Ca shows the highest concentration with a mean of 3.5 g kg^{-1}.

When focusing on the differences in the selective extractions between the four stages of thermokarst formation (Figure 8.2), we found that reactive (i.e., oxalate-extracted) Fe concentrations show a significant increase between Yedoma and Alas deposits (Wilcoxon test p-value <0.05) but similar concentrations between dry and lake cores (p-value = 0.19). Similarly, reactive Mn shows significantly higher concentrations in the Alas compared to Yedoma core but significantly higher concentrations in dry deposits compared to lake deposits (Figure 8.5b). Reactive Al concentrations show a similar trend to reactive Mn, with higher concentrations in Alas cores compared to Yedoma cores and higher concentration in dry deposits than in lake deposits. Mean reactive Mn and Al concentration is therefore the lowest in the Yedoma lake core and the highest in the Alas dry core. Oxalate-extracted Al concentration is higher than DCB-extracted Al (Figure 8.5c). Pyrophosphate-extracted Fe showed smaller concentrations in the Yedoma dry and Yedoma lake cores (mean: 0.41 g kg^{-1} and 0.35 g kg^{-1}) compared to the Alas dry and Alas lake cores (mean: 1.5 g kg^{-1} and 1.6 g kg^{-1}). This difference between Yedoma and Alas sediments is smaller for Mn and Al concentrations within pyrophosphate extraction (Figure 8.5). Pyrophosphate-extracted Mn concentrations are within the same order of magnitude as pyrophosphate-extracted Al (mean: 0.13 g kg^{-1} and 0.10 g kg^{-1}, respectively; Figure 8.4a) despite the huge difference (more than two orders of magnitude) in the bulk Al and Mn total concentrations in the sediments (Figure 8.5). Pyrophosphate-extracted Ca ranges from 0.542 and 6.86 g kg^{-1} with mean values decreasing from Alas dry (4.40 g kg^{-1}), Alas lake (4.26 g kg^{-1}), Yedoma dry (3.06 g kg^{-1}) to Yedoma lake (2.89 g kg^{-1}) cores. Pyrophosphate-extracted Ca concentrations show higher values than the sum of pyrophosphate-extracted Fe, Mn and Al combined.

Detailed graphs of the Fe, Mn and Al concentrations over depth can be found in the Supplements: total, DCB, oxalate and pyrophosphate extractions (Figure S.8.5 - Figure S.8.7), and total and pyrophosphate extracted Ca (Figure S.8.8). Overall, DCB-, oxalate- and pyrophosphate-extracted Fe and Mn

follow the same pattern as their total concentration profile. The Al total concentrations are two to three orders of magnitude higher than the concentration of selectively extracted Al. The sandy layer present in the Yedoma dry (between 19.3 and 10.1 m b.s.) is within the low range of values for all elements for their total, DCB-extracted, oxalate-extracted and pyrophosphate-extracted concentrations contributing to the greater variability (i.e., wider boxplot) within the Yedoma dry core (Figure 8.5). The total and selectively extracted Fe, Mn, Al and Ca concentrations are displayed in Table S.8.5.

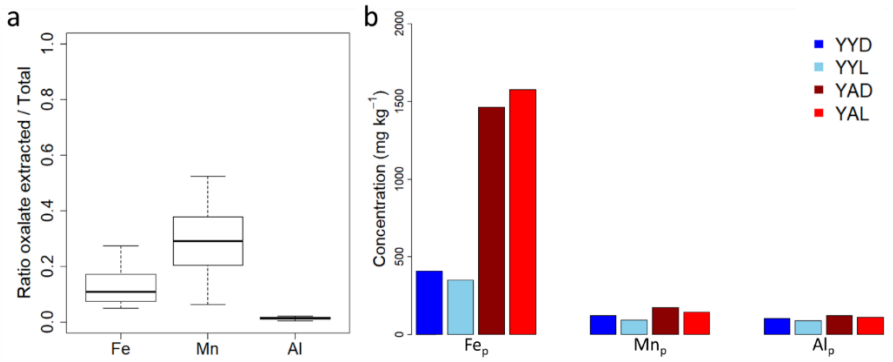

Figure 8.4: Boxplot of the ratio between oxalate-extracted (i.e. reactive) and total Fe, Mn and Al. (b) Histogram of mean concentrations in pyrophosphate extracted Fe, Mn and Al in the four sediment cores: Yedoma dry (YYD), Yedoma lake (YYL), Alas dry (YAD) and Alas lake (YAL).

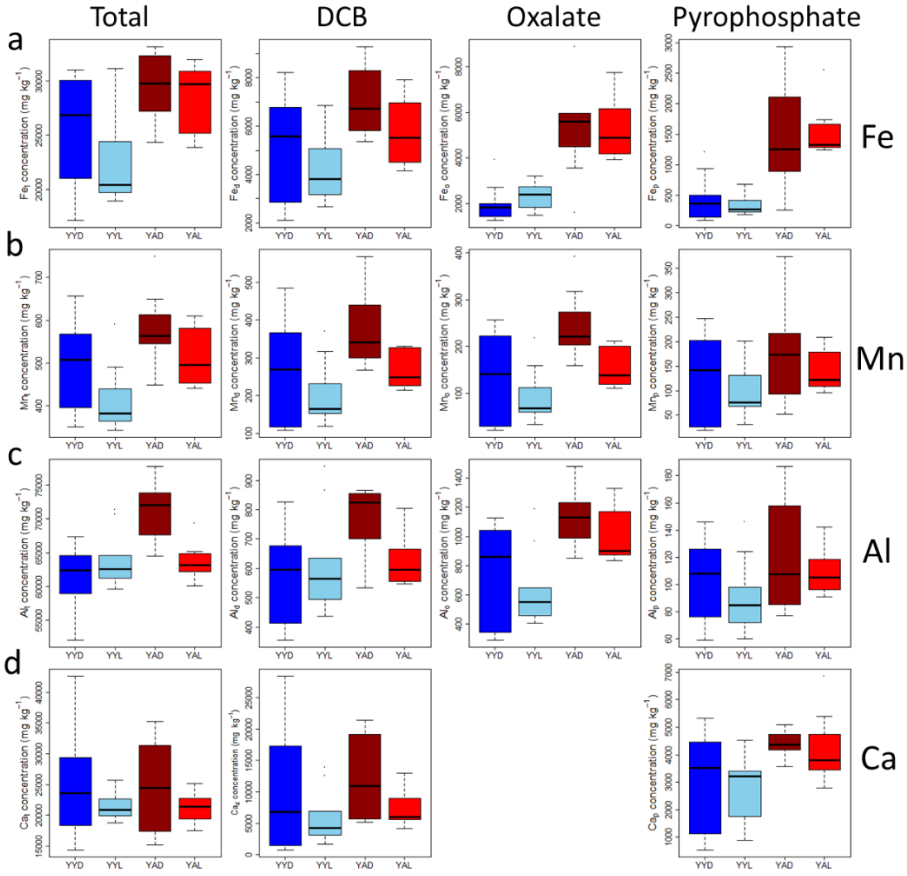

Figure 8.5: Boxplot of mineral element total concentrations and selectively extracted concentrations (expressed in mg kg^{-1}) using dithionite-citrate-bicarbonate (DCB), ammonium oxalate (oxalate) and Na-pyrophosphate (pyrophosphate) for (a) Fe, (b) Mn, (c) Al and (d) Ca for the four cores in Yukechi: Yedoma dry (YYD), Yedoma lake (YYL), Alas dry (YAD), Alas lake (YAL). Oxalate extraction of Ca is not shown due to precipitation issue (see methods Sect. 8.3.2). Yedoma cores are shown in blue and Alas cores in red. Indices are used for total, DCB, oxalate and pyrophosphate extracted metals, for instance in panel a, Fe_t, Fe_d, Fe_o and Fe_p, respectively. Note that the Y-scaling differs between plots for all elements.

8.4.3 Selective organic carbon extractions

Pyrophosphate-extracted C (C_p) concentration ranges are 2.2 - 15.4 g kg^{-1} (YYD), 1.6 - 6.6 g kg^{-1} (YYL), 4.1 - 9.2 g kg^{-1} (YAD) and 4.0 - 6.2 g kg^{-1} (YAL) (Figure 8.6a). Optical density of the oxalate extract (ODOE) ranges are 0.014 - 0.161 (YYD), 0.021 - 0.056 (YYL), 0.025 - 0.087 (YAD) and

0.049 - 0.106 (YAL) (Figure 8.6b). The Yedoma dry core shows the wider range of pyrophosphate-extracted C concentrations and Alas lake the narrower range (Figure 8.6a). Pyrophosphate-extracted C and optical density of the oxalate extract (ODOE) are positively correlated in the lower part of the Yedoma dry core (R^2 = 0.52), but not in the upper part (Figure S.8.9). The ODOE shows maximum values in the upper part of the Yedoma dry core. Notably, the sandy layer of the Yedoma dry core displays low range values for pyrophosphate-extracted C and ODOE (Figure 8.6 and Figure S.8.9). Absorbance and concentrations for selective carbon extractions are displayed in Table S.8.5.

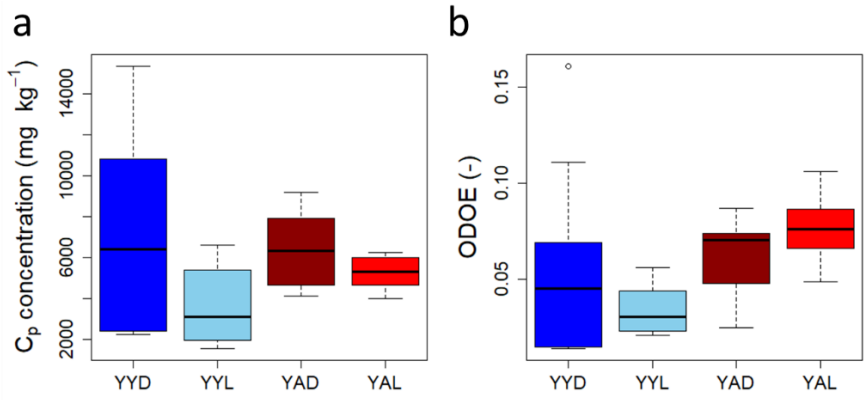

Figure 8.6: Boxplot of (a) pyrophosphate-extracted carbon concentration (C_P in mg kg^{-1}) and (b) optical density of the oxalate extract (ODOE) for Yedoma dry (YYD), Yedoma lake (YYL), Alas dry (YAD), and Alas lake (YAL) cores in Yukechi. Yedoma cores are shown in blue and Alas cores in red.

8.4.4 Statistical analysis of reactive metal and organic variables between stages of thermokarst process

Statistical analyses between the different cores highlight the significant differences occurring at each stage of the thermokarst process (Table 8.1). The initial lake formation (YYD to YYL; see Figure 8.3) triggered minor changes (not statistically significant; p-value > 0.05) in the concentration of the reactive metals (Fe_o, Mn_o, Al_o, Ca_p) and organic compounds (C_p and ODOE) (Table 8.1). The most significant differences during these stages are an increase in the concentration of reactive Fe phases and a decrease of complexed C (p-value slightly higher than 0.05 threshold). Note that the

average concentration of complexed C decreases significantly (p-value <0.05) when the sandy sediments from the Yedoma dry core are discarded. In comparison, the drainage and refreezing stage (YYL to YAD; Figure 8.3) shows a statistically significant change for every parameter (p-value <0.05; Table 8.1): the concentration of all reactive metals (Figure S.8.10) and organic compounds (ODOE and C_p) increased significantly. The secondary thawing and mature lake formation (YAD to YAL; Figure 8.3) triggered only significant changes on the reactive Mn, but had no significant effect on reactive Fe and Al nor on OC parameters (Figure 8.5 and Table 8.1). In combination, the evolution from the Yedoma dry to the Alas dry (YYD to YAD) shows a significant increase in the concentration of reactive Fe, Mn and Al, and no significant change for the other parameters (e.g., ODOE and C_p). The shift from Yedoma (YYD and YYL) to Alas (YAD and YAL) modifies the concentrations of reactive Fe, Mn, Al and Ca (Table 8.1 and Figure S.8.10). However, the shift from dry deposits (YYD and YAD) towards deposits beneath lakes (YYL and YAL) only significantly affects reactive Mn and complexed C (Table 8.1; p-value <0.05). We found that all reactive metals are positively correlated with complexed C (Figure 8.7). Complexed Fe which is the most abundant after Ca (Fe_p mean: 0.82 g kg^{-1}) shows the smallest correlation with complexed C (r = 0.29). On the other hand, complexed Mn (mean around 0.13 g kg^{-1}), which is the least abundant along with Al, shows the highest correlation with pyrophosphate extracted C (r = 0.74).

Table 8.1: P-value table of Wilcoxon test (two sided) to decipher statistical significance of subsets for reactive metals and organic compounds. These reactive metals gather oxalate-extracted Fe, Mn and Al (Fe_o, Mn_o and Al_o) and pyrophosphate-extracted Ca (Ca_p). Organic compounds are presented for optical density of the oxalate extract (ODOE) and pyrophosphate-extracted C (C_p). The p-values in bold character show statistical significant differences between the subsets. Subsets are the Yedoma dry (YYD), Yedoma lake (YYL), Alas dry (YAD) and Alas lake (YAL) cores. The (+) or (-) represents whether statistical differences is an increase or a decrease, respectively.

	Fe_o	Mn_o	Al_o	Ca_p	ODOE	C_p
*YYD vs YYL	0.0841	0.285	0.371	0.709	0.598	0.074
**YYL vs YAD	**<0.05 (+)**	**<0.05 (+)**	**<0.05 (+)**	**<0.05 (+)**	**<0.05 (+)**	**<0.05 (+)**
***YAD vs YAL	0.955	**<0.05 (-)**	0.336	0.336	0.148	0.397
****YYD vs YAD	**<0.05 (+)**	**<0.05 (+)**	**<0.05 (+)**	0.110	0.171	0.868
Yedoma vs Alas	**<0.05 (+)**	**<0.05 (+)**	**<0.05 (+)**	**<0.05 (+)**	**<0.05 (+)**	0.352
Dry vs Lake	0.190	**<0.05 (-)**	0.292	0.305	0.910	**<0.05 (-)**

*Initial lake formation effect (Figure 8.3c)

**Drainage and refreezing effect (Figure 8.3c)

***Second lake formation effect (Figure 8.3c)

**** Lake formation + drainage effects (combination of * and **)

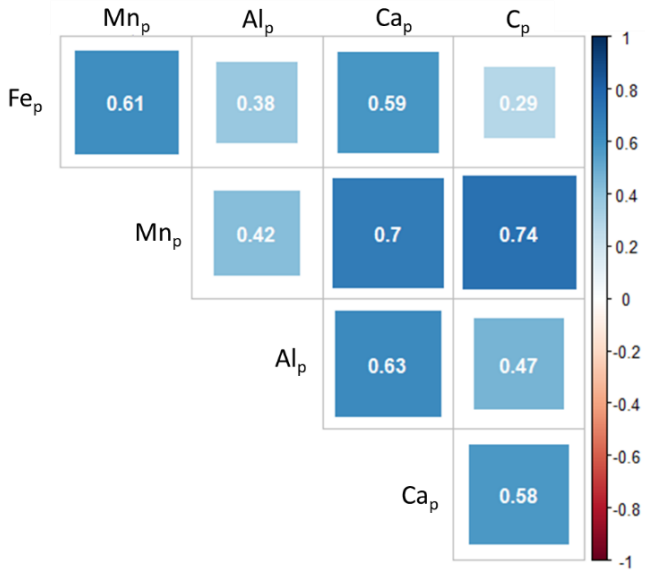

Figure 8.7: Upper correlation matrix using Pearson method of complexed (pyrophosphate-extracted) metals and organic carbon (n = 39). Correlation matrix with all parameters, including total, dithionite-extracted, oxalate-extracted, pyrophosphate extracted metals and C is available in Figure S.8.11.

8.5 Discussion

8.5.1 A typical Yedoma site modified by thermokarst process

Total mean Fe concentrations from all Yukechi cores (26.1 ± 4.9 g kg^{-1}, n = 39) are in the lower range of values compared to the median Fe concentration (31.7 ± 4.6 g kg^{-1}, n = 1,292) reported throughout the Yedoma domain (*Ch.2*). However, total mean Al and Mn concentrations fall in the same concentration range (Al = 66.5 ± 6.9 g kg^{-1}; Mn = 0.498 ± 0.119 g kg^{-1}) as presented in the Yedoma domain Mineral Concentration Assessment (YMCA) dataset (*Ch.1*). The total mean Ca concentration is twice as high (23.6 ± 6.8 g kg^{-1}) than the Yedoma domain median value (10.4 ± 4.7 g kg^{-1}, n = 1,292) (*Ch.1*). Indeed, previous studies from Central Yakutia showed that deposits in the area are rich in carbonates (Ulrich et al., 2019). This is further confirmed by the YMCA dataset (*Ch.1*), which highlights that Yukechi samples lie within the upper range of Ca concentration in Siberia (Figure S.8.12). The high pH values measured in Yukechi cores match previous findings from Central Yakutian

lakes which exhibit a pH range of 7 to 10 (Pestryakova et al., 2012), and in unconnected Alas lakes from Central Yakutia with a pH > 9 (Hughes-Allen et al., 2021). Despite the fact that carbonate presence was undetected with X-ray diffraction method, reaction of the samples to HCl supports the presence of calcite or other carbonates (including Na_2CO_3 if sample pH is above 9), which were previously reported in the area (Ulrich et al., 2019). The carbonate presence within the Yukechi deposits, the high pH values reported within our four cores, and the high range total Ca concentration emphasize that Ca is likely to be an important contributor for mineral OC interactions (Rowley et al., 2018; Sowers et al., 2020). Since redox and pH (to a lower extent) conditions can vary depending on the thawing history of deposits from each core, modifications in the contribution of each metal (Fe, Mn, Al, Ca) to mineral OC interactions are expected.

To support the findings of this space-for-time study design, the following assumptions about the four stages of thermokarst development are made. Within typical Yedoma deposits, there is a uniform mineralogical composition (Strauss et al., 2017) and little post-depositional processing (Ulrich et al., 2021). Previous work from Schirrmeister et al., (2013, 2020) in the Yedoma domain support this assumption, showing that the Yedoma deposits originated from local sources and a variety of transport mechanisms, which resulted in a polygenetic formation of Yedoma deposits. We further assume that Alas deposits formed within and from Yedoma deposits and are mainly composed of re-located and re-worked Yedoma sediments (Schirrmeister et al., 2022), although authigenic deposition upon lake formation and drainage is expected. The uniform mineralogical nature of the Yukechi site is confirmed by the similarity of detected crystalline minerals from X-ray diffraction analyses within the original Yedoma dry cores and within the other three cores (Table S.8.4). The variety of transport mechanisms is confirmed by different grain-size distributions reported in previous studies (Ulrich et al., 2019, 2021; Windirsch et al., 2020). Therefore, we expect the main changes on mineral OC interactions (i.e., Fe-, Mn-, Al-oxy(hydr)oxides and Fe, Mn, Al, Ca complexes and their associations to organic compounds) to be related to changing physico-chemical conditions in the sediment (i.e., redox state and pH), upon thermokarst processes and not related to a different composition of the original deposit. However, we acknowledge that spatial heterogeneity of the Yukechi site was not investigated and might explain part of the discrepancies observed in Yedoma and Alas deposits subjected to previous thaw. We acknowledge that additional factors not considered here such as the

diversity of microbial communities (e.g., modulating CO_2:CH_4 ratio or oxide dissolution rates), the spatial and functional complexity in the sediment (e.g., the structuring of space into a network of more or less connected microsites that determine local environment conditions), or the catalyst role of mineral elements for organic reactions (e.g., through the creation of centre of reactivity, proton transfer or electron acceptor) may also contribute to influence mineral OC interactions to some extent (Kleber et al., 2021).

8.5.2 Decoupling the influence of lake formation and lake drainage on mineral organic carbon interactions

Biogeochemical conditions in the sediment (here referring to redox and pH) are modified during lake formation and lake drainage (Lipson et al., 2012). Lake formation and lake drainage may lead to contrasted physico-chemical conditions for OC stabilization and modify mineral OC interactions. Indeed, mineral elements involved in mineral OC interactions are either redox sensitive (Fe, Mn) and/or pH sensitive (Fe, Mn, Al, Ca). We assume redox conditions to change significantly beneath lakes or in dry deposits (Kögel-Knabner et al., 2010; Lipson et al., 2012). However, the pH measured within the four cores (dry and lake cores) display high values (around 8) without significant differences between cores, which complicates the observation of modifications for pH sensitive elements. Combining our data of the four sediment cores, we are able to dissociate the impact of the following stages on mineral – OC interactions in the Yukechi sediments: i) the initial lake formation (modifications between the Yedoma dry and Yedoma lake cores); ii) the lake drainage and partial refreezing (modifications between the Yedoma lake and Alas dry cores); and iii) the second/mature lake formation (modifications between the Alas dry and Alas lake cores).

The difference in reactive Fe, Mn, Al across the sites of Yedoma and Alas show that there are opposing mechanisms upon lake formation and lake drainage. We demonstrate that the processes occurring during the intermediate steps are masked when comparing only the initial (YYD) and the final (YAD) deposits stage resulting from thermokarst processes. For instance, we observe that the combination of initial lake formation and drainage (YYD to YAD) shows no significant differences within the organic parameters concentrations (****; Table 8.1). Nonetheless, when considered separately, there is a decrease upon lake formation followed by an increase upon lake drainage for

most parameters, including reactive metals, ODOE and C_p. We highlight that initial (*; Figure 8.3b) and secondary (***; Figure 8.3b) stages of lake formation had only minor effects on pedogenic Fe, Mn, Al, Ca but greater effects on OC phases (Table 8.1). On the other hand, drainage and refreezing (**; Figure 8.3b) of the Alas dry formation corresponded to a significant increase in reactive metal (Fe, Mn, Al, Ca) oxides and complexes and also a significant increase in ODOE and C_p. We can therefore state that reactive mineral formation during drainage and refreezing outweighs any reactive mineral and organic carbon loss during the first thermokarst stage (i.e., initial lake formation). This finding supports that organic acid concentrations are unchanged between the Yedoma dry and the Alas dry (e.g., p-value = 0.87 for C_p). However, the intermediate stages involved in the formation of the Alas dry may have changed the form and properties of mineral OC interactions from the original deposit with an increase in the potential to stabilize OC. Consequently, the Alas dry core contained the largest pool size of DCB-extracted Fe and Mn, and the highest reactive Fe and Mn proportion within this pool (Figure 8.8). More specifically, the size of the DCB-extracted pool increased about 36% for both Fe and Mn between the Yedoma dry and the Alas dry core. Reactive (amorphous and complexed) Fe increased from 37% to 75% and Mn increased from 51% to 65% out of the DCB-extracted pool (Figure 8.8).

The proportion of crystalline, amorphous and complexed Fe and Mn phases evolves with lake formation and lake drainage (Figure 8.8). Between the least degraded (Yedoma dry; YYD) and the more degraded core (Alas lake; YAL), the total DCB-extracted pool is relatively unchanged (increase of 11% for Fe and decrease of 1.5% for Mn). However, if we look at the distribution of Fe and Mn between the reactive phases, we observed some differences. Firstly, for Fe, the proportion of the complexed Fe phases increase by threefold and the amorphous Fe phases double at the expense of the proportion of crystalline phases which drops significantly (63% of the dithionite-extracted pool in Yedoma dry to 8% in the Alas lake). More specifically, in the least degraded Yedoma dry core, the majority of the DCB-extracted Fe is present as crystalline phases (63%) followed by amorphous pool (29%) and complexed phases (8%) (Figure 8.8). The Alas lake sediment core shows a very distinct distribution of the different Fe pools with only 8% of the DCB-extracted Fe as crystalline phases and an increase to 65% of amorphous phases and 27% of complexed forms. Secondly, for Mn, the crystalline phases represent 50%, the amorphous only 5.5% and complexed forms 44.5% of the DCB-extracted pool

in the Yedoma dry core. The Alas lake shows a small depletion of crystalline phases (42%), amorphous phases stay unchanged (5%) and complexed forms increase (53%) in the DCB-extracted Mn pool (Figure 8.8). Overall, this supports a significant shift towards less crystalline and more reactive (amorphous and complexed) Fe compounds between the initial and the final step considered, and only a slight shift for reactive Mn compounds.

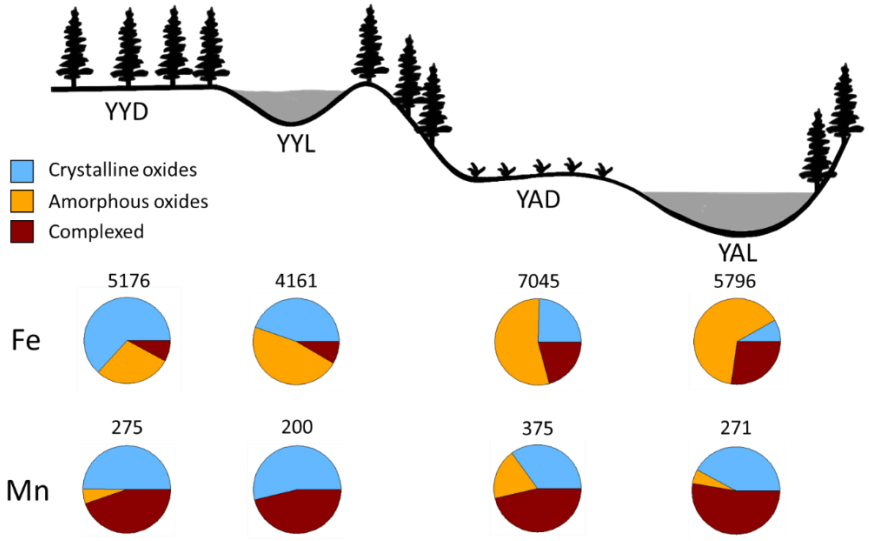

Figure 8.8: Proportion of crystalline oxides, amorphous oxides and complexed forms of Fe and Mn out of the oxide and complexed pool within the sequence of Yukechi cores. These values are based on selective extractions assuming crystalline oxide pool is the difference between DCB and oxalate-extracted and amorphous oxide pool the difference between oxalate and pyrophosphate-extracted. Complexed metals are pyrophosphate extracted. From left to right, cores represent the Yedoma dry (YYD), Yedoma lake (YYL), Alas dry (YAD) and Alas lake (YAL). The size of the total DCB-extracted pool, average in mg kg^{-1}, is given above each pie charts. The Al cannot be represented on the same basis because of higher proportion of oxalate-extracted Al than DCB-extracted Al.

The decrease in reactive Mn upon lake formation (Figure 8.5b), which is not the case for reactive Fe (Figure 8.5a), was not expected. Indeed, their similar properties related to redox sensitivity would suggest that both reactive Mn and Fe would increase upon oxidative conditions and decrease upon reductive conditions. We propose that the water saturation of Alas deposits beneath the lake might have decreased the redox potential only to a certain extent. To support this idea, Hughes-Allen et al. (2021) observed a decrease in dissolved

O_2 to below 5% during winter in the bottom of shallow (~2 m deep) unconnected lakes from Central Yakutia (located less than 100 km apart and with very similar properties as the lakes overlying Yedoma and Alas lake cores from this study). The depleted oxygen levels beneath those lakes is additional evidence for a lower redox potential in the below-lake deposits discussed here. According to the redox ladder (Figure 8.1), Mn species are thermodynamically more favourable to reduce before Fe reduction. This means that Mn is theoretically reduced before Fe species upon reduction and Fe should be oxidized before Mn species upon oxidation (Patrick Jr. and Jugsujinda, 1992; Kappler et al., 2021). As a consequence, reduction of Mn minerals may be spatially separated from reduction of Fe minerals (for example, in stratified lake sediments) (Kappler et al., 2021). The potential Mn reduction upon lake formation might have a protective effect towards Fe reduction and prevent reactive Fe decrease upon lake formation as observed here (Figure 8.5a). However, in many environments Mn cycling and Fe cycling are tightly coupled, where steep redox gradients exist on small scales (Kappler et al., 2021). Our data could be evidence for the preferential dissolution of Mn phases (relative to Fe phases) upon thermokarst lake formation.

Currently the increase in the number of lakes across the Circum-Arctic region is not offsetting the land area gained through lake drainage: this is suggesting that the transition from lake to drained thaw lake basins (i.e. Alas) is leading to permafrost aggradation and increasing carbon sequestration (Jones et al., 2022). However, future warming, reduced freezing and potential second lake formation may have a disruptive effect in this trajectory (Jones et al., 2022). Lake formation and lake drainage, and their intermediaries, are therefore highly relevant stages of permafrost condition today and in the future. We investigate the influence of the end-stages and intermediate stages of thermokarst processes on Fe- and Mn-OC interactions and show that drainage and refreezing triggered the increase in absolute and relative concentration of reactive Fe and Mn phases. In addition, the pool of reactive minerals is higher within the Alas lake than the Yedoma lake core suggesting an increase in mineral OC interactions. This suggests that secondary lake formation would have smaller impact on OC release and subsequent mineralization than initial lake formation. In summary, the increase of reactive Fe and Mn (poorly crystalline oxides and complexes) at the expense of well crystalline oxides from Yedoma to Alas cores is likely beneficial for OC stabilization (Wagai et al., 2013; Chen et al., 2014; Kleber et al., 2015).

8.5.3 Changing organo-metallic bindings with the thawing history of ice-rich permafrost deposits

The molar contribution of Ca, Fe, Al and Mn out of the sum of the complexed phases differs for each metal. On average, this contribution decreases following the sequence Ca, Fe, Al and Mn with 80.7%, 13.5%, 3.6%, and 2.2% of contribution, respectively. The high contribution of a metal (quantitatively) out of the total complexed metal pool is not the only criterion to prove that this metal is the most influential (qualitatively) on OC binding and protection. Within sediments (all characterized by high pH), we found that Ca is the dominant contributor for organo-metallic complexes. The high Ca concentration within these deposits and the poor solubility of Fe(III) under circumneutral pH might explain the higher contribution of Ca compared to Fe. However, organo-metallic complexes can involve both Fe(II) and Fe(III) and the reported co-occurrence of Fe(II) and Fe(III) in organic complexes from both oxic and anoxic sediments can explain the substantial role of Fe despite the alkaline pH and reductive conditions within sediments (Bhattacharyya et al., 2018b). Additionally, we found a strong correlation between Mn_p (a minor player quantitatively compared to Fe_p or Ca_p) and C_p (Figure 8.7), which emphasizes that Mn is likely an important player qualitatively to form association with C and increase its stabilization.

The saturation of functional groups within soluble organic acids can be approached by the metal:C molar ratio, i.e., the ratio between the sum of pyrophosphate-extracted metals (Fe_p, Mn_p, Al_p and Ca_p) and pyrophosphate-extracted C (C_p) (Stevenson, 1994; Nierop et al., 2002; Schwesig et al., 2003). As described by Boudot et al. (1989), organo-metallic complexes which exhibit a low metal:C molar ratio are easily biodegraded because of the lack of significant protective effect. In short, the higher the metal:C molar ratio, the better protected the organic matter may be against microbial degradation. In the Yedoma dry core (YYD), the metal:C molar ratio is around 0.1. Upon thermokarst process, this molar ratio increases and all other cores (YYL, YAD, YAL) display a metal:C molar ratio around 0.3 (Figure 8.9). Organic acids display thus fewer bindings with metals within the Yedoma dry core compared to other cores. The initial lake formation led to a depletion in complexed C and to a lesser extent in complexed metals (Figure 8.9b, arrow 1) with a significant shift from metal:C molar ratio from 0.1 to 0.3 ratio line

(Figure 8.9a). The second stage of the thermokarst process (i.e., drainage and refreezing; Figure 8.9b, arrow 2) led to an increase of both complexed C and complexed metals following the 0.3 ratio line. Finally, the second lake formation had no or few effects on C and metal molar concentrations compared to the initial lake formation. Complexation between organic acids and metals lowers the solubility of organic acids and hence its availability to microorganisms (Baldock and Skjemstad, 2000). This, in turn, can decrease the susceptibility to biological attack and hinders mineralization of organic molecules (Oades, 1988). Two hypotheses can explain an increase in metal:C molar ratio: i) the density of functional groups is constant and the quantity of metals binding to these functional groups is increasing, or ii) polyfunctional groups are saturated with metal cations but the density of polyfunctional groups is increasing. The abundance of metals cations (especially Ca) suggests that functional groups are likely saturated, and that the second hypothesis is more likely. Either way, the increase in metal:C ratio results in increasing protection for organic acids. Therefore, the increased metal:C ratio observed after thawing of the Yedoma dry deposits likely results in the increase of stability inferred from complexation between metals and OC and to the previous loss of unprotected OC.

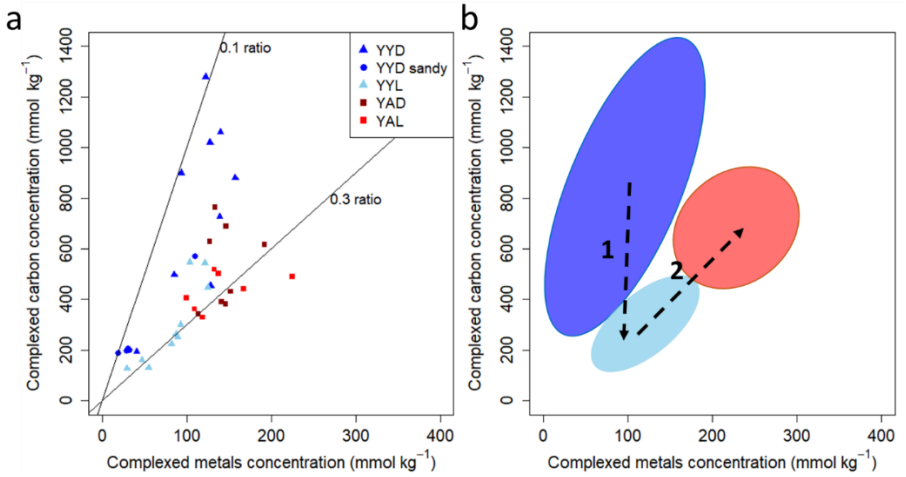

Figure 8.9: (a) Relation between the concentration (in mmol kg^{-1}) of complexed carbon (y-axis) and the sum of complexed metals (including Fe, Mn, Al and Ca) for Yedoma dry (YYD), Yedoma lake (YYL), Alas dry (YAD) and Alas lake (YAL) cores. (b) Conceptual view of the influence of lake formation (1) and lake drainage (2) on complexed mineral and organic phases.

Dissolved organic acids have a high density of carboxyl groups (on average one carboxyl group for every ten C atoms; pKa around 4-5) (Stevenson, 1994). For acidic pH, where we found a dominance of carboxylic polyfunctional group (Catrouillet et al., 2014), organic acids are thus considered saturated around a metal:C molar ratio of 0.1. Here, the high pH (mean around 8-9) allows the presence of other functional groups such as phenolic groups (pKa around 10) (Bell, 2013). Advanced stages of organic matter degradation and subsequent depolymerization and oxidation can also lead to the increase of abundance of polar functional groups and enhance their chemical reactivity towards metal cations and mineral surfaces (Kleber et al., 2021). Polyvalent cations (i.e., $Fe^{3+/2+}$, Al^{3+}, $Mn^{4+/3+/2+}$ and Ca^{2+}) can bind via coordination to those multiple functional groups and form stable organo-metallic complexes. Complexation mechanisms maintain OC stability and slow down its decomposition rate (Chen et al., 2022). The increase in metal:C ratio after thawing highlights the increase of metal-C coordination bindings and suggests a higher protective role against microbial mineralization.

8.5.4 Implications for greenhouse gas emissions

We have the excellent opportunity to combine data on mineral OC interactions presented in this study with incubation experiments quantifying CO_2 and CH_4 emissions from adjacent samples from the same sediment cores of Yedoma lake and Alas lake (Jongejans et al., 2021b). The cumulative greenhouse gas production after 1 year of incubation was the highest in Yedoma lake sediments, and was 3 and 1.5 times lower in Alas lake sediments for CO_2 and CH_4, respectively (Jongejans et al., 2021b). The authors concluded that the highest production in Yedoma deposits was likely due to the decomposition of readily bioavailable organic matter, and that the lower greenhouse gases production in the non-frozen Alas lake sediments likely resulted from advanced OM decomposition during Holocene talik development. Higher greenhouse gas emissions were reported in the Yedoma lake core despite the lower total OC content within this core (median YYL: 0.5 wt%) relative to the Alas lake core (median YAL: 0.8 wt%).

We suggest that the increase in stabilizing mechanisms (involving reactive Fe, Mn, Al, and Ca) in the Alas lake core compared to the Yedoma lake core (Figure 8.8) could also explain the lowest greenhouse gas production in Alas lake sediments (Figure 8.10). The lower CO_2 and slightly lower CH_4

production (Figure 8.10a and Figure 8.10b, respectively) in the Alas lake core relative to the Yedoma lake core is concomitant with an increase of both complexed C and sum of complexed metals concentrations (Figure 8.10). In addition, the increase in reactive Fe (Fe_o/Fe_t; Figure 8.10), and reactive Mn, Al and Ca after first lake drainage (Mn_o/Mn_t, Al_o/Al_t, Ca_p/Ca_t; Figure S.8.13) likely offers better protection for the OC in the sediment. There is also an increase in the total amount of stabilized complexed C upon the drainage process, a pool that is kept during the second lake formation (Figure 8.9b, arrow 2). All of these would contribute to the decrease of CO_2 and CH_4 emissions in Alas lake sediments relative to the Yedoma lake sediments. Quantitatively, metals participating in organo-metallic complexes increased by ~70% in the Alas lake relative to the Yedoma lake (83 mmol kg^{-1} in YYL to 141 mmol kg^{-1} in YAL; Figure 8.10) and may hinder the efficacy of microbial enzymes to degrade OC (Mikutta et al., 2006; Kleber et al., 2007). The amounts of poorly crystallized Fe oxides (Fe_o-Fe_p) almost doubled, from 1.96 g kg^{-1} in the Yedoma lake to 3.74 g kg^{-1} in the Alas lake, on average. Thanks to the high specific surface area of poorly crystallized oxides, iron oxy(hydr)oxides can sorb up to 0.22 g OC g Fe^{-1} (Wagai and Mayer, 2007). Based on this ratio, Yedoma lake sediments can sorb and protect up to 0.83 g OC kg^{-1} (mean YYL: 3.81 g Fe kg^{-1}) and Alas lake sediments up to 0.93 g OC kg^{-1} (mean YAL: 4.22 g Fe kg^{-1}), which represents a 12% increase.

Overall, we suggest that the shift in the proportion of reactive Fe (from 10.4% in Yedoma lake to 18.6% in Alas lake) and of reactive Mn (from 21.2% in Yedoma lake to 30% in Alas lake) out of their total concentration (also true for reactive Al and Ca; Figure S.8.13) might contribute to mitigate CO_2 and CH_4 emissions. In addition, the increased availability of Fe and Mn within the Alas lake core can promote anaerobic oxidation of CH_4 (Lipson et al., 2012; Miller et al., 2015, 2019). Under anaerobic conditions, a variety of microorganisms are capable of using Fe and Mn to oxidize CH_4 and mitigate CH_4 emissions (Blodau, 2002; Beal et al., 2009). The decrease in CH_4 production within the Alas lake core could be explained by an increase in reactive Fe and Mn. Further investigations are still needed to quantify the direct impact of such mineral OC interactions on methane production rates.

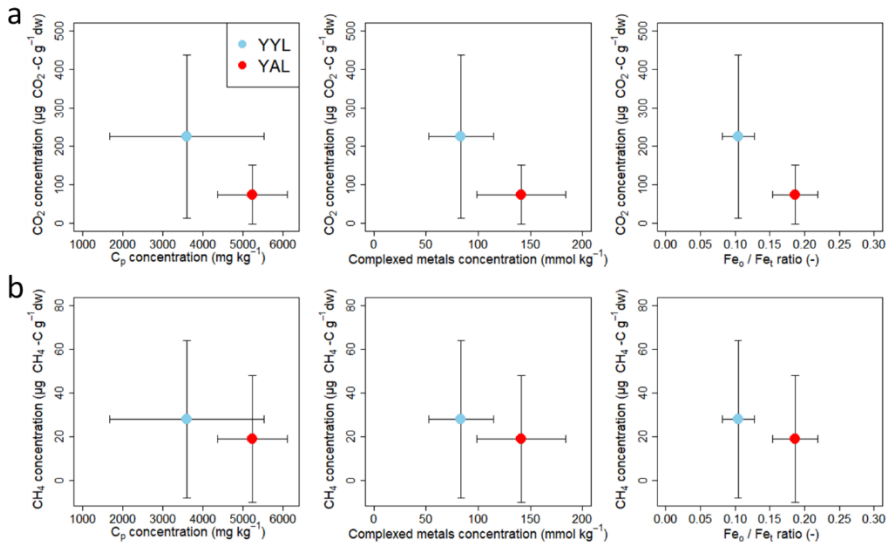

Figure 8.10: Mean and standard deviation of (a) CO_2 (expressed in µg CO_2-C g^{-1} dry weight) and (b) CH_4 (expressed in µg CH_4-C g^{-1} dry weight) emissions on the y-axis and mineral stabilization parameters (pyrophosphate extracted C, sum of complexed metals concentration and Fe_o/Fe_t ratio) on the x-axis for the Yedoma lake sediments (YYL, blue) and the Alas lake sediments (YAL, red). The mean greenhouse gases (CO_2 and CH_4) concentration values are from one-year long (4°C, dark) incubation experiments for Yedoma lake sediments (YYL; n = 7) and Alas lake sediments (YAL; n = 10)(Jongejans et al., 2021b). No incubation experiments are available in the Yedoma dry and Alas dry sediments to compare with the other cores.

In combination, sediment incubation data and mineral organic carbon characterization validate the increased attention given to mineral OC interactions for their potential influence on the permafrost carbon feedback. We demonstrate that the increased abundance in stabilizing surfaces and ions (i.e., via adsorption, co-precipitation, complexation) led to the decrease in microbial degradation and potentially to methanogenesis inhibition. While many other parameters can influence greenhouse gas emissions (carbon quality, quantity, microbial community diversity), we claim that mineral OC interactions cannot be neglected. Incubation experiments highlighted the contribution and importance of organo-mineral associations for soil OC sequestration in soils of the Siberian Arctic, with over 50% of soil OC bound to minerals (Gentsch et al., 2015a). The potential to increase CO_2 and CH_4 production in ecosystems vulnerable to thermokarst processes could be limited by the increase of reactive metals that enhance OC protection and by the increase of Fe and Mn availability that may inhibits CH_4 production

(Bodegom et al., 2004; Lipson et al., 2012). Our data support the overwhelming evidence that mineral OC interactions are key for a more comprehensive understanding of potential greenhouse gases emissions upon recent and future thermokarst processes.

8.6 Conclusion

This study investigated the role of the reactive metals Fe, Mn, Al and Ca in mineral organic carbon interactions along a landscape transect in Central Yakutia from undisturbed Yedoma uplands to drained lake and thermokarst lakes sediments from different generations. We quantified the influence of thermokarst lake formation and drainage on mineral OC interactions. Our main conclusions are the following:

(i) Intermediate stages of thermokarst processes like lake formation and lake drainage largely influence interactions between reactive metals and OC. Lake formation decreased the amount of complexed OC by 50% and reactive Mn phases by 33%. Lake drainage (disappearance) and refreezing substantially increased the amount of organic compounds (complexed OC and associated to mineral surfaces) and all reactive metals (Fe, Mn, Al, Ca). The maximum of reactive metals is found within the Alas dry core (YAD).

(ii) Upon the range of thermokarst process here considered (Yedoma dry (YYD) to Alas lake sediments (YAL), the amount of complexed Fe phases increases by threefold. The amount of amorphous Fe doubles at the expense of crystalline phases which drop significantly from the Yedoma dry to the Alas lake core (63% of crystalline Fe oxides in the free iron pool in the Yedoma dry (YYD) and 8% in the Alas lake (YAL)). Despite a significant increase of amorphous and complexed Mn concentrations in the Alas dry core (YAD), the amount of reactive Mn remains relatively similar from Yedoma dry (YYD) to Alas lake core (YAL). Reactive Al and Ca concentrations increase significantly with the thermokarst lake drainage whereas lake formation has only minor influence with a slight decrease in reactive Al and Ca concentrations.

(iii) Following thermokarst processes, organic carbon has more opportunity to bind with metal cations which likely increases the stability of organic matter and mitigate microbial degradation.

(iv) The higher proportion of reactive metals and complexed organic carbon in Alas lake deposits (YAL) than in Yedoma lake deposits (YYL) is concomitant with lower CO_2 and CH_4 emissions reported in Alas than in Yedoma deposits from the same cores via incubation experiments.

We found an increase in the supply of stabilizing Fe, Mn and Al surfaces, especially Fe-oxy(hydr)oxides and Fe, Mn, Al, Ca cations providing an increasing protection for OC. We found an increase in poorly crystalline oxides and in metal:C bindings within organo-metallic complexes upon thermokarst lake drainage and refreezing. All of these contributed to the concomitant decrease of CO_2 and CH_4 emission upon secondary thawing of Alas deposits. Overall, our data emphasize the overwhelming evidence that mineral OC interactions need to be considered in the estimates of future greenhouse gas emissions upon thawing of ice-rich permafrost deposits.

9. Chapter 4: Mineral organic carbon interactions in dry versus wet tundra soils

This chapter is a modified version of a research paper submitted in Geoderma special issue: "Permafrost affected soils and climate change - from soil development to carbon storage and biological functioning".

Monhonval, A., Mauclet, E., Hirst, C., Bemelmans, N., Eekman, E., Schuur., E.A.G., Opfergelt, S., 2022. Mineral organic carbon interactions in dry versus wet tundra soils, Geoderma (submitted).

Abstract

Mineral organic carbon interactions (aggregation, organo-mineral associations and organo-metallic complexes) enhance the protection of organic carbon (OC) from microbial degradation in soils. The northern circumpolar permafrost region stores between 1,440 and 1,600 Pg OC of which a significant portion is already thawed or about to thaw in coming years. In the light of this tipping point for climate change, any mechanism that can promote OC stabilization and hence mitigate OC mineralization and greenhouse gas emissions is of crucial interest. Here, we study interactions between metals (Fe, Al, Mn and Ca) and OC in the moist acidic tundra ecosystem of Eight Mile Lake, near Healy, AK, USA. We collected thirteen cores (124 soil samples) in late summer 2019 with shallow and deep active layers (45 to 109 cm deep) and varying water table depths. We find that, in combination, organo-mineral associations (association between ferrihydrite and OC) and organo-metallic complexes (associations between Fe, Mn, Al, Ca polyvalent cations and organic acids) stabilize between 6% and 59% of total OC in Eight Mile lake tundra soils (mean 20%). We find that total Fe and Mn concentrations can be used as good proxies to assess the reactive pool of these metals able to form associations with OC, i.e., poorly crystalline oxides or metals complexed with OC. We observe that in the active layer, mineral OC interactions are mostly as organo-metallic complexes with Fe cations, with an accumulation at the water table level acting as a soil redox interface. In waterlogged soils with a water table level above surface, no such accumulation of OC-Fe complexes is found due to the absence of a redox interface below soil surface. In the permafrost layer, we find that a combination of complexed metals and poorly crystalline Fe oxides act as reactive phases towards OC. Knowing that upon permafrost thaw tundra soils

will become wetter or drier, this assessment of mineral protection of OC in drier or wetter tundra soils is a needed step to better constrain the changes in the proportion of non-protected OC more likely to contribute to C emissions from tundra soils.

9.1 Introduction

The permafrost region occupies about 22%-24% of the exposed land surface of the Northern Hemisphere (Brown et al., 1998; Zhang et al., 1999; Obu et al., 2019). Total soil organic carbon (OC) in the northern circumpolar permafrost region is estimated to be 1,440-1,600 Pg OC, stored in surface and deeper (>3 m) soil layers (Hugelius et al., 2014; Schuur et al., 2015; Strauss et al., 2017). Rising temperatures, two times more rapid in northern regions compared to global warming, result in the gradual thaw (i.e., deepening of the soil layer that thaws every summer, referred as the active layer) of permafrost (Schuur et al., 2015; Luo et al., 2016). Permafrost thaw is a major tipping point in the climate system (Lenton et al., 2019; IPCC, 2021) because of its climate-sensitive OC pool under threat of being transferred to the atmosphere as greenhouse gases carbon dioxide (CO_2) and methane (CH_4) upon microbial degradation (Zimov, 2006; Schuur et al., 2008, 2013).

The impact of climate warming on the hydrology of northern permafrost soils is complex (Bring et al., 2016; Vonk et al., 2019). Permafrost tundra soils are expected to be drier with increasing evapotranspiration and drainage as a consequence of permafrost thaw (Avis et al., 2011; Bring et al., 2016). However, local increases in water saturation in soils are predicted in areas that collapse and fill with water because of the impermeable permafrost table that prevents drainage (Swindles et al., 2016). Waterlogged soils face major changes in biogeochemical conditions (Kögel-Knabner et al., 2010): the presence of the water table at the surface restricts oxygen diffusion which lowers the reductive-oxidative (redox) potential and promotes metal oxides dissolution or anaerobic processes (such as methane production). Most permafrost-affected ecosystems suffer from periodic or persistent anoxia due to soil water saturation (Street et al., 2016).

The mechanisms of OC stabilization involving mineral OC interactions, i.e., the mineral protection of OC, are highly dependent on the soil moisture and hence redox state of tundra soils (Fiedler and Sommer, 2004; Bhattacharyya et al., 2018a; Winkler et al., 2018; Herndon et al., 2020b). While the importance of such interactions for OC protection has been assessed in many environments, from temperate, forest and volcanic soils to paddy soils and marine sediments (e.g., Eglinton, 2012; Eusterhues et al., 2005; Inagaki et al., 2020; Kalbitz and Kaiser, 2008; Lalonde et al., 2012; Masiello et al., 2004; Mikutta et al., 2007; Pan et al., 2014; Wang et al., 2019), the focus on permafrost soils is only recently growing (Fiedler et al., 2004; Mu et al., 2016;

Herndon et al., 2017, 2020a; Patzner et al., 2020; Wang et al., 2021; Joss et al., 2022; Lim et al., 2022a, 2022b). Our understanding on the changes of mineral OC interactions between drier and wetter tundra soils remains incomplete, particularly with respect to changing water saturation in the active layer upon thawing.

Mineral OC interactions result in the protection of OC from degradation via aggregation, organo-mineral associations and organo-metallic complexes (Torn et al., 1997; Baldock and Skjemstad, 2000; von Lützow et al., 2006; Kleber et al., 2015). Aggregation offers physical protection whereas organo-mineral associations and organo-metallic complexes offer physico-chemical protection of OC. In aggregates, OC is occluded in the tridimensional arrangement of minerals involving metal oxides (e.g., goethite, hematite, ferrihydrite, birnessite), limiting the access for microorganisms to the trapped OC. Organo-mineral associations involve the ligand exchange (alongside other binding mechanisms) between organic carbon and phyllosilicates or metal oxide surfaces, which are among the most effective sorbent for dissolved OC (e.g., Kaiser et al., 1997; Stumm, 1992) or other important nutrients for plant growth (e.g., phosphorous (P); Giesler et al., 2005; Herndon et al., 2019). In organo-metallic complexes, metals (i.e., $Fe^{3+/2+}$, Al^{3+}, $Mn^{3+/2+}$ or Ca^{2+}) act as polyvalent cations and coordinate to the functional groups of organic acids (e.g., Boudot et al., 1989). In organo-mineral associations and organo-metallic complexes, OC is less soluble and therefore less available for microorganisms which contributes to mitigate greenhouse gas emissions from permafrost soils.

We hypothesize that soil moisture content is a major player in controlling mineral OC interactions in moist acidic tundra soils. Indeed, in poorly drained organic-rich soils well represented in moist acidic tundra soils, soluble Fe^{2+} present in the mineral horizons can migrate to more oxic zones and accumulate as a mixture of organic-bound (i.e., complexed) Fe^{2+} and Fe^{3+}, and Fe oxy(hydr)oxides (Lipson et al., 2012; Riedel et al., 2013; Herndon et al., 2017; Bhattacharyya et al., 2018b), thereby contributing to form mineral OC interactions. In contrast, in waterlogged soils, such accumulation of complexed Fe and Fe oxy(hydr)oxides is less likely. In the absence of oxic conditions within the soil profile, due to the high soil moisture content, soil redox potential decreases and in turn may increase oxide dissolution and release previously stabilized OC, hence increasing OC vulnerability to mineralization (Lipson et al., 2012). In addition to the major role of redox conditions, we also hypothesize that mineral OC interactions differ with

changing pH conditions between organic-rich surface horizons and mineral-rich deeper soil horizons (Parkinson, 1978; Ping et al., 2005). The soil pH controls oxides dissolution rates and can protonate or deprotonate organic acids functional groups or oxide surfaces, modifying organic acids-oxides association (Pan et al., 2014; Kleber et al., 2015, 2021). A shift in pH would change the relative importance of Fe, Al versus Ca metal as polyvalent cations participating in complexation (Rowley et al., 2018). Finally, we hypothesize that with permafrost thaw, additional minerals and OC stored in frozen layers will become available to form mineral OC interactions (Opfergelt, 2020; Hirst et al., 2022).

Testing these hypotheses requires a better understanding on the dynamics of Fe, Al, Mn and Ca and their interactions with organic acids in permafrost soil ecosystems. Here, we investigate the proportion of mineral OC interactions (including Fe, Al, Mn and Ca with a particular focus on Fe) in a range of dry and wet tundra soils. We study 13 profiles with varying active layer and water table depths from a well described moist acidic tundra site near Eight Mile Lake, Healy, AK, USA. We determine the total pool of Fe, Al, Mn and Ca and quantify the reactivity of these metals with OC.

9.2 Material and Methods

9.2.1 Site description and soil sampling

Soil profiles were collected at Gradient site from the Eight Mile Lake (EML) watershed in Turbic Cryosols (IUSS Working Group WRB, 2015) from a moist acidic tundra located near Healy, Alaska, USA (63.87°N; 149.25°W, 700 m elevation, Figure 9.1a) in late summer 2019, at the time of deepest active layer thaw. Gradient site is a natural gradient of permafrost thaw and thermokarst development (i.e., gullies and water tracks) monitored for ~40 years (Osterkamp et al., 2009; Schuur et al., 2009). The EML watershed lies at the continuous to discontinuous permafrost boundary but the Gradient site itself is underlain entirely by permafrost. Mean annual air temperature averaged -0.94°C from 1977 to 2015 with a non-summer (October-April) average of -10.09°C and summer (May-September) average of 11.91°C (Healy and McKinley Stations, Western Regional Climate Center and NOAA National Centers for Environmental Information) (Mauritz et al., 2017). Permafrost is close to thaw because its temperature approximates the mean

annual air temperature of - 1°C (Osterkamp and Romanovsky, 1999) and is still rising (Osterkamp et al., 2009). The area is characterized with thick peat accumulations (~40 cm) over fine-grained soils of loess origin associated with colluvial deposits. The upper 1 m of soils at Eight Mile Lake have characteristically high moisture content, within 48% - 60% by volume in 2009, and thus are highly vulnerable to the formation of thermokarst terrain (Osterkamp et al., 2009; Garnello et al., 2021). The Gradient site was historically determined based on increase subsidence and thaw settlements downslope previously referred as Minimal, Moderate and Extensive thaw (Osterkamp et al., 2009). Windblown snow always fills thermokarst depressions causing further warming and thawing of the underlying permafrost (Osterkamp et al., 2009). The thermokarst development at Eight Mile Lake has initiated a shift in vegetation cover, with evergreen and deciduous shrubs and forbs becoming dominant at the expense of tussock forming sedges in drier sites, and sedges and mosses being dominant in wetter sites (Schuur et al., 2007; Natali et al., 2011; Mauclet et al., 2021; Villani et al., 2022). Long-term monitoring at the Gradient site (between 2004-2021) supports the spatial and temporal change in active layer and water table depth with ongoing permafrost thaw (Schuur et al., 2021; Kelley et al., 2022; Schädel et al., 2022).

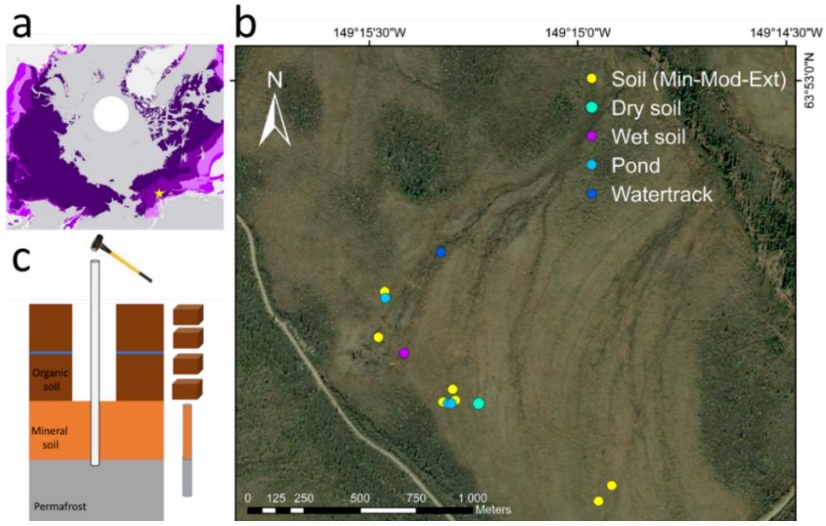

Figure 9.1: (a) Location (yellow star) of Eight Mile Lake Gradient site near Healy, Alaska, at the boundary between continuous and discontinuous permafrost. (b) Coring locations within the Gradient site for the thirteen soil profiles. Coordinates, active layer depth and water table depth are available in Table S.9.1. (c) Sampling scheme with chisel and knife in upper profile and steel pipe hammered down into active layer and permafrost. The blue line represents the water table position.

The first centimeters of soil cores (up to 45 cm) were collected using chisel and knife in 5 cm increments which prevented compaction within organic-rich layers. Below the water table (i.e., when chisel and knife was not applicable), cores were retrieved using a stainless-steel pipe (diameter 44 mm) which was manually hammered down into active layer and permafrost (Figure 9.1c). The core within the steel pipe was subdivided in 10 cm increments. All samples were stored in plastic bags and air dried in the laboratory before analysis. Note that compaction in the surface layers of waterlogged soils (i.e., especially ponds and water track (WT) profiles) was inevitable using the steel pipe method. This study presents 13 soil profiles combining a total of 124 samples from poorly thawed profiles (defined here as soils profiles with an active layer depth < 60 cm; n = 64; profiles Min1, Min3, Mod1, Ext1, Dry5, Pond10) and deeply thawed profiles (active layer depth > 60 cm; n = 60; profiles Mod3, Mod2, Ext3, Wet4, Pond1, Pond9, WT1) (Figure 9.1b; Table S.9.1). The 60 cm limit is representative of the modern day active layer reported in EML soils (Hutchings et al., 2019). Within the 13 profiles, active layer depth ranged between 45 and 109 cm b.s. (below surface; the surface here is defined as the bottom of vegetation) and water table depth between 45 cm b.s. and 15 cm a.s. (above surface). Permafrost was reached for all 13 profiles to a maximum depth of 150 cm. The length of soil cored varied: we stopped coring when the steel pipe hit rock fragments. At each sampling location, water table depth and active layer depth were recorded. In total, this study presents 73 samples from active layer soils and 51 from permafrost layers. Samples from the litter were shredded without anterior sieving while other samples were sieved at 2 mm and ground prior to laboratory analyses.

9.2.2 Total measurements of metals (Fe, Mn, Al and Ca), total P and organic carbon

We assessed total Fe, Mn, Al and Ca concentrations using a portable X-ray fluorescence (pXRF) device (*Niton^{TM} XL3t GOLDD+*, Thermo Fisher Scientific, Waltham, USA) following the method described fully in (*Ch.1*). The pXRF method needs to be calibrated to ensure trueness. We compared the total metal concentrations measured by pXRF with metal concentrations obtained using inductively coupled plasma optical-emission spectrometry (ICP-OES; iCAP 6500 Thermo Fisher Scientific) after sample dissolution by alkaline fusion (Chao and Sanzolone, 1992). The loss on ignition at 1,000°C allows to verify the sum of oxides (between 98 and 102%). Total elemental

content is expressed in reference to the soil dry weight at 105°C. We performed pXRF and ICP-OES measurements on 39 samples from Gradient site in addition to the 144 samples based on the work from *Ch.1* on ice-rich permafrost samples. We observed that two corrections were needed depending on total OC content. The pXRF measurement involves X-ray beam penetration of the sample and fluorescence energy needs to be detected back by the pXRF device. The density of the sample (i.e., the amount of air present in the porosity of the sample) may cause under estimation of metal concentration, hence correction to ensure trueness is needed (Ravansari and Lemke, 2018; Ravansari et al., 2020). Samples with lower total organic carbon content (TOC < 20 wt%), considered as mineral matrix, followed the linear regression previously assessed in *Ch.1* (Figure S.9.1). Samples with higher TOC (> 20 wt%) displayed another linear regression and therefore need to be corrected using another equation for Fe, Mn and Ca, whereas only one linear regression was necessary for Al ($R^2 = 0.91$). The coefficient of variation (i.e., CV, the ratio of the standard deviation to the mean concentration) of the pXRF method equals 0.74% (Fe), 3.7% (Al), 2.9% (Mn), 0.84% (Ca), and for ICP-OES method 0.50% (Fe), 0.43% (Al), 0.85% (Mn) and 0.99% (Ca) (*Ch.1*).

Total P concentrations were measured by ICP-OES after alkaline fusion (n = 39). The poor correlation between pXRF and ICP-OES method for P prevented the use of corrected pXRF concentration. Based on identical samples from *Ch.1*, the CV equal 2.1% and no sample was below detection limit (0.01 mg L^{-1}). The reference material $BHVO_2$ used to ensure trueness show a mean of 1178 ± 74 mg kg^{-1} (n = 10) within the certified value range of 1200 ± 100 mg kg^{-1} (Wilson, 1997).

The total soil carbon content was measured on all samples (n = 124). Air-dried samples were homogenized by grinding prior to a measurement of 5-7 mg of the sample with a Vario El cube elemental analyzer (Elementar, Langensebold, Germany). Every sample is weighed and processed twice for carbon analysis and the mean is calculated. The average standard deviation for C content is ~5% and the detection limit is <0.1%. Total C measurements are expressed as weight percentage (i.e., wt%) in reference to the soil dry weight at 105°C. With no presence of carbonates detected, the total soil carbon content is considered equivalent to soil OC content.

9.2.3 Selective extractions of metals (Fe, Mn, Al and Ca) and organic acids

Selective extractions of Fe, Mn, Al and Ca were performed on all samples (n = 124) using i) dithionite-citrate-bicarbonate (DCB), ii) ammonium oxalate in the dark for 4 hours, and iii) Na-pyrophosphate for 16 hours. The DCB extraction is presumed to remove oxides (well and poorly crystallized oxides) as well as complexed (i.e., organic-bound) metals (Mehra and Jackson, 1960). The ammonium oxalate in the dark extraction (in the following referred as oxalate extraction) is presumed to remove poorly crystalline oxides and complexed metals (Blakemore et al., 1981). This oxalate extracted pool will be defined as the reactive metals because of their high reactivity to bind with OC. The Na-pyrophosphate extraction is presumed to remove only organically complexed metals and also dispersible colloids (Bascomb, 1968; Parfitt and Childs, 1988). These extractions are not fully quantitative and some dissimilarities between the theoretical and practical extracted pool may appear (Rennert, 2019). However, these are commonly used extraction methods that can be used as indicators of the oxides and complexed pools within a particular soil. The amount of well crystallized Fe oxides is calculated as the difference between DCB- and oxalate-extracted Fe (i.e., $Fe_d - Fe_o$), and the amount of poorly crystalline Fe oxides (i.e., ferrihydrite) by the difference between oxalate and pyrophosphate-extracted Fe (i.e., $Fe_o - Fe_p$). The same can be done for Mn but not Al for which DCB extraction do not target Al oxides specifically (Rennert, 2019). Note that Ca concentration within the oxalate extraction is not relevant given that Ca oxalate precipitates and does not remain in solution for ICP-OES measurement. Metal concentrations (Fe, Mn, Al and Ca) in the extracts were analyzed by ICP-OES (iCAP 6500 Thermo Fisher Scientific) and are expressed in reference to the soil dry weight at 105°C (mg kg^{-1}). The limit of quantification (LOQ) was reached for oxalate-extracted Mn (< 0.008 mg L^{-1}, corresponding to 6 mg kg^{-1} in solid sample) for 30 out of 124 samples.

Organic acids were analyzed using indirect or direct measurements within the oxalate extract and the pyrophosphate extract, respectively. Note that the organic composition of the DCB and oxalate solutions do not allow direct measurement of OC. The optical density of oxalate extract (ODOE), considered as an indicator of reactive polyaromatic acid concentration, was measured by determining the absorbance at 430 nm on a Genesys 10 S VIS spectrophotometer, with the ammonium oxalate reagent as a blank (Daly,

1982). From the pyrophosphate extract, the concentration in dissolved OC released after dispersion by pyrophosphate (referred as C_p) was measured using a Shimadzu TOC-L Analyzer (measuring non purgeable OC; LOQ = 0.1 mg L^{-1}; accuracy ±2%). This indicates the amounts of C participating in organo-metallic complexes in soils (Bascomb, 1968). The LOQ was never reached for any samples.

9.2.4 Mineral element stocks in permafrost tundra and statistical analysis

The dataset built along this study was used to estimate reactive mineral stocks in Eight Mile Lake tundra soils. Given that bulk densities were not measured upon sampling, bulk densities were estimated based on measured TOC content. A quadratic model has been used to relate bulk density (BD) to TOC content based on 443 paired measurements on active layer and permafrost samples from a moist acidic tundra site analogous to Gradient located couple kilometers north-east from Gradient site, i.e., the Carbon in Permafrost Experimental Heating Research (CiPEHR; Plaza et al., 2019). The model used is: $BD=b_0+b_1\ x+b_2\ x^2$ where x represents the TOC expressed in % and b_0 = 1.08, $b_1 = -3.46 \times 10^{-2}$ and $b_2 = 2.81 \times 10^{-4}$ ($R^2 = 0.72$) (Figure S.9.2). Stocks of Fe_o were calculated for each layer following Eq. 9.1 and cumulative stock for a considered thickness was obtained from the sum of the stock of each layer. Similarly, stocks were computed for Al_o, Mn_o, TOC and C_p.

$$\textit{Fe}_o\ \textit{stock}\ [\text{kg m}^{-2}] = \textit{Fe}_o\ \textit{concentration}\ [\text{g kg}^{-1}] \times \textit{Bulk density}\ [\text{g cm}^{-3}] \times \textit{Thickness}\ [\text{m}] \quad \text{(Eq. 9.1)}$$

Correlation analysis using Pearson method between metal and organic parameters were constructed using *corrplot* package. All statistics were performed using R core software (R Core Team, 2018).

9.3 Results

9.3.1 Total and selectively extracted metals (Fe, Mn, Al and Ca) in permafrost tundra soils

Here we present the metal concentrations (Fe, Mn, Al and Ca) in a partially unsaturated (i.e., dry) profile which is poorly thawed and a waterlogged (i.e., wet) profile which is deeply thawed. The trends are similar in the other soil profiles available (Figure S.9.3-S.9.15). Total and selective concentrations for Fe, Mn, Al, Ca as well as total P concentration are available in Table S.9.2.

In partially unsaturated soils (i.e., when water table is below the soil surface), Fe is the only metal that accumulates at the water table level for both the total and selectively extracted concentrations (Figure 9.2a). In all soils, total and selectively extracted Fe are well correlated. The total Mn concentration is high in the litter horizon (0-5 cm layer), decreases within the organic layer and increases within the mineral soil. Selectively extracted Mn is in the high range of values within the litter and in the low range values in the remaining of the profile (except in the deepest samples where Mn accumulation is observed; Figure 9.2b). Total Al concentrations are higher in the mineral soil (below 30 cm in profile Min3) compared to the organic-rich soils (above 30 cm in profile Min3; Figure 9.2c). Selectively extracted Al concentrations are lower in organic and permafrost samples compared to mineral samples from the active layer (Figure 9.2c). Similarly, total Ca concentrations are high in mineral and low in organic layers but the opposite is observed for complexed (i.e., pyrophosphate extracted) Ca. The difference between total and complexed Ca concentrations is low in organic-rich soils but the total Ca is one order of magnitude higher than the complexed Ca in mineral soils.

In waterlogged soils where the water table depth is close to the surface, Fe accumulation at the water table depth and Mn accumulation in the litter horizons is limited (Figure 9.3a-b) or is absent (Figure S.9.3-S.9.15). Note that an accumulation of Fe and/or Mn concentration were observed in the permafrost layers of some profiles (i.e., Figure 9.2, Figure 9.3 but also in Pond 9 and Mod 3; Figure S.9.9 and S.9.14). Total and selective Al and Ca show the same trend for both dry and wet soils. In all profiles, DCB-extracted and oxalate-extracted Fe and Mn often overlap, which suggests no presence of well crystalline Fe or Mn-oxides. In addition, pyrophosphate–extracted and oxalate-extracted Fe and Mn concentrations often overlap within the organic

active layer and differ within the permafrost layer (Figure 9.2 and Figure 9.3).

Total P concentration assessed for the three soil profiles (Min1, Mod3 and Ext3) varies between 196 mg kg^{-1} and 1811 mg kg^{-1} with significantly ($p < 0.01$) higher total P concentration in active layer (mean; 925 mg kg^{-1}) compared to permafrost samples (mean; 549 mg kg^{-1}). In the active layer, total P concentration is lower in top surface litter and increases with depth. Below the organo-mineral transition, total P concentration decreases (Table S.9.2).

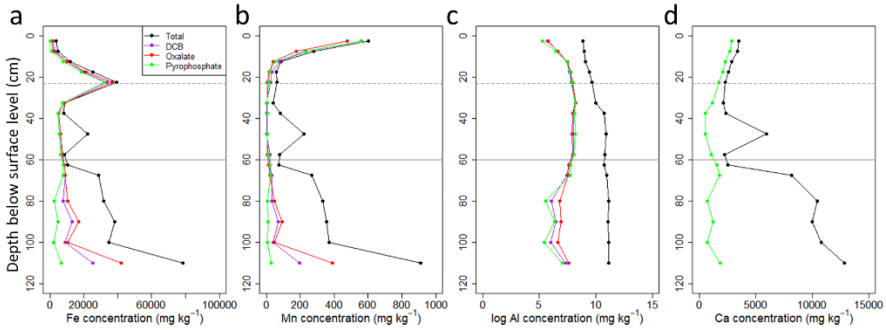

Figure 9.2: Partially unsaturated poorly thawed soil profile (Min 3) depth evolution of total metal concentrations and selectively extracted metals using dithionite-citrate-bicarbonate (DCB), ammonium oxalate (oxalate) and Na-pyrophosphate for (a) Fe, (b) Mn, (c) Al and (d) Ca. Dashed and continuous line represents the water table and permafrost table depth, respectively. A logarithmic scale is used for Al. The Ca is only represented for total and pyrophosphate concentrations. The organo-mineral transition (cut-off at 20 wt% TOC) is at 20 cm depth.

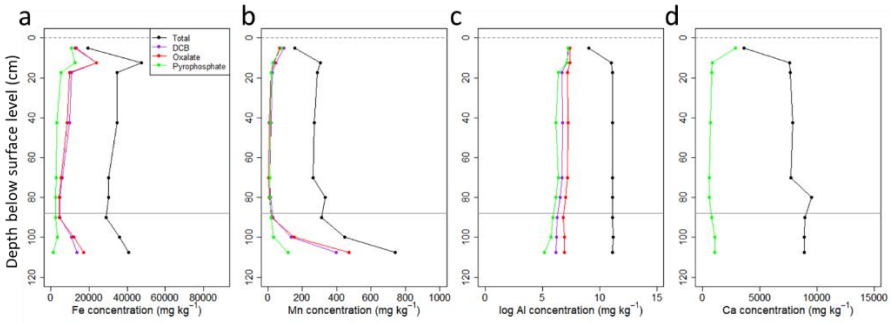

Figure 9.3: Waterlogged deeply thawed soil profile (Mod 2) depth evolution of total metal concentrations and selectively extracted metals using dithionite-citrate-bicarbonate (DCB), ammonium oxalate (oxalate) and Na-pyrophosphate for (a) Fe, (b) Mn, (c) Al and (d) Ca. Dashed and continuous line represents the water table and permafrost table depth, respectively. A logarithmic scale is used for Al. The Ca is only represented for total and pyrophosphate concentrations. The organo-mineral transition (cut-off at 20 wt% TOC) is at 10 cm depth.

9.3.2 Total carbon and organic acids in permafrost tundra soils

This section describes the total organic carbon content (TOC, in wt%), the optical density of the oxalate extract (ODOE, indicator of polyaromatic acids) and complexed (i.e., pyrophosphate extracted) C concentration in two typical soil profiles: a poorly thawed and a deeply thawed soil profile. Additional profiles with similar trends are available in Figure S.9.3-S.9.15.

Total OC content ranges between 0.7 and 49.7 wt% for all soil profiles (n = 124). The organo-mineral transition (i.e., where samples shift from TOC values higher than 20 wt% in organic horizons to TOC values lower than 20 wt% in mineral horizons) is generally found between 10 and 40 cm below surface. The organic samples present a mean of 40 wt% TOC and mineral samples of 5 wt% TOC. The ODOE and the complexed C are well correlated (r = 0.81). However, TOC content is poorly correlated with ODOE but better correlated with C_p (r = 0.36 and 0.73, respectively). The TOC content is high in the surface and decreases within the mineral horizons. Exceptionally, buried peat (organic-rich) layers were detected in some profiles (i.e., 34 wt% TOC at 110 cm in Pond 9, Figure S.9.14). The ODOE value increases at the water table level. Similarly, complexed C concentration accumulates at the water table level. This accumulation of ODOE and C_p values are sometimes found in buried frozen peat layers (Figure 9.4 and Figure S.9.5). In waterlogged soils, such accumulation in ODOE or C_p value is not found within surface soils or with significantly lower values (Figure 9.5).

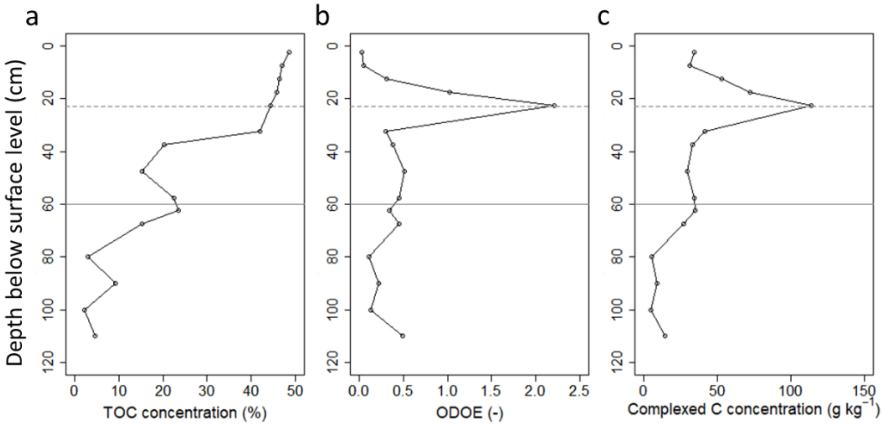

Figure 9.4: Partially unsaturated poorly thawed profile (Min 3) depth evolution of (a) total organic carbon (TOC) content (in %), (b) optical density of the oxalate extract (ODOE, adimensional) and (c) complexed carbon concentration (C_p, in g kg^{-1}). Dashed and continuous line represents the water table and permafrost table depth, respectively.

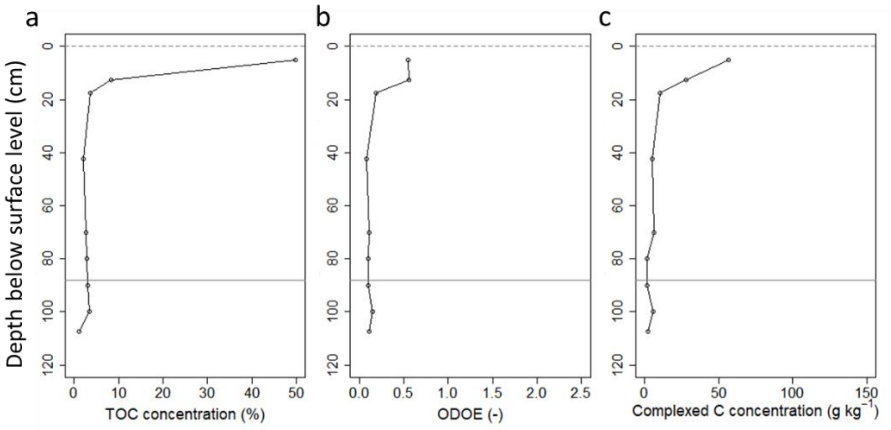

Figure 9.5: Waterlogged deeply thawed profile (Mod 2) depth evolution of (a) total organic carbon (TOC) content (%), (b) optical density of the oxalate extract (ODOE, adimensional) and (c) complexed carbon concentration (C_p, g kg^{-1}). Dashed and continuous line represents the water table and permafrost table depth, respectively.

9.3.3 Reactive metals, organic carbon stock estimations and correlations

The organic-rich samples are characterized by a low bulk density (BD = 0.052 g cm^{-3} for TOC = 50 wt%) compared to mineral samples (BD = 0.91 g cm^{-3} for TOC = 5 wt%). Therefore, element stock estimations clearly depend on the type of matrix (mineral or organic). Here, we estimated the stocks in reactive (i.e., oxalate-extracted) metals, TOC and complexed carbon. To allow comparison, stocks were estimated for each site-specific active layer depth and then normalized to 1 m depth for comparison between profiles (kg m^{-3}). The reactive Fe stock is 5-fold higher than reactive Al stock and about 3 orders of magnitude higher than reactive Mn stock (Table S.9.3). The OC stocks, total or complexed, are systematically higher than the reactive metals stocks. There is no significant statistical difference between poorly and deeply thawed profiles for all stocks calculated (p-values between 0.125 and 1).

A correlation matrix between all concentrations (total and selectively extracted metals, total and selectively extracted C) is shown in Figure S.9.16. Correlation coefficients show that the higher negative correlation lies between total Al and TOC (r = -0.99). The highest positive correlation lies between DCB- and oxalate-extracted Fe (r = 0.98) and DCB- and pyrophosphate extracted Al (r = 0.99). Overall, total concentrations of each metal are

positively correlated to their selective extracted concentrations. Total OC is positively correlated with complexed Fe, Mn, Al and Ca (r = 0.38, 0.39, 0.41 and 0.56, respectively) and with selectively extracted carbon (r = 0.36 for ODOE and r = 0.73 for C_p). All other parameters are negatively correlated or not correlated with TOC. The best correlation for ODOE is observed for selectively extracted Fe species (max correlation with Fe_p, r = 0.94) as well as complexed C (r = 0.81). Complexed C is positively correlated with selectively extracted Fe, Al and Ca but not correlated with selectively extracted Mn concentrations.

9.4 Discussion

9.4.1 Mechanisms of organic carbon stabilization within tundra soils

Complexation between OC and metals dominated by iron

The stabilization of OC with cations and mineral surfaces involves complexation (i.e., binding between polyvalent cations and functional groups of organic acids) or organo-mineral associations (i.e., adsorption of OC on metal oxide surfaces) mechanisms. Results suggest that complexation is the main mechanism (especially in active layer soils) to stabilize OC in these moist acidic tundra soils (Table S.9.4). This statement is supported by the overlap between the concentration of complexed and poorly crystalline minerals (oxalate extraction) and the concentration of complexed metals (pyrophosphate extraction) in soils (Figure 9.2 and Figure 9.3). The results demonstrate that all metal cations (Fe, Al, Mn, Ca) coordinate with the polyfunctional groups of organic acids but in various proportions. In the top of the soil profile, within the litter, organo-metallic complexes are dominated by Ca (contributing to 63% of total complexed metals) but the Ca contribution to organo-mineral complexation decreases in deeper soil layers (Figure 9.6a). Organic complexation with Mn is a minor contributor in the litter and is negligible compared to Fe, Al and Ca deeper in the soil profile. Organic complexation with Fe is dominant under unsaturated soil conditions while complexation with Al increases under waterlogged and likely long-term saturated soil conditions (Figure 9.6a and Figure S.9.17a). In most permafrost layers, Fe is the dominant polyvalent cation for complexation with OC, with the exception of some layers where Al is the dominant polyvalent cation

(Figure 9.6a). On average, all samples combined (n = 124 from 13 profiles), the molar contribution of each metal to complexation is decreasing from Fe (48.4%), Ca (25.9%), Al (24.3%) and Mn (1.4%). Note that Ca contribution is high on average because of its dominant contribution in surface soils (up to 75% in the litter). The correlation between the sum of complexed metals and complexed carbon is high (r = 0.9), and complexed C and the sum of complexed metals are both accumulating at the water table depth (Figure 9.6a-b). The positive correlation indicates a control of complexed metals on organic complexes stability (Lim et al., 2022a). This suggests that OC stabilization by complexation mechanism is dominated by different polyvalent cations depending on soil properties (e.g., OC content, soil water saturation and frozen state).

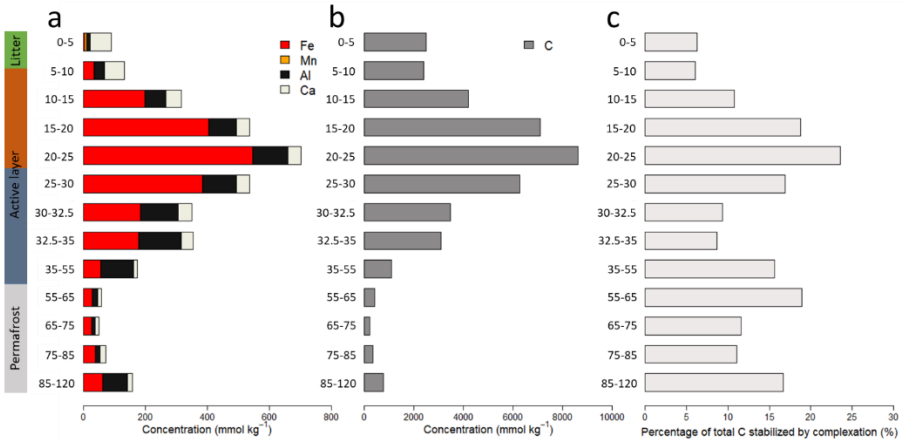

Figure 9.6: (a) Complexed metals (Fe, Mn, Al and Ca) in mmol kg^{-1} within a poorly thawed profile and (b) Complexed carbon (mmol kg^{-1}) and (c) percentage of total C stabilized by complexation in the Min 1 profile. The active layer thickness is 55 cm and water table depth is located 25 cm below surface. The stratigraphic column on the left represents permafrost (gray), saturated (blue) and unsaturated (brown) active layer and litter (green).

Influence of water saturation and pH on metals involved in complexation in tundra soils

All metals (Fe, Mn, Al and Ca) investigated in this study are likely influenced by pH conditions (von Lützow et al., 2006; Kleber et al., 2015), while some are redox sensitive (Fe and Mn). We found that Fe is the only redox-sensitive metal accumulating as Fe-OC complexes at the water table (i.e., likely acting as a redox interface with oxic conditions above and reducing conditions below

the water table; Lipson et al., 2012). However, Mn-OC complexes are not accumulating at the redox-interface but accumulate in the litter horizon (first 0-5 cm soil layer). Here, it appears that the soil conditions at the water table mainly promote the oxidation of Fe as complexed Fe rather than poorly crystalline oxide (i.e., ferrihydrite) as often stated in previous studies (Lipson et al., 2012; Riedel et al., 2013; Herndon et al., 2017; Bhattacharyya et al., 2018b). In addition, it was reported that a lower Fe/DOC ratio in soil solution promotes the formation of Fe-OC complexes instead of the precipitation of ferrihydrite (Jansen et al., 2003). The lower Fe/DOC ratio in soil solution (due to high DOC concentrations) reported in saturated zones compared to unsaturated conditions from EML tundra soils support the Fe-OC complexation at the redox interface (Hirst et al., 2022). For Mn, which is soluble in acidic soils, as observed in the surface layer of moist acidic tundra soils, cycling through vegetation (i.e., uptake and litter fall) results in Mn accumulation in surface soils year after year (Fiedler et al., 2004; Jobbágy and Jackson, 2004; Li et al., 2021) but still represent a minor fraction of organo-metallic complexes. In addition, it seems that the high Mn concentration found in plant leaves or biomass from such tundra ecosystems (especially mosses and shrubs) may accelerate accumulation within litter (Mauclet et al., 2021). Thus, the mechanism for the accumulation of Mn-OC complexes or Fe-OC complexes likely differs.

The contribution of Al complexation reaches 61% at 35-55 cm depth, located at the bottom of the active layer which is subject to long-term saturated conditions (WTD = 25 cm b.s.; Figure 9.6a). Organic carbon association with Al may be more important than Fe under long-term waterlogged conditions in soils (Inagaki et al., 2020). In addition, competition between Fe and Al cations to bind to functional groups of organic acids is very likely and mostly pH driven (Pinheiro et al., 2000; Hall and Thompson, 2022). Complexation with Al was found to be pH dependent according to several studies (Nierop et al., 2002; Jansen et al., 2003; Schwesig et al., 2003), with clearly less Al-OC complexes at pH 3.5 than at pH 4.5 (Scheel et al., 2008). The pH unit in soil pore water from this study ranges from 4-5 in top horizons and increase to 7 at the permafrost table (Hirst et al., 2022). Similarly, soil pH-H_20 from these soils ranges from 3.5 and 7.5 with lower values in organic-rich surface layers and higher values in permafrost (Mauclet et al., 2022). Our results suggest that complexation with Fe is dominant (especially under low pH and oxic conditions). However, in some persistent water saturated or permafrost layers, Al complexation increases and contributes equally or even more than Fe

complexation (Figure S.9.17a). Such layers are found deeper in the soil profile and are characterized with higher pH values than in oxic zones above the water table. The higher pH and long term saturated conditions promote Al-OC complexation in these soils. No clear effect of the soil pH is observed for Ca complexation with OC. The increase of Ca contribution to OC complexation in the litter is very likely vegetation-related (e.g., Mauclet et al., 2021; Villani et al., 2022) but the higher pH value found at the permafrost table or in permafrost (pH 7) did not resulted in a significant increase of Ca-complexation relative to Fe- or Al-complexation. Nonetheless, in deep permafrost layers, Ca-complexation sometimes exceeded Fe-complexation (Figure S.9.17b-c). Under alkaline conditions (pH above 7), Ca is expected to contribute more than Fe and Al to complexation and other binding mechanisms such as inner-sphere interactions, sorption or inclusion (Rowley et al., 2018).

Taken together, the complexed metals stabilize between 5% and 35% of TOC under dry and wet tundra soil conditions (range between 6-24% in Min1 profile; Figure 9.6c). The concentration of complexed metals is higher in active layer soils (mean = 266 mmol kg^{-1}) compared to underlying permafrost layers (173 mmol kg^{-1}). However, the percentage of TOC stabilized by complexation is significantly higher (p-value < 0.01) in permafrost soils (mean = 25.4%) than in active layer soils (16.5%) because of the higher TOC within the active layer.

Combined protection of complexation and ferrihydrite-bound OC

In addition to complexation, organo-mineral associations with poorly crystalline Fe oxides (i.e., ferrihydrite) might increase the overall potential for minerals to stabilize OC. Ferrihydrite minerals are highly effective sorbents characterized by a high specific surface area (200-800 $m^2\ g^{-1}$; Kleber et al., 2021) and are potentially present in mineral and permafrost soils which may offer additional stabilizing surfaces for OC. We assessed the overall percentage of OC out of the TOC that is stabilized by i) complexation and ii) organo-mineral associations.

For complexation, the amount of complexed carbon (C_p) has been measured and can be used as an indicator of stabilized C by complexation mechanism. The metal:C molar ratio of 0.15 (on average, Table S.9.2) for samples from this study suggests that polyfunctional groups of organic acids are saturated

with metals. Indeed, in moist acidic tundra soils, carboxylic groups (pKa around 4-5; Stevenson, 1994) are the most common polyfunctional group of organic acids and are characterized with one functional group (i.e., the part that bind to metal ions) for 10 atoms of C. This means that a metal:C molar ratio above 0.1 suggest that organic acids are considered as saturated (Boudot et al., 1989; Stevenson, 1994; Catrouillet et al., 2014). When organic acids are saturated, they are less soluble and therefore less available to microorganisms than unsaturated organic acids (Oades, 1988). In turn, the mechanism of complexation maintains OC stability and slows down its decomposition rate (Kalbitz et al., 2005; Kaiser and Guggenberger, 2007; Chen et al., 2022).

For organo-mineral associations, we were able to determine the concentration of ferrihydrite (Fe_o - Fe_p) which is the most important poorly crystalline metal oxide in moist acidic tundra soils (Herndon et al., 2017). It has been determined that up to 0.22 g OC g^{-1} Fe (as ferrihydrite) can be stabilized in soils (Wagai and Mayer, 2007). In this study, we found that most ferrihydrite-bound OC was found within permafrost. In addition, results emphasize that the proportion of ferrihydrite-bound OC is always smaller and often negligible compared to complexed C (Figure 9.7a; Table S.9.4 and Figure S.9.17d-e-f). While organo-mineral association mechanisms are involved to minor extent in active layer OC stabilization, they are of greater importance in permafrost OC stabilization which is the most vulnerable to thaw in the near future (Figure 9.7).

By adding both mechanisms (complexation and organo-mineral associations), we demonstrate that a significant percentage of total OC is potentially stabilized by these mineral OC interactions, both in permafrost and active layer soils. The soil profile (Min3) displays a range of C stabilization from 6.7% up to 48% (Figure 9.7b). The OC stored in the soil layers located at the water table level is at least 10% more mineral protected than in above or below soil layers thanks to the accumulation of organo-metallic complexes. The stabilizing potential at the water table (114 g kg^{-1} of complexed C and 1.0 g kg^{-1} of ferrihydrite-bound OC) is 25%. This is a lower proportion of stabilization than observed in permafrost soils, where the higher proportion of stabilized OC is found. One reason for this is that the TOC content in permafrost is lower than in active layer samples, so that any organo-mineral associations and cation complexation with TOC makes up a larger proportion of the stabilization.

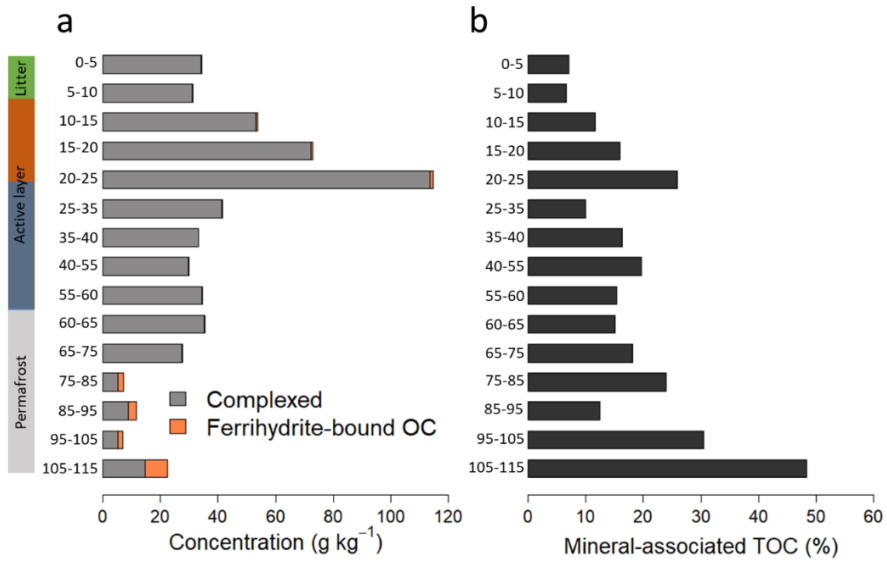

Figure 9.7: (a) Concentration of C associated with metal cations (Fe, Al, Ca and Mn) by complexation (gray) or by ferrihydrite within organo-mineral associations (Ferrihydrite-bound OC, orange) and (b) percentage of total OC stabilized by these two mineral OC interactions in the Min 3 profile. The active layer thickness is 60 cm and water table depth is located 23 cm below surface. The stratigraphic column on the left represents permafrost (gray), saturated (blue) and unsaturated (brown) active layer and litter (green).

The percentage of TOC stabilized with mineral OC interactions (as complexation and organo-mineral associations) ranges between 6% and 59% in EML tundra soils (n =124, mean 20%; Table S.9.4; Figure S.9.17h-i-j). This falls in line with previous findings in permafrost regions from the Qinghai-Tibetan Plateau where Mu et al., (2016) found that between 1% and 59% (mean 20%) of OC was associated to Fe (after DCB extraction protocol). Here because very few crystalline oxides are present or in other words that DCB-extracted and oxalate-extracted Fe are equal, these results are directly comparable with Mu et al., (2016). In this study we argue that complexation is the most abundant mechanism of mineral OC interaction in tundra soils, followed by association with ferrihydrite, and the role of well-crystalline oxides is negligible in moist acidic tundra soils. Scenarios to predict the evolution of mineral protected OC should take into account the type of binding given that these mechanisms evolve differently as a function of water saturation or frozen state.

9.4.2 Total Fe and Mn concentrations are good proxies to assess reactive minerals with a protective role for carbon

All metals in soils do not necessarily contribute to mineral protection of organic carbon. However, this study highlights that the proportion of metals that play a role in OC protection (i.e., ratio between oxalate-extracted metal and total metal concentration) is substantial. More precisely, on average, 76.5% of total Fe is present as reactive form (ferrihydrite or complexed) in organic samples (n = 57) and 29.8% in mineral samples (n = 67), and this is key for OC stabilization mechanisms. This percentage reaches 40.7% and 19.5% of reactive Mn out of total Mn in organic and mineral samples, respectively.

We pointed out in the previous section that the mineral cations and surfaces can stabilize on average 20% of TOC and up to 59% of TOC. However, data from selective extractions needed to quantify the reactive mineral pool are scarce around the permafrost regions and hinder the development of a comprehensive dataset of reactive Fe which is the pool strongly involved in OC stabilization (Kaiser and Guggenberger, 2003; Mikutta et al., 2006; Mu et al., 2016; Patzner et al., 2020; Joss et al., 2022). Nonetheless, we found a high correlation between the total Fe and reactive Fe (i.e., oxalate-extracted) and similar conclusions are drawn for Mn. For both metals, these linear regressions are a function of the matrix of the sample. In other words, mineral (TOC < 20 wt%) and organic (TOC > 20 wt%) samples follow different linear regressions with a high determination coefficient. For Fe, the organic samples have a $R^2 = 0.96$, and mineral samples an $R^2 = 0.84$ (Figure 9.8a). For Mn, organic and mineral samples have $R^2 = 0.97$ and 0.95, respectively (Figure 9.8b). No such correlations were observed for Al_o and Ca_p as function of their total concentration (not shown).

These regressions based on dry and wet tundra sites might be a useful tool to approximate the amount of reactive Fe and Mn. The reactive Fe and Mn pool is function of total Fe and Mn concentration, respectively, accounting for TOC content above or below 20%wt. In a large range of permafrost sites, the TOC is a commonly measured parameter, and the total concentrations in metals can be determined with minimal pre-treatment using the pXRF method providing a fast and reliable measurement (*Ch.1*). It follows that a wider estimation of reactive Fe and Mn minerals in permafrost soils could be achieved through total Fe and Mn concentration measurements.

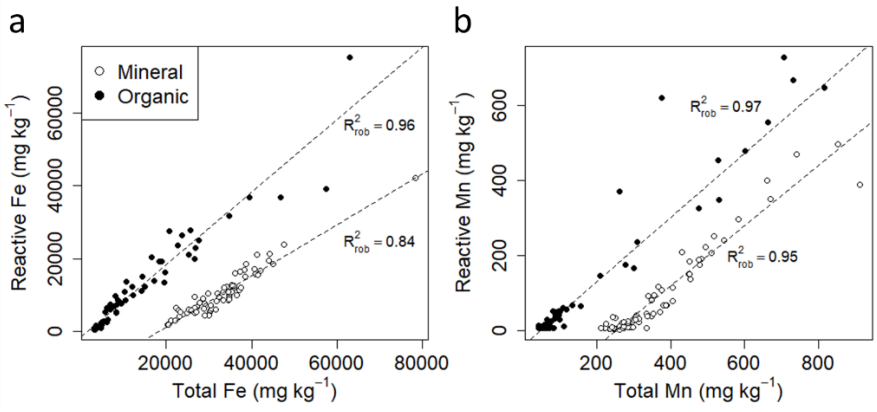

Figure 9.8: Total metal concentration (in mg kg^{-1}) as a function of reactive (i.e., oxalate extracted; in mg kg^{-1}) for (a) Fe and (b) Mn. Mineral samples (total carbon content < 20%) are open circles and organic samples (total carbon content > 20%) are full circles. Robust linear regressions are presented (dashed line, alpha = 0.95) for mineral (n = 67) and organic (n = 57) samples.

9.4.3 Mineral OC interactions hotspots

Mineral OC interactions hotspots within the active layer

In the active layer, we observe a marked Fe accumulation at the redox interface located at the water table, i.e., the border between unsaturated and saturated soil layers. This accumulation is spatially narrow: only a 5-10 cm soil layer presents higher Fe concentrations (Figure 9.9). This is consistent with previous observations showing that redox changes can occur at centimeter scale within flat tundra landscape characterized by poor drainage (Lipson et al., 2010; Liljedahl et al., 2011; Zona et al., 2011; Herndon et al., 2020b). We hypothesize that soluble Fe^{2+} from the deep active layer migrates upward with water table fluctuations and precipitates as complexed Fe under oxic conditions (Lipson et al., 2012; Colombo et al., 2014; Herndon et al., 2017). Similar immobilization of Fe has been explained by abrupt changes in redox potential under well-drained micro-highs of polygonal tundra sites (Fiedler et al., 2004). Selective extractions confirm that such Fe accumulation at the redox interface is dominated by complexed Fe forms (Sect. 9.3.1). Few to no Fe oxides were measured (negligible Fe_d-Fe_o and low Fe_o-Fe_p concentrations) in organic-rich samples from the active layer.

In this study organic compounds are classified as total OC (the sum of organic

carbon in the sample) and selectively extracted carbon (ODOE and C_p), indicators of organic acids potentially stabilized via mineral OC interactions (either as organo-mineral associations or organo-metallic complexes). It appears that the TOC content does not change at the redox interface where Fe accumulates (Figure 9.4a). However, the accumulation of reactive Fe (Figure 9.2a) is well correlated with both ODOE and C_p, which means that the accumulation of organic acids is co-located with reactive Fe accumulation (Figure 9.4b-c). This accumulation of organic acids is observed in poorly or deeply thawed soils, where a redox interface is present within the soil profile (Figure 9.6b and Figure S.9.17d-e). The accumulation of complexed Fe near the redox interface concomitant with the accumulation of complexed C (Figure 9.9b) promotes the protection of OC in a narrow band close to the water table (Figure 9.7b). However, the accumulation of organic acids disappears in waterlogged soils where no such redox interface exists (i.e., when the water table is at or above soil surface; Figure 9.5b-c and Figure S.9.17f). We demonstrate that the water table level is a transient zone for the accumulation of organic acids. It follows that fluctuations from wet to drier conditions (and in turn water table fluctuation) in permafrost soils result in the development of a hotspot where OC can be trapped.

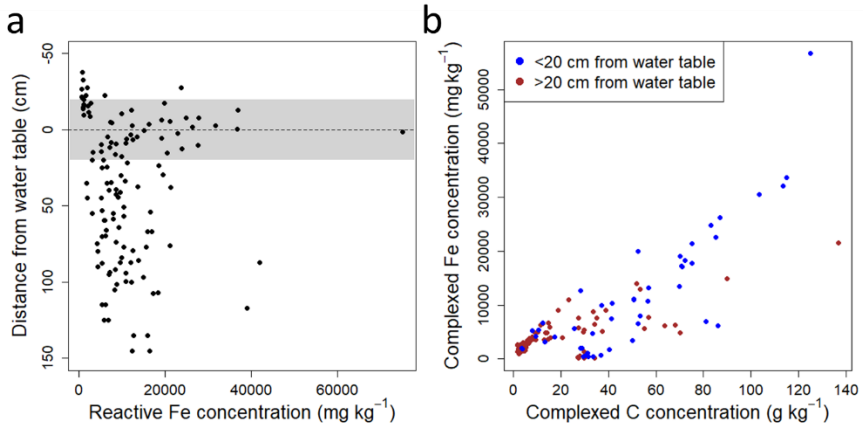

Figure 9.9: (a) Reactive Fe concentration as function of the distance of the sample to the water table. The grayish rectangle represents samples from a distance smaller than 20 cm above or below water table. (b) Complexed Fe concentration (mg kg^{-1}) as a function of complexed carbon concentration (g kg^{-1}) for samples located close to the water table (< 20 cm; blue points) and far from the water table (> 20 cm; brown points).

Hotspots of mineral OC interactions in the permafrost

Reactive Fe in permafrost is shown to be a combination of both complexed Fe (Fe_p) and poorly crystallized Fe oxides (Fe_o-Fe_p). In permafrost layers, Fe and Mn accumulation are often concomitant with TOC increase (Pond9; Figure S.9.14), with some exceptions. Similar Fe accumulation in frozen peat layers has already been described in deep sediments from the ice-rich permafrost region (*Ch.2*): in these buried peat layers, Fe accumulation was explained as a consequence of microscale oxic conditions promoted by the peat layer itself that favors Fe precipitation. Cryoturbation of surface soil could be another explanation and has been reported in this moist acidic tundra area below 1 m depth (Hutchings et al., 2019).

In organic-rich samples (TOC > 20wt%), reactive Fe is dominantly present as complexes with OC, while in mineral samples (TOC < 20wt%) reactive Fe is both in the poorly crystallized and complexed forms (Figure 9.10). Indeed, organic molecules can suppress iron oxy(hydr)oxide precipitation by complexing dissolved Fe (III) (Karlsson et al., 2008; Sundman et al., 2014; Herndon et al., 2017), and organic acids can also sorb to poorly crystalline ferrihydrite and prevent transition to more crystalline forms such as goethite or magnetite minerals (Schwertmann and Murad, 1988; Herndon et al., 2017). Ferric iron in peat soils with low pH and low Fe content (i.e., such as found in these active layer soils) tend to form mononuclear Fe(III)–OM complexes whereas in soils with high pH and high Fe content (i.e., such as found in permafrost) Fe(oxy)hydroxides are the dominant species (Karlsson et al., 2008). In addition, the poor leaching of soils can result in an overall decrease in the crystallinity of Fe oxides and promote re-crystallization as short range ordered (i.e., poorly crystallized) oxides (Winkler et al., 2018). Conversely, well drained soils showed an overall increase in oxides crystallinity, caused by the preferential removal of poorly crystallized oxides upon reduction. The high OC content, even in minerals soils, and impeded leaching of moist acidic tundra from this study, can explain the overall absence of well crystalline oxides.

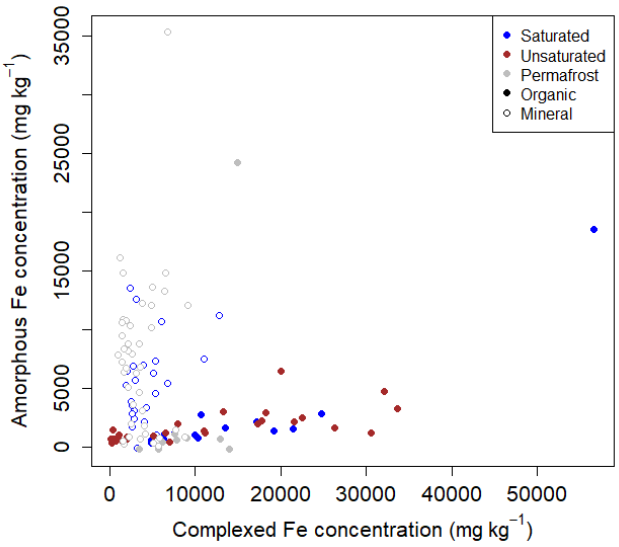

Figure 9.10: Concentration of complexed Fe as a function of Fe under poorly crystallized oxide form under different soil conditions (saturated, unsaturated, frozen). Mineral samples (total carbon content < 20%; empty circles) are separated from organic samples (total carbon content > 20%; plain circles).

Implication of redox interface on a limiting nutrient such as phosphorous

The reported Fe-OC complex accumulation at the redox interface might be of crucial importance for limiting nutrients such as phosphorous (P). Our results show an accumulation of P nearby the water table co-located with the accumulation of Fe (Figure 9.11). Some studies have described the importance of ferrihydrite as traps for P in permafrost soils (Giesler et al., 2005; Herndon et al., 2019). In addition, complexed Fe is also thought to be involved in P binding via organic-Fe-PO_4 ternary complexes (Giesler et al., 2005; Kizewski et al., 2010). Furthermore, the crystallinity of Fe-oxides has an influence on phosphate sorption and studies have highlighted that poorly crystalline Fe-oxides can better sorb phosphate than well crystalline Fe-oxides (Strauss et al., 1997; Herndon et al., 2019). Here we show that complexed Fe is well correlated with P accumulation, often at the redox interface (Figure 9.11). Uncertainties remain regarding the rate at which P would be released from that layer, i.e., lost upon leaching or gradually released allowing time for P assimilation by plant roots (Walker and Syers, 1976; Vitousek et al., 2010).

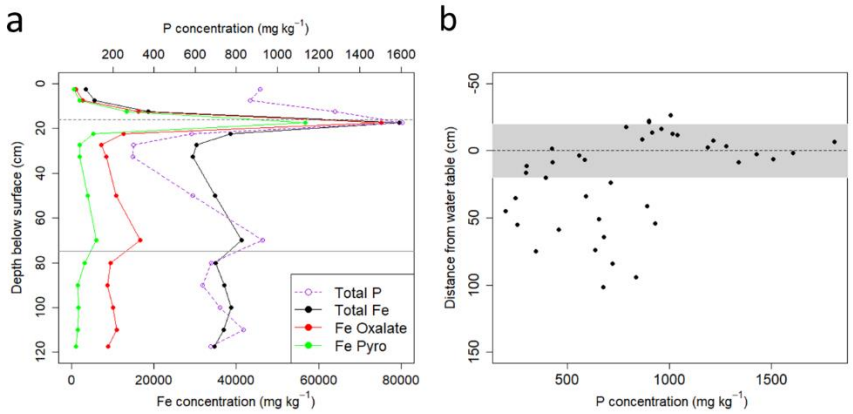

Figure 9.11: (a) Depth evolution (Mod3 soil profile) of total and selectively extracted Fe (continuous lines) and total P concentrations (dashed line) and (b) Total P concentration (n = 39, expressed in mg kg^{-1}) as function of the distance of the sample to the water table. The grayish rectangle represents samples from a distance smaller than 20 cm above or below water table.

Ongoing warming will more rapidly increase the pool of reactive Fe than the pool of OC in the active layer

Soil OC stocks at Eight Mile Lake estimated in this study are substantial and range between ~26 – 68 kg m^{-2} in the top meter (mean 47 kg m^{-2} OC; Table S.9.3). Our estimates using modelled bulk density values fall in line with results from other studies that estimated over 50 kg m^{-2} and up to 69 kg m^{-2} in Eight Mile Lake tundra soils top meter (Hicks Pries et al., 2012). It is projected that permafrost soils from Eight Mile Lake watershed will thaw deeper in the coming years (Garnello et al., 2021). Once mean annual air temperature will rise above the freezing point, the active layer thaw depth will increase by over 1 m for every 1°C rise in mean annual air temperature (Garnello et al., 2021). All of the warming scenarios (RCP 4.5, 6.0 and 8.5) projected that permafrost will disappear from the upper top 3 m by 2100 at this site (Garnello et al., 2021). If we assume that an additional 20 cm of the top permafrost layer will thaw in the coming decades, we can estimate the amount of OC and of reactive Fe that would be thawed. Our results show that the OC stored in the first 20 cm below the permafrost table (n = 13 soil profiles) represents about 11 ± 5.2 kg m^{-2} of OC (Table S.9.5). On average, this would represent an increase of 37 ± 20% OC in comparison to the actual OC stored in the active layer at maximum depth. This result is in the high range compared to another estimation that concluded that 15 kg m^{-2} of OC will be exposed if the next 60

cm below maximum active layer thaws in a similar moist acidic tundra site (with increasing active layer depth from 63 cm to 123 cm; Hutchings et al., 2019). Since the OC stock tends to decrease with depth in soils from EML watershed and that the first 20 cm likely store higher OC stock than the 40 cm layer located below (Hutchings et al., 2019), our estimation still fits within the same magnitude range. The same 20 cm of permafrost layer stores about 1.7 ± 1.0 kg m^{-2} of reactive Fe (Table S.9.5). The additional reactive Fe exposed would substantially increase (by 65% on average) the pool of reactive Fe compared to modern active layer reactive Fe stock. Therefore, with ongoing active layer deepening, the reactive Fe stock within the active layer will increase faster than the OC stock, likely increasing the potential for mineral OC interactions.

The OC stock found in permafrost layer is characterized by an increased mineral protection compared to active layer soils (p-value < 0.001; Figure 9.12). Older C as a function of depth has been reported in soils from this site (Hutchings et al., 2019). In summary, the deeper and the older the OC, the higher the proportion of mineral-protected OC (Figure S.9.18). This is also confirmed by other studies related to older OC being more protected by mineral OC interactions (Torn et al., 1997; Schmidt et al., 2011; Hemingway et al., 2019; Grant et al., 2022).

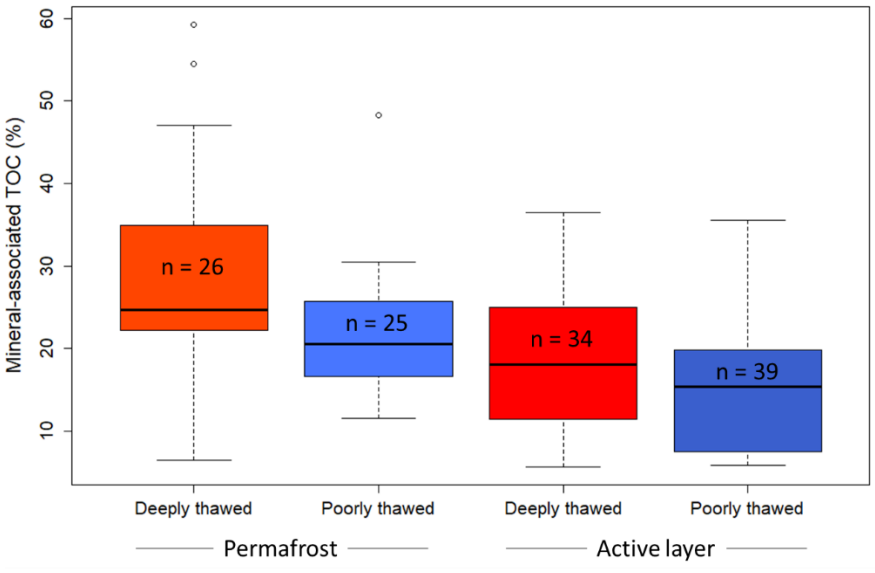

Figure 9.12: Percentage of total organic carbon (TOC) associated with metal cations (Fe, Mn, Al, Ca) via complexation and with ferrihydrite via organo-mineral-associations.

The proportion of mineral protected OC ranges between 5.7 and 36% within the active layer and between 6.5 and 59% in permafrost layers. These differences may result from soil forming processes and the duration of these processes. It is reported in this site that the OC accumulation rates are higher in the 0-66 cm layer (10.8 g OC m^{-2} a^{-1}) compared to the 66-123 cm layer (1.4 g OC m^{-2} a^{-1}; Hutchings et al., 2019). The active layer residence time (i.e., the time for which a soil layer is part of the active layer) is estimated to be 4.5 ka for the 0-66 cm and increases to 13.1 ka for the 66-123 cm layer (Hutchings et al., 2019). We argue that increased time under seasonal freeze-thaw cycle and above zero temperature led to the increase of mineral protection for deeper OC (currently found in permafrost layers). Overall, because permafrost layers about to thaw are characterized by a large pool of reactive Fe compared to the pool of OC and a high proportion of the OC protected via mineral OC interactions, we argue that active layer deepening will provide an additional pool of mineral-protected stabilized organic carbon.

9.5 Conclusions

This study offers a comprehensive assessment on mineral organic carbon interactions involving Fe, Al, Mn and Ca in a typical moist acidic tundra permafrost from the Eight Mile Lake gradient site, near Healy, AK, USA. Thirteen cores (up to 150 cm depth) were collected in late summer 2019, at time of maximum thaw in locations with varying active layer depth (from 45 to 109 cm below surface) and varying water table depth (from 15 cm above surface to 45 cm below surface). Because mineral organic carbon (OC) interactions involve redox- and pH-sensitive elements (Fe, Mn, Al and Ca), our study assessed the contribution of metals and their association to organic carbon within contrasted redox and pH soil conditions. From this study we conclude that:

(i) The combination of organo-mineral association (association between ferrihydrite and OC) and organo-metallic complexes (associations between organic acids and Fe, Mn, Al, Ca polyvalent cations) contributed to stabilize between 6% and 59% of total OC in Eight Mile Lake tundra soils (mean 20%). In soil profiles, we found a higher percentage of total OC stabilized in permafrost layers (mean 25.4%) compared to active layers (mean 16.5%).

(ii) Assessing reactive phases towards OC can be done for Fe using total Fe concentration to estimate reactive Fe i.e., sum of poorly crystalized Fe oxides and complexed Fe (with a $R^2 = 0.96$ for organic-rich samples$_{> 20wt\% OC}$) and $R^2 = 0.84$ for mineral samples$_{< 20wt\% OC}$), and for Mn using total Mn to estimate reactive Mn (with a $R^2 = 0.97$ for organic samples and $R^2 = 0.95$ for mineral samples).

(iii) The OC is protected as organo-metallic complexes in the active layer and permafrost, and organo-mineral associations contribute mainly in permafrost layers. In organo-metallic complexes, Fe cations prevails relative to other metals (Al, Ca, Mn) except in litter samples. Top surface OC (0-5 cm) is mostly stabilized by Ca cations with some contribution from Mn cations. In active layers soils, complexation is dominated by Fe but Al contribution increases under persistent waterlogged conditions.

(iv) The higher pool of mineral-protected OC in the active layer is found at the water table level, i.e., a redox interface where organo-metallic complexes dominated by Fe cations accumulate. In permafrost soil layers, the TOC content is lower than in the active layer but a higher proportion is mineral-protected relative to active layer soils.

(v) A permafrost thaw 20 cm deeper in the coming decades in these tundra soils would result in a 37% increase of the OC stock exposed to microbial degradation and a 65% increase in reactive Fe exposed. The permafrost layer expected to thaw in the next decades contains a large proportion of mineral-protected OC. However, different OC protection mechanisms between the active layer (i.e., complexation) and the permafrost (i.e., complexation and ferrihydrite-bound OC) suggest a change of mineral OC interactions upon thawing.

10. Chapter 5: Strontium isotopes trace the dissolution and precipitation of mineral organic carbon interactions in thawing permafrost

This chapter is a modified version of a research paper submitted in Geoderma special issue: "Permafrost affected soils and climate change - from soil development to carbon storage and biological functioning".

Monhonval, A., Hirst, C., Strauss, J., Schuur, E.A.G., Opfergelt, S., 2022. Strontium isotopes trace the dissolution and precipitation of mineral organic carbon interactions in thawing permafrost, Geoderma (submitted).

Abstract

Interactions between minerals and organic carbon (OC) in soils are key to stabilize carbon and mitigate greenhouse gas emissions upon permafrost thaw. However, changes in soil water pathways upon permafrost thaw are likely to affect the stability of mineral OC interactions by inducing processes of dissolution and precipitation of these interactions, but the effects of these changes remain poorly quantified. This study aims to assess under what conditions mineral OC interactions are affected by dissolution and precipitation upon permafrost thaw. We hypothesize that a change in the radiogenic strontium (Sr) isotopic ratio ($^{87}Sr/^{86}Sr$) involved in mineral OC interactions upon changing soil conditions imply a destabilization of the mineral OC interaction. We measured the $^{87}Sr/^{86}Sr$ ratio of selective extractions on soils or sediments targeting the Sr associated to mineral OC interactions in soils vulnerable to gradual thaw (Eight Mile Lake, AK, USA) and in deposits vulnerable to abrupt thaw (Duvanny Yar, Russia).

First, we found a difference in the $^{87}Sr/^{86}Sr$ ratio between water saturated layers with a higher proportion of mineral OC interactions relative and the surrounding layers which supports the preservation of a Sr "stable" pool in these interactions. We estimated that a portion of these interactions have remained undissociated since their formation (between 4% and 64% by Sr isotope mass balance). Second we found no difference in $^{87}Sr/^{86}Sr$ ratio between layers accumulating Fe oxides at redox interfaces regularly affected by water table changes (or upon thermokarst processes) relative to surrounding layers which supports the dominance of a Sr "labile" pool

inherited from processes of dissolution and precipitation of the mineral OC interactions. Third, our estimations based on a Sr isotope mass balance support that, as a consequence of permafrost thaw, a larger proportion of Sr from primary mineral weathering (> 80%) controls the Sr in mineral OC interactions in the saturated zone of deeply thawed soils relative to poorly thawed soils (~50%). In conclusion, we found that the radiogenic Sr isotope method, applied for the first time in this context, is promising to trace dissolution-precipitation processes of mineral OC interaction in thawing permafrost.

10.1 Introduction

Mineral organic carbon interactions provide a significant protective role for organic carbon (OC) in soils and sediments (von Lützow et al., 2006; Keil and Mayer, 2014; Kleber et al., 2015, 2021). Mineral-protected OC is known to be less available for microorganisms and is therefore less vulnerable to microbial degradation. In permafrost environments which store between 1,460 – 1,600 Pg C, twice the carbon stock currently found in the atmosphere, the OC enclosed in unfrozen and frozen layers below ground is highly sensitive to climate warming (Schuur et al., 2015; van Huissteden, 2020; Strauss et al., 2021a). Warming in northern latitudes is almost three times faster than the global warming and permafrost is currently thawing at unprecedented rate (IPCC, 2019). The interactions between mineral surfaces or cations and OC act as a protective shield and reduce the portion of OC emitted as greenhouse gases in the atmosphere upon permafrost thaw (e.g., Mu et al., 2016; Herndon et al., 2017; Hemingway et al., 2019; Patzner et al., 2020). Mineral OC interactions include aggregation, organo-mineral associations (involving Fe, Mn, Al oxides, clay minerals or carbonates) and organo-metallic complexes between polyvalent cations (e.g., Fe^{3+}, Al^{3+}, Ca^{2+}) and functional groups of organic acids. However, Fe oxides and organo-metallic complexes are known to be highly vulnerable with permafrost thaw due to changing soil conditions (Schwertmann, 1991; Colombo et al., 2014; Kleber et al., 2015; Winkler et al., 2018; Patzner et al., 2020). Permafrost thawing processes such as deepening of the active layer, thermokarst lake formation and drainage are responsible for changing moisture and hydrological pathways in permafrost regions (Grosse et al., 2013; Vonk et al., 2019; Rodenhizer et al., 2020) and likely influence mineral OC interactions (Opfergelt, 2020). Most permafrost-affected areas suffer from periodic or persistent anoxia due to soil water saturation (Street et al., 2016) which promotes the dissolution of Fe oxides and influences the formation of organo-metallic complexes (Schwertmann, 1991; Stumm and Sulzberger, 1992; Colombo et al., 2014; Kleber et al., 2015). The processes of dissolution and precipitation of such mineral OC interactions is a major concern to better predict future greenhouse gas emissions upon gradual (i.e., deepening of the active layer) or abrupt (i.e., thermokarst processes) thaw in permafrost regions. These processes of dissolution and precipitation of mineral OC interactions may result from multiple freeze-thaw cycles inherited from changing soil conditions extending back thousands of years depending on sediment deposition processes and permafrost thawing history.

To determine what drives the preservation of mineral OC interactions or under what conditions mineral OC interactions are altered by dissolution and precipitation upon permafrost thaw is a challenge. In mineral OC interactions, calcium (Ca) can act (i) as a cation bridge adsorbed to Fe oxide surfaces or be occluded within Fe oxides structure and (ii) as a polyvalent metal cation participating in the formation of organo-metallic complexes (von Lützow et al., 2006; Kleber et al., 2015; Rowley et al., 2018). Strontium (Sr) is an alkaline earth metal of similar ionic size and charge as Ca and is established as an analogue for Ca (Faure and Powell, 1972; Capo et al., 1998). Because of their similar properties, Sr often substitutes to Ca, and can therefore be part of mineral OC interactions, i.e., occluded or adsorbed onto Fe oxides or complexed with organic acids (Andersson et al., 1994; Wortberg et al., 2017). The radiogenic Sr isotope ratio ($^{87}Sr/^{86}Sr$) is commonly used as a source tracer in Earth surface processes (e.g., Miller et al., 1993; Capo et al., 1998; Banner, 2004). The $^{87}Sr/^{86}Sr$ ratio of each mineral is different and the bulk soil $^{87}Sr/^{86}Sr$ ratio is the weighted average of all its constituent minerals. A higher $^{87}Sr/^{86}Sr$ ratio enriched in the radiogenic isotope (^{87}Sr) is referred to as more radiogenic whereas a lower $^{87}Sr/^{86}Sr$ ratio is less radiogenic. Targeting the Sr within the mineral OC interactions requires the selective extraction of Fe oxides and organo-metallic complexes in soils. This can be achieved using the dithionite-citrate-bicarbonate (DCB) extraction method commonly used to selectively extracts Fe involved in Fe oxides (Mehra and Jackson, 1960) but which also extracts untargeted metals adsorbed to or occluded within Fe oxides or participating in organo-metallic complexes (Rennert, 2019).

In the context of permafrost thaw, we hypothesize that Sr within mineral OC interactions should display a "stable" pool that has not been submitted to dissolution processes since the formation of the mineral OC interaction. The Sr in the "stable" pool should reflect the original Sr source from the time of the formation of the interaction. Conversely, we hypothesize the presence of a Sr "labile" pool within mineral OC interactions that experienced ongoing dissolution-precipitation of these interactions and reflects the ultimate source of Sr. Since Sr is a highly soluble element (Gupta et al., 2018), the dissociation between Sr and the mineral OC interactions should release the original Sr into the soil solution. Upon subsequent precipitation of the mineral OC interactions, Sr from the new soil environment with a potentially different Sr isotopic signature may co-precipitate with mineral OC interactions (Andersson et al., 1994). If this hypothesis is true, a similar Sr isotopic signature in mineral OC interactions before and after changing soil conditions

(i.e., gradual thaw, thermokarst lake formation) would indicate that mineral OC interaction bonds with Sr are stable (no dissolution) or that the ultimate Sr from the new soil environment is characterized with similar Sr isotopic signature as the original Sr (Figure 10.1). However, a change in the isotopic signature of Sr within mineral OC interactions would suggest a dissolution step followed by the adsorption of ultimate Sr from an external source with a contrasting Sr isotopic signature (Figure 10.1). We consider that OC will be released together with Sr upon Fe oxide dissolution or organo-metallic complexes dissociation (von Lützow et al., 2006; Wortberg et al., 2017; Patzner et al., 2020). Hence, we use Sr as a witness of OC stabilization upon thawing permafrost and consequent changing environment conditions.

Upon gradual permafrost thaw, minerals (i.e., Sr-bearing minerals) are released from permafrost layers and can participate to biogeochemical processes in the active layer where they may interact with Fe oxide precipitation and organo-metallic complexes formation (Kokelj et al., 2013; Reyes and Lougheed, 2015). Lateral transport in the saturated active layer may also provide Sr from an external source with a distinct isotopic signature that differs from the Sr isotopic signature found in permafrost (Keller et al., 2007, 2010; Hirst et al., 2022). Upon abrupt thaw, thermokarst lake formation and drainage during the Holocene can provide Sr from external source with distinct isotopic signature compared to Yedoma deposits formed during the late Pleistocene (Biskaborn et al., 2013; Grosse et al., 2013). Therefore, both gradual and abrupt thaw can potentially modify the ultimate Sr isotopic signature which allows to trace the stability of mineral OC interactions in thawing permafrost.

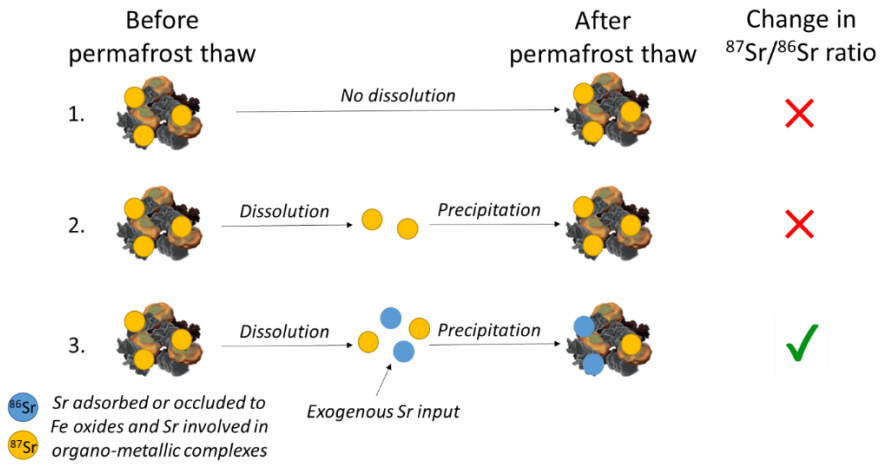

Figure 10.1: Hypothesis of stability of mineral organic carbon (OC) interactions upon permafrost thaw and changing soil conditions measuring $^{87}Sr/^{86}Sr$ ratio of the Sr occluded or adsorbed onto iron oxides and the Sr complexed with organic acids. In scenario 1, there is no dissolution of the mineral OC interactions and no change in $^{87}Sr/^{86}Sr$ ratio ("stable" pool). In scenario 2, there is a first dissolution step of the mineral OC interactions and subsequent precipitation with Sr of similar isotopic signature as the original Sr ("labile" pool). In scenario 3, there is a first dissolution step of the mineral OC interactions and subsequent precipitation with ultimate Sr of different isotopic signature than the original Sr ("labile" pool).

This study aims to open a new way to assess the stability of mineral OC interactions upon permafrost thaw, a key factor in the fate of OC which represents a source for greenhouse gas emissions. In detail we aim to test a method using radiogenic Sr isotopes measured from DCB extracts to trace dissolution-precipitation of mineral OC interactions upon thawing permafrost. We tested this idea (i) upon gradual thaw in six soil profiles from a moist acidic tundra of Eight Mile Lake site with varying active layer and water table depth and (ii) upon abrupt thaw of the ice-rich permafrost (i.e., Yedoma) region of Duvanny Yar in two Yedoma deposits that never thawed since deposition during late Pleistocene and in two previously thawed profiles (i.e., one Alas deposits and one lake sediments profile).

10.2 Material and methods

Two sites were investigated in this study (Figure 10.2). Both sites were selected as they showed iron redistribution upon permafrost thaw for Eight

Mile Lake (*Ch.4*) and for Duvanny Yar study sites (*Ch.2*). While the radiogenic Sr isotope is a commonly used tracer, its use on selective extractions targeting Fe oxides and organo-metallic complexes is a first, to the best of our knowledge.

10.2.1 Permafrost landscapes from Eight Mile Lake, Alaska

The first site is a moist acidic tundra site located in Eight Mile Lake watershed, Healy, AK, USA (63.87°N, 149.25°W). This site is characterized by gully formation and local subsidence. The gradient site from Eight Mile Lake is characterized as a moist acidic tundra, dominated by the tussock forming sedge (*Eriophorum vaginatum*), various small shrubs and *Sphagnum* spp. mosses (Schuur et al., 2007). The higher elevations have gravelly soils associated with glacial till and are covered with a thin aeolian silt cap. The lower slopes and valleys have a thick peat accumulation (up to 50 cm) over fine-grained soils associated with colluvial deposits (Osterkamp et al., 2009). The modern active layer at this site (0-66 cm) spans a range from 0 - 4.6 ka (i.e., thousand years) and the underlying permafrost layer (66-123 cm) spans a range from 4.6 to 15 ka (Hutchings et al., 2019). Permafrost in this region is vulnerable to gradual thaw, deepening of the active layer, subsidence and water table level rise (Osterkamp et al., 2009; Plaza et al., 2019; Rodenhizer et al., 2020). In addition, *Ch.4* highlighted the redistribution and accumulation of mineral OC interactions at the water table level. These characteristics make this site an ideal candidate to test potential dissolution-precipitation processes of mineral OC interactions with permafrost gradual thaw. Six profiles with varying active layer depth and water table depth were collected (Ext1, Mod1, Min1, Ext3, Mod3 and Mod2; Figure 10.2a-b). Cores were sampled in late-summer 2019 from six profiles (n = 72), at time of deepest active layer thaw, using chisel and knife in the upper part of the profile. Under water table or when chisel and knife was not applicable, the deepest soil layers were collected using a stainless-steel pipe hammered down into active layer and permafrost. The length cored varied with the presence of rocks in the deeper permafrost. Permafrost was reached for every core and up to a maximum depth of 120 cm. The active layer thickness varied with microtopography and ranges from 48 cm to 88 cm. These soil profiles have been characterized for their total organic carbon (TOC) content (*Ch.4*; Figure S.10.1).

10.2.2 Permafrost landscapes from Duvanny Yar, Yakutia

The second site is an ice-rich permafrost site from Duvanny Yar in the Kolyma Lowland, Siberia, Russia (68.63°N, 159.10°E; located in the Yedoma domain as defined by Strauss et al. (2017)). This site is affected by thermokarst lake formation and drainage. The Duvanny Yar site is considered to be a key site for late Pleistocene history and have a long history of study since 1950's (Popov, 1953; Tomirdiaro and Chernen'kiy, 1987; Rozenbaum and Shpolyanskaya, 1998; Zanina et al., 2011; Strauss et al., 2012; Murton et al., 2015). Duvanny Yar silty sediments from the Yedoma profiles are characterized as polygenetic and loess-related deposits (Strauss et al., 2012; Murton et al., 2015; Shmelev et al., 2021). The mineralogy of this deposit is characterized by the presence of pyroxene, hornblende, pyrope, magnetite, goethite, quartz, feldspar, calcite, illite, and chlorite (Shmelev et al., 2021). Samples were collected from an approximately 12-km-long outcrop, which consists of Yedoma hills as high as 50 m above river level (a.r.l.) dissected by deep thermo-erosional valleys and thermokarst depressions exposed along the Kolyma river (Figure 10.2c-d). This late Pleistocene syngenetic permafrost is vulnerable to abrupt thaw (i.e., thermokarst lake formation and drainage) and is also well suited to test the dissolution-precipitation dynamic of mineral OC interactions. Duvanny Yar Yedoma deposits span a range from >45 ka to 9 ka for uppermost Holocene sediments (Strauss, 2010). A total of 46 samples from two Yedoma profiles (DY-01 and DY-05) and two previously thawed profiles (one lake sediment profile (DY-02) and one Alas profile (DY-04)) were collected using hand-held drill or hammer after cleaning the first centimeters of the outcrop. These samples for which the TOC content is available (Figure S.10.2) represent a subset of the full profiles from this site studied in *Ch.2* (Figure S.10.3).

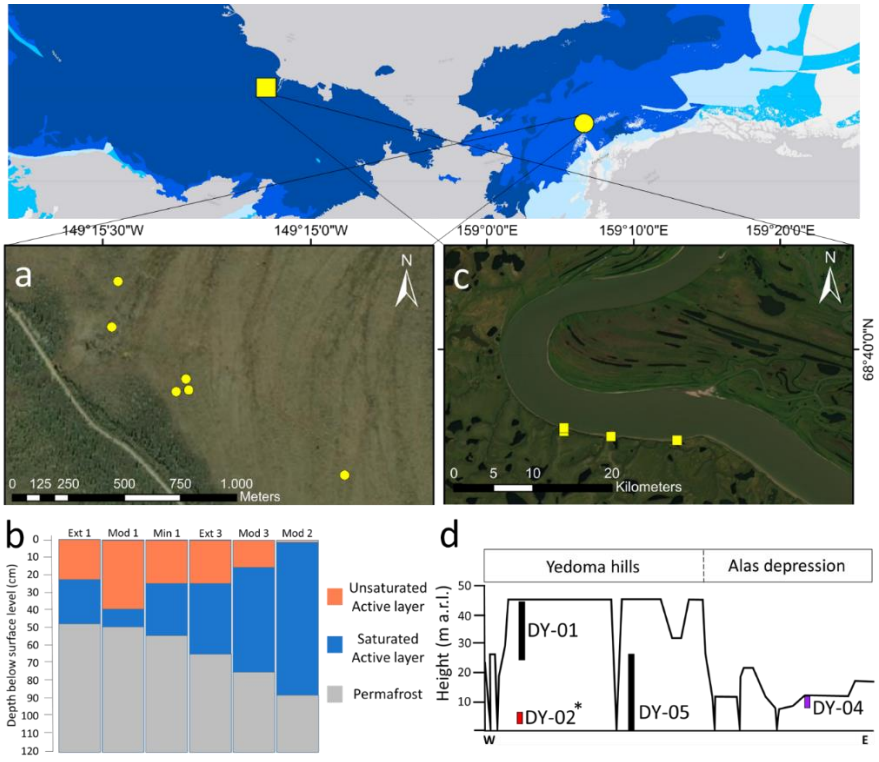

Figure 10.2: a) Eight Mile Lake location near Healy, AK, USA and the six soil profiles collected (yellow points); (b) Schematic of the six profiles investigated in this study. The unsaturated and saturated active layer is represented (orange and blue, respectively) and the permafrost is represented in gray. (c) Duvanny Yar location in the Kolyma Lowland, Siberia, Russia and the four sediment profiles collected (yellow squares); (d) Schematic of the Duvanny Yar section with position (height above river level; m. a.r.l.) of the studied profiles (modified from Strauss (2010)). Yedoma deposits are represented in black (DY-01 and DY-05), Alas deposits in purple (DY-04) and Lake sediments in red (DY-02). *DY-02 is a separate profile underlying the Yedoma deposits sequence. Maps were built with ArcGis software; source: Esri, DigitalGlobe, GeoEye, USDA, USGA, IGN and the GIS User community.

10.2.3 Selective Fe and Sr extraction

The concentrations of Fe and Sr selectively extracted by dithionite-citrate-bicarbonate (DCB; Mehra and Jackson, 1960) were determined on all samples from Eight Mile Lake study site (n = 72) and Duvanny Yar site (n = 46). The concentrations in DCB-extracted Fe are available from *Ch.4* for the Eight Mile Lake site (n = 72), and measured here for the Duvanny Yar site (n = 46). The concentrations in DCB-extracted Sr were measured in this study for both sites.

Briefly, 0.75 g of grind soil or sediment sample was mixed with 30 ml of citrate solution (sodium citrate $Na_3C_6H_5O_7$ $2H_2O$) 0.3 M buffered by sodium bicarbonate $NaHCO_3$ in centrifugal tubes. The dithionite (three to five times 0.75 g) was added to the tubes placed in a hot bath at 85°C while stirring. The DCB-extract was filtered (Whatman 41 filter, 20 µm retention size) and the Fe and Sr concentrations were measured by inductively coupled plasma optical emission spectrometry (ICP-OES, iCAP 6500 Thermo Fisher Scientific). The precision (coefficient of variation) of the ICP-OES measurement on permafrost samples is 0.5% and 1% for Fe and Sr, respectively *(Ch.1)* and limit of detection was never reached (0.004 mg L^{-1} and 0.0001 mg L^{-1} for Fe and Sr, respectively). The concentration of DCB-extracted Fe and Sr is expressed in reference to the soil or sediment dry weight (105°C) and will be referred as Fe_d and Sr_d (in mg kg^{-1}) in the following.

The proportion of DCB-extracted Sr over the total Sr concentration (Sr_d/Sr_{total}) was determined by measuring the total Sr concentrations in the bulk samples (Eight Mile Lake site, n = 72; Duvanny Yar site, n = 46) by portable X-ray fluorescence (pXRF) device and corrected using a regression with measurements by ICP-OES after alkaline fusion following the method described in *Ch.1* (Figure 10.3; $R^2 = 0.99$).

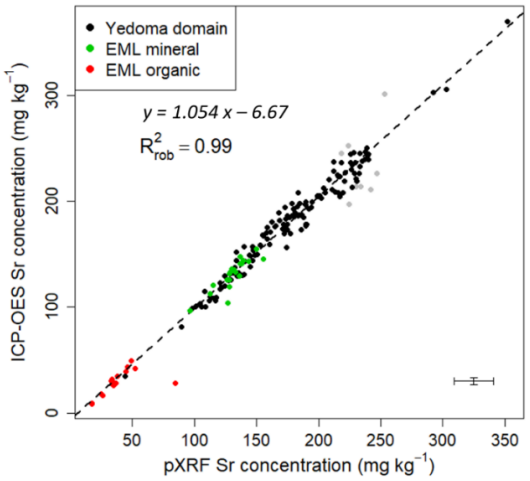

Figure 10.3: Total Sr concentrations (mg kg^{-1}) measured by the inductively coupled plasma optical-emission spectrometry (ICP-OES) method as a function of those measured by the portable X-ray fluorescence (pXRF) method on mineral and organic samples from Eight Mile Lake acidic tundra (green points; n = 21 and red points n = 18, respectively). Samples from the Yedoma domain deposits (black points; n = 144, *Ch.1*) are included. The robust linear regression for mineral and organic samples is presented (dashed black line; alpha= 0.95). Gray points are excluded from the robust linear regression. Mineral and organic samples are divided with 20 wt% organic carbon cutoff (Hicks Pries et al., 2012). Equation from linear regressions is provided with the robust determination coefficient. Errors bars (± 2σ) are taken from *Ch.1*.

10.2.4 Purification of Sr and radiogenic Sr isotope measurements

The radiogenic Sr isotopic ratio of the DCB extracts (Sect. 10.2.3) has been measured for all samples from Eight Mile Lake study site (n = 72) and Duvanny Yar site (n = 46). A volume of DCB extract corresponding to 500 ng of Sr was evaporated in Teflon vials on hot plate (50°C). The sample was then mixed with H_2O_2 and concentrated HNO_3 to remove organics: the sample reacted in sealed Teflon vials on a hot plate (180°C) and was then evaporated to dryness. This step was repeated 2 to 3 times. To purify Sr from the sample, the aliquot was dissolved in 3M HNO_3 and loaded on a Biorad microspin column containing 500 µl of Sr specific resin (50-100 µm Triskem), and eluted in several stages with HNO_3 (Aciego et al., 2009). The sample containing the purified Sr was evaporated to dryness and dissolved in HNO_3 2% for Sr isotope measurements. The total procedural Sr blank was < 0.1% of the total Sr analyzed.

Strontium isotope measurements were carried out by MC-ICP-MS (Neptune Plus TM High Resolution Multicollector ICP-MS, Thermo Fisher Scientific, Earth and Life Institute, UCLouvain, Belgium) in wet plasma mode using a PerFluoroAlkoxy (PFA) nebulizer of 100 µl min^{-1} uptake rate. Typical sensitivity for 100 ppb Sr was about 7V. Each sample was measured with three repetitions and the results are expressed as $^{87}Sr/^{86}Sr$ ratio (average ± 2SD on the three repetitions). The long term precision and accuracy was assessed using an in-house standard Sr ICP (0.708598 ± 0.000115; 2SD, n =75) and the reference material NIST SRM987 (0.710303 ± 0.000033; 2SD, n = 20), consistent with certified value for this reference material (0.71034 ± 0.00026; Standard Reference Material® 987, Strontium Carbonate, Isotopic Standard). The NIST SRM987 reference material was also used to validate that no interference was associated to the DCB matrix. The obtained value for the $^{87}Sr/^{86}Sr$ ratio after mixing the NIST SRM987 with DCB and column purification was 0.710313 ± 0.000073 (2SD, n = 27), also consistent with the certified value (0.71034 ± 0.00026).

10.3 Results

10.3.1 The Fe and Sr concentrations and radiogenic Sr ratio in DCB-extracts from soil profiles at Eight Mile Lake site

The concentration in DCB-extracted Fe in Eight Mile Lake soils ranges between 1.02 and 75.0 g kg^{-1} with the highest recorded values at the water table, as described in details in *Ch.4* (Figure 10.4). About 51% of total Sr is DCB-extractable (Sr_d/Sr_{total}) in organic samples and therefore half of the total Sr is found within mineral OC interactions. This percentage substantially decreases to 6.8% in mineral samples (Figure S.10.4; considering Figure S.10.1 to differentiate organic (TOC > 20%) from mineral samples (TOC < 20%; Hicks Pries et al. (2012)). Note that the concentration of Sr_d is lower in deeper soil and that a significant amount of Sr from deeper soil layers would be needed to slightly change the Sr isotopic ratio in DCB-extracted solution from surface soils.

In the moist acidic tundra site of Eight Mile Lake, the $^{87}Sr/^{86}Sr$ ratio ranges between 0.708309 and 0.710044 (Figure 10.4). Samples from the organic-rich layer are significantly more radiogenic than samples from mineral layers ($p < 0.001$; Figure S.10.5a). The maximum $^{87}Sr/^{86}Sr$ ratio is often found within the

first 15 cm depth of tundra soils. In addition, a significant decrease in the radiogenic Sr ratio is observed between active layer and permafrost ($p < 0.001$). Within the permafrost, the radiogenic ratio is constant with depth in profiles Min 1 and Mod 1 but increases with depth in all other profiles (Figure 10.4c-f). Despite the increase in permafrost layers, the radiogenic Sr isotopic signature is the highest in top surface horizons which allows us to decipher two isotopic signatures, one from the unsaturated layer (0.709590) and one from deeper frozen layers (0.708739). The $^{87}Sr/^{86}Sr$ ratio found in top of the waterlogged profile with deepest thaw (0.709288; 0-10 cm) is lower compared to top surface layer from adjacent profile (Mod1 and Mod3; Figure 10.4). Overall, a positive correlation is found between $^{87}Sr/^{86}Sr$ ratio and the TOC ($r = 0.81$; Pearson method; Figure S.10.5a). All data are available in Table S.10.1.

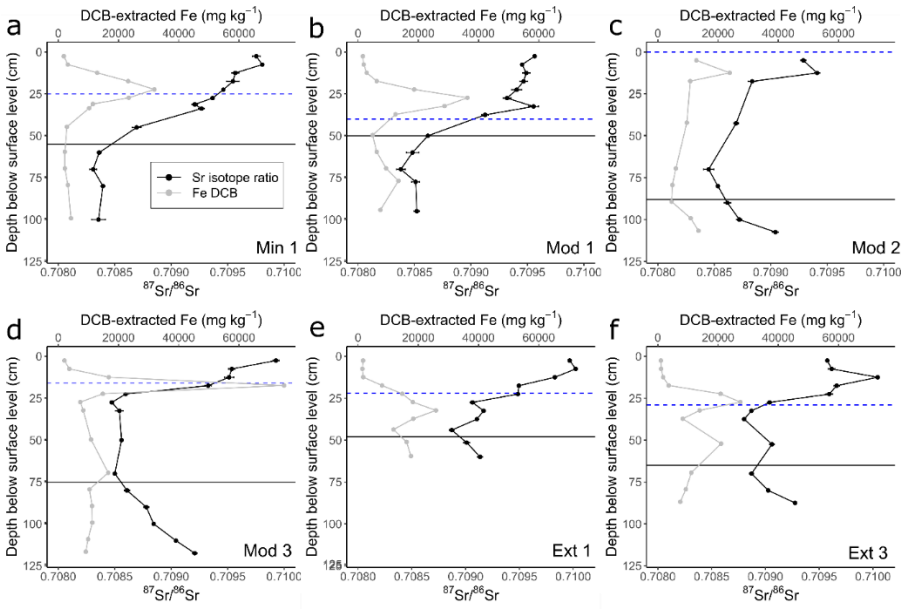

Figure 10.4: Radiogenic Sr isotopic ratio from DCB extraction ($^{87}Sr/^{86}Sr$; black points, bottom x-axis) and concentration in dithionite-citrate-bicarbonate (DCB) extracted Fe (in mg kg^{-1}; gray points, top x-axis) for Eight Mile Lake soil profiles Min 1 (a), Mod 1 (b), Mod 2 (c), Mod 3 (d), Ext 1 (e) and Ext 3 (f). Errors bars (±2SD) are represented for radiogenic Sr isotopic ratio. The water table (dashed blue line) and permafrost table (black line) are represented for each plot. The DCB-extracted Fe data are taken from *Ch.4*.

10.3.2 The Fe and Sr concentrations and radiogenic Sr ratio in DCB-extracts from sediment profiles at Duvanny Yar site

The concentration in DCB-extracted Fe in Duvanny Yar sediments ranges between 7.76 and 52.8 g kg^{-1} (Figure 10.5). The highest values are found as a narrow accumulation (less than 50 cm thick; Figure 10.5) in the thawed and refrozen deposits (DY-04 and DY-02 profiles). About 10% of total Sr is DCB-extractable with a range of 5 to 26% and the maximum found in an organic-rich layer of the Yedoma deposits (DY-01, 29 m a.r.l.; Figure S.10.6).

Both Yedoma deposit profiles span an identical range of DCB extracted $^{87}Sr/^{86}Sr$ ratio (0.709175 ± 0.000426 and 0.708980 ± 0.000221; mean ± 2SD for DY-01 and DY-05, respectively; Figure 10.5). Similarly, the $^{87}Sr/^{86}Sr$ ratio of Alas deposits and Lake sediment profile falls within similar range as the Yedoma profiles. The Alas profile (DY-04) shows a $^{87}Sr/^{86}Sr$ ratio of 0.708988 ± 0.000206 and the lake sediment profile (DY-02) a $^{87}Sr/^{86}Sr$ ratio of 0.709099 ± 0.000485. The highest Sr isotopic ratios are found in peat layers from the Yedoma (DY-01) and the lake sediments profile (DY-02; Figure 10.5; Figure S.10.5a). All data are available in Table S.10.1.

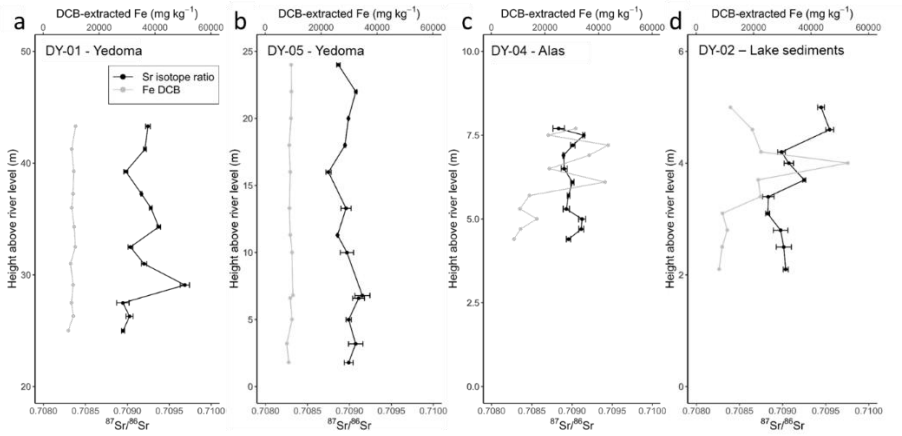

Figure 10.5: Radiogenic Sr isotopic ratio from dithionite-citrate-bicarbonate (DCB) extraction ($^{87}Sr/^{86}Sr$; black points, bottom x-axis) and concentration in dithionite-citrate-bicarbonate (DCB) extracted Fe (in mg kg^{-1}; gray points, top x-axis) for Duvanny Yar sediment profiles DY-01 (a), DY-05 (b), DY-04 (c) and DY-02 (d). The two Yedoma profiles are displayed on the left (a and b). The Alas profile (c) and lake sediment profile (d) on the right. Errors bars (±2SD) are represented for radiogenic Sr isotopic ratio.

10.4 Discussion

10.4.1 Controls on the variability of the radiogenic Sr ratio in mineral OC interactions from Eight Mile Lake soil profiles

General soil profile

We observe a general decrease in the $^{87}Sr/^{86}Sr$ ratio of the DCB-extracted Sr from surface to depth in the soil profiles from Eight Mile Lake (Figure 10.4). This is consistent with previous studies from other permafrost regions which highlighted similar decrease in radiogenic Sr ratio in deeper soil layers relative to top surface layer (Keller et al., 2010; Bagard et al., 2013). The mineralogy of Eight Mile Lake tundra soil is derived from a loess that accumulated during the late Pleistocene and Holocene period which is characterized by minerals such as K-feldspar, micas, illitic clay minerals (i.e., K-rich more radiogenic minerals), but also plagioclase and other Ca-bearing minerals (i.e., Ca-rich less radiogenic minerals) (Mauclet, 2022). The difference in radiogenic Sr isotopic composition with depth likely reflects a higher proportion of K-rich minerals (i.e., characterized with a high $^{87}Sr/^{86}Sr$ ratio) in the upper soil profile relative to a higher proportion of Ca-rich minerals (characterized with a low $^{87}Sr/^{86}Sr$ ratio) in the lower soil profile. This can be explained by dissolution of the more weatherable Ca-plagioclase and the relative increase in resistant K-rich minerals in the uppermost soil layers, thereby resulting in higher $^{87}Sr/^{86}Sr$ ratio in organic-rich layers in the upper part of the profile (Drouet et al., 2007).

The general decrease in the $^{87}Sr/^{86}Sr$ ratio of the DCB-extracted Sr from surface to depth is also observed for the exchangeable Sr extracted from the same samples (i.e., after ammonium acetate extraction; NH_4Ac; Metson et al. (1956)) (Mauclet, 2022). The concentration in exchangeable Sr is systematically lower than the concentration in DCB-extracted Sr (Figure S.10.7a) given that the DCB targets a larger Sr pool (i.e., occluded in Fe oxides or as organo-metallic complexes). This is confirmed by the less radiogenic $^{87}Sr/^{86}Sr$ ratio of the DCB-extracted Sr relative to the exchangeable Sr (Figure S.10.7b), resulting from the contribution from less radiogenic Sr from primary mineral weathering in deeper soil layers found within mineral OC interactions.

Atmospheric deposition is another process which could enrich surface soil horizons with exogenous inorganic rock-derived Sr and contribute to Sr

release for mineral OC interactions (Graustein and Armstrong, 1983; Derry and Chadwick, 2007). While Sr derived from marine aerosol was reported as an important source of Sr in some highly weathered and/or coastal systems (Graustein and Armstrong, 1983; Chadwick et al., 2009; Pearce et al., 2015), the influence of marine deposition is negligible in the continental environment of Interior Alaska (Hirst et al., 2022) and is therefore neglected in this study.

Specific soil layers

Here we assess the type of mineral OC interactions targeted by DCB extractions in Eight Mile Lake specific soil layers to understand if mineral OC interactions have been affected by dissolution-precipitation processes. In the unsaturated organic layer, no correlation is found between the amount of Fe involved in Fe oxides or participating in organo-metallic complexes (Fe_d concentrations) and the $^{87}Sr/^{86}Sr$ ratios (Figure 10.4 and Figure S.10.5b). This means that in unsaturated layers, the increase in mineral OC interactions involving Fe do not influence the Sr isotopic ratio. Instead, mineral OC interactions can involve organo-metallic complexes with elements such as Ca, and hence Sr, as supported by higher Sr_d/Sr_{total} in unsaturated soil layers (Figure S.10.4). *Ch.4* highlighted the higher and almost exclusive contribution of organo-metallic complexes compared to Fe oxide to mineral OC interactions in active layer samples from Eight Mile Lake. Building on this work, our results indicate a positive correlation for all samples (except unsaturated active layer samples within the top litter horizon) between the DCB-extracted Sr and the pyrophosphate-extracted Ca (Ca_p; Ca involved in organo-metallic complexes; Figure 10.6a; *Ch.4*). This supports that the existence of organo-metallic complexes with Sr^{2+} substituting for Ca^{2+} in Eight Mile Lake soils (saturated, unsaturated and permafrost) is very likely. Our results also indicate a positive correlation between Ca_p and radiogenic Sr signature ($r = 0.77$) with highest Sr isotopic ratio found in unsaturated soil layers (Figure 10.6b). The organo-metallic complexes with Ca, and likely with Sr were shown to accumulate in litter horizons where little Fe concentrations are observed (*Ch.4)*. The higher Sr isotopic ratio with higher organo-metallic complexes with Ca is likely explained by the location of the sample in the top surface layer of Eight Mile Lake tundra soils. Therefore, the high Sr isotopic ratio found in mineral OC interactions from unsaturated layers can be explained by mineralogical composition of the organic layer controlling the

source of Sr rather than by mineral OC interactions dissolution-precipitation or stabilization processes.

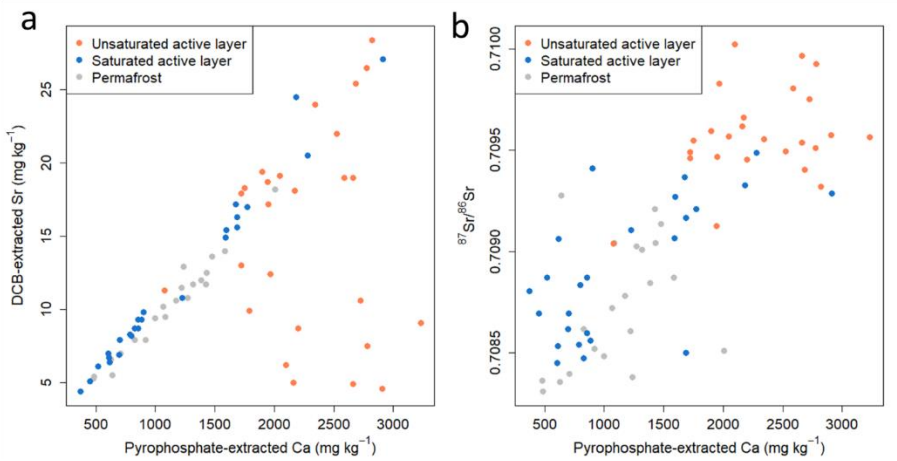

Figure 10.6: (a) Concentration of dithionite-citrate-bicarbonate (DCB) extracted Sr as a function of pyrophosphate-extracted Ca (mg kg^{-1}) in unsaturated active layer (orange), saturated active layer (blue) and permafrost (gray) in samples from Eight Mile Lake tundra soils. (b) Radiogenic Sr isotopic ratio ($^{87}Sr/^{86}Sr$) as a function of pyrophosphate-extracted Ca (mg kg^{-1}). Pyrophosphate-extracted Ca data are taken from *Ch.4*. Error bars for radiogenic Sr isotopic ratio are not represented on the plot.

An accumulation of mineral OC interactions (higher concentrations in Fe_d) is usually found close to the redox interface (Figure 10.4). We argue that the Fe_d accumulation location indicates the mean position of the water table fluctuation level during summer season for each specific soil profile (i.e., the water table level displayed on the plots refers to the water table at the moment of sampling; Figure 10.4). The Sr within such mineral OC interactions can be Sr adsorbed or occluded to Fe oxides or Sr involved in organo-metallic complexes. Here, the positive correlation in saturated soil layers between the concentration in DCB-extracted Sr and the organo-metallic complexes with Ca^{2+} (pyrophosphate-extracted Ca; Ca_p) (r = 0.99; Figure 10.6a) indicate a high proportion of organo-metallic complexes with Sr. The divalent cation Sr^{2+}, like Ca^{2+}, is potentially able to stabilize the negative charge of polyfunctional groups in organic acids. However, the accumulation of mineral OC interactions near the redox interface do not modify the overall $^{87}Sr/^{86}Sr$ ratio of that layer compared to the surrounding soil layers (i.e., located directly above or below; Figure 10.4). This can be explained by a large pool of labile Sr submitted to repeated dissolution-precipitation cycles or by the increased abundance of organo-metallic complexes with dynamic association-

dissociation processes. The interface between minerals and organic carbon evolves continuously with changes in the chemistry of aqueous phases, organic matter and mineralogy, and influences both magnitude and rate of OC adsorption (Kleber et al., 2021). This dynamic exchange between the mineral and organic compounds may be greater within organo-metallic complexes compared to spatially occluded Sr within Fe oxides (von Lützow et al., 2006). The mineral OC interactions found at the redox interface are substantial but our results indicate a poor stability in time of these interactions and rather highly dynamic cycles of dissolution-precipitation maintaining the isotopic ratio of the ultimate Sr source available in that specific soil layer.

The Fe accumulation at the water table is commonly explained with the hypothesis that Fe^{2+} is released from weathered minerals previously locked in permafrost which migrates upward towards oxic zones before oxidation and precipitation as poorly crystalline oxides or as organo-metallic complexes (Lipson et al., 2012; Herndon et al., 2017; Patzner et al., 2022). Another explanation could be that soluble organo-metallic complexes present in permafrost or formed above the permafrost table migrate upwards with water table fluctuations and settle at the redox interface. In the first scenario, Fe^{2+} mobility is independent of Sr because they are not interacting. The Sr adsorbed at the time of Fe oxidation is therefore the one found locally at the redox interface with a high $^{87}Sr/^{86}Sr$ ratio. This first scenario would not modify the Sr isotopic signature at the water table because Sr would originate from top surface layer close to the redox interface. In the second scenario, Sr is translocated upward together with soluble organo-metallic complexes. Under these conditions, the $^{87}Sr/^{86}Sr$ ratio at the Fe accumulation layer would decrease reflecting less radiogenic Sr from deeper source mixing with more radiogenic Sr from upper soil layer. Here, the results suggest that the first scenario is the more likely and that there is no mixing of Sr from deeper layers upon gradual thaw. In terms of organic carbon stabilization, this supports that mineral OC interactions must be disrupted on ascent and cannot migrate in a stable form towards the redox interface. Organic carbon is therefore more vulnerable upon Fe oxide dissolution in long-term saturated soil conditions with low potential to form mineral OC interactions.

In saturated soil layers, between the permafrost and the water table, the radiogenic Sr isotopic signature and Fe_d concentration are positively correlated ($r = 0.65$; Figure S.10.5b). For instance, the slight increase in Fe_d concentration in the saturated profile (10–15 cm in Mod 2; Figure 10.4c) is concomitant with an increase in radiogenic Sr isotopic signature. Similarly,

below the water table level of profiles Mod 1, Ext 1 and Ext 3, the higher Fe_d concentrations result in higher radiogenic Sr isotopic signature. As an example, the higher $^{87}Sr/^{86}Sr$ ratio found at 50 cm in Ext 3 (Figure 10.4f) likely reflects the original Sr isotopic signature preserved in a Sr "stable" pool induced by the higher proportion of mineral OC interactions. Our results suggest that under saturated conditions, the increase in mineral OC interactions increases the proportion of the stable pool of Sr and may provide a higher stability of Fe oxides and organo-metallic complexes with time. The different radiogenic Sr signatures found in mineral OC accumulation layers of saturated soil might reflect the presence of the original Sr source preserved upon changing soil conditions. A high rate of dissolution-precipitation of these interactions would likely result in the mixing of highly soluble Sr within the saturated active layer and hence in a constant $^{87}Sr/^{86}Sr$ ratio through the saturated portion of soil. Therefore, our data support that mineral OC interactions at these locations offer stable interactions for Sr preserving the radiogenic Sr isotopic signature over time despite gradual thaw.

10.4.2 Controls on the variability of the radiogenic Sr ratio in mineral OC interactions from Duvanny Yar sediment profiles

General sediment profile

We found homogeneous DCB-extracted Fe concentration with depth in both Yedoma profiles but a redistribution of mineral OC interactions in Alas deposits (DY-04) and Lake sediments (DY-02) (Figure 10.5). The DCB-extracted Fe concentrations support that, compared to Yedoma deposit profiles, Fe oxides and organo-metallic complexes are redistributed upon thermokarst process leading to layers of accumulation of mineral OC interactions in Alas and Lake sediment profiles (Figure 10.5). This is supported by the redistribution of total Fe concentration upon thermokarst processes highlighted in *Ch.2*, between the homogeneous Fe concentration in Yedoma profiles and the highly variable Fe concentration in Alas and Lake sediment profile (Figure S.10.3). However, the higher Fe_d concentration in previously thawed deposits compared to Yedoma deposits is not correlated with higher Sr isotopic ratio (Figure S.10.5c).

The identical radiogenic Sr signature in both Yedoma deposits profile was expected and is explained by the similar loess origin upon Yedoma formation during the late Pleistocene. Both Yedoma profiles were submitted to similar cold and dry climate conditions and therefore, Yedoma deposits were very likely to display identical $^{87}Sr/^{86}Sr$ reflecting their similar sources. Grain size analysis from Strauss et al. (2012) indicates stable sediment sources and persistent transport conditions with very likely loess origin (grain size distribution with a large peak at 20 to 60 µm; Smalley and Smalley, 1983). In addition, Yedoma deposits from the Kolyma Lowland and elsewhere are characterized by weak intensity of chemical weathering because of their specific mineralogy, continental origin, cold and arid climate conditions (Alekseev et al., 2003). The lack of chemical weathering could be partially responsible for the rather homogeneous $^{87}Sr/^{86}Sr$ ratio within Yedoma deposits. Such Yedoma formation should result in homogeneous radiogenic Sr isotopic signature with time. Note that slight differences might be explained by seasonal (summer and winter) variations in wind speed and directions likely modifying the origin of the loess material or by increased weathering before syngenetic freezing under warmer interstadial periods (Murton et al., 2015).

However, the identical $^{87}Sr/^{86}Sr$ ratio measured in deposits which experienced thermokarst processes was not expected and complicate the use of radiogenic Sr as a source tracer between deposits that never thawed since deposition and deposits that thawed during the Holocene. In this scenario where no change in Sr isotopic signature is found between Yedoma and previously thawed permafrost features, one cannot conclude about dissolution-precipitation processes of mineral OC interactions (Figure 10.1). Here, the identical Sr isotopic signature indicates that (i) mineral OC interactions were stable despite lake formation and drainage or (ii) mineral OC interactions were dissociated and subsequently precipitated with ultimate Sr of endogenous or exogenous source with similar radiogenic Sr isotopic signature. The fact that Alas deposits and Lake sediments are mainly composed of re-worked deposits from the former Yedoma deposits (Grosse et al., 2013) potentially promoted an endogenous Sr source and hence an homogeneous $^{87}Sr/^{86}Sr$ ratio despite abrupt thaw processes.

Specific sediment layers

The maximum $^{87}Sr/^{86}Sr$ ratio from Duvanny Yar is found in a peat layer from the Yedoma profile (DY-01; 29 m a.r.l.) (Figure 10.5a). The peat layer (10.5 wt% TOC) is a paleocryosol sequence with increased silt and lower sand content compared to other samples (mean grain size 16 µm; Strauss (2010)). The increased TOC found in Yedoma deposits could be caused by ponding water and boggy conditions in low-center polygons under warmer conditions (Strauss et al., 2012). Such conditions could have promoted increased weathering and subsequent enrichment in resistant K-rich (more radiogenic minerals). This specific layer is not characterized by an increase in Fe_d concentration but by an increase in Sr_d concentration (Figure S.10.6a). This could be evidence of increased mineral OC interactions in the form of organo-metallic complexes with Ca^{2+} and Sr^{2+} as previously hypothesized for Eight Mile Lake soils (Sect. 10.4.1), and identified in deposits from the Yedoma domain (*Ch.3*).

In previously thawed deposits, the top layer from the Lake sediment profile displays the highest $^{87}Sr/^{86}Sr$ ratio (Figure 10.5d). This layer is dated from the Holocene period and results from peat formation process. Like in the Yedoma profile DY-01, the highest radiogenic Sr isotopic ratio is not concomitant with an increase in mineral OC interactions involving Fe (Figure 10.5) but concomitant with a higher proportion of Sr participating in mineral OC interactions (Sr_d/Sr_{total}; Figure S.10.6d). This is supporting evidence for the importance of organo-metallic complexes with Ca^{2+} and Sr^{2+}.

10.4.3 Conditions for the preservation of mineral OC interactions upon permafrost thaw

Preservation of mineral OC interactions in saturated layers enriched in Fe-oxides and organo-metallic complexes

Saturated layers with an increase in mineral OC interactions (high Fe_d concentration) often display a different radiogenic Sr signature than layers located directly above or below (Figure 10.7). This suggests a conservative property of original Sr isotopic signature and a stability of mineral OC interactions upon thaw. We argue that soil or sediment layers with an accumulation of mineral OC interactions which is not affected by repetitive

redox fluctuations (i.e., redox fluctuation is enhanced at the water table level) kept a different radiogenic Sr signature with time than adjacent layers (Figure 10.4) indicating a stabilization of the mineral OC interactions. This stabilization of mineral OC interactions is observed in Eight Mile Lake soils despite seasonal thaw. In parallel, specific peat layers from Yedoma domain deposits also suggest rather stable mineral OC interactions from organo-metallic complexes involving Ca^{2+} and Sr^{2+} rather the Fe cations. The highest Sr isotopic ratios observed in these peat layers are concomitant with an increase in Sr_d, likely involved as organo-metallic complexes rather than occluded or adsorbed to Fe oxides because of the absence of Fe_d accumulation in these layers. This implies that saturated layer or peat layer with increased mineral OC interactions may offers highly stable conditions and could mitigate the OC vulnerability despite seasonal or abrupt thaw as already proposed in previous studies (Joss et al., 2022).

The layer of mineral OC interactions accumulation in the deeply thawed profile (Mod2) is well suited to test the stability of such mineral OC interactions despite waterlogged conditions. This specific layer is not classified as organic-rich (TOC = 8 wt%, i.e., below the cutoff at 20% for organic rich layers) but shows concomitant increase in Fe_d and $^{87}Sr/^{86}Sr$ ratio. The radiogenic Sr isotope ratio is a tool that can be used in mixing models to estimate the proportion of Sr in a specific layer that combines a more radiogenic source from upper soil layer with a less radiogenic source from deeper soil layers. This mixing tool can be used to estimate quantitatively the proportion of Sr preserved in a specific layer accumulating mineral OC interactions in the saturated soil layers. For instance, in EML, we can use the average $^{87}Sr/^{86}Sr$ ratio from unsaturated soil layer ($\text{Sr ratio}_{\text{Unsaturated}}$ = 0.7095897) and from permafrost layer ($\text{Sr ratio}_{\text{Permafrost}}$ = 0.7087378) as end-member values to estimate their contribution to a specific layer from the saturated layer using the following equation (Eq. 10.1):

$$\text{Sr ratio}_{\text{Saturated}} = \text{X} * \text{Sr ratio}_{\text{Permafrost}} + (1 - \text{X}) * \text{Sr ratio}_{\text{Unsaturated}} \quad (Eq.\ 10.1)$$

where, X refers to the contribution of permafrost Sr source in the specific saturated layer of interest.

The layer of accumulation of mineral OC interaction in the saturated zone of Mod2 profile (10-15 cm; Figure 10.4) display a Sr isotopic ratio of 0.7094107. According to Eq. 10.1, this indicates that 21% of the Sr originates from the permafrost layer and 79% from the top surface layer. In comparison, the unsaturated layer in Mod2 on average is characterized by 85% of the Sr with

a permafrost isotopic signature and only 15% from the top unsaturated layer. The increase in mineral OC interaction and subsequent increase in the $^{87}Sr/^{86}Sr$ ratio raised the amount of the stable pool of Sr that remained undissociated in mineral OC interaction compared to other layers with a lower potential for mineral OC interactions. These calculations indicate that 79% of Sr trapped in mineral OC interactions originates from the top surface layer when there is an accumulation of mineral OC interactions, but this proportion decreases to 15% in layers without mineral OC interactions accumulation. By difference between these two pools, this suggest that 64% of the Sr originating from top layer was preserved thanks to the accumulation of mineral OC interactions. The same calculation can be applied to the accumulation peak of mineral OC interactions in profile Ext1 and Ext3: this supports that 51% of the Sr originates from the upper part of the profile at Fe_d accumulation peak against 47% on average in the saturated layer for Ext1, and 38% against 20% on average in the saturated layer for Ext3. By difference between the area of Fe_d accumulation and the average of the saturated zone, overall this indicates a potential preservation of the original radiogenic Sr signature between 4% and 64% in the presence of mineral OC interactions accumulation in saturated soil layers.

Dissolution-precipitation of mineral OC interactions at redox interfaces

Despite the significant accumulation of Fe_d indicating increasing mineral OC interactions at the redox interface of Eight Mile Lake soils, no change in $^{87}Sr/^{86}Sr$ ratio in these layers relative to their surrounding layers is observed (Figure 10.7). The redox interface acts as an oxidative barrier that promotes Fe oxides precipitation with potential co-precipitation of Sr. The Fe_d accumulation found at the redox interface is the result of redox shift due to water table fluctuations and reported in many studies (Lipson et al., 2012; Riedel et al., 2013; Herndon et al., 2017; Patzner et al., 2022). Our approach is consistent with the observations from Wortberg et al. (2017) using radiogenic Sr isotopes to trace the source of Fe aggregates co-precipitated with Sr in rivers and originating from a redox interface between anoxic groundwater and oxic stream water. Here, to explain the unchanged Sr isotopic ratio at redox interface in soil layers characterized with little Fe oxides and mainly organo-metallic complexes accumulation, we argue that the ongoing aerobic-anaerobic conditions promoted by water table fluctuations

induces persistent and dynamic dissolution-precipitation of mineral OC interactions. In turn, this would favor an increased proportion of labile Sr pool vulnerable to dissolution and a precipitation of new mineral OC interactions with a lack of conservative property such as recorded in the stable pool of Sr from saturated layers.

In parallel, the accumulation of Fe_d in previously thawed profiles from the Yedoma domain (Figure 10.5) can also be explained by Fe redistribution and precipitation where local conditions favors oxidation reactions (*Ch.2*). The increase in Fe_d concentration without change in radiogenic Sr isotopic ratio is similar than what is observed at the redox interface of Eight Mile Lake. Therefore, this could be explained by similar processes of ongoing dissolution-precipitation processes in layers with mineral OC interactions accumulation promoting the formation of a Sr highly "labile" pool. Note that this could also be explained by the homogeneous Sr isotopic ratio with depth in both Yedoma and previously thawed profiles.

Overall, the lack of difference in $^{87}Sr/^{86}Sr$ ratio between layers accumulating Fe-oxides at redox interfaces regularly affected by water table changes (or upon thermokarst processes) relative to surrounding layers supports the dominance of a Sr "labile" pool inherited from processes of dissolution and precipitation of the mineral OC interactions characterized with a signature from the local environment (Figure 10.7).

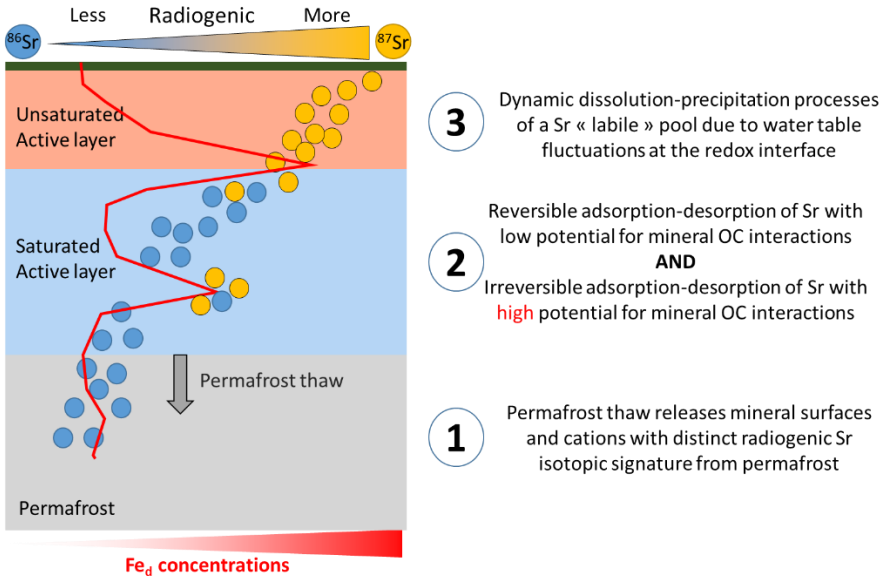

Figure 10.7: Schematic of permafrost soil radiogenic Sr isotope ratio in the DCB extract (blue and yellow Sr isotopes) and concentration in DCB-extracted Fe (Fe_d; red line) dynamic upon thaw. At the boundary between saturated and unsaturated soil layers (i.e., redox interface), the accumulation of Fe_d is not correlated with a change in radiogenic Sr ratio in the DCB extract. In saturated soil layer, the increase in Fe_d is concomitant with an increase in radiogenic Sr ratio in the DCB extract indicating a stable pool of Sr with a conservative property in mineral OC interactions rich layers.

Increasing contribution from mineral weathering to mineral OC interactions upon gradual permafrost thaw

In Eight Mile Lake soils, profiles can be divided as poorly thawed (Min1, Mod1 and Ext1; <60 cm active layer thickness) or deeply thawed (Mod2, Mod3, Ext1; >60 cm). Using a mixing equation identical to Eq. 10.1, we can determine the proportion of Sr adsorbed or occluded to Fe oxides and participating in organo-metallic complexes which found its source from the less radiogenic minerals in permafrost layers compared to the more radiogenic unsaturated layers. On average, the saturated active layer of poorly thawed soil profiles is characterized by a higher radiogenic Sr ratio of the DCB extracts (0.7091367 ± 0.000485) than the saturated active layer from deeply thawed profiles (0.7087963 ± 0.000661; p-value < 0.05). According to calculation based on Eq. 10.1, 53% of Sr in mineral OC interactions in the saturated layer of poorly thawed profiles is from permafrost layers in Min1

and Ext1 (Mod1 is left out because no samples are located in the saturated layer) while in deeply thawed profiles, this contribution increases to >80% (85% in Mod2, 100% in Mod3, 80% in Ext3). This higher contribution of less radiogenic Sr in mineral OC interactions in deeply thawed soil profiles is direct evidence of the contribution of mineral elements from newly thawed layers (weatherable minerals) to OC stabilization mechanisms. This hypothesis is supported by the two-fold higher values of Total Reserve in Bases (TRB = total concentration in Ca+Mg+K+Na; Herbillon, 1986) in saturated active layer from deeply thawed profile (Mod3 and Ext3 with TRB of 186 and 184 $cmol_c\ kg^{-1}$, respectively; Mauclet, 2022) compared to the saturated soil layer from poorly thawed profile (Min1 = 77 $cmol_c\ kg^{-1}$; Mauclet, 2022). The higher TRB value from deeply thawed profiles directly supports a larger weatherable mineral reserve in these soils originating from newly thawed poorly weathered soil layer, i.e., a direct source of Sr included in mineral OC interactions.

A mixing model using radiogenic Sr ratio is a powerful tool to estimate the contribution of different Sr source when end-members are clearly defined with different Sr isotopic signature and when additional end-members are not left out of the mixing model. We acknowledge that the end-members defined in this study have significantly different Sr ratio (p-value < 0.001; Wilcoxon test) but display a high variability within permafrost (0.7087378 ± 0.000625; mean ± 2SD). End-members are critical in mixing models and further investigations to define narrower ranges for the radiogenic Sr isotope composition of the Sr sources participating in mineral OC interactions in different permafrost systems might help to better constrain dissolution-precipitation processes of theses interactions as proposed in this study.

10.5 Conclusion

In conclusions, we found that:

(i) In saturated soil layers of tundra soils vulnerable to gradual thaw, the accumulation of mineral OC interactions is correlated with a more radiogenic Sr isotope signature in mineral OC interactions, supporting the preservation of 4 to 64% of Sr from top soil layer in a "stable" pool of Sr in mineral OC interactions, despite permafrost thaw.

(ii) At the redox interface of tundra soils accumulating mineral OC interactions, the absence of change in the radiogenic Sr ratio supports that the redox shift induced by fluctuating water table level promotes dynamic dissolution-precipitation of mineral OC interactions. This likely promotes a large contribution of a Sr "labile" pool reflecting the radiogenic Sr signature of the surrounding layers.

(iii) Ongoing permafrost thaw releases minerals likely to get involved in organic carbon stabilization mechanisms. This is supported by a larger contribution of Sr with a permafrost signature (> 80%) in mineral OC interactions in deeply thawed soil profile than in poorly thawed soils (~53%).

(iv) In Yedoma deposits vulnerable to abrupt thaw such as thermokarst lake formation and drainage, the similar range of Sr isotopic signature in the deposits prior and after thawing did not allow to determine whether or not the mineral OC interactions have been modified upon thermokarst process. Either mineral OC interactions are stable upon thermokarst process or, after Fe oxide dissolution or organo-metallic complexes dissociation, the newly available Sr occluded upon Fe oxide precipitation or complexing with OC display a similar isotopic signature than the previous Sr source.

In perspectives, this first attempt to use radiogenic Sr isotopes to trace the *in situ* dissolution-precipitation processes of mineral OC interactions was promising and should be tested in other thawing permafrost features.

Part IV
Conclusions and perspectives

11. CONCLUSIONS AND PERSPECTIVES

11.1 General conclusions

The overarching aim of the Ph.D. thesis was to improve our knowledge on mineral surfaces and cations involved in interactions with organic carbon (OC) in permafrost soils and sediments, and investigate the evolution of those mineral OC interactions upon permafrost thaw. Indeed, mineral OC interactions can stabilize OC and increase the proportion of mineral-protected OC less likely to be mineralized as greenhouse gases. However, mineral OC interactions are vulnerable to changes in soil conditions such as shift in pH or redox conditions. The different chapters of the Ph.D. thesis contribute to shed light on the following question: *What is the influence of permafrost thaw on mineral organic carbon interactions?*

The first step needed was to validate the use of a rapid methodology to accurately measure total concentration of specific mineral elements involved in mineral OC interactions. In the *Ch.1*, total concentrations of Si, Al, Fe, Ca, K, Ti, Mn, Zn, Sr and Zr were shown to be accurately measured using portable X-ray fluorescence (pXRF) method and corrected using alkaline fusion and inductively coupled plasma optical emissions spectrometry. These mineral elements include Fe, Al, Mn and Ca which play an important role in mineral OC interactions and have a direct influence on OC stabilization, but also other mineral elements (e.g., Si, K, Zn, Sr) which drive nutrient supply to plants or microorganisms with indirect influence on OC storage and degradation or other immobile element (e.g., Ti, Zr) which can be useful to evaluate the advance of weathering in permafrost soil or sediments. This fast and reliable methodology allowed the construction of the first Yedoma domain Mineral Concentration Assessment (YMCA) dataset (n = 1,292) and allowed the estimation of mineral element stocks within the Yedoma domain.

Then, to investigate the influence of permafrost thaw on mineral OC interactions, we characterized under different soil or sediment conditions (i) the elemental composition of the bulk soil (using the pXRF method developed in *Ch.1* in ice-rich permafrost region and in other permafrost regions), (ii) the proportion of metals contributing to mineral OC interactions and under which form these metals were present (i.e., crystallized and poorly crystalline oxides form or participating in organo-metallic complexes), and (iii) the total organic

carbon content and organic acids potentially stabilized by those mineral OC interactions.

The Ph.D. thesis addressed three specific research questions for which the conclusions are the following.

Q1. How do mineral organic carbon interactions change with thermokarst lake formation and drainage upon ice-rich permafrost *abrupt thaw*?

In ice-rich permafrost regions, Arctic warming induces thermokarst lake formation which may drain with time. These abrupt thaw processes significantly change soil conditions and likely influence the stability of mineral OC interactions. In this study, we were able to investigate the influence of abrupt thaw across the ice-rich permafrost region (i.e., Yedoma domain) in Yedoma deposits which never thawed since deposition and previously thawed and refrozen Alas deposits (*Ch.2*), and in a specific landscape transect in Central Yakutia from undisturbed sediments in Yedoma uplands to drained lake sediments and sediments below thermokarst lakes from different generations (*Ch.3*).

The YMCA dataset highlighted a significant total Fe redistribution upon thermokarst lake formation and drainage in Alas landforms across many parts of the ice-rich permafrost region. In addition, the total Fe redistribution was followed by the redistribution of Fe involved in mineral OC interactions suggesting higher potential for OC stabilization in previously thawed deposits compared to never thawed Yedoma deposits. More specifically, we found that 25% of the global Fe pool in Yedoma and Alas deposits was involved in mineral OC interactions (*Ch.2*). Similarly, the specific site of Yukechi highlighted an increase in the supply of stabilizing metal surfaces in thawed deposits, especially Fe-oxy(hydr)oxides and metal cations (Fe, Mn, Al and Ca) which provide an increasing protection for OC after drainage of thawed deposits. The drainage of thermokarst lakes studied promoted the increase in poorly crystalline oxides and the increase in metal:C bindings within organo-metallic complexes which both increases OC stabilization. Eventually, we found that the increased stabilizing surfaces and cations was concomitant with a partial decrease in both carbon dioxide and methane emissions (*Ch.3*).

Both chapters (*Ch.2* and *Ch.3*) highlighted that OC was potentially better protected after initial abrupt thaw, suggesting that abrupt thaw likely increases

the potential to stabilize OC and mitigate permafrost carbon emissions. We argue that thermokarst processes lead to the modifications of environmental conditions which increase mineral OC interactions potential and hence increase the proportion of the mineral-protected OC pool less vulnerable to be mineralized as greenhouse gases. With future permafrost thaw, our results suggest that the OC pool within never thawed Yedoma deposits is more vulnerable to microbial degradation than the OC pool from Alas landforms.

Q2. How do mineral organic carbon interactions change with the deepening of the active layer and subsidence upon permafrost *gradual thaw*?

In permafrost regions vulnerable to gradual thaw, active layer deepening and water table rise may lead to changing soils conditions and influence mineral OC interactions. The moist acidic tundra from Eight Mile Lake was well suited to investigate changes in soil conditions because of the varying active layer depth (45 to 109 cm deep) and water table depth from the studied soil profiles. Active layer deepening may increase the supply of metal surfaces or cations from permafrost and influence OC stabilization within the thawed layer. The acidic conditions from surface organic-rich layers compared to the neutral conditions found in permafrost mineral layers may influence pH-sensitive metal oxides or cations and their interactions with OC. In addition, the water table act as a redox interface likely to influence the stability of redox sensitive elements such as Fe and Mn. The simultaneous assessment of Fe, Mn, Al and Ca elements and their contribution to mineral OC interactions was required to better constrain their relative importance under such variable soil conditions.

In a permafrost vulnerable to gradual thaw, we found that the combination of organo-mineral associations (i.e., association between ferrihydrite and OC) and organo-metallic complexes involving Fe, Mn, Al and Ca polyvalent cations contributed to stabilize between 6% and 59% of total OC (mean 20%). This percentage was higher in the permafrost than in the active layer. Similarly to the conclusions from the Yedoma domain, we found a positive correlation between total Fe and Mn concentrations and the Fe and Mn involved in mineral OC interactions. We found that OC is mainly protected by organo-metallic complexes within the active layer and permafrost and organo-mineral associations with ferrihydrite contributed only in permafrost layers. In organo-

metallic complexes, Ca is the major contributor in litter while Fe prevails in other layers. The contribution of Al in organo-metallic complexes increases under persistent waterlogged conditions. Within the active layer, hotspots for mineral OC interactions and hence OC protection is found at the redox interface (i.e., water table level), however, the permafrost layer expected to thaw in the next decades contains the larger proportion of mineral-protected OC (*Ch.4*).

Q3. To what extent can we trace the dissolution-precipitation processes of mineral organic carbon interactions upon both gradual and abrupt thaw?

The stability of mineral OC interactions upon changing soil conditions is key to better estimate OC protection in thawing permafrost. However, determining the drivers of preservation of mineral OC interactions or the conditions in which these are affected by processes of dissolution and precipitation upon permafrost thaw is a challenge. Here we tested a new approach using radiogenic Sr isotopes to trace the *in situ* dissolution-precipitation processes related to mineral OC interactions upon permafrost thaw (i.e., abrupt thaw and gradual thaw). Radiogenic Sr isotopes is a common source tracer for provenance or cation mobility studies. In this Ph.D. thesis and for the first time to the best of our knowledge, we orientated the use of radiogenic Sr isotopes on Sr from selective extractions, targeting the Sr involved in mineral OC interactions either adsorbed or occluded to metal oxides or participating in organo-metallic complexes. We argue that a change in the Sr isotopic signature of such mineral OC interactions upon permafrost thaw indicates a destabilization of the binding between mineral surfaces and Sr, and hence OC.

In a permafrost subjected to gradual thaw, contrasted radiogenic Sr ratio in saturated layer characterized with accumulation of mineral OC interactions compared to surrounding layers indicated the presence of a Sr “stable” pool which supports a preservation of 4 to 64% of the original Sr within the mineral OC interaction despite gradual thaw. At the redox interface characterized by an accumulation of mineral OC interactions, identical radiogenic Sr ratio with surrounding layers suggested a rather “labile” Sr pool due to ongoing dissolution-precipitation processes induced by fluctuating redox conditions. Eventually, we were able to demonstrate that permafrost gradual thaw releases mineral elements becoming involved in OC stabilization mechanisms.

In an ice-rich permafrost subjected to abrupt thaw, the similar range in Sr isotopic signature in the deposits prior and after thawing did not allow to determine whether or not the mineral OC interactions have experienced dissolution-precipitation processes upon abrupt thaw. Mineral OC interactions are either (i) stable upon thermokarst processes (i.e., thermokarst lake formation and drainage) or (ii) dissolved but formed with a similar Sr source than the original Sr source.

11.2 Implications and perspectives

This Ph.D. thesis investigated the influence of changing soil conditions on mineral organic carbon (OC) interactions from large scale (i.e., Yedoma domain) to microscale (i.e., dissolution-precipitation processes within mineral OC interactions). This section summarizes the main integrated outcomes of the different chapters and opens up perspectives for future research.

11.2.1 Integrated outcomes

The *Ch.1* investigated the validation of portable X-ray fluorescence (pXRF) method for a fast assessment of total concentrations of mineral elements such as Fe, Al, Mn and Ca which are directly involved in mineral OC interactions and have a direct influence on OC stabilization.

The *Ch.2* focused on Fe redistribution upon thawing, a key cation ubiquitous in mineral OC interactions, and highlighted the increase in total Fe in deposits which experienced thermokarst lake formation and drainage concomitant with the increase in Fe involved in mineral OC interactions. The *Ch.2* confirmed that changing soil conditions influenced the distribution of redox-sensitive cations which are key for mineral OC interactions.

Following on this, the *Ch.3* and *Ch.4* investigated the potential contribution of Fe, Al, Mn and Ca elements in mineral OC interactions relative to their different stability domain (pH, redox). The *Ch.3* highlighted the influence of abrupt thaw on mineral OC interactions with Fe, Mn, Al and Ca while the *Ch.4* investigated the changes of those interactions for gradual thaw. The *Ch.3* and *Ch.4* highlighted the complexity and competition between these elements to form association with OC. These chapters shed light on the different

behavior of such metals relative to changing soil conditions and their different potential to stabilize OC.

Eventually, the *Ch.5* focused on the stability of those interactions upon gradual and abrupt thaw and highlighted the presence of a stable and labile pool for mineral OC interactions with contrasting stability depending on soil conditions and mineral OC interactions presence or absence.

Based on these findings, four main perspectives have been identified and are discussed in the following sections.

11.2.2 Total Fe concentration as a proxy of Fe involved in mineral organic carbon interactions at the Arctic scale

With Arctic warming, permafrost areas are likely to shrink substantially within decades or even disappear by 2100 (Biskaborn et al., 2019; IPCC, 2022; Smith et al., 2022). With this in mind, the assessment of potential OC stabilization by mineral OC interactions and the ultimate goal to implement those interactions in the next generation of climate models is urgent with time as a key constraint (Opfergelt, 2020). This Ph.D. thesis was thought on this basis. The validation of pXRF methodology for a rapid assessment of total bulk concentrations of main mineral elements involved in mineral OC interactions was a first key step. The scientific community and this Ph.D. thesis emphasize on the importance of Fe for mineral OC interactions. There is a general consensus on the importance of Fe oxy(hydr)oxides and organo-metallic complexes with Fe cations for OC stabilization in soils and sediment (von Lützow et al., 2006; Colombo et al., 2014; Kleber et al., 2015; Grant et al., 2022). The DCB-extracted Fe (Fe_d) is a good indicator of Fe involved in mineral OC interactions either as oxide surfaces for organo-mineral associations or as cations for the formation of organo-metallic complexes (Mehra and Jackson, 1960; Rennert, 2019). The pooling of the samples investigated within the different *Data chapters* highlights a positive correlation between total Fe and Fe_d concentrations (Figure 11.1). The Ph.D. thesis included samples with many different characteristics, from mineral sediments in deep Yedoma sediments from northern Alaska to organic rich-layer of Alas deposits in Interior Siberia or even to mineral or organic-rich samples from the tundra site of Eight Mile Lake. The positive correlation between total Fe and Fe_d seems to be influenced only by matrix effect which

depends on total organic carbon (TOC) content (cutoff at 20 wt% TOC; Hicks Pries et al. (2012)).

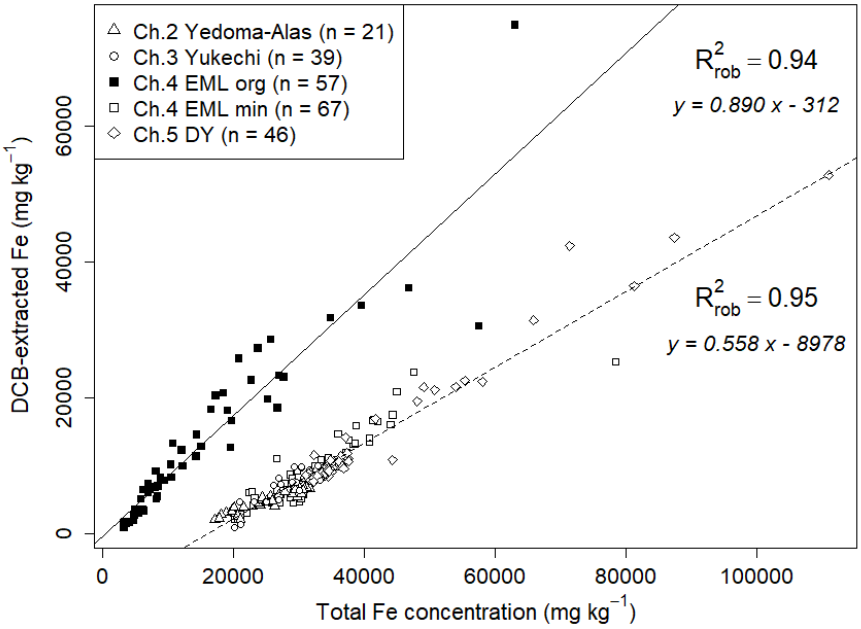

Figure 11.1: Dithionite-citrate-bicarbonate (DCB) extracted Fe concentration (mg kg^{-1}) as a function of total Fe concentration (mg kg^{-1}) (n = 230). Samples are taken from the *Ch.2* in the Yedoma domain, *Ch.3* from the Yukechi site, *Ch.4* for the Eight Mile Lake (EML) study site and *Ch.5* for the Duvanny Yar (DY) site. Organic-rich samples (>20 wt% total organic carbon content) are represented with full symbols and robust linear regression for organic samples with continuous line. Mineral samples (<20 wt% total organic carbon content) are represented with empty symbols and mineral linear regression with the dashed line. Robust linear regression (alpha = 0.95) coefficient of determination (R^2) and specific equations are provided in the plot.

The positive correlation between total and DCB-extracted Fe (R^2 > 0.94; Figure 11.1) opens an interesting possibility for the rapid assessment of the amount of Fe involved in mineral OC interactions in permafrost regions. We found that 27 ± 9 % (mean ± standard deviation) of total Fe was extracted with DCB and potentially involved in mineral OC interactions for mineral samples (TOC < 20 wt%) and 81 ± 25% for organic samples (TOC > 20 wt%). While many studies in permafrost regions include total Fe concentration assessment, the methods to target Fe involved in mineral OC interactions are tedious and therefore not systematic. In addition, extraction procedures may differ from

the commonly used DCB-extraction (Mehra and Jackson, 1960) with alternative such as DCB-extraction for 16 hours at room temperature, sequential extraction or HCl-based extractions (Wagai et al., 2013; Rennert, 2019). We acknowledge that selective extractions such as DCB extraction may extract some untargeted phases which is well reviewed in Rennert (2019). However we argue that standardized protocol from sampling to laboratory methodologies are essential to compare and share information with minimal bias from different sampling campaign across the Arctic. Given that the 230 samples presented in Figure 11.1 display a wide range of TOC content, grain-size and thawing history across multiple sites of the permafrost region, the use of total Fe as a proxy to estimate the Fe involved in mineral OC interactions should be scalable to all permafrost regions. The assessment of total Fe concentration using pXRF device and corrected following the method from *Ch.1* may offer a rapid and accurate alternative to assess total Fe concentration in permafrost regions where total Fe concentration remains unknown. Since this Ph.D. thesis highlighted that total Fe and Fe involved in mineral OC interactions may increase substantially at redox interfaces or in some buried peat layers, the complementary use of pXRF device and the linear regression presented in Figure 11.1 could help to identify areas enriched in reactive Fe (DCB-extracted Fe) and thereby potential mineral OC interactions hotspots with increased stabilization effect on OC in other permafrost regions. This complementary method minimizes analytical procedure and could allow a fast assessment of mineral OC interactions hotspots in the entire Arctic region. Nonetheless, we would recommend to validate that the equation to infer DCB-extractable Fe based on total Fe concentration works on a subset of sample with the matrix of interest provided that identical methodologies are used.

11.2.3 Incubation experiments in identified layers of mineral organic carbon interactions accumulation

The key outcome in studies investigating mineral OC interactions in permafrost regions is to decipher the increased OC stability relative to microbial degradation. In the *Ch.3*, we were able to highlight that the increase in mineral OC interactions in Alas lake sediments compared to Yedoma lake sediments was concomitant with a decrease in carbon dioxide (CO_2) and a slight decrease in methane (CH_4) emissions based on incubation experiments. However, samples submitted to incubation experiments to measure carbon

fluxes and OC decomposition rates are often characterized based on TOC content, dissolved OC, microbial community types and abundance but the assessment of mineral OC interactions involving Fe, Mn, Al and Ca are rare.

An interesting perspective to this Ph.D. work would be to carry out incubation experiments and measure greenhouse gas emissions in specific samples previously characterized with high or low potential for mineral OC interactions (i.e., redox interface, buried peat layers). Samples with similar properties which differ in the amount of organo-mineral associations or organo-metallic complexes would be nice candidate to test the direct effect of mineral OC interactions on the expected mitigation of OC microbial degradation. The Min 3 profile from Eight Mile Lake study site could be a nice candidate to test the influence of mineral OC accumulation at the redox interface or in permafrost layers (Figure 11.2). This soil profile is characterized by an accumulation of mineral OC interaction at the redox interface which may protect up to 26% of TOC. The layers located above or below this redox interface have high TOC content but lower potential for mineral OC interactions and protect up to 10% of TOC. The different water saturation conditions in these two layers might contribute to influence carbon fluxes after incubation experiments. In permafrost, samples are characterized with lower TOC content but can be enriched or not in mineral OC interactions (samples 5 and 4 in Figure 11.2, respectively). These samples can protect up to 48% of the OC and should display lower CO_2 and CH_4 emissions than samples from the redox interface.

Along this thesis we highlighted the accumulation of mineral OC interactions under specific soil conditions and suggested potential hotspots for OC protection. However, the degradation of OC via the oxidation of OC coupled with Fe or Mn reduction reactions was not investigated. During anoxic periods, microbial use of metals (e.g., Fe^{III}, Mn^{IV}) as an electron acceptor directly produces CO_2 from the metabolic coupling of organic matter oxidation to metal reduction (Lovley and Phillips, 1986; Lipson et al., 2010). These OC degradation mechanisms were recently reported to even counteract protection mechanisms inferred by mineral OC interactions (Chen et al., 2020; Li et al., 2021). Conversely, metal reduction mechanisms are also reported to inhibit methanogenesis and coupling of organic matter oxidation to metal reduction may influence the CO_2:CH_4 balance (Bodegom et al., 2004; Lipson et al., 2012). Given that organic matter can be oxidized by the reduction of Fe or Mn in soils undergoing changes in redox conditions, incubation experiments should include both OC stabilization and degradation processes.

This Ph.D. study did not investigate the rate of metal-mediated OC oxidation. We argue that carbon fluxes measurements (CO_2 and CH_4) from incubation studies of samples with different proportion of mineral OC interactions should help to fill the knowledge gap on the net response that include both the protection inferred by mineral surfaces and cations versus the degradation promoted by oxidative transformation of OC coupled with metal reduction.

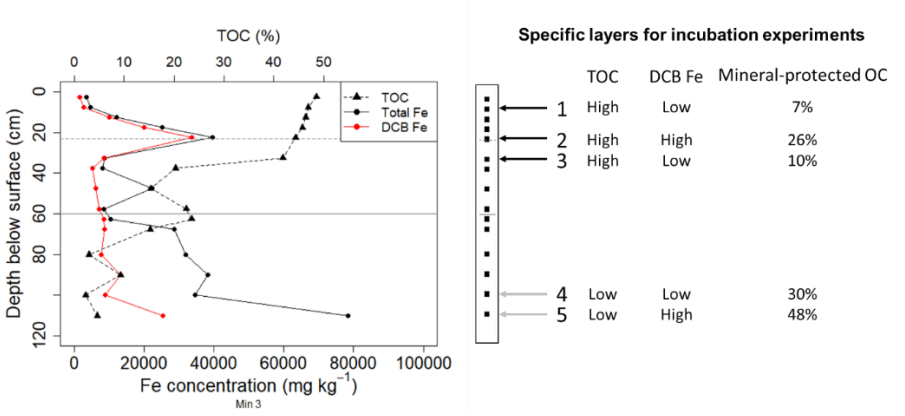

Figure 11.2: Proposed soils samples to test the influence of mineral organic carbon interaction at the redox interface or in permafrost layers via incubation experiment and greenhouse gas measurements. Samples (from 1 to 5) are characterized with varying total organic carbon (TOC) content, dithionite-citrate-bicarbonate (DCB) extracted Fe and have different potential to stabilize OC (*Ch.4*). The different soil conditions: unsaturated (1), redox interface (2), saturated (3) in the active layer and the different concentrations in DCB Fe involved in mineral OC interactions in permafrost layers (4 and 5) may influence the carbon fluxes measured upon incubation experiments of these specific layers.

11.2.4 Different contribution of Fe, Mn, Al and Ca in mineral OC interactions under varying geochemical conditions

This Ph.D. thesis gathers multiple permafrost sites with varying sample characteristics such as different TOC content, freezing and thawing history, pH and redox conditions, age of deposition, or grain-size distribution (Figure 11.3). We argue that the inheritance of the deposits, its history of deposition and time before permafrost formation together with the rate, duration and type of thawing processes are crucial parameters that determine the abundance and types of mineral OC interactions in a specific permafrost layer.

Along the different chapters, the aim was to investigate the processes such as dissolution or precipitation of metal oxides or association-dissociation of organo-metallic complexes affecting mineral OC interactions and hence the potential to stabilize OC upon permafrost thaw. Mineral elements investigated in this study (Fe, Mn, Al, Ca) have specific stability domains according to the local geochemical conditions (redox, pH) and may be influenced differently depending on initial conditions and changing soil conditions. Briefly, Ca is reported to have higher contribution in OC protection under neutral or alkaline conditions than Fe or Al which prevail under acidic conditions (Pan et al., 2014; Rowley et al., 2018). The alkaline conditions from Yukechi sediments (pH ~8-9; *Ch.3*) highlighted the increased contribution of Ca in organo-metallic complexes and supports the theory of Ca-mediated stabilization under alkaline conditions. However, Ca also prevailed in organo-metallic complexes from the litter of Eight Mile Lake tundra soils (*Ch.4*) which are characterized with acidic pH (~4). The negligible total Fe and Al concentrations in such specific layer may explain the high contribution of Ca despite acidic conditions. While Mn and Fe are both redox sensitive element, this Ph.D. thesis highlighted some discrepancies in their dissolution-precipitation dynamic. Thermodynamically, Mn should be reduced before Fe and Fe should be oxidized before Mn species (Melton et al., 2014; Kappler et al., 2021). At the Yukechi site, the increase in Fe oxides and organo-metallic complexes upon thermokarst processes was higher than observed for Mn species (*Ch.3*). Similarly, the Fe accumulation at the redox interface was not concomitant with an increase in Mn at the redox interface (*Ch.4*) which suggest other competition mechanisms which may imply different stability domain for both Fe and Mn accumulation and interactions with OC. Finally, grain-size characteristics within soils or sediments of interest may influence the overall stability of mineral OC interactions. The clay content in permafrost soils, not investigated here but reported to stabilize OC in many environments, might contribute significantly to OC stability (Saidy et al., 2012; Kleber et al., 2021). In addition, the grain-size influences the geochemical conditions in microsites and alters oxygen availability resulting in nanoscale redox modifications depending on grain-size and porosity within sediments (Keiluweit et al., 2018).

We hypothesize that the different conditions, especially pH and redox, may drive the competition between those metals for the formation of mineral OC interactions and influence their role for OC stabilization. We argue that future studies investigating the mineral OC interactions upon permafrost thaw should

combine the multiple metals capable of interacting with OC (Fe, Al, Mn, Ca) and relate their relative contribution to the specific geochemical conditions and inheritance of the deposits.

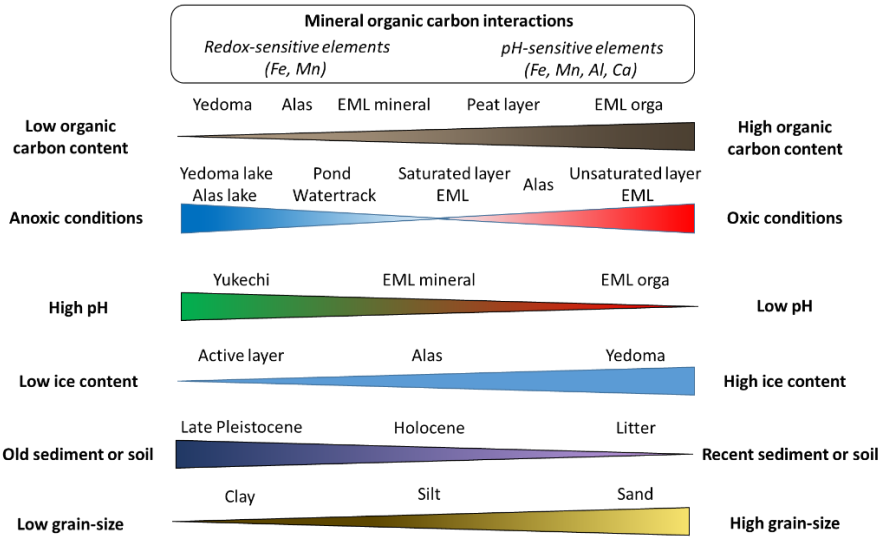

Figure 11.3: Overview of the soil or sediment conditions and characteristics within the multiple samples investigated from this Ph.D. thesis (EML = Eight Mile Lake). Mineral elements involved in mineral organic carbon interactions (Fe, Mn, Al and Ca) can be redox- or pH-sensitive potentially driving their contribution to participate in mineral organic carbon interactions. The different sample types are classified based on the relative difference specific for each parameters. This represents a general overview, note that not all sample types and local conditions or characteristics are represented.

11.2.5 Geochemical modelling to investigate stability of minerals surfaces with changing soil conditions

Geochemical modelling using computer program for simulating chemical reactions, processes, and transport could be used for further investigations. Simplified programming models could be used to check assumptions regarding the presence of mineral phases or their dissolution kinetics based on soil solution parameters and physico-chemical properties. The ubiquitous role of pH and redox on the stability of Fe-, Al-, Mn- and Ca-bearing phases makes PHREEQC (pH-REdox-EQuilibrium) a powerful tool to test the saturation index of specific mineral phases and their fate with changing soil conditions

(Parkhurst and Appelo, 2013). To integrate organic compounds, Visual MINTEQ would be more adapted to assess binding equilibrium between oxide surfaces and organic matter using complexation models (Gustafsson, 2011). The combination of both Visual MINTEQ program to assess saturation of organic acids in complexation and PHREEQC program to evaluate transport processes within a soil profile would be worth to quantify OC stability and mineralization potential (i.e., as free DOC not interacting with mineral surfaces or cations).

The modifications of initial and border conditions within the geochemical model could be tested in order to simulate i) redox fluctuations from oxygen-rich to oxygen depleted conditions (i.e., mimicking water table level variations) or ii) pH change such as acidification (i.e., mimicking cryoturbation of peat layer in deeper layers for instance) or alkalinization (i.e., mimicking the release of base cations from permafrost thaw). Ultimately, geochemical models may be used to predict the geochemical equilibrium which can be compared to the measured parameters in soil solution and solid phases. The comparison would emphasize how far the measured system is from the state of geochemical equilibrium.

11.2.6 Further investigations with radiogenic Sr isotope to trace the stability of mineral organic carbon upon permafrost thaw

The methodological design built in the *Ch.5* which aimed to use radiogenic Sr isotopes adsorbed or occluded to Fe oxides and participating in organo-metallic complexes to trace the *in situ* dissolution-precipitation processes of mineral OC interaction is a first, to the best of our knowledge. The extent to which radiogenic Sr isotopes can be used to trace the *in situ* stability of mineral OC interactions upon permafrost thaw relies on solid basis and reasonable assumptions. However, the high variability of Sr isotopic signature from Eight Mile Lake permafrost layers and chosen as an end-member for mixing model calculations should be tested in other permafrost environments. In addition, the similar Sr isotopic signature observed in Yedoma and in previously thawed deposits from the Yedoma domain made the interpretation related to dissolution-precipitation processes rather complex in the context of abrupt thaw.

A suggestion for future research would be to use the same methodological design in a single tundra soil profile at different stages of permafrost degradation (i.e., rather than on multiple profiles with different active layer at a specific time) and to track the dynamic change with time in the Sr participating in mineral OC interactions. A nice candidate for such experimental approach would be to test this on Eight Mile Lake tundra soil from the Carbon in Permafrost Experimental Heating Research (CIPEHR) experiment (Natali et al., 2011). At this site, tundra soils are sampled at different timescale (e.g., 2009 and 2017) at the exact same location but after increased subsidence, active layer deepening and water table rise (Rodenhizer et al., 2020). The changes in soil conditions in similar soils offer an advantage to better trace dissolution-precipitation processes using radiogenic Sr isotopes, especially now that we highlighted the less radiogenic Sr signature from deeper soils compared to surface soils at this site. Similarly, in order to trace the *in situ* mineral OC interactions stability in Yedoma deposits which experienced thermokarst lake formation and drainage, future studies should focus on permafrost locations where deposition during Holocene is likely to display contrasting Sr isotopic signature than the original Yedoma deposits in regions with greater lithological variability.

Another approach would be to test the hypotheses and conclusions highlighted in *Ch.5* under controlled conditions (Figure 11.4). For instance, to test the hypothesis of a labile pool of Sr involved in mineral OC interactions at the **redox interface**, we propose to conduct a batch experiment with ferrihydrite and Fe cations in presence of organic acids under fluctuating redox conditions (alternating under N_2 and O_2 conditions). By adding Sr in solution with a known contrasted Sr isotopic ratio (i.e., mimicking the exogenous Sr assumption from *Ch.5*), the determination of the Sr isotopic signature involved in mineral OC interactions before and after batch experiment could confirm or infirm the initial hypothesis. Under this scenario, mimicking redox interface, the radiogenic Sr signature of the Sr involved in mineral OC interactions should change with the addition of Sr of contrasting isotopic signature and ongoing dissolution-precipitation processes. Similarly, to confirm or infirm the hypothesis of a stable Sr pool in mineral OC interactions under reducing conditions in the **saturated soil layers**, we propose a batch experiment mimicking the influence of reducing conditions on the same material. Under such conditions, the radiogenic Sr signature of the Sr involved in mineral OC interactions should not change with the addition of Sr of

contrasting isotopic signature and confirm the stability of the mineral OC interactions under water saturated conditions (Figure 11.4).

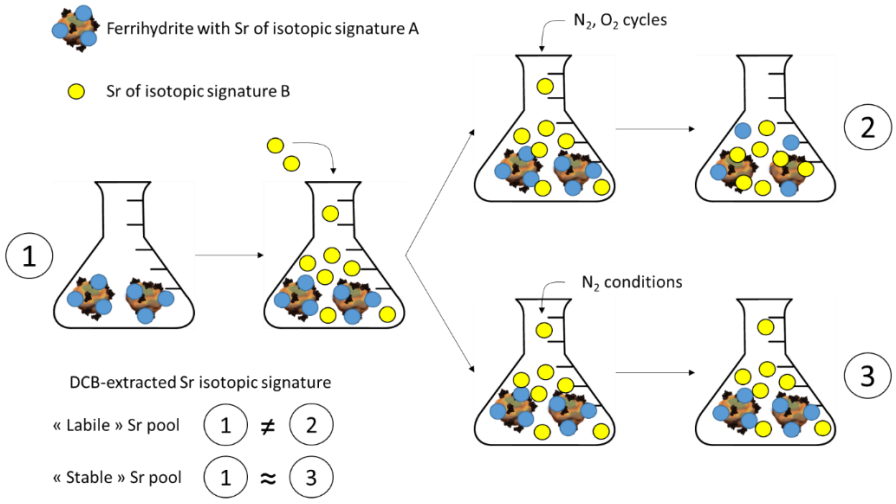

Figure 11.4: Batch experiment schematic to confirm or infirm conclusions from *Ch.5*. Erlenmeyer (1) contains organic carbon associated to ferrihydrite with adsorbed or occluded Sr of isotopic signature A in which we add Sr of contrasted isotopic signature B. In scenario (2), the experiment reproduces fluctuating redox conditions as found at the redox interface of permafrost soils by inducing anaerobic (N_2 atmosphere) and aerobic (O_2 atmosphere) conditions. In scenario (3), the experiment changes to reducing conditions (N_2) corresponding to soil saturated layers. To match findings from *Ch.5*, the results in the Sr isotopic signature from dithionite-citrate-bicarbonate (DCB) extraction should be different between (1) and (2) (i.e., "labile" Sr pool hypothesis) and roughly similar between (1) and (3) (i.e., "stable" Sr pool hypothesis).

GENERAL BIBLIOGRAPHY

Abbott, B.W., Brown, M., Carey, J.C., Ernakovich, J., Frederick, J.M., Guo, L., Hugelius, G., Lee, R.M., Loranty, M.M., Macdonald, R., Mann, P.J., Natali, S.M., Olefeldt, D., Pearson, P., Rec, A., Robards, M., Salmon, V.G., Sayedi, S.S., Schädel, C., Schuur, E.A.G., Shakil, S., Shogren, A.J., Strauss, J., Tank, S.E., Thornton, B.F., Treharne, R., Turetsky, M., Voigt, C., Wright, N., Yang, Y., Zarnetske, J.P., Zhang, Q., Zolkos, S., 2022. We Must Stop Fossil Fuel Emissions to Protect Permafrost Ecosystems. Frontiers in Environmental Science 10. https://doi.org/10.3389/fenvs.2022.889428

Abbott, B.W., Jones, J.B., 2015. Permafrost collapse alters soil carbon stocks, respiration, CH_4, and N_2O in upland tundra. Glob Change Biol 21, 4570–4587. https://doi.org/10.1111/gcb.13069

Aciego, S.M., Bourdon, B., Lupker, M., Rickli, J., 2009. A new procedure for separating and measuring radiogenic isotopes (U, Th, Pa, Ra, Sr, Nd, Hf) in ice cores. Chemical Geology 266, 194–204.

Adhikari, D., Yang, Y., 2015. Selective stabilization of aliphatic organic carbon by iron oxide. Sci Rep 5, 1–7. https://doi.org/10.1038/srep11214

Åkerman, H.J., Johansson, M., 2008. Thawing permafrost and thicker active layers in sub-arctic Sweden. Permafrost Periglac. Process. 19, 279–292. https://doi.org/10.1002/ppp.626

Alekseev, A., Alekseeva, T., Ostroumov, V., Siegert, C., Gradusov, B., 2003. Mineral Transformations in Permafrost-Affected Soils, North Kolyma Lowland, Russia. Soil Science Society of America Journal 67, 596. https://doi.org/10.2136/sssaj2003.0596

Alexander Bentley, R., 2006. Strontium Isotopes from the Earth to the Archaeological Skeleton: A Review. Journal of Archaeological Method and Theory 13, 135–187. https://doi.org/10.1007/s10816-006-9009-x

Andersson, P.S., Wasserburg, G.J., Ingri, J., Stordal, M.C., 1994. Strontium, dissolved and particulate loads in fresh and brackish waters: The Baltic Sea and Mississippi Delta. Earth and Planetary Science Letters 124, 195–210. https://doi.org/10.1016/0012-821X(94)00062-X

Andreev, A.A., Grosse, G., Schirrmeister, L., Kuznetsova, T.V., Kuzmina, S.A., Bobrov, A.A., Tarasov, P.E., Novenko, E.Y., Meyer, H., Derevyagin, A.Y., Kienast, F., Bryantseva, A., Kunitsky, V.V., 2009. Weichselian and Holocene palaeoenvironmental history of the Bol'shoy Lyakhovsky Island, New Siberian Archipelago, Arctic Siberia. Boreas 38, 72–110. https://doi.org/10.1111/j.1502-3885.2008.00039.x

Andreev, A.A., Schirrmeister, L., Siegert, C., Bobrov, A.A., Demske, D., Seiffert, M., Hubberten, H.-W., 2002. Paleoenvironmental Changes in Northeastern Siberia during the Late Quaternary - Evidence from Pollen Records of the Bykovsky Peninsula. Polarforschung 70 13–25.

Angelopoulos, M., Overduin, P.P., Miesner, F., Grigoriev, M.N., Vasiliev, A.A., 2020. Recent advances in the study of Arctic submarine permafrost. Permafrost and Periglac Process ppp.2061. https://doi.org/10.1002/ppp.2061

Anthony, K.M.W., Zimov, S.A., Grosse, G., Jones, M.C., Anthony, P.M., Iii, F.S.C., Finlay, J.C., Mack, M.C., Davydov, S., Frenzel, P., Frolking, S., 2014. A shift of thermokarst lakes from carbon sources to sinks during the Holocene epoch. Nature 511, 452–456. https://doi.org/10.1038/nature13560

Anzelmo, J.A., Lindsay, J.R., 1987. X-ray fluorescence spectrometric analysis of geologic materials Part 1. Principles and instrumentation. J. Chem. Educ. 64, A181. https://doi.org/10.1021/ed064pA181

Audry, S., Pokrovsky, O.S., Shirokova, L.S., Kirpotin, S.N., Dupre, B., 2011. Organic matter mineralization and trace element post-depositional redistribution in Western Siberia thermokarst lake sediments. Biogeosciences 3341–3358. https://doi.org/10.5194/bg-8-3341-2011

Avis, C.A., Weaver, A.J., Meissner, K.J., 2011. Reduction in areal extent of high-latitude wetlands in response to permafrost thaw. Nature Geosci 4, 444–448. https://doi.org/10.1038/ngeo1160

Bagard, M.-L., Schmitt, A.-D., Chabaux, F., Pokrovsky, O.S., Viers, J., Stille, P., Labolle, F., Prokushkin, A.S., 2013. Biogeochemistry of stable Ca and radiogenic Sr isotopes in a larch-covered permafrost-dominated watershed of Central Siberia. Geochimica et Cosmochimica Acta 114, 169–187. https://doi.org/10.1016/j.gca.2013.03.038

Baldock, J.A., Nelson, P.N., 2000. Soil organic matter. CRC press.

Baldock, J.A., Skjemstad, J.O., 2000. Role of the soil matrix and minerals in protecting natural organic materials against biological attack. Organic Geochemistry 31, 697–710. https://doi.org/10.1016/S0146-6380(00)00049-8

Banner, J.L., 2004. Radiogenic isotopes: systematics and applications to earth surface processes and chemical stratigraphy. Earth-Science Reviews 65, 141–194. https://doi.org/10.1016/S0012-8252(03)00086-2

Barber, A., Brandes, J., Leri, A., Lalonde, K., Balind, K., Wirick, S., Wang, J., Gélinas, Y., 2017. Preservation of organic matter in marine sediments by inner-sphere interactions with reactive iron. Sci Rep 7, 366. https://doi.org/10.1038/s41598-017-00494-0

Bartlett, R.J., Ross, D.S., 2005. Chemistry of Redox Processes in Soils, in: Chemical Processes in Soils. John Wiley & Sons, Ltd, pp. 461–487. https://doi.org/10.2136/sssabookser8.c9

Bascomb, C.L., 1968. Distribution of Pyrophosphate-Extractable Iron and Organic Carbon in Soils of Various Groups. Journal of Soil Science 19, 251–268. https://doi.org/10.1111/j.1365-2389.1968.tb01538.x

Baskaran, M. (Ed.), 2011. Handbook of environmental isotope geochemistry, Advances in isotope geochemistry. Springer, Berlin ; New York.

Bataille, C.P., Bowen, G.J., 2012. Mapping 87Sr/86Sr variations in bedrock and water for large scale provenance studies. Chemical Geology 304–305, 39–52. https://doi.org/10.1016/j.chemgeo.2012.01.028

Bataille, C.P., Brennan, S.R., Hartmann, J., Moosdorf, N., Wooller, M.J., Bowen, G.J., 2014. A geostatistical framework for predicting variations in strontium concentrations and isotope ratios in Alaskan rivers. Chemical Geology 389, 1–15. https://doi.org/10.1016/j.chemgeo.2014.08.030

Beal, E.J., House, C.H., Orphan, V.J., 2009. Manganese- and Iron-Dependent Marine Methane Oxidation. Science 325, 184–187. https://doi.org/10.1126/science.1169984

Bell, R.P., 2013. The Proton in Chemistry. Springer Science & Business Media.

Berner, R.A., Lasaga, A.C., Garrels, R.M., 1983. Carbonate-silicate geochemical cycle and its effect on atmospheric carbon dioxide over the past 100 million years. Am. J. Sci. 283, 641–683. https://doi.org/10.2475/ajs.283.7.641

Bhattacharyya, A., Campbell, A.N., Tfaily, M.M., Lin, Y., Kukkadapu, R.K., Silver, W.L., Nico, P.S., Pett-Ridge, J., 2018a. Redox Fluctuations Control the Coupled Cycling of Iron and Carbon in Tropical Forest Soils. Environ. Sci. Technol. 52, 14129–14139. https://doi.org/10.1021/acs.est.8b03408

Bhattacharyya, A., Schmidt, M.P., Stavitski, E., Martínez, C.E., 2018b. Iron speciation in peats: Chemical and spectroscopic evidence for the co-occurrence of ferric and ferrous iron in organic complexes and mineral precipitates. Organic Geochemistry 115, 124–137. https://doi.org/10.1016/j.orggeochem.2017.10.012

Biskaborn, B.K., Herzschuh, U., Bolshiyanov, D.Y., Schwamborn, G., Diekmann, B., 2013. Thermokarst Processes and Depositional Events in a Tundra Lake, Northeastern Siberia: Thermokarst processes in a Siberian tundra lake. Permafrost and Periglacial Processes 24, 160–174. https://doi.org/10.1002/ppp.1769

Biskaborn, B.K., Smith, S.L., Noetzli, J., Matthes, H., Vieira, G., Streletskiy, D.A., Schoeneich, P., Romanovsky, V.E., Lewkowicz, A.G., Abramov, A., Allard, M., Boike, J., Cable, W.L., Christiansen, H.H., Delaloye, R., Diekmann, B., Drozdov, D., Etzelmüller, B., Grosse, G., Guglielmin, M., Ingeman-Nielsen, T., Isaksen, K., Ishikawa, M., Johansson, M., Johannsson, H., Joo, A., Kaverin, D., Kholodov, A., Konstantinov,

P., Kröger, T., Lambiel, C., Lanckman, J.-P., Luo, D., Malkova, G., Meiklejohn, I., Moskalenko, N., Oliva, M., Phillips, M., Ramos, M., Sannel, A.B.K., Sergeev, D., Seybold, C., Skryabin, P., Vasiliev, A., Wu, Q., Yoshikawa, K., Zheleznyak, M., Lantuit, H., 2019. Permafrost is warming at a global scale. Nat Commun 10, 264. https://doi.org/10.1038/s41467-018-08240-4

Blakemore, L.C., Searle, P.L., Daly, B.K., 1981. Methods for chemical analysis of soils. New Zealand Soil Bureau Scientific Report 10 A, second revision 102. https://doi.org/10.7931/DL1-SBSR-10A

Blodau, C., 2002. Carbon cycling in peatlands — A review of processes and controls. Environmental Reviews 10, 111–134.

Bockheim, J.G., 2007. Importance of Cryoturbation in Redistributing Organic Carbon in Permafrost-Affected Soils. Soil Science Society of America Journal 71, 1335. https://doi.org/10.2136/sssaj2006.0414N

Bockheim, J.G., 1995. Permafrost distribution in the southern circumpolar region and its relation to the environment: A review and recommendations for further research. Permafrost and Periglacial Processes 6, 27–45. https://doi.org/10.1002/ppp.3430060105

Bodegom, P.M., Scholten, J.C.M., Stams, A.J.M., 2004. Direct inhibition of methanogenesis by ferric iron. FEMS Microbiology Ecology 49, 261–268. https://doi.org/10.1016/j.femsec.2004.03.017

Boiteau, R.M., Kukkadapu, R., Cliff, J.B., Smallwood, C.R., Kovarik, L., Wirth, M.G., Engelhard, M.H., Varga, T., Dohnalkova, A., Perea, D.E., Wietsma, T., Moran, J.J., Hofmockel, K.S., 2020. Calcareous organic matter coatings sequester siderophores in alkaline soils. Science of The Total Environment 724, 138250. https://doi.org/10.1016/j.scitotenv.2020.138250

Börker, J., Hartmann, J., Amann, T., Romero-Mujalli, G., 2018. Global Unconsolidated Sediments Map Database v1.0 (shapefile and gridded to 0.5° spatial resolution). https://doi.org/10.1594/PANGAEA.884822

Borzenkova, I., Zorita, E., Borisova, O., Kalniņa, L., Kisielienė, D., Koff, T., Kuznetsov, D., Lemdahl, G., Sapelko, T., Stančikaitė, M., Subetto, D., 2015. Climate Change During the Holocene (Past 12,000 Years), in: The BACC II Author Team (Ed.), Second Assessment of Climate Change for the Baltic Sea Basin, Regional Climate Studies. Springer International Publishing, Cham, pp. 25–49. https://doi.org/10.1007/978-3-319-16006-1_2

Bouchard, F., Fortier, D., Paquette, M., Boucher, V., Pienitz, R., Laurion, I., 2020. Thermokarst lake inception and development in syngenetic ice-wedge polygon terrain during a cooling climatic trend, Bylot Island (Nunavut), eastern Canadian Arctic. The Cryosphere 14, 2607–2627. https://doi.org/10.5194/tc-14-2607-2020

Bouchard, F., MacDonald, L.A., Turner, K.W., Thienpont, J.R., Medeiros, A.S., Biskaborn, B.K., Korosi, J., Hall, R.I., Pienitz, R., Wolfe, B.B., 2017. Paleolimnology of thermokarst lakes: a window into permafrost landscape evolution. Arctic Science 3, 91–117. https://doi.org/10.1139/as-2016-0022

Boudot, J.-P., 1992. Relative efficiency of complexed aluminum noncrystalline Al hydroxide, allophane and imogolite in retarding the biodegradation of citric acid. Geoderma 52, 29–39. https://doi.org/10.1016/0016-7061(92)90073-G

Boudot, J.P., Hadj, A.B., Steiman, R., Seigle-Murandi, F., 1989. Biodegradation of synthetic organo-metallic complexes of iron and aluminium with selected metal to carbon ratios. Soil Biology and Biochemistry 21, 961–966.

Brennan, S.R., Fernandez, D.P., Mackey, G., Cerling, T.E., Bataille, C.P., Bowen, G.J., Wooller, M.J., 2014. Strontium isotope variation and carbonate versus silicate weathering in rivers from across Alaska: Implications for provenance studies. Chemical Geology 389, 167–181. https://doi.org/10.1016/j.chemgeo.2014.08.018

Breton, J., Vallières, C., Laurion, I., 2009. Limnological properties of permafrost thaw ponds in northeastern Canada. Can. J. Fish. Aquat. Sci. 66, 1635–1648. https://doi.org/10.1139/F09-108

Bridgham, S.D., Updegraff, K., Pastor, J., 1998. Carbon, nitrogen, and phosphorus mineralization in northern wetlands. Ecology 79, 1545–1561.

Bring, A., Fedorova, I., Dibike, Y., Hinzman, L., Mård, J., Mernild, S.H., Prowse, T., Semenova, O., Stuefer, S.L., Woo, M.-K., 2016. Arctic terrestrial hydrology: A synthesis of processes, regional effects, and research challenges: Arctic Terrestrial Hydrology. J. Geophys. Res. Biogeosci. 121, 621–649. https://doi.org/10.1002/2015JG003131

Brosius, L.S., Anthony, K.M.W., Treat, C.C., Lenz, J., Jones, M.C., Bret-Harte, M.S., Grosse, G., 2021. Spatiotemporal patterns of northern lake formation since the Last Glacial Maximum. Quaternary Science Reviews 253, 106773. https://doi.org/10.1016/j.quascirev.2020.106773

Brown, J., Ferrians, O.J., Heginbottom, J.A., Melnikov, E.S., Akerman, J., 1998. Circum-Arctic map of permafrost and ground-ice conditions. Circum-Pacific Map Series CP-45, scale 1:10,000,000, Tech. rep.,. U.S.Geological Survey in Cooperation with the Circum-Pacific Council for Energy and Mineral Resources., Washington, DC,. https://doi.org/10.13140/RG.2.1.2994.9040

Brunner, W., Blaser, P., 1989. Mineralization of Soil Organic Matter and Added Carbon Substrates in Two Acidic Soils with High non-exchangeable Aluminum. Zeitschrift für Pflanzenernährung und Bodenkunde 152, 367–372. https://doi.org/10.1002/jpln.19891520405

Bullen, T., Chadwick, O., 2016. Ca, Sr and Ba stable isotopes reveal the fate of soil nutrients along a tropical climosequence in Hawaii. Chemical Geology 422, 25–45. https://doi.org/10.1016/j.chemgeo.2015.12.008

Burn, C.R., 2013. PERMAFROST AND PERIGLACIAL FEATURES | Thermokarst Topography, in: Elias, S.A., Mock, C.J. (Eds.), Encyclopedia of Quaternary Science (Second Edition). Elsevier, Amsterdam, pp. 574–581. https://doi.org/10.1016/B978-0-444-53643-3.00091-1

Canadell, J.G., Monteiro, P.M.S., Costa, M.H., Cotrim da Cunha, L., Cox, P.M., Eliseev, A.V., Henson, S., Ishii, M., Jaccard, S., Koven, C., Lohila, A., Patra, P.K., Piao, S., Rogelj, J., Syampungani, S., Zaehle, S., Zickfeld, K., 2021. Global Carbon and other Biogeochemical Cycles and Feedbacks, in: Masson-Delmotte, V., Zhai, P., Pirani, A., Connors, S.L., Péan, C., Berger, S., Caud, N., Chen, Y., Goldfarb, L., Gomis, M.I., Huang, M., Leitzell, K., Lonnoy, E., Matthews, J.B.R., Maycock, T.K., Waterfield, T., Yelekçi, O., Yu, R., Zhou, B. (Eds.), Climate Change 2021: The Physical Science Basis. Contribution of Working Group I to the Sixth Assessment Report of the Intergovernmental Panel on Climate Change. Cambridge University Press, Cambridge, United Kingdom and New York, NY, USA, pp. 673–816. https://doi.org/10.1017/9781009157896.007

Capo, R.C., Stewart, B.W., Chadwick, O.A., 1998. Strontium isotopes as tracers of ecosystem processes: theory and methods. Geoderma 82, 197–225. https://doi.org/10.1016/S0016-7061(97)00102-X

Catrouillet, C., Davranche, M., Dia, A., Bouhnik-Le Coz, M., Marsac, R., Pourret, O., Gruau, G., 2014. Geochemical modeling of Fe(II) binding to humic and fulvic acids. Chemical Geology 372, 109–118. https://doi.org/10.1016/j.chemgeo.2014.02.019

Chadwick, O.A., Derry, L.A., Bern, C.R., Vitousek, P.M., 2009. Changing sources of strontium to soils and ecosystems across the Hawaiian Islands. Chemical Geology 267, 64–76.

Chao, T.T., 1972. Selective Dissolution of Manganese Oxides from Soils and Sediments with Acidified Hydroxylamine Hydrochloride. Soil Science Society of America Journal 36, 764–768. https://doi.org/10.2136/sssaj1972.03615995003600050024x

Chao, T.T., Sanzolone, R.F., 1992. Decomposition techniques. J. Geochem. Explor. 65–106.

Chen, C., Dynes, J.J., Wang, J., Sparks, D.L., 2014. Properties of Fe-Organic Matter Associations via Coprecipitation versus Adsorption. Environ. Sci. Technol. 48, 13751–13759. https://doi.org/10.1021/es503669u

Chen, C., Hall, S.J., Coward, E., Thompson, A., 2020. Iron-mediated organic matter decomposition in humid soils can counteract protection. Nat Commun 11, 2255. https://doi.org/10.1038/s41467-020-16071-5

Chen, C., Thompson, A., 2018. Ferrous Iron Oxidation under Varying pO2 Levels: The Effect of Fe(III)/Al(III) Oxide Minerals and Organic Matter. Environ. Sci. Technol. 52, 597–606. https://doi.org/10.1021/acs.est.7b05102

Chen, Q., Zhang, P., Hu, Z., Li, S., Zhang, Y., Hu, L., Zhou, L., Lin, B., Li, X., 2022. Soil Organic Carbon and Geochemical Characteristics on Different Rocks and Their Significance for Carbon Cycles. Frontiers in Environmental Science 9.

Climate-data.org, 2022. Climate data for cities worldwide [WWW Document]. URL https://en.climate-data.org/asia/russian-federation/sakha-republic/yakutsk-1806/

Colombo, C., Palumbo, G., He, J.-Z., Pinton, R., Cesco, S., 2014. Review on iron availability in soil: interaction of Fe minerals, plants, and microbes. J Soils Sediments 14, 538–548. https://doi.org/10.1007/s11368-013-0814-z

Colombo, C., Torrent, J., 1991. Relationships between aggregation and iron oxides in Terra Rossa soils from southern Italy. CATENA 18, 51–59. https://doi.org/10.1016/0341-8162(91)90006-J

Cornelis, J.-T., Delvaux, B., Georg, R.B., Lucas, Y., Ranger, J., Opfergelt, S., 2011. Tracing the origin of dissolved silicon transferred from various soil-plant systems towards rivers: a review. Biogeosciences 8, 89–112. https://doi.org/10.5194/bg-8-89-2011

Cornell, R.M., Schwertmann, U., 2003. The iron oxides: structure, properties, reactions, occurrences and uses. John Wiley & Sons.

Côté, M.M., Burn, C.R., 2002. The oriented lakes of Tuktoyaktuk Peninsula, Western Arctic Coast, Canada: a GIS-based analysis. Permafrost and Periglacial Processes 13, 61–70. https://doi.org/10.1002/ppp.407

Crumbliss, A.L., Garrison, J.M., 1988. A Comparison of Some Aspects of the Aqueous Coordination Chemistry of Aluminum(III) and Iron(III). Comments on Inorganic Chemistry 8, 1–26. https://doi.org/10.1080/02603598808048670

Cudennec, Y., Lecerf, A., 2006. The transformation of ferrihydrite into goethite or hematite, revisited. Journal of Solid State Chemistry 179, 716–722. https://doi.org/10.1016/j.jssc.2005.11.030

DalCorso, G., Manara, A., Piasentin, S., Furini, A., 2014. Nutrient metal elements in plants. Metallomics 6, 1770–1788. https://doi.org/10.1039/c4mt00173g

Daly, B.K., 1982. Identification of podzols and podzolised soils in New Zealand by relative absorbance of oxalate extracts of A and B horizons. Geoderma 28, 29–38. https://doi.org/10.1016/0016-7061(82)90038-6

Davis, C.C., Edwards, M., 2017. Role of Calcium in the Coagulation of NOM with Ferric Chloride. Environ. Sci. Technol. 51, 11652–11659. https://doi.org/10.1021/acs.est.7b02038

Derry, L.A., Chadwick, O.A., 2007. Contributions from Earth's atmosphere to soil. Elements 3, 333–338.

Dobricic, S., Pozzoli, L., 2019. Arctic permafrost thawing : impacts on high latitude emissions of carbon dioxide and methane, Luxembourg: Publications Office of the European Union. Publications Office. https://doi.org/10.2760/007066

Drouet, T., Herbauts, J., Gruber, W., Demaiffe, D., 2007. Natural strontium isotope composition as a tracer of weathering patterns and of exchangeable calcium sources in acid leached soils developed on loess of central Belgium. European Journal of Soil Science 58, 302–319. https://doi.org/10.1111/j.1365-2389.2006.00840.x

Dutta, K., Schuur, E.A.G., Neff, J.C., Zimov, S.A., 2006. Potential carbon release from permafrost soils of Northeastern Siberia. Global Change Biol 12, 2336–2351. https://doi.org/10.1111/j.1365-2486.2006.01259.x

Eglinton, T.I., 2012. A rusty carbon sink. Nature 483, 165–166. https://doi.org/10.1038/483165a

Ernakovich, J.G., Lynch, L.M., Brewer, P.E., Calderon, F.J., Wallenstein, M.D., 2017. Redox and temperature-sensitive changes in microbial communities and soil chemistry

dictate greenhouse gas loss from thawed permafrost. Biogeochemistry 134, 183–200. https://doi.org/10.1007/s10533-017-0354-5
Estes, E.R., Andeer, P.F., Nordlund, D., Wankel, S.D., Hansel, C.M., 2017. Biogenic manganese oxides as reservoirs of organic carbon and proteins in terrestrial and marine environments. Geobiology 15, 158–172. https://doi.org/10.1111/gbi.12195
Eusterhues, K., Rumpel, C., Kögel-Knabner, I., 2005. Organo-mineral associations in sandy acid forest soils: importance of specific surface area, iron oxides and micropores. European Journal of Soil Science 56, 753–763. https://doi.org/10.1111/j.1365-2389.2005.00710.x
Eusterhues, K., Wagner, F.E., Häusler, W., Hanzlik, M., Knicker, H., Totsche, K.U., Kögel-Knabner, I., Schwertmann, U., 2008. Characterization of Ferrihydrite-Soil Organic Matter Coprecipitates by X-ray Diffraction and Mössbauer Spectroscopy. Environ. Sci. Technol. 42, 7891–7897. https://doi.org/10.1021/es800881w
Faure, G., 1977. Principles of isotope geology.
Faure, G., Mensing, T.M., 2005. Principles and applications. John Wiley & Sons, Inc.
Faure, G., Powell, J.L., 1972. Strontium Isotope Geology, Minerals, Rocks and Mountains. Springer-Verlag, Berlin Heidelberg. https://doi.org/10.1007/978-3-642-65367-4
Fedorov, A.N., Gavriliev, P.P., Konstantinov, P.Y., Hiyama, T., Iijima, Y., Iwahana, G., 2014. Estimating the water balance of a thermokarst lake in the middle of the Lena River basin, eastern Siberia. Ecohydrology 7, 188–196.
Fiedler, S., Sommer, M., 2004. Water and Redox Conditions in Wetland Soils—Their Influence on Pedogenic Oxides and Morphology. SOIL SCI. SOC. AM. J. 68, 10.
Fiedler, S., Wagner, D., Kutzbach, L., Pfeiffer, E.-M., 2004. Element Redistribution along Hydraulic and Redox Gradients of Low-Centered Polygons, Lena Delta, Northern Siberia. Soil Sci. Soc. Am. J. 68, 1002–1011. https://doi.org/10.2136/sssaj2004.1002
Fouché, J., Christiansen, C., Lafreniere, M., Grogan, P., Lamoureux, S., 2020. Canadian permafrost stores large pools of ammonium and optically distinct dissolved organic matter. Nature Communications 11, 4500. https://doi.org/10.1038/s41467-020-18331-w
French, H.M., 2007. The Periglacial Environment, 3rd ed. John Wiley and Sons. ed. Chichester, England.
French, H.M., Millar, S.W.S., 2014. Permafrost at the time of the Last Glacial Maximum (LGM) in North America: LGM permafrost in North America. Boreas 43, 667–677. https://doi.org/10.1111/bor.12036
Friedlingstein, P., Jones, M.W., O'Sullivan, M., Andrew, R.M., Bakker, D.C.E., Hauck, J., Le Quéré, C., Peters, G.P., Peters, W., Pongratz, J., Sitch, S., Canadell, J.G., Ciais, P., Jackson, R.B., Alin, S.R., Anthoni, P., Bates, N.R., Becker, M., Bellouin, N., Bopp, L., Chau, T.T.T., Chevallier, F., Chini, L.P., Cronin, M., Currie, K.I., Decharme, B., Djeutchouang, L.M., Dou, X., Evans, W., Feely, R.A., Feng, L., Gasser, T., Gilfillan, D., Gkritzalis, T., Grassi, G., Gregor, L., Gruber, N., Gürses, Ö., Harris, I., Houghton, R.A., Hurtt, G.C., Iida, Y., Ilyina, T., Luijkx, I.T., Jain, A., Jones, S.D., Kato, E., Kennedy, D., Klein Goldewijk, K., Knauer, J., Korsbakken, J.I., Körtzinger, A., Landschützer, P., Lauvset, S.K., Lefèvre, N., Lienert, S., Liu, J., Marland, G., McGuire, P.C., Melton, J.R., Munro, D.R., Nabel, J.E.M.S., Nakaoka, S.-I., Niwa, Y., Ono, T., Pierrot, D., Poulter, B., Rehder, G., Resplandy, L., Robertson, E., Rödenbeck, C., Rosan, T.M., Schwinger, J., Schwingshackl, C., Séférian, R., Sutton, A.J., Sweeney, C., Tanhua, T., Tans, P.P., Tian, H., Tilbrook, B., Tubiello, F., van der Werf, G.R., Vuichard, N., Wada, C., Wanninkhof, R., Watson, A.J., Willis, D., Wiltshire, A.J., Yuan, W., Yue, C., Yue, X., Zaehle, S., Zeng, J., 2022. Global Carbon Budget 2021. Earth System Science Data 14, 1917–2005. https://doi.org/10.5194/essd-14-1917-2022
Friedlingstein, P., O'Sullivan, M., Jones, M.W., Andrew, R.M., Hauck, J., Olsen, A., Peters, G.P., Peters, W., Pongratz, J., Sitch, S., Le Quéré, C., Canadell, J.G., Ciais, P., Jackson, R.B., Alin, S., Aragão, L.E.O.C., Arneth, A., Arora, V., Bates, N.R., Becker, M., Benoit-Cattin, A., Bittig, H.C., Bopp, L., Bultan, S., Chandra, N., Chevallier, F.,

Chini, L.P., Evans, W., Florentie, L., Forster, P.M., Gasser, T., Gehlen, M., Gilfillan, D., Gkritzalis, T., Gregor, L., Gruber, N., Harris, I., Hartung, K., Haverd, V., Houghton, R.A., Ilyina, T., Jain, A.K., Joetzjer, E., Kadono, K., Kato, E., Kitidis, V., Korsbakken, J.I., Landschützer, P., Lefèvre, N., Lenton, A., Lienert, S., Liu, Z., Lombardozzi, D., Marland, G., Metzl, N., Munro, D.R., Nabel, J.E.M.S., Nakaoka, S.-I., Niwa, Y., O'Brien, K., Ono, T., Palmer, P.I., Pierrot, D., Poulter, B., Resplandy, L., Robertson, E., Rödenbeck, C., Schwinger, J., Séférian, R., Skjelvan, I., Smith, A.J.P., Sutton, A.J., Tanhua, T., Tans, P.P., Tian, H., Tilbrook, B., van der Werf, G., Vuichard, N., Walker, A.P., Wanninkhof, R., Watson, A.J., Willis, D., Wiltshire, A.J., Yuan, W., Yue, X., Zaehle, S., 2020. Global Carbon Budget 2020. Earth System Science Data 12, 3269–3340. https://doi.org/10.5194/essd-12-3269-2020

Fritsch, E., Allard, T., Benedetti, M.F., Bardy, M., do Nascimento, N.R., Li, Y., Calas, G., 2009. Organic complexation and translocation of ferric iron in podzols of the Negro River watershed. Separation of secondary Fe species from Al species. Geochimica et Cosmochimica Acta 73, 1813–1825. https://doi.org/10.1016/j.gca.2009.01.008

Fritz, M., Opel, T., Tanski, G., Herzschuh, U., Meyer, H., Eulenburg, A., Lantuit, H., 2015. Dissolved organic carbon (DOC) in Arctic ground ice. The Cryosphere 9, 737–752. https://doi.org/10.5194/tc-9-737-2015

Fritz, M., Unkel, I., Lenz, J., Gajewski, K., Frenzel, P., Paquette, N., Lantuit, H., Körte, L., Wetterich, S., 2018. Regional environmental change versus local signal preservation in Holocene thermokarst lake sediments: A case study from Herschel Island, Yukon (Canada). Journal of Paleolimnology 60, 77–96. https://doi.org/10.1007/s10933-018-0025-0

Fritz, M., Wetterich, S., Meyer, H., Schirrmeister, L., Lantuit, H., Pollard, W.H., 2011. Origin and characteristics of massive ground ice on Herschel Island (western Canadian Arctic) as revealed by stable water isotope and Hydrochemical signatures: Origin and Characteristics of Massive Ground Ice on Herschel Island. Permafrost Periglac. Process. 22, 26–38. https://doi.org/10.1002/ppp.714

Fuchs, M., Grosse, G., Strauss, J., Günther, F., Grigoriev, M., Maximov, G.M., Hugelius, G., 2018. Carbon and nitrogen pools in thermokarst-affected permafrost landscapes in Arctic Siberia. Biogeosciences 15, 953–971. https://doi.org/10.5194/bg-15-953-2018

Fuchs, M., Lenz, J., Jock, S., Nitze, I., Jones, B.M., Strauss, J., Günther, F., Grosse, G., 2019. Organic Carbon and Nitrogen Stocks Along a Thermokarst Lake Sequence in Arctic Alaska. J. Geophys. Res. Biogeosci. 2018JG004591. https://doi.org/10.1029/2018JG004591

Fuchs, M., Nitze, I., Strauss, J., Günther, F., Wetterich, S., Kizyakov, A., Opel, T., Grigoriev, M.N., Maximov, G.M., Grosse, G., 2020. Rapid fluvio-thermal erosion of a yedoma permafrost cliff in the Lena River Delta (accepted). Front. Earth Sci., Frontiers in Earth Science.

Garnello, A., Marchenko, S., Nicolsky, D., Romanovsky, V., Ledman, J., Celis, G., Schädel, C., Luo, Y., Schuur, E. a. G., 2021. Projecting Permafrost Thaw of Sub-Arctic Tundra With a Thermodynamic Model Calibrated to Site Measurements. Journal of Geophysical Research: Biogeosciences 126, e2020JG006218. https://doi.org/10.1029/2020JG006218

Gasser, T., Kechiar, M., Ciais, P., Burke, E.J., Kleinen, T., Zhu, D., Huang, Y., Ekici, A., Obersteiner, M., 2018. Path-dependent reductions in CO2 emission budgets caused by permafrost carbon release. Nature Geosci 11, 830–835. https://doi.org/10.1038/s41561-018-0227-0

Genet, H., McGuire, A.D., Barrett, K., Breen, A., Euskirchen, E.S., Johnstone, J.F., Kasischke, E.S., Melvin, A.M., Bennett, A., Mack, M.C., Rupp, T.S., Schuur, A.E.G., Turetsky, M.R.M.R., Yuan, F., 2013. Modeling the effects of fire severity and climate warming on active layer thickness and soil carbon storage of black spruce forests across the landscape in interior Alaska. Environmental Research Letters 8. https://doi.org/10.1088/1748-9326/8/4/045016

Gentsch, N., Mikutta, R., Alves, R.J.E., Barta, J., Čapek, P., Gittel, A., Hugelius, G., Kuhry, P., Lashchinskiy, N., Palmtag, J., Richter, A., Šantrůčková, H., Schnecker, J., Shibistova, O., Urich, T., Wild, B., Guggenberger, G., 2015a. Storage and transformation of organic matter fractions in cryoturbated permafrost soils across the Siberian Arctic. Biogeosciences 12, 4525–4542. https://doi.org/10.5194/bg-12-4525-2015

Gentsch, N., Mikutta, R., Shibistova, O., Wild, B., Schnecker, J., Richter, A., Urich, T., Gittel, A., Šantrůčková, H., Bárta, J., Lashchinskiy, N., Mueller, C.W., Fuß, R., Guggenberger, G., 2015b. Properties and bioavailability of particulate and mineral-associated organic matter in Arctic permafrost soils, Lower Kolyma Region, Russia: Organic matter stabilization in permafrost soils. European Journal of Soil Science 66, 722–734. https://doi.org/10.1111/ejss.12269

Gentsch, N., Wild, B., Mikutta, R., Čapek, P., Diáková, K., Schrumpf, M., Turner, S., Minnich, C., Schaarschmidt, F., Shibistova, O., Schnecker, J., Urich, T., Gittel, A., Šantrůčková, H., Bárta, J., Lashchinskiy, N., Fuß, R., Richter, A., Guggenberger, G., 2018. Temperature response of permafrost soil carbon is attenuated by mineral protection. Global Change Biology 24, 3401–3415. https://doi.org/10.1111/gcb.14316

Giesler, R., Andersson, T., Lövgren, L., Persson, P., 2005. Phosphate Sorption in Aluminum- and Iron-Rich Humus Soils. Soil Sci. Soc. Am. J. 69, 77–86. https://doi.org/10.2136/sssaj2005.0077a

Goldich, S.S., 1938. A Study in Rock-Weathering. The Journal of Geology 46, 17–58. https://doi.org/10.1086/624619

Gorokhov, A.N., Fedorov, A.N., 2018. Current Trends in Climate Change in Yakutia. Geogr. Nat. Resour. 39, 153–161. https://doi.org/10.1134/S1875372818020087

Grant, K.E., Galy, V.V., Haghipour, N., Eglinton, T.I., Derry, L.A., 2022. Persistence of old soil carbon under changing climate: The role of mineral-organic matter interactions. Chemical Geology 587, 120629. https://doi.org/10.1016/j.chemgeo.2021.120629

Graustein, W.C., Armstrong, R.L., 1983. The use of strontium-87/strontium-86 ratios to measure atmospheric transport into forested watersheds. Science 219, 289–292.

Grigoriev, M.N., Rachold, V., Bolshiyanov, D., 2003. Russian-German cooperation System Laptev Sea : the expedition LENA 2002 , Berichte zur Polar- und Meeresforschung (Reports on Polar and Marine Research), Alfred Wegener Institute for Polar and Marine Research 466, 341 p. https://doi.org/10.2312/BzPM_0466_2003

Grosse, G., Harden, J., Turetsky, M., McGuire, A.D., Camill, P., Tarnocai, C., Frolking, S., Schuur, E.A.G., Jorgenson, T., Marchenko, S., Romanovsky, V., Wickland, K.P., French, N., Waldrop, M., Bourgeau-Chavez, L., Striegl, R.G., 2011. Vulnerability of high-latitude soil organic carbon in North America to disturbance. J. Geophys. Res. 116, G00K06. https://doi.org/10.1029/2010JG001507

Grosse, G., Jones, B., Arp, C., 2013. 8.21 Thermokarst Lakes, Drainage, and Drained Basins, in: Treatise on Geomorphology. Elsevier, pp. 325–353. https://doi.org/10.1016/B978-0-12-374739-6.00216-5

Grosse, G., Jones, B.M., Schirrmeister, L., Meyer, H., Wetterich, S., Strauss, J., Gaglioti, B.V., Mann, D.H., Romanovsky, V.E., 2015. Late Pleistocene and Holocene ice-rich permafrost in the Colville River valley, northern Alaska, in: EPIC3PAST Gateways 2015, Potsdam, 18 May 2015 - 22 May 2015, Geophysical Research Abstracts. Presented at the PAST Gateways 2015, EGU2015-10607, Potsdam.

Grosse, G., Schirrmeister, L., Siegert, C., Kunitsky, V.V., Slagoda, E.A., Andreev, A.A., Dereviagyn, A.Y., 2007. Geological and geomorphological evolution of a sedimentary periglacial landscape in Northeast Siberia during the Late Quaternary. Geomorphology 86, 25–51. https://doi.org/10.1016/j.geomorph.2006.08.005

Grotzinger, J., Jordan, T.H., 2010. Understanding Earth, 6th edition. ed. W.H. Freeman and Company, New York.

Grybos, M., Davranche, M., Gruau, G., Petitjean, P., Pédrot, M., 2009. Increasing pH drives organic matter solubilization from wetland soils under reducing conditions. Geoderma 154, 13–19. https://doi.org/10.1016/j.geoderma.2009.09.001

Gundelwein, A., Müller-Lupp, T., Sommerkorn, M., Haupt, E.T.K., Pfeiffer, E.-M., Wiechmann, H., 2007. Carbon in tundra soils in the Lake Labaz region of arctic Siberia. Eur J Soil Science 58, 1164–1174. https://doi.org/10.1111/j.1365-2389.2007.00908.x

Günther, F., Overduin, P.P., Yakshina, I.A., Opel, T., Baranskaya, A.V., Grigoriev, M.N., 2015. Observing Muostakh disappear: permafrost thaw subsidence and erosion of a ground-ice-rich island in response to arctic summer warming and sea ice reduction. The Cryosphere 9, 151–178. https://doi.org/10.5194/tc-9-151-2015

Gupta, D.K., Deb, U., Walther, C., Chatterjee, S., 2018. Strontium in the Ecosystem: Transfer in Plants via Root System, in: Gupta, D.K., Walther, C. (Eds.), Behaviour of Strontium in Plants and the Environment. Springer International Publishing, Cham, pp. 1–18. https://doi.org/10.1007/978-3-319-66574-0_1

Gustafsson, J.P., 2011. Visual MINTEQ Version 3.1: A windows version of MINTEQA2.

Hajj, F., Poszwa, A., Bouchez, J., Guérold, F., 2017. Radiogenic and "stable" strontium isotopes in provenance studies: A review and first results on archaeological wood from shipwrecks. Journal of Archaeological Science 86, 24–49. https://doi.org/10.1016/j.jas.2017.09.005

Hall, S.J., Thompson, A., 2022. What do relationships between extractable metals and soil organic carbon concentrations mean? Soil Science Soc of Amer J 86, 195–208. https://doi.org/10.1002/saj2.20343

Harden, J.W., Koven, C.D., Ping, C.-L., Hugelius, G., McGuire, A.D., Camill, P., Jorgenson, T., Kuhry, P., Michaelson, G.J., O'Donnell, J.A., Schuur, E.A.G., Tarnocai, C., Johnson, K., Grosse, G., 2012. Field information links permafrost carbon to physical vulnerabilities of thawing. Geophysical Research Letters 39. https://doi.org/10.1029/2012GL051958

Hartmann, J., Moosdorf, N., 2012. Global Lithological Map Database v1.0 (gridded to 0.5° spatial resolution). https://doi.org/10.1594/PANGAEA.788537

Hedges, J.I., Keil, R.G., 1999. Organic geochemical perspectives on estuarine processes: sorption reactions and consequences. Marine Chemistry 65, 55–65. https://doi.org/10.1016/S0304-4203(99)00010-9

Hemingway, J.D., Rothman, D.H., Grant, K.E., Rosengard, S.Z., Eglinton, T.I., Derry, L.A., Galy, V.V., 2019. Mineral protection regulates long-term global preservation of natural organic carbon. Nature 570, 228–231. https://doi.org/10.1038/s41586-019-1280-6

Herbillon, A.J., 1986. Chemical estimation of weatherable minerals present in the diagnostic horizons of low activity clay soils, in: Proceedings of the 8th International Clay Classification Workshop: Classification, Characterization and Utilization of Oxisols (Part 1)[Beinroth, FH, Camargo, MN and Eswaran (Ed.)][39–48](Rio de Janeiro, 1986).

Herndon, E., AlBashaireh, A., Singer, D., Roy Chowdhury, T., Gu, B., Graham, D., 2017. Influence of iron redox cycling on organo-mineral associations in Arctic tundra soil. Geochimica et Cosmochimica Acta 207, 210–231. https://doi.org/10.1016/j.gca.2017.02.034

Herndon, E., Kinsman-Costello, L., Di Dominico, N., Duroe, K.A., Barczok, M., Smith, C., Wullschleger, S.D., 2020a. Iron and iron-bound phosphate accumulate in surface soils of ice-wedge polygons in arctic tundra. Environ. Sci.: Processes Impacts 20, 747–756. https://doi.org/10.1039/D0EM00142B

Herndon, E., Kinsman-Costello, L., Godsey, S., 2020b. Biogeochemical Cycling of Redox-Sensitive Elements in Permafrost-Affected Ecosystems, in: Dontsova, K., Balogh-Brunstad, Z., Le Roux, G. (Eds.), Geophysical Monograph Series. Wiley, pp. 245–265. https://doi.org/10.1002/9781119413332.ch12

Herndon, E.M., 2018. Permafrost slowly exhales methane. Nature Clim Change 8, 273–274. https://doi.org/10.1038/s41558-018-0129-6

Herndon, E.M., Kinsman-Costello, L., Duroe, K.A., Mills, J., Kane, E.S., Sebestyen, S.D., Thompson, A.A., Wullschleger, S.D., 2019. Iron (Oxyhydr)Oxides Serve as

Phosphate Traps in Tundra and Boreal Peat Soils. J. Geophys. Res. Biogeosci. 124, 227–246. https://doi.org/10.1029/2018JG004776
Herndon, E.M., Mann, B.F., Roy Chowdhury, T., Yang, Z., Wullschleger, S.D., Graham, D., Liang, L., Gu, B., 2015. Pathways of anaerobic organic matter decomposition in tundra soils from Barrow, Alaska: Biogeochemistry Of Anoxic Arctic Tundra. J. Geophys. Res. Biogeosci. 120, 2345–2359. https://doi.org/10.1002/2015JG003147
Hicks Pries, C.E., Schuur, E.A.G., Crummer, K.G., 2012. Holocene Carbon Stocks and Carbon Accumulation Rates Altered in Soils Undergoing Permafrost Thaw. Ecosystems 15, 162–173. https://doi.org/10.1007/s10021-011-9500-4
Hinkel, K.M., Jones, B.M., Eisner, W.R., Cuomo, C.J., Beck, R.A., Frohn, R., 2007. Methods to assess natural and anthropogenic thaw lake drainage on the western Arctic coastal plain of northern Alaska. Journal of Geophysical Research: Earth Surface 112.
Hirst, C., Mauclet, E., Monhonval, A., Tihon, E., Ledman, J., Schuur, E.A.G., Opfergelt, S., 2022. Seasonal Changes in Hydrology and Permafrost Degradation Control Mineral Element-Bound DOC Transport From Permafrost Soils to Streams. Global Biogeochemical Cycles 36, e2021GB007105. https://doi.org/10.1029/2021GB007105
Hodson, M.E., 2002. Experimental evidence for mobility of Zr and other trace elements in soils. Geochimica et Cosmochimica Acta 66, 819–828. https://doi.org/10.1016/S0016-7037(01)00803-1
Höfle, S., Rethemeyer, J., Mueller, C.W., John, S., 2013. Organic matter composition and stabilization in a polygonal tundra soil of the Lena Delta. Biogeosciences 10, 3145–3158. https://doi.org/10.5194/bg-10-3145-2013
Holland, H.D., 2020. The chemical evolution of the atmosphere and oceans. Princeton University Press.
Huang, W., Hall, S.J., 2017. Elevated moisture stimulates carbon loss from mineral soils by releasing protected organic matter. Nat Commun 8, 1–10. https://doi.org/10.1038/s41467-017-01998-z
Hugelius, G., Bockheim, J.G., Camill, P., Elberling, B., Grosse, G., Harden, J.W., Johnson, K., Jorgenson, T., Koven, C.D., Kuhry, P., Michaelson, G., Mishra, U., Palmtag, J., Ping, C.-L., O'Donnell, J., Schirrmeister, L., Schuur, E.A.G., Sheng, Y., Smith, L.C., Strauss, J., Yu, Z., 2013. A new data set for estimating organic carbon storage to 3 m depth in soils of the northern circumpolar permafrost region. Earth System Science Data 5, 393–402. https://doi.org/10.5194/essd-5-393-2013
Hugelius, G., Loisel, J., Chadburn, S., Jackson, R.B., Jones, M., MacDonald, G., Marushchak, M., Olefeldt, D., Packalen, M., Siewert, M.B., Treat, C., Turetsky, M., Voigt, C., Yu, Z., 2020. Large stocks of peatland carbon and nitrogen are vulnerable to permafrost thaw. PNAS 117, 20438–20446. https://doi.org/10.1073/pnas.1916387117
Hugelius, G., Strauss, J., Zubrzycki, S., Harden, J.W., Schuur, E.A.G., Ping, C.-L., Schirrmeister, L., Grosse, G., Michaelson, G.J., Koven, C.D., O'Donnell, J.A., Elberling, B., Mishra, U., Camill, P., Yu, Z., Palmtag, J., Kuhry, P., 2014. Estimated stocks of circumpolar permafrost carbon with quantified uncertainty ranges and identified data gaps. Biogeosciences 11, 6573–6593. https://doi.org/10.5194/bg-11-6573-2014
Hughes-Allen, L., Bouchard, F., Laurion, I., Séjourné, A., Marlin, C., Hatté, C., Costard, F., Fedorov, A., Desyatkin, A., 2021. Seasonal patterns in greenhouse gas emissions from thermokarst lakes in Central Yakutia (Eastern Siberia). Limnology and Oceanography 66, S98–S116. https://doi.org/10.1002/lno.11665
Hutchings, J.A., Bianchi, T.S., Kaufman, D.S., Kholodov, A.L., Vaughn, D.R., Schuur, E.A.G., 2019. Millennial-scale carbon accumulation and molecular transformation in a permafrost core from Interior Alaska. Geochimica et Cosmochimica Acta 253, 231–248. https://doi.org/10.1016/j.gca.2019.03.028
Inagaki, T.M., Possinger, A.R., Grant, K.E., Schweizer, S.A., Mueller, C.W., Derry, L.A., Lehmann, J., Kögel-Knabner, I., 2020. Subsoil organo-mineral associations under

contrasting climate conditions. Geochimica et Cosmochimica Acta 270, 244–263. https://doi.org/10.1016/j.gca.2019.11.030

International Centre for Diffraction Data, 2013. Be confident with pdf2 [WWW Document]. URL http://www.icdd.com/products/technicalbulletins/PDF-2_Technical_%20Bulletin.pdf (accessed 6.20.20).

IPCC, 2022. Climate Change 2022: Impacts, Adaptation, and Vulnerability. Contribution of Working Group II to the Sixth Assessment Report of the Intergovernmental Panel on Climate Change, H.-O. Pörtner, D.C. Roberts, M. Tignor, E.S. Poloczanska, K. Mintenbeck, A. Alegría, M. Craig, S. Langsdorf, S. Löschke, V. Möller, A. Okem, B. Rama (eds.)]. Cambridge University Press. In Press.

IPCC, 2021. Summary for Policymakers. In: Climate Change 2021: The Physical Science Basis. Contribution of Working Group I to the Sixth Assessment Report of the Intergovernmental Panel on Climate Change [Masson-Delmotte, V., P. Zhai, A. Pirani, S. L. Connors, C. Péan, S. Berger, N. Caud, Y. Chen, L. Goldfarb, M. I. Gomis, M. Huang, K. Leitzell, E. Lonnoy, J.B.R. Matthews, T. K. Maycock, T. Waterfield, O. Yelekçi, R. Yu and B. Zhou (eds.)]. Cambridge University Press. In Press.

IPCC, 2019. Special Report on the Ocean and Cryosphere in a Changing Climate. eds H-O Pörtner et al in press.

IUSS Working Group WRB, 2015. World Reference Base for Soil Resources 2014, update 2015 International soil classification system for naming soils and creating legends for soil maps. World Soil Resources Reports No. 106. FAO, Rome.

Jackson, R.B., Lajtha, K., Crow, S.E., Hugelius, G., Kramer, M.G., Piñeiro, G., 2017. The Ecology of Soil Carbon: Pools, Vulnerabilities, and Biotic and Abiotic Controls. Annu. Rev. Ecol. Evol. Syst. 48, 419–445. https://doi.org/10.1146/annurev-ecolsys-112414-054234

Jakobsen, B.H., Siegert, C., Ostroumov, V., 1996. Effect of permafrost and palaeo-environmental history on soil formation in the lower Kolyma Lowland, Siberia. Danish J Geogr 96, 40–50.

Jansen, B., Nierop, K.G.., Verstraten, J.M., 2003. Mobility of Fe(II), Fe(III) and Al in acidic forest soils mediated by dissolved organic matter: influence of solution pH and metal/organic carbon ratios. Geoderma 113, 323–340. https://doi.org/10.1016/S0016-7061(02)00368-3

Jastrow, J.D., Miller, R.M., Boutton, T.W., 1996. Carbon dynamics of aggregate-associated organic matter estimated by carbon-13 natural abundance. Soil Science Society of America Journal 60, 801–807.

Jeanroy, E., Guillet, B., 1981. The occurrence of suspended ferruginous particles in pyrophosphate extracts of some soil horizons. Geoderma 26, 95–105. https://doi.org/10.1016/0016-7061(81)90078-1

Jiang, K., Qi, H.-W., Hu, R.-Z., 2018. Element mobilization and redistribution under extreme tropical weathering of basalts from the Hainan Island, South China. Journal of Asian Earth Sciences 158, 80–102. https://doi.org/10.1016/j.jseaes.2018.02.008

Jin, H.J., Chang, X.L., Wang, S.L., 2007. Evolution of permafrost on the Qinghai-Xizang (Tibet) Plateau since the end of the late Pleistocene. Journal of Geophysical Research: Earth Surface 112. https://doi.org/10.1029/2006JF000521

Jobbágy, E.G., Jackson, R.B., 2004. The Uplift of Soil Nutrients by Plants: Biogeochemical Consequences Across Scales. Ecology 85, 2380–2389. https://doi.org/10.1890/03-0245

Johnson, K., Purvis, G., Lopez-Capel, E., Peacock, C., Gray, N., Wagner, T., März, C., Bowen, L., Ojeda, J., Finlay, N., Robertson, S., Worrall, F., Greenwell, C., 2015. Towards a mechanistic understanding of carbon stabilization in manganese oxides. Nature Communications 6, 7628. https://doi.org/10.1038/ncomms8628

Jones, A., Stolbovoy, V., Tarnocai, C., Broll, G., Spaargaren, O., Montanarella, L., 2009. Soil atlas of the northern circumpolar region.

Jones, B.M., Grosse, G., Farquharson, L.M., Roy-Léveillée, P., Veremeeva, A., Kanevskiy, M.Z., Gaglioti, B.V., Breen, A.L., Parsekian, A.D., Ulrich, M., Hinkel, K.M., 2022. Lake and drained lake basin systems in lowland permafrost regions. Nat Rev Earth Environ 3, 85–98. https://doi.org/10.1038/s43017-021-00238-9

Jones, M.C., Grosse, G., Jones, B.M., Walter Anthony, K., 2012. Peat accumulation in drained thermokarst lake basins in continuous, ice-rich permafrost, northern Seward Peninsula, Alaska: peat accumulation in drained lake basins. J. Geophys. Res. 117, G00M07. https://doi.org/10.1029/2011JG001766

Jongejans, L.L., Liebner, S., Knoblauch, C., Mangelsdorf, K., Strauss, J., 2021a. Cumulative greenhouse gas production in thawed sediments underneath a Yedoma and Alas thermokarst lake in Eastern Siberia. https://doi.org/10.1594/PANGAEA.928140

Jongejans, L.L., Liebner, S., Knoblauch, C., Mangelsdorf, K., Ulrich, M., Grosse, G., Tanski, G., Fedorov, A.N., Konstantinov, P.Y., Windirsch, T., Wiedmann, J., Strauss, J., 2021b. Greenhouse gas production and lipid biomarker distribution in Yedoma and Alas thermokarst lake sediments in Eastern Siberia. Global Change Biology 27, 2822–2839. https://doi.org/10.1111/gcb.15566

Jongejans, L.L., Strauss, J., 2020. Bootstrapping approach for permafrost organic carbon pool estimation. https://doi.org/10.5281/zenodo.3734247

Jongejans, L.L., Strauss, J., Lenz, J., Peterse, F., Mangelsdorf, K., Fuchs, M., Grosse, G., 2018. Organic matter characteristics in yedoma and thermokarst deposits on Baldwin Peninsula, west Alaska. Biogeosciences 15, 6033–6048. https://doi.org/10.5194/bg-15-6033-2018

Jorgenson, M.T., Yoshikawa, K., Kanveskiy, M., Shur, Y., Romanovsky, V., Marchenko, S., Grosse, G., Brown, J., Jones, B., 2008. Permafrost characteristics of Alaska.

Joss, H., Patzner, M.S., Maisch, M., Mueller, C.W., Kappler, A., Bryce, C., 2022. Cryoturbation impacts iron-organic carbon associations along a permafrost soil chronosequence in northern Alaska. Geoderma 413, 115738. https://doi.org/10.1016/j.geoderma.2022.115738

Kahle, M., Kleber, M., Jahn, R., 2004. Retention of dissolved organic matter by phyllosilicate and soil clay fractions in relation to mineral properties. Organic Geochemistry, Selected papers from the Eleventh International Humic Substances Society Conference 35, 269–276. https://doi.org/10.1016/j.orggeochem.2003.11.008

Kaiser, K., Guggenberger, G., 2007. Sorptive stabilization of organic matter by microporous goethite: sorption into small pores vs. surface complexation. European Journal of Soil Science 58, 45–59. https://doi.org/10.1111/j.1365-2389.2006.00799.x

Kaiser, K., Guggenberger, G., 2003. Mineral surfaces and soil organic matter. European Journal of Soil Science 54, 219–236. https://doi.org/10.1046/j.1365-2389.2003.00544.x

Kaiser, K., Guggenberger, G., Haumaier, L., Zech, W., 1997. Dissolved organic matter sorption on sub soils and minerals studied by 13C-NMR and DRIFT spectroscopy. European Journal of Soil Science 48, 301–310. https://doi.org/10.1111/j.1365-2389.1997.tb00550.x

Kalbitz, K., Kaiser, K., 2008. Contribution of dissolved organic matter to carbon storage in forest mineral soils. Journal of Plant Nutrition and Soil Science 171, 52–60. https://doi.org/10.1002/jpln.200700043

Kalbitz, K., Schwesig, D., Rethemeyer, J., Matzner, E., 2005. Stabilization of dissolved organic matter by sorption to the mineral soil. Soil Biology and Biochemistry 37, 1319–1331. https://doi.org/10.1016/j.soilbio.2004.11.028

Kanevskiy, M., Shur, Y., Fortier, D., Jorgenson, M.T., Stephani, E., 2011. Cryostratigraphy of late Pleistocene syngenetic permafrost (yedoma) in northern Alaska, Itkillik River exposure. Quaternary Research 75, 584–596. https://doi.org/10.1016/j.yqres.2010.12.003

Kanevskiy, M., Shur, Y., Strauss, J., Jorgenson, T., Fortier, D., Stephani, E., Vasiliev, A., 2016. Patterns and rates of riverbank erosion involving ice-rich permafrost (yedoma) in northern Alaska. Geomorphology 253, 370–384. https://doi.org/10.1016/j.geomorph.2015.10.023

Kappler, A., Bryce, C., Mansor, M., Lueder, U., Byrne, J.M., Swanner, E.D., 2021. An evolving view on biogeochemical cycling of iron. Nat Rev Microbiol. https://doi.org/10.1038/s41579-020-00502-7

Karlsson, T., Persson, P., Skyllberg, U., Mörth, C.-M., Giesler, R., 2008. Characterization of Iron(III) in Organic Soils Using Extended X-ray Absorption Fine Structure Spectroscopy. Environ. Sci. Technol. 42, 5449–5454. https://doi.org/10.1021/es800322j

Kaufman, D.S., Ager, T.A., Anderson, N.J., Anderson, P.M., Andrews, J.T., Bartlein, P.J., Brubaker, L.B., Coats, L.L., Cwynar, L.C., Duvall, M.L., Dyke, A.S., Edwards, M.E., Eisner, W.R., Gajewski, K., Geirsdóttir, A., Hu, F.S., Jennings, A.E., Kaplan, M.R., Kerwin, M.W., Lozhkin, A.V., MacDonald, G.M., Miller, G.H., Mock, C.J., Oswald, W.W., Otto-Bliesner, B.L., Porinchu, D.F., Rühland, K., Smol, J.P., Steig, E.J., Wolfe, B.B., 2004. Holocene thermal maximum in the western Arctic (0–180°W). Quaternary Science Reviews 23, 529–560. https://doi.org/10.1016/j.quascirev.2003.09.007

Keil, R.G., Mayer, L.M., 2014. Mineral Matrices and Organic Matter, in: Treatise on Geochemistry. Elsevier, pp. 337–359. https://doi.org/10.1016/B978-0-08-095975-7.01024-X

Keiluweit, M., Gee, K., Denney, A., Fendorf, S., 2018. Anoxic microsites in upland soils dominantly controlled by clay content. Soil Biology and Biochemistry 118, 42–50. https://doi.org/10.1016/j.soilbio.2017.12.002

Keller, J.K., Medvedeff, C.A., 2016. Soil organic matter, in: Wetland Soils: Genesis, Hydrology, Landscapes, and Classification. M.J. Vepraskas, C.B. Craft, and J.L. Richardson, eds. (CRC Press: Boca Raton, FL), pp. 165–188.

Keller, K., Blum, J.D., Kling, G.W., 2010. Stream geochemistry as an indicator of increasing permafrost thaw depth in an arctic watershed. Chemical Geology 273, 76–81. https://doi.org/10.1016/j.chemgeo.2010.02.013

Keller, K., Blum, J.D., Kling, G.W., 2007. Geochemistry of Soils and Streams on Surfaces of Varying Ages in Arctic Alaska. Arctic, Antarctic, and Alpine Research 39, 84–98. https://doi.org/10.1657/1523-0430(2007)39[84:GOSASO]2.0.CO;2

Kelley, A.K., Pegoraro, E., Mauritz, M., Hutchings, J., Natali, S., Hicks-Pries, C.E., Schuur, E., Bonanza Creek LTER, 2022. Eight Mile Lake Research Watershed, Thaw Gradient: Seasonal thaw depth 2004-2021. https://doi.org/10.6073/pasta/854b92439ccceec557a810d09dfaf174

Kizewski, F.R., Boyle, P., Hesterberg, D., Martin, J.D., 2010. Mixed Anion (Phosphate/Oxalate) Bonding to Iron(III) Materials. J. Am. Chem. Soc. 132, 2301–2308. https://doi.org/10.1021/ja908807b

Kleber, M., Bourg, I.C., Coward, E.K., Hansel, C.M., Myneni, S.C.B., Nunan, N., 2021. Dynamic interactions at the mineral–organic matter interface. Nat Rev Earth Environ. https://doi.org/10.1038/s43017-021-00162-y

Kleber, M., Eusterhues, K., Keiluweit, M., Mikutta, C., Mikutta, R., Nico, P.S., 2015. Mineral–Organic Associations: Formation, Properties, and Relevance in Soil Environments, in: Advances in Agronomy. Elsevier, pp. 1–140. https://doi.org/10.1016/bs.agron.2014.10.005

Kleber, M., Sollins, P., Sutton, R., 2007. A conceptual model of organo-mineral interactions in soils: self-assembly of organic molecular fragments into zonal structures on mineral surfaces. Biogeochemistry 85, 9–24. https://doi.org/10.1007/s10533-007-9103-5

Kögel-Knabner, I., Amelung, W., Cao, Z., Fiedler, S., Frenzel, P., Jahn, R., Kalbitz, K., Kölbl, A., Schloter, M., 2010. Biogeochemistry of paddy soils. Geoderma 157, 1–14. https://doi.org/10.1016/j.geoderma.2010.03.009

Kögel-Knabner, I., Guggenberger, G., Kleber, M., Kandeler, E., Kalbitz, K., Scheu, S., Eusterhues, K., Leinweber, P., 2008. Organo-mineral associations in temperate soils: Integrating biology, mineralogy, and organic matter chemistry. Journal of Plant Nutrition and Soil Science 171, 61–82. https://doi.org/10.1002/jpln.200700048

Kokelj, S.V., Jorgenson, M.T., 2013. Advances in Thermokarst Research: Recent Advances in Research Investigating Thermokarst Processes. Permafrost and Periglac. Process. 24, 108–119. https://doi.org/10.1002/ppp.1779

Kokelj, S.V., Lacelle, D., Lantz, T.C., Tunnicliffe, J., Malone, L., Clark, I.D., Chin, K.S., 2013. Thawing of massive ground ice in mega slumps drives increases in stream sediment and solute flux across a range of watershed scales: FLUVIAL IMPACTS OF THERMOKARST. Journal of Geophysical Research: Earth Surface 118, 681–692. https://doi.org/10.1002/jgrf.20063

Kokelj, S.V., Smith, C.A.S., Burn, C.R., 2002. Physical and chemical characteristics of the active layer and permafrost, Herschel Island, western Arctic Coast, Canada. Permafrost and Periglacial Processes 13, 171–185. https://doi.org/10.1002/ppp.417

Konishchev, V.N., Rogov, V.V., 1993. Investigations of cryogenic weathering in Europe and Northern Asia. Permafrost and Periglacial Processes 4, 49–64. https://doi.org/10.1002/ppp.3430040105

Koven, C.D., Ringeval, B., Friedlingstein, P., Ciais, P., Cadule, P., Khvorostyanov, D., Krinner, G., Tarnocai, C., 2011. Permafrost carbon-climate feedbacks accelerate global warming. Proceedings of the National Academy of Sciences 108, 14769–14774. https://doi.org/10.1073/pnas.1103910108

Koven, C.D., Schuur, E.A.G., Schädel, C., Bohn, T.J., Burke, E.J., Chen, G., Chen, X., Ciais, P., Grosse, G., Harden, J.W., Hayes, D.J., Hugelius, G., Jafarov, E.E., Krinner, G., Kuhry, P., Lawrence, D.M., MacDougall, A.H., Marchenko, S.S., McGuire, A.D., Natali, S.M., Nicolsky, D.J., Olefeldt, D., Peng, S., Romanovsky, V.E., Schaefer, K.M., Strauss, J., Treat, C.C., Turetsky, M., 2015. A simplified, data-constrained approach to estimate the permafrost carbon–climate feedback. Phil. Trans. R. Soc. A 373, 20140423. https://doi.org/10.1098/rsta.2014.0423

Kramer, M.G., Chadwick, O.A., 2018. Climate-driven thresholds in reactive mineral retention of soil carbon at the global scale. Nature Climate Change 8, 1104–1108. https://doi.org/10.1038/s41558-018-0341-4

Krishnaswami, S., Trivedi, J.R., Sarin, M.M., Ramesh, R., Sharma, K.K., 1992. Strontium isotopes and rubidium in the Ganga-Brahmaputra river system: Weathering in the Himalaya, fluxes to the Bay of Bengal and contributions to the evolution of oceanic87Sr/86Sr. Earth and Planetary Science Letters 109, 243–253. https://doi.org/10.1016/0012-821X(92)90087-C

Kuhry, P., Bárta, J., Blok, D., Elberling, B., Faucherre, S., Hugelius, G., Jørgensen, C.J., Richter, A., Šantrůčková, H., Weiss, N., 2020. Lability classification of soil organic matter in the northern permafrost region. Biogeosciences 17, 361–379. https://doi.org/10.5194/bg-17-361-2020

Kurtz, A.C., Derry, L.A., Chadwick, O.A., Alfano, M.J., 2000. Refractory element mobility in volcanic soils. Geology 28, 683–686.

Lacelle, D., Bjornson, J., Lauriol, B., 2010. Climatic and geomorphic factors affecting contemporary (1950-2004) activity of retrogressive thaw slumps on the Aklavik Plateau, Richardson Mountains, NWT, Canada. Permafrost Periglac. Process. 21, 1–15. https://doi.org/10.1002/ppp.666

Lai, R., 2004. Soil Carbon Sequestration in Natural and Managed Tropical Forest Ecosystems. Journal of Sustainable Forestry 21, 1–30. https://doi.org/10.1300/J091v21n01_01

Lalonde, K., Mucci, A., Ouellet, A., Gélinas, Y., 2012. Preservation of organic matter in sediments promoted by iron. Nature 483, 198–200. https://doi.org/10.1038/nature10855

Langer, M., Westermann, S., Walter Anthony, K., Wischnewski, K., Boike, J., 2015. Frozen ponds: production and storage of methane during the Arctic winter in a lowland tundra landscape in northern Siberia, Lena River delta. Biogeosciences 12, 977–990. https://doi.org/10.5194/bg-12-977-2015

Lawrence, D.M., Koven, C.D., Swenson, S.C., Riley, W.J., Slater, A.G., 2015. Permafrost thaw and resulting soil moisture changes regulate projected high-latitude CO_2 and CH_4

emissions. Environ. Res. Lett. 10, 094011. https://doi.org/10.1088/1748-9326/10/9/094011
Lehmann, J., Kleber, M., 2015. The contentious nature of soil organic matter. Nature 528, 60–68. https://doi.org/10.1038/nature16069
Lehn, G.O., Jacobson, A.D., Douglas, T.A., McClelland, J.W., Barker, A.J., Khosh, M.S., 2017. Constraining seasonal active layer dynamics and chemical weathering reactions occurring in North Slope Alaskan watersheds with major ion and isotope (δ 34 S SO4 , δ 13 C DIC , 87 Sr/ 86 Sr, δ 44/40 Ca, and δ 44/42 Ca) measurements. Geochimica et Cosmochimica Acta 217, 399–420. https://doi.org/10.1016/j.gca.2017.07.042
Lehner, B., Döll, P., 2004. Development and validation of a global database of lakes, reservoirs and wetlands. Journal of hydrology 296, 1–22.
Lenton, T.M., 2012. Arctic climate tipping points. Ambio 41, 10–22. https://doi.org/10.1007/s13280-011-0221-x
Lenton, T.M., Rockström, J., Gaffney, O., Rahmstorf, S., Richardson, K., Steffen, W., Schellnhuber, H.J., 2019. Climate tipping points — too risky to bet against. Nature 575, 592–595. https://doi.org/10.1038/d41586-019-03595-0
Lenz, J., Wetterich, S., Jones, B.M., Meyer, H., Bobrov, A., Grosse, G., 2016. Evidence of multiple thermokarst lake generations from an 11 800-year-old permafrost core on the northern Seward Peninsula, Alaska. Boreas 45, 584–603. https://doi.org/10.1111/bor.12186
Li, H., Santos, F., Butler, K., Herndon, E., 2021. A Critical Review on the Multiple Roles of Manganese in Stabilizing and Destabilizing Soil Organic Matter. Environ. Sci. Technol. 55, 12136–12152. https://doi.org/10.1021/acs.est.1c00299
Liao, P., Li, W., Jiang, Y., Wu, J., Yuan, S., Fortner, J.D., Giammar, D.E., 2017. Formation, Aggregation, and Deposition Dynamics of NOM-Iron Colloids at Anoxic–Oxic Interfaces. Environ. Sci. Technol. 51, 12235–12245. https://doi.org/10.1021/acs.est.7b02356
Liese, A., Romeis, T., 2013. Biochemical regulation of in vivo function of plant calcium-dependent protein kinases (CDPK). Biochimica et Biophysica Acta (BBA) - Molecular Cell Research, 12th European Symposium on Calcium 1833, 1582–1589. https://doi.org/10.1016/j.bbamcr.2012.10.024
Liljedahl, A.K., Hinzman, L.D., Harazono, Y., Zona, D., Tweedie, C.E., Hollister, R.D., Engstrom, R., Oechel, W.C., 2011. Nonlinear controls on evapotranspiration in arctic coastal wetlands. Biogeosciences 8, 3375–3389. https://doi.org/10.5194/bg-8-3375-2011
Lim, A.G., Loiko, S.V., Kuzmina, D.M., Krickov, I.V., Shirokova, L.S., Kulizhsky, S.P., Pokrovsky, O.S., 2022a. Organic carbon, and major and trace elements reside in labile low-molecular form in the ground ice of permafrost peatlands: a case study of colloids in peat ice of Western Siberia. Environ. Sci.: Processes Impacts. https://doi.org/10.1039/D1EM00547B
Lim, A.G., Loiko, S.V., Pokrovsky, O.S., 2022b. Sizable pool of labile organic carbon in peat and mineral soils of permafrost peatlands, western Siberia. Geoderma 409, 115601. https://doi.org/10.1016/j.geoderma.2021.115601
Lindgren, A., Hugelius, G., Kuhry, P., Christensen, T.R., Vandenberghe, J., 2016. GIS-based Maps and Area Estimates of Northern Hemisphere Permafrost Extent during the Last Glacial Maximum. Permafrost and Periglacial Processes 27, 6–16. https://doi.org/10.1002/ppp.1851
Lindsay, W.L., 1972. Zinc in Soils and Plant Nutrition, in: Brady, N.C. (Ed.), Advances in Agronomy. Academic Press, pp. 147–186. https://doi.org/10.1016/S0065-2113(08)60635-5
Lipson, D.A., Jha, M., Raab, T.K., Oechel, W.C., 2010. Reduction of iron (III) and humic substances plays a major role in anaerobic respiration in an Arctic peat soil. J. Geophys. Res. 115, G00I06. https://doi.org/10.1029/2009JG001147
Lipson, D.A., Zona, D., Raab, T.K., Bozzolo, F., Mauritz, M., Oechel, W.C., 2012. Water-table height and microtopography control biogeochemical cycling in an Arctic coastal

tundra ecosystem. Biogeosciences 9, 577–591. https://doi.org/10.5194/bg-9-577-2012
Lovley, D.R., Phillips, E.J.P., 1987. Competitive Mechanisms for Inhibition of Sulfate Reduction and Methane Production in the Zone of Ferric Iron Reduction in Sediments. Appl Environ Microbiol 53, 2636–2641.
Lovley, D.R., Phillips, E.J.P., 1986. Organic Matter Mineralization with Reduction of Ferric Iron in Anaerobic Sediments. APPL. ENVIRON. MICROBIOL. 51, 7.
Luo, D., Wu, Q., Jin, H., Marchenko, S.S., Lü, L., Gao, S., 2016. Recent changes in the active layer thickness across the northern hemisphere. Environ Earth Sci 75, 555. https://doi.org/10.1007/s12665-015-5229-2
MacDougall, A.H., Knutti, R., 2016. Projecting the release of carbon from permafrost soils using a perturbed parameter ensemble modelling approach. Biogeosciences 13, 2123–2136. https://doi.org/10.5194/bg-13-2123-2016
Mackay, J.R., 1992. Lake stability in an ice-rich permafrost environment: examples from the western Arctic coast, in: Aquatic Ecosystems in Semi-Arid Regions: Implications for Resource Management. NHRI Symposium Series. pp. 1–26.
Mackay, J.R., 1988. Catastrophic lake drainage, Tuktoyaktuk peninsula area, District of Mackenzie. Current research, part D, geological survey of Canada, paper 88, 83–90.
Manabe, S., Stouffer, R.J., 1980. Sensitivity of a global climate model to an increase of CO2 concentration in the atmosphere. Journal of Geophysical Research: Oceans 85, 5529–5554. https://doi.org/10.1029/JC085iC10p05529
Manasypov, R.M., Vorobyev, S.N., Loiko, S.V., Kritzkov, I.V., Shirokova, L.S., Shevchenko, V.P., Kirpotin, S.N., Kulizhsky, S.P., Kolesnichenko, L.G., Zemtzov, V.A., Sinkinov, V.V., Pokrovsky, O.S., 2015. Seasonal dynamics of organic carbon and metals in thermokarst lakes from the discontinuous permafrost zone of western Siberia. Biogeosciences 12, 3009–3028. https://doi.org/10.5194/bg-12-3009-2015
Marschner, P., 2012. Marschner's Mineral Nutrition of Higher Plants. https://doi.org/10.1016/C2009-0-63043-9
Marsh, P., Neumann, N.N., 2001. Processes controlling the rapid drainage of two ice-rich permafrost-dammed lakes in NW Canada. Hydrological Processes 15, 3433–3446.
Masiello, C.A., Chadwick, O.A., Southon, J., Torn, M.S., Harden, J.W., 2004. Weathering controls on mechanisms of carbon storage in grassland soils. Global Biogeochemical Cycles 18. https://doi.org/10.1029/2004GB002219
Mauclet, E., 2022. Influence of permafrost degradation on the mineral nutrient cycling by Arctic tundra vegetation. Université catholique de Louvain, Louvain-la-Neuve.
Mauclet, E., Agnan, Y., Hirst, C., Monhonval, A., Pereira, B., Vandeuren, A., Villani, M., Ledman, J., Taylor, M., Jasinski, B.L., Schuur, E.A.G., Opfergelt, S., 2021. Changing sub-Arctic tundra vegetation upon permafrost degradation: impact on foliar mineral element cycling. Biogeosciences Discussions 1–34. https://doi.org/10.5194/bg-2021-263
Mauclet, E., Villani, M., Monhonval, A., Hirst, C., Schuur, E.A.G., Opfergelt, S., 2022. Characterization of permafrost soil exchange properties and quantification of stocks in soil exchangeable base cations. https://doi.org/10.14428/DVN/FQVMEP
Mauritz, M., Bracho, R., Celis, G., Hutchings, J., Natali, S.M., Pegoraro, E., Salmon, V.G., Schädel, C., Webb, E.E., Schuur, E.A.G., 2017. Nonlinear CO2 flux response to 7 years of experimentally induced permafrost thaw. Global Change Biology 23, 3646–3666. https://doi.org/10.1111/gcb.13661
McKeague, J.A., Day, J.H., 1966. Dithionite- and oxalate-extractable Fe and Al as aids in differentiating various classes of soils. Canadian Journal of Soil Science, Canadian Journal of Soil Science 46, 13–22. https://doi.org/10.4141/cjss66-003
McLaren, T.I., Guppy, C.N., Tighe, M.K., Forster, N., Grave, P., Lisle, L.M., Bennett, J.W., 2012. Rapid, Nondestructive Total Elemental Analysis of Vertisol Soils using Portable X-ray Fluorescence. Soil Science Society of America Journal 76, 1436–1445. https://doi.org/10.2136/sssaj2011.0354

Mehra, O.P., Jackson, M.L., 1960. Iron oxide removal from soils and clays by a dithionite-citrate system buffered with sodium bicarbonate. Proc. 7th Natl. Conf. Clays Clay Minerals 317–327. https://doi.org/10.1016/B978-0-08-009235-5.50026-7

Melton, E.D., Swanner, E.D., Behrens, S., Schmidt, C., Kappler, A., 2014. The interplay of microbially mediated and abiotic reactions in the biogeochemical Fe cycle. Nature Reviews Microbiology 12, 797–808. https://doi.org/10.1038/nrmicro3347

Meredith, M., Sommerkorn, M., Cassotta, S., Derksen, C., Ekaykin, A., Hollowed, A., Kofinas, G., Mackintosh, A., Melbourne-Thomas, J., Muelbert, M.M.C., Ottersen, G., Pritchard, H., Schuur, A.E.G., 2019. Polar Regions. In: IPCC Special Report on the Ocean and Cryosphere in a Changing Climate. Cambridge University Press, Cambridge, UK and New York, NY, USA, pp. 203–320.

Metson, A.J., New Zealand, Department of Scientific and Industrial Research, New Zealand, Soil Bureau, 1956. Methods of chemical analysis for soil survey samples. D.S.I.R., Wellington.

Michaelson, G.J., Ping, C.L., Kimble, J.M., 1996. Carbon storage and distribution in tundra soils of Arctic Alaska, USA. Arctic and Alpine Research 28, 414–424.

Mikutta, C., Wiederhold, J.G., Cirpka, O.A., Hofstetter, T.B., Bourdon, B., Gunten, U.V., 2009. Iron isotope fractionation and atom exchange during sorption of ferrous iron to mineral surfaces. Geochimica et Cosmochimica Acta 73, 1795–1812. https://doi.org/10.1016/j.gca.2009.01.014

Mikutta, R., Kleber, M., Torn, M.S., Jahn, R., 2006. Stabilization of Soil Organic Matter: Association with Minerals or Chemical Recalcitrance? Biogeochemistry 77, 25–56. https://doi.org/10.1007/s10533-005-0712-6

Mikutta, R., Mikutta, C., Kalbitz, K., Scheel, T., Kaiser, K., Jahn, R., 2007. Biodegradation of forest floor organic matter bound to minerals via different binding mechanisms. Geochimica et Cosmochimica Acta 71, 2569–2590. https://doi.org/10.1016/j.gca.2007.03.002

Miller, E.K., Blum, J.D., Friedland, A.J., 1993. Determination of soil exchangeable-cation loss and weathering rates using Sr isotopes. Nature 362, 438–441. https://doi.org/10.1038/362438a0

Miller, G.H., Lehman, S.J., Refsnider, K.A., Southon, J.R., Zhong, Y., 2013. Unprecedented recent summer warmth in Arctic Canada. Geophysical Research Letters 40, 5745–5751. https://doi.org/10.1002/2013GL057188

Miller, K., Lai, C.-T., Dahlgren, R., Lipson, D., 2019. Anaerobic Methane Oxidation in High-Arctic Alaskan Peatlands as a Significant Control on Net CH4 Fluxes. Soil Syst. 3, 7. https://doi.org/10.3390/soilsystems3010007

Miller, K.E., Lai, C.-T., Friedman, E.S., Angenent, L.T., Lipson, D.A., 2015. Methane suppression by iron and humic acids in soils of the Arctic Coastal Plain. Soil Biology and Biochemistry 83, 176–183. https://doi.org/10.1016/j.soilbio.2015.01.022

Millot, R., Gaillardet, J. érôm., Dupré, B., Allègre, C.J., 2003. Northern latitude chemical weathering rates: clues from the Mackenzie River Basin, Canada. Geochimica et Cosmochimica Acta 67, 1305–1329. https://doi.org/10.1016/S0016-7037(02)01207-3

Mitsch, W.J., Bernal, B., Nahlik, A.M., Mander, Ü., Zhang, L., Anderson, C.J., Jørgensen, S.E., Brix, H., 2013. Wetlands, carbon, and climate change. Landscape Ecology 28, 583–597.

Morgan, J.B., Connolly, E.L., 2013. Plant-Soil Interactions: Nutrient Uptake [WWW Document]. Nature Education Knowledge 4(8):2. URL https://www.nature.com/scitable/knowledge/library/plant-soil-interactions-nutrient-uptake-105289112/ (accessed 11.2.20).

Morgenstern, A., 2012. Thermokarst and thermal erosion: Degradation of Siberian ice-rich permafrost (PhD Thesis). Institutional Repository of the University of Potsdam.

Morgenstern, A., Ulrich, M., Günther, F., Roessler, S., Fedorova, I.V., Rudaya, N.A., Wetterich, S., Boike, J., Schirrmeister, L., 2013. Evolution of thermokarst in East

Siberian ice-rich permafrost: A case study. Geomorphology 201, 363–379. https://doi.org/10.1016/j.geomorph.2013.07.011

Mu, C.C., Zhang, T.J., Zhao, Q., Guo, H., Zhong, W., Su, H., Wu, Q.B., 2016. Soil organic carbon stabilization by iron in permafrost regions of the Qinghai-Tibet Plateau. Geophysical Research Letters 43, 10,286-10,294. https://doi.org/10.1002/2016GL070071

Mueller, C.W., Rethemeyer, J., Kao-Kniffin, J., Löppmann, S., Hinkel, K.M., Bockheim, J.G., 2015. Large amounts of labile organic carbon in permafrost soils of northern Alaska. Global Change Biology 21, 2804–2817. https://doi.org/10.1111/gcb.12876

Murton, J.B., Goslar, T., Edwards, M.E., Bateman, M.D., Danilov, P.P., Savvinov, G.N., Gubin, S.V., Ghaleb, B., Haile, J., Kanevskiy, M., Lozhkin, A.V., Lupachev, A.V., Murton, D.K., Shur, Y., Tikhonov, A., Vasil'chuk, A.C., Vasil'chuk, Y.K., Wolfe, S.A., 2015. Palaeoenvironmental Interpretation of Yedoma Silt (Ice Complex) Deposition as Cold-Climate Loess, Duvanny Yar, Northeast Siberia. Permafrost and Periglacial Processes 26, 208–288. https://doi.org/10.1002/ppp.1843

Natali, S.M., Holdren, J.P., Rogers, B.M., Treharne, R., Duffy, P.B., Pomerance, R., MacDonald, E., 2021. Permafrost carbon feedbacks threaten global climate goals. Proceedings of the National Academy of Sciences 118, e2100163118. https://doi.org/10.1073/pnas.2100163118

Natali, S.M., Schuur, E.A.G., Trucco, C., Hicks Pries, C.E., Crummer, K.G., Baron Lopez, A.F., 2011. Effects of experimental warming of air, soil and permafrost on carbon balance in Alaskan tundra: WARMING OF ALASKAN TUNDRA. Global Change Biology 17, 1394–1407. https://doi.org/10.1111/j.1365-2486.2010.02303.x

Natali, S.M., Watts, J.D., Rogers, B.M., Potter, S., Ludwig, S.M., Selbmann, A.-K., Sullivan, P.F., Abbott, B.W., Arndt, K.A., Birch, L., Björkman, M.P., Bloom, A.A., Celis, G., Christensen, T.R., Christiansen, C.T., Commane, R., Cooper, E.J., Crill, P., Czimczik, C., Davydov, S., Du, J., Egan, J.E., Elberling, B., Euskirchen, E.S., Friborg, T., Genet, H., Göckede, M., Goodrich, J.P., Grogan, P., Helbig, M., Jafarov, E.E., Jastrow, J.D., Kalhori, A.A.M., Kim, Y., Kimball, J.S., Kutzbach, L., Lara, M.J., Larsen, K.S., Lee, B.-Y., Liu, Z., Loranty, M.M., Lund, M., Lupascu, M., Madani, N., Malhotra, A., Matamala, R., McFarland, J., McGuire, A.D., Michelsen, A., Minions, C., Oechel, W.C., Olefeldt, D., Parmentier, F.-J.W., Pirk, N., Poulter, B., Quinton, W., Rezanezhad, F., Risk, D., Sachs, T., Schaefer, K., Schmidt, N.M., Schuur, E.A.G., Semenchuk, P.R., Shaver, G., Sonnentag, O., Starr, G., Treat, C.C., Waldrop, M.P., Wang, Y., Welker, J., Wille, C., Xu, X., Zhang, Z., Zhuang, Q., Zona, D., 2019. Large loss of CO2 in winter observed across the northern permafrost region. Nat. Clim. Chang. 9, 852–857. https://doi.org/10.1038/s41558-019-0592-8

National Research Centre for CRM, 1986. Institute of Geophysical and Geochemical Exploration component (GBW 07401- GBW 07404.

Nierop, K.G.J.J., Jansen, B., Verstraten, J.M., 2002. Dissolved organic matter, aluminium and iron interactions: precipitation induced by metal/carbon ratio, pH and competition. Science of The Total Environment 300, 201–211. https://doi.org/10.1016/S0048-9697(02)00254-1

Nitzbon, J., Westermann, S., Langer, M., Martin, L.C.P., Strauss, J., Laboor, S., Boike, J., 2020. Fast response of cold ice-rich permafrost in northeast Siberia to a warming climate. Nat Commun 11, 2201. https://doi.org/10.1038/s41467-020-15725-8

Oades, J.M., 1988. The retention of organic matter in soils. Biogeochemistry 5, 35–70. https://doi.org/10.1007/BF02180317

Obu, J., Westermann, S., Bartsch, A., Berdnikov, N., Christiansen, H.H., Dashtseren, A., Delaloye, R., Elberling, B., Etzelmüller, B., Kholodov, A., Khomutov, A., Kääb, A., Leibman, M.O., Lewkowicz, A.G., Panda, S.K., Romanovsky, V., Way, R.G., Westergaard-Nielsen, A., Wu, T., Yamkhin, J., Zou, D., 2019. Northern Hemisphere permafrost map based on TTOP modelling for 2000–2016 at 1 km2 scale. Earth-Science Reviews 193, 299–316. https://doi.org/10.1016/j.earscirev.2019.04.023

Oldham, V.E., Mucci, A., Tebo, B.M., Luther, G.W., 2017. Soluble Mn(III)–L complexes are abundant in oxygenated waters and stabilized by humic ligands. Geochimica et Cosmochimica Acta 199, 238–246. https://doi.org/10.1016/j.gca.2016.11.043

Olefeldt, D., Goswami, S., Grosse, G., Hayes, D., Hugelius, G., Kuhry, P., McGuire, A.D., Romanovsky, V.E., Sannel, A.B.K., Schuur, E.A.G., Turetsky, M.R., 2016. Circumpolar distribution and carbon storage of thermokarst landscapes. Nature Communications 7, 13043. https://doi.org/10.1038/ncomms13043

O'Neill, H.B., Roy-Leveillee, P., Lebedeva, L., Ling, F., 2020. Recent advances (2010–2019) in the study of taliks. Permafrost and Periglacial Processes 31, 346–357. https://doi.org/10.1002/ppp.2050

Opel, T., Meyer, H., Wetterich, S., Laepple, T., Dereviagin, A., Murton, J., 2018. Ice wedges as archives of winter paleoclimate: A review. Permafrost and Periglacial Processes 29, 199–209. https://doi.org/10.1002/ppp.1980

Opel, T., Wetterich, S., Meyer, H., Dereviagin, A.Y., Fuchs, M.C., Schirrmeister, L., 2017. Ground-ice stable isotopes and cryostratigraphy reflect late Quaternary palaeoclimate in the Northeast Siberian Arctic (Oyogos Yar coast, Dmitry Laptev Strait). Climate of the Past 13, 587–611. https://doi.org/10.5194/cp-13-587-2017

Opfergelt, S., 2020. The next generation of climate model should account for the evolution of mineral-organic interactions with permafrost thaw. Environ. Res. Lett. 15, 091003. https://doi.org/10.1088/1748-9326/ab9a6d

Osterkamp, T.E., Jorgenson, M.T., Schuur, E.A.G., Shur, Y.L., Kanevskiy, M.Z., Vogel, J.G., Tumskoy, V.E., 2009. Physical and ecological changes associated with warming permafrost and thermokarst in Interior Alaska. Permafrost Periglac. Process. 20, 235–256. https://doi.org/10.1002/ppp.656

Osterkamp, T.E., Romanovsky, V.E., 1999. Evidence for warming and thawing of discontinuous permafrost in Alaska. Permafrost and Periglacial Processes 10, 17–37. https://doi.org/10.1002/(SICI)1099-1530(199901/03)10:1<17::AID-PPP303>3.0.CO;2-4

Page, A.L., Miller, R.H., Keeney, D.R., 1982. Methods of soil analysis; part 2. Chemical and Microbiological Properties. American Soc. of Agronomy (Publ.) 363–364.

Palmer, M.R., Edmond, J.M., 1992. Controls over the strontium isotope composition of river water. Geochimica et Cosmochimica Acta 56, 2099–2111. https://doi.org/10.1016/0016-7037(92)90332-D

Pan, Y., Koopmans, G.F., Bonten, L.T.C., Song, J., Luo, Y., Temminghoff, E.J.M., Comans, R.N.J., 2014. Influence of pH on the redox chemistry of metal (hydr)oxides and organic matter in paddy soils. J Soils Sediments 14, 1713–1726. https://doi.org/10.1007/s11368-014-0919-z

Parfitt, R.L., Childs, C.W., 1988. Estimation of forms of Fe and Al - a review, and analysis of contrasting soils by dissolution and Mossbauer methods. Soil Res. 26, 121–144. https://doi.org/10.1071/sr9880121

Parkhurst, D.L., Appelo, C.A.J., 2013. Description of input and examples for PHREEQC version 3—A computer program for speciation, batch-reaction, one-dimensional transport, and inverse geochemical calculations: U.S. Geological Survey Techniques and Methods, book 6, chap. A43, 497 p. [WWW Document]. URL https://pubs.usgs.gov/tm/06/a43/pdf/tm6-A43.pdf (accessed 9.8.22).

Parkinson, R.J., 1978. Genesis and classification of arctic coastal plain soils, Prudhoe Bay, Alaska. Institute of Polar Studies, The Ohio State University.

Patrick Jr., W.H., Jugsujinda, A., 1992. Sequential Reduction and Oxidation of Inorganic Nitrogen, Manganese, and Iron in Flooded Soil. Soil Science Society of America Journal 56, 1071–1073. https://doi.org/10.2136/sssaj1992.03615995005600040011x

Patzner, M.S., Kainz, N., Lundin, E., Barczok, M., Smith, C., Herndon, E., Kinsman-Costello, L., Fischer, S., Straub, D., Kleindienst, S., Kappler, A., Bryce, C., 2022. Seasonal Fluctuations in Iron Cycling in Thawing Permafrost Peatlands. Environ. Sci. Technol. 56, 4620–4631. https://doi.org/10.1021/acs.est.1c06937

Patzner, M.S., Mueller, C.W., Malusova, M., Baur, M., Nikeleit, V., Scholten, T., Hoeschen, C., Byrne, J.M., Borch, T., Kappler, A., Bryce, C., 2020. Iron mineral dissolution releases iron and associated organic carbon during permafrost thaw. Nat Commun 11, 6329. https://doi.org/10.1038/s41467-020-20102-6

Pearce, C.R., Parkinson, I.J., Gaillardet, J., Charlier, B.L., Mokadem, F., Burton, K.W., 2015. Reassessing the stable (δ88/86Sr) and radiogenic (87Sr/86Sr) strontium isotopic composition of marine inputs. Geochimica et Cosmochimica Acta 157, 125–146.

Pearsall, W., Mortimer, C., 1939. Oxidation-reduction potentials in waterlogged soils, natural waters and muds. The Journal of Ecology 483–501.

Peng, X., Yan, X., Zhou, H., Zhang, Y.Z., Sun, H., 2015. Assessing the contributions of sesquioxides and soil organic matter to aggregation in an Ultisol under long-term fertilization. Soil and Tillage Research, Soil Structure and its Functions in Ecosystems: Phase matter & Scale matter 146, 89–98. https://doi.org/10.1016/j.still.2014.04.003

Pestryakova, L.A., Herzschuh, U., Wetterich, S., Ulrich, M., 2012. Present-day variability and Holocene dynamics of permafrost-affected lakes in central Yakutia (Eastern Siberia) inferred from diatom records. Quaternary Science Reviews 51, 56–70. https://doi.org/10.1016/j.quascirev.2012.06.020

Pewe, T.L., Journaux, A., 1983. Origin and character of loesslike silt in unglaciated south-central Yakutia, Siberia, USSR. US Geological Survey Professional Paper 1262.

Ping, C.L., Bockheim, J.G., Kimble, J.M., Michaelson, G.J., Walker, D.A., 1998. Characteristics of cryogenic soils along a latitudinal transect in arctic Alaska. Journal of Geophysical Research: Atmospheres 103, 28917–28928. https://doi.org/10.1029/98JD02024

Ping, C.-L., Michaelson, G.J., Kimble, J.M., Walker, D.A., 2005. Soil Acidity and Exchange Properties of Cryogenic Soils in Arctic Alaska. Soil Science and Plant Nutrition 51, 649–653. https://doi.org/10.1111/j.1747-0765.2005.tb00083.x

Pinheiro, J.P., Mota, A.M., Benedetti, M.F., 2000. Effect of Aluminum Competition on Lead and Cadmium Binding to Humic Acids at Variable Ionic Strength. Environ. Sci. Technol. 34, 5137–5143. https://doi.org/10.1021/es0000899

Plaza, C., Pegoraro, E., Bracho, R., Celis, G., Crummer, K.G., Hutchings, J.A., Hicks Pries, C.E., Mauritz, M., Natali, S.M., Salmon, V.G., Schädel, C., Webb, E.E., Schuur, E.A.G., 2019. Direct observation of permafrost degradation and rapid soil carbon loss in tundra. Nat. Geosci. 12, 627–631. https://doi.org/10.1038/s41561-019-0387-6

Pohlman, A.A., McColl, J.G., 1988. Soluble organics from forest litter and their role in metal dissolution. Soil Science Society of America Journal 52, 265–271.

Pokrovsky, O.S., Shirokova, L.S., Manasypov, R.M., Kirpotin, S.N., Kulizhsky, S.P., Kolesnichenko, L.G., Loiko, S.V., Vorobyev, S.N., 2014. Thermokarst lakes of Western Siberia: a complex biogeochemical multidisciplinary approach. International Journal of Environmental Studies 71, 733–748. https://doi.org/10.1080/00207233.2014.942535

Popov, A.I., 1953. Lithogenesis of alluvial lowlands in the cold climatic conditions. Izvestiya (Transactions) of the USSR Academy of Sciences. Geography 2, 29–41.

Porter, T.J., Opel, T., 2020. Recent advances in paleoclimatological studies of Arctic wedge- and pore-ice stable-water isotope records. Permafrost and Periglac Process ppp.2052. https://doi.org/10.1002/ppp.2052

Porter, T.J., Schoenemann, S.W., Davies, L.J., Steig, E.J., Bandara, S., Froese, D.G., 2019. Recent summer warming in northwestern Canada exceeds the Holocene thermal maximum. Nat Commun 10, 1631. https://doi.org/10.1038/s41467-019-09622-y

Possinger, A.R., Bailey, S.W., Inagaki, T.M., Kögel-Knabner, I., Dynes, J.J., Arthur, Z.A., Lehmann, J., 2020. Organo-mineral interactions and soil carbon mineralizability with variable saturation cycle frequency. Geoderma 375, 114483. https://doi.org/10.1016/j.geoderma.2020.114483

Pye, K., 1995. The nature, origin and accumulation of loess. Quaternary Science Reviews, Aeolian Sediments in the Quaternary Record 14, 653–667. https://doi.org/10.1016/0277-3791(95)00047-X

R Core Team, 2018. R: A language and environment for statistical computing. R Foundation for Statistical Computing, Vienna, Austria. URL https://www.R-project.org/.

Rantanen, M., Karpechko, A.Y., Lipponen, A., Nordling, K., Hyvärinen, O., Ruosteenoja, K., Vihma, T., Laaksonen, A., 2022. The Arctic has warmed nearly four times faster than the globe since 1979. Commun Earth Environ 3, 1–10. https://doi.org/10.1038/s43247-022-00498-3

Rauch, J.N., Pacyna, J.M., 2009. Earth's global Ag, Al, Cr, Cu, Fe, Ni, Pb, and Zn cycles. Global Biogeochemical Cycles 23. https://doi.org/10.1029/2008GB003376

Ravansari, R., Lemke, L.D., 2018. Portable X-ray fluorescence trace metal measurement in organic rich soils: pXRF response as a function of organic matter fraction. Geoderma 319, 175–184. https://doi.org/10.1016/j.geoderma.2018.01.011

Ravansari, R., Wilson, S.C., Tighe, M., 2020. Portable X-ray fluorescence for environmental assessment of soils: Not just a point and shoot method. Environment International 134, 105250. https://doi.org/10.1016/j.envint.2019.105250

Regelink, I.C., Voegelin, A., Weng, L., Koopmans, G.F., Comans, R.N.J., 2014. Characterization of Colloidal Fe from Soils Using Field-Flow Fractionation and Fe K-Edge X-ray Absorption Spectroscopy. Environ. Sci. Technol. 48, 4307–4316. https://doi.org/10.1021/es405330x

Reimann, C., Filzmoser, P., Garrett, R., Dutter, R., 2008. Statistical Data Analysis Explained: Applied Environmental Statistics with R |.

Rekant, P., Bauch, H.A., Schwenk, T., Portnov, A., Gusev, E., Spiess, V., Cherkashov, G., Kassens, H., 2015. Evolution of subsea permafrost landscapes in Arctic Siberia since the Late Pleistocene: a synoptic insight from acoustic data of the Laptev Sea. Arktos 1, 11. https://doi.org/10.1007/s41063-015-0011-y

Remucal, C.K., Ginder-Vogel, M., 2014. A critical review of the reactivity of manganese oxides with organic contaminants. Environmental Science: Processes & Impacts 16, 1247–1266.

Rennert, T., 2019. Wet-chemical extractions to characterise pedogenic Al and Fe species – a critical review. Soil Res. 57, 1. https://doi.org/10.1071/SR18299

Reyes, F.R., Lougheed, V.L., 2015. Rapid Nutrient Release from Permafrost Thaw in Arctic Aquatic Ecosystems. Arctic, Antarctic, and Alpine Research 47, 35–48. https://doi.org/10.1657/AAAR0013-099

Richmond, K.E., Sussman, M., 2003. Got silicon? The non-essential beneficial plant nutrient. Curr Opin Plant Biol 6, 268–272. https://doi.org/10.1016/s1369-5266(03)00041-4

Riedel, T., Biester, H., Dittmar, T., 2012. Molecular Fractionation of Dissolved Organic Matter with Metal Salts. Environ. Sci. Technol. 46, 4419–4426. https://doi.org/10.1021/es203901u

Riedel, T., Zak, D., Biester, H., Dittmar, T., 2013. Iron traps terrestrially derived dissolved organic matter at redox interfaces. Proceedings of the National Academy of Sciences 110, 10101–10105. https://doi.org/10.1073/pnas.1221487110

Rivkina, E.M., Fedorov-Davydov, D.G., Zakharyuk, A.G., Shcherbakova, V.A., Vishnivetskaya, T.A., 2020. Free Iron and Iron-Reducing Microorganisms in Permafrost and Permafrost-Affected Soils of Northeastern Siberia. Eurasian Soil Sc. 53, 1455–1468. https://doi.org/10.1134/S1064229320100166

Robert, M., Tessier, D., 1974. Méthode de préparation des argiles des sols pour des études minéralogiques. Méthode de préparation des argiles des sols pour des études minéralogiques, Annales agronomiques 25, 859–882.

Rodenhizer, H., Ledman, J., Mauritz, M., Natali, S.M., Pegoraro, E., Plaza, C., Romano, E., Schädel, C., Taylor, M., Schuur, E., 2020. Carbon Thaw Rate Doubles When Accounting for Subsidence in a Permafrost Warming Experiment. J. Geophys. Res. Biogeosci. 125. https://doi.org/10.1029/2019JG005528

Röhl, U., Abrams, L.J., 2000. High-resolution, downhole, and nondestructive core measurements from sites 999 and 1001 in the caribbean sea: application to the Late Pleistocene Thermal Maximum. Proceedings of the Ocean Drilling Program, Scientific Results 165, 191–203.

Romanovskii, N.N., 1993. Fundamentals of cryogenesis of lithosphere. Moscow University Press, Moscow.

Romanovsky, V.E., Drozdov, D.S., Oberman, N.G., Malkova, G.V., Kholodov, A.L., Marchenko, S.S., Moskalenko, N.G., Sergeev, D.O., Ukraintseva, N.G., Abramov, A.A., 2010. Thermal state of permafrost in Russia. Permafrost and Periglacial Processes 21, 136–155.

Rouiller, J., Burtin, G., Souchier, B., 1972. La dispersion des sols dans l'analyse granulométrique. Méthode utilisant les résines échangeuses d'ions. ENSAIA Nancy 14, 194–205.

Rouillon, M., Taylor, M.P., 2016. Can field portable X-ray fluorescence (pXRF) produce high quality data for application in environmental contamination research? Environmental Pollution 214, 255–264. https://doi.org/10.1016/j.envpol.2016.03.055

Rowley, M.C., Grand, S., Verrecchia, É.P., 2018. Calcium-mediated stabilisation of soil organic carbon. Biogeochemistry 137, 27–49. https://doi.org/10.1007/s10533-017-0410-1

Rowley, T., Giardino, J.R., Granados-Aguilar, R., Vitek, J.D., 2015. Periglacial Processes and Landforms in the Critical Zone, in: Developments in Earth Surface Processes. Elsevier, pp. 397–447. https://doi.org/10.1016/B978-0-444-63369-9.00013-6

Roy, M., McManus, J., Goñi, M.A., Chase, Z., Borgeld, J.C., Wheatcroft, R.A., Muratli, J.M., Megowan, M.R., Mix, A., 2013. Reactive iron and manganese distributions in seabed sediments near small mountainous rivers off Oregon and California (USA). Continental Shelf Research 54, 67–79. https://doi.org/10.1016/j.csr.2012.12.012

Rozenbaum, G.E., Shpolyanskaya, N.A., 1998. Late Cenozoic permafrost history of the Russian Arctic. Permafrost and periglacial processes 9, 247–273.

Rudnick, R., Gao, S., 2003. Composition of the Continental Crust. Treatise on Geochemistry 3, 1–64. https://doi.org/10.1016/B0-08-043751-6/03016-4

Saidy, A.R., Smernik, R.J., Baldock, J.A., Kaiser, K., Sanderman, J., Macdonald, L.M., 2012. Effects of clay mineralogy and hydrous iron oxides on labile organic carbon stabilisation. Geoderma 173–174, 104–110. https://doi.org/10.1016/j.geoderma.2011.12.030

Salvadó, J.A., Tesi, T., Andersson, A., Ingri, J., Dudarev, O.V., Semiletov, I.P., Gustafsson, Ö., 2015. Organic carbon remobilized from thawing permafrost is resequestered by reactive iron on the Eurasian Arctic Shelf. Geophysical Research Letters 42, 8122–8130. https://doi.org/10.1002/2015GL066058

Schädel, C., Rodenhizer, H.G., Celis, G., Ledman, J., Schuur, E., Bonanza Creek LTER, 2022. Eight Mile Lake Research Watershed, Thaw Gradient: Seasonal water table depth from 2004-2021. https://doi.org/10.6073/pasta/854cb809639b3173dfb2c9f2ee098f98

Schädel, C., Schuur, E.A.G., Bracho, R., Elberling, B., Knoblauch, C., Lee, H., Luo, Y., Shaver, G.R., Turetsky, M.R., 2014. Circumpolar assessment of permafrost C quality and its vulnerability over time using long-term incubation data. Glob Change Biol 20, 641–652. https://doi.org/10.1111/gcb.12417

Scheel, T., Dörfler, C., Kalbitz, K., 2007. Precipitation of Dissolved Organic Matter by Aluminum Stabilizes Carbon in Acidic Forest Soils. Soil Sci. Soc. Am. J. 71, 64–74. https://doi.org/10.2136/sssaj2006.0111

Scheel, T., Jansen, B., Van Wijk, A.J., Verstraten, J.M., Kalbitz, K., 2008. Stabilization of dissolved organic matter by aluminium: a toxic effect or stabilization through precipitation? European Journal of Soil Science 59, 1122–1132. https://doi.org/10.1111/j.1365-2389.2008.01074.x

Schirrmeister, L., Dietze, E., Matthes, H., Grosse, G., Strauss, J., Laboor, S., Ulrich, M., Kienast, F., Wetterich, S., 2020. The genesis of Yedoma Ice Complex permafrost -

grain-size endmember modeling analysis from Siberia and Alaska. E&G Quaternary Sci. J. 69, 33–53. https://doi.org/10.5194/egqsj-69-33-2020

Schirrmeister, L., Froese, D., Tumskoy, V., Grosse, G., Wetterich, S., 2013. Yedoma: Late Pleistocene Ice-Rich Syngenetic Permafrost of Beringia, in: Encyclopedia of Quaternary Science. Elsevier, Amsterdam, pp. 542–552. https://doi.org/10.1016/B978-0-444-53643-3.00106-0

Schirrmeister, L., Grosse, G., Kunitsky, V., Magens, D., Meyer, H., Dereviagin, A., Kuznetsova, T., Andreev, A., Babiy, O., Kienast, F., Grigoriev, M., Pier Overduin, P., Preusser, F., 2008. Periglacial landscape evolution and environmental changes of Arctic lowland areas for the last 60 000 years (western Laptev Sea coast, Cape Mamontov Klyk). Polar Research 27, 249–272. https://doi.org/10.1111/j.1751-8369.2008.00067.x

Schirrmeister, L., Grosse, G., Kunitsky, V.V., Fuchs, M.C., Krbetschek, M., Andreev, A.A., Herzschuh, U., Babyi, O., Siegert, C., Meyer, H., Derevyagin, A.Y., Wetterich, S., 2010. The mystery of Bunge Land (New Siberian Archipelago): implications for its formation based on palaeoenvironmental records, geomorphology, and remote sensing. Quaternary Science Reviews 29, 3598–3614. https://doi.org/10.1016/j.quascirev.2009.11.017

Schirrmeister, L., Grosse, G., Kunitsky, V.V., Meyer, H., Dereviagyn, A.Y., Kuznetsova, T.V., 2003a. Permafrost, periglacial and paleo-environmental studies on New Siberian Islands. Reports on Polar Research 466 195–314.

Schirrmeister, L., Grosse, G., Schwamborn, G., Andreev, A.A., Meyer, H., Kunitsky, V.V., Kuznetsova, T.V., Dorozhkina, M.V., Pavlova, E.Y., Bobrov, A.A., Oezen, D., 2003b. Late Quaternary History of the Accumulation Plain North of the Chekanovsky Ridge (Lena Delta, Russia): A Multidisciplinary Approach. Polar Geography 27, 277–319. https://doi.org/10.1080/789610225

Schirrmeister, L., Kunitsky, V., Grosse, G., Wetterich, S., Meyer, H., Schwamborn, G., Babiy, O., Derevyagin, A., Siegert, C., 2011. Sedimentary characteristics and origin of the Late Pleistocene Ice Complex on north-east Siberian Arctic coastal lowlands and islands – A review. Quaternary International 241, 3–25. https://doi.org/10.1016/j.quaint.2010.04.004

Schirrmeister, L., Meyer, H., Andreev, A., Wetterich, S., Kienast, F., Bobrov, A., Fuchs, M., Sierralta, M., Herzschuh, U., 2016. Late Quaternary paleoenvironmental records from the Chatanika River valley near Fairbanks (Alaska). Quaternary Science Reviews 147, 259–278. https://doi.org/10.1016/j.quascirev.2016.02.009

Schirrmeister, L., Schwamborn, G., Overduin, P.P., Strauss, J., Fuchs, M.C., Grigoriev, M., Yakshina, I., Rethemeyer, J., Dietze, E., Wetterich, S., 2017. Yedoma Ice Complex of the Buor Khaya Peninsula (southern Laptev Sea). Biogeosciences 14, 1261–1283. https://doi.org/10.5194/bg-14-1261-2017

Schirrmeister, L., Siegert, C., Kunitzky, V.V., Grootes, P.M., Erlenkeuser, H., 2002a. Late Quaternary ice-rich permafrost sequences as a paleoenvironmental archive for the Laptev Sea Region in northern Siberia. Int J Earth Sci 91, 154–167. https://doi.org/10.1007/s005310100205

Schirrmeister, L., Siegert, C., Kuznetsova, T., Kuzmina, S., Andreev, A., Kienast, F., Meyer, H., Bobrov, A., 2002b. Paleoenvironmental and paleoclimatic records from permafrost deposits in the Arctic region of Northern Siberia. Quaternary International 89, 97–118. https://doi.org/10.1016/S1040-6182(01)00083-0

Schirrmeister, L., Wagner, D., Grigoriev, M., Bolshiyanov, D., 2007. The Expedition LENA 2005 , Berichte zur Polar- und Meeresforschung (Reports on Polar and Marine Research), Bremerhaven, Alfred Wegener Institute for Polar and Marine Research 550, 289 p. https://doi.org/10.2312/BzPM_0550_2007

Schirrmeister, L., Wetterich, S., Schwamborn, G., Matthes, H., Grosse, G., Klimova, I., Kunitsky, V.V., Siegert, C., 2022. Heavy and Light Mineral Association of Late Quaternary Permafrost Deposits in Northeastern Siberia. Frontiers in Earth Science 10. https://doi.org/10.3389/feart.2022.741932

Schmidt, M.W.I., Torn, M.S., Abiven, S., Dittmar, T., Guggenberger, G., Janssens, I.A., Kleber, M., Kögel-Knabner, I., Lehmann, J., Manning, D.A.C., Nannipieri, P., Rasse, D.P., Weiner, S., Trumbore, S.E., 2011. Persistence of soil organic matter as an ecosystem property. Nature 478, 49–56. https://doi.org/10.1038/nature10386

Schneider von Deimling, T., Grosse, G., Strauss, J., Schirrmeister, L., Morgenstern, A., Schaphoff, S., Meinshausen, M., Boike, J., 2015. Observation-based modelling of permafrost carbon fluxes with accounting for deep carbon deposits and thermokarst activity. Biogeosciences 12, 3469–3488. https://doi.org/10.5194/bg-12-3469-2015

Schneider von Deimling, T., Meinshausen, M., Levermann, A., Huber, V., Frieler, K., Lawrence, D.M., Brovkin, V., 2012. Estimating the near-surface permafrost-carbon feedback on global warming. Biogeosciences 9, 649–665. https://doi.org/10.5194/bg-9-649-2012

Schuur, E.A., Abbott, B., 2011. High risk of permafrost thaw. Nature 480, 32–33.

Schuur, E.A.G., Abbott, B.W., Bowden, W.B., Brovkin, V., Camill, P., Canadell, J.G., Chanton, J.P., Chapin, F.S., Christensen, T.R., Ciais, P., Crosby, B.T., Czimczik, C.I., Grosse, G., Harden, J., Hayes, D.J., Hugelius, G., Jastrow, J.D., Jones, J.B., Kleinen, T., Koven, C.D., Krinner, G., Kuhry, P., Lawrence, D.M., McGuire, A.D., Natali, S.M., O'Donnell, J.A., Ping, C.L., Riley, W.J., Rinke, A., Romanovsky, V.E., Sannel, A.B.K., Schädel, C., Schaefer, K., Sky, J., Subin, Z.M., Tarnocai, C., Turetsky, M.R., Waldrop, M.P., Walter Anthony, K.M., Wickland, K.P., Wilson, C.J., Zimov, S.A., 2013. Expert assessment of vulnerability of permafrost carbon to climate change. Climatic Change 119, 359–374. https://doi.org/10.1007/s10584-013-0730-7

Schuur, E.A.G., Bockheim, J., Canadell, J.G., Euskirchen, E., Field, C.B., Goryachkin, S.V., Hagemann, S., Kuhry, P., Lafleur, P.M., Lee, H., Mazhitova, G., Nelson, F.E., Rinke, A., Romanovsky, V.E., Shiklomanov, N., Tarnocai, C., Venevsky, S., Vogel, J.G., Zimov, S.A., 2008. Vulnerability of Permafrost Carbon to Climate Change: Implications for the Global Carbon Cycle. BioScience 58, 701–714. https://doi.org/10.1641/B580807

Schuur, E.A.G., Bracho, R., Celis, G., Belshe, E.F., Ebert, C., Ledman, J., Mauritz, M., Pegoraro, E.F., Plaza, C., Rodenhizer, H., Romanovsky, V., Schädel, C., Schirokauer, D., Taylor, M., Vogel, J.G., Webb, E.E., 2021. Tundra Underlain By Thawing Permafrost Persistently Emits Carbon to the Atmosphere Over 15 Years of Measurements. Journal of Geophysical Research: Biogeosciences 126, e2020JG006044. https://doi.org/10.1029/2020JG006044

Schuur, E.A.G., Crummer, K.G., Vogel, J.G., Mack, M.C., 2007. Plant Species Composition and Productivity following Permafrost Thaw and Thermokarst in Alaskan Tundra. Ecosystems 10, 280–292. https://doi.org/10.1007/s10021-007-9024-0

Schuur, E.A.G., Mack, M.C., 2018. Ecological Response to Permafrost Thaw and Consequences for Local and Global Ecosystem Services. Annu. Rev. Ecol. Evol. Syst. 49, 279–301. https://doi.org/10.1146/annurev-ecolsys-121415-032349

Schuur, E.A.G., McGuire, A.D., Schädel, C., Grosse, G., Harden, J.W., Hayes, D.J., Hugelius, G., Koven, C.D., Kuhry, P., Lawrence, D.M., Natali, S.M., Olefeldt, D., Romanovsky, V.E., Schaefer, K., Turetsky, M.R., Treat, C.C., Vonk, J.E., 2015. Climate change and the permafrost carbon feedback. Nature 520, 171–179. https://doi.org/10.1038/nature14338

Schuur, E.A.G., Vogel, J.G., Crummer, K.G., Lee, H., Sickman, J.O., Osterkamp, T.E., 2009. The effect of permafrost thaw on old carbon release and net carbon exchange from tundra. Nature 459, 556–559. https://doi.org/10.1038/nature08031

Schwamborn, G., Rachold, V., Grigoriev, M.N., 2002. Late Quaternary sedimentation history of the Lena Delta. Quaternary International, Late Pleistocene and Holocene Climate and Geoarchaeology Internat ional Conference on Past Global Changes (PAGES) 89, 119–134. https://doi.org/10.1016/S1040-6182(01)00084-2

Schwertmann, U., 1991. Solubility and dissolution of iron oxides. Plant Soil 130, 1–25. https://doi.org/10.1007/BF00011851

Schwertmann, U., 1988. Occurrence and formation of iron oxides in various pedoenvironments, in: Iron in Soils and Clay Minerals. Springer, pp. 267–308.
Schwertmann, U., Kodama, H., Fischer, W. r., 1986. Mutual Interactions Between Organics and Iron Oxides, in: Interactions of Soil Minerals with Natural Organics and Microbes. John Wiley & Sons, Ltd, pp. 223–250. https://doi.org/10.2136/sssaspecpub17.c7
Schwertmann, U., Murad, E., 1988. The nature of an iron oxide—organic iron association in a peaty environment. Clay Minerals 23, 291–299. https://doi.org/10.1180/claymin.1988.023.3.06
Schwesig, D., Kalbitz, K., Matzner, E., 2003. Effects of aluminium on the mineralization of dissolved organic carbon derived from forest floors. European Journal of Soil Science 54, 311–322. https://doi.org/10.1046/j.1365-2389.2003.00523.x
Shand, C.A., Wendler, R., 2014. Portable X-ray fluorescence analysis of mineral and organic soils and the influence of organic matter. Journal of Geochemical Exploration 143, 31–42. https://doi.org/10.1016/j.gexplo.2014.03.005
Shmelev, D., Cherbunina, M., Rogov, V., Opfergelt, S., Monhonval, A., Strauss, J., 2021. Reconstructing Permafrost Sedimentological Characteristics and Post-depositional Processes of the Yedoma Stratotype Duvanny Yar, Siberia. Frontiers in Earth Science 9.
Shur, Y., Kanevskiy, M., Jorgenson, T., Dillon, M., Stephani, E., Bray, M., Fortier, D., 2012. Permafrost Degradation and Thaw Settlement under Lakes in Yedoma Environment 7.
Siegert, C., Schirrmeister, L., Babiy, O., 2002. The sedimentological, mineralogical and geochemical composition of late Pleistocene deposits from the ice complex on the Bykovsky peninsula, northern Siberia. Polarforschung, 70 2000, 3–11.
Six, J., Conant, R.T., Paul, E.A., Paustian, K., 2002. Review: Stabilization mechanisms of soil organic matter: Implications for C-saturation of soils. Plant and Soil 241, 155–176.
Sizov, O., Konstantinov, A., Volvakh, A., Molodkov, A., 2020. Timing and Sedimentary Record of Late Quaternary Fluvio-Aeolian Successions of the Tura-Pyshma Interfluve (SW Western Siberia, Russia). Geosciences 10, 396. https://doi.org/10.3390/geosciences10100396
Smalley, I.J., Smalley, V., 1983. Loess Material and Loess Deposits: Formation, Distribution and Consequences, in: Brookfield, M.E., Ahlbrandt, T.S. (Eds.), Developments in Sedimentology, Eolian Sediments and Processes. Elsevier, pp. 51–68. https://doi.org/10.1016/S0070-4571(08)70788-X
Smetacek, V., 1999. Diatoms and the Ocean Carbon Cycle. Protist 150, 25–32. https://doi.org/10.1016/S1434-4610(99)70006-4
Smith, L.C., Sheng, Y., MacDonald, G.M., 2007. A first pan-Arctic assessment of the influence of glaciation, permafrost, topography and peatlands on northern hemisphere lake distribution. Permafrost and Periglacial Processes 18, 201–208. https://doi.org/10.1002/ppp.581
Smith, S.L., O'Neill, H.B., Isaksen, K., Noetzli, J., Romanovsky, V.E., 2022. The changing thermal state of permafrost. Nat Rev Earth Environ 3, 10–23. https://doi.org/10.1038/s43017-021-00240-1
Soloviev, P.A., 1973. Thermokarst phenomena and land-forms due to frost heaving in Central Yakutia. Biuletyn Peryglacialny 23, 135–155.
Soloviev, P.A., 1959. Cryolithic Zone of the Northern Part of Lena-Amga Interfluve. Izdatel'stvo Akademii SSSR 142.
Souza, I.F., Archanjo, B.S., Hurtarte, L.C.C., Oliveros, M.E., Gouvea, C.P., Lidizio, L.R., Achete, C.A., Schaefer, C.E.R., Silva, I.R., 2017. Al-/Fe-(hydr)oxides–organic carbon associations in Oxisols — From ecosystems to submicron scales. CATENA 154, 63–72. https://doi.org/10.1016/j.catena.2017.02.017
Sowers, T.D., Stuckey, J.W., Sparks, D.L., 2018. The synergistic effect of calcium on organic carbon sequestration to ferrihydrite. Geochem Trans 19, 4. https://doi.org/10.1186/s12932-018-0049-4

Sowers, T.D., Wani, R.P., Coward, E.K., Fischel, M.H.H., Betts, A.R., Douglas, T.A., Duckworth, O.W., Sparks, D.L., 2020. Spatially Resolved Organomineral Interactions across a Permafrost Chronosequence. Environ. Sci. Technol. acs.est.9b06558. https://doi.org/10.1021/acs.est.9b06558

Sposito, G., Skipper, N.T., Sutton, R., Park, S., Soper, A.K., Greathouse, J.A., 1999. Surface geochemistry of the clay minerals. Proc Natl Acad Sci U S A 96, 3358–3364.

Stevenson, E.I., Aciego, S.M., Chutcharavan, P., Parkinson, I.J., Burton, K.W., Blakowski, M.A., Arendt, C.A., 2016. Insights into combined radiogenic and stable strontium isotopes as tracers for weathering processes in subglacial environments. Chemical Geology 429, 33–43. https://doi.org/10.1016/j.chemgeo.2016.03.008

Stevenson, F.J., 1994. Humus chemistry: genesis, composition, reactions. John Wiley & Sons.

Stone, A.T., Morgan, J.J., 1984. Reduction and dissolution of managese (IV) oxides by organics: 2. Survey of the reactivity of organids. Environ Sci Technol 18, 617–624.

Strauss, J., 2010. Late Quaternary environmental dynamics at the Duvanny Yar key section, Lower Kolyma, East Siberia. Universität Potsdam, Potsdam.

Strauss, J., Abbott, B., Hugelius, G., Schuur, A.E.G., Treat, C., Fuchs, M., Schädel, C., Ulrich, M., Turetsky, M., Keuschnig, M., Biasi, C., Yang, Y., Grosse, G., 2021a. Permafrost, in: Recarbonizing global soils – A technical manual of recommended management practices. : Food and Agriculture Organization of the United Nations (FAO), Rome, Italy, pp. 127–147.

Strauss, J., Laboor, S., Fedorov, A.N., Fortier, D., Froese, D., Fuchs, M., Grosse, G., Günther, F., Harden, J.W., Hugelius, G., Kanevskiy, M.Z., Kholodov, A.L., Kunitsky, V.V., Kraev, G., Lapointe-Elmrabti, L., Lozhkin, A.V., Rivkina, E., Robinson, J., Schirrmeister, L., Shmelev, D., Shur, Y., Siegert, C., Spektor, V., Ulrich, M., Vartanyan, S.L., Veremeeva, A., Walter Anthony, K.M., Zimov, S.A., 2016. Database of Ice-Rich Yedoma Permafrost (IRYP). https://doi.org/10.1594/PANGAEA.861733

Strauss, J., Laboor, S., Schirrmeister, L., Fedorov, A.N., Fortier, D., Froese, D., Fuchs, M., Günther, F., Grigoriev, M., Harden, J., Hugelius, G., Jongejans, L.L., Kanevskiy, M., Kholodov, A., Kunitsky, V., Kraev, G., Lozhkin, A., Rivkina, E., Shur, Y., Siegert, C., Spektor, V., Streletskaya, I., Ulrich, M., Vartanyan, S., Veremeeva, A., Anthony, K.W., Wetterich, S., Zimov, N., Grosse, G., 2021b. Circum-Arctic Map of the Yedoma Permafrost Domain. Frontiers in Earth Science 9. https://doi.org/10.3389/feart.2021.758360

Strauss, J., Schirrmeister, L., Grosse, G., Fortier, D., Hugelius, G., Knoblauch, C., Romanovsky, V., Schädel, C., Schneider von Deimling, T., Schuur, E.A.G., Shmelev, D., Ulrich, M., Veremeeva, A., 2017. Deep Yedoma permafrost: A synthesis of depositional characteristics and carbon vulnerability. Earth-Science Reviews 172, 75–86. https://doi.org/10.1016/j.earscirev.2017.07.007

Strauss, J., Schirrmeister, L., Grosse, G., Wetterich, S., Ulrich, M., Herzschuh, U., Hubberten, H.-W., 2013. The deep permafrost carbon pool of the Yedoma region in Siberia and Alaska: Deep carbon of Siberia and Alaska. Geophys. Res. Lett. 40, 6165–6170. https://doi.org/10.1002/2013GL058088

Strauss, J., Schirrmeister, L., Wetterich, S., Borchers, A., Davydov, S.P., 2012. Grain-size properties and organic-carbon stock of Yedoma Ice Complex permafrost from the Kolyma lowland, northeastern Siberia. Global Biogeochemical Cycles 26. https://doi.org/10.1029/2011GB004104

Strauss, R., Brümmer, G. w., Barrow, N. j., 1997. Effects of crystallinity of goethite: II. Rates of sorption and desorption of phosphate. European Journal of Soil Science 48, 101–114. https://doi.org/10.1111/j.1365-2389.1997.tb00189.x

Street, L.E., Dean, J.F., Billett, M.F., Baxter, R., Dinsmore, K.J., Lessels, J.S., Subke, J.-A., Tetzlaff, D., Wookey, P.A., 2016. Redox dynamics in the active layer of an Arctic headwater catchment; examining the potential for transfer of dissolved methane from soils to stream water. Journal of Geophysical Research: Biogeosciences 121, 2776–2792. https://doi.org/10.1002/2016JG003387

Streletskiy, D.A., Tananaev, N.I., Opel, T., Shiklomanov, N.I., Nyland, K.E., Streletskaya, I.D., Tokarev, I., Shiklomanov, A.I., 2015. Permafrost hydrology in changing climatic conditions: seasonal variability of stable isotope composition in rivers in discontinuous permafrost. Environmental Research Letters 10, 095003. https://doi.org/10.1088/1748-9326/10/9/095003

Stumm, W., 1992. Chemistry of the solid-water interface: processes at the mineral-water and particle-water interface in natural systems.

Stumm, W., Morgan, J.J., 1995. Aquatic Chemistry: Chemical Equilibria and Rates in Natural Waters, 3rd Edition | Wiley.

Stumm, W., Sulzberger, B., 1992. The cycling of iron in natural environments: Considerations based on laboratory studies of heterogeneous redox processes. Geochimica et Cosmochimica Acta 56, 3233–3257. https://doi.org/10.1016/0016-7037(92)90301-X

Sunda, W.G., Kieber, D.J., 1994. Oxidation of humic substances by manganese oxides yields low-molecular-weight organic substrates. Nature 367, 62–64. https://doi.org/10.1038/367062a0

Sundman, A., Karlsson, T., Laudon, H., Persson, P., 2014. XAS study of iron speciation in soils and waters from a boreal catchment. Chemical Geology 364, 93–102. https://doi.org/10.1016/j.chemgeo.2013.11.023

Swindles, G.T., Morris, P.J., Mullan, D., Watson, E.J., Turner, T.E., Roland, T.P., Amesbury, M.J., Kokfelt, U., Schoning, K., Pratte, S., Gallego-Sala, A., Charman, D.J., Sanderson, N., Garneau, M., Carrivick, J.L., Woulds, C., Holden, J., Parry, L., Galloway, J.M., 2016. The long-term fate of permafrost peatlands under rapid climate warming. Sci Rep 5, 17951. https://doi.org/10.1038/srep17951

Tanski, G., Wagner, D., Knoblauch, C., Fritz, M., Sachs, T., Lantuit, H., 2019. Rapid CO2 Release From Eroding Permafrost in Seawater. Geophysical Research Letters 46, 11244–11252. https://doi.org/10.1029/2019GL084303

Tarasenko, T.V., 2013. Interannual variations in the areas of thermokarst lakes in Central Yakutia. Water Resour 40, 111–119. https://doi.org/10.1134/S0097807813010107

Thermo Fisher Scientific, 2018. Neptune XT MC-ICP-MS 16.

Till, A.B., Dumoulin, J.A., Harris, A.G., Moore, T.E., Bleick, H.A., Siwiec, B.R., 2008. Bedrock Geologic Map of the southern Brooks Range, Alaska, and accompanying Conodont Data 70.

Tipping, E., 2005. Modelling Al competition for heavy metal binding by dissolved organic matter in soil and surface waters of acid and neutral pH. Geoderma 127, 293–304.

Tjallingii, R., Röhl, U., Kölling, M., Bickert, T., 2007. Influence of the water content on X-ray fluorescence core-scanning measurements in soft marine sediments: XRF core scanning. Geochem. Geophys. Geosyst. 8, n/a-n/a. https://doi.org/10.1029/2006GC001393

Tomirdiaro, S.V., Chernen'kiy, O., 1987. Cryogenic deposits of East Arctic and Sub Arctic. - AN SSSR Far-East-Science Centre 196 pp.

Torn, M.S., Trumbore, S.E., Chadwick, O.A., Vitousek, P.M., Hendricks, D.M., 1997. Mineral control of soil organic carbon storage and turnover. Nature 389, 170–173. https://doi.org/10.1038/38260

Treat, C.C., Kleinen, T., Broothaerts, N., Dalton, A.S., Dommain, R., Douglas, T.A., Drexler, J.Z., Finkelstein, S.A., Grosse, G., Hope, G., Hutchings, J., Jones, M.C., Kuhry, P., Lacourse, T., Lähteenoja, O., Loisel, J., Notebaert, B., Payne, R.J., Peteet, D.M., Sannel, A.B.K., Stelling, J.M., Strauss, J., Swindles, G.T., Talbot, J., Tarnocai, C., Verstraeten, G., Williams, C.J., Xia, Z., Yu, Z., Väliranta, M., Hättestrand, M., Alexanderson, H., Brovkin, V., 2019. Widespread global peatland establishment and persistence over the last 130,000 y. Proc Natl Acad Sci USA 116, 4822–4827. https://doi.org/10.1073/pnas.1813305116

Turetsky, M.R., Abbott, B.W., Jones, M.C., Anthony, K.W., Olefeldt, D., Schuur, E.A.G., Grosse, G., Kuhry, P., Hugelius, G., Koven, C., Lawrence, D.M., Gibson, C., Sannel, A.B.K., McGuire, A.D., 2020. Carbon release through abrupt permafrost thaw. Nature Geoscience 13, 138–143. https://doi.org/10.1038/s41561-019-0526-0

Ulrich, M., Jongejans, L.L., Grosse, G., Schneider, B., Opel, T., Wetterich, S., Fedorov, A.N., Schirrmeister, L., Windirsch, T., Wiedmann, J., Strauss, J., 2021. Geochemistry and Weathering Indices of Yedoma and Alas Deposits beneath Thermokarst Lakes in Central Yakutia. Frontiers in Earth Science 9, 701. https://doi.org/10.3389/feart.2021.704141

Ulrich, M., Matthes, H., Schirrmeister, L., Schütze, J., Park, H., Iijima, Y., Fedorov, A.N., 2017. Differences in behavior and distribution of permafrost-related lakes in Central Yakutia and their response to climatic drivers. Water Resources Research 53, 1167–1188. https://doi.org/10.1002/2016WR019267

Ulrich, M., Matthes, H., Schmidt, J., Fedorov, A.N., Schirrmeister, L., Siegert, C., Schneider, B., Strauss, J., Zielhofer, C., 2019. Holocene thermokarst dynamics in Central Yakutia – A multi-core and robust grain-size endmember modeling approach. Quaternary Science Reviews 218, 10–33. https://doi.org/10.1016/j.quascirev.2019.06.010

van Everdingen, R.O., 1998. Multi-language glossary of permafrost and related ground-ice terms, International Permafrost Association. The Arctic Institute of North America, Boulder, CO: National Snow and Ice Data Center/World Data Center for Glaciology.

van Hees, P.A.W., Lundström, U.S., Starr, M., Giesler, R., 2000. Factors influencing aluminium concentrations in soil solution from podzols. Geoderma 94, 289–310. https://doi.org/10.1016/S0016-7061(98)00138-4

van Huissteden, J., 2020. Thawing Permafrost: Permafrost Carbon in a Warming Arctic. Springer International Publishing, Cham. https://doi.org/10.1007/978-3-030-31379-1

Van Huissteden, J., Berrittella, C., Parmentier, F.J.W., Mi, Y., Maximov, T.C., Dolman, A.J., 2011. Methane emissions from permafrost thaw lakes limited by lake drainage. Nature Climate Change 1, 119–123.

Velichko, A.A., Catto, N., Drenova, A.N., Klimanov, V.A., Kremenetski, K.V., Nechaev, V.P., 2002. Climate changes in East Europe and Siberia at the Late glacial–holocene transition. Quaternary International, Late Pleistocene and Holocene Investigations in Europe. Internati onal Conference on Past Global Changes (PAGES) 91, 75–99. https://doi.org/10.1016/S1040-6182(01)00104-5

Verink, E., 2011. Simplified procedure for constructing Pourbaix diagrams. Uhlig's corrosion handbook 7, 111–124.

Villani, M., Mauclet, E., Agnan, Y., Druel, A., Jasinski, B.L., Taylor, M., Schuur, E.A.G., Opfergelt, S., 2022. Mineral element recycling in topsoil following permafrost degradation and a vegetation shift in sub-Arctic tundra. Geoderma.

Vitousek, P.M., Porder, S., Houlton, B.Z., Chadwick, O.A., 2010. Terrestrial phosphorus limitation: mechanisms, implications, and nitrogen–phosphorus interactions. Ecological Applications 20, 5–15. https://doi.org/10.1890/08-0127.1

Voigt, C., Marushchak, M.E., Abbott, B.W., Biasi, C., Elberling, B., Siciliano, S.D., Sonnentag, O., Stewart, K.J., Yang, Y., Martikainen, P.J., 2020. Nitrous oxide emissions from permafrost-affected soils. Nature Reviews Earth & Environment 1, 420–434. https://doi.org/10.1038/s43017-020-0063-9

von Lützow, M., Kögel-Knabner, I., Ekschmitt, K., Flessa, H., Guggenberger, G., Matzner, E., Marschner, B., 2007. SOM fractionation methods: Relevance to functional pools and to stabilization mechanisms. Soil Biology and Biochemistry 39, 2183–2207. https://doi.org/10.1016/j.soilbio.2007.03.007

von Lützow, M., Kogel-Knabner, I., Ekschmitt, K., Matzner, E., Guggenberger, G., Marschner, B., Flessa, H., 2006. Stabilization of organic matter in temperate soils: mechanisms and their relevance under different soil conditions - a review. Eur J Soil Science 57, 426–445. https://doi.org/10.1111/j.1365-2389.2006.00809.x

Vonk, J.E., Tank, S.E., Walvoord, M.A., 2019. Integrating hydrology and biogeochemistry across frozen landscapes. Nat Commun 10, 5377. https://doi.org/10.1038/s41467-019-13361-5

Wagai, R., Mayer, L.M., 2007. Sorptive stabilization of organic matter in soils by hydrous iron oxides. Geochimica et Cosmochimica Acta 71, 25–35. https://doi.org/10.1016/j.gca.2006.08.047

Wagai, R., Mayer, L.M., Kitayama, K., Shirato, Y., 2013. Association of organic matter with iron and aluminum across a range of soils determined via selective dissolution techniques coupled with dissolved nitrogen analysis. Biogeochemistry 112, 95–109. https://doi.org/10.1007/s10533-011-9652-5

Walker, D.A., Everett, K.R., 1991. Loess Ecosystems of Northern Alaska: Regional Gradient and Toposequence at Prudhoe Bay. Ecological Monographs 61, 437–464. https://doi.org/10.2307/2937050

Walker, T.W., Syers, J.K., 1976. The fate of phosphorus during pedogenesis. Geoderma 15, 1–19. https://doi.org/10.1016/0016-7061(76)90066-5

Walter Anthony, K., Schneider von Deimling, T., Nitze, I., Frolking, S., Emond, A., Daanen, R., Anthony, P., Lindgren, P., Jones, B., Grosse, G., 2018. 21st-century modeled permafrost carbon emissions accelerated by abrupt thaw beneath lakes. Nat Commun 9, 3262. https://doi.org/10.1038/s41467-018-05738-9

Walter, K.M., Edwards, M.E., Grosse, G., Zimov, S.A., Chapin, F.S., 2007. Thermokarst Lakes as a Source of Atmospheric CH_4 During the Last Deglaciation. Science 318, 633–636. https://doi.org/10.1126/science.1142924

Wang, J., Yang, W., Yu, B., Li, Z., Cai, C., Ma, R., 2016. Estimating the influence of related soil properties on macro- and micro-aggregate stability in ultisols of south-central China. CATENA 137, 545–553. https://doi.org/10.1016/j.catena.2015.11.001

Wang, S., Jia, Y., Liu, T., Wang, Y., Liu, Z., Feng, X., 2021. Delineating the Role of Calcium in the Large-Scale Distribution of Metal-Bound Organic Carbon in Soils. Geophysical Research Letters 48. https://doi.org/10.1029/2021GL092391

Wang, X., Toner, B.M., Yoo, K., 2019. Mineral vs. organic matter supply as a limiting factor for the formation of mineral-associated organic matter in forest and agricultural soils. Science of The Total Environment 692, 344–353. https://doi.org/10.1016/j.scitotenv.2019.07.219

Washburn, A.L., 1980. Geocryology: a survey of periglacial processes and environments. Wiley.

Weindorf, David C., Bakr, N., Zhu, Y., 2014a. Advances in Portable X-ray Fluorescence (PXRF) for Environmental, Pedological, and Agronomic Applications, in: Advances in Agronomy. Elsevier, pp. 1–45. https://doi.org/10.1016/B978-0-12-802139-2.00001-9

Weindorf, David C., Bakr, N., Zhu, Y., Mcwhirt, A., Ping, C.L., Michaelson, G., Nelson, C., Shook, K., Nuss, S., 2014b. Influence of Ice on Soil Elemental Characterization via Portable X-Ray Fluorescence Spectrometry. Pedosphere 24, 1–12. https://doi.org/10.1016/S1002-0160(13)60076-4

Weiss, N., Blok, D., Elberling, B., Hugelius, G., Jørgensen, C.J., Siewert, M.B., Kuhry, P., 2016. Thermokarst dynamics and soil organic matter characteristics controlling initial carbon release from permafrost soils in the Siberian Yedoma region. Sedimentary Geology 340, 38–48. https://doi.org/10.1016/j.sedgeo.2015.12.004

Weltje, G.J., Tjallingii, R., 2008. Calibration of XRF core scanners for quantitative geochemical logging of sediment cores: Theory and application. Earth and Planetary Science Letters 274, 423–438. https://doi.org/10.1016/j.epsl.2008.07.054

Wetterich, S., Grosse, G., Schirrmeister, L., Andreev, A.A., Bobrov, A.A., Kienast, F., Bigelow, N.H., Edwards, M.E., 2012. Late Quaternary environmental and landscape dynamics revealed by a pingo sequence on the northern Seward Peninsula, Alaska. Quaternary Science Reviews 39, 26–44. https://doi.org/10.1016/j.quascirev.2012.01.027

Wetterich, S., Kuzmina, S., Andreev, A.A., Kienast, F., Meyer, H., Schirrmeister, L., Kuznetsova, T., Sierralta, M., 2008. Palaeoenvironmental dynamics inferred from late Quaternary permafrost deposits on Kurungnakh Island, Lena Delta, Northeast

Siberia, Russia. Quaternary Science Reviews 27, 1523–1540. https://doi.org/10.1016/j.quascirev.2008.04.007
Wetterich, S., Rudaya, N., Tumskoy, V., Andreev, A.A., Opel, T., Schirrmeister, L., Meyer, H., 2011a. Last Glacial Maximum records in permafrost of the East Siberian Arctic. Quaternary Science Reviews 30, 3139–3151. https://doi.org/10.1016/j.quascirev.2011.07.020
Wetterich, S., Schirrmeister, L., Andreev, A.A., Pudenz, M., Plessen, B., Meyer, H., Kunitsky, V.V., 2009. Eemian and Late Glacial/Holocene palaeoenvironmental records from permafrost sequences at the Dmitry Laptev Strait (NE Siberia, Russia). Palaeogeography, Palaeoclimatology, Palaeoecology 279, 73–95. https://doi.org/10.1016/j.palaeo.2009.05.002
Wetterich, S., Schirrmeister, L., Kholodov, A.L., 2011b. The joint Russian-German Expedition BERINGIA/KOLYMA 2008 during the International Polar Year (IPY) 2007/2008, Berichte zur Polar- und Meeresforschung = Reports on Polar and Marine Research. Alfred-Wegener-Institut für Polar- und Meeresforschung, Bremerhaven, Germany.
Wetterich, S., Tumskoy, V., Rudaya, N., Andreev, A.A., Opel, T., Meyer, H., Schirrmeister, L., Hüls, M., 2014. Ice Complex formation in arctic East Siberia during the MIS3 Interstadial. Quaternary Science Reviews 84, 39–55. https://doi.org/10.1016/j.quascirev.2013.11.009
Williams Jr, R.S., Ferrigno, J.G., 2012. State of the Earth's cryosphere at the beginning of the 21st century: Glaciers, global snow cover, floating ice, and permafrost and periglacial environments. Director 508, 344–6840.
Wilson, M., 2004. Weathering of the primary rock-forming minerals: processes, products and rates. Clay Minerals 39, 233–266. https://doi.org/10.1180/0009855043930133
Wilson, M.J., 2013. Sheet Silicates: Clay Minerals. Geological Society.
Wilson, S.A., 1997. Data compilation for USGS reference material BHVO-2, Hawaian Basalt. U.S. Geological Survey Open-File Report, U.S. Geological Survey Open-File Report 2.
Windirsch, T., Grosse, G., Ulrich, M., Schirrmeister, L., Fedorov, A.N., Konstantinov, P.Y., Fuchs, M., Jongejans, L.L., Wolter, J., Opel, T., Strauss, J., 2020. Organic carbon characteristics in ice-rich permafrost in alas and Yedoma deposits, central Yakutia, Siberia. Biogeosciences 17, 3797–3814. https://doi.org/10.5194/bg-17-3797-2020
Winkler, P., Kaiser, K., Thompson, A., Kalbitz, K., Fiedler, S., Jahn, R., 2018. Contrasting evolution of iron phase composition in soils exposed to redox fluctuations. Geochimica et Cosmochimica Acta 235, 89–102. https://doi.org/10.1016/j.gca.2018.05.019
Winton, M., 2006. Amplified Arctic climate change: What does surface albedo feedback have to do with it? Geophys. Res. Lett. 33, L03701. https://doi.org/10.1029/2005GL025244
Wiseman, C.L.S., Püttmann, W., 2005. Soil organic carbon and its sorptive preservation in central Germany. European Journal of Soil Science 56, 65–76. https://doi.org/10.1111/j.1351-0754.2004.00655.x
Wortberg, K., Conrad, S., Andersson, P.S., Ingri, J., 2017. Strontium isotopes – A tracer for river suspended iron aggregates. Applied Geochemistry 79, 85–90. https://doi.org/10.1016/j.apgeochem.2017.02.012
Wrona, F.J., Johansson, M., Culp, J.M., Jenkins, A., Mård, J., Myers-Smith, I.H., Prowse, T.D., Vincent, W.F., Wookey, P.A., 2016. Transitions in Arctic ecosystems: Ecological implications of a changing hydrological regime: Terrestrial and freshwater ecosystems. J. Geophys. Res. Biogeosci. 121, 650–674. https://doi.org/10.1002/2015JG003133
Xue, B., Huang, L., Huang, Y., Zhou, F., Li, F., Kubar, K.A., Li, X., Lu, J., Zhu, J., 2019. Roles of soil organic carbon and iron oxides on aggregate formation and stability in two paddy soils. Soil and Tillage Research 187, 161–171. https://doi.org/10.1016/j.still.2018.12.010

Yang, Z., You, J., Yang, Z.-M., 2008. Manganese uptake and transportation as well as antioxidant response to excess manganese in plants. Zhi wu sheng li yu fen zi sheng wu xue xue bao = Journal of plant physiology and molecular biology 33, 480–8.

Yershov, E.D., 2004. General geocryology. Cambridge university press.

Yool, A., Tyrrell, T., 2003. Role of diatoms in regulating the ocean's silicon cycle. Global Biogeochemical Cycles 17. https://doi.org/10.1029/2002GB002018

Young, K.E., Evans, C.A., Hodges, K.V., Bleacher, J.E., Graff, T.G., 2016. A review of the handheld X-ray fluorescence spectrometer as a tool for field geologic investigations on Earth and in planetary surface exploration. Applied Geochemistry 72, 77–87. https://doi.org/10.1016/j.apgeochem.2016.07.003

Zanina, O.G., Gubin, S.V., Kuzmina, S.A., Maximovich, S.V., Lopatina, D.A., 2011. Late-Pleistocene (MIS 3-2) palaeoenvironments as recorded by sediments, palaeosols, and ground-squirrel nests at Duvanny Yar, Kolyma lowland, northeast Siberia. Quaternary Science Reviews 30, 2107–2123. https://doi.org/10.1016/j.quascirev.2011.01.021

Zhang, T., Barry, R., Knowles, K., Heginbottom, J.A., Brown, J., 1999. Statistics and characteristics of permafrost and ground-ice distribution in the Northern Hemisphere. Polar Geography, 23 132–154. https://doi.org/10.1080/10889370802175895

Zhao, Q., Adhikari, D., Huang, R., Patel, A., Wang, X., Tang, Y., Obrist, D., Roden, E.E., Yang, Y., 2017. Coupled dynamics of iron and iron-bound organic carbon in forest soils during anaerobic reduction. Chemical Geology 464, 118–126. https://doi.org/10.1016/j.chemgeo.2016.12.014

Zimov, S.A., 2006. Climate Change: Permafrost and the Global Carbon Budget. Science 312, 1612–1613. https://doi.org/10.1126/science.1128908

Zolkos, S., Tank, S.E., 2020. Experimental Evidence That Permafrost Thaw History and Mineral Composition Shape Abiotic Carbon Cycling in Thermokarst-Affected Stream Networks. Front. Earth Sci. 8. https://doi.org/10.3389/feart.2020.00152

Zona, D., Lipson, D.A., Zulueta, R.C., Oberbauer, S.F., Oechel, W.C., 2011. Microtopographic controls on ecosystem functioning in the Arctic Coastal Plain. J. Geophys. Res. 116, G00I08. https://doi.org/10.1029/2009JG001241

APPENDICES

Part III Data Chapters

Chapter 1: Mineral element stocks in the Yedoma domain: a novel method applied to ice-rich permafrost regions

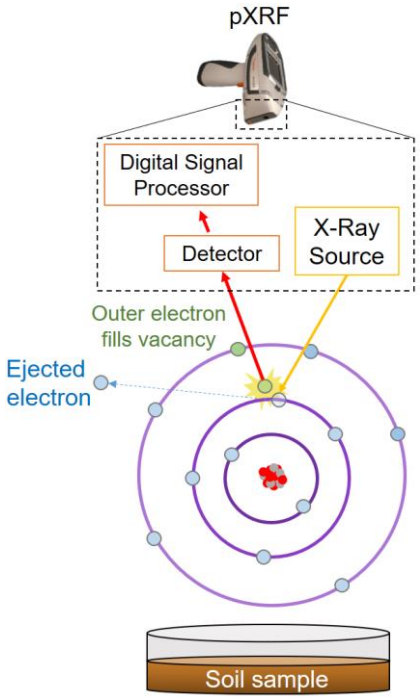

Figure S.6.1: Principles of the X-ray fluorescence methodology. An X-ray source emitted by the portable XRF device (here, *Niton XL3t GOLDD+*, Thermo Fisher Scientific) excites and ejects an electron from a specific atom. An outer electron fills vacancy to stabilize the overall atom and the electron translocation process implies an energy loss (fluorescence). This energy, specific to each atom, is detected, amplified and processed by the pXRF device. The processing converts photon energy of a specific wavelength to counts per seconds to concentration of a specific element.

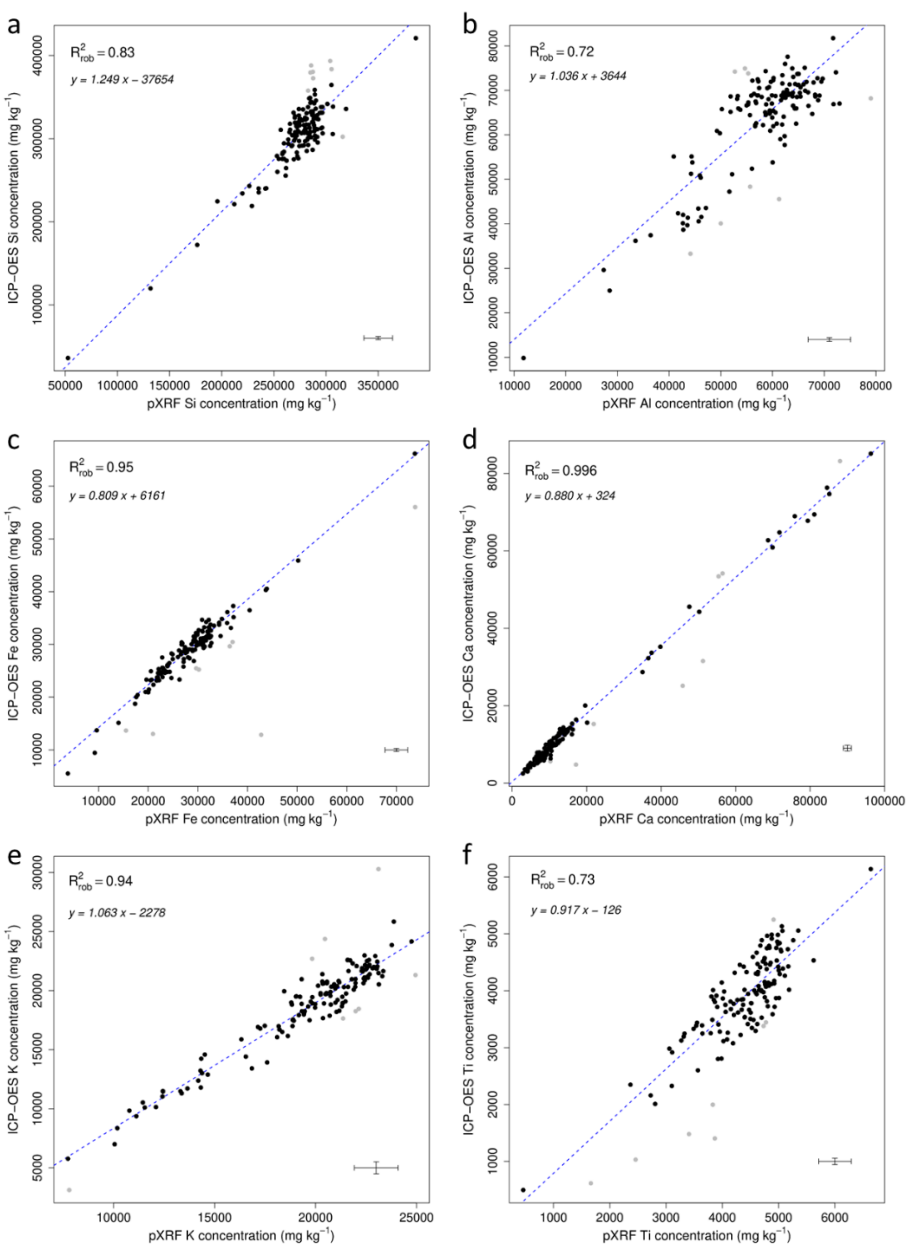
a
$R^2_{rob} = 0.83$
y = 1.249 x − 37654
ICP–OES Si concentration (mg kg^{-1})
pXRF Si concentration (mg kg^{-1})
b
$R^2_{rob} = 0.72$
y = 1.036 x + 3644
ICP–OES Al concentration (mg kg^{-1})
pXRF Al concentration (mg kg^{-1})
c
$R^2_{rob} = 0.95$
y = 0.809 x + 6161
ICP–OES Fe concentration (mg kg^{-1})
pXRF Fe concentration (mg kg^{-1})
d
$R^2_{rob} = 0.996$
y = 0.880 x + 324
ICP–OES Ca concentration (mg kg^{-1})
pXRF Ca concentration (mg kg^{-1})
e
$R^2_{rob} = 0.94$
y = 1.063 x − 2278
ICP–OES K concentration (mg kg^{-1})
pXRF K concentration (mg kg^{-1})
f
$R^2_{rob} = 0.73$
y = 0.917 x − 126
ICP–OES Ti concentration (mg kg^{-1})
pXRF Ti concentration (mg kg^{-1})

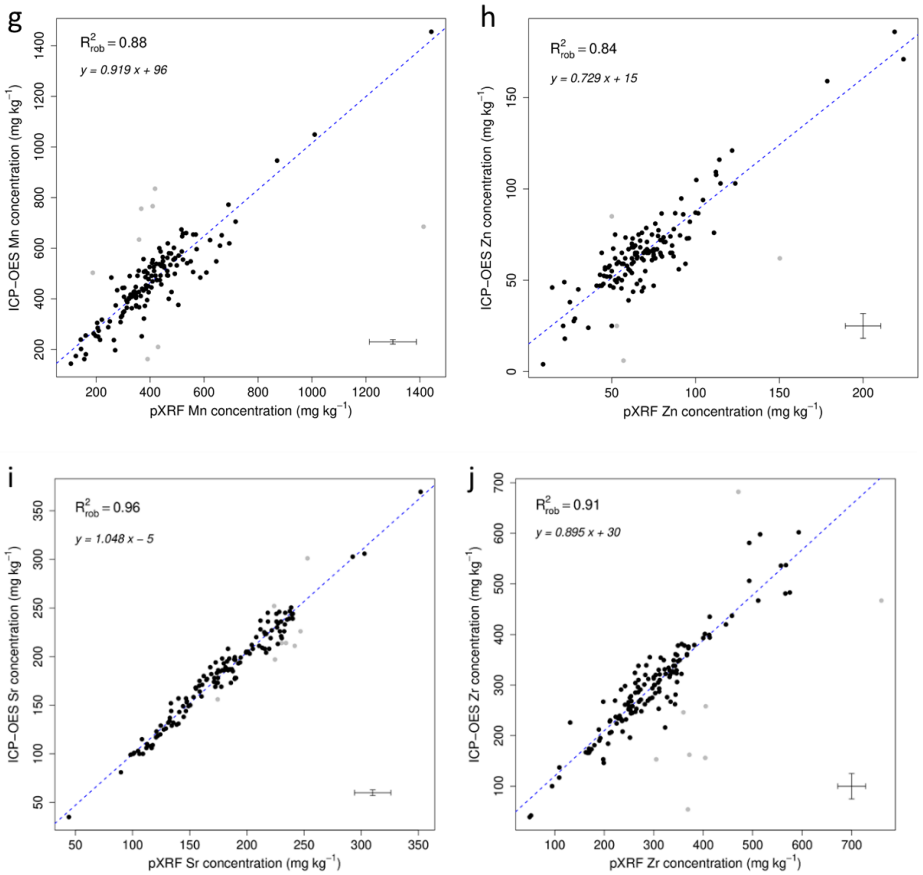

Figure S.6.2: Robust linear regressions (blue line) between element concentrations obtained by the inductively coupled plasma optical emission spectrometry (ICP-OES) method after alkaline fusion as a function of the raw concentrations obtained by the portable X-ray fluorescence (pXRF) method. The data are presented for the 10 elements considered: Si (a), Al (b), Fe (c), Ca (d), K (e), Ti (f), Mn (g), Zn (h), Sr (i), and Zr (j) with n = 144 for all elements, except for Zn where n = 119. Gray points (which include organic-rich samples; TOC > 40 wt%) were excluded from the robust linear regression. Errors bar (±2 pooled σ) were calculated based on three repetitions of three samples for ICP-OES method and on three to five repetitions of 20 samples for pXRF method. Robust linear regression R^2 and equation are provided for each element.

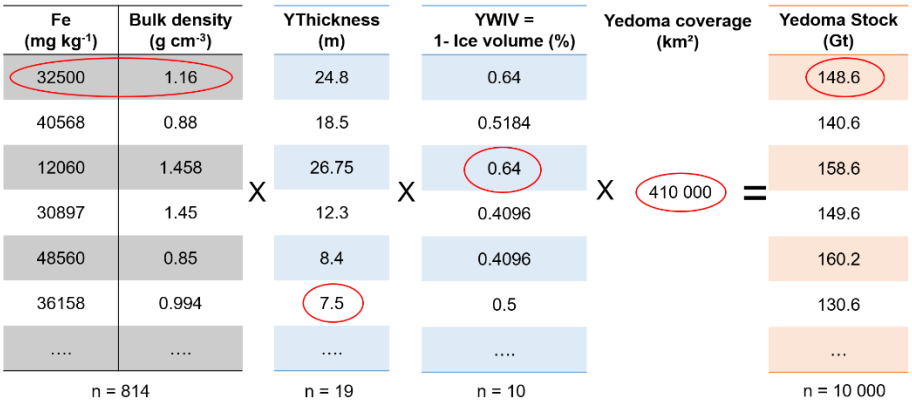

Figure S.6.3: Principles of the mean-bootstrapping technique to calculate mineral element stock in Yedoma domain deposits illustrated for Fe in Yedoma (Y). The bootstrapping statistical method use resampled (10,000 times) observed values (circled in red; i.e., mineral element concentration, bulk density, deposits thickness (mean = 19.6 m; n = 19) and ice-wedge volume (WIV; mean = 49.1%; n = 10)) and derive the mean afterward. This bootstrapping technique is used due to the non-normal distribution of the parameters. We used sampling with replacement, which means that after each step of the random draw from the original sample, we put the observation back before the following step. The process is done with 10,000 steps from which a stock density distribution is obtained. To estimate mineral elements stocks, we use the arithmetic mean and standard deviation assuming normality of the stock estimate distribution (Strauss et al., 2013).

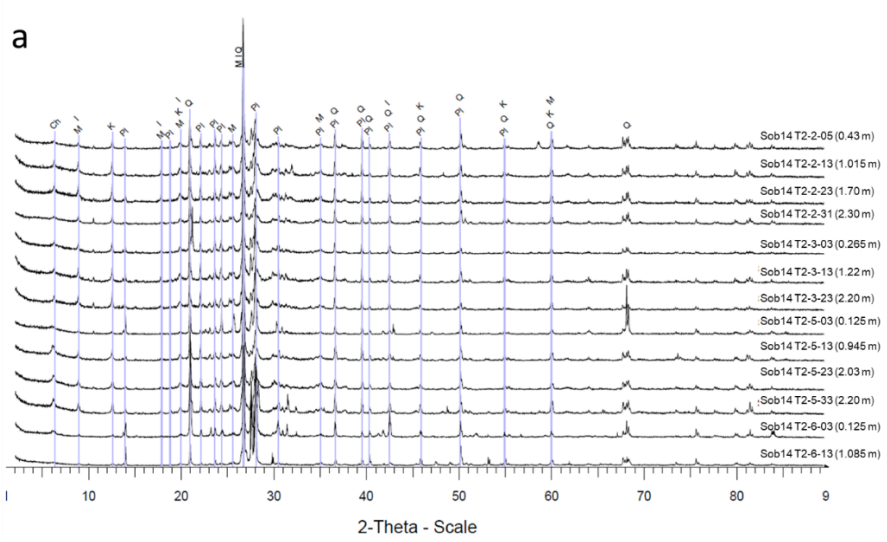
a
Sob14 T2-2-05 (0.43 m)
Sob14 T2-2-13 (1.015 m)
Sob14 T2-2-23 (1.70 m)
Sob14 T2-2-31 (2.30 m)
Sob14 T2-3-03 (0.265 m)
Sob14 T2-3-13 (1.22 m)
Sob14 T2-3-23 (2.20 m)
Sob14 T2-5-03 (0.125 m)
Sob14 T2-5-13 (0.945 m)
Sob14 T2-5-23 (2.03 m)
Sob14 T2-5-33 (2.20 m)
Sob14 T2-6-03 (0.125 m)
Sob14 T2-6-13 (1.085 m)
10
20
30
40
50
60
70
80
2-Theta - Scale

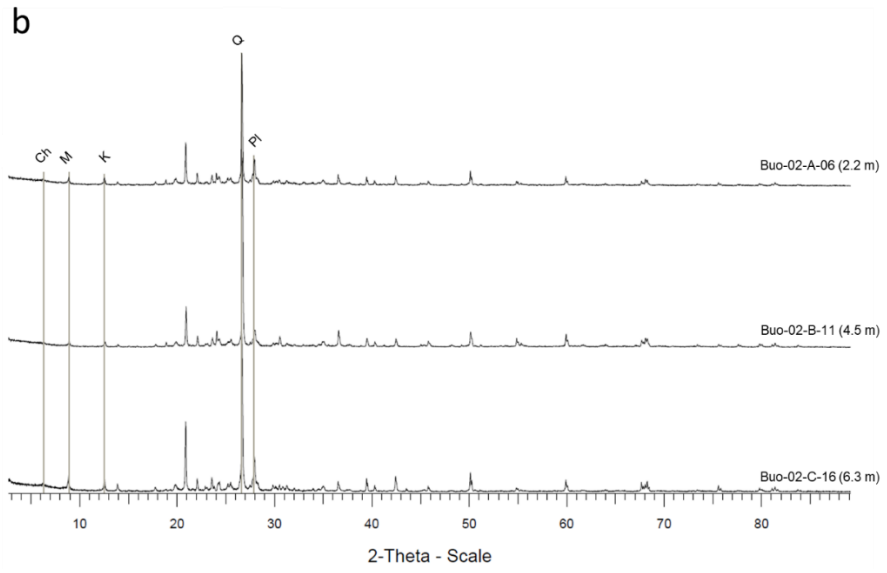
b
Q
Ch
M
K
Pl
Buo-02-A-06 (2.2 m)
Buo-02-B-11 (4.5 m)
Buo-02-C-16 (6.3 m)
10
20
30
40
50
60
70
80
2-Theta - Scale

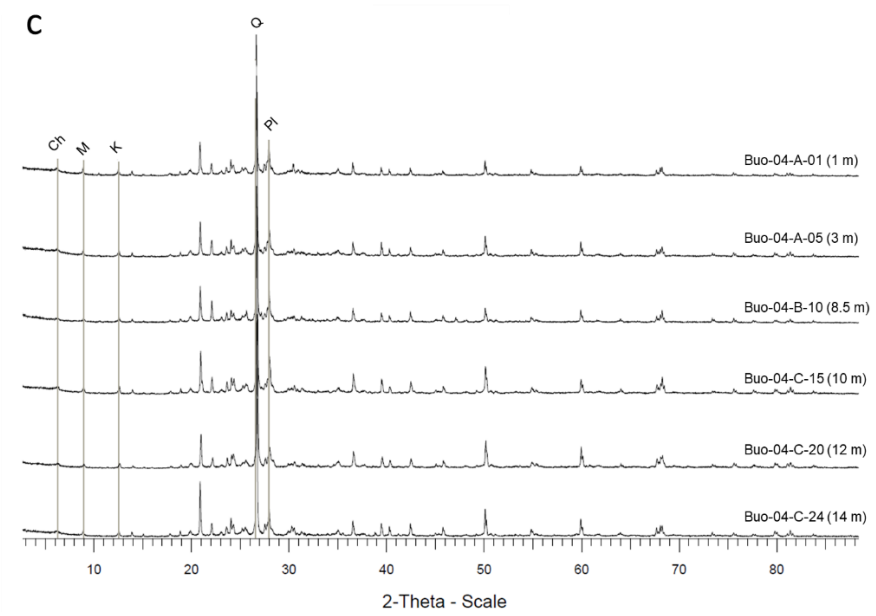
c
Q
Ch
M
K
Pl
Buo-04-A-01 (1 m)
Buo-04-A-05 (3 m)
Buo-04-B-10 (8.5 m)
Buo-04-C-15 (10 m)
Buo-04-C-20 (12 m)
Buo-04-C-24 (14 m)
10
20
30
40
50
60
70
80
2-Theta - Scale

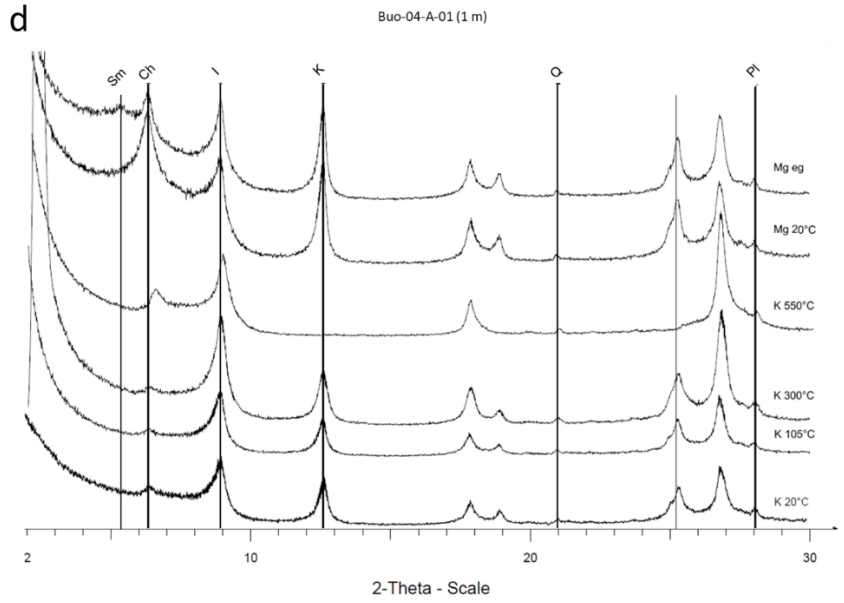
d
Buo-04-A-01 (1 m)
Sm
Ch
I
K
Q
Pl
Mg eg
Mg 20°C
K 550°C
K 300°C
K 105°C
K 20°C
2
10
20
30
2-Theta - Scale

e

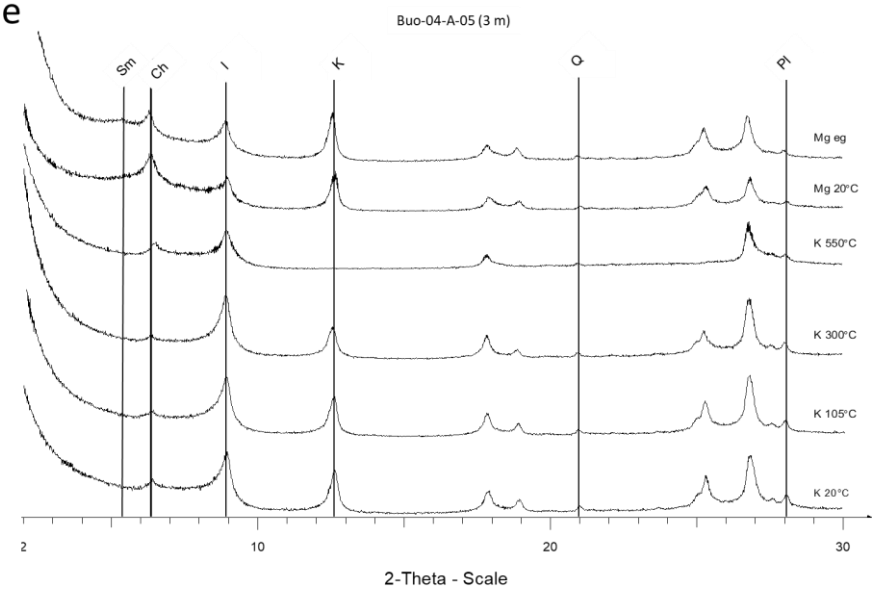
Buo-04-A-05 (3 m)
Sm
Ch
I
K
Q
Pl
Mg eg
Mg 20°C
K 550°C
K 300°C
K 105°C
K 20°C
2
10
20
30
2-Theta - Scale

f

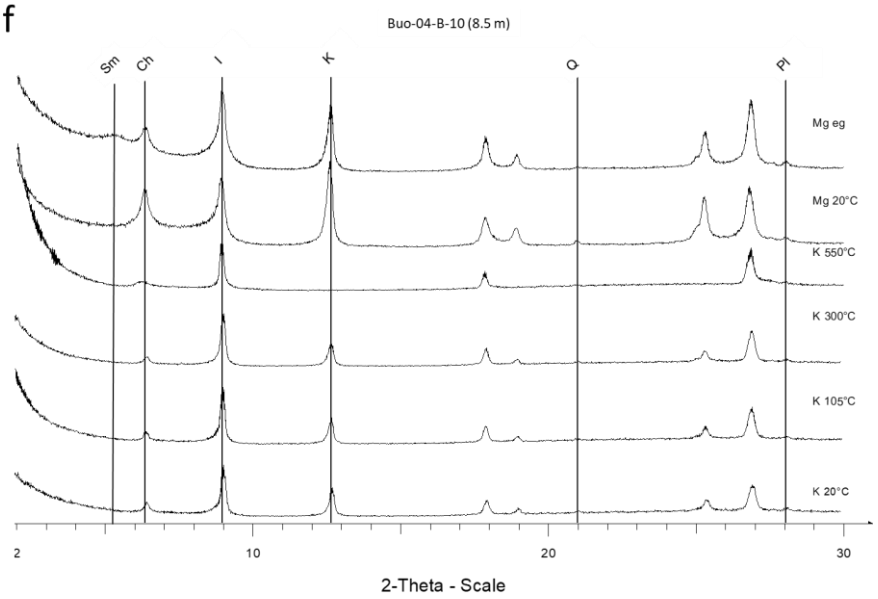
Buo-04-B-10 (8.5 m)
Sm
Ch
I
K
Q
Pl
Mg eg
Mg 20°C
K 550°C
K 300°C
K 105°C
K 20°C
2
10
20
30
2-Theta - Scale

g

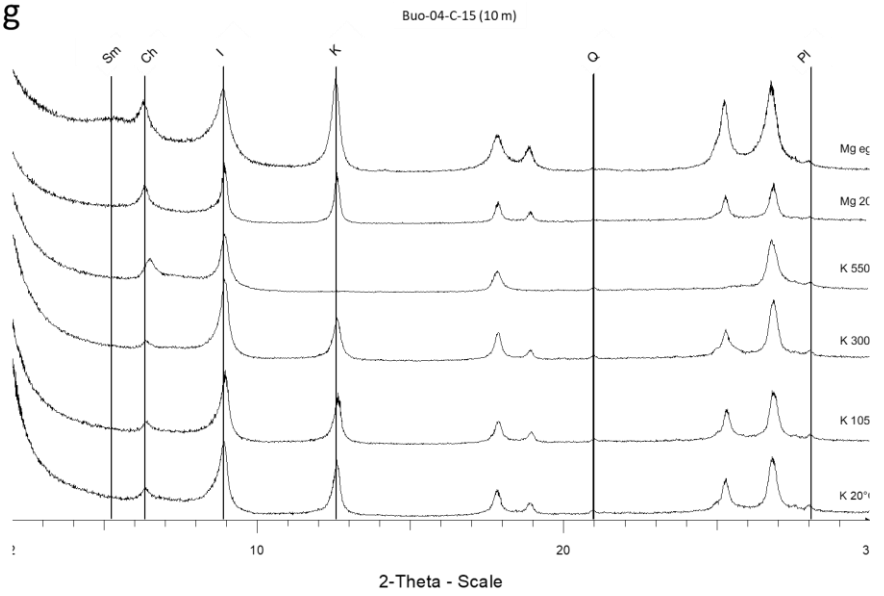
Buo-04-C-15 (10 m)
Sm
Ch
I
K
Q
Pl
Mg eg
Mg 20
K 550
K 300
K 105
K 20°
10
20
2-Theta - Scale

h

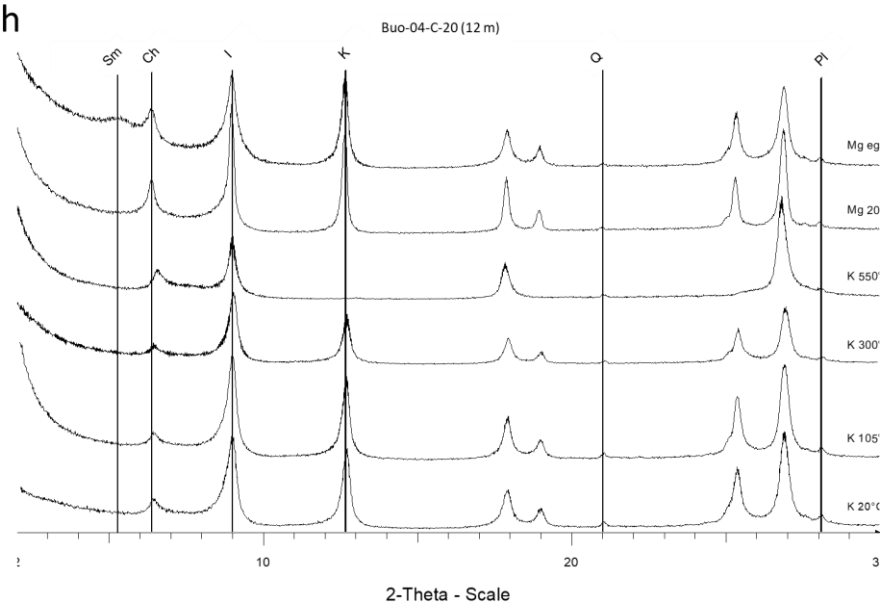
Buo-04-C-20 (12 m)
Sm
Ch
I
K
Q
Pl
Mg eg
Mg 20
K 550
K 300
K 105
K 20°
10
20
2-Theta - Scale

i

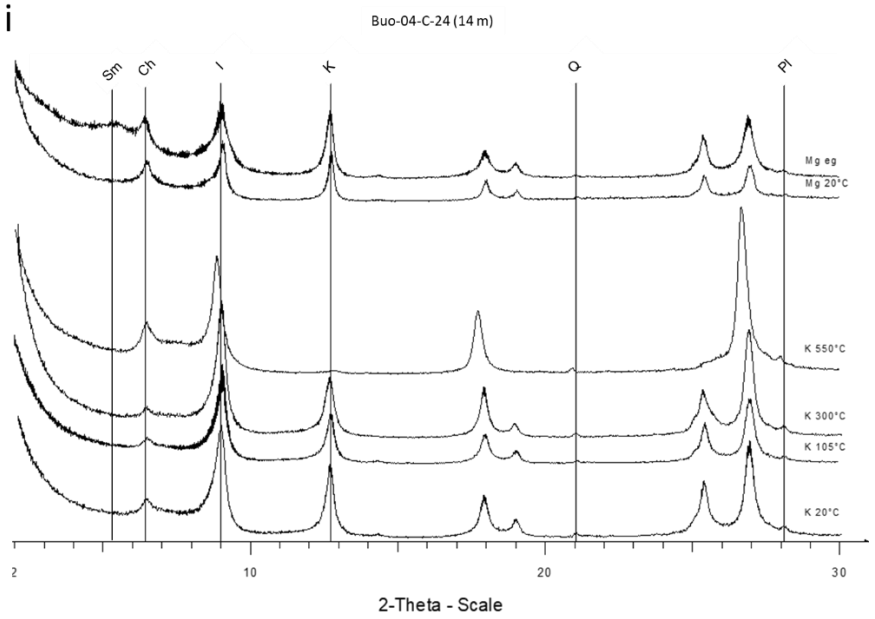
Buo-04-C-24 (14 m)
Sm
Ch
I
K
Q
Pl
Mg eg
Mg 20°C
K 550°C
K 300°C
K 105°C
K 20°C
2
10
20
30
2-Theta - Scale

j

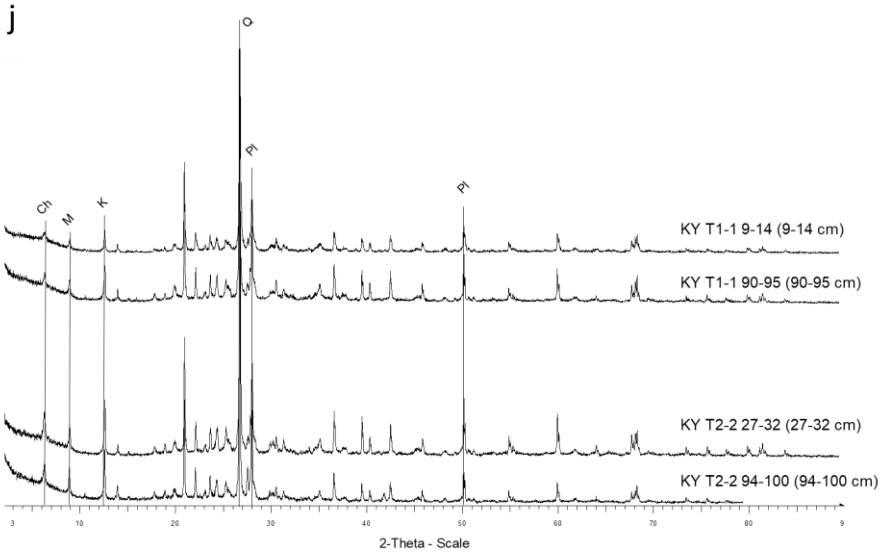
Q
Pl
Pl
Ch
M
K
KY T1-1 9-14 (9-14 cm)
KY T1-1 90-95 (90-95 cm)
KY T2-2 27-32 (27-32 cm)
KY T2-2 94-100 (94-100 cm)
3
10
20
30
40
50
60
70
80
9
2-Theta - Scale

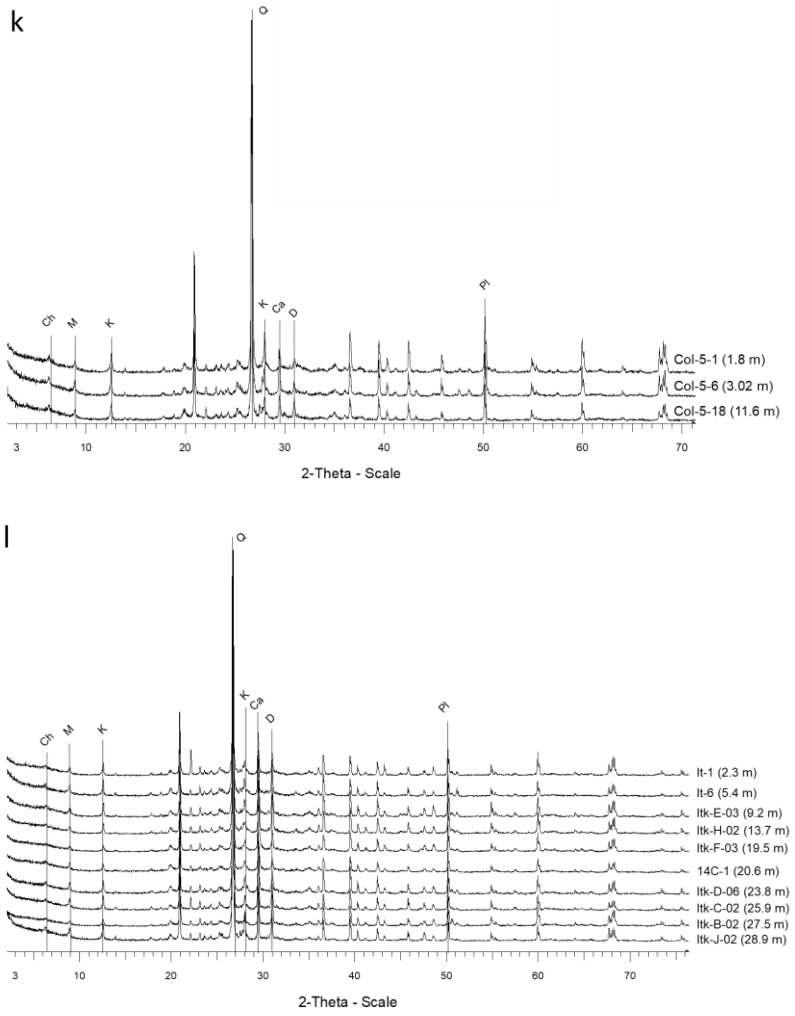

Figure S.6.4: X-ray diffractograms of Yedoma, Alas and fluvial deposits in Siberia and Alaska (Q, quartz; Pl, Plagioclase; Ch, Chlorite; M, Mica; I, Illite; K, Kaolinite; D, Dolomite; Ca, Calcite; Sm, Smectite). Each diffractogram is labelled according to label code from Table 6.1 and samples depth is specified next to each label. (a) Sobo Sise profiles, (b) Buo-02 profile, (c) Buo-04 profile, (d) to (i) Buo-04 clay fractions (including the following treatments: K^+ and Mg^{2+} saturation, ethylene glycol (eg) solvation and thermal treatments at 300 and 550°C), (j) Kytalyk profiles, (k) Colville profile and (l) Itkillik profile. Diffractograms include Yedoma (Sob T2-2, Sob T2-3, Buo-02, Buo-04, KY T1-1, Col, Itk) and Alas or fluvial deposits (Sob T2-5, Sob T2-6, KY T2-2). A summary of the mineral phases identified in each location is provided in Table 6.6.

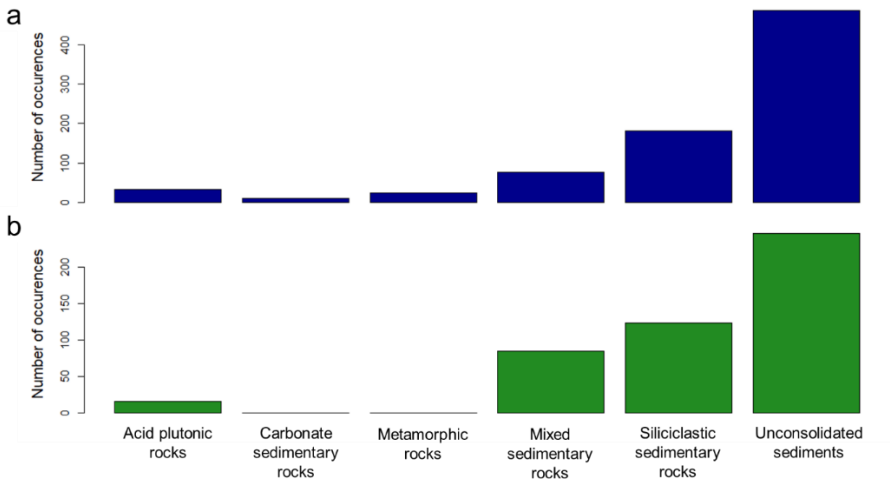

Figure S.6.5: Lithology of the bedrock underlying (a) Yedoma deposits (in blue, n=814) and (b) Alas deposits (in green, n=470) inferred from the Global Lithological Map (GLiM; Hartmann and Moosdorf, 2012).

Table S.6.1: Studied locations from the Yedoma domain with associated labels, total number of sampled profiles, number of samples analyzed with portable X-ray fluorescence (pXRF), inductively coupled plasma optical emission spectrometry (ICP-OES) after alkaline fusion and X-ray diffraction method (XRD). A simplified geomorphological description of each sampling location is presented (detailed information is provided in the reference papers cited in Table 6.1). The site numbers (Site Nb) 1-17 are from Siberia, and 18-22 are from Alaska.

Site Nb	Site Name	Label	Total profiles	Samples with pXRF method	Samples with ICP-OES method	Samples with XRD method	Geomorphology of sampling location
1	Cape Mamontov Klyk	Mak	3	80	-	-	Sedimentary coastal plain
2	Nagym (Ebe Sise Island)	Nag	3	29	-	-	Cliff section with thermokarst mounds
3	Khardang Island	Kha	1	31	1	-	Cliff section with thermokarst mounds
4	Kurungnakh Island	Bkh, KUR	4	143	2	-	Fragment of a broad foreland plain north of the Chekanovsky Ridge
5	Sobo Sise Island	Sob	4	58	58	13	Yedoma uplands but also features permafrost degradation landforms (thermokarst lakes, drained thaw lake basin, and thermo-erosional gullies)
6	Bykovsky Peninsula	Mkh, BYK	7	150	2	-	Remnants of an accumulation plain
7	Muostakh Island	Muo	1	11	-	-	Remnants of an accumulation plain
8	Buor Khaya Peninsula	Buo	5	80	44	10	Coastal lowlands - late Pleistocene accumulation plains
9	Stolbovoy Island	Sto	4	16	1	-	Step-like cryoplanation terraces with several levels
10	Belkovsky Island	Bel	2	12	-	-	Step-like cryoplanation terraces with several levels
11	Kotel'ny Island	KyS	1	10	-	-	Step-like cryoplanation terraces with several levels
12	Bunge Land	Bun	1	8	-	-	More-or-less homogeneous flat sandy plain
13	Bol'shoy Lyakhovsky Island	TZ, R, L	15	150	3	-	Gradually sloping terrain intersected by rivers and thermo-erosional valleys
14	Oyogos Yar coast	Oy	2	50	1	-	Very gently inclined step-like surface of the Yana-Indigirka Lowland
15	Kytalyk	KY, KH	3	50	4	4	Recent and sub-recent floodplains, Yedoma and Alas
16	Duvanny Yar	DY	6	143	5	-	Hills dissected by deep thermos-erosional valleys and thermokarst depressions
17	Yukechi	Yuk-Yul	4	87	2	-	Yedoma uplands and drained alas basins, indicating active thermokarst processes
18	Kitluk	Kit	2	45	2	-	Tundra-covered coastal plain
19	Baldwin Peninsula	Bal	4	70	1	-	Sequence of marine, fluvial and glaciogenic sediments, which are well exposed along coastal bluffs and in some regions covered by loess-like deposits
20	Colville	Col	1	23	8	3	High exposure along the Colville River
21	Itkillik	Itk, It	1	22	10	10	High exposure along the lower Itkillik River formed by active river erosion of a large remnant of originally gently undulating Yedoma terrain
22	Vault Creek Tunnel	FAI	1	24	-	-	Permafrost tunnel about 40 m deep and 220 m long on north facing slope
TOTAL			75	1292	144	40	

Table S.6.2: Accuracy on the measurement by inductively coupled plasma optical-emission spectrometry (ICP-OES) after alkaline fusion for three certified reference materials: i) USGS BHVO-2 (Wilson, 1997), ii) GBW07401 (GSS-1) and iii) GBW07404 (GSS-4) (National Research Centre for CRM, 1986). The mean and standard deviation (SD; n= number of repetitions) of ICP-OES values and certified values are shown. The offset, defined as the difference between certified and ICP-OES value over the certified value, expressed in %, is provided for each reference material.

	Si	Al	Fe	Ca	K	Ti	Mn	Zn	Sr	Zr
Units	Wt %						mg kg^{-1}			
BHVO-2										
n	12	12	12	12	12	12	12	5	11	12
ICP-OES mean (SD)	23.2 (0.2)	7.16 (0.07)	8.56 (0.14)	8.06 (0.11)	0.43 (0.03)	1.61 (0.02)	1291 (49)	110 (7)	392 (29)	176 (9)
Certified values mean (SD)	23.3 (0.3)	7.16 (0.08)	8.63 (0.14)	8.17 (0.12)	0.43 (0.01)	1.63 (0.02)	1290 (40)	103 (6)	389 (23)	172 (11)
Offset (%)	-0.3	0.02	-0.8	-1.4	0.5	-1.2	0.05	7.2	0.8	2.4
GBW07401 (GSS-1)										
n	5	5	5	5	5	5	5	5	5	5
ICP-OES mean (SD)	28.7 (0.79)	7.43 (0.16)	3.48 (0.05)	1.15 (0.01)	2.09 (0.04)	0.47 (0.01)	1703 (30)	666 (9)	152 (3)	239 (10)
Certified values mean (SD)	29.3 (0.07)	7.50 (0.07)	3.63 (0.06)	1.23 (0.04)	2.15 (0.03)	0.48 (0.02)	1760 (63)	680 (25)	155 (7)	245 (12)
Offset (%)	-2.0	-0.9	-4.2	-6.2	-2.6	-2.8	-3.2	-2.1	-1.9	-2.3
GBW07404 (GSS-4)										
n	5	5	5	5	5	5	5	5	5	5
ICP-OES mean (SD)	23.7 (0.4)	12.3 (0.3)	6.76 (0.15)	0.15 (0.01)	0.87 (0.02)	1.06 (0.02)	1404 (19)	209 (3)	78 (1)	518 (4)
Certified values mean (SD)	23.8 (0.1)	12.4 (0.1)	7.20 (0.08)	0.19 (0.03)	0.86 (0.05)	1.08 (0.03)	1420 (75)	210 (13)	77 (6)	500 (42)
Offset (%)	-0.3	-0.6	-6.1	-21	1.3	-2.1	-1.2	-0.4	1.0	3.7

Table S.6.3: List of samples (n=144) analysed by both inductively coupled plasma optical-emission spectrometry (ICP-OES) and portable X-ray fluorescence (XRF) method for linear regressions determination. Depth (below surface level) or *height (above sea level) are provided (in meters) if available. Labels are associated to labels from the Yedoma domain Mineral Concentration Assessment (YMCA) dataset for additional characteristics.

n	Sample	Depth/ *Height (m)	n	Sample	Depth/ *Height (m)	n	Sample	Depth/ *Height (m)
1	Sob14-T2-2-03	0.225	49	Sob14-T2-6-09	0.775	97	Buo-02-D-23	7
2	Sob14-T2-2-05	0.43	50	Sob14-T2-6-11	0.96	98	Col-5-1	1.8
3	Sob14-T2-2-07	0.6	51	Sob14-T2-6-13	1.085	99	Col-5-6	3.02
4	Sob14-T2-2-09	0.745	52	Sob14-T2-6-15	1.15	100	Col-5-10	5.4
5	Sob14-T2-2-11	0.87	53	Sob14-T2-6-16	1.2	101	Col-5-13	6.9
6	Sob14-T2-2-13	1.015	54	Buo-04-A-00	0.1	102	Col-5-15	9
7	Sob14-T2-2-15	1.15	55	Buo-04-A-01	1	103	Col-5-18	11.6
8	Sob14-T2-2-17	1.25	56	Buo-04-A-02	1.5	104	It-1	2.3
9	Sob14-T2-2-19	1.4	57	Buo-04-A-03	2	105	It-6	5.4
10	Sob14-T2-2-21	1.565	58	Buo-04-A-04	2.5	106	Itk-E-03	9.2
11	Sob14-T2-2-23	1.7	59	Buo-04-A-05	3	107	Itk-H-02	13.7
12	Sob14-T2-2-25	1.82	60	Buo-04-A-06	3.5	108	Itk-F-03	19.5
13	Sob14-T2-2-27	1.935	61	Buo-04-A-07	4.5	109	14C-1	20.6
14	Sob14-T2-2-29	2.14	62	Buo-04-A-08	5	110	Itk-D-06	23.8
15	Sob14-T2-2-31	2.3	63	Buo-04-B-09	8	111	Itk-C-02	25.9
16	Sob14-T2-3-03	0.265	64	Buo-04-B-10	8.5	112	Itk-B-02	27.5
17	Sob14-T2-3-05	0.52	65	Buo-04-B-11	9	113	Itk-J-02	28.9
18	Sob14-T2-3-07	0.66	66	Buo-04-B-12	9.5	114	Sob14-T2-2-03bis	0.225
19	Sob14-T2-3-09	0.835	67	Buo-04-B-13	10	115	Sob14-T2-2-07bis	0.6
20	Sob14-T2-3-11	1.045	68	Buo-04-C-14	9.5	116	Sob14-T2-2-15bis	1.15
21	Sob14-T2-3-13	1.22	69	Buo-04-C-15	10	117	Sob14-T2-2-20bis	1.5
22	Sob14-T2-3-15	1.45	70	Buo-04-C-16	10.5	118	Sob14-T2-2-30bis	2.2
23	Sob14-T2-3-17	1.685	71	Buo-04-C-17	11	119	KY-T1-1-9-14	0.125
24	Sob14-T2-3-19	1.885	72	Buo-04-C-19	11.7	120	KY-T1-1-90-95	0.925
25	Sob14-T2-3-21	2.04	73	Buo-04-C-20	12	121	KY-T2-2-27-32	0.295
26	Sob14-T2-3-23	2.2	74	Buo-04-C-21	12.5	122	KY-T2-2-94-100	0.97
27	Sob14-T2-3-25	2.4	75	Buo-04-C-22	13	123	Oy7-11-16	11.9*
28	Sob14-T2-5-03	0.125	76	Buo-04-C-23	13.5	124	52Mkh-KB-7-5	22.3*
29	Sob14-T2-5-05	0.375	77	Buo-02-A-01	0.3	125	DY-01-F-34	29.1*
30	Sob14-T2-5-07	0.48	78	Buo-02-A-02	0.6	126	DY-02-A-01	5*
31	Sob14-T2-5-09	0.635	79	Buo-02-A-03	0.7	127	DY-04-A-01	7.85*
32	Sob14-T2-5-11	0.775	80	Buo-02-A-04	1.2	128	DY-04-A-02	7.7*
33	Sob14-T2-5-13	0.945	81	Buo-02-A-05	1.7	129	DY-05-B-05	2.7*
34	Sob14-T2-5-15	1.15	82	Buo-02-A-06	2.2	130	Kit-8-5	-
35	Sob14-T2-5-17	1.32	83	Buo-02-B-07	2.5	131	Col-5-2	-
36	Sob14-T2-5-19	1.505	84	Buo-02-B-08	3	132	Col-5-17	-
37	Sob14-T2-5-21	1.75	85	Buo-02-B-09	3.5	133	Sto-1-1	0.25
38	Sob14-T2-5-23	2.03	86	Buo-02-B-10	4	134	1TZ-2-2	17.65*
39	Sob14-T2-5-25	2.19	87	Buo-02-B-11	4.5	135	L21+50-S-3	4.3*
40	Sob14-T2-5-27	2.39	88	Buo-02-B-13	5.5	136	L7-08-03	4.5*
41	Sob14-T2-5-29	2.57	89	Buo-02-C-14	5.2	137	126Mkh-6.1.1	1.25*
42	Sob14-T2-5-31	2.76	90	Buo-02-C-15	5.7	138	11KH-3007-1-4	0.6
43	Sob14-T2-5-33	2.94	91	Buo-02-C-16	6.3	139	Bkh2002 S17	32.5*
44	Sob14-T2-5-35	3.075	92	Buo-02-C-17	6.9	140	BAL16-B2-30	10.97
45	Sob14-T2-5-36	3.1525	93	Buo-02-D-18	4.5	141	YUK15-YUL7-5	7.75*
46	Sob14-T2-6-03	0.125	94	Buo-02-D-19	5	142	YUK15-YUL7-15	17.96*
47	Sob14-T2-6-05	0.325	95	Buo-02-D-20	5.5	143	K-10-14-4	14.38
48	Sob14-T2-6-07	0.525	96	Buo-02-D-22	6.5	144	Kit-7-2	-

Table S.6.4: Precision of portable X-ray fluorescence (pXRF) method on the element concentrations expressed pooled standard deviations (i.e., 2 pooled standard deviations, expressed in mg kg^{-1}) for the 10 elements considered. The values are based on a subset of Yedoma and Alas deposit samples with three to five repetitions of 20 samples. The coefficient of variation (CV; expressed in %), defined as the ratio of the standard deviation to the mean is available. The error bars on Figure S.6.2 are based on the following standard deviations for pXRF method.

		Si	Al	Fe	Ca	K	Ti	Mn	Zn	Sr	Zr
pXRF	$\pm 2SD_{pooled}$ (mg kg^{-1})	± 3675	± 4107	± 2288	± 1066	± 1084	± 88.5	± 87	± 0.587	± 15.88	± 28.2
	CV (%)	2.14	3.07	3.44	5.46	2.77	3.62	8.74	7.78	4.09	4.93

Table S.6.5: Mineral elements density (kg m^{-3}) summary in Yedoma and Alas deposits (n=814 and 470, respectively). This mineral element density neglects the presence of ice-wedges.

	Mineral element density (kg m^{-3})			
	Yedoma deposits		Alas deposits	
Element	Mean	± 2σ	Mean	± 2σ
Si	345.6	8.34	335.3	14.07
Al	75.4	1.74	73.0	2.96
Fe	36.0	0.843	35.3	1.38
Ca	17.3	0.916	13.1	1.02
K	22.0	0.572	21.3	0.98
Ti	4.64	0.107	4.42	0.18
Mn	0.626	0.0883	0.587	0.035
Zn	0.080	0.0019	0.078	0.0039
Sr	0.235	0.0085	0.235	0.016
Zr	0.332	0.0094	0.315	0.017

Chapter 2: Iron redistribution upon thermokarst processes in the Yedoma domain

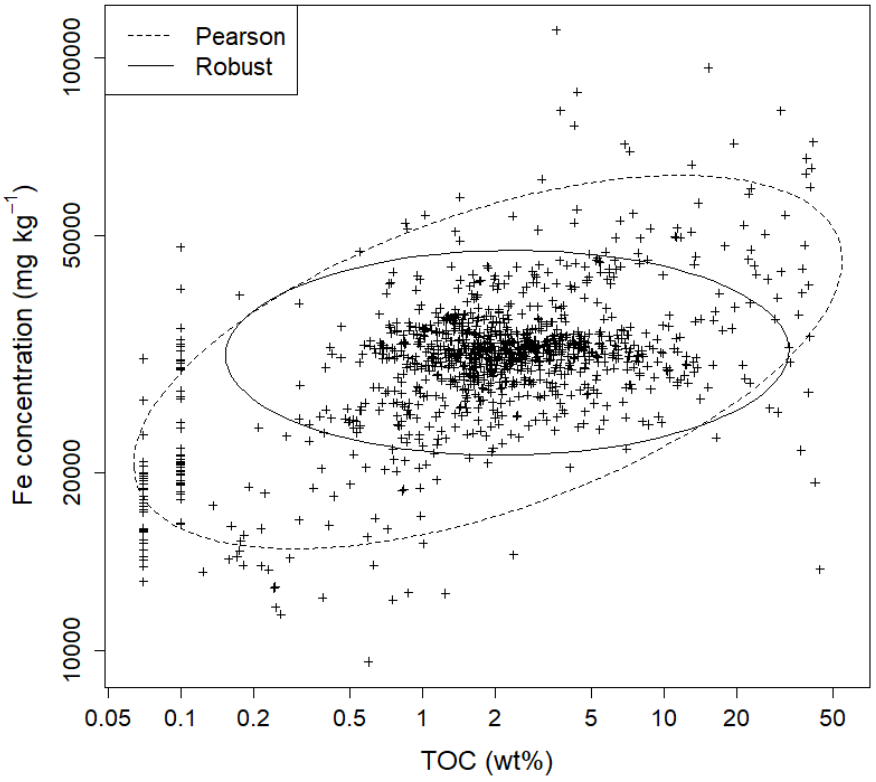

Figure S.7.1: Correlation plot of total Fe concentration (mg kg^{-1}) as a function of total organic carbon (TOC) content (wt%) from Yedoma Ice Complex and Alas deposits for which TOC data are available (n=1182). Points vertically distributed on the left of the plot refers to sample with limit of detection regarding TOC content (0.07 or 0.1 wt% depending on the method used). Pearson (dashed) and robust correlation (continuous ellipse) are shown on the plot and display values of 0.55 and 0.02, respectively. Samples with high TOC content (>20 wt%) and with lower Fe concentration refers to samples from top surface layers of deposits profiles (within active layer). Note that x and y-axis are logarithmic scale.

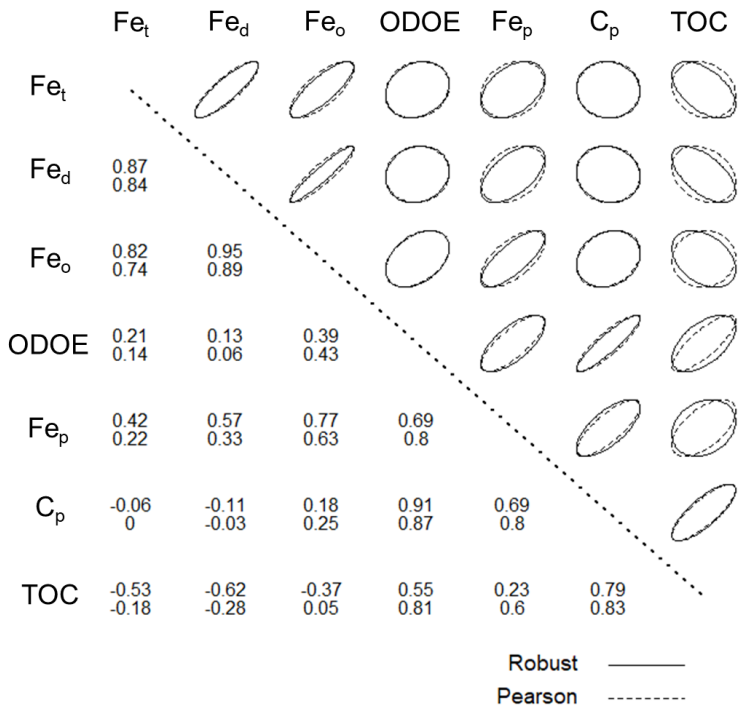

Figure S.7.2: Robust (full ellipse) and Pearson (dashed ellipse) correlation matrix of studied parameters: total Fe concentrations (Fe_t), Fe selectively extracted by dithionite-citrate-bicarbonate (Fe_d), Fe selectively extracted by ammonium oxalate (Fe_o), optical density of the oxalate extract (ODOE), Fe selectively extracted by Na-pyrophosphate (Fe_p), C selectively extracted by Na-pyrophosphate (C_p), total organic carbon (TOC) from Yedoma Ice Complex and Alas deposits. Robust correlation is the upper value and Pearson correlation the lower value displayed at the bottom part of the matrix.

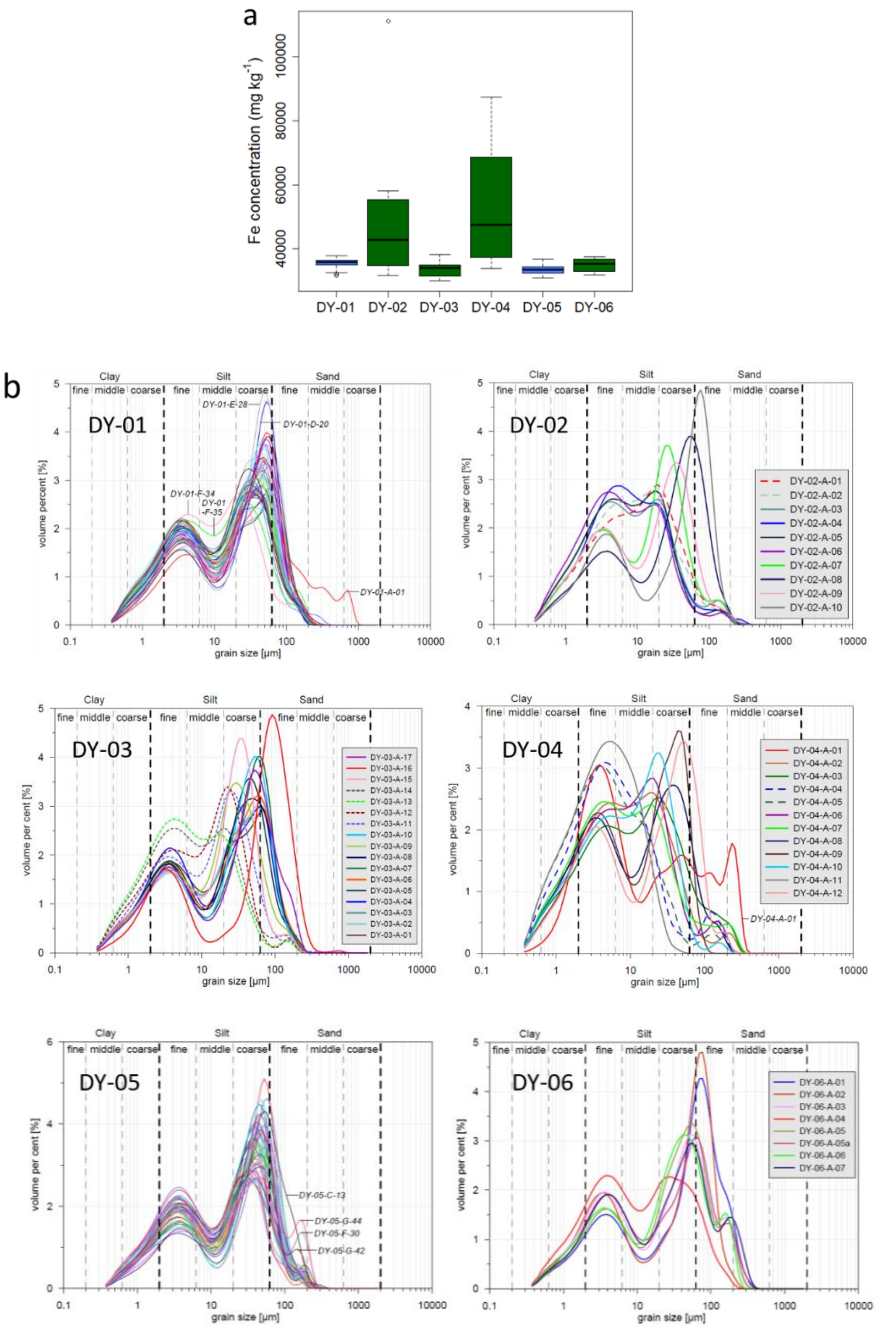

Figure S.7.3: (a) Boxplot of total Fe concentrations from Yedoma Ice Complex (blue) and Alas or thermokarst lake sediment (green) profiles from Duvanny Yar and (b) associated grain-size distribution (Strauss, 2010).

Table S.7.1: Label identification for each profile from sites of the Yedoma domain. These labels are sometimes part of composite profiles. Details about sampling campaign are provided in reference papers from Table 7.1.

Site Nb	Site Name	Label		
		Yedoma	Alas	Deltaic/fluvial
1	Cape Mamontov Klyk	Mak-2 to 10 Mak-12 to 19	Mak-14	
2	Nagym (Ebe Sise Island)	Nag 4+50 Nag 4+80 Nag 6+20	Nag 1+80	
3	Khardang Island	Kha-2		
4	Kurungnakh Island	Bkh-3 Bkh 2002	Bkh-4 K-10	
5	Sobo Sise Island	Sob14 T2-2 Sob14 T2-3	Sob14 T2-5	Sob14 T2-6
6	Bykovsky Peninsula	Mkh1 Mkh2 Mkh99 Mkh00	BYK-Mkh 6.2 MB 6.3	
7	Muostakh Island	Muo-3		
8	Buor Khaya Penisula	Buo-02 Buo-04	Buo-03 Buo-05	
9	Stolbovoy Island	Sto-1 Sto-2 Sto-3	Sto-4	
10	Belkovsky Island		Bel-7 Bel-8	
11	Kotel'ny Island	KyS-2		
12	Bunge Land			Bun-4
13	Bol'shoy Lyakhovsky Island	1TZ 2TZ 3TZ L7-18 L7-07	R33-A1 L21+50 L7-08	
14	Oyogos Yar coast	Oy7-08	Oy7-11	
15	Kytalyk	11KH-3007 KY T1-1	KY T2-2	
16	Duvanny Yar	DY-01 DY-05	DY-02 DY-03 DY-04 DY-06	
17	Yukechi	YUK15-YUL15 YUK15-YED1	YUK15-YUL7 YUK15-Alas1	
18	Kitluk	Kit	Kit	
19	Baldwin Peninsula	BAL16-B2	BAL16-B3 BAL16-B4 BAL16-B5	
20	Colville	Col-5		
21	Itkillik	Itk		
22	Vault Creek Tunnel	FAI		

Table S.7.2: Precision of selective iron extractions. The mean and associated coefficient of variation (CV, ratio of the standard deviation divided by the mean) were calculated on three samples from Yedoma and Alas deposits located in Yukechi site. Precision was assessed for Fe extracted using dithionite-citrate-bicarbonate extraction (Fe_d), dark ammonium oxalate extraction (Fe_o), and sodium pyrophosphate extraction (Fe_p) on three repetitions (n=3). The mean is expressed in g kg^{-1}, and the CV in %.

Sample	n	Fe_d		Fe_o		Fe_p	
		Mean (g kg^{-1})	CV (%)	Mean (g kg^{-1})	CV (%)	Mean (g kg^{-1})	CV (%)
A	3	7.93	2.3	7.75	0.9	2.56	1.8
B	3	5.64	3.3	5.41	1.5	1.52	6.8
C	3	2.33	4.9	1.26	32	0.11	6.0

Table S.7.3: Precision of selective carbon extractions. The mean and associated coefficient of variation (CV, ratio of the standard deviation divided by the mean, expressed in %) were calculated on three samples from Yedoma and Alas deposits located in Yukechi site. Precision was assessed for optical density of the oxalate extract (ODOE, with oxalate extractant as a blank) and concentration of dissolved organic carbon released after dispersion by pyrophosphate (C_p, expressed in g kg^{-1} dry soil) on three repetitions (n=3).

Sample	n	ODOE		C_p	
		Absorbance (-)	CV (%)	Mean (g kg^{-1})	CV (%)
A	3	0.083	0.0	5.89	3.5
B	3	0.070	2.2	8.30	3.4
C	3	0.015	14.2	2.46	2.3

Chapter 3: Thermokarst processes increase the supply of stabilizing surfaces and elements (Fe, Mn, Al, Ca) for mineral organic carbon interactions

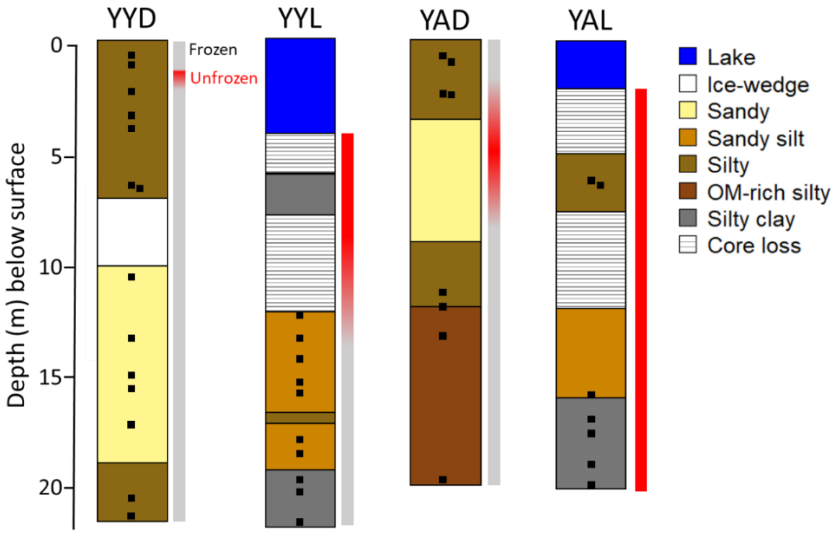

Figure S.8.1: Stratigraphic scheme and taliks (unfrozen portion of the core) for the Yedoma dry (YYD), Yedoma lake (YYL), Alas dry (YAD) and Alas lake (YAL) profiles in the Yukechi site. Samples analysed in this study are represented by the black squares.

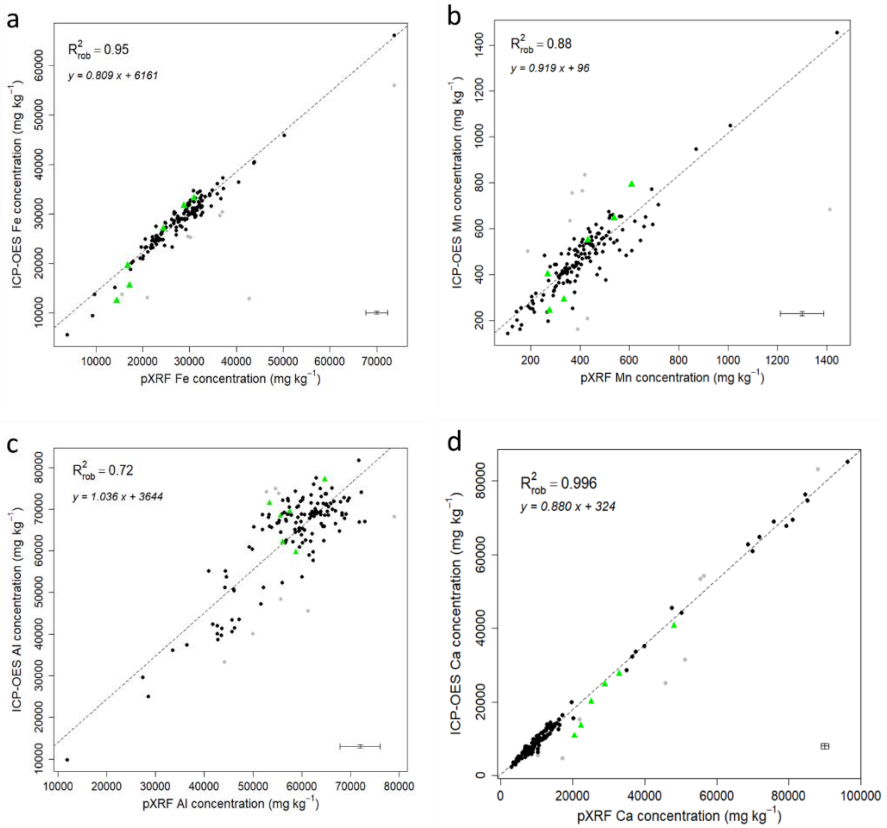

Figure S.8.2 : Total Fe (a), Mn (b), Al (c) and Ca (d) concentrations (mg kg^{-1}) measured by the inductively coupled plasma optical emission spectrometry (ICP-OES) method as a function of those measured by the portable X-ray Fluorescence (pXRF) method) on Yukechi deposit samples (green triangles, n=6) and Yedoma domain deposits (black and gray dots, n=144, *Ch.1*). Errors bars (±2σ) are based on three repetitions of three samples for the ICP-OES method and five or three repetitions of twenty samples for the pXRF method. The robust linear regression is presented (black line; alpha = 0.95; n=144), excluding the gray points (i.e., outside of robust regression), and the equation is provided.

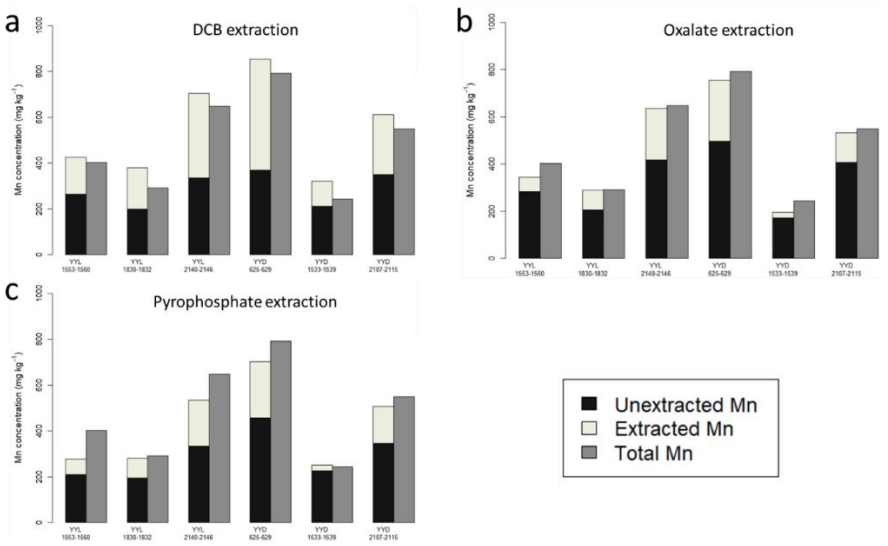

Figure S.8.3: Barplot of Mn concentrations (mg kg^{-1}) of the YYL and YYD cores measured by the inductively coupled plasma optical emission spectrometry (ICP-OES) method for total bulk concentration (gray barplot), extracted (white barplot) and unextracted (black barplot) Mn. (a) Dithionite-citrate-bicarbonate (DCB) extraction, (b) ammonium-oxalate extraction and (c) Na-pyrophophate extraction.

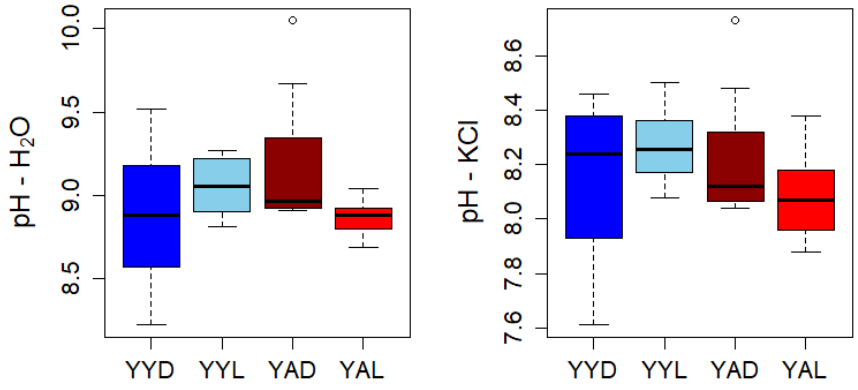

Figure S.8.4: Boxplot of pH-H_20 and pH-KCl values of bulk sediment samples for Yedoma dry (YYD, n=14), Yedoma lake (YYL; n=10), Alas dry (YAD, n=8) and Alas lake (YAL, n=7).

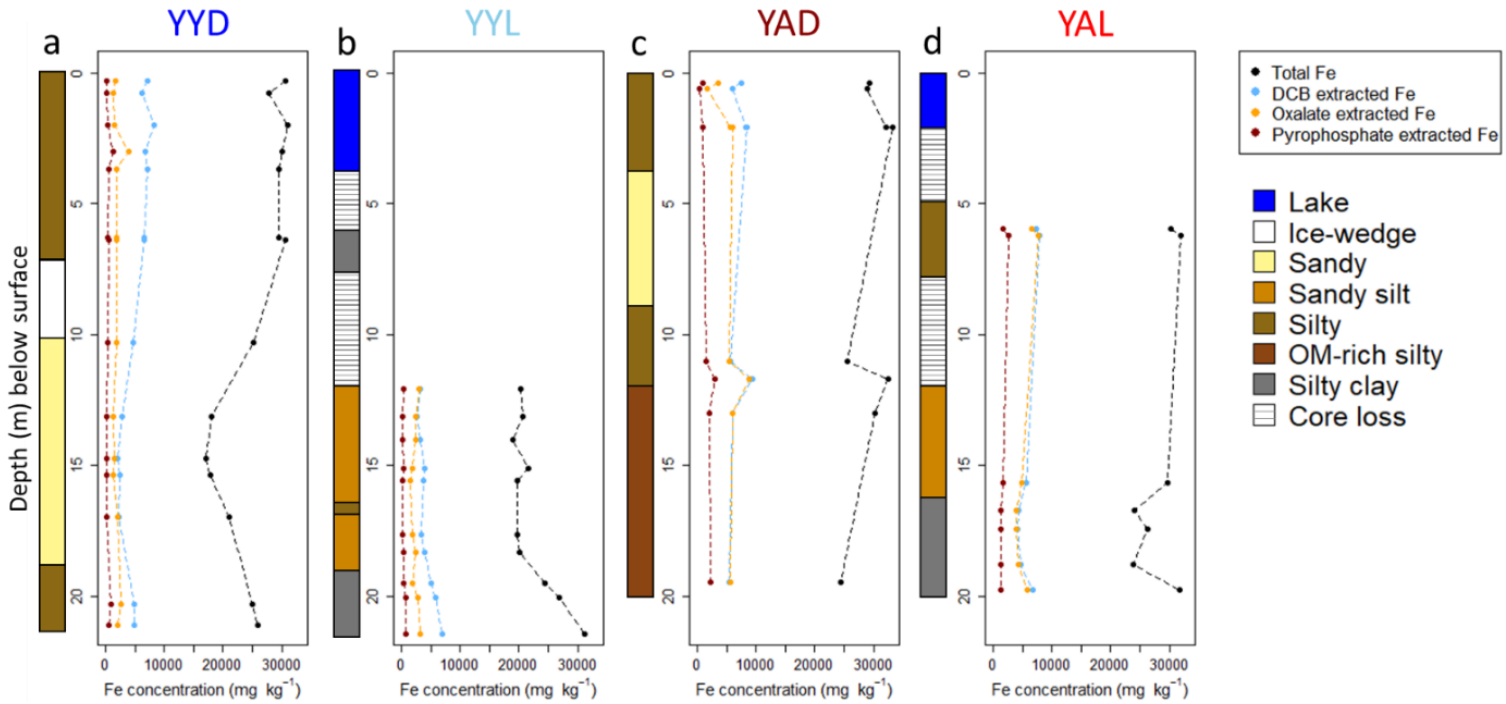

Figure S.8.5 : Depth evolution of total Fe concentrations and Fe extracted using dithionite-citrate-bicarbonate (DCB), ammonium oxalate and Na-pyrophosphate for (a) Yedoma dry (YYD), (b) Yedoma lake (YYL), (c) Alas dry (YAD), and (d) Alas lake (YAL) profiles in Yukechi. A stratigraphic column gives the sediment unit properties for each profile.

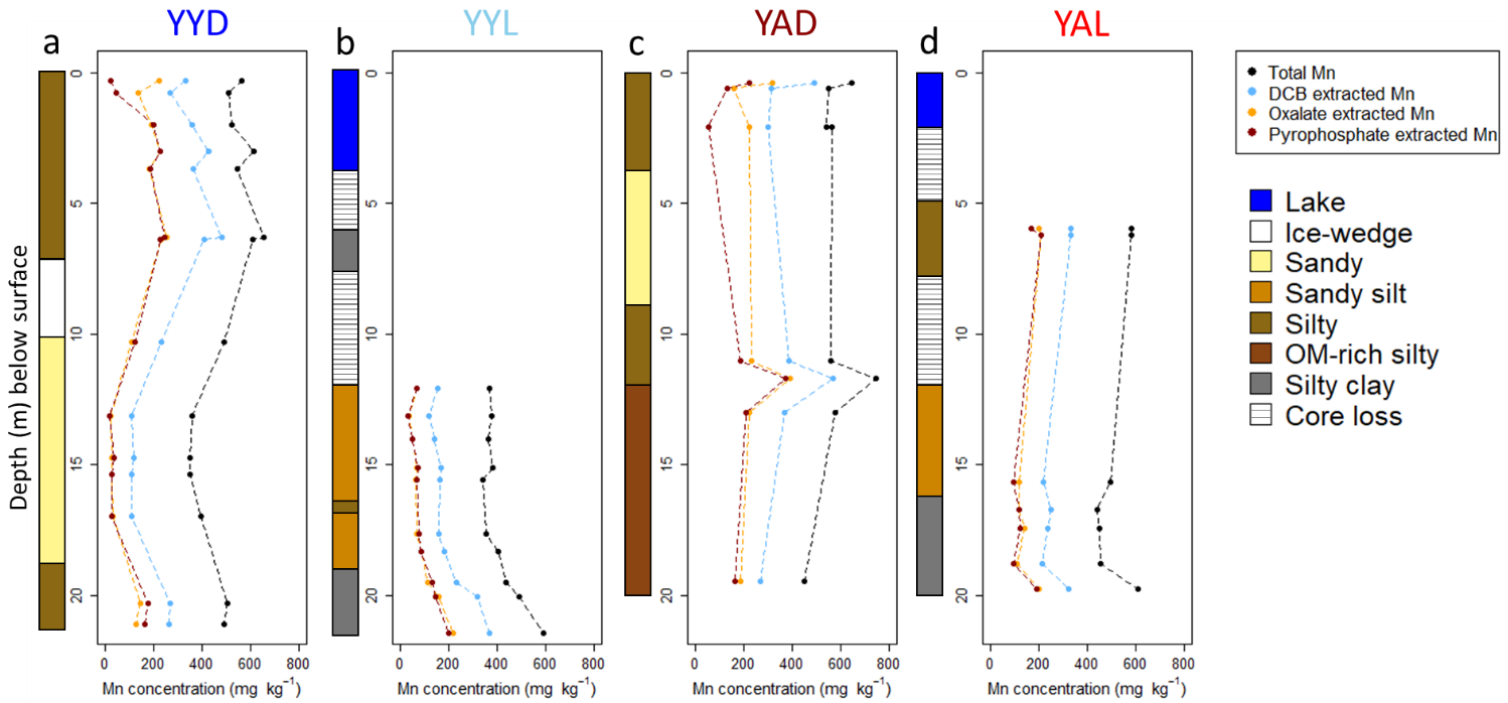

Figure S.8.6 : Depth evolution of total Mn concentrations and Mn extracted using dithionite-citrate-bicarbonate (DCB), ammonium oxalate and Na-pyrophosphate for (a) Yedoma dry (YYD), (b) Yedoma lake (YYL), (c) Alas dry (YAD), and (d) Alas lake (YAL) profiles in Yukechi. A stratigraphic column gives the sediment unit properties for each profile.

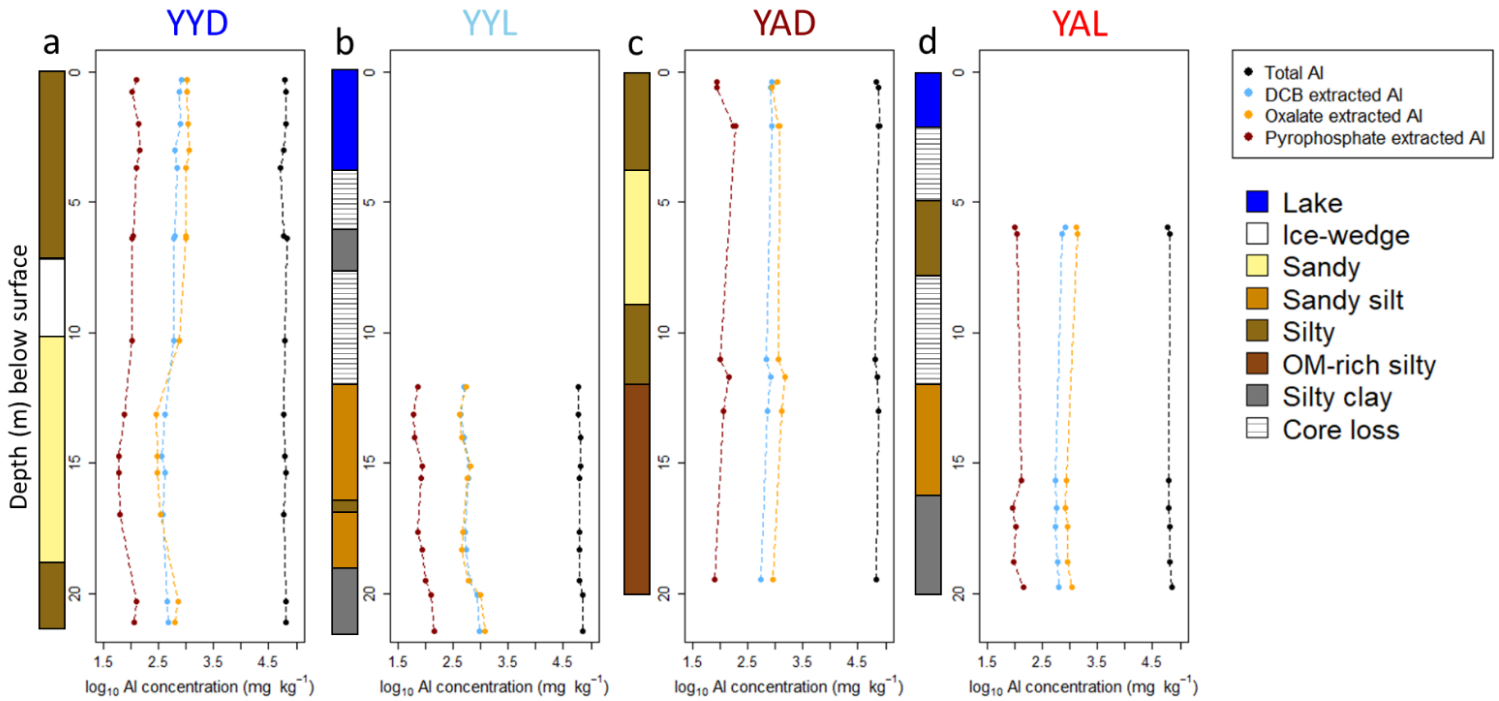

Figure S.8.7 : Depth evolution of total Al concentrations for (a) Yedoma dry (YYD), (b) Yedoma lake (YYL), (c) Alas dry (YAD), and (d) Alas lake (YAL) profiles in Yukechi. A stratigraphic column gives the sediment unit properties for each profile. The x-axis is logarithmic scale.

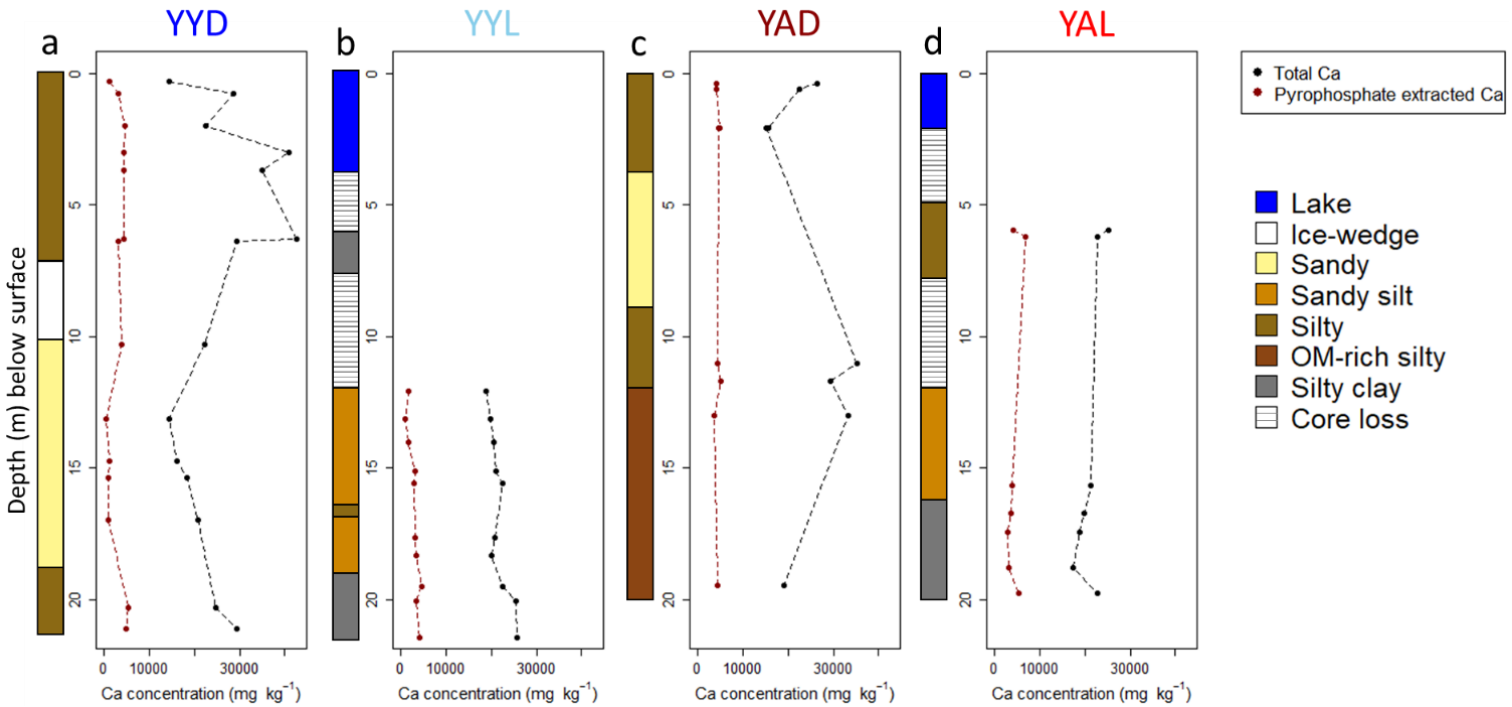

Figure S.8.8 : Depth evolution of total Ca and Na-pyrophosphate extracted Ca for (a) Yedoma dry (YYD), (b) Yedoma lake (YYL), (c) Alas dry (YAD), and (d) Alas lake (YAL) profiles in Yukechi. A stratigraphic column gives the sediment unit properties for each profile.

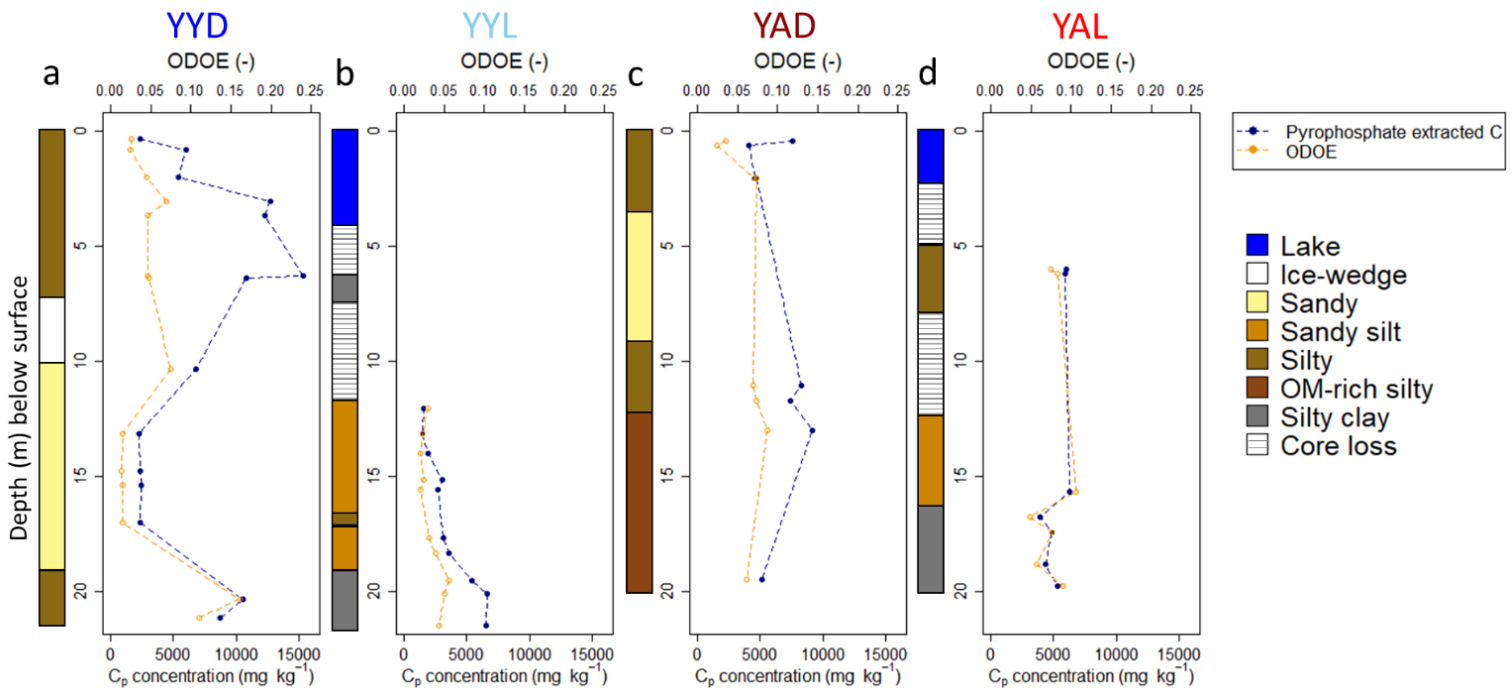

Figure S.8.9: Depth evolution of pyrophosphate-extracted C expressed in mg kg^{-1} (dashed purple line) and optical density of the oxalate extract (ODOE; dashed orange line). A stratigraphic column gives the sediment unit properties for each profile.

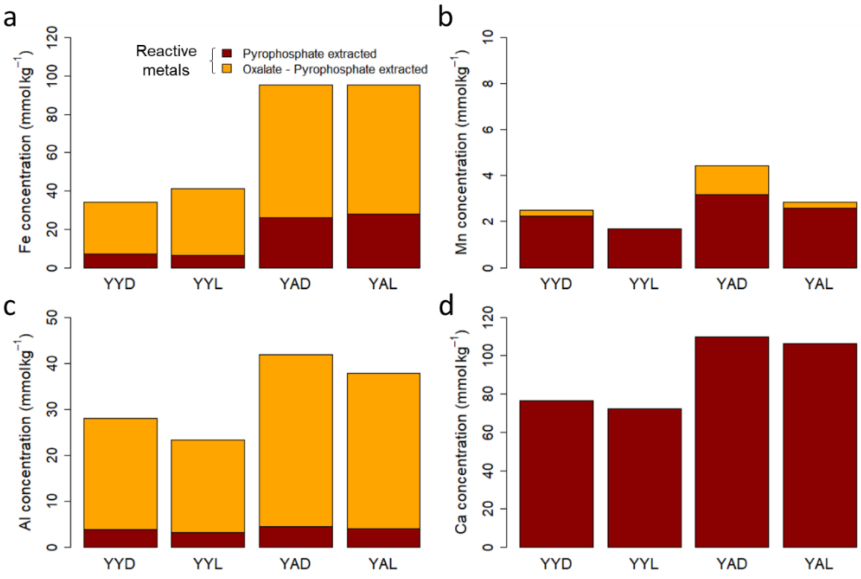

Figure S.8.10 : Mean reactive (a) Fe, (b) Mn, (c) Al and (d) Ca molar concentrations (mmol kg^{-1}) for Yedoma dry (YYD, n=14), Yedoma lake (YYL; n=10), Alas dry (YAD, n=8) and Alas lake (YAL, n=7). The reactive metals concentration combine the complexed (pyrophosphate extracted, black bar) and poorly cristalline oxides (differnece betwwen oxalate and pyrophossphate extracted, white bar) phases. Reactive Ca is defined here as the pyrophosphate extracted only.

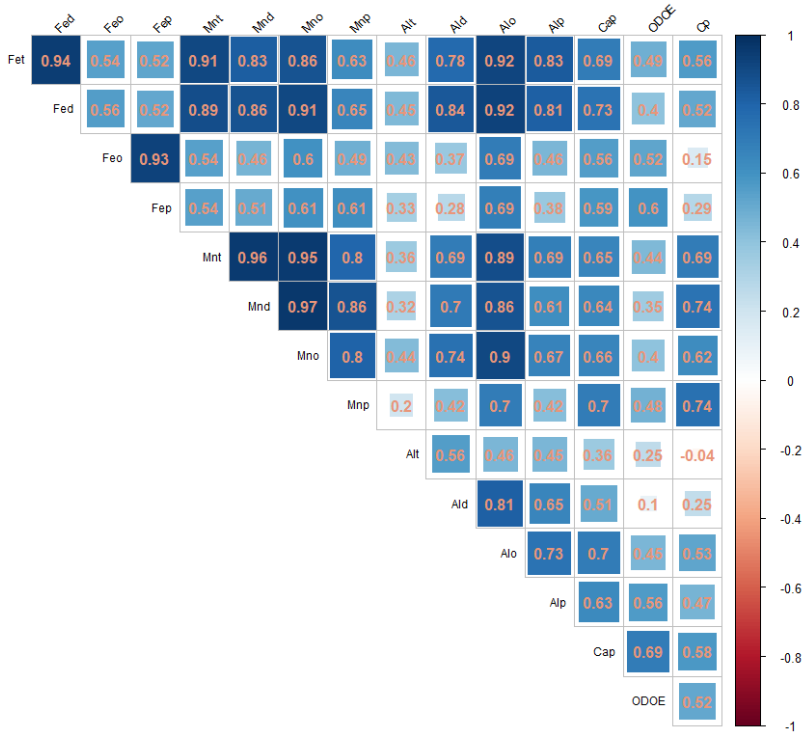

Figure S.8.11 : Correlation matrix including all studied parameters: total (t), dithionite-citrate-bicarbonate extracted (d), ammonium oxalated extracted (o), Na-pyrophophate extracted (p), for metals (Fe, Mn, Al and Ca) and include also optical density of the oxalate extract (ODOE) and complexed C within the pyrophosphate extract (C_p). Positive correlation is shown in blue and negative correlation in red.

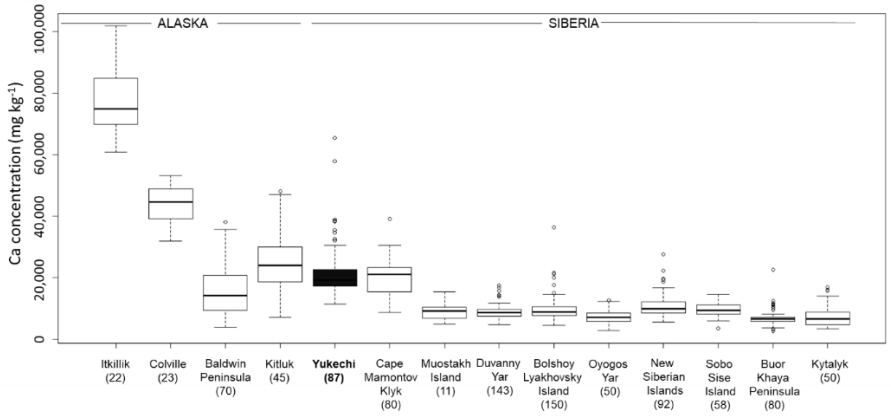

Figure S.8.12 : Boxplot of total Ca concentrations (in mg kg^{-1}) from various sites within the Yedoma domain (data from *Ch.1*). Yukechi site is shown in black and number of observations are shown between brakets below each boxplot).

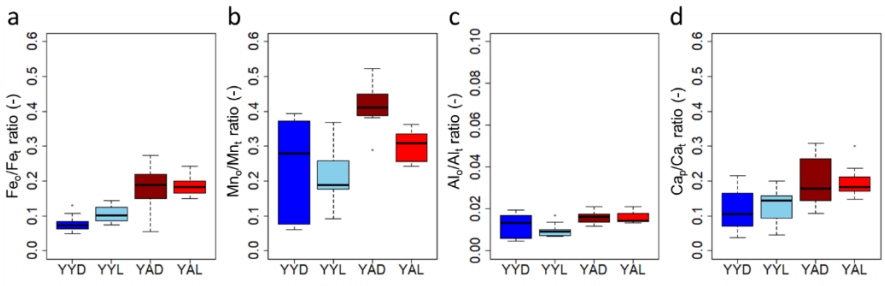

Figure S.8.13 : Boxplot of the ratio of reactive (a) Fe, (b) Mn, (c) Al and (d) Ca out of the total pool concentrations for Yedoma dry (YYD, n=14), Yedoma lake (YYL; n=10), Alas dry (YAD, n=8) and Alas lake (YAL, n=7). Yedoma profiles are in blue and Alas profiles in red.

Table S.8.1: Yukechi profiles locations and number of samples analysed.

Profile	Label		Latitude	Longitude	Windirsch et al., (2020)	Jongejans et al., (2021)	Ulrich et al., (2019)	This study
	This study	Other studies	°N	°E		n		
Yedoma dry	YYD	YED1	61.75967	130.47438	36			14
Yedoma lake	YYL	YU-L15	61.76086	130.47466		10	49	10
Alas dry	YAD	Alas1	61.76490	130.46503	28			8
Alas lake	YAL	YU-L7	61.76397	130.46442		10	19	7

Table S.8.2: Solubility of iron and aluminium phases commonly found in soils and sediments by commonly-used extractants used in this study (adapted from Rennert (2019); Wagai et al., (2013)).

Metal phase	Dithionite-citrate-bicarbonate (DCB) pH 7	Ammonium oxalate 4h in the dark pH 3	Na-pyrophosphate pH 10
OM-metal complex	●	●	●
Allophane/Imogolite	◊	●	□
Ferrihydrite	●	●	#
Al-oxides	◊	●	□
Goethite	●	X	#
Hematite	◊ ~ ●	X	X
Lepidocrocite	◊	□ ~ ◊	X
Magnetite	◊	□ ~ ◊	X
Gibbsite	X	□	X
Halloysite	X	X	X
Clay minerals	X	X	X

● 80-100% dissolution
◊ 10-80% dissolution
□ <10% dissolution
X No dissolution
Dispersion of small colloids

Table S.8.3: Precision of selective extractions method for dithionite-citrate-bicarbonate (DCB), ammonium oxalate (Oxalate) and Na-pyrophosphate (Pyro) for Fe, Mn, Al and Ca (expressed in mg kg^{-1}). The optical density of the oxalate extract (ODOE, adimensional) and the Na-pyrophosphate extracted C (mg kg^{-1}) are also shown. The mean values and standard deviation are shown. Each sample (A: YYD 1533-1539; B: YAD 1095-1109; C: YAL 615-622) was analysed three time to assess precision of the method.

Sample	Fe			Mn			Al			Ca	Carbon	
n=3	DCB	Oxalate	Pyro	DCB	Oxalate	Pyro	DCB	Oxalate	Pyro	Pyro	ODOE	Pyro
A	2328 ± 114	1257 ± 397	105 ± 6	110 ± 1	26 ± 2	25 ± 1	412 ± 43	292 ± 20	59 ± 3	1062 ± 99	0.015 ± 0.002	2459 ± 60
B	5643 ± 187	5406 ± 82	1517 ± 103	385 ± 1	231 ± 10	186 ± 6	687 ± 63	1141 ± 52	101 ± 2	4488 ± 731	0.070 ± 0.002	8296 ± 280
C	7933 ± 184	7755 ± 66	2557 ± 47	331 ± 2	211 ± 2	209 ± 8	704 ± 54	1331 ± 60	109 ± 2	6859 ± 654	0.083 ± 0	5894 ± 210

Table S.8.4: Detection of crystalline mineral phases in Yukechi sediments for the Yukechi Yedoma dry (YYD), Yukechi Yedoma lake (YYL), Yukechi Alas dry (YAD) and Yukechi Alas lake (YAL). Mineral phases detected by diffraction are marked with "X", detection with lower intensity peak or in some samples from the profiles are marked with "(X)" and undetected mineral phases are marked with "-".

	Primary minerals						Secondary minerals	
	Quartz	Plagioclase	Mica	Pyroxene	Amphibole	Dolomite	Serpentine	Vermiculite
YYD	X	X	X	X	(X)	(X)	X	X
YYD (sandy unit)	X	X	(X)	(X)	(X)	X	-	-
YYL	X	X	X	(X)	(X)	X	X	(X)
YAD	X	X	X	(X)	(X)	(X)	X	(X)
YAL	X	X	X	(X)	(X)	X	X	(X)

Table S.8.5: All data related to total and selective extractions and pH of Yukechi sites for Yedoma dry (YYD), Yedoma lake (YYL), Alas dry (YAD) and Alas lake (YAL). Total, dithionite-citrate-bicarbonate (DCB), oxalate, pyrophosphate (pyro) concentrations of Fe, Mn, Al and Ca expressed in mg kg^{-1}. Optical density of the oxalate extract (ODOE) and pyrophosphate extracted C and pH-H_2O and pH-KCl.

Profil	Sample ID	Depth b.s.	Fe Total	Fe DCB	Fe oxalate	Fe pyro	Mn Total	Mn DCB	Mn oxalate	Mn pyro	Al Total	Al DCB	Al oxalate	Al pyro	Ca Total	Ca pyro	ODOE	C pyro	pH water	pH KCl
		m	mg/kg														-	mg/kg	-	-
YYD	YYD 28-33	0.305	30621	7162	1623	247	567	331	223	23	62610	826	1051	124	14484	1260	0.026	2327	9.43	7.61
YYD	YYD 76-80	0.78	27802	6255	1364	135	511	269	136	45	63972	756	1044	106	28533	3130	0.025	5992	9.52	8.26
YYD	YYD 198-202	2	31021	8227	1557	351	523	358	190	202	64933	801	1082	135	22419	4553	0.045	5452	8.57	8.06
YYD	YYD 301-302	3.015	30103	6775	3912	1210	615	426	229	227	58156	630	1126	146	40970	4359	0.069	12757	8.65	8.22
YYD	YYD 364-367	3.655	29438	7029	1844	460	547	366	182	186	52079	677	976	127	34942	4461	0.046	12264	9.01	8.3
YYD	YYD 625-629	6.27	29461	6541	1888	426	656	485	257	247	58926	620	986	110	42627	4268	0.047	15367	9.29	8.46
YYD	YYD 637-640	6.385	30603	6508	1931	500	611	410	233	228	67311	598	974	106	29419	3079	0.048	10816	9.18	8.39
YYD	YYD 1028-1035	10.315	25139	4691	1824	377	491	232	107	121	62268	590	751	105	22181	3906	0.075	6846	8.67	7.93
YYD	YYD 1308-1315	13.115	18125	2844	1333	162	359	109	22	19	57975	405	291	76	14364	542	0.015	2238	8.22	8.08
YYD	YYD 1472-1476	14.74	17145	2102	1435	128	351	116	25	35	60217	355	294	61	16098	1117	0.014	2390	8.86	8.38
YYD	YYD 1533-1539	15.36	17827	2328	1257	105	350	110	26	25	64557	412	292	59	18308	1062	0.015	2459	8.9	8.4
YYD	YYD 1694-1701	16.975	21001	2221	1985	87	396	108	30	25	59947	373	346	64	20697	985	0.015	2371	9.03	8.27
YYD	YYD 2027-2032	20.295	24953	4884	2691	934	505	268	147	175	65594	444	726	126	24735	5328	0.161	10574	8.26	7.91
YYD	YYD 2107-2115	21.11	25891	4899	1990	617	493	263	126	162	63265	475	633	112	29265	4842	0.111	8740	8.26	7.82
YYL	YYL 1200-1210	12.05	20222	3120	2904	414	370	153	66	69	59959	486	531	72	18744	1753	0.03	1569	8.9	8.3
YYL	YYL 1308-1314	13.11	20589	2653	2374	223	380	119	35	31	59663	437	404	60	19847	904	0.023	1533	9.26	8.43
YYL	YYL 1398-1400	13.99	18923	3180	2392	252	364	142	49	50	63653	494	460	64	20513	1576	0.021	1928	9.22	8.35
YYL	YYL 1508-1514	15.11	21562	3966	1832	265	383	168	68	72	64618	635	651	88	21035	3213	0.025	3040	9	8.09
YYL	YYL 1553-1560	15.565	19732	3657	1473	217	343	162	61	68	61272	591	570	83	22453	2961	0.021	2697	9.06	8.21

Table S.8.5: (continued)

Profil	Sample ID	Depth b.s.	Fe Total	Fe DCB	Fe oxalate	Fe pyro	Mn Total	Mn DCB	Mn oxalate	Mn pyro	Al Total	Al DCB	Al oxalate	Al pyro	Ca Total	Ca pyro	ODOE	C pyro	pH water	pH KCl
		m	mg/kg														-	mg/kg	-	-
YYL	YYL 1764-1767	17.655	19734	3331	1861	184	353	161	70	78	63023	509	479	73	20699	3211	0.031	3164	9.27	8.5
YYL	YYL 1830-1832	18.31	20041	3963	2473	269	403	180	84	85	61734	538	447	86	19953	3348	0.04	3608	9.05	8.36
YYL	YYL 1948-1954	19.51	24451	5074	1815	359	439	231	113	131	62203	627	601	98	22619	4526	0.056	5378	8.9	8.17
YYL	YYL 2002-2010	20.06	26934	5800	2719	638	490	317	159	146	71359	866	966	124	25392	3414	0.051	6591	8.81	8.08
YYL	YYL 2140-2146	21.43	31182	6864	3212	681	591	370	218	201	70716	948	1187	146	25713	4020	0.044	6549	9.07	8.17
YAD	YAD 37-43	0.4	29267	7461	3545	838	649	494	317	222	67164	867	1088	85	26451	4201	0.035	7556	10.05	8.73
YAD	YAD 58-64	0.61	28888	5974	1595	259	549	314	159	133	73590	823	852	85	22450	4136	0.025	4128	9.67	8.48
YAD	YAD 201-209A	2.05	32163	8180	5659	987	542	302	222	53	77796	861	1117	170	15666	4843	0.071	4599	8.93	8.12
YAD	YAD 201-209B	2.05	33208	8441	5967	955	563	299	221	52	73798	849	1179	187	15168	4634	0.074	4722	8.94	8.08
YAD	YAD 1095-1109	11.02	25601	5643	5406	1517	562	385	231	185	64529	687	1141	101	35281	4488	0.07	8296	9.02	8.16
YAD	YAD 1161-1175	11.68	32561	9303	8892	2939	749	569	392	374	70399	825	1481	146	29389	5091	0.074	7416	8.92	8.05
YAD	YAD 1294-1307	13.005	30318	5997	5937	2016	578	369	221	211	74001	714	1288	114	33336	3573	0.087	9183	8.99	8.12
YAD	YAD 1944-1950	19.47	24382	5365	5531	2200	449	267	185	162	68121	534	893	77	19163	4264	0.061	5195	8.91	8.04
YAL	YAL 594-600	5.97	30198	7222	6554	1604	581	331	202	169	60097	805	1269	99	25176	4088	0.075	6050	8.97	8.29
YAL	YAL 615-622	6.185	31975	7933	7755	2557	581	331	211	209	65179	704	1331	109	22812	6859	0.083	5894	9.04	8.38
YAL	YAL 1562-1568	15.65	29742	5536	4891	1736	495	216	120	95	61518	548	859	128	21399	3796	0.106	6243	8.69	7.99
YAL	YAL 1670-1675	16.725	24045	4343	3989	1270	441	249	118	119	62903	562	835	91	19842	3610	0.049	3970	8.88	8.07
YAL	YAL 1739-1745	17.42	26296	4155	3930	1329	451	235	139	122	64658	547	889	105	18955	2797	0.076	4880	8.75	7.88
YAL	YAL 1877-1880	18.785	23857	4647	4353	1242	455	214	111	97	63129	594	903	93	17489	3269	0.057	4367	8.88	7.93
YAL	YAL 1969-1977	19.73	31687	6738	5777	1299	610	324	198	189	69340	626	1070	142	22772	5400	0.09	5317	8.84	8.07

Chapter 4: Mineral organic carbon interactions in dry versus wet tundra soils

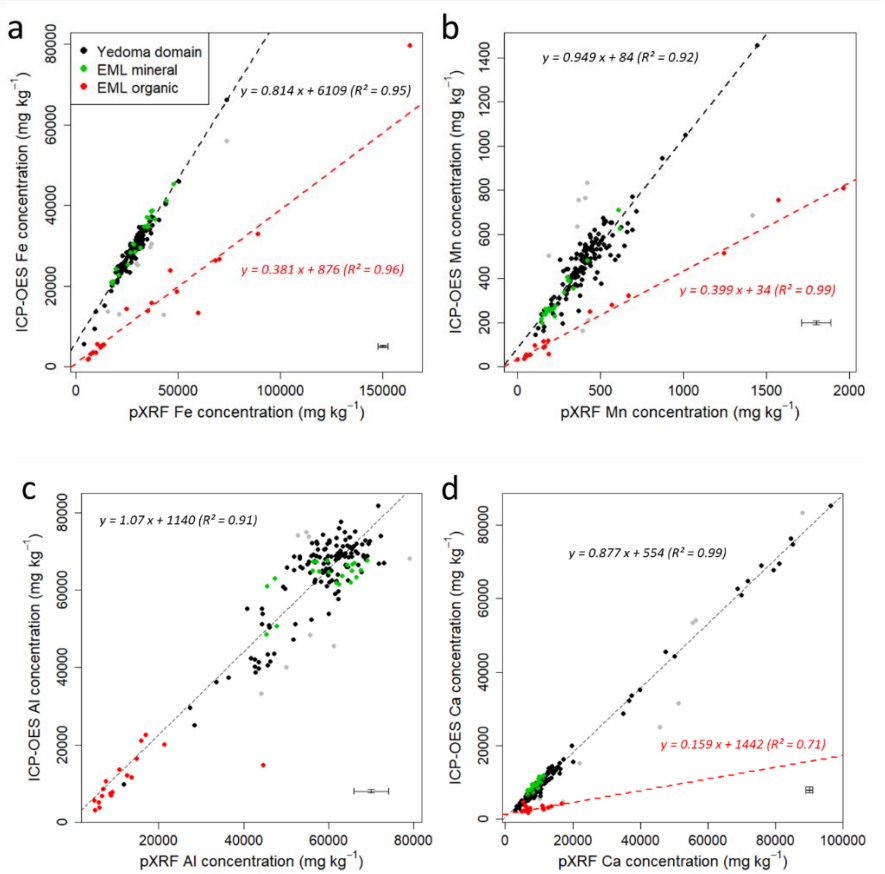

Figure S.9.1: Total (a) Fe, (b) Mn, (c) Al, and (d) Ca) concentrations (mg kg^{-1}) measured by the inductively coupled plasma optical-emission spectrometry (ICP-OES) method as a function of those measured by the portable X-ray fluorescence (pXRF) method on mineral and organic samples from Eight Mile Lake acidic tundra (green points; n = 21 and red points n = 18, respectively). Samples from the Yedoma domain deposits (black points; n = 144, *Ch.1*) are included. The robust linear regression for mineral samples is presented (black line; alpha= 0.95) and for organic samples (red line; alpha = 0.95). Gray points are excluded from the robust linear regression. Mineral and organic samples are divided with 20 wt% OC cutoff. Equations from linear regressions are provided with the robust determination coefficient. Errors bars (± 2σ) are taken from *Ch.1*.

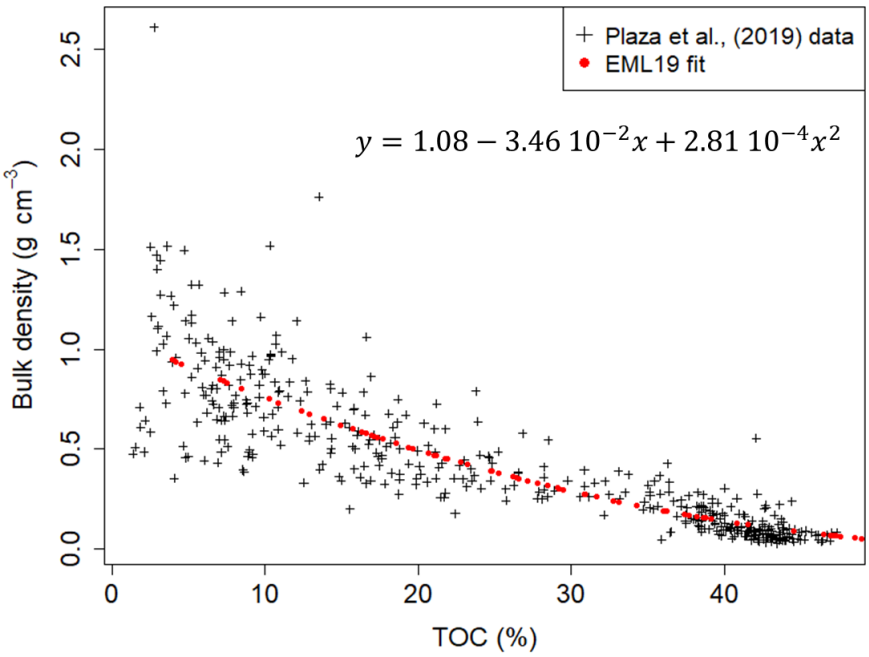

Figure S.9.2: Total organic carbon (TOC) percentage as a function of bulk density (g cm^{-3}) reported from Plaza et al. (2019) in analogous moist acidic tundra site near Eight Mile Lake watershed (black crosses). A quadratic model is used to estimate bulk densities based on TOC content from EML samples from this study (red points). The equation of the model used is shown.

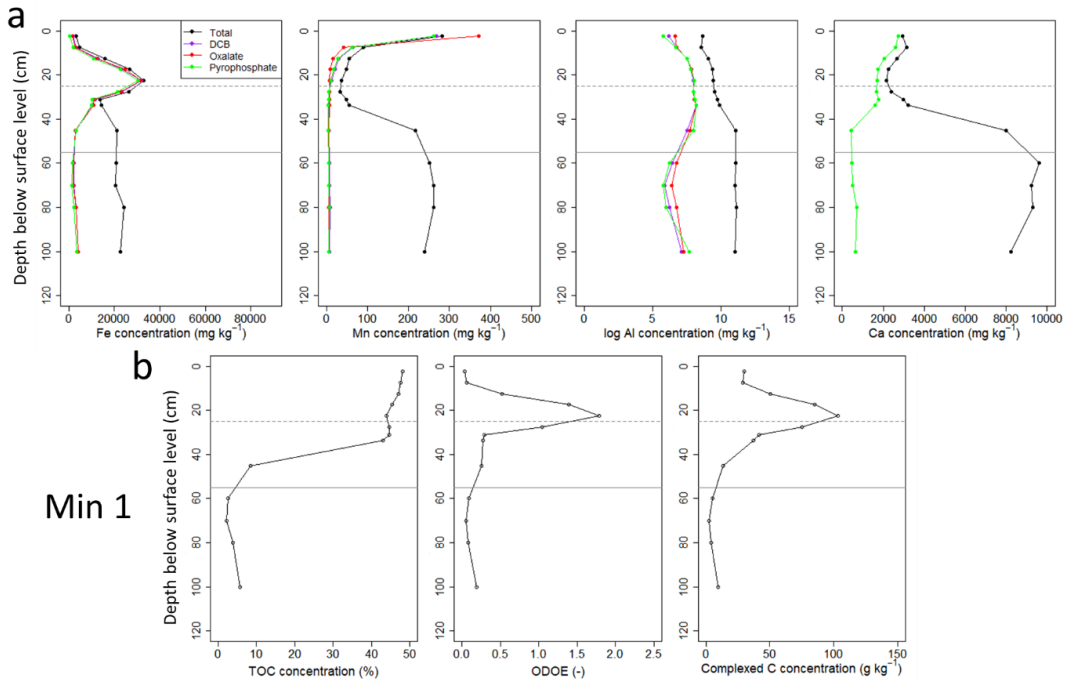

Figure S.9.3: (a) Total and selectively extracted metals (Fe, Mn, Al and Ca) for dithionite-citrate-bicarbonate (DCB), oxalate and pyrophosphate for the Min 1 profile. Note that Al plot is logarithmic scale. (b) Total organic carbon (TOC, %), optical density of the oxalate extract (-) and pyrophosphate-extracted C (g kg^{-1}). Dashed and continuous horizontal lines refer to the water table and active layer depth, respectively.

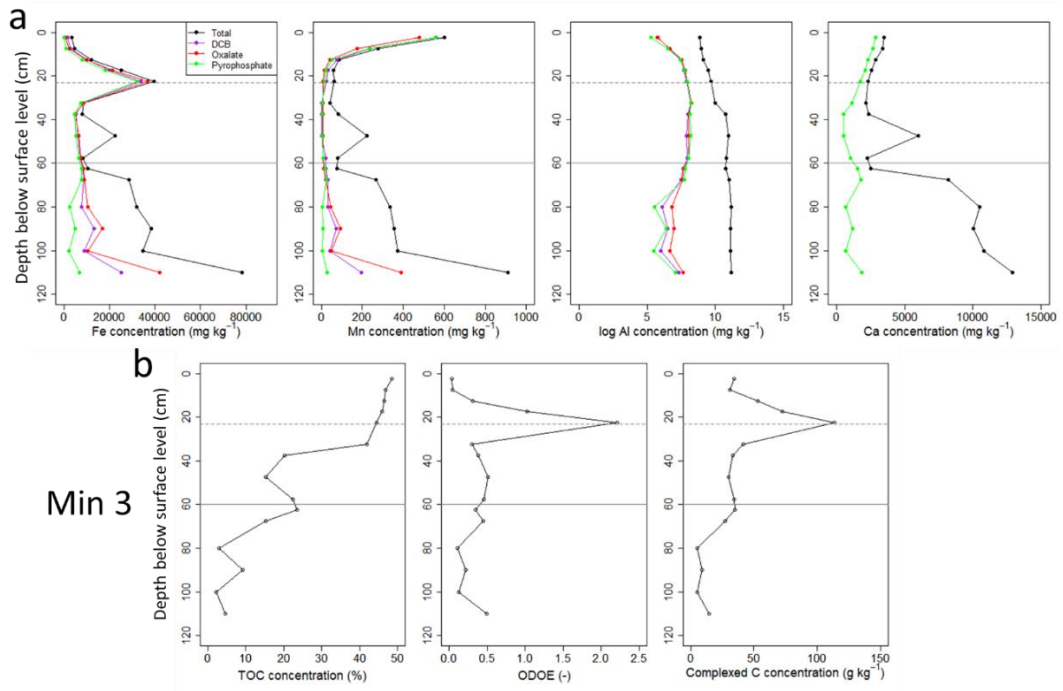

Figure S.9.4: (a) Total and selectively extracted metals (Fe, Mn, Al and Ca) for dithionite-citrate-bicarbonate (DCB), oxalate and pyrophosphate for the Min 3 profile. Note that Al plot is logarithmic scale. (b) Total organic carbon (TOC, %), optical density of the oxalate extract (-) and pyrophosphate-extracted C (g kg^{-1}). Dashed and continuous horizontal lines refer to the water table and active layer depth, respectively.

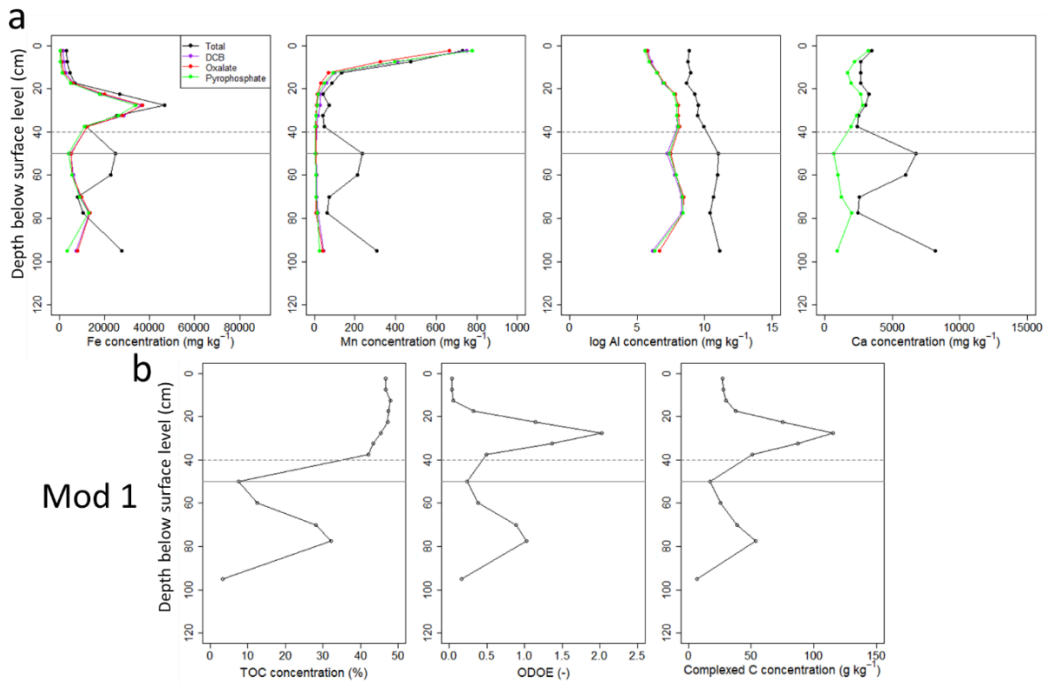

Figure S.9.5: (a) Total and selectively extracted metals (Fe, Mn, Al and Ca) for dithionite-citrate-bicarbonate (DCB), oxalate and pyrophosphate for the Mod 1 profile. Note that Al plot is logarithmic scale. (b) Total organic carbon (TOC, %), optical density of the oxalate extract (-) and pyrophosphate-extracted C (g kg^{-1}). Dashed and continuous horizontal lines refer to the water table and active layer depth, respectively.

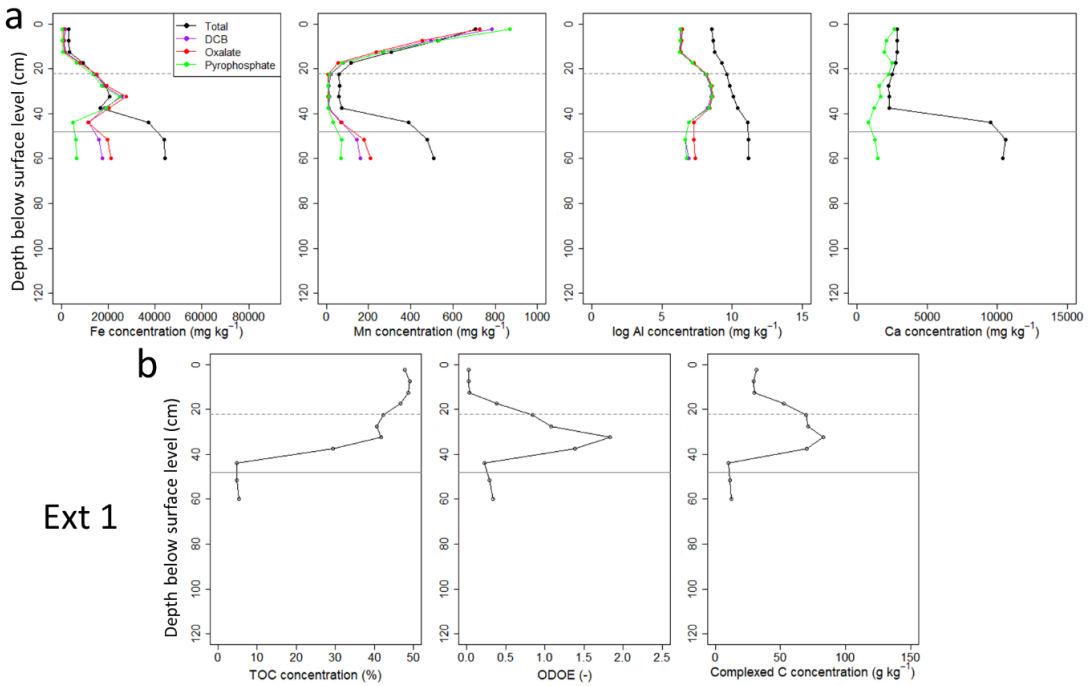

Figure S.9.6: (a) Total and selectively extracted metals (Fe, Mn, Al and Ca) for dithionite-citrate-bicarbonate (DCB), oxalate and pyrophosphate for the Ext 1 profile. Note that Al plot is logarithmic scale. (b) Total organic carbon (TOC, %), optical density of the oxalate extract (-) and pyrophosphate-extracted C (g kg^{-1}). Dashed and continuous horizontal lines refer to the water table and active layer depth, respectively.

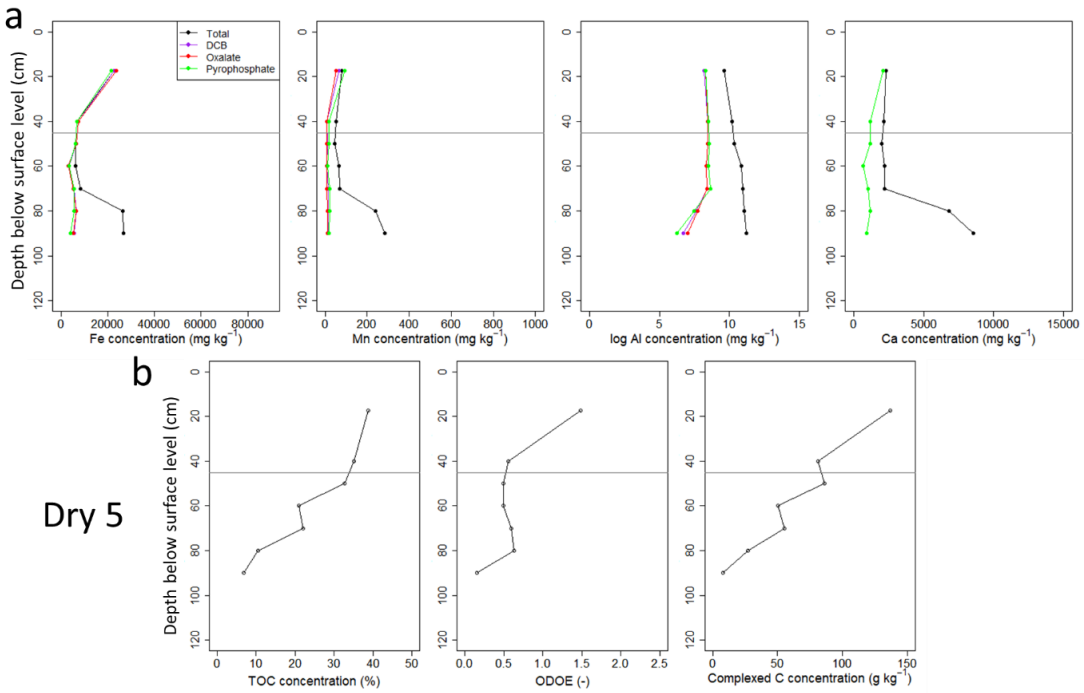

Figure S.9.7: (a) Total and selectively extracted metals (Fe, Mn, Al and Ca) for dithionite-citrate-bicarbonate (DCB), oxalate and pyrophosphate for the Dry 5 profile. Note that Al plot is logarithmic scale. (b) Total organic carbon (TOC, %), optical density of the oxalate extract (-) and pyrophosphate-extracted C (g kg^{-1}). Dashed and continuous horizontal lines refer to the water table and active layer depth, respectively.

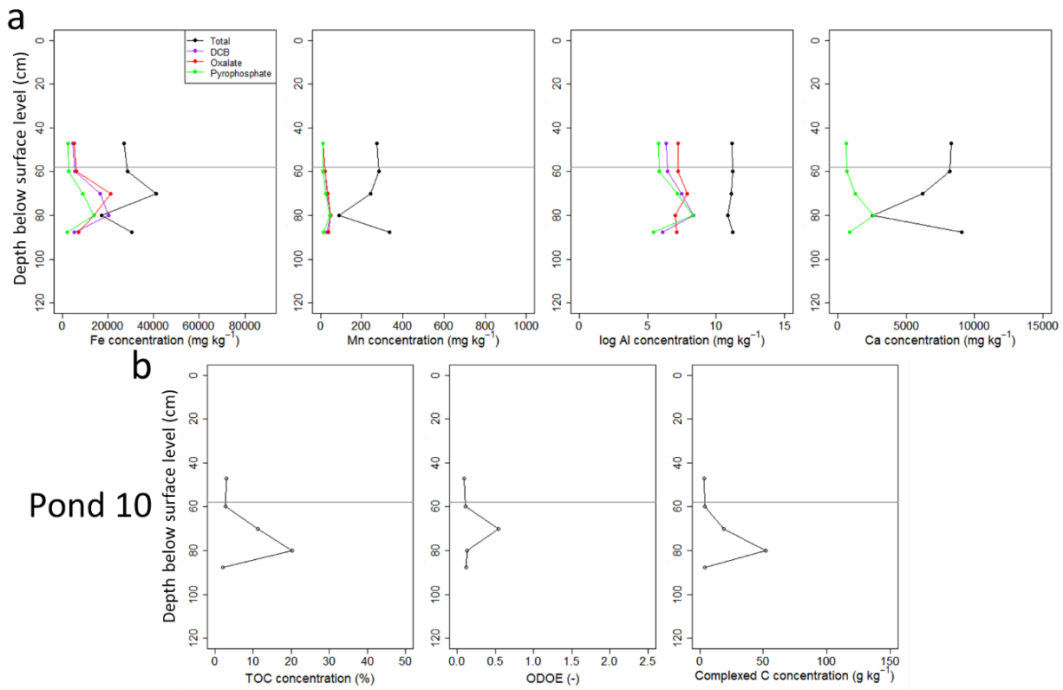

Figure S.9.8: (a) Total and selectively extracted metals (Fe, Mn, Al and Ca) for dithionite-citrate-bicarbonate (DCB), oxalate and pyrophosphate for the Pond 10 profile. Note that Al plot is logarithmic scale. (b) Total organic carbon (TOC, %), optical density of the oxalate extract (-) and pyrophosphate-extracted C (g kg^{-1}). Dashed and continuous horizontal lines refer to the water table and active layer depth, respectively.

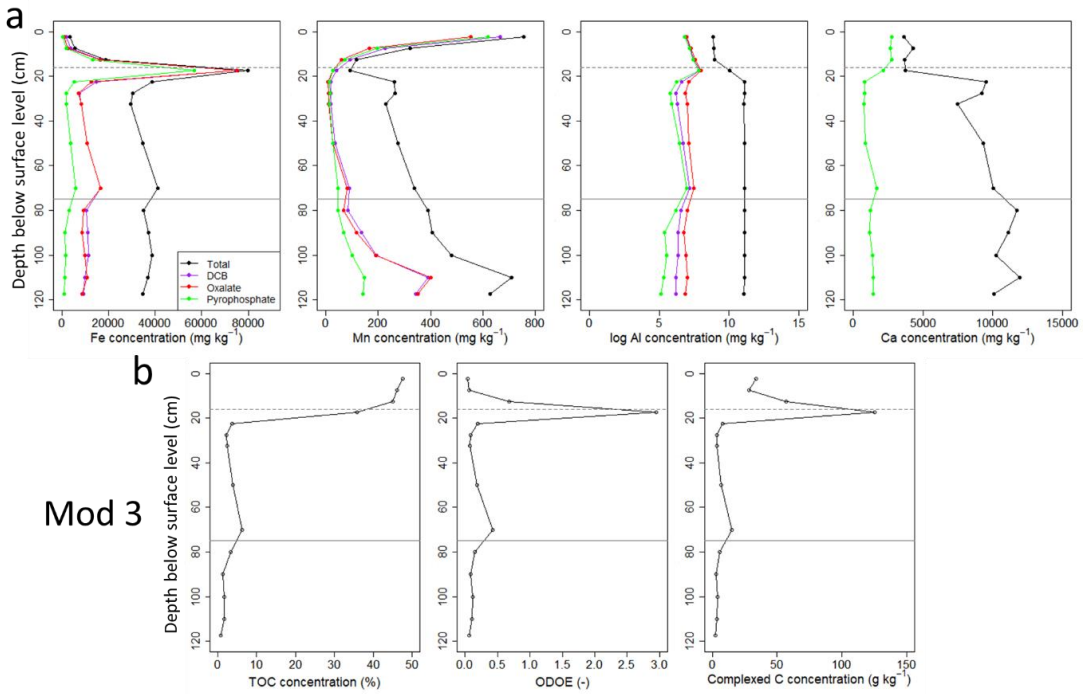

Figure S.9.9: (a) Total and selectively extracted metals (Fe, Mn, Al and Ca) for dithionite-citrate-bicarbonate (DCB), oxalate and pyrophosphate for the Mod 3 profile. Note that Al plot is logarithmic scale. (b) Total organic carbon (TOC, %), optical density of the oxalate extract (-) and pyrophosphate-extracted C (g kg^{-1}). Dashed and continuous horizontal lines refer to the water table and active layer depth, respectively.

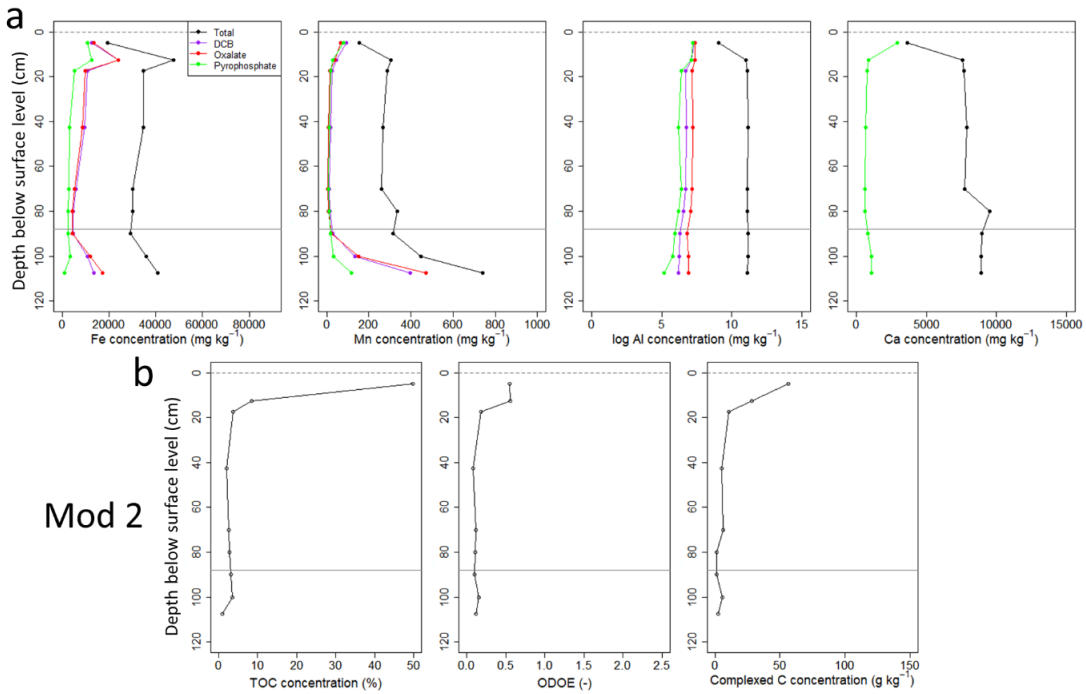

Figure S.9.10: (a) Total and selectively extracted metals (Fe, Mn, Al and Ca) for dithionite-citrate-bicarbonate (DCB), oxalate and pyrophosphate for the Mod 2 profile. Note that Al plot is logarithmic scale. (b) Total organic carbon (TOC, %), optical density of the oxalate extract (-) and pyrophosphate-extracted C (g kg^{-1}). Dashed and continuous horizontal lines refer to the water table and active layer depth, respectively.

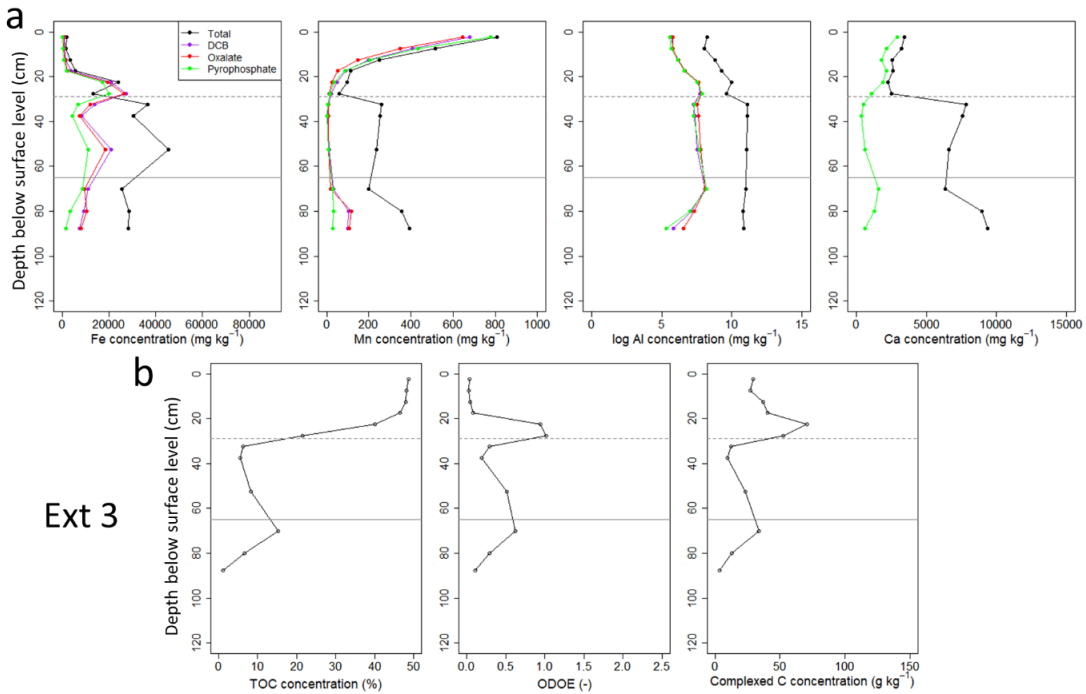

Figure S.9.11: (a) Total and selectively extracted metals (Fe, Mn, Al and Ca) for dithionite-citrate-bicarbonate (DCB), oxalate and pyrophosphate for the Ext 3 profile. Note that Al plot is logarithmic scale. (b) Total organic carbon (TOC, %), optical density of the oxalate extract (-) and pyrophosphate-extracted C (g kg^{-1}). Dashed and continuous horizontal lines refer to the water table and active layer depth, respectively.

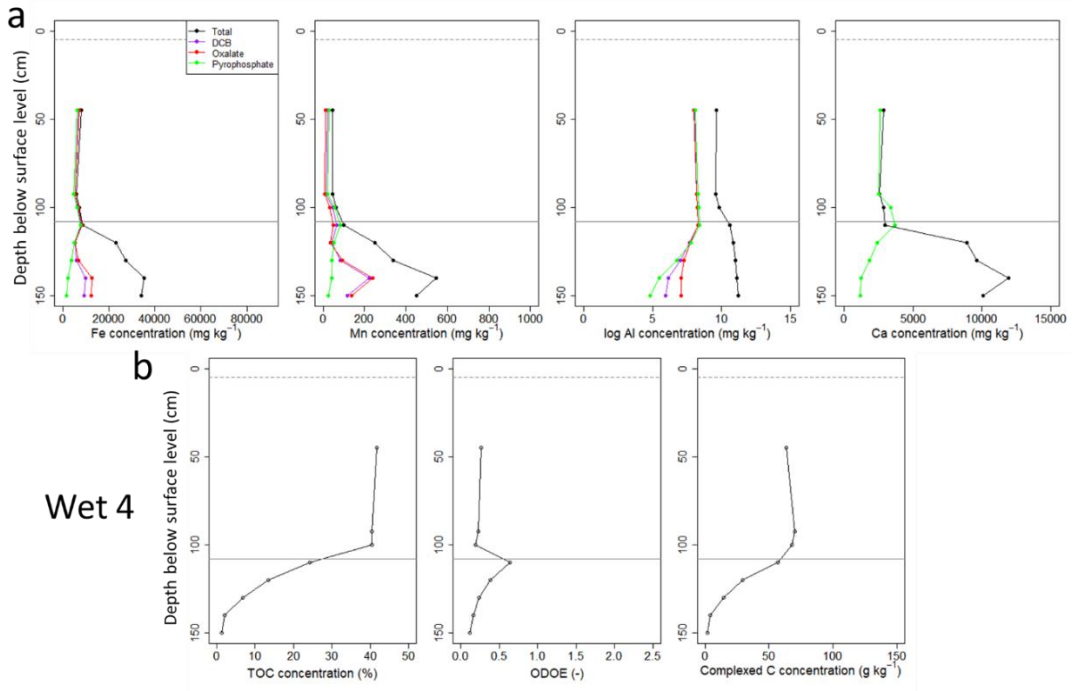

Figure S.9.12: (a) Total and selectively extracted metals (Fe, Mn, Al and Ca) for dithionite-citrate-bicarbonate (DCB), oxalate and pyrophosphate for the Wet 4 profile. Note that Al plot is logarithmic scale. (b) Total organic carbon (TOC, %), optical density of the oxalate extract (-) and pyrophosphate-extracted C (g kg^{-1}). Dashed and continuous horizontal lines refer to the water table and active layer depth, respectively.

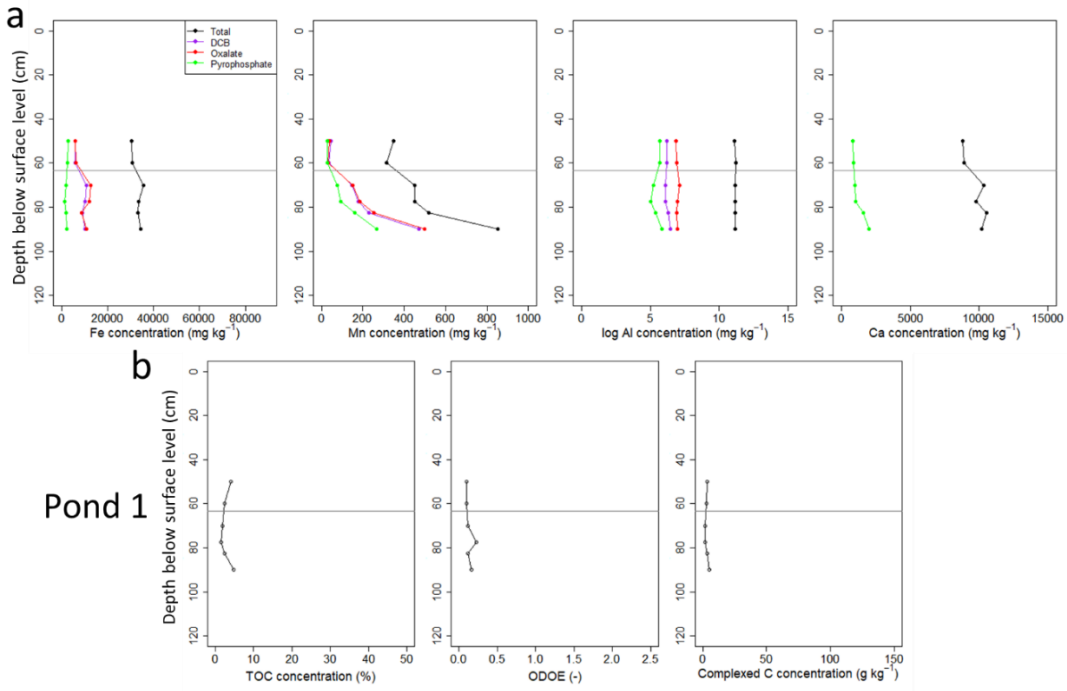

Figure S.9.13: (a) Total and selectively extracted metals (Fe, Mn, Al and Ca) for dithionite-citrate-bicarbonate (DCB), oxalate and pyrophosphate for the Pond 1 profile. Note that Al plot is logarithmic scale. (b) Total organic carbon (TOC, %), optical density of the oxalate extract (-) and pyrophosphate-extracted C (g kg^{-1}). Dashed and continuous horizontal lines refer to the water table and active layer depth, respectively.

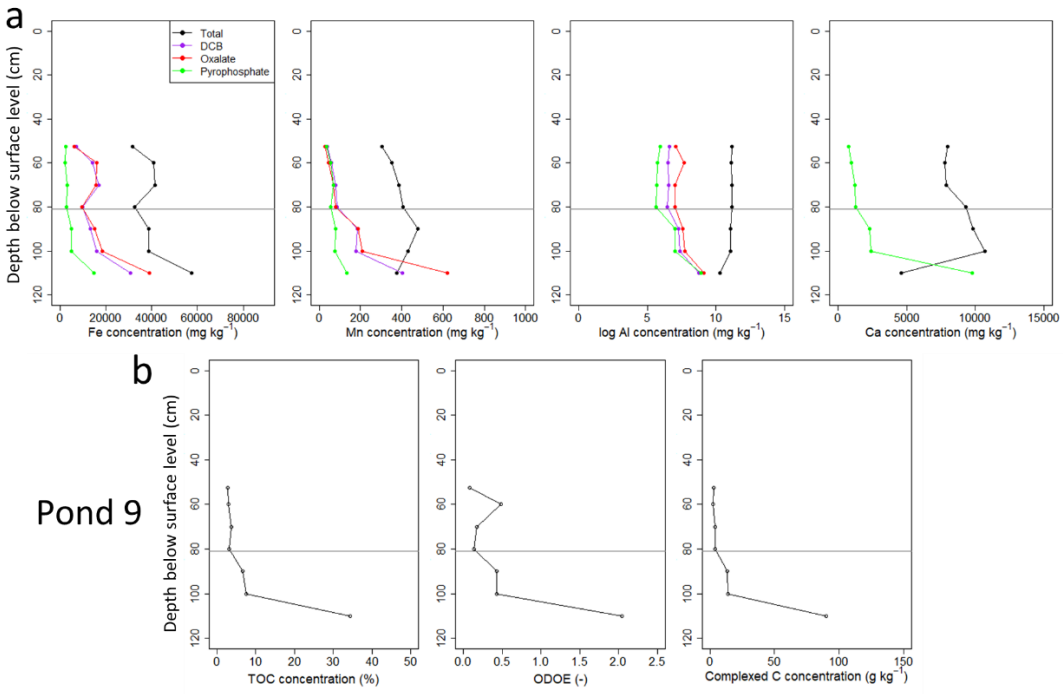

Figure S.9.14: (a) Total and selectively extracted metals (Fe, Mn, Al and Ca) for dithionite-citrate-bicarbonate (DCB), oxalate and pyrophosphate for the watertrack (WT1) profile. Note that Al plot is logarithmic scale. (b) Total organic carbon (TOC, %), optical density of the oxalate extract (-) and pyrophosphate-extracted C (g kg^{-1}). Dashed and continuous horizontal lines refer to the water table and active layer depth, respectively.

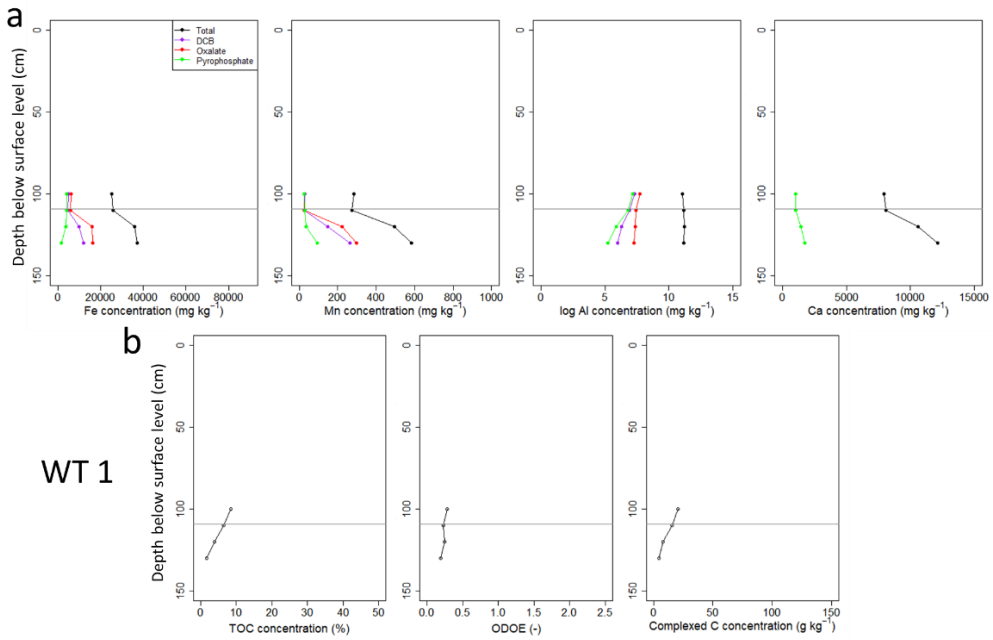

Figure S.9.15: (a) Total and selectively extracted metals (Fe, Mn, Al and Ca) for dithionite-citrate-bicarbonate (DCB), oxalate and pyrophosphate for the Pond 9 profile. Note that Al plot is logarithmic scale. (b) Total organic carbon (TOC, %), optical density of the oxalate extract (-) and pyrophosphate-extracted C (g kg^{-1}). Dashed and continuous horizontal lines refer to the water table and active layer depth, respectively.

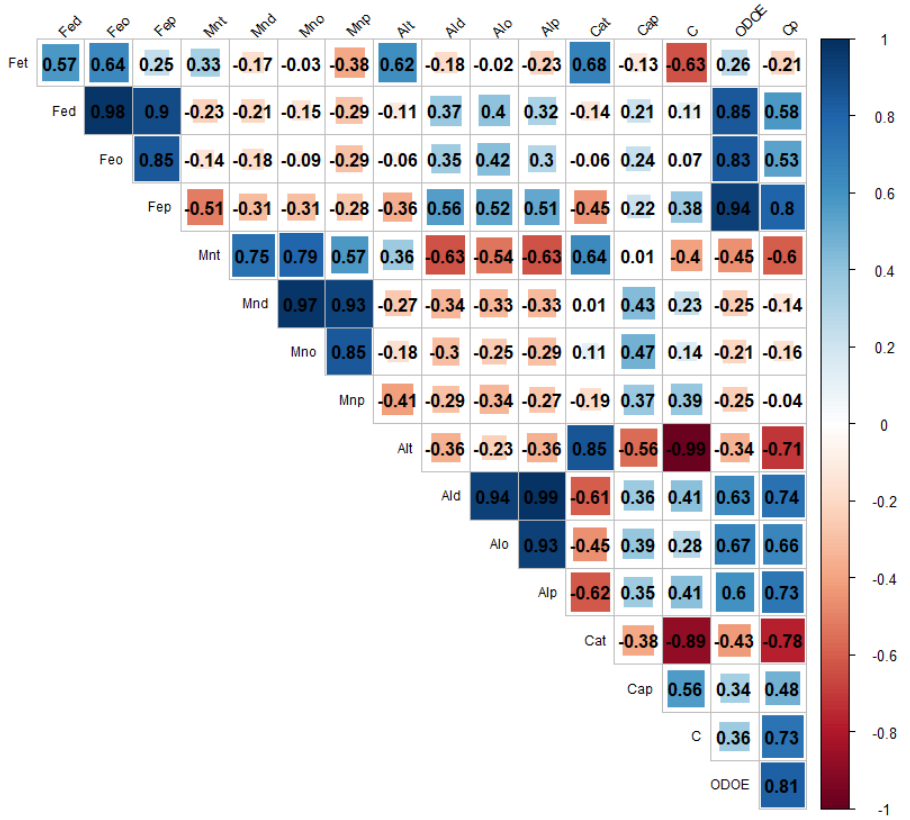

Figure S.9.16: Upper correlation matrix using Pearson method of total concentrations (e.g., Fe_t) and selectively extracted metal concentrations (Fe, Mn, Al and Ca) using dithionite-citrate-bicarbonate (Fe_d), oxalate (Fe_o) and pyrophosphate (Fe_p) and total organic carbon content (C), optical density of the oxalate extract (ODOE) and complexed C concentration (C_p) (n= 124).

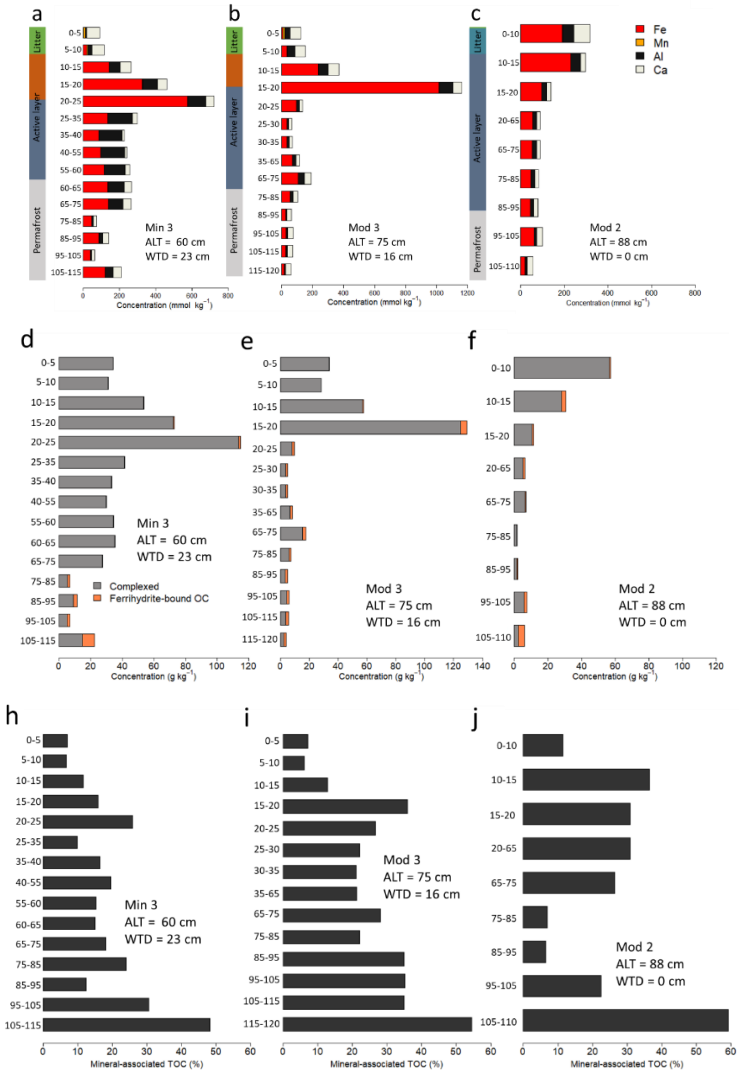

Figure S.9.17: Percentage of complexed metals (Fe, Mn, Al and Ca) in mmol kg^{-1} as a function of depth (cm) within profile (a) Min 3, (b) Mod 3 and (c) Mod 2. Active layer and water table depth are given within each panel. The stratigraphic column on the left represents permafrost (gray), saturated (blue) and unsaturated (brown) active layer and litter (green). (d-e-f) Concentration of C associated with metal cations (Fe, Al, Ca and Mn) by complexation (gray) or by ferrihydrite within organo-mineral associations (Ferrihydrite-bound OC, orange) within profiles Min 3, Mod 3 and Mod 2, respectively and; (h-i-j) percentage of total organic carbon (TOC) stabilized by complexation or bound to ferrihydrite (mineral-associated TOC) within profiles Min 3, Mod 3 and Mod 2, respectively.

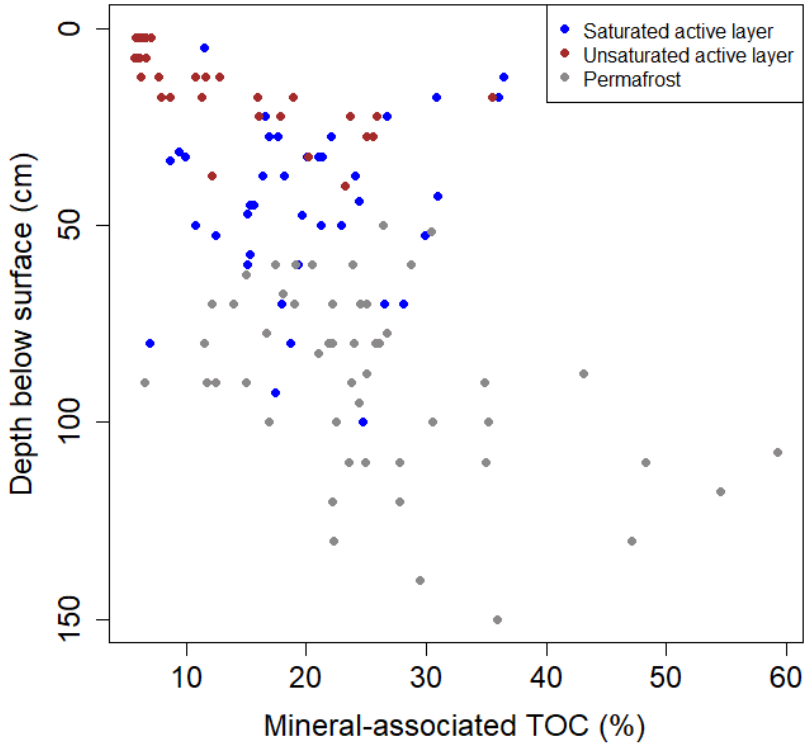

Figure S.9.18: Percentage of total organic carbon (TOC) stabilized by ferrihydrite and complexed metals (Fe, Al, Mn and Ca) as a function of depth under different soil conditions (saturated, unsaturated, permafrost).

Table S.9.1: The thirteen collected cores are divided as poorly thawed (i.e., active layer smaller than 60 cm) and deeply thawed (active layer higher than 60 cm). This table describes numbers of samples per core, active layer and water table depths (negative value means above surface level). and geographical coordinates.

Thaw	Site	n	Active layer depth (cm)	Water table depth (cm)	Latitude N	Longitude W
Poorly thawed	Min 1	13	55	25	63°52'34.3"	149°14'55.1"
	Min 3	15	60	23	63°52'33.3"	149°14'57.9"
	Mod 1	13	50	40	63°52'40.4"	149°15'18.0"
	Ext 1	11	48	22	63°52'43.7"	149°15'28.7"
	Dry 5	7	45	45	63°52'39.5"	149°15'14.3"
	Pond 10	5	58	-6	63°52'39.5"	149°15'18.2"
Deeply thawed	Mod 3	14	75	16	63°52'39.7"	149°15'17.6"
	Mod 2	9	88	0	63°52'39.6"	149°15'19.4"
	Ext 3	12	65	29	63°52'46.6"	149°15'27.8"
	Wet 4	8	108	5	63°52'42.7"	149°15'25.0"
	Pond 1	6	63.5	-9.5	63°52'46.2"	149°15'27.7"
	Pond 9	7	81	-7	63°52'39.5"	149°15'18.7"
	WT 1	4	109	-15	63°52'49.1"	149°15'19.7"

Table S.9.2: Characterization of the total organic carbon (TOC, in wt%), bulk density (BD, in g cm^{-3}), optical density of the oxalate extract (ODOE) and pyrophosphate-extracted C, total and selectively extracted metals (in mg kg^{-1}) including dithionite-citrate-bicaronate (DCB), oxalate (oxa) and pyrophosphate (pyro) extractions and pH-H_2O values for the soil profiles in Eight Mile Lake study site.

#	Sample ID	Depth	TOC	BD (model)	ODOE	C pyro	Fe Total	Fe DCB	Fe Oxa	Fe Pyro	Al Total	Al DCB	Al Oxa	Al Pyro	Mn Total	Mn DCB	Mn Oxa	Mn Pyro	Ca Total	Ca Pyro	P Total	pH H_2O
		cm	wt%	g cm^{-3}	-	g kg^{-1}	mg kg^{-1}															
1	Min1 0-5	2.5	48.11	0.0604	0.037	30.1	3591	1829	1690	294	6260	472	783	325	261	269	371	261	3205	2725	901	3.88
2	Min1 5-10	7.5	47.56	0.0646	0.06	28.9	5447	3175	2836	2006	7399	862	855	821	97	64	42	62	3210	2590	788	3.85
3	Min1 10-15	12.5	46.96	0.0695	0.522	50.5	15025	12917	12254	11086	8507	1823	1871	1797	65	30	16	28	2589	2047	1016	3.81
4	Min1 15-20	17.5	45.25	0.0845	1.394	85.1	27584	23174	24977	22550	15649	2359	2538	2407	56	20	9.3	17	2294	1751	1215	3.93
5	Min1 20-25	22.5	43.85	0.0979	1.784	103.4	34753	31916	31711	30533	14623	2971	3057	3052	50	12	7.0	11	2209	1722	1188	3.97
6	Min1 25-30	27.5	44.58	0.0908	1.041	75.2	26873	23411	22971	21464	12608	2870	2918	2970	41	5.5	6.9	6.2	2376	1678	1428	4.03
7	Min1 30-32.5	31.25	44.65	0.0901	0.296	41.6	14194	11483	11039	10314	17079	3202	3120	3291	53	5.4	6.8	4.5	2617	1772	1510	4.21
8	Min1 32.5-35	33.75	42.91	0.1076	0.276	37.1	10329	10266	10970	9968	24003	3592	3695	3694	56	5.4	6.8	3.9	2473	1594	1341	4.17
9	Min1 35-55	45	8.46	0.8036	0.255	13.3	21005	2862	3017	3164	65430	1837	2278	2863	221	5.7	6.2	3.2	6318	450	392	nd
10	Min1 55-65	60	2.64	0.9868	0.088	5.0	20206	2168	1862	1600	68891	633	839	502	250	7.0	6.1	5.0	8372	480	244	4.65
11	Min1 65-75	70	2.19	1.0019	0.056	2.5	20601	2180	1961	1469	67954	362	605	319	264	7.2	6.0	6.2	8673	487	196	4.68
12	Min1 75-85	80	3.91	0.9452	0.083	4.3	22047	3193	3055	2192	71862	515	866	389	244	8.8	6.0	6.9	8084	708	255	4.78
13	Min1 85-120	100	5.62	0.8906	0.188	9.4	23054	4220	4154	3512	67433	1205	1456	2150	233	7.4	6.0	6.1	7256	625	346	4.64
14	Min3 0-5	2.5	48.53	0.0572	0.034	34.2	3520	1613	776	143	7114	331	309	195	602	561	478	555	3480	2853	nd	4.11
15	Min3 5-10	7.5	46.88	0.0701	0.046	31.0	4673	2753	2125	1102	7954	753	769	663	278	234	176	232	3368	2686	nd	3.81
16	Min3 10-15	12.5	46.37	0.0745	0.312	53.3	12154	10054	9916	7941	9002	1722	1810	1668	87	77	40	53	2866	2334	nd	3.88
17	Min3 15-20	17.5	45.79	0.0795	1.021	72.2	25155	19950	21171	18255	12800	2120	2410	2230	58	33	15	22	2591	2084	nd	3.85
18	Min3 20-25	22.5	44.36	0.0929	2.208	113.6	39528	33683	36838	32133	15882	2618	2861	2721	63	26	7.2	15	2298	1746	nd	3.93
19	Min3 25-35	30	41.86	0.1189	0.302	41.3	8744	8403	8689	7539	21619	3622	3721	3650	41	1.0	6.6	5.1	2148	1154	nd	4.35
20	Min3 35-40	37.5	20.27	0.4900	0.381	33.2	8166	5189	5131	4813	46273	2875	3073	3456	82	1.0	6.4	4.0	2388	545	nd	4.57
21	Min3 40-55	47.5	15.31	0.6123	0.508	29.8	22314	6113	6450	5424	56032	2629	3052	3565	222	1.0	6.3	4.9	5976	519	nd	4.32
22	Min3 55-60	57.5	22.46	0.4404	0.456	34.3	8398	7104	7529	6397	48832	2799	3074	3144	79	20	6.4	8.7	2272	1027	nd	4.49
23	Min3 60-65	62.5	23.53	0.4171	0.344	35.2	10402	8380	8686	7625	47240	2019	2205	2449	75	20	12	19	2542	1558	nd	4.71
24	Min3 65-75	67.5	15.27	0.6131	0.449	27.3	28599	8750	9095	7643	58662	1732	1934	2219	268	31	20	26	8191	1783	nd	4.84
25	Min3 75-85	80	2.95	0.9767	0.111	5.3	31883	7711	10427	2557	71504	443	920	255	333	31	46	6.0	10486	696	nd	5.12
26	Min3 85-95	90	9.27	0.7795	0.219	8.9	38328	13251	16944	4872	66159	657	1049	587	355	72	94	9.0	10009	1208	nd	5.35
27	Min3 95-105	100	2.28	0.9990	0.127	5.1	34627	8837	10363	2164	67911	400	764	236	371	41	49	5.1	10811	690	nd	5.46
28	Min3 105-115	110	4.65	0.9214	0.49	14.7	78386	25331	42065	6761	70331	1519	2024	1155	912	196	390	28	12883	1862	nd	5.84

Table S.9.2: (continued)

#	Sample ID	Depth	TOC	BD (model)	ODOE	C pyro	Fe Total	Fe DCB	Fe Oxa	Fe Pyro	Al Total	Al DCB	Al Oxa	Al Pyro	Mn Total	Mn DCB	Mn Oxa	Mn Pyro	Ca Total	Ca Pyro	P Total	pH H_2O
		cm	wt%	g cm^{-3}	-	g kg^{-1}	mg kg^{-1}															
29	Mod 1 0-5	2.5	46.66	0.0720	0.031	27.1	3277	1596	774	313	7109	322	303	266	731	750	666	779	3469	3233	nd	4.16
30	Mod 1 5-10	7.5	46.68	0.0718	0.035	27.9	3340	1864	999	525	6330	418	388	362	475	410	325	396	2672	2200	nd	3.76
31	Mod 1 10-15	12.5	47.85	0.0624	0.052	29.9	4815	2889	1872	1364	7859	665	657	623	134	99	68	92	2673	1723	nd	3.54
32	Mod 1 15-20	17.5	47.39	0.0660	0.323	37.5	6919	6205	6002	5090	5617	1020	1134	1073	86	58	32	49	2655	1951	nd	3.56
33	Mod 1 20-25	22.5	47.17	0.0678	1.148	75.2	26682	18613	19915	17729	10720	2230	2572	2279	41	27	14	19	3302	2683	nd	4.05
34	Mod 1 25-30	27.5	45.27	0.0843	2.028	115.1	46741	36309	36909	33704	13637	2862	3101	2812	73	28	12	15	3035	2822	nd	4.07
35	Mod 1 30-35	32.5	43.25	0.1040	1.368	87.0	25648	28724	27914	26273	12908	2851	3016	2774	41	19	6.9	9.0	2500	2345	nd	4.25
36	Mod 1 35-40	37.5	42.06	0.1168	0.496	50.7	11997	12428	12375	10997	20477	2970	3358	3081	50	11	6.7	5.5	2396	1945	nd	4.45
37	Mod 1 40-55	50	7.61	0.8292	0.232	17.2	24821	4845	5205	4126	60015	1351	1769	1609	236	7.0	6.1	6.0	6760	698	nd	4.47
38	Mod 1 55-65	60	12.46	0.6887	0.383	25.5	22790	6180	5709	5626	57976	2417	2639	2645	211	10	6.2	8.9	6007	998	nd	4.58
39	Mod 1 65-75	70	28.00	0.3270	0.891	38.8	8069	9334	9787	9032	41389	4005	4619	4243	71	13	6.4	8.1	2593	1238	nd	4.78
40	Mod 1 75-80	77.5	32.09	0.2545	1.023	53.4	10638	13419	13600	12941	31855	4039	4431	4416	61	18	6.5	15	2489	2009	nd	4.86
41	Mod 1 85-105	95	3.31	0.9649	0.162	7.0	27775	7416	8013	3377	65180	466	785	544	307	46	41	26	8173	918	nd	5.25
42	Mod 2 0-10	5	49.72	0.0488	0.548	56.5	19476	12795	13441	10674	8692	1497	1596	1380	155	92	67	79	3632	2910	nd	3.92
43	Mod 2 10-15	12.5	8.38	0.8060	0.562	28.1	47566	23862	23877	12729	60005	1262	1604	1254	303	45	37	29	7601	901	nd	4.24
44	Mod 2 15-20	17.5	3.74	0.9507	0.186	10.6	34768	10756	9853	5351	67343	826	1297	610	286	24	16	19	7680	800	nd	4.47
45	Mod 2 20-65	42.5	2.07	1.0059	0.085	5.2	34618	9643	8632	3000	68823	851	1389	489	268	17	7.1	12	7892	699	nd	4.64
46	Mod 2 65-75	70	2.62	0.9876	0.114	6.4	30271	5980	5290	2883	67493	834	1320	592	261	12	3.7	8.8	7735	603	nd	4.5
47	Mod 2 75-85	80	2.78	0.9823	0.106	1.5	30067	4834	4325	2614	67778	717	1150	494	334	15	7.8	10	9537	613	nd	4.41
48	Mod 2 85-95	90	3.09	0.9721	0.101	1.6	29090	4580	4465	2477	68705	541	925	377	313	29	22	17	8941	826	nd	4.69
49	Mod 2 95-105	100	3.43	0.9610	0.152	5.8	35840	10912	12176	3411	70388	506	988	321	448	134	152	31	8897	1064	nd	5.05
50	Mod2 105-110	107.5	1.02	1.0412	0.115	2.5	40742	13506	17248	1131	67400	489	1008	178	741	397	470	118	8928	1082	nd	6.21

Table S.9.2: (continued)

#	Sample ID	Depth	TOC	BD (model)	ODOE	C pyro	Fe Total	Fe DCB	Fe Oxa	Fe Pyro	Al Total	Al DCB	Al Oxa	Al Pyro	Mn Total	Mn DCB	Mn Oxa	Mn Pyro	Ca Total	Ca Pyro	P Total	pH H_2O
		cm	wt%	g cm^{-3}	-	g kg^{-1}	mg kg^{-1}															
51	Mod3 0-5	2.5	47.46	0.0654	0.043	33.7	4651	2038	1002	492	10495	1026	1064	900	662	666	554	618	3598	2781	916	3.87
52	Mod3 5-10	7.5	46.00	0.0777	0.063	28.2	6017	3663	2612	1953	10317	1368	1465	1307	301	226	167	197	4094	2662	868	3.99
53	Mod3 10-15	12.5	45.00	0.0868	0.681	56.8	19681	16755	16229	13258	10797	1774	1936	1668	108	93	61	74	3183	2774	1278	3.96
54	Mod3 15-20	17.5	35.83	0.1963	2.95	124.9	62955	74979	75253	56706	19201	2731	2874	2480	100	41	29	27	2364	2182	1607	4.22
55	Mod3 20-25	22.5	3.60	0.9554	0.193	8.0	35979	14789	12610	5281	65075	752	1220	529	291	19	10	14	7512	856	584	4.57
56	Mod3 25-30	27.5	2.18	1.0023	0.082	3.7	29125	7314	7158	1917	75127	492	944	319	261	19	12	16	7827	829	300	4.78
57	Mod3 30-35	32.5	2.32	0.9976	0.079	3.5	31749	8301	8389	1973	72334	551	1096	361	297	19	11	15	7733	788	298	4.85
58	Mod3 35-65	50	3.87	0.9468	0.182	6.7	33347	10887	10798	3864	62384	811	1244	633	301	35	27	27	7859	884	590	4.89
59	Mod3 65-75	70	6.20	0.8724	0.422	15.1	41997	16580	16650	5985	61595	1302	1755	1056	349	91	81	47	9139	1686	929	5.25
60	Mod3 75-85	80	3.27	0.9661	0.155	5.9	34661	10359	9352	3070	71423	706	1106	480	381	85	68	48	10040	1221	679	5.34
61	Mod3 85-95	90	1.38	1.0291	0.089	3.2	34467	11217	8593	1403	71182	559	866	216	367	136	118	69	9094	1173	636	6.01
62	Mod3 95-105	100	1.73	1.0172	0.117	4.3	36589	11289	10005	1666	62956	581	997	253	483	195	192	100	9105	1385	721	6.2
63	Mod3 105-115	110	1.63	1.0206	0.111	3.6	35267	9903	10846	1429	61348	485	1088	209	661	391	400	148	10558	1430	836	6.57
64	Mod3 115-120	117.5	0.75	1.0506	0.069	2.4	34661	9137	8754	942	70992	488	962	165	669	344	351	143	9882	1424	675	7.52
65	Ext1 0-5	2.5	47.73	0.0633	0.026	31.6	3169	1671	1063	403	5273	585	632	541	707	786	727	869	2878	2660	nd	3.81
66	Ext1 5-10	7.5	49.02	0.0536	0.025	29.4	3138	1444	985	403	5673	563	601	531	529	494	455	532	2852	2098	nd	3.73
67	Ext1 10-15	12.5	48.59	0.0567	0.035	29.9	3376	1719	1215	645	6174	537	585	518	308	266	236	271	2873	1967	nd	3.74
68	Ext1 15-20	17.5	46.64	0.0722	0.385	52.4	9413	7945	7707	6533	10328	1301	1429	1297	118	80	56	76	2782	2525	nd	3.91
69	Ext1 20-25	22.5	42.15	0.1157	0.846	69.8	14307	14690	15172	13534	15192	3298	3653	3439	58	22	8.9	15	2505	2281	nd	3.92
70	Ext1 25-30	27.5	40.64	0.1329	1.078	71.0	18970	18199	19289	17147	18885	4538	5124	4806	62	12	6.7	8.4	2273	1593	nd	4.26
71	Ext1 30-35	32.5	41.68	0.1210	1.836	83.0	20755	25872	27597	24796	23768	4814	5452	5150	60	14	6.7	10	2303	1687	nd	4.29
72	Ext1 35-40	37.5	29.35	0.3021	1.385	70.3	16501	18348	20471	19137	32942	3707	4362	4160	71	12	6.6	9.2	2328	1223	nd	4.47
73	Ext1 40-48	44	4.76	0.9179	0.223	10.2	37093	11773	11308	5022	66162	1004	1411	985	389	72	68	32	9505	856	nd	4.83
74	Ext1 48-55	51.5	4.73	0.9189	0.288	11.5	44020	16117	19578	6332	69212	770	1404	779	479	144	177	71	10616	1315	nd	5.16
75	Ext1 55-65	60	5.40	0.8976	0.339	12.3	44304	17577	21354	6539	71444	991	1618	869	510	163	208	69	10396	1479	nd	5.12

Table S.9.2: (continued)

#	Sample ID	Depth	TOC	BD (model)	ODOE	C pyro	Fe Total	Fe DCB	Fe Oxa	Fe Pyro	Al Total	Al DCB	Al Oxa	Al Pyro	Mn Total	Mn DCB	Mn Oxa	Mn Pyro	Ca Total	Ca Pyro	P Total	pH H_2O
		cm	wt%	g cm^{-3}	-	g kg^{-1}	mg kg^{-1}															
76	Ext3 0-5	2.5	48.66	0.0563	0.033	29.6	3291	1018	595	171	7644	313	330	260	817	680	646	778	3452	2908	1007	3.78
77	Ext3 5-10	7.5	48.06	0.0607	0.03	27.2	3072	1078	581	242	6446	319	321	293	530	405	349	435	3257	2161	900	3.84
78	Ext3 10-15	12.5	47.97	0.0615	0.042	36.9	4017	1767	1174	722	8339	493	503	463	209	197	147	204	2590	1791	960	3.6
79	Ext3 15-20	17.5	46.43	0.0740	0.081	40.3	4798	3618	2280	1809	9155	759	764	723	97	89	52	85	2612	2169	1040	3.83
80	Ext3 20-25	22.5	39.92	0.1416	0.942	70.6	18418	20844	19251	17276	18198	2005	2077	1894	76	47	26	34	2281	1899	1811	3.87
81	Ext3 25-30	27.5	21.50	0.4619	1.016	52.3	23657	27411	26447	19971	48834	2310	2569	2647	110	22	11	15	2518	1076	423	4.43
82	Ext3 30-35	32.5	6.27	0.8704	0.291	12.2	37579	13887	12116	6755	70111	1415	1829	1507	272	6.4	6.2	3.2	7840	522	558	4.53
83	Ext3 35-40	37.5	5.59	0.8915	0.194	9.4	28941	8272	7560	4245	73514	1583	2024	1450	271	4.3	6.2	1.2	7589	369	428	4.53
84	Ext3 40-65	52.5	8.36	0.8065	0.51	23.3	44955	21013	18505	11041	51844	1890	2338	2162	245	10	6.2	7.0	6610	619	713	4.6
85	Ext3 65-75	70	15.23	0.6143	0.625	33.6	26599	11111	9617	8744	49838	3207	3182	3547	225	31	19	27	6367	1588	891	4.85
86	Ext3 75-85	80	6.54	0.8621	0.289	12.8	29702	9299	10376	3582	49779	1203	1476	1131	405	102	116	30	8957	1271	653	5.29
87	Ext3 85-90	87.5	1.09	1.0390	0.11	3.3	27798	7442	7935	1601	52379	337	693	210	374	101	108	29	9350	640	457	5.52
88	Wet4 85-90	45	41.60	0.1219	0.261	63.7	7908	6945	7003	6197	15134	3014	2875	3194	46	22	13	30	2865	2617	nd	nd
89	Wet4 90-95	92.5	40.30	0.1371	0.224	70.2	5780	5174	5353	4820	14530	3691	3616	3904	45	13	6.5	21	2590	2523	nd	nd
90	Wet4 95-105	100	40.36	0.1363	0.187	68.1	7144	6639	6959	6271	18524	3840	3792	4139	64	46	31	57	2883	3396	nd	nd
91	Wet4 105-115	110	24.23	0.4023	0.637	56.9	8780	7994	8357	7750	40151	3900	4002	4380	99	67	50	81	2994	3717	nd	nd
92	Wet4 115-125	120	13.33	0.6649	0.379	29.6	23213	5402	5339	5065	51591	2163	2247	2428	249	43	34	53	8920	2422	nd	nd
93	Wet4 125-135	130	6.84	0.8529	0.239	14.5	27238	5903	6855	3743	60887	1112	1436	863	338	81	92	42	9598	1877	nd	nd
94	Wet4 135-145	140	2.12	1.0044	0.163	4.0	35380	9934	12690	2367	65392	470	1199	244	545	221	240	42	11899	1228	nd	nd
95	Wet4 145-155	150	1.24	1.0340	0.113	2.1	34108	9241	12326	1522	74599	386	1181	126	452	115	137	25	10103	1178	nd	nd
96	Dry5 25-35	17.5	38.69	0.1571	1.483	136.9	22643	22728	23700	21540	15449	3652	4056	3927	79	67	52	93	2315	2106	nd	nd
97	Dry5 35-45	40	35.03	0.2080	0.558	81.1	6915	7402	7394	6957	27005	4678	4639	4951	53	7.4	6.3	17	2137	1179	nd	nd
98	Dry5 45-55	50	32.64	0.2455	0.496	86.2	6075	6575	6616	6192	30628	4697	4754	5283	47	10	6.5	17	2028	1184	nd	nd
99	Dry5 55-65	60	20.95	0.4744	0.489	50.2	6262	3489	3249	3457	51092	4220	4117	4951	67	9.2	6.2	12	2233	656	nd	nd
100	Dry5 65-75	70	21.97	0.4513	0.598	55.1	8255	5622	5426	5652	55677	4431	4345	5577	69	14	8.9	21	2218	1059	nd	nd
101	Dry5 75-85	80	10.53	0.7430	0.63	27.3	26575	6499	6458	5744	64473	2078	2263	1805	241	13	10	21	6792	1189	nd	nd
102	Dry5 85-95	90	6.89	0.8512	0.152	7.9	26719	5479	5147	4095	72617	818	1098	524	283	14	10	18	8550	957	nd	nd

Table S.9.2: (continued)

#	Sample ID	Depth	TOC	BD (model)	ODOE	C pyro	Fe Total	Fe DCB	Fe Oxa	Fe Pyro	Al Total	Al DCB	Al Oxa	Al Pyro	Mn Total	Mn DCB	Mn Oxa	Mn Pyro	Ca Total	Ca Pyro	P Total	pH H_2O
		cm	wt%	g cm^{-3}	-	g kg^{-1}	mg kg^{-1}															
103	Pond1 45-55	50	4.08	0.9398	0.101	3.7	30398	6054	5888	2800	67041	497	947	298	347	44	38	28	8779	844	nd	nd
104	Pond1 55-65	60	2.48	0.9924	0.102	2.9	30633	5895	6251	2440	73365	500	1017	292	313	36	31	28	8914	890	nd	nd
105	Pond1 65-75	70	1.77	1.0160	0.116	2.0	35611	10696	12577	1861	69122	455	1202	184	451	149	152	75	10339	979	nd	nd
106	Pond1 75-80	77.5	1.50	1.0252	0.223	1.7	33596	10094	12012	1418	68427	451	1045	152	451	177	184	93	9765	1017	nd	nd
107	Pond1 80-85	82.5	2.48	0.9922	0.119	3.8	33274	8996	8539	1871	69175	536	1018	215	518	228	251	163	10557	1583	nd	nd
108	Pond1 85-95	90	4.86	0.9149	0.165	5.3	34550	10203	10881	2143	69431	648	1077	344	853	472	498	265	10183	1990	nd	nd
109	Pond9 50-55	52.5	2.85	0.9802	0.081	2.8	31573	7097	6088	2608	68889	733	1146	386	305	37	29	35	7981	763	nd	nd
110	Pond9 55-65	60	2.92	0.9778	0.486	2.7	40755	14129	15886	2363	66312	675	2137	309	352	58	45	55	7773	969	nd	nd
111	Pond9 65-75	70	3.77	0.9499	0.169	4.0	41382	16806	15592	3025	68410	693	1105	297	386	79	69	70	7903	1241	nd	nd
112	Pond9 75-85	80	3.10	0.9719	0.135	4.3	32436	9979	9597	2699	68129	648	1099	273	405	85	79	54	9290	1312	nd	nd
113	Pond9 85-95	90	6.63	0.8592	0.433	13.6	38571	13366	15027	4890	61927	1449	1987	1098	476	185	189	80	9835	2338	nd	nd
114	Pond9 95-105	100	7.55	0.8312	0.429	14.0	38682	16000	18451	4903	62622	1610	2266	1140	430	179	210	76	10693	2412	nd	nd
115	Pond9 105-115	110	34.25	0.2200	2.041	89.9	57507	30689	39082	14900	29177	6300	9118	7427	376	404	619	132	4589	9768	nd	nd
116	Pond10 43-55	47	2.92	0.9777	0.088	3.8	27043	4605	5322	2540	68976	581	1338	318	273	13	11	11	8308	635	nd	nd
117	Pond10 55-65	60	2.72	0.9845	0.111	4.0	28705	5450	6282	2714	72860	640	1332	335	285	20	22	13	8200	654	nd	nd
118	Pond10 65-75	70	11.25	0.7226	0.538	18.7	41315	16730	21117	9076	65579	1791	2652	1293	242	32	36	26	6205	1290	nd	nd
119	Pond10 75-85	80	20.16	0.4925	0.122	52.0	17213	20412	13816	13985	50893	4289	1127	4073	88	49	50	45	2572	2624	nd	nd
120	Pond10 85-90	87.5	2.11	1.0047	0.113	4.2	30290	5275	7204	2119	74308	449	1219	229	335	33	38	16	9044	885	nd	nd
121	WT1 95-105	100	8.54	0.8012	0.284	20.6	25238	5012	6113	4010	62211	1502	2243	1301	283	27	25	26	7933	1050	nd	nd
122	WT1 105-115	110	6.39	0.8666	0.229333	15.5	25865	4674	5788	3992	68155	1020	1642	905	272	26	24	27	8092	1049	nd	nd
123	WT1 115-125	120	3.88	0.9463	0.246	8.1	36017	9907	15966	3769	71790	544	1599	367	494	148	223	35	10592	1429	nd	nd
124	WT1 125-135	130	1.70	1.0185	0.191	4.7	37196	12039	16359	1553	70660	410	1400	190	582	262	297	93	12117	1743	nd	nd

Table S.9.3: Stock of reactive metals (Fe_o, Al_o, Mn_o), total organic carbon (TOC) and complexed C (C_p). The stock represents only active layer samples and is normalized to kg m^{-3} for all profiles. These stocks were estimated using the cumulative stock within the active layer of each site and normalized to one meter deep (stock expressed in kg m^{-3}) to allow comparison between profiles. The active layer depth (ALD) is shown. The bulk density used is estimated based on linear regression presented in Sect. 9.2.4.

Thaw	Site	ALD	Fe_o	Al_o	Mn_o	TOC	C_p
		cm			kg m^{-3}		
Poorly	Min 1	55	1.75	0.79	0.0044	48.1	7.1
	Min 3	60	2.15	0.83	0.0053	62.6	10.0
	Mod 1	50	2.42	0.51	0.014	61.1	9.1
	Ext 1	48	3.25	0.56	0.020	44.7	7.6
	Dry 5	45	3.24	0.71	0.0066	63.5	20.5
	Pond 10	58	5.25	1.31	0.011	28.5	3.7
Deeply	Mod 3	75	8.96	0.95	0.026	38.9	7.5
	Mod 2	88	7.36	1.17	0.0086	26.3	5.8
	Ext 3	65	8.24	1.11	0.0089	55.2	12.0
	Wet 4	108	0.93	0.41	0.0023	52.6	8.4
	Pond 1	63.5	5.62	0.91	0.035	36.5	3.4
	Pond 9	81	8.49	1.23	0.039	29.1	2.9
	WT 1	109	4.90	1.78	0.020	67.9	16.4

Table S.9.4: Mean concentration of complexed carbon (Cp) with metals cations (Fe, Al, Mn and Ca) and ferrihydrite-bound organic carbon (OC). The mean percentage of TOC associated with minerals as organo-mineral associations or organo-metallic complexes is given as well as the range for each profile.

	Site	n	Mean complexed C_p (g kg^{-1})	Mean ferrihydrite-bound OC (g kg^{-1})	Mean % of TOC associated with minerals (%)	Range (min – max) TOC associated (%)
Poorly thawed	Min 1	13	37.4	0.21	13.4	6.1 – 23.6
	Min 3	15	36.0	1.19	18.5	6.7 – 48.3
	Mod 1	13	45.6	0.30	15.3	5.8 – 25.6
	Ext 1	11	42.9	0.90	17.5	6.0 – 30.4
	Dry 5	7	63.5	0.14	24.6	11.8 – 35.5
	Pond10	5	16.5	1.03	20.5	15.2 – 25.8
Deeply thawed	Mod 3	14	21.4	1.55	25.9	6.2 – 54.5
	Mod 2	9	13.1	1.35	25.7	6.5 – 59.3
	Ext 3	12	29.3	0.74	19.0	5.7 – 43.2
	Wet 4	8	38.6	0.75	22.9	15.4 – 36.0
	Pond 1	6	3.2	1.6	18.9	10.8 – 26.7
	Pond 9	7	18.7	2.65	20.4	12.5 – 27.8
	WT 1	4	12.2	1.7	31.1	24.7 – 47.1
Total		124	31.4	1.0	20.2	5.8 – 59.3

Table S.9.5: Projected OC stock and reactive Fe stock exposed (in kg m^{-2} and in percentage relative to the current stock in the active layer) upon a projection of 20 cm deepening of the active layer. ALT = active layer thickness, AL = active layer, OC = organic carbon, Feo = oxalate-extracted Fe.

Thaw	Site	ALT	Projected ALT	Additional OC exposed (kg m^{-2})	Additional OC stock exposed compare to AL stock (%)	Additional Fe_o stock exposed (kg m^{-2})	Additional Fe_o stock exposed compare to AL stock (%)
Poorly	Min 1	55	75	4.8	18	0.38	40
	Min 3	60	80	16	42	1.2	97
	Mod 1	50	70	16	53	0.77	63
	Ext 1	48	68	9.3	44	3.7	240
	Dry 5	45	65	18	63	0.32	22
	Pond 10	58	78	13	79	2.2	71
Deeply	Mod 3	75	95	4.6	16	1.8	27
	Mod 2	88	108	6.0	26	2.1	32
	Ext 3	65	85	15	42	1.5	28
	Wet 4	108	128	17	31	0.77	76
	Pond 1	63.5	83.5	3.8	16	2.3	64
	Pond 9	81	101	11	45	2.6	38
	WT 1	109	129	7.7	10	2.5	46
Mean ± SD				11 ± 5.2	37 ± 20	1.7 ± 1.0	65 ± 57

Chapter 5: Strontium isotopes trace the dissolution and precipitation of mineral organic carbon interactions in thawing permafrost

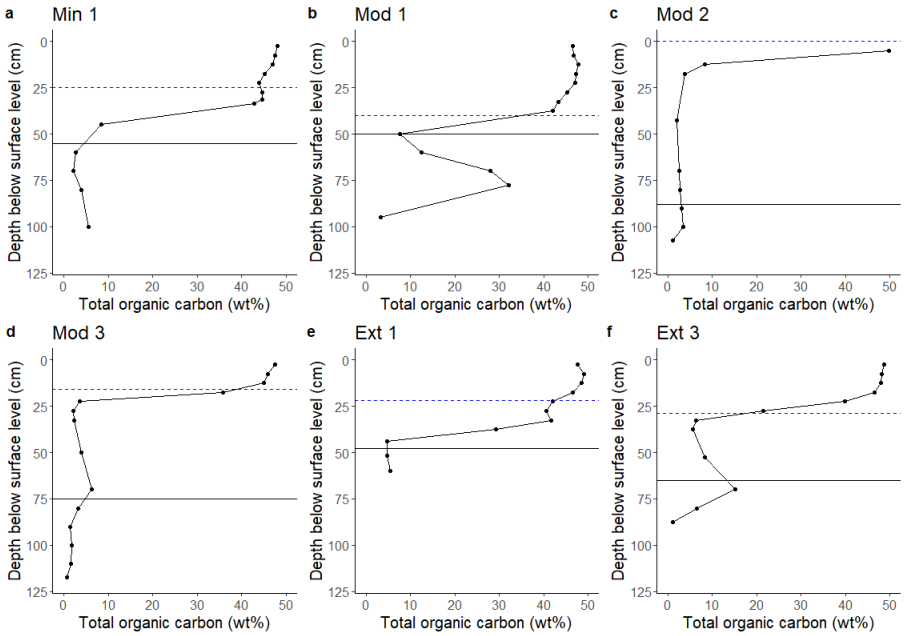

Figure S.10.1: Total organic carbon content (TOC; wt%) with depth in Eight Mile Lake soil profiles Min 1 (a); Mod 1 (b), Mod 2 (c), Mod 3 (d), Ext 1 (e) and Ext 3 (f). The water table (blue dashed line) and the permafrost table (black line) are represented for each plot. Data taken from *Ch.4.*

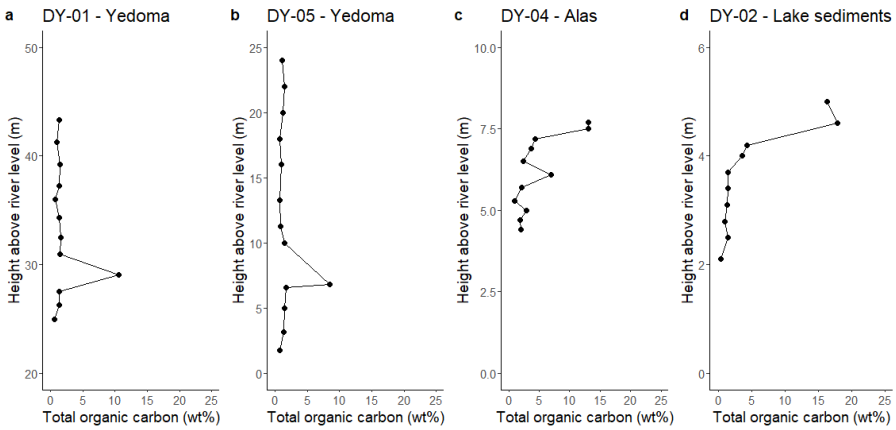

Figure S.10.2: Total organic carbon (TOC; wt%) as a function of height above river level in Duvanny Yar site for Yedoma deposits profile (a) DY-01 and (b) DY-05, and for previously thawed (c) Alas profile and (d) Lake sediment profile. Data are taken from *Ch.2*.

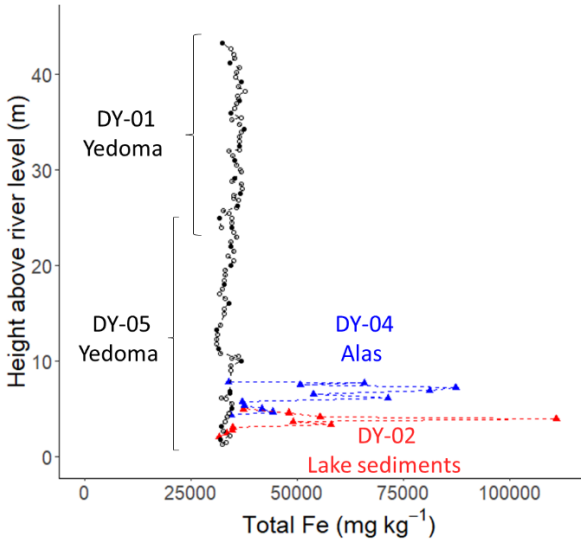

Figure S.10.3: Total Fe concentration (in mg kg^{-1}) as a function of height above river level in Duvanny Yar site for Yedoma deposits profiles (DY-01 and DY-05; black dots), Alas profile (DY-04; blue triangles) and lake sediement profile (DY-02; red triangles). All samples from Alas and lake sediments, and a subset of Yedoma deposits (full symbols) were used for DCB extractions of Fe and Sr and further determination of their radiogenic Sr ratio.

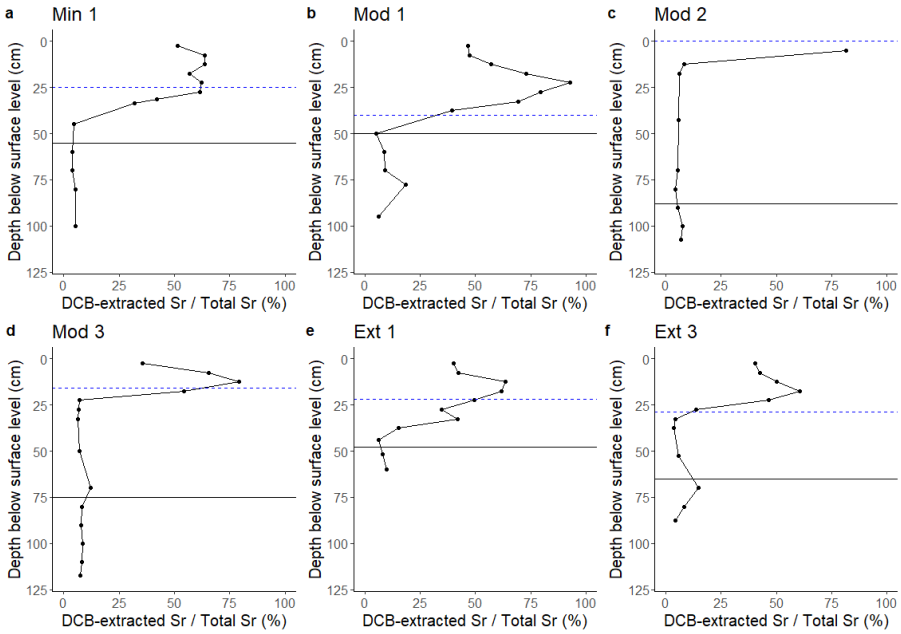

Figure S.10.4: Percentage of dithionite-citrate-bicarbonate (DCB) extracted Sr out of the total Sr with depth in Eight Mile Lake tundra soil profiles Min 1 (a); Mod 1 (b), Mod 2 (c), Mod 3 (d), Ext 1 (e) and Ext 3 (f). The water table (blue dashed line) and the permafrost table (black line) are represented for each plot.

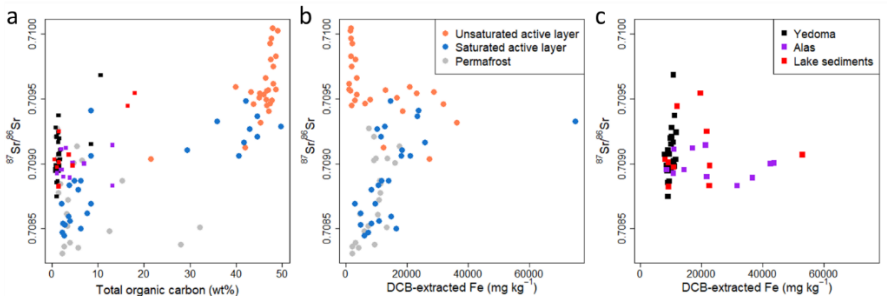

Figure S.10.5: (a) Radiogenic Sr isotopic signature ($^{87}Sr/^{86}Sr$) as a function of total organic carbon content (wt%) in Eight Mile Lake soil samples (points) and Duvanny Yar sediments (square). (b) Radiogenic Sr isotopic signature ($^{87}Sr/^{86}Sr$) as a function of dithionite-citrate-bicarbonate (DCB) extracted Fe (mg kg^{-1}) in Eight Mile Lake soil samples for unsaturated (orange points), saturated (blue points) and permafrost (gray points). (c) Radiogenic Sr isotopic signature ($^{87}Sr/^{86}Sr$) as a function of DCB extracted Fe (in mg kg^{-1}) in Duvanny Yar deposits samples for Yedoma deposits (black squares), Alas deposits (purple squares) and Lake sediments (red squares). The symbols used for Eight Mile Lake (b) and Duvanny Yar (c) are applicable to plot (a).

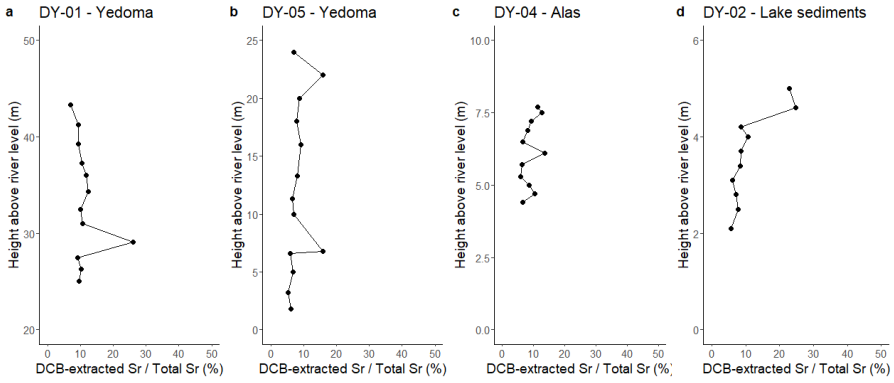

Figure S.10.6: Percentage of dithionite-citrate-bicarbonate (DCB) extracted Sr out of the total Sr with height in Duvanny Yar deposit for the Yedoma profiles DY-01 (a) and DY-05 (b) and for previously thawed Alas profile DY-04 (c) and Lake sediment profile DY-02 (d).

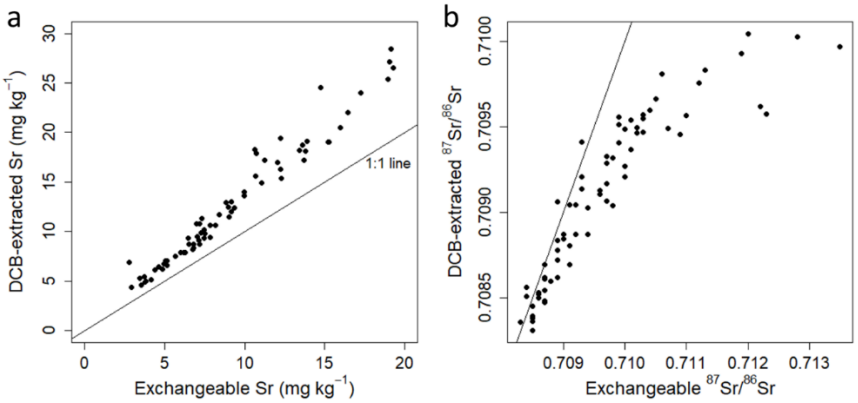

Figure S.10.7: (a) Concentration of dithionite-citrate-bicarbonate (DCB) extracted Sr (in mg kg^{-1}) as a function of exchangeable Sr extracted by ammonium acetate (in mg kg^{-1}). (b) Radiogenic Sr isotopic signature ($^{87}Sr/^{86}Sr$ ratio) of DCB-extracted Sr as a function of exchangeable Sr isotopic ratio. Data for exchangeable Sr concentration and isotopic ratio are taken from (Mauclet, 2022).

Table S.10.1: Characterization of samples from Eight Mile Lake (Min1, Mod1, Mod2, Mod3, Ext1 and Ext3) and Duvanny Yar Yedoma profile (DY-01; DY-05), Alas profile (DY-04) and Lake sediment profile (DY-02) for total organic carbon (TOC) content, total and dithionite-citrate-bicarbonate (DCB)-extracted Fe and Sr, radiogenic Sr isotopic ratio ($^{87}Sr/^{86}Sr$) mean and standard deviation (SD; n = 3) and pyrophosphate (Pyro) extracted Ca (data taken from *Ch.4*).

Nb	Sample ID	Sample depth	ALD	WTD	TOC	Fe Total	Fe DCB	Sr Total	Sr DCB	Ca Pyro	$^{87}Sr/^{86}Sr$ Mean	$^{87}Sr/^{86}Sr$ SD
			cm	cm	wt%			mg kg^{-1}			-	-
1	Min 1 0-5	2.5	55	25	48	3591	1829	21	11	2725	0.709753	1.70E-05
2	Min 1 5-10	7.5	55	25	48	5447	3175	30	19	2590	0.709806	3.65E-06
3	Min 1 10-15	12.5	55	25	47	15025	12917	30	19	2047	0.709567	1.53E-05
4	Min 1 15-20	17.5	55	25	45	27584	23174	32	18	1751	0.709546	2.78E-05
5	Min 1 20-25	22.5	55	25	44	34753	31916	29	18	1722	0.709461	6.57E-06
6	Min 1 25-30	27.5	55	25	45	26873	23411	28	17	1678	0.709366	8.08E-06
7	Min 1 30-32.5	31.25	55	25	45	14194	11483	40	17	1772	0.709209	1.27E-05
8	Min 1 32.5-35	33.75	55	25	43	10329	10266	48	15	1594	0.709268	1.35E-05
9	Min 1 35-55	45	55	25	8.5	21005	2862	115	5	450	0.708694	2.00E-05
10	Min 1 55-65	60	55	25	2.6	20206	2168	139	5	480	0.708362	8.53E-06
11	Min 1 65-75	70	55	25	2.2	20601	2180	145	5	487	0.708309	1.54E-05
12	Min 1 75-85	80	55	25	3.9	22047	3193	132	7	708	0.708395	9.86E-06
13	Min 1 85-120	100	55	25	5.6	23054	4220	128	7	625	0.708356	3.05E-05
14	Mod 1 0-5	2.5	50	40	47	3277	1596	20	9	3233	0.709564	4.04E-06
15	Mod 1 5-10	7.5	50	40	47	3340	1864	18	9	2200	0.709453	5.78E-06
16	Mod 1 10-15	12.5	50	40	48	4815	2889	23	13	1723	0.709489	1.59E-05
17	Mod 1 15-20	17.5	50	40	47	6919	6205	24	17	1951	0.709466	1.67E-05
18	Mod 1 20-25	22.5	50	40	47	26682	18613	27	25	2683	0.709404	2.31E-05
19	Mod 1 25-30	27.5	50	40	45	46741	36309	36	28	2822	0.709319	1.78E-05
20	Mod 1 30-35	32.5	50	40	43	25648	28724	35	24	2345	0.709554	2.14E-05
21	Mod 1 35-40	37.5	50	40	42	11997	12428	47	19	1945	0.709125	1.45E-05
22	Mod 1 45-55	50	50	40	7.6	24821	4845	129	7	698	0.708618	7.21E-06
23	Mod 1 55-65	60	50	40	12	22790	6180	107	9	998	0.708482	2.72E-05
24	Mod 1 65-75	70	50	40	28	8069	9334	140	13	1238	0.708379	1.91E-05
25	Mod 1 75-80	77.5	50	40	32	10638	13419	98	18	2009	0.708510	1.76E-05
26	Mod 1 85-105	95	50	40	3.3	27775	7416	129	8	918	0.708520	1.29E-05
27	Mod 2 0-10	5	88	0	50	19476	12795	33	27	2910	0.709288	1.19E-05
28	Mod 2 10-15	12.5	88	0	8.4	47566	23862	121	10	901	0.709411	1.23E-05
29	Mod 2 15-20	17.5	88	0	3.7	34768	10756	131	8	800	0.708835	1.82E-05
30	Mod 2 20-65	42.5	88	0	2.1	34618	9643	134	8	699	0.708694	1.08E-05
31	Mod 2 65-75	70	88	0	2.6	30271	5980	133	7	603	0.708450	2.23E-05
32	Mod 2 75-85	80	88	0	2.8	30067	4834	161	7	613	0.708531	5.34E-06
33	Mod 2 85-95	90	88	0	3.1	29090	4580	145	8	826	0.708616	1.44E-05
34	Mod 2 95-105	100	88	0	3.4	35840	10912	132	10	1064	0.708722	1.18E-05
35	Mod 2 105-110	107.5	88	0	1.0	40742	13506	140	10	1082	0.709042	1.33E-05

Table S.10.1: (continued)

Nb	Sample ID	Sample depth	ALD	WTD	TOC	Fe Total	Fe DCB	Sr Total	Sr DCB	Ca Pyro	$^{87}Sr/^{86}Sr$ Mean	$^{87}Sr/^{86}Sr$ SD
		cm	cm	cm	wt%			mg kg^{-1}			-	-
36	Mod 3 0-5	2.5	75	16	47	4651	2038	21	8	2781	0.709927	1.35E-05
37	Mod 3 5-10	7.5	75	16	46	6017	3663	29	19	2662	0.709537	1.44E-05
38	Mod 3 10-15	12.5	75	16	45	19681	16755	33	27	2774	0.709512	2.11E-05
39	Mod 3 15-20	17.5	75	16	36	62955	74979	45	25	2182	0.709327	1.39E-05
40	Mod 3 20-25	22.5	75	16	3.6	35979	14789	128	9	856	0.708597	6.36E-06
41	Mod 3 25-30	27.5	75	16	2.2	29125	7314	130	9	829	0.708474	5.44E-06
42	Mod 3 30-35	32.5	75	16	2.3	31749	8301	128	8	788	0.708541	1.73E-05
43	Mod 3 35-65	50	75	16	3.9	33347	10887	129	9	884	0.708560	5.24E-06
44	Mod 3 65-75	70	75	16	6.2	41997	16580	134	16	1686	0.708501	4.06E-06
45	Mod 3 75-85	80	75	16	3.3	34661	10359	138	12	1221	0.708608	1.18E-05
46	Mod 3 85-95	90	75	16	1.4	34467	11217	138	11	1173	0.708779	1.18E-05
47	Mod 3 95-105	100	75	16	1.7	36589	11289	140	12	1385	0.708845	4.22E-06
48	Mod 3 105-115	110	75	16	1.6	35267	9903	152	13	1430	0.709042	5.18E-06
49	Mod 3 115-120	117.5	75	16	0.75	34661	9137	158	12	1424	0.709209	1.03E-05
50	Ext 1 0-5	2.5	48	22	48	3169	1671	12	5	2660	0.709967	5.16E-06
51	Ext1 5-10	7.5	48	22	49	3138	1444	15	6	2098	0.710024	9.09E-06
52	Ext1 10-15	12.5	48	22	49	3376	1719	20	12	1967	0.709830	3.22E-06
53	Ext1 15-20	17.5	48	22	47	9413	7945	36	22	2525	0.709495	2.76E-06
54	Ext 1 20-25	22.5	48	22	42	14307	14690	42	21	2281	0.709486	1.17E-06
55	Ext 1 25-30	27.5	48	22	41	18970	18199	43	15	1593	0.709064	1.16E-05
56	Ext 1 30-35	32.5	48	22	42	20755	25872	37	16	1687	0.709167	8.69E-06
57	Ext 1 35-40	37.5	48	22	29	16501	18348	71	11	1223	0.709105	6.52E-06
58	Ext 1 40-48	44	48	22	4.8	37093	11773	138	9	856	0.708872	1.12E-05
59	Ext 1 48-55	51.5	48	22	4.7	44020	16117	144	12	1315	0.709010	1.47E-05
60	Ext 1 55-65	60	48	22	5.4	44304	17577	140	14	1479	0.709135	1.25E-05
61	Ext 3 0-5	2.5	65	29	49	3291	1018	11	5	2908	0.709576	1.54E-06
62	Ext 3 5-10	7.5	65	29	48	3072	1078	12	5	2161	0.709617	1.52E-05
63	Ext 3 10-15	12.5	65	29	48	4017	1767	20	10	1791	0.710045	6.39E-06
64	Ext 3 15-20	17.5	65	29	46	4798	3618	30	18	2169	0.709663	1.28E-05
65	Ext 3 20-25	22.5	65	29	40	18418	20844	42	19	1899	0.709594	1.52E-05
66	Ext 3 25-30	27.5	65	29	21	23657	27411	83	11	1076	0.709039	1.05E-05
67	Ext 3 30-35	32.5	65	29	6.3	37579	13887	137	6	522	0.708871	3.54E-06
68	Ext 3 35-40	37.5	65	29	5.6	28941	8272	127	4	369	0.708803	7.07E-06
69	Ext 3 40-65	52.5	65	29	8.4	44955	21013	112	6	619	0.709062	1.02E-05
70	Ext 3 65-75	70	65	29	15	26599	11111	95	14	1588	0.708871	8.93E-06
71	Ext 3 75-85	80	65	29	6.5	29702	9299	127	11	1271	0.709026	5.57E-06
72	Ext 3 85-90	87.5	65	29	1.1	27798	7442	129	6	640	0.709276	7.31E-06

Table S.10.1: (continued)

Nb	Sample ID	Sample height	ALD	WTD	TOC	Fe Total	Fe DCB	Sr Total	Sr DCB	Ca Pyro	$^{87}Sr/^{86}Sr$ Mean	$^{87}Sr/^{86}Sr$ SD
		m	cm	cm	wt%			mg kg^{-1}			-	-
73	DY-01-A-02	43.3	nd	nd	1.3	32305	11580	165	12	nd	0.709246	1.42E-05
74	DY-01-B-06	41.25	nd	nd	0.92	34165	10211	175	16	nd	0.709209	8.58E-06
75	DY-01-B-10	39.25	nd	nd	1.4	36793	10955	169	16	nd	0.708983	1.22E-05
76	DY-01-B-14	37.25	nd	nd	1.3	36486	10674	163	17	nd	0.709168	3.82E-06
77	DY-01-C-18	36	nd	nd	0.74	34327	10215	176	21	nd	0.709280	8.18E-06
78	DY-01-D-22	34.3	nd	nd	1.4	37560	11078	166	21	nd	0.709375	1.13E-05
79	DY-01-D-26	32.5	nd	nd	1.6	36394	11482	153	15	nd	0.709036	1.40E-05
80	DY-01-E-30	31	nd	nd	1.5	35222	9801	172	18	nd	0.709199	1.63E-05
81	DY-01-F-34	29.1	nd	nd	11	35200	10700	150	39	nd	0.709686	2.78E-05
82	DY-01-F-38	27.5	nd	nd	1.4	36559	10103	164	15	nd	0.708947	3.71E-05
83	DY-01-G-42	26.3	nd	nd	1.3	35978	10773	163	17	nd	0.709026	2.04E-05
84	DY-01-H-46	25	nd	nd	0.64	31732	9006	180	17	nd	0.708949	9.27E-06
85	DY-02-A-01	5	nd	nd	16	37325	11951	109	25	nd	0.709447	1.98E-05
86	DY-02-A-02	4.6	nd	nd	18	48092	19585	103	25	nd	0.709546	2.28E-05
87	DY-02-A-03	4.2	nd	nd	4.4	55415	22583	134	12	nd	0.708988	2.21E-05
88	DY-02-A-04	4	nd	nd	3.6	111049	52801	124	13	nd	0.709072	2.72E-05
89	DY-02-A-05	3.7	nd	nd	1.4	49045	21613	148	13	nd	0.709251	9.26E-06
90	DY-02-A-06	3.4	nd	nd	1.4	58055	22429	142	12	nd	0.708834	3.39E-05
91	DY-02-A-07	3.1	nd	nd	1.4	34938	9171	166	10	nd	0.708826	1.14E-05
92	DY-02-A-08	2.8	nd	nd	1.0	34826	10849	169	12	nd	0.708977	4.22E-05
93	DY-02-A-09	2.5	nd	nd	1.4	33505	9073	174	13	nd	0.709014	4.41E-05
94	DY-02-A-10	2.1	nd	nd	0.42	31674	7998	180	10	nd	0.709036	1.46E-05
95	DY-04-A-02	7.7	nd	nd	13	65868	31482	113	13	nd	0.708834	3.58E-05
96	DY-04-A-03	7.5	nd	nd	13	50763	21247	125	16	nd	0.709146	6.41E-06
97	DY-04-A-04	7.2	nd	nd	4.4	87415	43612	111	10	nd	0.709010	1.34E-05
98	DY-04-A-05	6.9	nd	nd	3.7	81267	36510	120	10	nd	0.708895	4.07E-06
99	DY-04-A-06	6.5	nd	nd	2.4	53936	21653	141	9	nd	0.708902	1.87E-05
100	DY-04-A-07	6.1	nd	nd	6.9	71412	42398	126	17	nd	0.709005	1.02E-05
101	DY-04-A-08	5.7	nd	nd	2.1	37106	14236	161	10	nd	0.708956	8.40E-06
102	DY-04-A-09	5.3	nd	nd	1.0	37542	10683	164	9	nd	0.708929	1.93E-05
103	DY-04-A-10	5	nd	nd	3.0	41698	16982	155	13	nd	0.709125	2.18E-05
104	DY-04-A-11	4.7	nd	nd	1.9	44248	10946	142	15	nd	0.709115	1.58E-05
105	DY-04-A-12	4.4	nd	nd	1.9	34484	8486	171	11	nd	0.708956	1.41E-05
106	DY-05-A-02	1.8	nd	nd	0.77	32046	8417	179	11	nd	0.708992	2.65E-05
107	DY-05-B-06	3.2	nd	nd	1.3	32235	7757	189	10	nd	0.709074	4.25E-05
108	DY-05-B-10	5	nd	nd	1.5	34680	9586	167	11	nd	0.708992	1.57E-05
109	DY-05-C-14	6.6	nd	nd	1.7	34274	8945	166	10	nd	0.709110	3.53E-05
110	DY-05-C-15	6.8	nd	nd	8.4	34261	9928	151	24	nd	0.709154	4.51E-05
111	DY-05-D-18	10	nd	nd	1.5	36824	9613	159	11	nd	0.708971	3.94E-05
112	DY-05-E-22	11.3	nd	nd	0.8	31500	8969	182	12	nd	0.708859	2.08E-06
113	DY-05-E-26	13.3	nd	nd	0.68	31025	8688	181	15	nd	0.708960	3.00E-05
114	DY-05-F-30	16	nd	nd	1.0	34055	8967	190	17	nd	0.708751	1.53E-05
115	DY-05-F-34	18	nd	nd	0.69	32733	8612	178	14	nd	0.708947	4.05E-06
116	DY-05-F-38	20	nd	nd	1.2	34401	9230	172	15	nd	0.708988	1.99E-06
117	DY-05-G-42	22	nd	nd	1.5	34362	9386	176	28	nd	0.709077	6.34E-06
118	DY-05-H-46	24	nd	nd	1.1	34554	9307	169	12	nd	0.708869	1.09E-05